



Room 14-0551
77 Massachusetts Avenue
Cambridge, MA 02139
Ph: 617.253.5668 Fax: 617.253.1690
Email: docs@mit.edu
<http://libraries.mit.edu/docs>

DISCLAIMER OF QUALITY

Due to the condition of the original material, there are unavoidable flaws in this reproduction. We have made every effort possible to provide you with the best copy available. If you are dissatisfied with this product and find it unusable, please contact Document Services as soon as possible.

Thank you.

Some pages in the original document contain color pictures or graphics that will not scan or reproduce well.

**Use of Sterically Hindered Carboxylate Ligands to Model
Structural and Functional Features of
Dioxygen-Activating Centers in Non-Heme Diiron Enzymes**

by

Dongwhan Lee

B.S., Chemistry, Seoul National University, Seoul, Korea (1993)

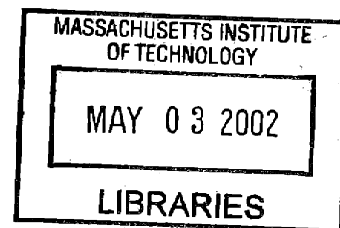
M.S., Chemistry, Seoul National University, Seoul, Korea (1996)

SUBMITTED TO THE DEPARTMENT OF CHEMISTRY IN PARTIAL
FULFILLMENT OF THE REQUIREMENT FOR THE DEGREE OF

DOCTOR OF PHILOSOPHY IN CHEMISTRY
AT THE
MASSCHUSETTS INSTITUTE OF TECHNOLOGY

February 2002

© 2002 Massachusetts Institute of Technology
All rights reserved



V.1

Signature of Author: _____

Department of Chemistry
September 17, 2001

Certified by: _____

Stephen J. Lippard
Thesis Supervisor

Accepted by: _____

Robert W. Field
Chairman, Departmental Committee on Graduate Studies

This doctoral thesis has been examined by a Committee of the Department of Chemistry as follows:

Daniel G. Nocera
Professor of Chemistry
Committee Chairman

Stephen J. Lippard
Arthur Amos Noyes Chair and Professor of Chemistry
Thesis Supervisor

Alan Davison
Professor of Chemistry

Use of Sterically Hindered Carboxylate Ligands to Model Structural and Functional Features of Dioxygen-Activating Centers in Non-Heme Diiron Enzymes

by

Dongwhan Lee

Submitted to the Department of Chemistry on September 17, 2001, in partial fulfillment of the requirements for the Degree of Doctor of Philosophy

Abstract

Chapter I. Modeling Dioxygen-Activating Centers in Non-Heme Diiron Enzymes: Carboxylate Shifts in Diiron(II) Complexes Supported by Sterically Hindered Carboxylate Ligands

General synthetic routes are described for a series of diiron(II) complexes supported by sterically demanding carboxylate ligands 2,6-di(*p*-tolyl)benzoate ($\text{Ar}^{\text{Tol}}\text{CO}_2^-$) and 2,6-di(4-fluorophenyl)benzoate ($\text{Ar}^{4\text{-FPH}}\text{CO}_2^-$). The interlocking nature of the *m*-terphenyl units in self-assembled $[\text{Fe}_2(\mu\text{-O}_2\text{CAr}^{\text{Tol}})_2(\text{O}_2\text{CAr}^{\text{Tol}})_2\text{L}_2]$ ($\text{L} = \text{C}_5\text{H}_5\text{N}$ (**4**); 1-MeIm (**5**)) promotes the formation of coordination geometries analogous to those of the non-heme diiron cores in the enzymes RNR-R2 and $\Delta 9\text{D}$. Magnetic susceptibility and Mössbauer studies of **4** and **5** revealed properties consistent with weak antiferromagnetic coupling between the high-spin iron(II) centers. Structural studies of several derivatives obtained by ligand substitution reactions demonstrated that the $[\text{Fe}_2(\text{O}_2\text{CAr}')_2\text{L}_2]$ ($\text{Ar}' = \text{Ar}^{\text{Tol}}, \text{Ar}^{4\text{-FPH}}$) module is geometrically quite flexible. Details of the core rearrangement within the tetracarboxylate diiron framework, facilitated by carboxylate shifts, were probed by solution VT ^{19}F -NMR spectroscopic studies of $[\text{Fe}_2(\mu\text{-O}_2\text{CAr}^{4\text{-FPH}})_2(\text{O}_2\text{CAr}^{4\text{-FPH}})_2(\text{THF})_2]$ (**8**) and $[\text{Fe}_2(\mu\text{-O}_2\text{CAr}^{4\text{-FPH}})_4(4\text{-}^t\text{BuC}_5\text{H}_4\text{N})_2]$ (**12**). The dynamic motion in the primary coordination sphere controls the positioning of open sites and regulates the access of exogenous ligands, processes that also occur at the catalytic sites of non-heme diiron enzymes.

Chapter II. Structural Flexibility within a Sterically Hindered Ligand Platform: Mononuclear Iron(II) Carboxylate Complexes as Subsite Models for Diiron(II) Centers

The synthesis and characterization of a series of mononuclear iron(II) carboxylate complexes are described. By using sterically hindered carboxylate ligands, 2,6-di(*p*-tolyl)benzoate ($\text{Ar}^{\text{Tol}}\text{CO}_2^-$) and 2,6-di(4-*tert*-butylphenyl)benzoate ($\text{Ar}^{4\text{-}^t\text{BuPh}}\text{CO}_2^-$), a series of four-, five-, and six-coordinate iron(II) complexes were synthesized. The compounds are $[\text{Fe}(\text{O}_2\text{CAr}^{\text{Tol}})_2(1\text{-BnIm})_2]$ (**3**), $[\text{Fe}(\text{O}_2\text{CAr}^{\text{Tol}})_2(1\text{-MeBzIm})_2]$ (**4**), $[\text{Fe}(\text{O}_2\text{CAr}^{4\text{-}^t\text{BuPh}})_2(2,2'\text{-bipy})_2]$ (**5**), $[\text{Fe}(\text{O}_2\text{CAr}^{\text{Tol}})_2(\text{TMEDA})]$ (**6**), and $[\text{Fe}(\text{O}_2\text{CAr}^{\text{Tol}})_2(\text{BPTA})]$ (**7**). Structural analyses of **3–7** revealed that the overall stereochemistry of the

[Fe(O₂CAr')₂L_n] units is dictated by electronic and steric factors of the N-donor ligands (L), as well as by the flexible coordination of the carboxylate ligands. Distinctive Mössbauer parameters obtained for these and related compounds facilitated the spectral assignment of a diiron(II) complex having asymmetric metal sites, [Fe₂(μ-O₂CAr^{Tol})₃(O₂CAr^{Tol})(2,6-lutidine)] (**2**). Well-defined mononuclear iron carboxylate complexes thus may serve as subsite models for higher nuclearity species in both synthetic and biological systems.

Chapter III. Functional Mimic of Dioxygen-Activating Centers in Non-Heme Diiron Enzymes: Mechanistic Implications of Paramagnetic Intermediates in the Reactions between Diiron(II) Complexes and Dioxygen

Tetracarboxylate diiron(II) complexes, [Fe₂(μ-O₂CAr^{Tol})₂(O₂CAr^{Tol})₂(C₅H₅N)₂] (**1a**) and [Fe₂(μ-O₂CAr^{Tol})₄(4-^tBuC₅H₄N)₂] (**2a**), where Ar^{Tol}CO₂⁻ = 2,6-di(*p*-tolyl)benzoate, react with O₂ in CH₂Cl₂ at -78 °C to afford deep green intermediates **1b** (λ_{max} ≅ 660 nm; ε = 1600 M⁻¹cm⁻¹) and **2b** (λ_{max} ≅ 670 nm; ε = 1700 M⁻¹cm⁻¹), respectively. Upon warming to room temperature, the solutions turn yellow, ultimately converting to isolable diiron(III) compounds [Fe₂(μ-OH)₂(μ-O₂CAr^{Tol})₂(O₂CAr^{Tol})₂(C₅H₅N)₂] (**1c**) and [Fe₂(μ-OH)₂(μ-O₂CAr^{Tol})₂(O₂CAr^{Tol})₂(4-^tBuC₅H₄N)₂] (**2c**). EPR and Mössbauer spectroscopic studies revealed the presence of equimolar amounts of valence-delocalized Fe₂(II,III) and valence-trapped Fe(III)Fe(IV) species as major components of solution **2b**. The spectroscopic and reactivity properties of the Fe(III)Fe(IV) component are similar to those of the intermediate X in the RNR-R2 catalytic cycle. EPR kinetic studies revealed that the processes leading to the formation two distinctive paramagnetic components in **2b** are coupled to one another. A mechanism for this reaction is proposed and compared with those of other synthetic and biological systems, in which electron transfer occurs from a low-valent starting material to putative high-valent dioxygen-adduct(s).

Chapter IV. Structural and Spectroscopic Studies of Valence-Delocalized Diiron(II,III) Complexes Supported by Carboxylate-Only Bridging Ligands

The synthesis, molecular structures, and spectroscopic properties of a series of valence-delocalized diiron(II,III) complexes are described. Chemical oxidation of diiron(II) tetracarboxylate complexes afforded the compounds [Fe₂(μ-O₂CAr^{Tol})₄L₂]X, where L = 4-^tBuC₅H₄N (**1b**), C₅H₅N (**2b**), and THF (**3b**); X = PF₆⁻ (**1b** and **3b**) and OTf⁻ (**2b**). In **1b–3b**, four μ-1,3 carboxylate ligands span relatively short Fe...Fe distances of 2.6633(11) – 2.713(3) Å. The ground state ferromagnetism of these compounds was characterized by magnetic susceptibility data (μ_{eff} = 10.5 – 11.0 μ_B at 300 K). Mössbauer and XAS experiments disclosed the valence-delocalized nature of **1b–3b**. The electron delocalization between paramagnetic centers is described by double exchange, which, for the first time, is observed in diiron clusters having no single-atom bridging ligand(s). In the absence of efficient ligand-mediated coupling pathways, double exchange in **1b–3b** is apparently facilitated by the direct through-space interaction between the metal centers.

Chapter V. Spectroscopic Studies of a Putative O₂-Adduct of a Carboxylate-Bridged Diiron Complex: Effects of Nitrogen-Rich Coordination in Dioxygen Activation

The synthesis, molecular structures, and dioxygen reactivity studies of di(μ -carboxylato)diiron(II) complexes are described. The compounds $[(\text{Me}_3\text{TACN})_2\text{Fe}_2(\mu\text{-O}_2\text{CAr}^{\text{Tol}})_2\text{L}_2](\text{OTf})_2$ ($\text{L} = \text{MeCN}$ (**1a**); H_2O (**2a**)), where $\text{Ar}^{\text{Tol}}\text{CO}_2^- = 2,6\text{-di}(p\text{-tolyl})\text{benzoate}$ and $\text{Me}_3\text{TACN} = 1,4,7\text{-trimethyl-}1,4,7\text{-triazacyclononane}$, were synthesized. Structural analyses of **1a** and **2a** revealed relatively long Fe...Fe distances of 4.6787(15) – 4.7127(13) Å spanned by two μ -1,3 bridging carboxylate ligands. Oxygenation of **1a** in THF at -78 °C afforded a dark blue-green intermediate **1b** with a broad absorption band centered at 640 nm ($\epsilon \approx 2000 \text{ M}^{-1}\text{cm}^{-1}$). The EPR and Mössbauer properties of **1b** is consistent with the presence of a (peroxo)diiron(III) core. A relatively short metal...metal distance of 3.09 Å was assigned for a model of **1b** derived from EXAFS spectroscopy. At -78 °C, **1b** gradually decays ($t_{1/2} \cong 20$ min) to afford **1c** displaying optical bands at 483 nm, 525 nm, and 750 nm. The UV-vis, Mössbauer, and EXAFS studies indicate the presence of a bent (μ -oxo)diiron(III) core in **1c**. The distinctive reactivity pattern of **1a** is compared with that of related neutral diiron(II) compounds. Biological implications of such structure–function correlation are discussed, in the context of dioxygen activation by non-heme diiron centers.

Chapter VI. Biomimetic Access to the Elusive $\{\text{Fe}_2(\mu\text{-OH})_2(\mu\text{-O}_2\text{CR})\}^{3+}$ Core of Soluble Methane Monooxygenase Hydroxylase: Synthesis, Characterization, and Dioxygen Reactivity Studies of Carboxylate-Bridged Diiron(II) Complexes Supported by Bidentate Amine Ligands

Synthesis and reactivity studies of diiron(II) tetracarboxylate complexes are described. Oxidizable C–H bonds were integrated as part of the diamine ligands bound to carboxylate-bridged diiron(II) centers. One such compound, $[\text{Fe}_2(\mu\text{-O}_2\text{CAr}^{\text{Tol}})_2(\text{O}_2\text{CAr}^{\text{Tol}})_2(\text{N},\text{N}\text{-Bn}_2\text{en})_2]$ (**6**), reacts with dioxygen to afford the diiron(III) complex $[\text{Fe}_2(\mu\text{-OH})_2(\mu\text{-O}_2\text{CAr}^{\text{Tol}})(\text{O}_2\text{CAr}^{\text{Tol}})_3(\text{N},\text{N}\text{-Bn}_2\text{en})(\text{N}\text{-Bnen})]$ (**8**). This process closely parallels the activation of dioxygen by non-heme diiron enzymes and afforded the first diiron(III) complex having the $\{\text{Fe}_2(\mu\text{-OH})_2(\mu\text{-O}_2\text{CR})\}^{3+}$ core structure of MMOH_{ox} . A reaction model is provided and compared with mechanistic frameworks previously developed for related cP450 or copper(I) dioxygen chemistry

Chapter VII. Hydroxo-Bridged Cubane-Type Tetrairon(II) Clusters Supported by Sterically-Hindered Carboxylate Ligands

A series of hydroxo-bridged cubane-type tetrairon(II) clusters, $[\text{Fe}_4(\mu\text{-OH})_4(\mu\text{-O}_2\text{CAr}^{4\text{-tBuPh}})_2(\mu\text{-OTf})_2\text{L}_4]$ ($\text{L} = \text{C}_5\text{H}_5\text{N}$ (**1**); $4\text{-}^t\text{BuC}_5\text{H}_4\text{N}$ (**2**); $3\text{-FC}_5\text{H}_4\text{N}$ (**3**)), were synthesized by using a sterically hindered carboxylate ligand 2,6-di(4-*tert*-butylphenyl)benzoate ($\text{Ar}^{4\text{-tBuPh}}\text{CO}_2^-$). Three different bridging units that mediate weak antiferromagnetic coupling interactions between the metal centers support the unprecedented cubane-type $[\text{Fe}_4(\mu\text{-OH})_4]^{4+}$ cores in **1–3**. The solution structures of **1** and **3** probed by FT-IR and ^{19}F -NMR spectroscopy are consistent with the solid state geometry deter-

mined by X-ray crystallography. Zero-field Mössbauer spectra of **1–3** at 4.2 K are characteristic of high-spin iron(II) centers in nearly identical coordination environments. Compound **1** undergoes two irreversible oxidation processes at ca -10 mV and $+880$ mV (vs Fc/Fc⁺), the former approaching quasi-reversible behavior with increased scan rates and a narrow potential sweep range. Comparisons are made with analogous known $\{\text{Fe}_4\text{X}_4\}^{n+}$ (X = O, S) units, and the structural integrity of tetrairon fragments upon change in oxidation state is discussed together with some possible biological implications.

Chapter VIII. Sterically Hindered Carboxylate Ligands Support Water-Bridged Dimetallic Centers That Model Features of Metallohydrolase Active Sites

The synthesis and characterization of carboxylate-bridged dimetallic complexes are described. By using *m*-terphenyl-derived carboxylate ligands, a series of dicobalt(II), dicobalt(III), dinickel(II), and dizinc(II) complexes were synthesized. The compounds are $[\text{Co}_2(\mu\text{-O}_2\text{CAr}^{\text{Tol}})_2(\text{O}_2\text{CAr}^{\text{Tol}})_2\text{L}_2]$ (**1**), $[\text{Co}_2(\mu\text{-OH}_2)_2(\mu\text{-O}_2\text{CAr}^{\text{Tol}})_2(\text{O}_2\text{CAr}^{\text{Tol}})_2\text{L}_2]$ (**2a–c**), $[\text{Co}_2(\mu\text{-OH})_2(\mu\text{-O}_2\text{CAr}^{\text{Tol}})_2(\text{O}_2\text{CAr}^{\text{Tol}})_2\text{L}_2]$ (**3**), $[\text{Ni}_2(\mu\text{-O}_2\text{CAr}^{\text{Tol}})_4\text{L}_2]$ (**4**), $[\text{Ni}_2(\mu\text{-HO}\cdots\text{H})_2(\mu\text{-O}_2\text{CAr}^{\text{Tol}})_2(\text{O}_2\text{CAr}^{\text{Tol}})_2\text{L}_2]$ (**5**), and $[\text{Zn}_2(\mu\text{-O}_2\text{CAr}^{\text{Tol}})_2(\text{O}_2\text{CAr}^{\text{Tol}})_2\text{L}_2]$ (**6**), where $\text{Ar}^{\text{Tol}}\text{CO}_2\text{H} = 2,6\text{-di}(p\text{-tolyl})\text{benzoic acid}$ and L = pyridine, THF, or *N,N*-dibenzylethylenediamine. Structural analysis of these complexes revealed that additional bridging ligands can be readily accommodated within the $\{\text{M}_2(\mu\text{-O}_2\text{CAr}^{\text{Tol}})_2\}^{2+}$ core, allowing a wide distribution of M \cdots M distances from 2.5745(6) Å to 4.0169(9) Å. Unprecedented bridging units $\{\text{M}_2(\mu\text{-OH}_2)_2(\mu\text{-O}_2\text{CR})_2\}^{n+}$ and $\{\text{M}_2(\mu\text{-HO}\cdots\text{H})_2(\mu\text{-O}_2\text{CR})_2\}^{n+}$ were identified in **2a** and **5**, respectively, in which strong hydrogen bonding accommodates shifts of protons from bridging water molecules toward the dangling oxygen atoms of terminal monodentate carboxylate groups. Such a proton shift along the O \cdots H \cdots O coordinate attenuates the donor ability of the anionic carboxylate ligand, which can translate into increased Lewis acidity at the metal centers. Such double activation of bridging water molecules by a Lewis acidic metal center and a metal-bound general base may facilitate the reactivity of metallohydrolases such as methionine aminopeptidase (MAP).

Thesis Supervisor: Stephen J. Lippard

Title: Arthur Amos Noyes Professor of Chemistry

To my wife, Mina

Acknowledgments

For more than four months since I moved out of Rm 18-506 to settle in another room at the other end of the floor, I've been waiting for this moment. Now I can sit down a little bit relaxed, looking back over the five years I spent at MIT, as I am about to start this part of my thesis. Like so many other things in life, once you reach the point you've been waiting for with such great expectation, all of a sudden, it looks so different from what you've been dreaming of, be it good or bad.

Looking at these eight chapters as a proof of my exploration into the small uncharted waters left behind by those who went ahead of me, I would first like to thank my thesis advisor, Steve Lippard, for guiding me throughout the past five years. With his unparalleled enthusiasm about science and deep insights into seemingly unconnected phenomena, Steve helped to shape the way I look at chemistry. Sometimes I wonder what convinced Steve to take this clueless Korean guy who could barely express himself in the fall of 1996. The five years I spent under the guidance of Steve has been a valuable period for my intellectual growth as a chemist and I really appreciate his patience and understanding during that time.

I truly believe that it takes more than one Ph.D. to make another Ph.D. I cannot recall my life on the fifth floor of Bldg 18 without thanking all the great people I was lucky to work with. Dr. Tadashi Jack Mizoguchi was my first baymate when I was in Rm 18-527 during the winter of 1997, making hundreds of grams of tosylated amines. He dragged me into the group responsibility of Mössbauer spectroscopy, without bothering to tell me that it predominantly involved delivering frozen samples to Northeastern University. Thanks to the unpredictable schedule of MBTA buses, we often had to take an hour walk all the way to Prof. Reiff's lab, carrying liquid nitrogen dewars in our hands. Jack was patient enough to answer all my stupid questions during our excursions across the Harvard Bridge. I really thank him for teaching me a lot of spectroscopy, not to mention all the good skills for handling thermally sensitive samples. He was indeed like a big brother to me. Drs. Xiao-Xiang Zhang and Maria Bautista are thanked for watching over me while I was learning glovebox techniques. Dr. Justin Du Bois joined the group in the spring of 1997, kicking me out of Rm 18-527. We later landed at Rm 18-506 and shared the same hood for two years, working on some of the diiron projects together. He was one the most passionate and hardworking chemists I have ever seen in my life, and brought an incredible amount of intellectual stimulation to our synthetic bay. Our brief conversations after department seminars often lead to lengthy discussions, which undoubtedly helped to nurture a young graduate student. I really thank Justin for teaching me organic chemistry as well as critical ways of thinking. It is quite gratifying to see the growing publication list of this Stanford assistant professor these days. Dr. Dirk Burdinski became my new (and last) baymate after Justin left. Although I am not really sure whether Dirk liked the idea of sharing the hood and most of the glassware with such a sloppy person like me, I learned a lot from this well-organized German chemist. I have to say that I was never able to convince him with any of my argument (not even once!) but I always knew he was right. Dr. Josh Farrell joined our construction team in 1999 with his ample experience in synthetic inorganic chemistry. He was a responsible and careful chemist and I really thank him for helping me with so

many things during various stages of my thesis work. He took much trouble to keep the dry-boxes in good shape and spared his valuable time to look over my poorly written manuscripts.

My graduate career overlaps with three generations of talented X-ray postdocs, who taught me this amazing methodology that I knew nothing about when I first joined the group. Dr. Peter Fuhrmann solved the structure of my first crystal (tetrabutylammonium hexafluorophosphate) and decided afterwards to train me to pick and mount more interesting crystals by myself. I thank him for all his efforts to make a "part-time crystallographer" out of me and for not yelling at me when I asked him to bike all the way to MIT at midnight to fix the goniometer and the compound turned out to be a simple salt the next morning. He had a great personality and kept the X-ray lab a friendly place to work in. Dr. Bernhard Spingler was the tallest person I ever made friends with in my life. He had a good balance between chemistry and crystallography and helped me a lot with twinned crystals. I thank Dr. Weiming Bu for keeping the X-ray lab in excellent shape during our transition to the 4th-floor-era and bearing with me when I was really stressed out locating and working up old X-ray data files during my write-up.

Former and current Lippardians were a great collection of outstanding chemists, who I am greatly indebted to. Dietrich Steinhuebel impressed me with his profound knowledge of organometallic chemistry, as well as his dedication to science. I still haven't figured out how a person can live on a piece of bread and a few carrots and continue such an endless lab work. I thank him for many helpful comments and well-intended criticisms. I was lucky to have Chuan He as a solid labmate as well as a good friend. He was always willing to share his unlimited knowledge of "everything" and cheered me up in the dark days of my science. Kathy Franz taught me SQUID, EPR, and electrochemistry. Amy Barrios and Joey Bautista made frequent trips to the Spec Lab to run resonance Raman spectra for me. Ann Valentine helped me with stopped-flow kinetic experiments. Jane Kuzelka shared the small drybox with me during the last two and half years and became a logical successor to our Mössbauer business, which culminated in installing our own machine in the basement of Bldg 18 in 1999. I was very lucky to have this very understanding and devoted chemist working next to me, as a good consultant to talk about science, as well as so many other things. Although our projects did not overlap much with one another, it was nice to have good synthetic chemists like Shawn Burdette and Scott Hilderbrand around the lab to ask for help. Pei-Lin Hung worked as a UROP student for me and made some of the wonderful compounds described in the last chapter of this thesis. I wish her the best in her graduate studies at Stanford. Drs. Sudhakar Marla and Chris Ziegler were excellent resources for heme chemistry in this non-heme group and Dr. Natasha Kaminskaia's profound knowledge of chemical kinetics was something I always envied. Drs. Seth Cohen, Ariel Haskel, Jens Müller were there to keep me up and running during this exhausting period of thesis writing. Although I have to admit that five years' group meetings pathetically failed to teach me biology, people in the MMO subgroup continuously provided thoughtful insights, from which I tremendously benefited. I thank Drs. George Gassner, Shannon Stahl, Maarten Merckx, as well as Douglas Whittington and Daniel Kopp for that. I also wish good luck to Sungho Yoon, Emily Carrig, and Dr. Edit Tshuva, who took over the better part of the diiron projects that I was not able to complete. I am waiting to see their smiling faces with Steve in a future issue of C&EN News on cracking the secret codes of biological C-H activation.

With the finding of the “green monster” (as Justin used to call it) described in the Chapter 3 of this thesis, my research moved into a new phase. Collaborations made with gurus in Mössbauer, EPR and XAS incredibly enriched my chemistry. I thank Prof. Vincent Huynh and Dr. Carsten Krebs at Emory, Prof. Michael P. Hendrich and Brad Pierce at Carnegie Mellon, Profs. Britt Hedman, Keith O. Hodgson and their talented grad student Jennifer DuBois at Stanford, for their tremendous contribution. Drs. Jeffrey Simpson and Mark Wall in DCIF at MIT helped me a lot with Mössbauer and VT NMR experiments. Prof. William Reiff and Dr. Christopher Frommen at Northeastern University are also acknowledged for allowing me to use their instruments and teaching me the underlying physics of Mössbauer spectroscopy. Dr. Mookie (Mu-Hyun) Baik at Columbia and Dr. Jorge Rodriguez at Berkeley independently worked on the DFT part of the diiron chemistry. Dr. Catalina Achim at Harvard was an excellent consultant for Mössbauer spectroscopy and I wish her good luck in her independent academic career at Carnegie Mellon. My four Inorganic classmates, Daniel Mindiola, Yann Schrodi, Jane Brock, and Evan Freiberg, now all doctors, made my early days at MIT more bearable. We were like parachute troops, each landing at small unmapped islands scattered across a vast ocean of chemistry in the summer of 1996. I look forward to seeing how our paths will cross in the days to come, with utmost confidence that we will help one another just as we did during all the cumes and orals we went through together.

I started my graduate work at SNU as an organic chemistry major, fascinated by the elegant reaction mechanisms (almost always) explained by pushing only a pair of electrons. Under the guidance of Profs. Junghun Suh and Myunghyun Paik Suh, however, I came to realize that there’s more excitement where there are more than two electrons to take into account. From there I decided to pursue inorganic chemistry for my Ph.D. Their guidance during and after my SNU days is highly acknowledged. Prof. Kimoon Kim at POSTECH encouraged me to work for Steve and I really thank him for his advice. My parents have always supported my decisions and I cannot thank them enough for their love. They did everything for me, not wanting anything from me. I am proud not because I’m an MIT Ph.D. but because I am the second inorganic chemistry Ph.D. in my family after my father. My special thanks go to my wife, Mina, for all her support and understanding during that time, without which I don’t think I would have been able to finish my degree. With love and wisdom, she shared our journey through the ups and downs of our Cambridge days. This thesis is thus dedicated to her, although she deserves much, much more than this.

Table of Contents

Abstract.....	3
Dedication.....	7
Acknowledgments.....	8
Table of Contents.....	11
List of Tables.....	17
List of Schemes.....	19
List of Figures.....	20
Chapter I. Modeling Dioxygen-Activating Centers in Non-Heme Diiron Enzymes: Carboxylate Shifts in Diiron(II) Complexes Supported by Sterically Hindered Carboxylate Ligands.....	28
Introduction.....	29
Experimental Section.....	32
General Considerations.....	32
Synthetic Procedures.....	33
X-ray Crystallographic Studies.....	38
Physical Measurements.....	39
Results.....	40
Ligand Synthesis and Initial Metallation Attempts.....	40
Preparation and Structural Characterization of Complexes.....	41
Mössbauer Spectroscopy.....	46
Magnetic Susceptibility Studies.....	47
¹⁹ F-NMR Spectroscopic Studies.....	48
Discussion.....	49
Ligand Design.....	49
Synthetic Routes to Diiron(II) Complexes.....	52
Structural Models of Δ^9 D and RNR-R2 Active Sites.....	52
Ligand Substitution and Core Rearrangement.....	56
Doubly- versus Quadruply-Bridged Tetracarboxylate Diiron(II) Complexes.....	58
Structural Rearrangement Probed by VT ¹⁹ F-NMR Spectroscopy.....	59
Flexibility versus Rigidity.....	62
Summary and Conclusion.....	64
Acknowledgment.....	64
References.....	65

Chapter II. Structural Flexibility within a Sterically Hindered Ligand Platform: Mononuclear Iron(II) Carboxylate Complexes as Subsite

Models for Diiron(II) Centers	113
Introduction.....	114
Experimental Section.....	115
General Considerations.....	115
Physical Measurements.....	116
Synthetic Procedures.....	116
X-ray Crystallographic Studies.....	118
Results.....	119
Synthesis and Structural Characterization of Complexes.....	119
Mössbauer Spectroscopy.....	122
Discussion.....	123
Synthesis of Iron(II) Carboxylate Complexes.....	123
Mössbauer Spectroscopy.....	126
Summary and Conclusions.....	127
Acknowledgment.....	128
References.....	129

Chapter III. Functional Mimic of Dioxygen-Activating Centers in Non-Heme Diiron Enzymes: Mechanistic Implications of Paramagnetic Intermediates in the Reactions between Diiron(II) Complexes and

Dioxygen	143
Introduction.....	144
Experimental Section.....	146
General Considerations.....	146
Synthetic Procedures.....	147
X-ray Crystallographic Studies.....	148
Physical Measurements.....	148
Redox Titration.....	152
EPR Kinetics.....	153
Ligand Recovery.....	153
Reactions with Phenol Substrates.....	154
Results.....	155
Reactions of Diiron(II) Complexes with Dioxygen.....	155
Reactions of the Oxygenation Intermediates with External Reagents.....	165
Synthesis, Structural Characterization, and Physical Properties of	

Diiron(III) Complexes.....	166
Discussion.....	169
Spectroscopic Properties of the O ₂ Reaction Intermediates.....	169
Proposed Mechanisms.....	170
Biomimetic Formation of Fe(III)Fe(IV) Species:	
Relevance to RNR-R2.....	177
Comparison with Copper(I) Dioxygen Activation.....	178
Summary and Perspective.....	179
Acknowledgment.....	179
References.....	181
Chapter IV. Structural and Spectroscopic Studies of Valence-Delocalized Diiron(II,III) Complexes Supported by Carboxylate-Only	
Bridging Ligands.....	221
Introduction.....	222
Experimental Section.....	224
General Considerations.....	224
Synthetic Procedures.....	224
X-ray Crystallographic Studies.....	226
Physical Measurements.....	227
Results.....	228
Electrochemistry of Diiron(II) Complexes.....	228
Synthesis and Structural Characterization of Diiron(II,III) Complexes.....	229
Physical Properties.....	230
Mössbauer Spectroscopy.....	231
X-ray Absorption Spectroscopy.....	232
Discussion.....	232
Synthesis, Structures, and Electrochemical Properties of Diiron(II,III) Complexes.....	232
XAS: Valence-Delocalized Photoexcited States.....	234
Valence Delocalization.....	235
Acknowledgment.....	236
References.....	237
Chapter V. Spectroscopic Studies of a Putative O₂-Adduct of a Carboxylate-Bridged Diiron Complex: Effects of Nitrogen-Rich Coordination in Dioxygen Activation.....	262
Introduction.....	263

Experimental Section.....	265
General Considerations.....	265
Synthetic Procedures.....	265
X-ray Crystallographic Studies.....	266
Physical Measurements.....	267
Results.....	271
Synthesis and Structural Characterization of Complexes.....	271
Reactions of Diiron(II) Complexes with Dioxygen.....	272
Discussion.....	277
Structural Properties of Diiron(II) Complexes.....	277
Proposed O ₂ -Activation Mechanism.....	279
Effects of Nitrogen-Rich Coordination on Dioxygen Activation.....	280
Acknowledgment.....	281
References.....	282
Chapter VI. Biomimetic Access to the Elusive {Fe₂(μ-OH)₂(μ-O₂CR)}³⁺	
Core of Soluble Methane Monooxygenase Hydroxylase: Synthesis,	
Characterization, and Dioxygen Reactivity Studies of Carboxylate-Bridged	
Diiron(II) Complexes Supported by Bidentate Amine Ligands.....	312
Introduction.....	313
Experimental Section.....	315
General Considerations.....	315
Physical Measurements.....	316
Synthetic Procedures.....	316
X-ray Crystallographic Studies.....	318
Amine N-Dealkylation Studies.....	319
GC Analyses.....	320
Isotope Labeling Experiments.....	320
Results.....	321
Synthesis and Structural Characterization of Complexes.....	321
Oxidative N-Dealkylation.....	324
Discussion.....	325
Synthetic Routes to Diiron(II) Complexes.....	325
Structural Model of MMOHox.....	326
Mechanism of Oxidative N-Dealkylation.....	328
Summary and Perspective.....	330
Acknowledgment.....	330

References.....	331
Chapter VII. Hydroxo-Bridged Cubane-Type Tetrairon(II) Clusters	
Supported by Sterically-Hindered Carboxylate Ligands.....	361
Introduction.....	362
Experimental Section.....	363
General Considerations.....	363
Physical Measurements.....	364
Synthetic Procedures.....	364
X-ray Crystallographic Studies.....	366
Results.....	368
Synthesis and Structural Characterization of Complexes.....	368
UV/vis and IR Spectroscopy.....	370
¹⁹ F-NMR Spectroscopy.....	371
Mössbauer Spectroscopy.....	371
Magnetochemistry.....	372
Electrochemistry.....	376
Discussion.....	376
Acknowledgment.....	379
References.....	380
Chapter VIII. Sterically Hindered Carboxylate Ligands Support	
Water-Bridged Dimetallic Centers That Model Features of	
Metallohydrolase Active Sites.....	400
Introduction.....	401
Experimental Section.....	402
General Procedures and Methods.....	402
Synthetic Procedures.....	402
X-ray Crystallographic Studies.....	406
Results.....	407
Preparation and Structural Characterization of Complexes.....	407
Discussion.....	412
Structures and Physical Properties.....	412
Proton Shifts in Carboxylate-Bridged Dimetallic Centers.....	415
Biological Relevance: Dicobalt(II) Centers in Methionine Aminopeptidases.....	417
Summary and Conclusions.....	417
Acknowledgment.....	418
References.....	419

Biographical Note..... 443
Curriculum Vitae..... 444

List of Tables

Table 1.1.	Summary of X-ray Crystallographic Data.....	73
Table 1.2.	Selected Bond Lengths and Angles for 1–5 and 8	76
Table 1.3.	Selected Bond Lengths and Angles for 6, 7, and 9–12	77
Table 1.4.	Mössbauer and Magnetic Parameters for $[\text{Fe}_2(\mu\text{-O}_2\text{CAr}^{\text{Tol}})_2\text{-}(\text{O}_2\text{CAr}^{\text{Tol}})_2(\text{THF})_2]$ (2), $[\text{Fe}_2(\mu\text{-O}_2\text{CAr}^{\text{Tol}})_2(\text{O}_2\text{CAr}^{\text{Tol}})_2(\text{C}_5\text{H}_5\text{N})_2]$ (4), $[\text{Fe}_2(\mu\text{-O}_2\text{CAr}^{\text{Tol}})_2(\text{O}_2\text{CAr}^{\text{Tol}})_2(1\text{-MeIm})_2]$ (5), $[\text{Fe}_2(\mu\text{-O}_2\text{CAr}^{\text{Tol}})_4\text{-}(4\text{-}^t\text{BuC}_5\text{H}_4\text{N})_2]$ (7), MMOH, RNR-R2, and $\Delta 9\text{D}$	78
Table 2.1.	Summary of X-ray Crystallographic Data.....	133
Table 2.2.	Selected Bond Lengths and Angles for 3–7	134
Table 2.3.	4.2 K Zero-Field Mössbauer Parameters for $[\text{Fe}_2(\mu\text{-O}_2\text{CAr}^{\text{Tol}})_3\text{-}(\text{O}_2\text{CAr}^{\text{Tol}})(2,6\text{-lutidine})]$ (2), $[\text{Fe}(\mu\text{-O}_2\text{CAr}^{\text{Tol}})_2(1\text{-BnIm})_2]$ (3), $[\text{Fe}(\text{O}_2\text{CAr}^{\text{Tol}})_2(1\text{-MeBzIm})_2]$ (4), $[\text{Fe}(\text{O}_2\text{CAr}^{4\text{-}t\text{BuPh}})_2(2,2'\text{-bipy})]$ (5), $[\text{Fe}(\text{O}_2\text{CAr}^{\text{Tol}})_2(\text{BPTA})]$ (7), and Related Diiron(II) complexes.....	136
Table 3.1.	Summary of X-ray Crystallographic Data.....	189
Table 3.2.	Spectroscopic Properties of Peroxo Diiron(III) Enzyme Intermediates and Their Synthetic Analogs.....	190
Table 3.3.	Mössbauer Parameters of the Fe(III)Fe(IV) Component in 2b and Related Valence-Trapped Fe(III)Fe(IV) Centers Having $S = 1/2$ Ground State.....	191
Table 3.4.	Mössbauer Parameters of the Fe(II)Fe(III) Component in 2b , $[\text{Fe}_2(\mu\text{-O}_2\text{CAr}^{\text{Tol}})_4(4\text{-}^t\text{BuC}_5\text{H}_4\text{N})_2]^+$, and Related Valence-Delocalized Fe(II)Fe(III) centers Having $S = 9/2$ Gound State.....	192
Table 3.5.	Selected Bond Lengths and Angles for 1c and 2c	193
Table 4.1.	Summary of X-ray Crystallographic Data.....	241
Table 4.2.	Selected Bond Lengths and Angles for 2b and 3b	242
Table 4.3.	Summary of Pertinent Structural and Spectroscopic Data for 1b–3b and Related Mixed-Valence $S = 9/2$ Diiron(II,III) Systems.....	243
Table 5.1.	Summary of X-ray Crystallographic Data.....	289
Table 5.2.	Selected Bond Lengths and Angles for 1a and 2a	290
Table 5.3.	Spectroscopic Properties of Peroxo Diiron(III) Enzyme Intermediates and their Synthetic Analogs.....	291
Table 5.4.	4.2 K Zero-field Mössbauer Parameters for $[(\text{Me}_3\text{TACN})_2\text{Fe}_2\text{-}(\mu\text{-O}_2\text{CAr}^{\text{Tol}})_2(\text{MeCN})_2](\text{OTf})_2$ (1a), $[(\text{Me}_3\text{TACN})_2\text{Fe}_2(\mu\text{-O}_2\text{CAr}^{\text{Tol}})_2\text{-}(\text{H}_2\text{O})_2](\text{OTf})_2$ (2a), 1b , 1c , and Related Diiron Clusters.....	292
Table 5.5.	EXAFS Fit Results for 1a , 1b , and 1c	293
Table 6.1.	Summary of X-ray Crystallographic Data.....	338
Table 6.2.	Selected Bond Lengths and Angles for 2 and 5–7	339
Table 6.3.	Selected Bond Lengths and Angles for 8	340
Table 6.4.	Mössbauer Parameters of the Diiron(III) Centers in MMOH _{ox} , 8 , and $[\text{Fe}_2(\mu\text{-OH})_2(\mu\text{-O}_2\text{CAr}^{\text{Tol}})_2(\text{O}_2\text{CAr}^{\text{Tol}})_2(4\text{-}^t\text{BuC}_5\text{H}_4\text{N})_2]$	

	Measured at 4 K.....	341
Table 7.1.	Summary of X-ray Crystallographic Data.....	385
Table 7.2.	Selected Bond Lengths and Angles for 2	386
Table 7.3.	Zero-Field Mössbauer Parameters for 1–3 and Related Tetrairon(II) Clusters.....	387
Table 8.1.	Summary of X-ray Crystallographic Data.....	424
Table 8.2.	Selected Bond Lengths and Angles for 1, 2a, and 3	426
Table 8.3.	Selected Bond Lengths and Angles for 4, 5, and 6	427

List of Schemes

Scheme 1.1.....	79
Scheme 1.2.....	80
Scheme 1.3.....	81
Scheme 1.4.....	82
Scheme 1.5.....	83
Scheme 1.6.....	84
Scheme 2.1.....	137
Scheme 3.1.....	194
Scheme 3.2.....	195
Scheme 3.3.....	196
Scheme 4.1.....	244
Scheme 4.2.....	245
Scheme 5.1.....	294
Scheme 5.2.....	295
Scheme 6.1.....	342
Scheme 6.2.....	343
Scheme 6.3.....	344
Scheme 6.4.....	345
Scheme 6.5.....	346
Scheme 7.1.....	388
Scheme 8.1.....	428
Scheme 8.2.....	429
Scheme 8.3.....	430

List of Figures

Figure 1.1.	Structures of the diiron(II) centers in hemerythrin (Hr), the hydroxylase component of soluble methane monooxygenase (MMOH) from <i>M. capsulatus</i> (Bath), R2 subunit of ribonucleotide reductase (RNR-R2) from <i>Escherichia coli</i> , and stearyl-acyl carrier protein Δ^9 desaturase.....	85
Figure 1.2.	ORTEP diagram of $[\text{Fe}_2(\mu\text{-O}_2\text{CAr}^{\text{Tol}})_2(\text{THF})_2\text{Br}_2]$ (1) with thermal ellipsoids at 50% probability.....	86
Figure 1.3.	ORTEP diagram of $[\text{Fe}_2(\mu\text{-O}_2\text{CAr}^{\text{Tol}})_2(\text{O}_2\text{CAr}^{\text{Tol}})_2(\text{THF})_2]$ (2) with thermal ellipsoids at 50% probability.....	87
Figure 1.4.	ORTEP diagram of $[\text{Fe}_2(\mu\text{-O}_2\text{CAr}^{\text{Tol}})_2(\text{O}_2\text{CAr}^{\text{Tol}})_2(\text{MeCN})_2]$ (3) with thermal ellipsoids at 50% probability.....	88
Figure 1.5.	Solid-state structure of $[\text{Fe}_2(\mu\text{-O}_2\text{CAr}^{\text{Tol}})_2(\text{O}_2\text{CAr}^{\text{Tol}})_2(\text{C}_5\text{H}_5\text{N})_2]$ (4): ORTEP diagram with thermal ellipsoids at 50% probability and space-filling representation.....	89
Figure 1.6.	ORTEP diagram of $[\text{Fe}_2(\mu\text{-O}_2\text{CAr}^{\text{Tol}})_2(\text{O}_2\text{CAr}^{\text{Tol}})_2(1\text{-MeIm})_2]$ (5) with thermal ellipsoids at 50% probability.....	90
Figure 1.7.	ORTEP diagram of $[\text{FeTl}(\mu\text{-O}_2\text{CAr}^{\text{Tol}})_3(\text{C}_5\text{H}_5\text{N})]$ with thermal ellipsoids at 50% probability and a space-filling representation.....	91
Figure 1.8.	ORTEP diagram of $[\text{FeTl}(\mu\text{-O}_2\text{CAr}^{\text{Tol}})_3(1\text{-MeIm})]$ with thermal ellipsoids at 50% probability.....	92
Figure 1.9.	ORTEP diagram of $[\text{Fe}_2(\mu\text{-O}_2\text{CAr}^{\text{Tol}})_3(\text{O}_2\text{CAr}^{\text{Tol}})(2,6\text{-lutidine})]$ (6) with thermal ellipsoids at 50% probability.....	93
Figure 1.10.	ORTEP diagram of $[\text{Fe}_2(\mu\text{-O}_2\text{CAr}^{\text{Tol}})_4(4\text{-}^t\text{BuC}_5\text{H}_4\text{N})_2]$ (7) with thermal ellipsoids at 50% probability.....	94
Figure 1.11.	ORTEP diagram of $[\text{Fe}_2(\mu\text{-O}_2\text{CAr}^{4\text{-FPH}})_2(\text{O}_2\text{CAr}^{4\text{-FPH}})_2(\text{THF})_2]$ (8) with thermal ellipsoids at 50% probability.....	95
Figure 1.12.	ORTEP diagram of $[\text{Fe}_2(\mu\text{-O}_2\text{CAr}^{4\text{-FPH}})_4(\text{THF})_2]$ (9) with thermal ellipsoids at 50% probability.....	96
Figure 1.13.	ORTEP diagram of $[\text{Fe}_2(\mu\text{-O}_2\text{CAr}^{4\text{-FPH}})_4(\text{C}_5\text{H}_5\text{N})_2]$ (10) with thermal ellipsoids at 50% probability.....	97
Figure 1.14.	ORTEP diagram of $[\text{Fe}_2(\mu\text{-O}_2\text{CAr}^{4\text{-FPH}})_4(1\text{-MeIm})_2]$ (11) with thermal ellipsoids at 50% probability.....	98
Figure 1.15.	ORTEP diagram of $[\text{Fe}_2(\mu\text{-O}_2\text{CAr}^{4\text{-FPH}})_4(4\text{-}^t\text{BuC}_5\text{H}_4\text{N})_2]$ (12) with thermal ellipsoids at 50% probability.....	99
Figure 1.16.	Zero-field Mössbauer spectrum recorded at 4.2 K for $[\text{Fe}_2(\mu\text{-O}_2\text{CAr}^{\text{Tol}})_2(\text{O}_2\text{CAr}^{\text{Tol}})_2(\text{C}_5\text{H}_5\text{N})_2]$ (4) in the solid state.....	100
Figure 1.17.	Zero-field Mössbauer spectrum recorded at 4.2 K for $[\text{Fe}_2(\mu\text{-O}_2\text{CAr}^{\text{Tol}})_2(\text{O}_2\text{CAr}^{\text{Tol}})_2(\text{THF})_2]$ (2) (A), $[\text{Fe}_2(\mu\text{-O}_2\text{CAr}^{\text{Tol}})_2(\text{O}_2\text{CAr}^{\text{Tol}})_2(1\text{-MeIm})_2]$ (5) (B), and $[\text{Fe}_2(\mu\text{-O}_2\text{CAr}^{\text{Tol}})_4(4\text{-}^t\text{BuC}_5\text{H}_4\text{N})_2]$ (7) (C) in the solid state.....	101
Figure 1.18.	Plots of effective moment (μ_{eff}) per molecule versus	

	temperature (A) and molar susceptibility (χ_M) versus temperature (B) for $[\text{Fe}_2(\mu\text{-O}_2\text{CAr}^{\text{Tol}})_2(\text{O}_2\text{CAr}^{\text{Tol}})_2(\text{C}_5\text{H}_5\text{N})_2]$ (4).....	102
Figure 1.19.	Plots of effective moment (μ_{eff}) per molecule versus temperature (A) and molar susceptibility (χ_M) versus temperature (B) for $[\text{Fe}_2(\mu\text{-O}_2\text{CAr}^{\text{Tol}})_2(\text{O}_2\text{CAr}^{\text{Tol}})_2(1\text{-MeIm})_2]$ (5).....	103
Figure 1.20.	Plots of effective moment (μ_{eff}) per molecule versus temperature (A) and molar susceptibility (χ_M) versus temperature (B) for $[\text{Fe}_2(\mu\text{-O}_2\text{CAr}^{\text{Tol}})_4(4\text{-}^t\text{BuC}_5\text{H}_4\text{N})_2]$ (7)	104
Figure 1.21.	Variable temperature (+20 – –70 °C) ^{19}F -NMR spectra (vs CFCl_3) of $[\text{Fe}_2(\mu\text{-O}_2\text{CAr}^{4\text{-FPH}})_4(4\text{-}^t\text{BuC}_5\text{H}_4\text{N})_2]$ (12) in CH_2Cl_2 at 470 MHz.....	105
Figure 1.22.	Variable temperature (+20 – –80 °C) ^{19}F -NMR spectra (vs CFCl_3) of $[\text{Fe}_2(\mu\text{-O}_2\text{CAr}^{4\text{-FPH}})_2(\text{O}_2\text{CAr}^{4\text{-FPH}})_2(\text{THF})_2]$ (8) in CH_2Cl_2 at 470 MHz.....	106
Figure 1.23.	Ball and stick representation of the solid-state structures of $[\text{Fe}_2(\mu\text{-O}_2\text{CAr}^{\text{Tol}})_2(\text{O}_2\text{CAr}^{\text{Tol}})_2(\text{C}_5\text{H}_5\text{N})_2]$ (4), $[\text{Fe}_2(\mu\text{-O}_2\text{CAr}^{\text{Tol}})_2(\text{O}_2\text{CAr}^{\text{Tol}})_2(1\text{-MeIm})_2]$ (5), $[\text{Fe}_2(\mu\text{-O}_2\text{CAr}^{\text{Tol}})_3(\text{O}_2\text{CAr}^{\text{Tol}})(2,6\text{-lutidine})]$ (6), and $[\text{Fe}_2(\mu\text{-O}_2\text{CAr}^{\text{Tol}})_2(\text{O}_2\text{CAr}^{\text{Tol}})_2(4\text{-}^t\text{BuC}_5\text{H}_4\text{N})_2]$ (7) generated using the crystallographic coordinates.....	107
Figure 1.24.	Ball and stick representation of the crystallographically determined diiron(II) active site of $\Delta 9\text{D}$ and 4	108
Figure 1.25.	Structures of $[\text{Fe}_2(\mu\text{-O}_2\text{CAr}^{\text{Tol}})_2(\text{THF})_2\text{Br}_2]$ (1) and $[\text{Fe}_2(\mu\text{-O}_2\text{CAr}^{\text{Tol}})_2(\text{O}_2\text{CAr}^{\text{Tol}})_2(\text{THF})_2]$ (2) generated using the crystallographic coordinates.....	109
Figure 1.26.	Ball and stick representation of the crystallographically determined diiron(II) active site of RNR-R2 and 5	110
Figure 1.27.	Structures of $[\text{Fe}_2(\mu\text{-O}_2\text{CAr}^{\text{Mes}})_2(\text{O}_2\text{CAr}^{\text{Mes}})_2(\text{MeCN})_2]$ and $[\text{Fe}_2(\mu\text{-O}_2\text{CAr}^{\text{Tol}})_2(\text{O}_2\text{CAr}^{\text{Tol}})_2(\text{MeCN})_2]$ (3) generated using the crystallographic coordinates.....	111
Figure 1.28.	Distribution of torsion angles (τ) of $\text{Ar}^{\text{Mes}}\text{CO}_2^-$ and $\text{Ar}^{\text{Tol}}\text{CO}_2^-$	112
Figure 2.1.	ORTEP diagrams of $[\text{Fe}(\text{O}_2\text{CAr}^{\text{Tol}})_2(1\text{-BnIm})_2]$ (3) and $[\text{Fe}(\text{O}_2\text{CAr}^{\text{Tol}})_2(1\text{-MeBzIm})_2]$ (4) with thermal ellipsoids at 50% probability.....	138
Figure 2.2	ORTEP diagrams of $[\text{Fe}(\text{O}_2\text{CAr}^{4\text{-tBuPh}})_2(2,2'\text{-bipy})]$ (5) and $[\text{Fe}(\text{O}_2\text{CAr}^{\text{Tol}})_2(\text{TMEDA})]$ (6) with thermal ellipsoids at 50% probability.....	139
Figure 2.3.	ORTEP diagram of $[\text{Fe}(\text{O}_2\text{CAr}^{\text{Tol}})_2(\text{BPTA})]$ (7) with thermal ellipsoids at 50% probability.....	140
Figure 2.4.	Zero-field Mössbauer spectra recorded at 4.2 K for a solid sample of $[\text{Fe}_2(\mu\text{-O}_2\text{CAr}^{\text{Tol}})_3(\text{O}_2\text{CAr}^{\text{Tol}})(2,6\text{-lutidine})]$ (2)	141
Figure 2.5.	Zero-field Mössbauer spectra recorded at 4.2 K for solid samples of $[\text{Fe}(\text{O}_2\text{CAr}^{\text{Tol}})_2(1\text{-BnIm})_2]$ (3) (A); $[\text{Fe}(\text{O}_2\text{CAr}^{\text{Tol}})_2(1\text{-MeBzIm})_2]$ (4) (B); $[\text{Fe}(\text{O}_2\text{CAr}^{4\text{-tBuPh}})_2(2,2'\text{-bipy})]$ (5);	

	[Fe(O ₂ CAr ^{Tol}) ₂ (BPTA)] (7)	142
Figure 3.1.	Electronic absorption spectra for the formation of dioxygen adducts of diiron(II) complexes in CH ₂ Cl ₂ at -78 °C and their thermal decay products.....	197
Figure 3.2.	Kinetic data for the reaction of [Fe ₂ (μ-O ₂ CAr ^{Tol}) ₄ (4- ^t BuC ₅ H ₄ N) ₂] (2a) with O ₂ in CH ₂ Cl ₂ at -78 °C (UV-vis traces for the development of 2b and a plot of A ₆₇₀ versus time and a fit to a first-order exponential buildup)	198
Figure 3.3.	Resonance Raman spectra of fluid solutions of [Fe ₂ (μ-O ₂ CAr ^{Tol}) ₂ -(O ₂ CAr ^{Tol}) ₂ (C ₅ H ₅ N) ₂] (1a), 1a + ¹⁶ O ₂ (1b), and 1a + ¹⁸ O ₂ (1b*) in CH ₂ Cl ₂ at -78 °C.....	199
Figure 3.4.	Resonance Raman spectra of fluid solutions of [Fe ₂ (μ-O ₂ CAr ^{Tol}) ₄ -(4- ^t BuC ₅ H ₄ N) ₂] (2a) and 2a + ¹⁶ O ₂ (2b) in CH ₂ Cl ₂ at -78 °C.....	200
Figure 3.5.	Resonance Raman spectra of fluid solutions of [Fe ₂ (μ-O ₂ CAr ^{Tol}) ₄ -(C ₅ H ₅ N) ₂](OTf) (1mv) and [Fe ₂ (μ-O ₂ CAr ^{Tol}) ₄ (4- ^t BuC ₅ H ₄ N) ₂](PF ₆) (2mv) in CH ₂ Cl ₂ at -78 °C.....	201
Figure 3.6.	X-band (9.4 GHz) and Q-band (34.1 GHz) EPR spectra of a frozen CH ₂ Cl ₂ solution of 2b for microwave fields parallel and perpendicular to the static field.....	202
Figure 3.7.	X-band and Q-band EPR spectra of a frozen CH ₂ Cl ₂ solution sample of 2mv	203
Figure 3.8.	Perpendicular mode X-band EPR spectra of a frozen CH ₂ Cl ₂ solution sample of 2b and its thermolysis product. Parallel mode X-band EPR spectra of 2c , thermolysis product of 2b , and a sample prepared by exposing a CH ₂ Cl ₂ solution of 2a to dioxygen at room temperature and freezing.....	204
Figure 3.9.	Mössbauer spectra of the solid powder sample of 2b recorded at 4.2 K with a 50-mT magnetic field applied parallel and perpendicular to the γ-rays, and a difference spectrum thereof.....	205
Figure 3.10.	Deconvolution of the Mössbauer spectrum of the solid powder sample of 2b recorded at 4.2 K in an applied field of 8 T.....	206
Figure 3.11.	4.2 K Mössbauer spectra of [Fe ₂ (μ-O ₂ CAr ^{Tol}) ₄ (4- ^t BuC ₅ H ₄ N) ₂](PF ₆) (2mv) in the form of solid and the Fe(II)Fe(III) component in 2b	207
Figure 3.12.	4.2 K Mössbauer spectra of the Fe(III)Fe(IV) component in the solid powder sample of 2b in applied fields of 4 T and 8 T.....	208
Figure 3.13.	Time-dependent development of the S = 1/2 and S = 9/2 components in 2b as determined by X-band EPR spectra.....	209
Figure 3.14.	X-band EPR spectra of a frozen CH ₂ Cl ₂ solution of 2b obtained by quenching the reaction 5 min after exposing 2a to dioxygen at -78 °C, in the absence and presence of [H(OEt ₂) ₂](BAR' ₄)	210
Figure 3.15.	UV-vis spectra for the reaction of 2b with Cp* ₂ Fe in CH ₂ Cl ₂ at -78 °C.....	211

Figure 3.16.	UV/vis and EPR spectra of the reactions between 1b and 2,4,6-tri- <i>tert</i> -butylphenol in CH ₂ Cl ₂	212
Figure 3.17.	ORTEP diagram of [Fe(O ₂ CAr ^{Tol}) ₂ (2,4- ^t Bu ₂ C ₆ H ₃ O)-(4- ^t BuC ₅ H ₄ N)] with thermal ellipsoids at 50% probability.....	213
Figure 3.18.	ORTEP diagram of [Fe ₂ (μ-OH) ₂ (μ-O ₂ CAr ^{Tol}) ₂ (O ₂ CAr ^{Tol}) ₂ -(C ₅ H ₅ N) ₂] (1c) with thermal ellipsoids at 50% probability.....	214
Figure 3.19.	ORTEP diagram of [Fe ₂ (μ-OH) ₂ (μ-O ₂ CAr ^{Tol}) ₂ (O ₂ CAr ^{Tol}) ₂ -(4- ^t BuC ₅ H ₄ N) ₂] (2c) with thermal ellipsoids at 50% probability.....	215
Figure 3.20.	Zero-field Mössbauer spectra recorded at 4.2 K for [Fe ₂ (μ-OH) ₂ -(μ-O ₂ CAr ^{Tol}) ₂ (O ₂ CAr ^{Tol}) ₂ (4- ^t BuC ₅ H ₄ N) ₂] (2c) as a solid state sample and as a THF frozen solution sample.....	216
Figure 3.21.	Plots of effective moment (μ _{eff}) per molecule versus temperature and molar susceptibility (χ _M) versus temperature for [Fe ₂ (μ-OH) ₂ (μ-O ₂ CAr ^{Tol}) ₂ (O ₂ CAr ^{Tol}) ₂ (C ₅ H ₅ N) ₂] (1c).....	217
Figure 3.22.	Plots of effective moment (μ _{eff}) per molecule versus temperature and molar susceptibility (χ _M) versus temperature for [Fe ₂ (μ-OH) ₂ (μ-O ₂ CAr ^{Tol}) ₂ (O ₂ CAr ^{Tol}) ₂ (4- ^t BuC ₅ H ₄ N) ₂] (2c).....	218
Figure 3.23.	Comparison of the electronic absorption spectra of [Fe ₂ (μ-O ₂ CAr ^{Tol}) ₄ (4- ^t BuC ₅ H ₄ N) ₂](PF ₆) (2mv) and 2b	219
Figure 3.24.	Space-filling representations of [Fe ₂ (μ-O ₂ CAr ^{Tol}) ₂ (O ₂ CAr ^{Tol}) ₂ -(C ₅ H ₅ N) ₂] (1a) and [Fe ₂ (μ-O ₂ CAr ^{Tol}) ₄ (4- ^t BuC ₅ H ₄ N) ₂] (2a).....	220
Figure 4.1.	Solid-state structures of the cations in [(Me ₃ TACN) ₂ Fe(μ-OH) ₃](ClO ₄) ₂ (A), [L ¹ Fe ₂ (μ-OAc) ₂](ClO ₄) (B), and [Fe ₂ (μ-O ⁱ Pr) ₂ -(μ-O ₂ CAr ^{Mes})(O ₂ CAr ^{Mes}) ₂] (C) generated using the crystallographic coordinates.....	246
Figure 4.2.	Cyclic voltammograms of [Fe ₂ (μ-O ₂ CAr ^{Tol}) ₄ (4- ^t BuC ₅ H ₄ N) ₂] (1a) in CH ₂ Cl ₂ with 0.5 M (Bu ₄ N)(PF ₆) as supporting electrolyte.....	247
Figure 4.3.	Cyclic voltammograms of [Fe ₂ (μ-O ₂ CAr ^{4-FPh}) ₄ (4- ^t BuC ₅ H ₄ N) ₂] in CH ₂ Cl ₂ with 0.5 M (Bu ₄ N)(PF ₆) as supporting electrolyte.....	248
Figure 4.4.	Cyclic voltammograms of [Fe ₂ (μ-O ₂ CAr ^{Tol}) ₂ (O ₂ CAr ^{Tol}) ₂ (THF) ₂] (3a) in CH ₂ Cl ₂ with 0.5 M (Bu ₄ N)(PF ₆) as supporting electrolyte.....	249
Figure 4.5.	Ball and stick (top) and space-filling (bottom) representation of the solid-state structure of [Fe ₂ (μ-O ₂ CAr ^{Tol}) ₄ (4- ^t BuC ₅ H ₄ N) ₂] ⁺ cation generated using the crystallographic coordinates.....	250
Figure 4.6.	ORTEP diagram of the cation in [Fe ₂ (μ-O ₂ CAr ^{Tol}) ₄ (C ₅ H ₅ N) ₂](OTf) (2b) with thermal ellipsoids at 50% probability.....	251
Figure 4.7.	ORTEP diagram of the cation in [Fe ₂ (μ-O ₂ CAr ^{Tol}) ₄ (THF) ₂](PF ₆) (3b) with thermal ellipsoids at 50% probability.....	252
Figure 4.8.	Electronic absorption spectra of 1b–3b in CH ₂ Cl ₂ showing the IVCT transitions.....	253
Figure 4.9.	First-derivative electronic absorption spectra of 1b–3b in CH ₂ Cl ₂	254
Figure 4.10.	Electronic absorption spectra (UV–vis–NIR) of [Fe ₂ (μ-O ₂ CAr ^{Tol}) ₄ -	

	(4- ^t BuC ₅ H ₄ N) ₂](PF ₆) (1b) in CH ₂ Cl ₂	255
Figure 4.11.	Effective magnetic moments, T 5–300 K, for [Fe ₂ (μ-O ₂ CAr ^{Tol}) ₄ -(4- ^t BuC ₅ H ₄ N) ₂](PF ₆) (1b), [Fe ₂ (μ-O ₂ CAr ^{Tol}) ₄ (C ₅ H ₅ N) ₂](OTf) (2b), and [Fe ₂ (μ-O ₂ CAr ^{Tol}) ₄ (THF) ₂](PF ₆) (3b)	256
Figure 4.12.	Mössbauer spectra of the solid powder sample of [Fe ₂ (μ-O ₂ CAr ^{Tol}) ₄ (4- ^t BuC ₅ H ₄ N) ₂](PF ₆) (1b) recorded at 4.2 K with a magnetic field of 4 T and 8 T parallel to the γ-rays.....	257
Figure 4.13.	Fe K-edge and pre-edge transitions for [Fe ₂ (μ-O ₂ CAr ^{Tol}) ₄ -(4- ^t BuC ₅ H ₄ N) ₂](PF ₆) (1b), [Fe ₂ (μ-O ₂ CAr ^{Tol}) ₄ (C ₅ H ₅ N) ₂](OTf) (2b), and [Fe ₂ (μ-O ₂ CAr ^{Tol}) ₄ (THF) ₂](PF ₆) (3b)	258
Figure 4.14.	Fe K-edge and pre-edge transitions for [Fe ₂ (μ-O ₂ CAr ^{Tol}) ₄ -(4- ^t BuC ₅ H ₄ N) ₂] (1a), [Fe ₂ (μ-O ₂ CAr ^{Tol}) ₄ (4- ^t BuC ₅ H ₄ N) ₂](PF ₆) (1b), [Fe ₂ (μ-OH) ₂ (μ-O ₂ CAr ^{Tol}) ₂ (O ₂ CAr ^{Tol}) ₂ (4- ^t BuC ₅ H ₄ N) ₂] (1c), and a 50:50 weighted addition of the edges for 1a and 1c	259
Figure 4.15.	Second derivatives of the K-edge spectra for [Fe ₂ (μ-O ₂ CAr ^{Tol}) ₄ -(4- ^t BuC ₅ H ₄ N) ₂] (1a), [Fe ₂ (μ-O ₂ CAr ^{Tol}) ₄ (4- ^t BuC ₅ H ₄ N) ₂](PF ₆) (1b), and [Fe ₂ (μ-OH) ₂ (μ-O ₂ CAr ^{Tol}) ₂ (O ₂ CAr ^{Tol}) ₂ (4- ^t BuC ₅ H ₄ N) ₂] (1c).....	260
Figure 4.16.	Second derivatives of the pre-edge region (1s → 3d transition) for [Fe ₂ (μ-O ₂ CAr ^{Tol}) ₄ (4- ^t BuC ₅ H ₄ N) ₂] (1a), [Fe ₂ (μ-O ₂ CAr ^{Tol}) ₄ -(4- ^t BuC ₅ H ₄ N) ₂](PF ₆) (1b), and [Fe ₂ (μ-OH) ₂ (μ-O ₂ CAr ^{Tol}) ₂ -(O ₂ CAr ^{Tol}) ₂ (4- ^t BuC ₅ H ₄ N) ₂] (1c)	261
Figure 5.1.	ORTEP diagram of [Fe ₂ (μ-O ₂ CAr ^{Tol}) ₂ (Me ₃ TACN) ₂ (MeCN) ₂] ²⁺ (1a) with thermal ellipsoids at 50% probability.....	296
Figure 5.2.	ORTEP diagram of [Fe ₂ (μ-O ₂ CAr ^{Tol}) ₂ (Me ₃ TACN) ₂ (H ₂ O) ₂] ²⁺ (2a) with thermal ellipsoids at 50% probability.....	297
Figure 5.3.	Comparison of the solid state structures of [Fe ₂ (μ-O ₂ CAr ^{Tol}) ₂ -(Me ₃ TACN) ₂ (MeCN) ₂] ²⁺ (1a) and [(Me ₃ TACN) ₂ Fe ₂ (μ-O ₂ CAr ^{Tol}) ₂ -(H ₂ O) ₂] ²⁺ (1b) (bottom)	298
Figure 5.4.	Electronic absorption spectra of (A) [(Me ₃ TACN) ₂ Fe ₂ -(μ-O ₂ CAr ^{Tol}) ₂ (MeCN) ₂](OTf) ₂ (1a) in THF at -78 °C before and after addition of dioxygen, (B) the decay of 1b at -78 °C (inset: a plot of A ₆₄₀ versus time and a fit to a first-order exponential decay), and (C) 1c formed by warming 1b to 25 °C in air.....	299
Figure 5.5.	Zero-field Mössbauer spectra recorded at 4.2 K for [(Me ₃ TACN) ₂ -Fe ₂ (μ-O ₂ CAr ^{Tol}) ₂ (MeCN) ₂](OTf) ₂ (1a) and [(Me ₃ TACN) ₂ Fe ₂ -(μ-O ₂ CAr ^{Tol}) ₂ (H ₂ O) ₂](OTf) ₂ (1b).....	300
Figure 5.6.	Zero-field Mössbauer spectra recorded at 4.2 K of [(Me ₃ TACN) ₂ -Fe ₂ (μ-O ₂ CAr ^{Tol}) ₂ (MeCN) ₂](OTf) ₂ (1a) as a THF frozen solution, and 1a + O ₂ as a THF solution.....	301
Figure 5.7.	Zero-field Mössbauer spectra recorded at 4.2 K of 1b as a THF solution.....	302
Figure 5.8.	Zero-field Mössbauer spectra recorded at 4.2 K of 1c as a THF solution.....	303

Figure 5.9.	Resonance Raman spectra of fluid solutions of [(Me ₃ TACN) ₂ -Fe ₂ (μ-O ₂ CAr ^{Tol}) ₂ (MeCN) ₂](OTf) ₂ (1a), 1a + ¹⁶ O ₂ (1b), and 1a + ¹⁸ O ₂ in THF at -78 °C.....	304
Figure 5.10.	Fe K-edge and pre-edge transitions for 1a in THF and in the solid state.....	305
Figure 5.11.	Fe K-edge and pre-edge transitions for 1a , 1a + O ₂ , and the putative (peroxo)diiron(III) species 1b (1a + O ₂] - 40%[1a]).....	306
Figure 5.12.	EXAFS and Fourier transformed EXAFS for 1a in THF and in the solid state.....	307
Figure 5.13.	Fourier transform data and fits for 1a in THF.....	308
Figure 5.14.	Fourier transform data and fits for 1a in the solid state.....	309
Figure 5.15.	Fourier transform data and fits for 1b	310
Figure 5.16.	Fourier transform data and representative best fit for 1c	311
Figure 6.1.	ORTEP diagram of [Fe ₂ (μ-O ₂ CAr ^{Tol}) ₂ (O ₂ CAr ^{Tol}) ₂ (N,N-Me ₂ en) ₂] (2) with thermal ellipsoids at 50% probability.....	347
Figure 6.2.	ORTEP diagram of [Fe ₂ (μ-O ₂ CAr ^{Tol}) ₃ (O ₂ CAr ^{Tol})(N,N-Me ₂ en)] (3) with thermal ellipsoids at 50% probability.....	348
Figure 6.3.	ORTEP diagram of [Fe(O ₂ CAr ^{Tol}) ₂ (N,N-Me ₂ en) ₂] (4) with thermal ellipsoids at 50% probability.....	349
Figure 6.4.	ORTEP diagram of [Fe ₂ (μ-O ₂ CAr ^{4-tBuPh}) ₂ (OTf) ₂ (N,N-Bn ₂ en) ₂] (5) with thermal ellipsoids at 50% probability.....	350
Figure 6.5.	ORTEP diagram of [Fe ₂ (μ-O ₂ CAr ^{Tol}) ₂ (O ₂ CAr ^{Tol}) ₂ (N,N-Bn ₂ en) ₂] (6) with thermal ellipsoids at 50% probability.....	351
Figure 6.6.	ORTEP diagram of [Fe ₂ (μ-O ₂ CAr ^{4-FPh}) ₂ (O ₂ CAr ^{4-FPh}) ₂ (N,N-Bn ₂ en) ₂] (7) with thermal ellipsoids at 50% probability.....	352
Figure 6.7.	Zero-field Mössbauer spectrum recorded at 4.2 K for [Fe ₂ (μ-O ₂ CAr ^{Tol}) ₂ (O ₂ CAr ^{Tol}) ₂ (N,N-Bn ₂ en) ₂] (6) in the solid state.....	353
Figure 6.8.	ORTEP diagram of [Fe ₂ (μ-OH) ₂ (μ-O ₂ CAr ^{Tol})(O ₂ CAr ^{Tol}) ₃ (N-Bnen)-(N,N-Bn ₂ en)] (8) with thermal ellipsoids at 50% probability.....	354
Figure 6.9.	Electronic absorption spectrum of [Fe ₂ (μ-OH) ₂ (μ-O ₂ CAr ^{Tol})-(O ₂ CAr ^{Tol}) ₃ (N-Bnen)(N,N-Bn ₂ en)] (8) in CH ₂ Cl ₂	355
Figure 6.10.	Zero-field Mössbauer spectrum recorded at 77 K for [Fe ₂ (μ-OH) ₂ -(μ-O ₂ CAr ^{Tol})(O ₂ CAr ^{Tol}) ₃ (N-Bnen)(N,N-Bn ₂ en)] (8) in the solid state.....	356
Figure 6.11.	Zero-field Mössbauer spectrum recorded at 4.2 K for [Fe ₂ (μ-OH) ₂ -(μ-O ₂ CAr ^{Tol})(O ₂ CAr ^{Tol}) ₃ (N-Bnen)(N,N-Bn ₂ en)] (8) in the solid state.....	357
Figure 6.12.	A representative GC chromatogram for the oxidative N-dealkylation reactions of 6	358
Figure 6.13.	Oxidative N-dealkylation of internal versus external substrates by mono- and dinuclear iron(II) complexes.....	359
Figure 6.14.	Comparison of the diiron(III) core structures of MMOH _{ox} and compound 8	360
Figure 7.1.	Ball and stick representation of the solid-state structure of [Fe ₄ (μ-OH) ₄ (μ-O ₂ CAr ^{4-tBuPh}) ₂ (μ-OTf) ₂ (C ₅ H ₅ N) ₄] (1)	389

Figure 7.2.	ORTEP diagram of $[\text{Fe}_4(\mu\text{-OH})_4(\mu\text{-O}_2\text{CAr}^{4\text{-tBuPh}})_2(\mu\text{-OTf})_2\text{-}(4\text{-tBuC}_5\text{H}_4\text{N})_4]$ (2) with thermal ellipsoids at 50% probability.....	390
Figure 7.3.	Ball and stick representation of the solid-state structure of $[\text{Fe}_4(\mu\text{-OH})_4(\mu\text{-O}_2\text{CAr}^{4\text{-tBuPh}})_2(\mu\text{-OTf})_2(3\text{-FC}_5\text{H}_4\text{N})_4]$ (3).....	391
Figure 7.4.	Electronic absorption spectra of 1–3 showing the MLCT transitions.....	392
Figure 7.5.	IR spectra of $[\text{Fe}_4(\mu\text{-OH})_4(\mu\text{-O}_2\text{CAr}^{4\text{-tBuPh}})_2(\mu\text{-OTf})_2(\text{C}_5\text{H}_5\text{N})_4]$ (A) in KBr; (B) in KBr as a mixture with OD ⁻ substituted cluster $[\text{Fe}_4(\mu\text{-OD})_4(\mu\text{-O}_2\text{CAr}^{4\text{-tBuPh}})_2(\mu\text{-OTf})_2(\text{C}_5\text{H}_5\text{N})_4]$; (C) in CH ₂ Cl ₂	393
Figure 7.6.	470-MHz ¹⁹ F-NMR spectra of $[\text{Fe}_4(\mu\text{-OH})_4(\mu\text{-O}_2\text{CAr}^{4\text{-tBuPh}})_2(\mu\text{-OTf})_2(\text{C}_5\text{H}_5\text{N})_4]$ (1) (A) and $[\text{Fe}_4(\mu\text{-OH})_4(\mu\text{-O}_2\text{CAr}^{4\text{-tBuPh}})_2(\mu\text{-OTf})_2(3\text{-FC}_5\text{H}_4\text{N})_4]$ (3) (B) in CH ₂ Cl ₂	394
Figure 7.7.	Zero-field Mössbauer spectra recorded at 4.2 K for $[\text{Fe}_4(\mu\text{-OH})_4(\mu\text{-O}_2\text{CAr}^{4\text{-tBuPh}})_2(\mu\text{-OTf})_2(\text{C}_5\text{H}_5\text{N})_4]$ (1) (A), $[\text{Fe}_4(\mu\text{-OH})_4(\mu\text{-O}_2\text{CAr}^{4\text{-tBuPh}})_2(\mu\text{-OTf})_2(4\text{-tBuC}_5\text{H}_4\text{N})_4]$ (2) (B), and $[\text{Fe}_4(\mu\text{-OH})_4(\mu\text{-O}_2\text{CAr}^{4\text{-tBuPh}})_2(\mu\text{-OTf})_2(3\text{-FC}_5\text{H}_4\text{N})_4]$ (3) (C) in the solid state.....	395
Figure 7.8.	Plot of χT versus temperature for $[\text{Fe}_4(\mu\text{-OH})_4(\mu\text{-O}_2\text{CAr}^{4\text{-tBuPh}})_2\text{-}(\mu\text{-OTf})_2(\text{C}_5\text{H}_5\text{N})_4]$ (1).....	396
Figure 7.9.	Magnetization curves versus field of $[\text{Fe}_4(\mu\text{-OH})_4(\mu\text{-O}_2\text{CAr}^{4\text{-tBuPh}})_2\text{-}(\mu\text{-OTf})_2(\text{C}_5\text{H}_5\text{N})_4]$ (1).....	397
Figure 7.10.	Plots of calculated χT versus T for $S = 1\text{--}8$ with $D = 5\text{ cm}^{-1}$	398
Figure 7.11.	Cyclic voltammograms of $[\text{Fe}_4(\mu\text{-OH})_4(\mu\text{-O}_2\text{CAr}^{4\text{-tBuPh}})_2\text{-}(\mu\text{-OTf})_2(\text{C}_5\text{H}_5\text{N})_4]$ (1) in CH ₂ Cl ₂	399
Figure 8.1.	ORTEP drawing of $[\text{Co}_2(\mu\text{-O}_2\text{CAr}^{\text{Tol}})_2(\text{O}_2\text{CAr}^{\text{Tol}})_2(\text{C}_5\text{H}_5\text{N})_2]$ (1) showing 50% probability thermal ellipsoids.....	431
Figure 8.2.	ORTEP drawing of $[\text{Co}_2(\mu\text{-OH}_2)_2(\mu\text{-O}_2\text{CAr}^{\text{Tol}})_2(\text{O}_2\text{CAr}^{\text{Tol}})_2\text{-}(\text{C}_5\text{H}_5\text{N})_2]$ (2a) showing 50% probability thermal ellipsoids.....	432
Figure 8.3.	ORTEP diagram of $[\text{Co}_2(\mu\text{-OH}_2)_2(\mu\text{-O}_2\text{CAr}^{\text{Tol}})_2(\text{O}_2\text{CAr}^{\text{Tol}})_2\text{-}(\text{THF})_2]$ (2b) with thermal ellipsoids at 50% probability.....	433
Figure 8.4.	ORTEP diagram of $[\text{Co}_2(\mu\text{-OH}_2)_2(\mu\text{-O}_2\text{CAr}^{\text{Tol}})_2(\text{O}_2\text{CAr}^{\text{Tol}})_2\text{-}(N,N\text{-Bn}_2\text{en})_2]$ (2c) with thermal ellipsoids at 50% probability.....	434
Figure 8.5.	ORTEP diagram of a mixture of $[\text{Co}_2(\mu\text{-O}_2\text{CAr}^{\text{Tol}})_2(\text{O}_2\text{CAr}^{\text{Tol}})_2\text{-}(\text{C}_5\text{H}_5\text{N})_2]$ (1) and $[\text{Co}_2(\mu\text{-OH}_2)_2(\mu\text{-O}_2\text{CAr}^{\text{Tol}})_2(\text{O}_2\text{CAr}^{\text{Tol}})_2\text{-}(\text{C}_5\text{H}_5\text{N})_2]$ (2a) with thermal ellipsoids at 50% probability.....	435
Figure 8.6.	ORTEP drawing of $[\text{Co}_2(\mu\text{-OH})_2(\mu\text{-O}_2\text{CAr}^{\text{Tol}})_2(\text{O}_2\text{CAr}^{\text{Tol}})_2\text{-}(\text{C}_5\text{H}_5\text{N})_2]$ (3) showing 50% probability thermal ellipsoids.....	436
Figure 8.7.	ORTEP drawing of $[\text{Ni}_2(\mu\text{-O}_2\text{CAr}^{\text{Tol}})_4(\text{C}_5\text{H}_5\text{N})_2]$ (4) showing 50% probability thermal ellipsoids.....	437
Figure 8.8.	ORTEP drawing of $[\text{Ni}_2(\mu\text{-HO}\cdots\text{H})(\mu\text{-O}_2\text{CAr}^{\text{Tol}})_2(\text{O}_2\text{CAr}^{\text{Tol}})_2\text{-}(\text{C}_5\text{H}_5\text{N})_2]$ (5) showing 50% probability thermal ellipsoids.....	438
Figure 8.9.	ORTEP drawing of $[\text{Zn}_2(\mu\text{-O}_2\text{CAr}^{\text{Tol}})_2(\text{O}_2\text{CAr}^{\text{Tol}})_2(\text{C}_5\text{H}_5\text{N})_2]$ (6) showing 50% probability thermal ellipsoids.....	439

Figure 8.10. Schematic representation of carboxylate-bridged dimetallic centers having hydroxo or aqua bridging ligands.....	440
Figure 8.11. Core structures of $[\text{Co}_2(\mu\text{-O}_2\text{CAr}^{\text{Tol}})_2(\text{O}_2\text{CAr}^{\text{Tol}})_2(\text{C}_5\text{H}_5\text{N})_2]$ (1), $[\text{Co}_2(\mu\text{-OH}_2)_2(\mu\text{-O}_2\text{CAr}^{\text{Tol}})_2(\text{O}_2\text{CAr}^{\text{Tol}})_2(\text{C}_5\text{H}_5\text{N})_2]$ (2a), $[\text{Ni}_2(\mu\text{-HO}\cdots\text{H})_2(\mu\text{-O}_2\text{CAr}^{\text{Tol}})_2(\text{O}_2\text{CAr}^{\text{Tol}})_2(\text{C}_5\text{H}_5\text{N})_2]$ (5), and $[\text{Co}_2(\mu\text{-OH})_2(\mu\text{-O}_2\text{CAr}^{\text{Tol}})_2(\text{O}_2\text{CAr}^{\text{Tol}})_2(\text{C}_5\text{H}_5\text{N})_2]$ (3).....	441
Figure 8.12. Structures of the dicobalt centers in methionine aminopeptidases from <i>E. coli</i> and <i>P. furiosus</i>	442

* Each chapter in this thesis was prepared independently, based on the manuscripts submitted for publication. As a result, different numbering schemes were used to denote identical compounds as described below. These labels, however, are internally consistent within each chapter.

compounds	chapters				
	I	II	III	IV	IV
$[\text{Fe}_2(\mu\text{-O}_2\text{CAr}^{\text{Tol}})_2(\text{O}_2\text{CAr}^{\text{Tol}})_2(\text{THF})_2]$	2	1		3a	1
$[\text{Fe}_2(\mu\text{-O}_2\text{CAr}^{\text{Tol}})_2(\text{O}_2\text{CAr}^{\text{Tol}})_2(\text{C}_5\text{H}_5\text{N})_2]$	4		1a	2a	
$[[\text{Fe}_2(\mu\text{-O}_2\text{CAr}^{\text{Tol}})_3(\text{O}_2\text{CAr}^{\text{Tol}})(2,6\text{-lutidine})_2]$	6	2			
$[\text{Fe}_2(\mu\text{-O}_2\text{CAr}^{\text{Tol}})_4(4\text{-}^t\text{BuC}_5\text{H}_4\text{N})_2]$	7		2a	1a	
$[\text{Fe}_2(\mu\text{-O}_2\text{CAr}^{\text{Tol}})_4(\text{C}_5\text{H}_5\text{N})_2](\text{OTf})$			1mv	2b	
$[\text{Fe}_2(\mu\text{-O}_2\text{CAr}^{\text{Tol}})_4(4\text{-}^t\text{BuC}_5\text{H}_4\text{N})_2](\text{PF}_6)$			2mv	1b	
$[\text{Fe}_2(\mu\text{-O}_2\text{CAr}^{\text{Tol}})_4(\text{THF})_2](\text{PF}_6)$				3b	
$[\text{Fe}_2(\mu\text{-OH})_2(\mu\text{-O}_2\text{CAr}^{\text{Tol}})_2(\text{O}_2\text{CAr}^{\text{Tol}})_2(\text{C}_5\text{H}_5\text{N})_2]$			1c		
$[\text{Fe}_2(\mu\text{-OH})_2(\mu\text{-O}_2\text{CAr}^{\text{Tol}})_2(\text{O}_2\text{CAr}^{\text{Tol}})_2(4\text{-}^t\text{BuC}_5\text{H}_4\text{N})_2]$			2c	1c	

Chapter I

Modeling Dioxygen-Activating Centers in Non-Heme Diiron Enzymes: Carboxylate Shifts in Diiron(II) Complexes Supported by Sterically Hindered Carboxylate Ligands*

Introduction

Carboxylate-bridged diiron centers are encountered at the active sites of several proteins that bind or activate dioxygen (Figure 1.1).¹ Hemerythrin (Hr) is a dioxygen-carrier protein that utilizes the (μ -hydroxo)di(μ -carboxylato)diiron(II) core for reversible binding of dioxygen.² Binding and release of dioxygen are accompanied by a two-electron change in the redox state of the diiron unit, which undergoes minimal structural rearrangement. The hydroxylase component of soluble methane monooxygenase (MMOH),³⁻⁵ the R2 component of class I ribonucleotide reductase (RNR-R2),^{6,7} and stearyl-acyl carrier protein (ACP) Δ^9 -desaturase ($\Delta 9D$)^{8,9} bind and reductively activate dioxygen. The active site structures of these enzymes are closely related to each other. Two bridging carboxylates support coordinatively unsaturated iron(II) centers, each having one terminal carboxylate and one histidine ligand.^{6,8,10} In contrast to Hr, these proteins exhibit structural flexibility at their carboxylate-rich diiron centers, as exemplified by crystallographic studies on MMOH at various oxidation states.¹¹

Despite the essentially identical first coordination spheres derived from the polypeptide side chains and solvent molecules in MMOH, RNR-R2, and $\Delta 9D$, however, the ultimate fate of dioxygen molecules that react with their diiron(II) centers is strikingly different.¹ MMOH catalyzes the oxidation of various organic substrates including CH_4 . Formal four-electron oxidation by dioxygen affords a high-valent diiron(IV) species Q ^{12,13} that inserts an O_2 -derived oxygen atom into a C-H bond.^{5,14} RNR-R2 generates a catalytically active tyrosyl radical. One electron reduction of an initial dioxygen-adduct affords a high-valent iron(III)iron(IV) intermediate X ,¹⁵ which effects the oxidation of an adjacent tyrosine residue. $\Delta 9D$ catalyzes the insertion of a cis double bond in stearyl-bound ACP. Although the details of the $\Delta 9D$ reaction mechanism are less clear, a (peroxo)diiron(III) intermediate has recently been identified,^{16,17} which is closely re-

lated to intermediates in the MMOH and RNR-R2 reaction cycles that precede the formation of iron(IV) centers.¹

The diiron(II) active sites in these functionally distinctive enzymes have attracted much attention. In parallel with direct studies of the biological systems, chemists have tried to construct and study synthetic analogs of their active sites.^{1c,1e,18-22} Low molecular weight diiron(II) synthetic models have afforded benchmarks for calibrating the assignment of spectra in their biological counterparts.^{1f,19,23} For example, highly reactive diiron(III) peroxo complexes were isolated at low temperatures and structurally characterized,²⁴⁻²⁶ providing insights into the electronic and geometric structures of the enzyme intermediates. Such efforts have enriched our knowledge of the underlying chemical principles that govern the enzyme reaction mechanism. The quest for a unifying theory of dioxygen activation lies at the heart of such efforts, which have engendered significant advances in ligand design, synthesis, and mechanistic understanding of small molecule surrogates.^{1e,22}

Unlike metal ions stabilized within tetrapyrrole macrocyclic ligands such as porphyrin²⁷ or corrin derivatives,²⁸ carboxylate-bridged iron(II) units are kinetically labile and have a strong propensity to assemble into higher nuclearity species.¹⁸ In the absence of a well-structured three-dimensional framework stabilizing the metal-ligand assembly, an initial and desirable kinetic product may be diverted into an unwanted thermodynamic one. Controlling the nuclearity and coordination geometry of labile metal ions on a labile ligand platform thus presents a formidable synthetic challenge. In order to stabilize diiron(II) complexes having coordinatively unsaturated metal centers, earlier efforts were directed toward elaborating terminal ancillary ligands. By using an imidazole-based bidentate ligand, a discrete tetra(carboxylato)diiron(II) complex $[\text{Fe}_2(\mu\text{-O}_2\text{CH})_3(\text{O}_2\text{CH})(\text{BIPhMe})_2]$ ²⁹ could be assembled that has an open coordination

site for dioxygen binding.^{30,31} The doubly-bridged diiron(II) core structure at the RNR-R2 and Δ 9D active sites was subsequently modeled by $[\text{Fe}_2(\mu\text{-OAc})_2(\text{TPA})_2](\text{BPh}_4)_2$ ³² and $[\text{Fe}_2(\mu\text{-OAc})_2(\text{BPMEN})_2](\text{ClO}_4)_2$.³³ Polypyridyl-derived tetradentate capping ligands TPA²⁹ or BPMEN²⁹ in these compounds, however, rendered the metal centers coordinatively saturated.

Conformationally well-defined dinucleating dicarboxylate ligands, XDK^{29,34} and its derivatives,^{35,36} and Ph₄DBA,^{29,37,38} have been extensively used in our laboratory in order to assemble coordinatively unsaturated diiron(II) complexes. With an additional two carboxylate and two N-donor ligands, a series of diiron(II) complexes $[\text{Fe}_2(\mu\text{-XDK}')(\mu\text{-O}_2\text{CR})(\text{O}_2\text{CR})(\text{N})_2]$ (XDK' = XDK-derivatives; N = pyridine or imidazole derivatives) were prepared.^{35,39} For the first time, the exact ligand compositions of MMOH, RNR-R2, and Δ 9D were reproduced on a non-peptidyl framework. The triply-bridged diiron(II) centers in these compounds, however, do not exactly mimic the doubly-bridged cores in their biological counterparts.^{6,8,10} The inherent asymmetry of the diiron(II) site in Hr was successfully modeled in $[\text{Fe}_2(\mu\text{-OH})(\mu\text{-Ph}_4\text{DBA})\text{L}_2(\text{OTf})]$ (L = TMEDA or DPE),^{29,37,38} in which a triply-bridged diiron(II) core presents five- and six-coordinate metal sites. Upon reaction with dioxygen at low temperature, biomimetic peroxo species were obtained from these compounds.^{35,37-39}

Despite the advances in synthetic modeling afforded by these designer carboxylate ligands, however, certain limitations exist. To achieve the desired functional chemistry, the structural rigidity imparted by conformationally restrictive semi-rigid dinucleating carboxylates can be a liability. DFT calculations on MMOH indicate significant geometric rearrangement of carboxylate ligands during the reaction cycle.^{5,40} Current information points toward *trans*-disposed carboxylate ligands across the putative $\{\text{Fe}_2(\mu\text{-O})_2\}^{4+}$ core in MMOH_Q.^{13,40-42} Such a structural requirement can be accommodated neither by the convergent

dicarboxylate fragment in XDK nor by the orthogonal dicarboxylate unit in Ph₄DBA, demanding a new synthetic strategy for this long-standing problem.

In this chapter we present a full description of our synthetic efforts to reproduce the key structural features of the foregoing non-heme diiron enzyme active sites. With the use of sterically demanding *m*-terphenyl-derived carboxylate ligands, 2,6-di(*p*-tolyl)benzoate (Ar^{Tol}CO₂⁻) and 2,6-di(4-fluorophenyl)benzoate (Ar^{4-FPh}CO₂⁻),⁴³ a series of tetra(carboxylato)diiron(II) complexes [Fe₂(O₂CAr')₄L_n] (Ar' = Ar^{Tol} or Ar^{4-FPh}; L = O- or N-donor ligands; n = 1 or 2) were accessed that bear a close structural resemblance to the diiron(II) centers in MMOH, RNR-R2, and Δ9D.^{6,8,10} Divergent synthetic routes from a common precursor compound afforded a variety of diiron(II) complexes having unprecedented coordination, the detailed structural and spectroscopic properties of which are described. The dynamic rearrangement of the core within a labile carboxylate-bridged diiron(II) construct was probed by VT ¹⁹F-NMR studies. The functional relevance of such a process is discussed and compared with related systems. Collectively, these findings represent a significant advance in our ability to control the geometry of biomimetic non-heme diiron(II) compounds, laying the foundation for exploring functional chemistry of dioxygen-activating models.^{44,45} Aspects of this work have been previously communicated.^{44,46}

Experimental Section

General Considerations. All reagents were obtained from commercial suppliers and used as received unless otherwise noted. Dichloromethane was distilled over CaH₂ under nitrogen. Diethyl ether, THF, and pentanes were saturated with nitrogen and purified by passage through activated Al₂O₃ columns under nitrogen.⁴⁷ The compounds Fe(OTf)₂·2MeCN,⁴⁸ Ar^{Tol}CO₂H, and Ar^{4-FPh}CO₂H⁴³ were prepared according to literature procedures. The sodium

salts of the carboxylic acids, $\text{NaO}_2\text{CAr}^{\text{Tol}}$ and $\text{NaO}_2\text{CAr}^{4\text{-FPh}}$, were prepared by treating a MeOH solution of the free acid with 1 equiv of NaOH and removing the volatile fractions under reduced pressure. Air-sensitive manipulations were carried out under nitrogen in a Vacuum Atmospheres drybox or by standard Schlenk line techniques.

Physical Measurements. ^1H -NMR and ^{19}F -NMR spectra were recorded on Varian Mercury 300 MHz and Inova 500 MHz spectrometers, respectively. Chemical shifts of the ^1H -NMR spectra are reported versus tetramethylsilane and were referenced to the residual solvent peaks. ^{19}F chemical shifts are reported with reference to external CFCl_3 (0.0 ppm). FT-IR spectra were recorded on a Bio Rad FTS-135 instrument with Win-IR software. UV-vis spectra were recorded on a Hewlett Packard 8453 diode array spectrophotometer.

$\text{TlO}_2\text{CAr}^{\text{Tol}}$. To a rapidly stirred THF (40 mL) solution of $\text{Ar}^{\text{Tol}}\text{CO}_2\text{H}$ (3.00 g, 9.92 mmol) was added dropwise TlOEt (2.72 g, 10.9 mmol) diluted in THF (5 mL). The resulting white suspension was stirred for 3 h. The off-white $\text{TlO}_2\text{CAr}^{\text{Tol}}$ solid (4.60 g, 9.10 mmol, 98%) was isolated by filtration, washed with 50 mL of THF, and dried in vacuo. ^1H -NMR (300 MHz, DMSO, 20 °C) δ 7.51 (d, 4H), 7.30 (t, 1H), 7.20 (t, 6H), 2.34 (s, 6H) ppm. FT-IR (KBr, cm^{-1}) 2916, 1554, 1515, 1362, 831, 818, 798, 786, 766, 740, 702, 584, 539, 515. Anal. Calcd for $\text{C}_{21}\text{H}_{17}\text{O}_2\text{Tl}$: C, 49.87; H, 3.39. Found: C, 49.83; H, 3.35.

$[\text{Fe}_2(\mu\text{-O}_2\text{CAr}^{\text{Tol}})_2(\text{THF})_2\text{Br}_2]$ (1) and $[\text{Fe}_2(\mu\text{-O}_2\text{CAr}^{\text{Tol}})_2(\text{O}_2\text{CAr}^{\text{Tol}})_2(\text{THF})_2]$ (2). *Method 1.* To a rapidly stirred THF solution (45 mL) of FeBr_2 (397 mg, 1.84 mmol) was added $\text{TlO}_2\text{CAr}^{\text{Tol}}$ (2.00 g, 3.95 mmol) in a single portion. The resulting heterogeneous mixture was stirred overnight (> 10 h). The suspension was filtered through Celite and the pale yellow filtrate was concentrated under reduced pressure to give a beige solid. Vapor diffusion of pentanes into a concentrated $\text{CH}_2\text{Cl}_2/\text{THF}$ solution of this material afforded colorless blocks of 2

(1.03 g, 0.705 mmol, 77 % yield), which were suitable for X-ray crystallography. When a similar reaction was conducted for a shorter period of time (< ~3 h), yellow blocks of **1** were isolated as yellow crystals by recrystallization from CH₂Cl₂/pentanes. No further attempts were made to purify this material from [FeBr₂(THF)₂]_n, a byproduct obtained as yellow blocks from the same crystallization batch.

Method 2. To a rapidly stirred THF (20 mL) solution of Fe(OTf)₂·2MeCN (327 mg, 0.750 mmol) was added NaO₂CAr^{Tol} (492 mg, 1.52 mmol) in a single portion. The heterogeneous mixture was stirred overnight at room temperature. Volatile fractions were removed under reduced pressure and the residual white solid was extracted into CH₂Cl₂ (10 mL). Insoluble fractions were filtered off and the pale yellow filtrate was treated with THF (0.5 mL). Vapor diffusion of pentanes into the filtrate afforded **2** as colorless blocks (365 mg, 0.250 mmol, 67%). FT-IR (KBr, cm⁻¹) 2918, 1605, 1543, 1515, 1456, 1410, 1384, 1187, 1110, 1037, 1020, 882, 858, 819, 801, 784, 765, 736, 714, 699, 584, 546, 539, 521. Anal. Calcd for C₉₂H₈₄O₁₀Fe₂: C, 75.62; H, 5.79. Found: C, 75.37; H, 6.03.

[Fe₂(μ-O₂CAr^{Tol})₂(O₂CAr^{Tol})₂(MeCN)₂] (**3**). A pale yellow CH₂Cl₂ (2 mL) solution of **2** (100 mg, 68.4 μmol) was treated with MeCN (1 mL). Vapor diffusion of pentanes into the colorless reaction mixture afforded **3** (76 mg, 54 μmol, 79%) as colorless blocks. FT-IR(KBr, cm⁻¹) 3051, 3021, 2918, 2862, 2307, 2281, 1589, 1541, 1515, 1456, 1412, 1384, 1307, 1213, 1186, 1149, 1110, 1073, 1033, 1020, 858, 818, 800, 790, 767, 738, 714, 702, 585, 540, 519. Anal. Calcd for C₈₈H₇₄N₂O₈Fe₂: C, 75.54; H, 5.33; N, 2.00. Found: C, 75.21; H, 5.31; N, 1.85.

[Fe₂(μ-O₂CAr^{Tol})₂(O₂CAr^{Tol})₂(C₅H₅N)₂] (**4**). To a rapidly stirred pale yellow CH₂Cl₂ solution (15 mL) of **2** (675 mg, 0.462 mmol) was added dropwise neat pyridine (82 μL, 1.0 mmol). The solution immediately turned intense yellow and microcrystalline material began to precipitate within minutes. The reaction

mixture was kept at $-30\text{ }^{\circ}\text{C}$ overnight. Ivory microcrystals of **4** (510 mg, 0.346 mmol, 75%) were isolated by filtration, washed with pentanes, and dried in vacuo. Colorless blocks suitable for X-ray crystallography were obtained by vapor diffusion of pentanes into a saturated CH_2Cl_2 solution of this material at room temperature. FT-IR (KBr, cm^{-1}) 2918, 1605, 1554, 1515, 1489, 1457, 1447, 1408, 1383, 1189, 1112, 1070, 1041, 857, 817, 802, 785, 764, 758, 736, 714, 696, 584, 545, 522; UV-vis (CH_2Cl_2 , λ_{max} , nm (ϵ , $\text{M}^{-1}\text{cm}^{-1}$)) 375 (1100). Anal. Calcd for $\text{C}_{94}\text{H}_{78}\text{N}_2\text{O}_8\text{Fe}_2$: C, 76.53; H, 5.33; N, 1.90. Found: C, 76.18; H, 5.21; N, 1.93.

$[\text{Fe}_2(\mu\text{-O}_2\text{CAr}^{\text{Tol}})_2(\text{O}_2\text{CAr}^{\text{Tol}})_2(1\text{-MeIm})_2]$ (**5**). This compound was prepared from **2** (266 mg, 0.182 mmol) and 1-methylimidazole (32 μL , 0.40 mmol) by a procedure analogous to that used to obtain **4**. Colorless blocks of **5** (187 mg, 0.126 mmol, 69%) precipitated upon vapor diffusion of pentanes into the reaction mixture and were analyzed by X-ray crystallography. FT-IR (KBr, cm^{-1}) 3119, 3055, 3021, 2919, 2863, 1608, 1541, 1516, 1454, 1409, 1378, 1306, 1287, 1241, 1188, 1147, 1111, 1095, 1071, 1020, 945, 847, 819, 800, 783, 765, 736, 713, 701, 656, 615, 543, 520, 453. Anal. Calcd for $\text{C}_{92}\text{H}_{80}\text{N}_4\text{O}_8\text{Fe}_2$: C, 74.59; H, 5.44; N, 3.78. Found: C, 74.26; H, 5.49; N, 3.48.

$[\text{Fe}_2(\mu\text{-O}_2\text{CAr}^{\text{Tol}})_3(\text{O}_2\text{CAr}^{\text{Tol}})(2,6\text{-lutidine})]$ (**6**). A rapidly stirred CH_2Cl_2 (4 mL) solution of **2** (130 mg, 89.0 μmol) was treated with neat 2,6-lutidine (250 μL , 2.15 mmol). A flash of intense yellow color appeared, which gradually faded during the addition. Vapor diffusion of Et_2O into the reaction mixture afforded **6** as an off-white solid (81 mg, 57 μmol , 64%). Colorless blocks of **6** suitable for X-ray crystallography were obtained by vapor diffusion of Et_2O into a concentrated CH_2Cl_2 solution of this material at $-30\text{ }^{\circ}\text{C}$. FT-IR (KBr, cm^{-1}) 3054, 3024, 2971, 2920, 2864, 1601, 1580, 1541, 1515, 1454, 1407, 1382, 1305, 1184, 1150, 1111, 1072, 1021, 860, 844, 834, 819, 799, 784, 709, 585, 531, 470. Anal. Calcd for $\text{C}_{91}\text{H}_{77}\text{NO}_8\text{Fe}_2$: C, 76.74; H, 5.45; N, 0.98. Found: C, 76.55; H, 5.95; N, 0.96.

$[\text{Fe}_2(\mu\text{-O}_2\text{CAr}^{\text{Tol}})_4(4\text{-}^t\text{BuC}_5\text{H}_4\text{N})_2]$ (**7**). *Method 1.* To a rapidly stirred pale yellow CH_2Cl_2 solution (5 mL) of **2** (144 mg, 99 μmol) was added dropwise neat 4-*tert*-butylpyridine (32 μL , 0.22 mmol). The solution was intense greenish yellow following the addition. Greenish yellow blocks of **7** (100 mg, 63 μmol , 64%) were obtained by vapor diffusion of Et_2O into the reaction mixture. Layering of benzene over a CH_2Cl_2 solution of this material provided crystals suitable for X-ray crystallography.

Method 2. To a rapidly stirred THF (20 mL) suspension of $\text{NaO}_2\text{CAr}^{\text{Tol}}$ (570 mg, 1.76 mmol) was added $\text{Fe}(\text{OTf})_2\cdot 2\text{MeCN}$ (385 mg, 0.883 mmol) in a single portion. The heterogeneous mixture was stirred overnight and volatile fractions were removed under reduced pressure. The residual ivory solid was extracted into CH_2Cl_2 (10 mL) and filtered. A portion of 4-*tert*-butylpyridine (130 μL , 0.880 mmol) was added to the filtrate and the greenish yellow solution was concentrated to ca 3 mL. Vapor diffusion of Et_2O into the solution afforded **7** (373 mg, 0.235 mmol, 53%) as greenish yellow blocks. FT-IR (KBr, cm^{-1}) 3051, 3020, 2965, 2919, 2866, 1614, 1585, 1514, 1502, 1438, 1422, 1404, 1384, 1304, 1273, 1185, 1150, 1109, 1072, 2029, 1021, 842, 830, 812, 786, 763, 726, 712, 706, 584, 568, 525, 458; UV-vis (CH_2Cl_2 , λ_{max} , nm (ϵ , $\text{M}^{-1}\text{cm}^{-1}$)) 370 (1400). Anal. Calcd for $\text{C}_{102}\text{H}_{94}\text{N}_2\text{O}_8\text{Fe}_2$: C, 77.17; H, 5.97; N, 1.76. Found: C, 77.31; H, 6.06; N, 1.64.

$[\text{Fe}_2(\mu\text{-O}_2\text{CAr}^{4\text{-FPh}})_2(\text{O}_2\text{CAr}^{4\text{-FPh}})_2(\text{THF})_2]$ (**8**). This compound was prepared from $\text{Fe}(\text{OTf})_2\cdot 2\text{MeCN}$ (221 mg, 0.507 mmol) and $\text{NaO}_2\text{CAr}^{4\text{-FPh}}$ (375 mg, 1.13 mmol) by a procedure analogous to that used to prepare **2**. Colorless blocks of **8** (192 mg, 0.129 mmol, 51%) were obtained by recrystallization from CH_2Cl_2 /petanes/hexanes and analyzed by X-ray crystallography. FT-IR (KBr, cm^{-1}) 3063, 2975, 2886, 1608, 1514, 1458, 1413, 1384, 1300, 1219, 1186, 1160, 1094, 1071, 1035, 1014, 938, 882, 836, 809, 792, 773, 739, 712, 700, 602, 582, 555, 531, 462.

Anal. Calcd for $C_{84}H_{60}O_{10}F_8Fe_2 \cdot 0.25CH_2Cl_2$: C, 66.82; H, 4.03. Found: C, 66.65; H, 4.05.

$[Fe_2(\mu-O_2CAr^{4-FPh})_4(THF)_2]$ (**9**). To a rapidly stirred pale yellow CH_2Cl_2 (5 mL) solution of **8** (57 mg, 38 μ mol) was added dropwise $[Cp_2Fe](PF_6)$ (28 mg, 84 μ mol) suspended in CH_2Cl_2 (3 mL). The dark blue-green reaction mixture was stirred at room temperature for 1.5 h. Volatile fractions were removed under reduced pressure and the residual dark green solid was washed repeatedly with pentanes. The remaining solid material was extracted into CH_2Cl_2 (4 mL) and filtered. Vapor diffusion of pentanes into the filtrate afforded **9** as pale green blocks suitable for X-ray crystallography. No further attempts were made to purify this material, which was obtained together with purple powders.

$[Fe_2(\mu-O_2CAr^{4-FPh})_4(C_5H_5N)_2]$ (**10**). This compound was prepared from **8** (95 mg, 64 μ mol) and pyridine (10 μ L, 0.12 mmol) by a procedure analogous to that used to obtain **4**. Vapor diffusion of pentanes into the reaction mixture afforded **10** (61 mg, 40 μ mol, 67%) as a yellow microcrystalline solid. Single crystals suitable for X-ray crystallography were obtained by vapor diffusion of pentanes into a saturated CH_2Cl_2 solution of this material at -30 °C. FT-IR (KBr, cm^{-1}) 3057, 1605, 1551, 1510, 1488, 1449, 1404, 1381, 1300, 1225, 1160, 1096, 1071, 1042, 1011, 843, 809, 792, 771, 704, 582, 555, 530, 464; UV-vis (CH_2Cl_2 , λ_{max} , nm (ϵ , $M^{-1}cm^{-1}$)) 366 (930). Anal. Calcd for $C_{86}H_{54}N_2O_8F_8Fe_2$: C, 68.54; H, 3.61; N, 1.86. Found: C, 68.49; H, 3.70; N, 1.92.

$[Fe_2(\mu-O_2CAr^{4-FPh})_4(1-MeIm)_2]$ (**11**). This compound was prepared in a manner similar to that described for **10**, except that 1-methylimidazole was used instead of pyridine. Pale yellow blocks of **11** (44%) suitable for X-ray crystallography were obtained by vapor diffusion of pentanes/hexanes (1:1) into the reaction mixture. FT-IR (KBr, cm^{-1}) 3136, 3059, 2962, 2928, 1605, 1535, 1511, 1454, 1404, 1381, 1222, 1160, 1094, 1015, 948, 842, 809, 792, 771, 714, 705, 655, 555, 531,

466. Anal. Calcd for $C_{84}H_{56}N_4O_8F_8Fe_2$: C, 66.68; H, 3.73; N, 3.70. Found: C, 66.71; H, 4.03; N, 3.67.

$[Fe_2(\mu-O_2CAr^{4-FPh})_4(4-tBuC_5H_4N)_2]$ (**12**). This compound was prepared in a manner similar to that described for **10**, except that 4-*tert*-butylpyridine was used instead of pyridine. Greenish yellow blocks of **12** (62%) were obtained by vapor diffusion of pentanes into the reaction mixture and analyzed by X-ray crystallography. FT-IR (KBr, cm^{-1}) 3057, 2966, 2905, 2870, 1614, 1580, 1554, 1510, 1452, 1403, 1382, 1222, 1159, 1095, 1074, 844, 831, 818, 793, 772, 727, 706, 555, 530, 468; UV-vis (CH_2Cl_2 , λ_{max} , nm (ϵ , $M^{-1}cm^{-1}$)) 365 (1200). Anal. Calcd for $C_{94}H_{70}N_2O_8F_8Fe_2$: C, 69.72; H, 4.36; N, 1.73. Found: C, 69.97; H, 4.45; N, 1.64.

X-ray Crystallographic Studies. Intensity data were collected on a Bruker (formerly Siemens) CCD diffractometer with graphite-monochromated Mo K α radiation ($\lambda = 0.71073 \text{ \AA}$), controlled by a Pentium-based PC running the SMART software package.⁴⁹ Single crystals were mounted at room temperature on the tips of quartz fibers, coated with Paratone-N oil, and cooled to 188 K under a stream of cold nitrogen maintained by a Bruker LT-2A nitrogen cryostat. Data collection and reduction protocols are described elsewhere.⁵⁰ The structures were solved by direct methods and refined on F^2 by using the SHELXTL software package.⁵¹ Empirical absorption corrections were applied with SADABS,⁵² part of the SHELXTL program package, and the structures were checked for higher symmetry by the program PLATON.⁵³ All non-hydrogen atoms were refined anisotropically unless otherwise noted. Hydrogen atoms were assigned idealized positions and given thermal parameters equivalent to either 1.5 (methyl hydrogen atoms) or 1.2 (all other hydrogen atoms) times the thermal parameter of the carbon atom to which they were attached. The hydrogen atoms associated with the disordered solvent molecules were not included in the refinement. The THF ligands in **1** were disordered over two positions. The occupancy of four

carbons was equally distributed and refined isotropically. A disordered CH_2Cl_2 molecule in the structure of **2** was distributed over two positions and refined. The disordered MeCN and CH_2Cl_2 solvent molecules in the structure of **3** were equally distributed over two positions and refined isotropically. The lattice solvent molecules in the structure of **5** were modeled as partially occupied CH_2Cl_2 (0.75 occupancy) and pentane (0.25 occupancy). The *tert*-butyl groups on each of the 4-*tert*-butylpyridine in the structure of **7** is distributed over two positions and refined isotropically. In the structure of **8** each coordinated THF molecule was disordered over two positions. In each case, two of the carbon atoms and the oxygen atom were refined at full occupancy, and the occupancies of the remaining two carbon atoms were equally distributed over two positions and refined isotropically. The THF ligands in **9** were disordered over two positions. In one molecule, three carbon atoms were distributed at 0.7 and 0.3 occupancies and refined. In the other, the occupancy of four carbon atoms was distributed at 0.7 and 0.3 occupancies and refined isotropically. One of the chlorine atoms in the disordered CH_2Cl_2 molecule was equally distributed over two positions. Three carbon atoms of a disordered pentane molecule were distributed at 0.6 and 0.4 occupancies and refined. A disordered CH_2Cl_2 molecule in the structure of **10** was equally distributed over two positions and refined isotropically. The other CH_2Cl_2 molecule was refined with 0.8 and 0.2 occupancies. Each of the three CH_2Cl_2 solvent molecules in the structure of **11** were distributed over two positions with equal occupancies. One carbon atom of a lattice solvent Et_2O in **12** was equally distributed over two positions and refined isotropically. Pertinent crystallographic information is provided in Table 1.1.

^{57}Fe Mössbauer Spectroscopy. Mössbauer spectra of **2**, **4**, **5**, and **7** were obtained on an MS1 spectrometer (WEB Research Co.) with a ^{57}Co source in a Rh matrix maintained at room temperature in the MIT Department of Chemistry In-

strumentation Facility. Solid samples were prepared by suspending ~0.04 mmol of the powdered material in Apeizon N grease and packing the mixture into a nylon sample holder. All data were collected at 4.2 K and the isomer shift (δ) values are reported with respect to natural iron foil that was used for velocity calibration at room temperature. The spectra were fit to Lorentzian lines by using the WMOSS plot and fit program.⁵⁴

Magnetic Susceptibility. Magnetic susceptibility data for polycrystalline powders of **4**, **5**, and **7** were measured between 5 K and 300 K with applied magnetic fields of 0.5 T using a Quantum Design MPMS SQUID susceptometer. Samples were loaded in gel capsules under nitrogen and suspended in plastic straws. Data were corrected for the magnetism of the sample holder, which was independently determined at the same temperature range and field. Underlying diamagnetism of the sample was estimated from Pascal's constants.⁵⁵ The molar magnetic susceptibility data were fit to the expression derived from the spin-only isotropic HDvV exchange Hamiltonian $\mathcal{H} = -2J\mathbf{S}_1 \cdot \mathbf{S}_2$, where $\mathbf{S}_1 = \mathbf{S}_2 = 2$. This expression is given in eq 1, where $x = J/kT$. No corrections were made for TIP or paramagnetic impurities.

$$\chi_M = \frac{N g^2 \mu_B^2}{kT} \frac{2e^{2x} + 10e^{6x} + 28e^{12x} + 60e^{20x}}{1 + 3e^{2x} + 5e^{6x} + 7e^{12x} + 9e^{20x}} \quad (1)$$

Results

Ligand Synthesis and Initial Metallation Attempts. A tandem benzyne generation–nucleophilic capture–electrophilic quench protocol, involving a modification^{43b} of the Hart reaction,^{43a} afforded gram quantities of Ar'CO₂H (Ar' = Ar^{Tol} or Ar^{4-FPh}) as crystalline solids. The corresponding metal salts, MO₂CAr' (M = Tl or Na), were readily obtained by treating the free acid with either TlOEt or NaOH. They were used in anion metathesis reactions with FeBr₂

or $\text{Fe}(\text{OTf})_2 \cdot 2\text{MeCN}$ in anhydrous THF. When reactions between FeBr_2 and 2 equiv of $\text{TiO}_2\text{CAr}^{\text{Tol}}$ were conducted for less than ~3 h in THF, yellow blocks of $[\text{Fe}_2(\mu\text{-O}_2\text{CAr}^{\text{Tol}})_2(\text{THF})_2\text{Br}_2]$ (**1**) were obtained following recrystallization from CH_2Cl_2 /pentanes. The crystal structure of **1** is shown in Figure 1.2; selected bond lengths and angles are listed in Table 1.2. The two iron atoms in **1** are connected by two μ -1,3-bridging carboxylate ligands that span a $\text{Fe}\cdots\text{Fe}$ distance of 3.5684(13) Å. Terminal bromide and THF ligands complete the pseudo-tetrahedral coordination of iron. Since **1** did not contain the desired $\{\text{Fe}_2(\text{O}_2\text{CAr}^{\text{Tol}})_4\}$ unit, it was not further characterized.

Synthesis and Structural Characterization of Doubly-Bridged Diiron(II) Complexes $[\text{Fe}_2(\mu\text{-O}_2\text{CAr}^{\text{Tol}})_2(\text{O}_2\text{CAr}^{\text{Tol}})_2\text{L}_2]$, L = THF (2**), MeCN (**3**), pyridine (**4**), and 1-MeIm (**5**).** Compound **2** (Figure 1.3) was prepared in good yield (~77%) from a reaction between FeBr_2 and 2 equiv of $\text{TiO}_2\text{CAr}^{\text{Tol}}$ in anhydrous THF. An extended reaction period (> 10 h) was required for complete metathesis of bromide with the carboxylate ligands (vide supra). The two five-coordinate iron atoms in **2** are related by a crystallographic inversion center. The relatively long $\text{Fe}\cdots\text{Fe}$ separation of 4.2822(7) Å is spanned by two bridging carboxylate ligands. The unsymmetrical *syn,syn*-bidentate mode of μ -1,3 carboxylate ligand coordination is reflected by distinctive Fe-O-C angles of 156.64(19)° and 135.98(18)°. These wide angles are a consequence of the long intermetallic distance. The remaining coordination sites are occupied by THF and bidentate terminal carboxylate ligands, which complete the distorted trigonal bipyramidal coordination geometry. The same air-sensitive compound can be prepared in comparable yield (~67%) from $\text{Fe}(\text{OTf})_2 \cdot 2\text{MeCN}$ and 2 equiv of $\text{NaO}_2\text{CAr}^{\text{Tol}}$ in THF.

The weakly bound THF molecules in **2** can be readily displaced by N-donor ligands (L), allowing access to derivatives sharing the common molecular

formula $[\text{Fe}_2(\mu\text{-O}_2\text{CAr}^{\text{Tol}})_2(\text{O}_2\text{CAr}^{\text{Tol}})_2\text{L}_2]$ (Scheme 1.1). Simply by recrystallizing **2** in a mixture of MeCN/CH₂Cl₂/pentanes, we obtained **3** (Figure 1.4) in good yield (~79%). Two essentially identical dinuclear complexes were identified in the crystallographic asymmetric unit, for which comparable Fe...Fe distances of 3.9602(13) and 3.9754(12) Å were observed. Upon treating a CH₂Cl₂ solution of **2** with 2 equiv of pyridine, the reaction mixture turned intense yellow, and pale ivory microcrystals of **4** immediately deposited. As shown in Figure 1.5, a crystallographic inversion center in **4** requires the two iron and four oxygen atoms of the μ -1,3 carboxylates to lie in the same plane. Two pyridine and two terminal carboxylate ligands are disposed anti to each other across this {Fe₂O₄} plane, a situation similar to that in **2** and **3**. When **2** was allowed to react with 2 equiv of 1-methylimidazole (1-MeIm), colorless crystals of **5** were obtained following recrystallization from CH₂Cl₂/pentanes. X-ray structure analysis revealed two chemically identical but crystallographically inequivalent molecules of **5** in the unit cell (Figure 1.6). In one molecule, the terminal carboxylates are bidentate chelating, as in **2**, **3**, and **4**, whereas these ligands have undergone carboxylate shifts to afford monodentate terminal coordination and four-coordinate iron centers in the other molecule. The Fe...Fe separation is not significantly affected by this structural variation. Comparable intermetallic distances of 4.2029(10) Å and 4.1967(11) Å were obtained for the 4,4-coordinate and 5,5-coordinate complex, respectively. Selected bond lengths and angles in **2**–**5** are listed in Table 1.2.

Strict exclusion of $\text{TiO}_2\text{CAr}^{\text{Tol}}$ impurity from the reaction mixture is essential for the preparation of pure **4** and **5**. When similar synthetic procedures were followed by using a crude batch of **2**, heterodimetallic complexes $[\text{FeTi}(\mu\text{-O}_2\text{CAr}^{\text{Tol}})_3\text{L}]$ ($\text{L} = \text{C}_5\text{H}_5\text{N}$ or 1-MeIm) were isolated. The structures of these compounds were determined by X-ray crystallography.^{56,57} Two chemically equivalent $[\text{FeTi}(\mu\text{-O}_2\text{CAr}^{\text{Tol}})_3(\text{C}_5\text{H}_5\text{N})]$ molecules were identified in the unit cell,

which have comparable Fe...Tl distances of 3.7100(14) Å and 3.7425(10) Å (Figure 1.7). In one molecule, the four-coordinate iron atom has three carboxylate oxygen and one pyridine nitrogen atom donors, affording trigonal pyramidal ($N_{\text{axial}}\text{-Fe-O}_{\text{base}} = 88.6(2) - 98.9(2)^\circ$) stereochemistry. In the other molecule, one of the three μ -1,3 bridging carboxylate ligands shifts to become μ -1,1 bridging as well as bidentate chelating to iron. Consequently, the coordination number of the iron atom increases from four to five. The highly distorted trigonal pyramidal geometry adopted by the iron center is reflected by the $N_{\text{axial}}\text{-Fe-O}_{\text{axial}}$ angle of $138.9(2)^\circ$. Unlike $[\text{FeTl}(\mu\text{-O}_2\text{CAr}^{\text{Tol}})_3(\text{C}_5\text{H}_5\text{N})]$, the pseudo-tetrahedral iron atom in $[\text{FeTl}(\mu\text{-O}_2\text{CAr}^{\text{Tol}})_3(1\text{-MeIm})]$ is connected to the thallium atom ($\text{Fe}\cdots\text{Tl} = 3.6014(6)$ Å) by two μ -1,3 and one μ -1,1 bridging carboxylate ligands (Figure 1.8).

As shown in Figures 1.7 and 1.8, the thallium(I) ion in these compounds is coordinated to three carboxylate oxygen atoms (Tl-O , 2.589(4) – 2.766(4) Å) and further bound to *p*-tolyl groups on the μ -1,3 carboxylate ligands. The pseudo- C_3 symmetric conical cavity and the $\text{Tl}\cdots\text{arene}$ interaction in $[\text{FeTl}(\mu\text{-O}_2\text{CAr}^{\text{Tol}})(\text{C}_5\text{H}_5\text{N})]$ are illustrated in Figure 1.7. The $\text{Tl}\cdots\text{arene}_{\text{centroid}}$ distances range from 3.24 to 3.67 Å with an average of 3.43 Å, compared to a value of 3.73 Å for the sum of their van der Waals radii.⁵⁸ In $[\text{FeTl}(\mu\text{-O}_2\text{CAr}^{\text{Tol}})_3(1\text{-MeIm})]$, only two *p*-tolyl groups interact with Tl ($\text{Tl}\cdots\text{arene}_{\text{centroid}} = 3.15$ and 3.50 Å). The $\text{Tl}\cdots\text{arene}_{\text{centroid}}$ distances for other structurally characterized compounds range between 2.85 and 3.22 Å.⁵⁹ The $[\text{FeTl}(\mu\text{-O}_2\text{CAr}^{\text{Tol}})_3\text{L}]$ module might serve as a starting material for transmetallation reactions with appropriate metal halides (MX_n) that could afford heterodimetallic compounds of the kind $[\text{FeM}(\mu\text{-O}_2\text{CAr}^{\text{Tol}})_3\text{L}]\text{X}_{n-1}$, following loss of one equiv of TlX .

Synthesis and Structural Characterization of Triply- and Quadruply-Bridged Diiron(II) Complexes $[\text{Fe}_2(\mu\text{-O}_2\text{CAr}^{\text{Tol}})_3(\text{O}_2\text{CAr}^{\text{Tol}})(2,6\text{-lutidine})]$ (6) and $[\text{Fe}_2(\mu\text{-O}_2\text{CAr}^{\text{Tol}})_4(4\text{-}^t\text{BuC}_5\text{H}_4\text{N})_2]$ (7). A triply-bridged diiron(II) complex 6

was obtained by treating a CH₂Cl₂ solution of **2** with 2,6-lutidine. Even when an excess (> 10 equiv) amount of 2,6-lutidine was used, only one equivalent of the N-donor ligand was incorporated upon displacement of two THF molecules from **2**. The crystal structure of **6** is shown in Figure 1.9; selected bond distances and angles are available in Table 1.3. Unlike the di(μ -carboxylato)diiron(II) complexes **2–5**, in **6** the two iron atoms are not symmetry-related, but are bridged by three μ -1,3 carboxylate ligands. The Fe...Fe distance of 3.2342(4) Å is significantly shorter than those (3.9602(13) – 4.2822(7) Å) in the doubly-bridged complexes **2–5**. Coordination of two different terminal ligands, a bidentate carboxylate and 2,6-lutidine, renders the diiron(II) core asymmetric. One iron atom (Fe1) is five-coordinate with all oxygen donors; the other (Fe2) is four-coordinate with a NO₃ donor atom set.

Substitution of THF ligands in **2** with 2 equiv of 4-*tert*-butylpyridine afforded the paddle-wheel compound **7**. Air-sensitive yellow blocks of **7** were obtained following recrystallization from CH₂Cl₂/Et₂O. The same compound can be directly prepared by a reaction between Fe(OTf)₂·2MeCN, NaO₂CAr^{Tol}, and 4-*tert*-butylpyridine in a 1:2:1 ratio. The crystal structure of **7** is depicted in Figure 1.10; selected bond distances and angles are listed in Table 1.3. The Fe...Fe distance is 2.8229(9) Å and there are four μ -1,3 carboxylate ligands disposed around a pseudo-C₄ axis along the Fe–Fe vector. The crystallographically inequivalent iron(II) centers have similar square-pyramidal coordination geometries with comparable average Fe–O distances of 2.09(6) Å for Fe(1) and 2.09(7) Å for Fe(2).

Doubly- and Quadruply-Bridged Diiron(II) Complexes Having Identical Ligand Combinations: Synthesis and Structural Characterization of [Fe₂(μ -O₂CAr^{4-FPh})₂(O₂CAr^{4-FPh})₂(THF)₂] (8**) and [Fe₂(μ -O₂CAr^{4-FPh})₄(THF)₂] (**9**).** Reaction of Fe(OTf)₂·2MeCN with 2 equiv of NaO₂CAr^{4-FPh} in anhydrous THF afforded colorless blocks of **8** in modest yield (~50%). The crystal structure of **8** is

shown in Figure 1.11; selected bond lengths and angles are listed in Table 1.2. The lateral width occupied by the *m*-terphenyl unit is diminished when the 2,6-substituents are changed from *p*-tolyl to 4-fluorophenyl groups. The corresponding van der Waals radii of CH₃ and F are 2.0 Å and 1.47 Å, respectively.^{58,60} The solid state geometry of **8**, however, is similar to that of the analogous THF complex **2** prepared from Ar^{Tol}CO₂⁻, suggesting that the steric properties of Ar^{4-FPh}CO₂⁻ are comparable to those of Ar^{Tol}CO₂⁻. Unlike **2**, two chemically equivalent dinuclear units of **8** were identified in the unit cell. In one molecule, the terminal carboxylate ligands are bidentate, affording five-coordinate iron centers. In the other molecule, monodentate coordination of terminal carboxylate renders the iron centers four-coordinate. The co-existence of both 4,4- and 5,5-coordinate diiron(II) complexes in the same crystal is reminiscent of the situation in **5**. The metal...metal separation is not significantly affected by this structural variation, as indicated by the comparable intermetallic distances of 4.1869(9) Å and 4.1452(8) Å observed for the 4,4-coordinate and 5,5-coordinate complexes, respectively.

A paddle-wheel diiron(II) compound **9** was obtained as a product of an unsuccessful attempt to oxidize **8** with 2 equiv of [Cp₂Fe](PF₆) in CH₂Cl₂. Pale green blocks were obtained by recrystallization from CH₂Cl₂/pentanes and analyzed by X-ray crystallography. The crystal structure of **9** is shown in Figure 1.12; selected bond lengths and angles are listed in Table 1.3. As in **7**, there are four bridging carboxylate ligands related by a pseudo-C₄ axis along the Fe-Fe vector. The metal...metal distance of 2.7277(7) Å is significantly shorter than those of the doubly-bridged dimetallic cores in the precursor complex **8**. Although further characterization of this compound was hampered by contamination with unidentified dark colored materials, the structure of **9** clearly indicates that both doubly- and quadruply-bridged isomers of a diiron(II) complex can be

accessed from an identical ligand set, and their interconversion is likely to occur in solution (*vide infra*).

Synthesis and Structural Characterization of Quadruply-Bridged Diiron(II) Complexes $[\text{Fe}_2(\mu\text{-O}_2\text{CAr}^{4\text{-FPh}})_4\text{L}_2]$, $\text{L} = \text{C}_5\text{H}_5\text{N}$ (**10**), 1-MeIm (**11**), and 4-^tBuC₅H₄N (**12**). Neutral paddle-wheel diiron(II) compounds **10–12** were conveniently prepared by ligand substitution of **8** with 2 equiv of the appropriate N-donor ligand (Scheme 1.2). Recrystallization from CH₂Cl₂/pentanes afforded X-ray quality crystalline materials in modest yields (44–67%). The crystal structures of **10–12** are shown in Figures 1.13–1.15; selected bond distances and angles are listed in Table 1.3. The metal centers in **10–12** all have square pyramidal geometry similar to that of the Ar^{Tol}CO₂[−]-supported analog **7**. All metric parameters are normal and the Fe...Fe distances range from 2.8247(5) to 2.8475(7) Å.

Mössbauer Spectroscopy. Zero-field Mössbauer spectra of solid samples of **2**, **4**, **5**, and **7** were collected at 4.2 K. Figures 1.16 and 1.17 display the spectra; the corresponding parameters derived from fits of the spectra are provided in Table 1.4 along with those of related diiron(II) centers in non-heme enzymes.^{9,12,61–65} Compounds **2** and **4** exhibit single sharp ($\Gamma = 0.25 - 0.28 \text{ mm s}^{-1}$) quadrupole doublets, consistent with two iron centers related by a crystallographic inversion center. Although there are two crystallographically unique iron sites in **7**, their nearly identical coordination environments produce unresolved Mössbauer spectra with a sharp ($\Gamma = 0.24 - 0.26 \text{ mm s}^{-1}$) quadrupole doublet. Significant broadening of the peaks ($\Gamma = 0.34 - 0.40 \text{ mm s}^{-1}$) occurs for **5**, however, which exists in two crystallographically inequivalent dinuclear units in the solid state (*vide supra*). No attempt was made to deconvolute the unresolved quadrupole doublet into contributions from the 4,4-coordinate and 5,5-coordinate components. The isomer shifts and quadrupole splittings of **2**, **4**, **5**, and **7** are typical of high-spin iron(II) sites in a N/O coordination environment^{19,66,67} and

comparable to those obtained for related biological clusters (Table 1.4).^{1b,1f} The similar Mössbauer parameters obtained for **2**, **4**, and **5** suggest that the electronic environment around the metal center is not significantly perturbed upon ligand substitution within the $[\text{Fe}_2(\mu\text{-O}_2\text{CAr}^{\text{Tot}})_2(\text{O}_2\text{CAr}^{\text{Tot}})\text{L}_2]$ module.

Magnetic Susceptibility Studies. The two iron(II) centers in the di(μ -carboxylato)diiron(II) compounds **4** and **5** display similarly weak antiferromagnetic (AF) coupling. Plots of the effective magnetic moment (μ_{eff}) and molar susceptibility (χ_{M}) versus temperature for **4** and **5** are shown in Figures 1.18 and 1.19. The measured values of $\mu_{\text{eff}} = 7.60$ (for **4**) and $7.45 \mu_{\text{B}}$ (for **5**) at 300 K are close to the theoretical value of $7.62 \mu_{\text{B}}$ calculated for the effective moment of two uncoupled $S = 2$ centers with $g = 2.2$.⁶⁸ Upon lowering the temperature, μ_{eff} gradually decreases to ca $7.0 \mu_{\text{B}}$ at 50 K, below which it rapidly drops to $4.14 \mu_{\text{B}}$ and $3.72 \mu_{\text{B}}$ at 5 K for **4** and **5**, respectively. These relatively high μ_{B} values indicate that excited magnetic states are still populated at the lowest temperature.

The magnetic susceptibility data were fit by using an expression derived from the spin-only isotropic HDvV exchange Hamiltonian $\mathcal{H} = -2J\mathbf{S}_1 \cdot \mathbf{S}_2$, where $\mathbf{S}_1 = \mathbf{S}_2 = 2$. The best fit was obtained for $J = -0.90(3) \text{ cm}^{-1}$ and $g = 2.16(1)$ for **4** (Figure 1.18). Similar treatment afforded $J = -1.04(2) \text{ cm}^{-1}$ and $g = 2.14(1)$ for **5** (Figure 1.19). This simplified analysis, however, does not take into account spin-orbit coupling and zero-field splitting (ZFS). Although the orbital contribution is significantly quenched with a deviation from ideal octahedral geometry,⁶⁹ ZFS of iron(II) complexes can be on the same order of magnitude as the exchange coupling.⁷⁰ This effect would result in a complicated energy level distribution. Given these features, it should be noted that the calculated fit may not be a unique solution for the observed magnetic behavior. Nevertheless, the weak AF coupling interaction exhibited by **4** and **5** is consistent with the absence of a more efficient exchange pathway between two iron(II) centers separated by $> 4 \text{ \AA}$. Pa-

rameters derived from fits of the curves are provided in Table 1.4 along with those of related diiron(II) centers in the biological systems.

The magnetic behavior of the paddle wheel diiron(II) compound **7**, however, is significantly different from that of **4** and **5**. The μ_{eff} vs T as well as χ_M vs T curves for **7** are displayed in Figure 1.20. The measured values of $\mu_{\text{eff}} = 6.52 \mu_B$ at 300 K is substantially lower than those of **4** and **5**, in which there are two uncoupled S = 2 centers. From 300 K to 5 K, this value almost linearly decreases to $0.42 \mu_B$ (Figure 1.20). Although this apparent strong AF coupling can be attributed to an increased number of bridging ligands as well as the shorter metal...metal distance in **7**, a satisfactory theoretical model to reproduce the magnetic behavior is currently unavailable.

¹⁹F-NMR Spectroscopic Studies. The solution structures of **8** and **12** were probed by VT ¹⁹F-NMR spectroscopy. In CH₂Cl₂ at 20 °C, **12** exhibits a sharp ($\Delta\nu_{1/2} = 43$ Hz) resonance at -117.4 ppm (Figure 1.21). This signal arises from the four μ -1,3 Ar^{4-FPh}CO₂⁻ ligands, related by the pseudo-C₄ axis along the Fe-Fe vector. The local C₂ symmetry of the Ar^{4-FPh}CO₂⁻ ligand apparently gives rise to a single fluorine resonance. The corresponding signal occurs at -115.5 ppm for diamagnetic Ar^{4-FPh}CO₂H, which shifts to -117.7 ppm upon deprotonation with excess Et₃N (data not shown). Within the temperature range of +20 – -70 °C, no significant spectral change was observed for **12** (Figure 1.21).

Under similar conditions, however, **8** displays much different spectral patterns (Figure 1.22). At 20 °C, a single broad ($\Delta\nu_{1/2} = 213$ Hz) resonance occurs at -118.5 ppm, which significantly broadens ($\Delta\nu_{1/2} = 438$ Hz) upon cooling to 10 °C. This signal splits into a set of three peaks between -120 and -116 ppm below 0 °C, with enhanced resolution at lower temperatures. At -20 °C, well-resolved three resonances occur at -120.1, -118.2, and -116.4 ppm. Notable spectral changes from -10 °C to -40 °C include sharpening of the peak at -118 ppm, along

with significant broadening of the flanking two resonances at -120 and -116 ppm. These signals become barely resolved at -50 °C. The middle resonance at -118 ppm is slightly upfield shifted upon cooling. Below -60 °C, the three peaks merge into one broad resonance, which becomes narrower upon cooling. At -80 °C, a single resonance at -115.6 ppm ($\Delta\nu_{1/2} = 508$ Hz) dominates the ^{19}F -NMR spectrum of **8**. Along with this dramatic temperature-dependent spectral change, minor fluorine-containing species were also detected. Although their presence was obscured by overlap with the major signals at certain temperature ranges, four small peaks are persistent in the spectra obtained below -60 °C. At -80 °C, peaks at -104.4, -109.1, -115.1, and -122.1 ppm are observed in addition to the major resonance at -115.6 ppm.

Discussion

Ligand Design. The development of sterically demanding ligands has significantly advanced the chemistry of low-coordinate metal complexes.^{71,72} Bulky *m*-terphenyl fragments have been previously used in main group organometallic chemistry to stabilize compounds having unusual structural or electronic properties.⁷²⁻⁷⁴ Aryloxy,⁷⁵ -thiolate,⁷⁶ -amidinate,⁷⁷ or -imide⁷⁸ derivatives having 2,6-aryl substituents stabilize coordinatively unsaturated metal sites. Conformationally well-defined aryl moieties provide binding pockets for substrates or a steric shield against unwanted side reactions of highly reactive intermediates.

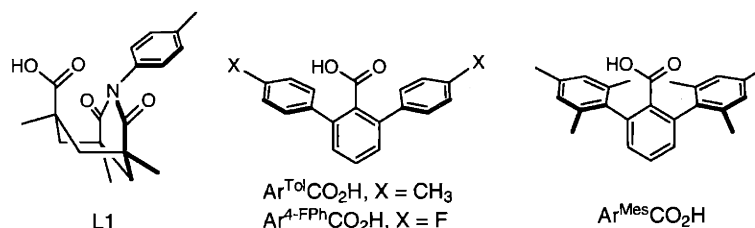
In contrast to the widespread use of the *m*-terphenyl ligand fragments mentioned above, however, analogous platforms incorporating carboxylate functionalities have found limited applications in synthetic inorganic chemistry. Prior to our initial exploration of this area, there were only two structurally characterized transition metal complexes supported by *m*-terphenyl-derived car-

boxylate ligands. They are $[\text{Rh}_2(\text{TTB})_3(\text{OAc})(\text{py})_2]$ and $[\text{Rh}_2(\text{TTB})_4(\text{py})_2]$, where $\text{TTB} = 2,4,6\text{-tri}(p\text{-tolyl})\text{benzoate}$.⁷⁹ In this case, however, the steric constraint imposed by the bulky carboxylate ligand was a liability, as indicated by the significantly reduced activity of these dirhodium(II) compounds in catalyzing the cyclopropanation of olefin substrates.⁷⁹ Related *m*-terphenyl-derived carboxylate units have been used to model host-guest interactions in organic chemistry. Encapsulation of guest components was assisted by integrating the V-shaped shallow concave cavity into a rigid cyclophane framework.^{80,81} Extended hydrophobic fragments flanking the carboxylate group facilitated recognition of organic substrates by through-space polar- π interactions.^{43c}

Our investigation of diiron complexes coordinated by *m*-terphenyl-derived carboxylate ligands was inspired by the unusual spatial orientation of the two μ -1,3 carboxylate groups supporting the diiron(II) centers in RNR-R2 and Δ 9D.^{6,8} A survey of the CSD revealed that a majority of structurally characterized carboxylate-bridged diiron complexes has triply-bridged $\{\text{Fe}_2(\mu\text{-O}_2\text{CR})_2(\mu\text{-X})\}^{n+}$ cores, where $X = \text{O}, \text{OH}, \text{or OR}$. Single atom bridging ligands X in such dinuclear centers apparently enforce a geometry in which the two bridging carboxylate ligands occupy nearly orthogonal positions of face-shared octahedral metal centers (**A**, Scheme 1.3). We envisioned that, by increasing the steric repulsion between adjacent bridging carboxylate ligands, the $\text{O}_{\text{carboxylate}}\text{-Fe-O}_{\text{carboxylate}}$ dihedral angle would open to such a degree that the triply-bridged core geometry would be highly crowded (**B**, Scheme 1.3). Formal extrusion of the single atom bridging ligand would afford the desired di(μ -carboxylato)diiron(II) cores in the resulting complexes (**C**, Scheme 1.3). For Hr models, geometries like **A** are preferred,^{37,38} whereas geometry **C** best mimics that in MMOH, RNR-R2, and Δ 9D.

Unlike amine- or phosphine-based ligands, in which the immediate metal coordination can be controlled by direct substitution on the N or P donor atoms, modifications of a carboxylate ligand can only start from the carbon α to the carboxylate group, three atoms away from the metal center. We reasoned that the desired *trans* configuration of two bridging carboxylate ligands would not be achieved simply by installing bulky substituents on the α -carbons. Steric effects of the radially disposed bulky α -substituents would propagate *away from* the metal center, significantly reducing the desired inter-ligand steric repulsion. In order to maximize such steric crowding, bulky components on carboxylate ligands should be directed *toward* the dimetallic core.

In the quest for such a ligand system, we were attracted by the unique structural features of *m*-terphenyl-derived carboxylates. In these V-shaped molecules, aryl substituents flanking the CO_2^- group are directed *toward* the oxygen atoms and terminate nearly at their level. Although such structural features are shared by the ligand L1,⁸² previously employed to support $(\mu\text{-aqua})\text{di}(\mu\text{-carboxylato})\text{dimetallic}$ cores, steric shielding around the carboxylate group within the *m*-terphenyl unit is amplified by the pseudo- C_2 symmetry within the ligand. Preliminary CPK modeling studies suggested that 2,6-di(*p*-tolyl)benzoate ($\text{Ar}^{\text{Tol}}\text{CO}_2^-$) would facilitate the assembly of the desired $\text{di}(\mu\text{-carboxylato})\text{-diiron(II)}$ cores. The requirement for the *trans*-disposed bridging carboxylate ligands in the $\{\text{Fe}_2(\mu\text{-O}_2\text{CAr}^{\text{Tol}})_2\}^{2+}$ unit minimizes steric interactions between the *p*-tolyl groups. The related ligand 2,6-di(4-fluorophenyl)benzoate ($\text{Ar}^{4\text{-FPh}}\text{CO}_2^-$)



was also targeted in order to provide a handle for solution ^{19}F -NMR spectroscopic studies.

The *m*-terphenyl unit is modular in nature and variations can be readily made on the 2,6-substituents. Electronic perturbation introduced by such variations is substantially minimized since the conjugation between the central ring and the flanking substituents is conformationally prohibited. The C–C rotation responsible for such deconjugation of the aryl system, however, renders a certain degree of conformationally flexibility to the terphenyl system, the importance of which can be highlighted by comparison with a more rigid 2,6-dimesitylbenzoate ($\text{Ar}^{\text{Mes}}\text{CO}_2^-$) system used by others (*vide infra*).⁸³

Synthetic Routes to Diiron(II) Complexes. Synthetic routes to the tetracarboxylate diiron(II) complexes developed in this investigation are summarized in Schemes 1.1 and 1.2. Neutral THF complexes **2** and **8** were readily obtained through efficient self-assembly from simple starting materials. Weakly bound THF molecules in these compounds can be readily displaced by stronger N-donor ligands such as MeCN, pyridine, 1-methylimidazole, 2,6-lutidine, or 4-*tert*-butylpyridine. This divergent synthetic strategy from a common diiron(II) precursor readily generates substantial structural diversity within the $\{\text{Fe}_2(\text{O}_2\text{CAr}')_4\}$ ($\text{Ar}' = \text{Ar}^{\text{Tol}}$ and $\text{Ar}^{4\text{-FPH}}$) platform. One of the most notable aspects of the ligand substitution reactions is the dramatic core rearrangement assisted by carboxylate shifts.⁸⁴ This feature is exemplified by the rich structural variety of doubly-, triply-, and quadruply-bridged diiron(II) complexes supported by $\text{Ar}^{\text{Tol}}\text{CO}_2^-$ and $\text{Ar}^{4\text{-FPH}}\text{CO}_2^-$ (Figure 1.23).

Structural Models of $\Delta 9\text{D}$ and RNR-R2 Active Sites. Compounds **1–5** and **8** belong to a rare class of diiron(II) compounds in which two metal centers are bridged solely by two carboxylate ligands. This structural motif is encountered at diiron(II) centers in the active sites of reduced RNR-R2 and $\Delta 9\text{D}$,^{6,8} as

well as that in MMOH_{red} ,^{10,11} and shared by a few structurally characterized complexes such as $[\text{Fe}_2(\mu\text{-OAc})_2(\text{TPA})_2](\text{BPh}_4)_2$,³² $[\text{Fe}_2(\mu\text{-OAc})_2(\text{BPMEN})_2](\text{ClO}_4)_2$,³³ and $[\text{Fe}_2(\mu\text{-O}_2\text{CPh})_2(\text{O}_2\text{CPh})_2(\text{C}_5\text{H}_5\text{N})_4]$.^{8,5} Although the doubly-bridged dimetallic cores in these compounds are reminiscent of those in non-heme diiron enzyme active sites, neither the ligand type/composition nor the coordination geometry reproduce the properties of their biological counterparts. Polyamine/imine ancillary capping ligands render the metal coordinatively saturated with no open coordination sites available for exogenous ligand binding. This structural feature has a significant influence on the reactivity. For example, $[\text{Fe}_2(\mu\text{-OAc})_2(\text{TPA})_2]^{2+}$ dissociates into two monomeric units in order to react with dioxygen.³² Di(μ -carboxylato)diiron(II) complexes having coordinatively unsaturated metal centers were previously unknown in synthetic inorganic chemistry.

The diiron(II) core structure of **4** bears a close structural resemblance to the catalytic site of $\Delta 9\text{D}$ (Figure 1.24). The two μ -1,3-bridging carboxylate ligands of the model simulate the Glu143 and Glu229 residues, which span two iron(II) centers in the protein. Bidentate binding of Glu105 and Glu196, as well as the coordination of two nitrogen donors, His146 and His232, are reproduced by the terminal carboxylate and pyridine ligands. The Fe...Fe separation of 4.2189(13) Å in **4** models the corresponding value of 4.2 Å in $\Delta 9\text{D}$.⁸ This relatively long metal...metal distance results from steric interactions between bridging and terminal carboxylate ligands, as clearly indicated by the solid state structures of the related compounds **1** and **2** (Figure 1.25). Here the identical $\{\text{Fe}_2(\mu\text{-O}_2\text{CAr}^{\text{Tol}})_2(\text{THF})_2\}^{2+}$ cores are capped either by Br^- (**1**) or by a bidentate $\text{Ar}^{\text{Tol}}\text{CO}_2^-$ (**2**) ligand. Steric repulsion between the *p*-tolyl groups on the bridging and terminal carboxylate ligands apparently pushes the two iron atoms away from each other, increasing the Fe...Fe distance by as much as ca 0.7 Å, from

3.568(1) Å in **1** to 4.2822(7) Å in **2**. The geometry of the first coordination sphere thus can be tuned by non-covalent interaction in the second coordination sphere, which comprises four interlocking *m*-terphenyl units. Although the diiron core in **4** is effectively shielded by these sterically hindered ligands, the open coordination site of the five-coordinate iron atom is well-exposed (Figure 1.5) for reaction with exogenous reagents including dioxygen.⁴⁶

Features of the doubly-bridged four-coordinate diiron(II) centers in the active site of RNR-R2 are mimicked by **5** (Figure 1.26).⁶ The coordination of μ -1,3 bridging Glu115 and Glu238, terminal monodentate Asp84 and Glu204, and N-donor His118 and His241 residues in the protein are faithfully represented by the diiron(II) core in 4,4-coordinate **5**. The Fe...Fe separation of 4.2029(10) Å is comparable to that (3.9 Å) in the protein. The Mössbauer and magnetic parameters of **4** and **5** are comparable to the corresponding properties of Δ 9D and RNR-R2, for which weak AF coupling between high-spin iron(II) centers afford a $S = 0$ ground state (Table 1.4).

Notable structural features of **5** include the co-existence of 4,4-coordinate and 5,5-coordinate dinuclear complexes in the crystal lattice. This structural variation results from a shift in the denticity of the terminal carboxylate ligand, which can be correlated to the electron density at the metal center. Coordination of more electron-donating ligands attenuates the Lewis acidity at the metal center, inducing a carboxylate shift from bidentate to monodentate in low-spin cobalt(III) complexes.⁸⁶ Recent structural analyses of a series of dinuclear and mononuclear iron(II) complexes having different N-donor ligands also corroborate this notion.^{39,83c} Accordingly, the shift in the coordination number from pyridine-bound five-coordinate iron (**4**) to 1-methyl-imidazole-bound four-coordinate iron (**5**) may be rationalized by invoking the enhanced donor ability (pyridine < 1-methylimidazole) of the ancillary ligand. The co-existence of both

five-coordinate and four-coordinate metal centers in the solid state structure of **5**, however, calls into question the generality of such a rationale. A simple electronic model does not explain the fact that **8** also exists as both 4,4- and 5,5-coordinate dimers in the solid state. Moreover, in the corresponding $\text{Ar}^{\text{Tol}}\text{CO}_2^-$ -supported THF complex **2**, the iron(II) centers are five-coordinate. This shift to lower coordination number as the carboxylate becomes less electron-donating ($\text{Ar}^{4\text{-FPh}}\text{CO}_2^- < \text{Ar}^{\text{Tol}}\text{CO}_2^-$) is difficult to rationalize.

Taken together, these findings suggest that both four- and five-coordinate iron(II) centers may be readily accessible in tetracarboxylate diiron(II) cores without significant thermodynamic penalty. Interconversion between these isoenergetic units can be facilitated by carboxylate shifts,⁸⁴ which may be relevant to the different coordination numbers determined for the diiron(II) centers of $\Delta 9\text{D}$ (5,5-coordinate)⁸ and RNR-R2 (4,4-coordinate)⁶ by X-ray crystallography, and RNR-R2 (4,5-coordinate) by CD and MCD studies.⁶⁴ The energetics of different coordination modes of carboxylate ligands were studied by DFT calculations on zinc(II) complexes $[\text{Zn}(\text{OAc})_x\text{L}_y]^{n+}$.⁸⁷ The potential energy surface of carboxylate coordination in this model is extremely flat and, depending on the ancillary ligands, the interconversion between bidentate and monodentate coordination can be almost barrierless.

Although **4** and **5** faithfully reproduce the ligand composition and coordination number of the diiron(II) active sites of $\Delta 9\text{D}$ and RNR-R2, certain limitations exist. The relative positioning of the N-donor ligands is different. They are disposed anti in the model compound (Figure 1.23) and syn in the protein (Figure 1.1). If such an asymmetric ligand arrangement is crucial in order to bind substrates in the right orientation, the symmetry-related iron sites in **4** or **5** may not be ideal for the desired biomimetic chemical transformations. Spatial disposition of the ancillary ligands can have a significant influence on chemical reac-

tivity by affecting the structures and energies of the molecular orbitals involved. These stereoelectronic issues remain to be addressed by future work.

Ligand Substitution and Core Rearrangement. Unlike dinucleating dicarboxylate ligands such as XDK or Ph₄DBA,^{29,34,37} unrestricted motion of the carboxylate ligands within the self-assembled [Fe₂(μ-O₂CAr')₄L₂] (Ar' = Ar^{Tol} and Ar^{4-FPh}) module allows significant structural flexibility. The interlocking *m*-terphenyl moieties apparently help to sustain the dinuclear core units during ligand substitution, a process that requires displacement of terminal ligands and interconversion between bridging and terminal carboxylates.

Depending on the choice of N-donor ligands, doubly-, triply-, or quadruply-bridged diiron(II) cores can be accessed (Schemes 1.1 and 1.2). Reaction of **2** with MeCN, pyridine, or 1-methylpyridine introduces minimal structural perturbation at the metal centers. The {Fe₂(μ-O₂CAr^{Tol})₂(O₂CAr^{Tol})₂} core structure is retained. Shifts of one or two carboxylate ligands occur, however, upon ligand substitution of **2** with 2,6-lutidine or 4-*tert*-butylpyridine. One possible mechanism for such core conversions is postulated in Scheme 1.4. Formal shift of one carboxylate from terminal bidentate to μ-1,3-bridging is triggered by displacing the THF ligand in **2** with 2,6-lutidine. The two α-methyl groups of 2,6-lutidine induce steric crowding around the Fe–N bond, lowering the coordination number of Fe(2) from five to four. Such a carboxylate shift would displace the THF ligand on Fe(1) and afford the asymmetric 4,5-coordination encountered in **6**. The metal...metal distance of 3.2342(4) Å in the triply-bridged diiron(II) core of **6** is significantly shortened from the 4.2822(7) Å value of the doubly-bridged precursor **2**. Comparable Fe...Fe distances of 3.51 – 3.67 Å occur in the tri(μ-carboxylato)-diiron(II) centers supported by XDK derivatives.^{35,39}

Formal double carboxylate shifts within the {Fe₂(μ-O₂CAr^{Tol})₂(O₂CAr^{Tol})₂} unit triggered by ligand substitution would afford the paddle wheel complex **7**

(Scheme 1.4). The 4-*tert*-butylpyridine ligand was initially employed to enhance the solubility of **4**, which hampered solution spectroscopic studies. The bulky 4-*tert*-butyl group was installed distal to the N-donor atom, in order to minimize structural perturbation. A space-filling model indicated little steric crowding in the desired compound $[\text{Fe}_2(\mu\text{-O}_2\text{CAr}^{\text{Tol}})_2(\mu\text{-O}_2\text{CAr}^{\text{Tol}})_2(4\text{-}^t\text{BuC}_5\text{H}_4\text{N})_2]$. The quadruply-bridged diiron(II) core in **7**, therefore, was not anticipated before its structural characterization by X-ray crystallography. Although two metal ions bridged by four carboxylate ligands define a well-known unit in inorganic chemistry, **7** is only the third structurally characterized example in iron(II) chemistry. The others are $[\text{Fe}_2(\mu\text{-O}_2\text{CCMe}_3)_4(\text{C}_5\text{H}_5\text{N})_2]$ and $[\text{Fe}_2(\mu\text{-O}_2\text{CPh})_4(\text{C}_5\text{H}_5\text{N})_2]$.⁸⁵ A gradual decrease in metal...metal distance with additional bridging ligands places the Fe...Fe distance of 2.8229(9) Å in **7** at the low end of the range obtained for the $\text{Ar}^{\text{Tol}}\text{CO}_2^-$ -based tetracarboxylate diiron(II) complexes (Tables 1.2 and 1.3). Comparable metal...metal distances of 2.792 and 2.851 Å were obtained for $[\text{Fe}_2(\mu\text{-O}_2\text{CCMe}_3)_4(\text{C}_5\text{H}_5\text{N})_2]$ and $[\text{Fe}_2(\mu\text{-O}_2\text{CPh})_4(\text{C}_5\text{H}_5\text{N})_2]$, respectively.⁸⁸ Unlike the paddle wheel complexes supported by small carboxylate ligands, however, the spatial arrangement of the *p*-tolyl groups on the $\text{Ar}^{\text{Tol}}\text{CO}_2^-$ generates a unique steric environment for the N-donor ligands. There is a pseudo- C_4 axis along the Fe–Fe vector in **7** and the four *p*-tolyl groups on either side of the dimetallic center are disposed nearly orthogonal to each other along this axis. The roughly parallel orientation of the *p*-tolyl planes along the Fe–Fe vector results in a tetragonal pocket surrounding the axial position of the square pyramidal iron(II) centers. In order to minimize steric repulsion with the *p*-tolyl groups, pyridine rings lie along the diagonal inside the cavity and rotation around the Fe–N bond is significantly restricted. Preliminary DFT calculations indicate that such rotation barrier is dominated by steric factors, and the near orthogonal orientation of the pyridine rings is favored both sterically and

electronically.⁸⁹ The dihedral angle between the two pyridine rings in **7** is 71.4(2)°. Detailed theoretical studies are in progress to address the energetic consequence of such stereochemical preferences.

Doubly- vs Quadruply-Bridged Tetracarboxylate Diiron(II) Complexes.

Two geometric isomers, $[\text{Fe}_2(\mu\text{-O}_2\text{CAr}^{4\text{FPh}})_2(\text{O}_2\text{CAr}^{4\text{FPh}})_2(\text{THF})_2]$ (**8**) and $[\text{Fe}_2(\mu\text{-O}_2\text{CAr}^{4\text{FPh}})_4(\text{THF})_2]$ (**9**), were obtained for $[\text{Fe}_2(\text{O}_2\text{CAr}^{4\text{FPh}})(\text{THF})_2]$. Isolation and structural characterization of **8** and **9** strongly indicate that both doubly- and quadruply-bridged diiron(II) cores can be accessed without substantial steric or electronic preference under the conditions employed.

The substitution reactions of **8** with N-donor ligands afford only quadruply-bridged diiron(II) complexes (**10–12**), whereas both doubly- and quadruply-bridged complexes are accessible by similar synthetic routes from **2**. As evident from Schemes 1.1 and 1.2, no obvious correlation can be drawn between the preferred solid state structures and the steric/electronic properties of the ancillary ligands within a homologous series. For example, both pyridine and 4-*tert*-butylpyridine afford tetra(μ -carboxylato)diiron(II) cores supported by $\text{Ar}^{4\text{FPh}}\text{CO}_2^-$, whereas they provide doubly- and quadruply-bridged diiron(II) complexes, respectively, for the $\text{Ar}^{\text{Tol}}\text{CO}_2^-$ system. Although the ability to acquire X-ray crystal structures of these complexes assured their structural homogeneity in the solid state, there is no clear answer as to why a given complex prefers one isomer over the other and how both isomers can be accessed for a certain ligand combination.

These findings led us to speculate that at least two isomeric forms exist for $[\text{Fe}_2(\mu\text{-O}_2\text{CAr}')_4\text{L}_2]$ complexes in solution, the interconversion between which is assisted by carboxylate shifts (Scheme 1.5). Equilibration among these species can be affected by various factors including solvent polarity and temperature. At the early stage of crystallization, a weak packing interaction may lead to selective

deposition of one isomer, and the thermodynamically driven crystallization process can afford structural homogeneity in the solid state. In order to probe the possibility that such dynamic structural rearrangements occur within the tetracarboxylate diiron(II) platform, solution NMR studies were carried out.

Structural Rearrangement Probed by VT ^{19}F -NMR Spectroscopy. The presence of fluorine nuclei in the $\text{Ar}^{4\text{-FPh}}\text{CO}_2^-$ ligands allowed the use of ^{19}F -NMR spectroscopy to investigate the solution structures of **8** and **12**, despite their paramagnetism. ^{19}F -NMR spectroscopy is a good structural probe for paramagnetic iron(II) or cobalt(II) complexes.^{82,90-92} The number and symmetry of the species in solution can often be inferred from the spectral pattern, which is significantly simplified compared with that of ^1H -NMR.

Unlike the large isotropic shifts ($\Delta\text{ppm} > \sim 55$) of iron(II)-bound CF_3CO_2^- or OTf^- ,^{90,92} coordinated $\text{Ar}^{\text{F}}\text{CO}_2^-$ ligands in **8** and **12** display resonances (-118.5 – -117.4 ppm) only slightly shifted from that (-117.7 ppm) of the diamagnetic free $\text{Ar}^{\text{F}}\text{CO}_2^-$ anion at 20°C . This narrow range of chemical shifts may result from the relatively long $\text{F}\cdots\text{Fe}$ distances of $> \sim 5.87$ Å in **8** and $> \sim 5.62$ Å in **12**, as well as by the absence of efficient spin delocalization pathways. Nevertheless, the temperature-dependent changes in the ^{19}F -NMR spectral patterns are markedly different for **8** and **12**, allowing us to draw conclusions about the solution behavior.

Consistent with the pseudo- C_4 symmetry found for the paddle wheel structure of **12** in the solid state, a single fluorine resonance was observed at 20°C . Combined with the local pseudo- C_2 symmetry of the $\text{Ar}^{\text{F}}\text{CO}_2^-$ ligand, the disposition of the four ligand fragments along the $\text{Fe}\text{--}\text{Fe}$ vector places the eight fluorine nuclei at the corners of an approximately rectangular parallelepiped. The $\text{F}\cdots\text{Fe}$ distances are distributed over a narrow range of 5.62 – 6.22 Å in the solid state and the fluorine atoms experience similar local magnetic environ-

ments. This simple spectral pattern is displayed from +20 – -70 °C, suggesting that the quadruply-bridged core structure of **12** is retained in CH₂Cl₂ over this temperature range.

A significantly broadened ($\Delta\nu_{1/2} = 213$ Hz) fluorine resonance of **8**, compared with that ($\Delta\nu_{1/2} = 43$ Hz) of **12**, at 20 °C indicates either rapid equilibration between multiple Ar^FCO₂⁻-containing species or different chemical environments for the fluorine nuclei of a single species. Either explanation can be invoked in order to explain the dramatic spectral change of **8** from +20 to -80 °C (Figure 1.22). As depicted in Scheme 1.6, we postulate an equilibration between doubly-bridged (**D** and **D'**) and quadruply-bridged (**E**) isomers of [Fe₂(O₂C-Ar^{4-FPh})₄(THF)₂] in CH₂Cl₂ at 20 °C. This assignment is strongly supported by the isolation of **8** and **9** (vide supra) at room temperature (~25 °C). The individual fluorine signals arising from such an equilibrium mixture are unresolved above +10 °C, which we ascribe to dynamic interconversion between isomers. Three distinct peaks emerge below 0 °C. Such a pattern could be accounted for by the μ -1,3-bridging and terminal Ar^{4-FPh}CO₂⁻ ligands in **D**, which are rendered inequivalent due to their different chemical environments (Scheme 1.6). Alternatively, the sharp peak in the middle of the three signals can be assigned to **E**, by analogy to the narrow fluorine resonance observed for **12** under similar conditions. With the latter model, the two broader flanking signals are assigned to the μ -1,3-bridging and terminal carboxylate ligands in **D**. The ¹H-NMR spectrum obtained for the diamagnetic compound [Zn₂(μ -O₂CAr^{Tol})₂(O₂CAr^{Tol})₂(C₅H₅N)₂], which is structurally related to **D**, displays two different methyl resonances at 2.07 and 2.02 ppm in CH₂Cl₂ at 20 °C.⁹³ This behavior is consistent with the different magnetic environments of the *p*-tolyl groups on the bridging and terminal Ar^{Tol}CO₂⁻ ligands. A mixture of **D/D'** and **E** would result in the three major fluorine resonances observed experimentally. The lack of definitive

peak assignments, however, precluded quantitative analysis of the dynamic processes in solution.

At lower temperatures, the exchange rate of the carboxylate ligands in **D** between the bridging and terminal positions slows down, as reflected by significant broadening of the signals at -116 and -120 ppm, which merge into the resonance arising from **E**. Below -60 °C, **D** eventually converts to **E** and a single fluorine signal from its equivalent $\text{Ar}^{4\text{-FPh}}\text{CO}_2^-$ groups dominate the spectra. The four well-resolved small peaks between -104 and -122 ppm, partially overlapping the major fluorine resonances, may arise from other $\text{Ar}^{4\text{-FPh}}\text{CO}_2^-$ -containing species. One possibility would be a triply-bridged diiron(II) species structurally related to the $\text{Ar}^{\text{Tol}}\text{CO}_2^-$ -supported complex **6**, in which all four fluorine resonances are inequivalent.

Although a more definitive proof of the foregoing core rearrangement mechanism is currently unavailable, the dynamic nature of the carboxylate ligands within the tetracarboxylate diiron framework is clearly demonstrated. Similar processes can be operative within a related construct. Previous Mössbauer studies of $[\text{Fe}_2(\mu\text{-BXDK})(\mu\text{-O}_2\text{CPhCy})(\text{O}_2\text{CPhCy})(\text{C}_5\text{H}_5\text{N})_2]$ revealed that its solid and solution structures may not be the same.³⁹ In the solid state, this compound consists of one six-coordinate and one four-coordinate iron atom, which afford two distinct quadrupole doublets. The Mössbauer spectrum obtained for a frozen THF solution sample, however, displays a single broad quadrupole doublet. This spectral behavior may arise from scrambling between the μ -1,3-bridging and terminal bidentate carboxylate ligand in solution, which would render the two iron sites equivalent.

Carboxylate shifts within a diiron(II) core have a significant mechanistic implication for its reaction with dioxygen. Positioning of the open coordination sites for exogenous ligands can be adjusted by the ancillary ligands. For a mole-

cule in which such structural variation is temperature-dependent, the functionally reactive isomer may be accessed under conditions mapped out by solution spectroscopic studies. Spectroscopic data obtained on frozen solutions of samples reflect the static structural properties of the molecules at the freezing point of the solution, which may not be the functionally relevant temperature.

Flexibility versus Rigidity. A sterically more demanding *m*-terphenyl-derived carboxylate ligand, 2,6-dimesitylbenzoate ($\text{Ar}^{\text{Mes}}\text{CO}_2^-$), was used by others to assemble a related diiron(II) complex $[\text{Fe}_2(\mu\text{-O}_2\text{CAr}^{\text{Mes}})_2(\text{O}_2\text{CAr}^{\text{Mes}})_2(\text{MeCN})_2]$.^{83a} The relatively long Fe...Fe distance of 4.122(1) Å, as well as the composition of two μ -1,3-bridging and two terminal bidentate carboxylate ligands, in this compound is reminiscent of the structural features of 2–5 and 8. Coordination of this more sterically crowded ligand, however, affords a geometry that is significantly more rigid than that imposed by the less sterically demanding $\text{Ar}^{\text{Tol}}\text{CO}_2^-$, although the lateral width spanned by both compounds is identical. The presence of four ortho methyl groups in the biphenyl units of $\text{Ar}^{\text{Mes}}\text{CO}_2^-$ apparently restricts rotation around the C–C bonds and enhances interligand steric repulsions. This behavior is clearly evident by a comparison of the $[\text{Fe}_2(\mu\text{-O}_2\text{CAr}^{\text{Mes}})_2(\text{O}_2\text{CAr}^{\text{Mes}})_2(\text{MeCN})_2]$ and $[\text{Fe}_2(\mu\text{-O}_2\text{CAr}^{\text{Tol}})_2(\text{O}_2\text{CAr}^{\text{Tol}})_2(\text{MeCN})_2]$ (3) structures. As displayed in Figure 1.27, in order to minimize steric interactions with the bridging carboxylate ligands, the terminal carboxylates in $[\text{Fe}_2(\mu\text{-O}_2\text{CAr}^{\text{Mes}})_2(\text{O}_2\text{CAr}^{\text{Mes}})_2(\text{MeCN})_2]$ approach the iron atoms along the Fe–Fe vector, the Fe...Fe...C_{carboxylate} angle being 177.5°. Such mutual orthogonality of the four $\text{Ar}^{\text{Mes}}\text{CO}_2^-$ fragments alleviates steric crowding between the conformationally more demanding ligands. Such a spatial disposition of ligands effectively shields the dimetallic core from external nucleophiles, and only the small rod-shaped MeCN ligand could be accommodated in the sterically crowded intermetallic cavity. Notably, the methyl group of the MeCN ligand is

directing *toward* the diiron core. Attempts to install other N-donor ligands on the $\{\text{Fe}_2(\mu\text{-O}_2\text{CAr}^{\text{Mes}})_2(\text{O}_2\text{CAr}^{\text{Mes}})_2\}$ platform resulted in core disassembly, affording mononuclear species.^{83a,c}

Unlike the situation in $[\text{Fe}_2(\mu\text{-O}_2\text{CAr}^{\text{Mes}})_2(\text{O}_2\text{CAr}^{\text{Mes}})_2(\text{MeCN})_2]$, positioning of the two terminal bidentate $\text{Ar}^{\text{Tol}}\text{CO}_2^-$ ligands in **3** significantly displaces them from the Fe–Fe vector, with a $\text{Fe}\cdots\text{Fe}\cdots\text{C}_{\text{carboxylate}}$ angle of 125.5° (Figure 1.27). Rotation about the C–C bonds within the $\text{Ar}^{\text{Tol}}\text{CO}_2^-$ ligand apparently reduces the steric repulsion, as the terminal carboxylates tilt toward the bridging carboxylates to open up a binding site for MeCN. Coordination of the MeCN ligand directs the methyl group *away from* the dimetallic core, and bulkier N-donor ligands can occupy this position without inter-ligand steric repulsion. The $\{\text{Fe}_2(\mu\text{-O}_2\text{CAr}^{\text{Tol}})_2(\text{O}_2\text{CAr}^{\text{Tol}})_2\}$ module retains its structural integrity upon coordination of biomimetic N-donor ligands, allowing the formation of a variety of diiron(II) complexes that are apparently inaccessible to the $\text{Ar}^{\text{Mes}}\text{CO}_2^-$ system.

The ability to compare solid state structures of both $\text{Ar}^{\text{Tol}}\text{CO}_2^-$ and $\text{Ar}^{\text{Mes}}\text{CO}_2^-$ -supported diiron(II) complexes enabled us to assess the flexibility of the ligand system as measured by the dihedral angle (τ) defined in Figure 1.28. Since the four carbon atoms C_b , C_c , C_d , and C_e may not lie in the same plane, an average value (τ) of the two angles (τ_1 and τ_2) was taken. Depending on the relative orientation of the two aryl rings, this value can range from 90° (orthogonal) to 0° (coplanar). The torsional confinement in $\text{Ar}^{\text{Mes}}\text{CO}_2^-$ is reflected by the narrow range of τ values, between 80° and 87° . For $\text{Ar}^{\text{Tol}}\text{CO}_2^-$, this value is distributed between 40° and 74° , indicating a significantly greater degree of freedom in aryl–aryl rotations. Such rotational flexibility within a conformationally rigid framework clearly distinguishes $\text{Ar}^{\text{Tol}}\text{CO}_2^-$ from $\text{Ar}^{\text{Mes}}\text{CO}_2^-$, the consequence of which is reflected in distinctive structural and reactivity properties of the diiron complexes supported thereupon.^{44-46,83,94}

Summary and Conclusion

General synthetic routes were developed that allowed access to carboxylate-bridged diiron(II) complexes having unprecedented coordination geometries. Sterically demanding *m*-terphenyl-derived carboxylate ligands stabilize coordinatively unsaturated diiron(II) centers, some of which faithfully reproduce key architectural aspects of the catalytic sites of selected non-heme diiron enzyme. Ligand substitution reactions revealed significant structural flexibility within the carboxylate-rich ligand framework, which was further demonstrated by solution VT ^{19}F -NMR spectroscopic studies. Analogous carboxylate shifts may facilitate the required structural changes of the enzyme active sites during the catalytic cycle, for which binding and activation of dioxygen is controlled by the delicate interplay between geometric and electronic factors.

Acknowledgment. This work was supported by grants from the National Science Foundation and National Institute of General Medical Sciences. I thank Ms. J. Kuzelka for help in acquiring the Mössbauer spectra, Drs. T. J. Mizoguchi and J. Du Bois for helpful discussions, and Prof. K. S. Hagen for providing the X-ray coordinates of the compounds $[\text{Fe}_2(\mu\text{-O}_2\text{CCMe}_3)_4(\text{C}_5\text{H}_5\text{N})_2]$ and $[\text{Fe}_2(\mu\text{-O}_2\text{CPh})_4(\text{C}_5\text{H}_5\text{N})_2]$.

References

- (*) Part of this work has appeared previously in references 44 and 46, © 1998, 1999 American Chemical Society. A slightly modified version of this work has been submitted for publication. Lee, D.; Lippard, S. J. **2001**.
- (1) (a) Feig, A. L.; Lippard, S. J. *Chem. Rev.* **1994**, *94*, 759-805. (b) Wallar, B. J.; Lipscomb, J. D. *Chem. Rev.* **1996**, *96*, 2625-2657. (c) Que, L., Jr.; Dong, Y. *Acc. Chem. Res.* **1996**, *29*, 190-196. (d) Lange, S. J.; Que, L., Jr. *Curr. Opin. Chem. Biol.* **1998**, *2*, 159-172. (e) Du Bois, J.; Mizoguchi, T. J.; Lippard, S. J. *Coord. Chem. Rev.* **2000**, *200-202*, 443-485. (f) Solomon, E. I.; Brunold, T. C.; Davis, M. I.; Kemsley, J. N.; Lee, S.-K.; Lehnert, N.; Neese, F.; Skulan, A. J.; Yang, Y.-S.; Zhou, J. *Chem. Rev.* **2000**, *100*, 235-349.
- (2) Stenkamp, R. E. *Chem. Rev.* **1994**, *94*, 715-726.
- (3) Valentine, A. M.; Lippard, S. J. *J. Chem. Soc., Dalton Trans.* **1997**, 3925-3931.
- (4) Whittington, D. A.; Lippard, S. J. *Handbook of Metalloproteins*; Messerschmidt, A., Huber, R., Poulos, T. and Wieghardt, K., Ed.; John Wiley & Sons: Chichester, 2001, pp 712-724.
- (5) Merckx, M.; Kopp, D. A.; Sazinsky, M. H.; Blazyk, J. L.; Müller, J.; Lippard, S. J. *Angew. Chem., Int. Ed. Engl.* **2001**, *40*, 2782-2807.
- (6) Logan, D. T.; Su, X.-D.; Åberg, A.; Regnström, K.; Hajdu, J.; Eklund, H.; Nordlund, P. *Structure* **1996**, *4*, 1053-1064.
- (7) Stubbe, J.; van der Donk, W. A. *Chem. Rev.* **1998**, *98*, 705-762.
- (8) Lindqvist, Y.; Huang, W.; Schneider, G.; Shanklin, J. *EMBO J.* **1996**, *15*, 4081-4092.
- (9) Yang, Y.-S.; Broadwater, J. A.; Pulver, S. C.; Fox, B. G.; Solomon, E. I. *J. Am. Chem. Soc.* **1999**, *121*, 2770-2783.
- (10) Rosenzweig, A. C.; Nordlund, P.; Takahara, P. M.; Frederick, C. A.; Lippard, S. J. *Chem. Biol.* **1995**, *2*, 409-418.

- (11) Whittington, D. A.; Lippard, S. J. *J. Am. Chem. Soc.* **2001**, *123*, 827-838.
- (12) Liu, K. E.; Valentine, A. M.; Wang, D.; Huynh, B. H.; Edmondson, D. E.; Salifoglou, A.; Lippard, S. J. *J. Am. Chem. Soc.* **1995**, *117*, 10174-10185.
- (13) Shu, L.; Nesheim, J. C.; Kauffmann, K.; Münck, E.; Lipscomb, J. D.; Que, L., Jr. *Science* **1997**, *275*, 515-518.
- (14) Valentine, A. M.; Stahl, S. S.; Lippard, S. J. *J. Am. Chem. Soc.* **1999**, *121*, 3876-3887.
- (15) (a) Sturgeon, B. E.; Burdi, D.; Chen, S.; Huynh, B. H.; Edmondson, D. E.; Stubbe, J.; Hoffman, B. M. *J. Am. Chem. Soc.* **1996**, *118*, 7551-7557. (b) Burdi, D.; Sturgeon, B. E.; Tong, W. H.; Stubbe, J.; Hoffman, B. M. *J. Am. Chem. Soc.* **1996**, *118*, 281-282. (c) Willems, J.-P.; Lee, H.-I.; Burdi, D.; Doan, P. E.; Stubbe, J.; Hoffman, B. M. *J. Am. Chem. Soc.* **1997**, *119*, 9816-9824. (d) Burdi, D.; Willems, J.-P.; Riggs-Gelasco, P.; Antholine, W. E.; Stubbe, J.; Hoffman, B. M. *J. Am. Chem. Soc.* **1998**, *120*, 12910-12919.
- (16) Broadwater, J. A.; Ai, J.; Loehr, T. M.; Sanders-Loehr, J.; Fox, B. G. *Biochemistry* **1998**, *37*, 14664-14671.
- (17) Broadwater, J. A.; Achim, C.; Münck, E.; Fox, B. G. *Biochemistry* **1999**, *38*, 12197-12204.
- (18) Lippard, S. J. *Angew. Chem. Int. Ed. Engl.* **1988**, *27*, 344-361.
- (19) Kurtz, D. M., Jr. *Chem. Rev.* **1990**, *90*, 585-606.
- (20) Que, L., Jr. *J. Chem. Soc., Dalton Trans.* **1997**, 3933-3940.
- (21) Westerheide, L.; Pascaly, M.; Krebs, B. *Curr. Opin. Chem. Biol.* **2000**, *4*, 235-241.
- (22) Tolman, W. B.; Spencer, D. J. E. *Curr. Opin. Chem. Biol.* **2001**, *5*, 188-195.
- (23) Solomon, E. I. *Inorg. Chem.* **2001**, *40*, 3656-3669.
- (24) Kim, K.; Lippard, S. J. *J. Am. Chem. Soc.* **1996**, *118*, 4914-4915.

- (25) Ookubo, T.; Sugimoto, H.; Nagayama, T.; Masuda, H.; Sato, T.; Tanaka, K.; Maeda, Y.; Okawa, H.; Hayashi, Y.; Uehara, A.; Suzuki, M. *J. Am. Chem. Soc.* **1996**, *118*, 701-702.
- (26) Dong, Y.; Yan, S.; Young, V. G., Jr.; Que, L., Jr. *Angew. Chem., Int. Ed. Engl.* **1996**, *35*, 618-620.
- (27) (a) Collman, J. P.; Fu, L. *Acc. Chem. Res.* **1999**, *32*, 455-463. (b) Feiters, M. C.; Rowan, A. E.; Nolte, R. J. M. *Chem. Soc. Rev.* **2000**, *29*, 375-384. (c) Woggon, W.-D.; Wagenknecht, H.-A.; Claude, C. *J. Inorg. Biochem.* **2001**, *83*, 289-300.
- (28) (a) Pratt, J. M. *Pure and Appl. Chem.* **1993**, *65*, 1513-1520. (b) Hirota, S.; Marzilli, L. G. *Chemistry and Biochemistry of B₁₂*; Banerjee, R., Ed.; John Wiley & Sons: New York, 1999, pp 239-260.
- (29) Abbreviations: BIPhMe, 2,2'-bis(1-methylimidazolyl)phenylmethoxymethane; TPA, tris(2-pyridylmethyl)amine; BPMEN, *N,N'*-dimethyl-*N,N'*-bis(2-pyridyl-methyl)ethylene-1,2-diamine; XDK, *m*-xylenediamine bis-(Kemp's triacid imide); Ph₄DBA, dibenzofuran-4,6-bis(diphenylacetate); TMEDA, *N,N,N',N'*-tetramethylethylenediamine; DPE, dipyrrolidinoethane; OTf⁻, triflate
- (30) Tolman, W. B.; Bino, A.; Lippard, S. J. *J. Am. Chem. Soc.* **1989**, *111*, 8522-8523.
- (31) Tolman, W. B.; Liu, S.; Bentsen, J. G.; Lippard, S. J. *J. Am. Chem. Soc.* **1991**, *113*, 152-164.
- (32) Ménage, S.; Zang, Y.; Hendrich, M. P.; Que, L., Jr. *J. Am. Chem. Soc.* **1992**, *114*, 7786-7792.
- (33) Hazell, R.; Jensen, K. B.; McKenzie, C. J.; Toftlund, H. *J. Chem. Soc., Dalton Trans.* **1995**, 707-717.
- (34) Rebek, J., Jr.; Marshall, L.; Wolak, R.; Parris, K.; Killoran, M.; Askew, B.; Nemeth, D.; Islam, N. *J. Am. Chem. Soc.* **1985**, *107*, 7476-7481.
- (35) Herold, S.; Lippard, S. J. *J. Am. Chem. Soc.* **1997**, *119*, 145-156.

- (36) LeCloux, D. D.; Lippard, S. J. *Inorg. Chem.* **1997**, *36*, 4035-4046.
- (37) Mizoguchi, T. J.; Lippard, S. J. *J. Am. Chem. Soc.* **1998**, *120*, 11022-11023.
- (38) Mizoguchi, T. J.; Kuzelka, J.; Spingler, B.; DuBois, J. L.; Davydov, R. M.; Hedman, B.; Hodgson, K. O.; Lippard, S. J. *Inorg. Chem.* **2001**, *in press*.
- (39) LeCloux, D. D.; Barrios, A. M.; Mizoguchi, T. J.; Lippard, S. J. *J. Am. Chem. Soc.* **1998**, *120*, 9001-9014.
- (40) Dunietz, B. D.; Beachy, M. D.; Cao, Y.; Whittington, D. A.; Lippard, S. J.; Friesner, R. A. *J. Am. Chem. Soc.* **2000**, *122*, 2828-2839.
- (41) Siegbahn, P. E. M. *Inorg. Chem.* **1999**, *38*, 2880-2889.
- (42) Gherman, B. J.; Dunietz, B. D.; Whittington, D. A.; Lippard, S. J.; Friesner, R. A. *J. Am. Chem. Soc.* **2001**, *123*, 3836-3837.
- (43) (a) Du, C.-J. F.; Hart, H.; Ng, K.-K. D. *J. Org. Chem.* **1986**, *51*, 3162-3165. (b) Saednya, A.; Hart, H. *Synthesis* **1996**, 1455-1458. (c) Chen, C.-T.; Siegel, J. S. *J. Am. Chem. Soc.* **1994**, *116*, 5959-5960.
- (44) Lee, D.; Du Bois, J.; Petasis, D.; Hendrich, M. P.; Krebs, C.; Huynh, B. H.; Lippard, S. J. *J. Am. Chem. Soc.* **1999**, *121*, 9893-9894.
- (45) Lee, D.; Lippard, S. J. *J. Am. Chem. Soc.* **2001**, *123*, 4611-4612.
- (46) Lee, D.; Lippard, S. J. *J. Am. Chem. Soc.* **1998**, *120*, 12153-12154.
- (47) Pangborn, A. B.; Giardello, M. A.; Grubbs, R. H.; Rosen, R. K.; Timmers, F. J. *Organometallics* **1996**, *15*, 1518-1520.
- (48) Hagen, K. S. *Inorg. Chem.* **2000**, *39*, 5867-5869.
- (49) *SMART v5.05: Software for the CCD Detector System*; Bruker AXS: Madison, WI, 1998.
- (50) Feig, A. L.; Bautista, M. T.; Lippard, S. J. *Inorg. Chem.* **1996**, *35*, 6892-6898.
- (51) Sheldrick, G. M. *SHELXTL97-2: Program for the Refinement of Crystal Structures*; University of Göttingen, Germany, 1997.

- (52) Sheldrick, G. M. *SADABS: Area-Detector Absorption Correction*; University of Göttingen, Germany, 1996.
- (53) Spek, A. L. *PLATON, A Multipurpose Crystallographic Tool*; Utrecht University: Utrecht, The Netherlands, 1998.
- (54) Kent, T. A. *WMOSS v2.5: Mössbauer Spectral Analysis Software*; WEB Research Co.: Minneapolis, MN, 1998.
- (55) Carlin, R. L. *Magnetochemistry*; Springer-Verlag: New York, 1986.
- (56) Crystal data for $[\text{FeTl}(\mu\text{-O}_2\text{CAr}^{\text{Tol}})_3(\text{C}_5\text{H}_5\text{N})]$: space group $P\bar{1}$ with $a = 11.097(2) \text{ \AA}$, $b = 23.499(4) \text{ \AA}$, $c = 25.524(9) \text{ \AA}$, $\alpha = 68.759(14)^\circ$, $\beta = 78.926(14)^\circ$, $\gamma = 85.259(12)^\circ$, $V = 6088(3) \text{ \AA}^3$, $Z = 4$, $R = 5.20 \%$, $wR^2 = 14.52 \%$.
- (57) Crystal data for $[\text{FeTl}(\mu\text{-O}_2\text{CAr}^{\text{Tol}})_3(1\text{-MeIm})]$: space group $P\bar{1}$ with $a = 13.9499(3) \text{ \AA}$, $b = 14.8627(3) \text{ \AA}$, $c = 15.2549(2) \text{ \AA}$, $\alpha = 88.374(1)^\circ$, $\beta = 87.776(1)^\circ$, $\gamma = 83.896(1)^\circ$, $V = 3141.6(1) \text{ \AA}^3$, $Z = 2$, $R = 4.57\%$, $wR^2 = 13.19\%$.
- (58) Bondi, A. J. *Phys. Chem.* **1964**, *68*, 441-451.
- (59) (a) Schmidbaur, H.; Bublak, W.; Riede, J.; Müller, G. *Angew. Chem., Int. Ed. Engl.* **1985**, *24*, 414-416. (b) Trofimenko, S.; Calabrese, J. C.; Thompson, J. S. *Inorg. Chem.* **1987**, *26*, 1507-1514. (c) Noirod, M. D.; Anderson, O. P.; Strauss, S. H. *Inorg. Chem.* **1987**, *26*. (d) Waezsda, S. D.; Belgardt, T.; Noltemeyer, M.; Roesky, H. W. *Angew. Chem., Int. Ed. Engl.* **1994**, *33*, 1351-1352. (e) Frank, W.; Korrell, G.; Reiss, G. J. Z. *Anorg. Allg. Chem.* **1995**, *621*, 765-770. (f) Fillebeen, T.; Hascall, T.; Parkin, G. *Inorg. Chem.* **1997**, *36*, 3787-3790. (g) Schebler, P. J.; Riordan, C. G.; Guzei, I. A.; Rheingold, A. L. *Inorg. Chem.* **1998**, *37*, 4754-4755.
- (60) Pauling, L. *The Nature of the Chemical Bond*; 3rd ed.; Cornell University Press: Ithaca, NY, 1960.
- (61) Pulver, S.; Froland, W. A.; Fox, B. G.; Lipscomb, J. D.; Solomon, E. I. *J. Am. Chem. Soc.* **1993**, *115*, 12409-12422.

- (62) Fox, B. G.; Hendrich, M. P.; Surerus, K. K.; Andersson, K. K.; Froland, W. A.; Lipscomb, J. D.; Münck, E. *J. Am. Chem. Soc.* **1993**, *115*, 3688-3701.
- (63) Lynch, J. B.; Juarez-Garcia, C.; Münck, E.; Que, L., Jr. *J. Biol. Chem.* **1989**, *264*, 8091-8096.
- (64) Pulver, S. C.; Tong, W. H.; Bollinger, M. J., Jr.; Stubbe, J.; Solomon, E. I. *J. Am. Chem. Soc.* **1995**, *117*, 12664-12678.
- (65) Fox, B. G.; Shanklin, J.; Somerville, C.; Münck, E. *Proc. Natl. Acad. Sci. USA* **1993**, *90*, 2486-2490.
- (66) Gütlich, P.; Ensling, J. *Inorganic Electronic Structure and Spectroscopy*; Solomon, E. I. and Lever, A. B. P., Ed.; John Wiley & Sons: New York, 1999; Vol. I, pp 161-211.
- (67) Münck, E. *Physical Methods in Bioinorganic Chemistry: Spectroscopy and Magnetism*; Que, L., Jr., Ed.; University Science Books: Sausalito, CA, 2000, pp 287-319.
- (68) Girerd, J.-J.; Journaux, Y. *Physical Methods in Bioinorganic Chemistry: Spectroscopy and Magnetism*; Que, L., Jr., Ed.; University Science Books: Sausalito, CA, 2000, pp 321-374.
- (69) Borrás-Almenar, J. J.; Clemente-Juan, J. M.; Coronado, E.; Pali, A. V.; Tsukerblat, B. S. *J. Phys. Chem. A* **1998**, *102*, 200-213.
- (70) Varret, F. *J. Phys. Chem. Solids* **1976**, *37*, 257-263.
- (71) Cummins, C. C. *Prog. Inorg. Chem.* **1998**, *47*, 685-836.
- (72) Twamley, B.; Haubrich, S. T.; Power, P. P. *Adv. Organomet. Chem.* **1999**, *44*, 1-65.
- (73) (a) Robinson, G. H. *Acc. Chem. Res.* **1999**, *32*, 773-782. (b) Robinson, G. H. *Chem. Commun.* **2000**, 2175-2181.
- (74) Clyburne, J. A. C.; McMullen, N. *Coord. Chem. Rev.* **2000**, *210*, 73-99.

- (75) (a) O'Donoghue, M. B.; Schrock, R. R.; LaPointe, A. M.; Davis, W. M. *Organometallics* **1996**, *15*, 1334-1336. (b) Thorn, M. G.; Hill, J. E.; Waratuke, S. A.; Johnson, E. S.; Fanwick, P. E.; Rothwell, I. P. *J. Am. Chem. Soc.* **1997**, *119*, 8630-8641. (c) Thorn, M. G.; Etheridge, Z. C.; Fanwick, P. E.; Rothwell, I. P. *Organometallics* **1998**, *17*, 3636-3638. (d) Ooi, T.; Kondo, Y.; Maruoka, K. *Angew. Chem., Int. Ed. Engl.* **1998**, *37*, 3039-3041. (e) Vilardo, J. S.; Thorn, M. G.; Fanwick, P. E.; Rothwell, I. P. *Chem. Commun.* **1998**, 2425-2426. (f) Thorn, M. G.; Vilardo, J. S.; Fanwick, P. E.; Rothwell, I. P. *Chem. Commun.* **1998**, 2427-2428. (g) Darensbourg, D. J.; Niezgodna, S. A.; Draper, J. D.; Reibenspies, J. H. *J. Am. Chem. Soc.* **1998**, *120*, 4690-4698.
- (76) (a) Ellison, J. J.; Ruhlandt-Senge, K.; Power, P. P. *Angew. Chem., Int. Ed. Engl.* **1994**, *33*, 1178-1180. (b) Niemeyer, M.; Power, P. P. *Inorg. Chem.* **1996**, *35*, 7264-7272. (c) Buyuktas, B. S.; Olmstead, M. M.; Power, P. P. *Chem. Commun.* **1998**, 1689-1690. (d) Stange, A. F.; Sixt, T.; Kaim, W. *Chem. Commun.* **1998**, 469-470.
- (77) Schmidt, J. A. R.; Arnold, J. *Chem. Commun.* **1999**, 2149-2150.
- (78) Clark, G. R.; Nielson, A. J.; Rickard, C. E. F. *J. Chem. Soc., Dalton Trans.* **1996**, 4265-4268.
- (79) Callot, H. J.; Albrecht-Gary, A.-M.; Joubbeh, M. A.; Metz, B. *Inorg. Chem.* **1989**, *28*, 3633-3640.
- (80) Vinod, T. K.; Hart, H. *Topics in Current Chemistry*; Weber, E., Ed.; Springer-Verlag: Berlin, 1994; Vol. 172, pp 119-178.
- (81) Kannan, A.; Rajakumar, P.; Kabaleeswaran, V.; Rajan, S. S. *J. Org. Chem.* **1996**, *61*, 5090-5102.
- (82) Hagen, K. S.; Lachicotte, R.; Kitaygorodskiy, A. *J. Am. Chem. Soc.* **1993**, *115*, 12617-12618.

- (83) (a) Hagadorn, J. R.; Que, L., Jr.; Tolman, W. B. *J. Am. Chem. Soc.* **1998**, *120*, 13531-13532. (b) Hagadorn, J. R.; Que, L., Jr.; Tolman, W. B.; Prisecaru, I.; Münck, E. *J. Am. Chem. Soc.* **1999**, *121*, 9760-9761. (c) Hagadorn, J. R.; Que, L., Jr.; Tolman, W. B. *Inorg. Chem.* **2000**, *39*, 6086-6090.
- (84) Rardin, R. L.; Tolman, W. B.; Lippard, S. J. *New J. Chem.* **1991**, *15*, 417-430.
- (85) Randall, C. R.; Shu, L.; Chiou, Y.-M.; Hagen, K. S.; Ito, M.; Kitajima, N.; Lachicotte, R. J.; Zang, Y.; Que, L., Jr. *Inorg. Chem.* **1995**, *34*, 1036-1039.
- (86) Connolly, J. A.; Kim, J. H.; Banaszczyk, M.; Drouin, M.; Chin, J. *Inorg. Chem.* **1995**, *34*, 1094-1099.
- (87) Ryde, U. *Biophys. J.* **1999**, *77*, 2777-2787.
- (88) Hagen, K. S., personal communication.
- (89) Baik, M.-H.; Lee, D.; Lippard, S. J.; Friesner, R., unpublished results.
- (90) Hagen, K. S.; Lachicotte, R.; Kitaygorodskiy, A.; Elbouadili, A. *Angew. Chem., Int. Ed. Engl.* **1993**, *32*, 1321-1324.
- (91) Lachicotte, R.; Kitaygorodskiy, A.; Hagen, K. S. *J. Am. Chem. Soc.* **1993**, *115*, 8883-8884.
- (92) Blakesley, D. W.; Payne, S. C.; Hagen, K. S. *Inorg. Chem.* **2000**, *39*, 1979-1989.
- (93) Lee, D.; Lippard, S. J., unpublished results.
- (94) Lee, D.; Krebs, C.; Huynh, B. H.; Hendrich, M. P.; Lippard, S. J. *J. Am. Chem. Soc.* **2000**, *122*, 5000-5001.

Table 1.1. Summary of X-ray Crystallographic Data

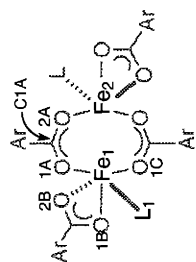
	1	2·2CH ₂ Cl ₂	3·CH ₂ Cl ₂ ·MeCN	4
formula	Fe ₂ C ₅₀ H ₅₀ O ₆ Br ₂	Fe ₂ C ₉₄ H ₈₄ O ₁₀ Cl ₄	Fe ₂ C ₉₃ H ₇₄ N ₄ O ₈ Cl ₂	Fe ₂ C ₉₄ H ₇₈ N ₂ O ₈
fw	1018.42	1627.12	1558.16	1475.28
space group	P2 ₁ /c	P $\bar{1}$	P $\bar{1}$	P $\bar{1}$
<i>a</i> , Å	9.5511(6)	10.7768(3)	12.5735(18)	10.6013(7)
<i>b</i> , Å	12.5628(7)	14.2356(3)	16.646(3)	13.5990(9)
<i>c</i> , Å	19.5714(11)	15.1219(4)	20.595(4)	14.9139(10)
α , deg		107.549(1)	78.725(15)	68.8480(10)
β , deg	103.0780(10)	98.414(1)	81.744(12)	71.5410(10)
γ , deg		105.762(1)	79.915(11)	78.886(2)
<i>V</i> , Å ³	2287.4(2)	2061.87(9)	4135.3(12)	1894.6(2)
<i>Z</i>	2	1	2	1
ρ calc. g/cm ³	1.479	1.310	1.251	1.293
<i>T</i> , °C	-85	-85	-85	-85
μ (Mo K α), mm ⁻¹	2.429	0.541	0.473	0.444
θ limits, deg	1.94–28.27	1.46–28.29	1.84–28.28	1.52–28.25
total no. of data	13120	12551	26327	8860
no. of unique data	5148	8751	18388	7145
no. of params	267	519	964	634
R (%) ^a	6.64	5.17	6.76	6.77
wR ² (%) ^b	11.44	13.20	16.09	13.33
max, min peaks, e/Å ³	0.532, -0.531	0.659, -0.597	0.646, -0.538	0.511, -0.784
a R = $\Sigma F_o - F_c / \Sigma F_o $. b wR ² = $\{\Sigma [w(F_o^2 - F_c^2)^2] / \Sigma [w(F_o^2)^2]\}^{1/2}$.				

Table 1.1, continued. Summary of X-ray Crystallographic Data

	5·0.75CH ₂ Cl ₂ ·0.25C ₅ H ₁₂	6·Et ₂ O	7·C ₆ H ₁₄	8·C ₅ H ₁₂
formula	Fe ₂ C ₉₄ H ₈₀ N ₄ O ₈ Cl _{1.5}	Fe ₂ C ₉₅ H ₈₇ NO ₉	Fe ₂ C ₁₀₈ H ₁₀₀ N ₂ O ₈	Fe ₂ C ₈₈ H ₆₀ O ₁₀ F ₈
fw	1647.12	1498.36	1665.60	1541.06
space group	$P\bar{1}$	$P\bar{1}$	$P\bar{1}$	$P\bar{1}$
<i>a</i> , Å	11.1846(2)	12.8331(2)	14.9812(3)	13.5775(2)
<i>b</i> , Å	17.3132(2)	17.0361(3)	16.4516(4)	16.49110(10)
<i>c</i> , Å	22.5524(3)	18.63320(10)	19.8007(4)	16.7091(2)
α , deg	84.4790(10)	96.3402(9)	105.6310(10)	93.7940(10)
β , deg	84.1290(10)	92.9808(9)	92.0760(10)	107.1610(10)
γ , deg	73.6050(10)	103.6906(8)	109.4020(10)	93.5930(10)
<i>V</i> , Å ³	4157.14(10)	3920.85(9)	4390.12(16)	3553.62(7)
<i>Z</i>	2	2	2	2
ρ calc. g/cm ³	1.316	1.269	1.260	1.440
<i>T</i> , °C	-85	-85	-85	-85
μ (Mo K α), mm ⁻¹	0.537	0.430	0.391	0.493
θ limits, deg	1.48–28.27	2.05–28.21	1.46–28.27	1.58–28.32
total no. of data	17450	24671	27652	21281
no. of unique data	10972	17121	19326	14929
no. of params	1023	964	1077	1013
R (%) ^a	0.0671	4.44	6.45	5.70
wR ² (%) ^b	0.1673	10.60	14.60	12.98
max, min peaks, e/Å ³	0.964, -0.468	0.396, -0.389	0.472, -0.437	1.076, -0.700
a $R = \Sigma F_o - F_c / \Sigma F_o $. b $wR^2 = \{\Sigma [w(F_o^2 - F_c^2)^2] / \Sigma [w(F_o^2)^2]\}^{1/2}$.				

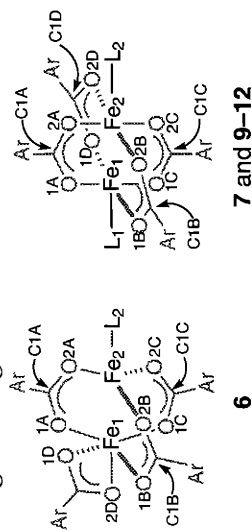
Table 1.1, continued. Summary of X-ray Crystallographic Data

	9·CH ₂ Cl ₂ ·C ₅ H ₁₂	10·3CH ₂ Cl ₂	11·3CH ₂ Cl ₂	12·Et ₂ O
formula	Fe ₂ C ₉₀ H ₅₈ O ₁₀ F ₈ Cl ₂	Fe ₂ C ₈₉ H ₅₄ N ₂ O ₈ F ₈ Cl ₆	Fe ₂ C ₈₇ H ₅₆ N ₄ O ₈ F ₈ Cl ₆	Fe ₂ C ₉₈ H ₇₀ N ₂ O ₉ F ₈
fw	1633.96	1755.74	1761.76	1683.26
space group	$P\bar{1}$	$P\bar{1}$	$P\bar{1}$	$P\bar{1}$
<i>a</i> , Å	13.9997(3)	14.5513(2)	14.7618(4)	14.9070(3)
<i>b</i> , Å	16.4453(6)	16.33130(10)	16.2466(4)	14.93700(10)
<i>c</i> , Å	17.0489(6)	16.9140(3)	16.9722(5)	20.1380(4)
α , deg	91.580(2)	93.6872(10)	93.6210(10)	69.4930(6)
β , deg	91.590(2)	91.2981(10)	92.9080(10)	89.6860(10)
γ , deg	99.4854(18)	101.9649(9)	99.5840(10)	80.7690(7)
<i>V</i> , Å ³	3867.9(2)	3921.34(9)	3997.84(19)	4139.26(12)
<i>Z</i>	2	2	2	2
ρ_{calc} , g/cm ³	1.403	1.487	1.464	1.351
<i>T</i> , °C	-85	-85	-85	-85
μ (Mo K α), mm ⁻¹	0.525	0.654	0.642	0.430
θ limits, deg	1.26–28.26	1.69–28.28	1.69–28.25	1.71–28.28
total no. of data	34614	23470	25107	26284
no. of unique data	17300	16466	17572	18335
no. of params	973	1038	1031	1082
<i>R</i> (%) ^a	6.39	7.76	6.72	5.37
<i>wR</i> ² (%) ^b	16.50	20.67	18.08	11.61
max, min peaks, e/Å ³	0.793, -0.799	0.994, -1.044	1.092, -1.128	0.413, -0.438
<i>a</i> $R = \Sigma F_o - F_c / \Sigma F_o $. <i>b</i> $wR^2 = \{\Sigma [w(F_o^2 - F_c^2)^2] / \Sigma [w(F_o^2)^2]\}^{1/2}$.				

Table 1.2. Selected Bond Lengths (Å) and Angles (deg) for 1–5 and 8. ^a

	1	2	3	4	5	8
Fe1...Fe2	3.5684(13)	4.2822(7)	3.9754(12) ^b	4.2189(13)	4.2029(10) ^d	4.1869(9) ^d
Fe1-O1A	1.967(3)	1.9428(19)	3.9602(13) ^c	1.957(3)	4.1967(11) ^e	4.1452(8) ^e
Fe1-O1C ^f	1.995(3)	2.0061(18)	1.920(3) ^b	2.006(3)	1.950(3) ^d	1.949(2) ^d
Fe1-O1B			1.910(3) ^c		1.980(3) ^e	1.968(2) ^e
Fe1-O2B			1.994(3) ^b	2.047(3)	2.015(3) ^d	1.993(2) ^d
			2.000(3) ^c		2.017(3) ^e	1.995(2) ^e
			2.048(2) ^b		2.025(3) ^d	1.980(2) ^d
			2.049(3) ^c		2.090(3) ^e	2.029(2) ^e
			2.327(2) ^b	2.358(3)	2.463(3) ^{d,g}	2.661(3) ^{d,g}
			2.318(2) ^c		2.315(3) ^e	2.342(2) ^e
			2.123(3) ^b	2.132(4)	2.092(3) ^d	2.088(2) ^d
			2.130(3) ^c		2.085(3) ^e	2.082(2) ^e
			155.4(3) ^b	152.8(3)	153.9(3) ^d	147.4(2) ^d
			159.1(3) ^c		140.0(3) ^e	151.2(2) ^e
			129.2(3) ^b	135.6(3)	137.0(2) ^d	140.9(2) ^d
			127.3(3) ^c		147.9(3) ^e	132.0(2) ^e

^a Numbers in parentheses are estimated standard deviations of the last significant figures. ^b Molecule 1 in the asymmetric unit. ^c Molecule 2 in the asymmetric unit. ^d 4,4-Coordinate isomer. ^e 5,5-Coordinate isomer. ^f Fe1-O1C and Fe2-O2A are identical. ^g Fe...O_{non-coordinating} ^h Fe-O_{THF}.

Table 1.3. Selected Bond Lengths (Å) and Angles (deg) for 6, 7, and 9–12.^a

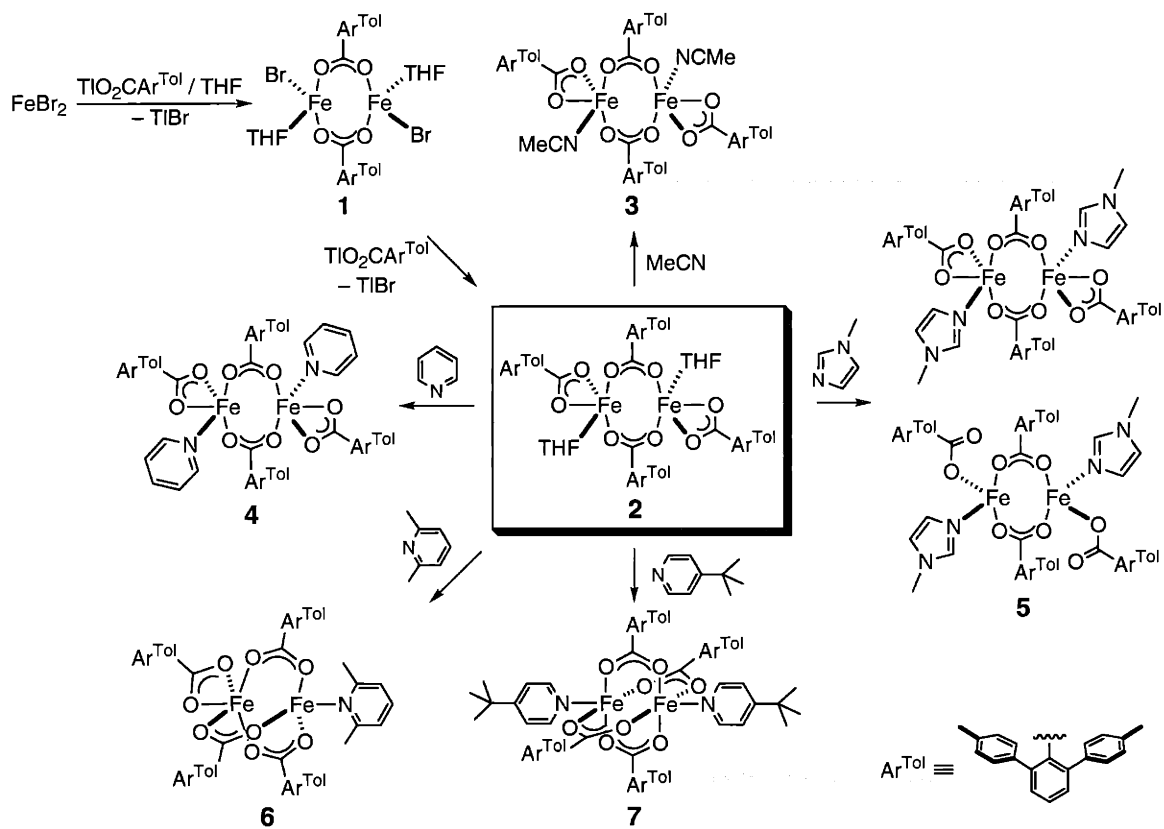
	6	7	9	10	11	12
Fe1...Fe2	3.2342(4)	2.8229(9)	2.7277(7)	2.8249(9)	2.8475(7)	2.8247(5)
Fe1-O1A	2.0698(14)	2.136(3)	2.060(2)	2.196(3)	2.162(3)	2.1165(19)
Fe1-O1B	2.0645(15)	2.031(3)	2.061(2)	2.161(3)	2.208(3)	2.0526(19)
Fe1-O1C	2.0443(15)	2.028(3)	2.072(2)	2.031(3)	2.039(3)	2.0383(19)
Fe1-O1D	2.0776(15)	2.145(3)	2.079(2)	2.033(3)	2.036(2)	2.1152(19)
Fe1-O2D	2.2137(14)					
Fe1-L1		2.105(4)	2.041(3)	2.094(4)	2.068(3)	2.098(2)
Fe2-O2A	1.9968(14)	2.026(3)	2.155(2)	2.018(3)	2.024(3)	2.0460(19)
Fe2-O2B	1.9836(15)	2.160(3)	2.068(2)	2.012(3)	2.024(3)	2.1278(19)
Fe2-O2C	1.9968(14)	2.156(3)	2.075(2)	2.135(3)	2.156(3)	2.1174(19)
Fe2-O2D		2.034(3)	2.101(2)	2.129(3)	2.151(3)	2.0507(18)
Fe2-L2	2.1102(17)	2.098(4)	2.038(3)	2.081(4)	2.066(3)	2.086(2)
Fe1-O1A-C1A	127.58(13)	119.1(3)	121.1(2)	120.0(3)	112.9(2)	118.20(18)
Fe1-O1B-C1B	132.63(14)	130.4(3)	125.5(2)	113.2(3)	127.5(2)	130.23(17)
Fe1-O1C-C1C	142.78(15)	132.2(3)	121.6(2)	131.1(3)	128.4(2)	130.15(18)
Fe1-O1D-C1D		117.4(3)	127.1(2)	126.2(3)	131.5(2)	118.48(17)
Fe2-O2A-C1A	130.16(13)	130.9(3)	122.7(2)	127.3(3)	135.9(2)	129.45(18)
Fe2-O2B-C1B	126.71(13)	117.4(3)	120.7(2)	136.3(3)	127.5(2)	117.84(17)
Fe2-O2C-C1C	115.68(14)	115.2(3)	123.1(2)	116.7(3)	119.1(2)	117.81(18)
Fe2-O2D-C1D		130.9(3)	118.0(2)	121.2(3)	116.3(2)	128.72(17)

^a Numbers in parentheses are estimated standard deviations of the last significant figures.

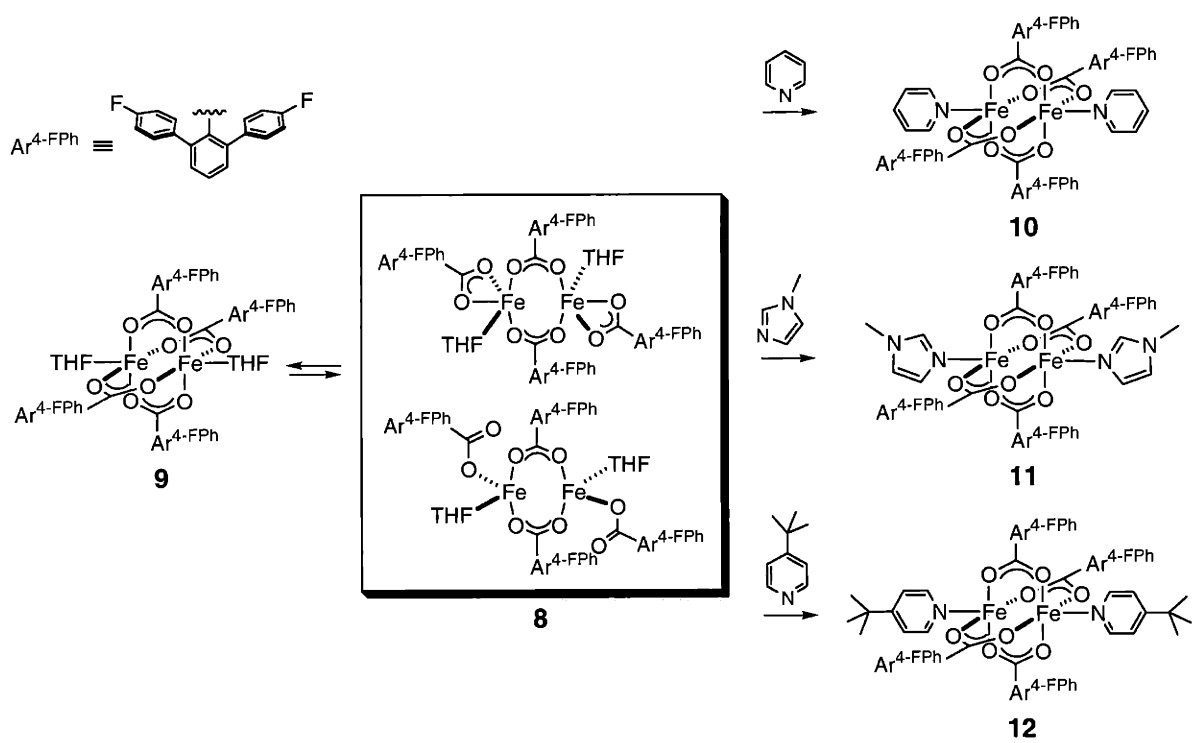
Table 1.4. Mössbauer and Magnetic Parameters for $[\text{Fe}_2(\mu\text{-O}_2\text{CAr}^{\text{Tot}})_2(\text{O}_2\text{CAr}^{\text{Tot}})_2(\text{THF})_2]$ (2), $[\text{Fe}_2(\mu\text{-O}_2\text{CAr}^{\text{Tot}})_2(\text{O}_2\text{CAr}^{\text{Tot}})(\text{C}_5\text{H}_5\text{N})_2]$ (4), $[\text{Fe}_2(\mu\text{-O}_2\text{CAr}^{\text{Tot}})_2(\text{O}_2\text{CAr}^{\text{Tot}})_2(1\text{-MeIm})_2]$ (5), $[\text{Fe}_2(\mu\text{-O}_2\text{CAr}^{\text{Tot}})_4(4\text{-}^t\text{BuC}_5\text{H}_4\text{N})_2]$ (7), MMOH, RNR-R2, and $\Delta 9\text{D}$

	δ (mm/s)	ΔE_{Q} (mm/s)	Γ_{L} (mm/s)	Γ_{R} (mm/s)	J (cm^{-1})	g	ref
2	1.26(2) ^a	2.90(2) ^a	0.27 ^a	0.28 ^a			this work
4	1.19(2) ^a	3.02(2) ^a	0.25 ^a	0.25 ^a	-0.90(3) ^b	2.16(1)	this work
5	1.19(2) ^a	3.01(2) ^a	0.34 ^a	0.40 ^a	-1.04(2) ^b	2.14(1)	this work
7	1.12(2) ^a	3.05(2) ^a	0.24 ^a	0.26 ^a			this work
MMOH	1.30 ^{a,c}	2.87 ^{a,c}					12
RNR-R2	1.3 ^{a,d,e}	2.4-3.1 ^{a,d,e}			0.3-0.5 ^{b,d}		61, 62
$\Delta 9\text{D}$	1.26 ^a	3.13 ^a			-0.5 ^b		63, 64
	1.30 ^{a,e}	3.04-3.36 ^{a,e}			$\sim < -1$ ^b		9, 65

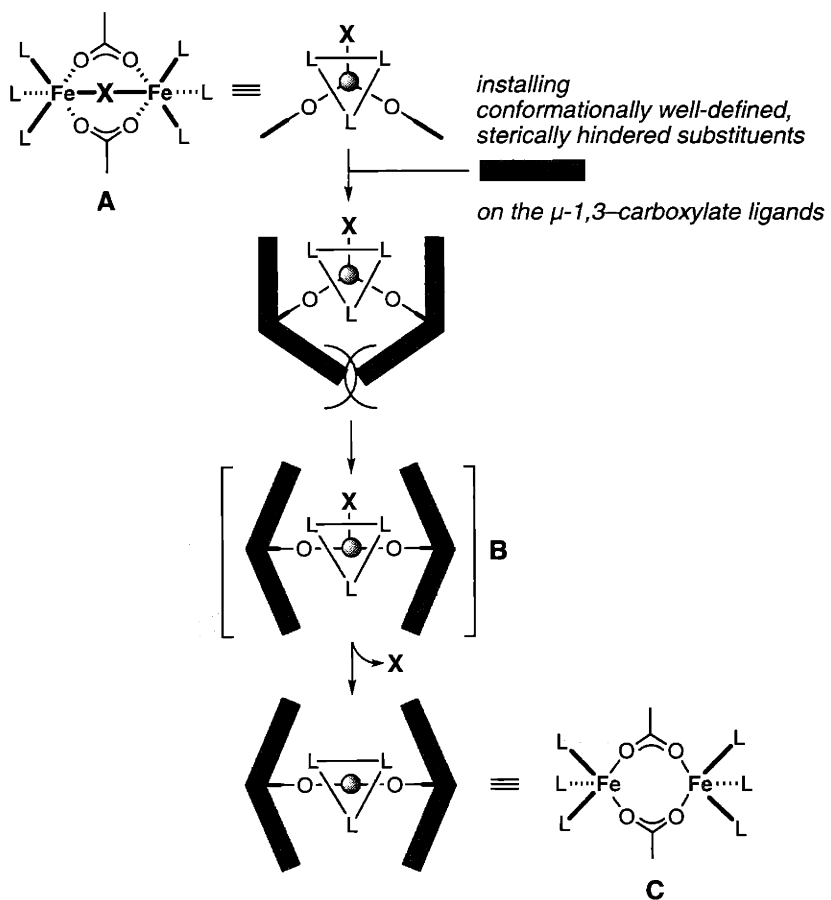
^a Measured at 4.2 K. ^b $\mathcal{H} = -2J\mathbf{S}_1 \cdot \mathbf{S}_2$. ^c *Methylococcus capsulatus* (Bath). ^d *Methylosinus trichosporium* OB3b. ^e Two quadrupole doublets.



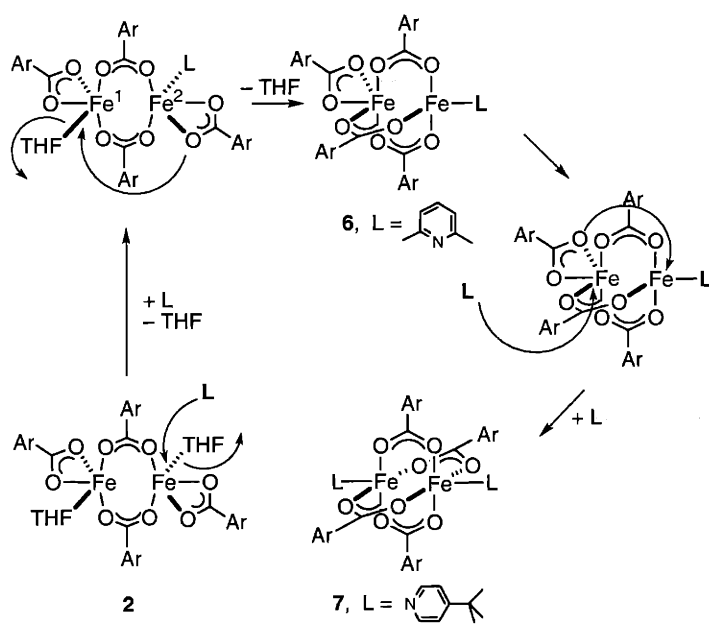
Scheme 1.1.



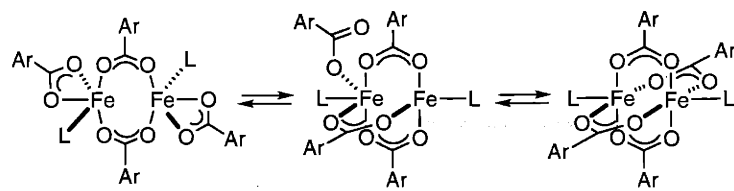
Scheme 1.2.



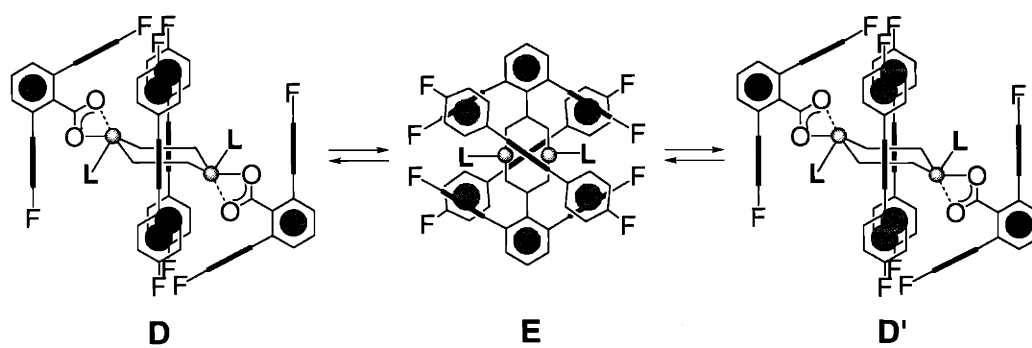
Scheme 1.3.



Scheme 1.4.



Scheme 1.5.



Scheme 1.6.

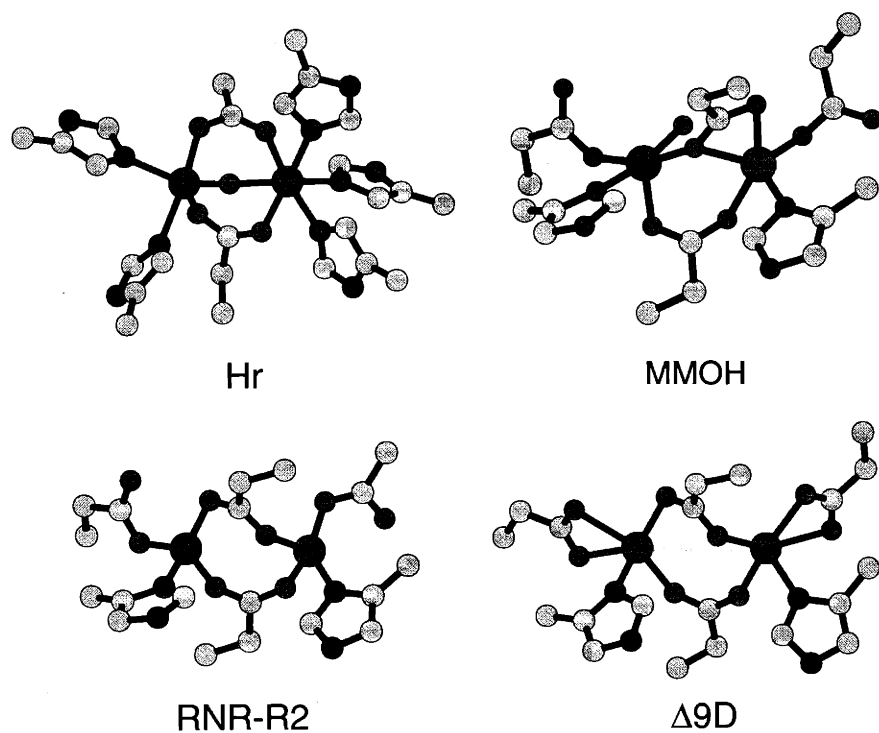


Figure 1.1. Structures of the diiron(II) centers in hemerythrin (Hr), the hydroxylase component of soluble methane monooxygenase (MMOH) from *M. capsulatus* (Bath), R2 subunit of ribonucleotide reductase (RNR-R2) from *Escherichia coli*, and stearoyl-acyl carrier protein Δ^9 desaturase (Δ^9 D). Generated using the crystallographic coordinates.

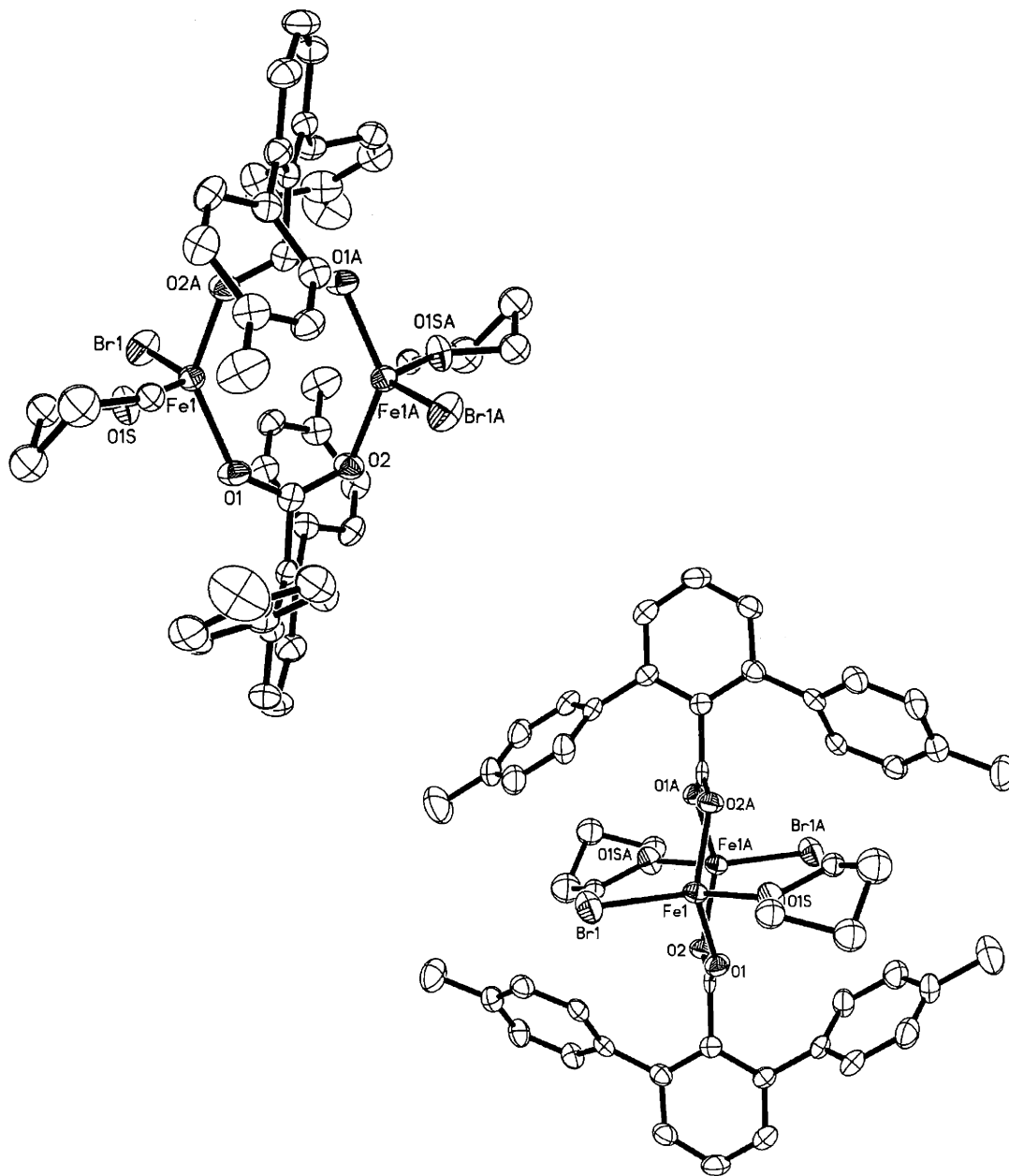


Figure 1.2. ORTEP diagram of [Fe₂(μ-O₂CAr^{Tol})₂(THF)₂Br₂] (1) with thermal ellipsoids at 50% probability.

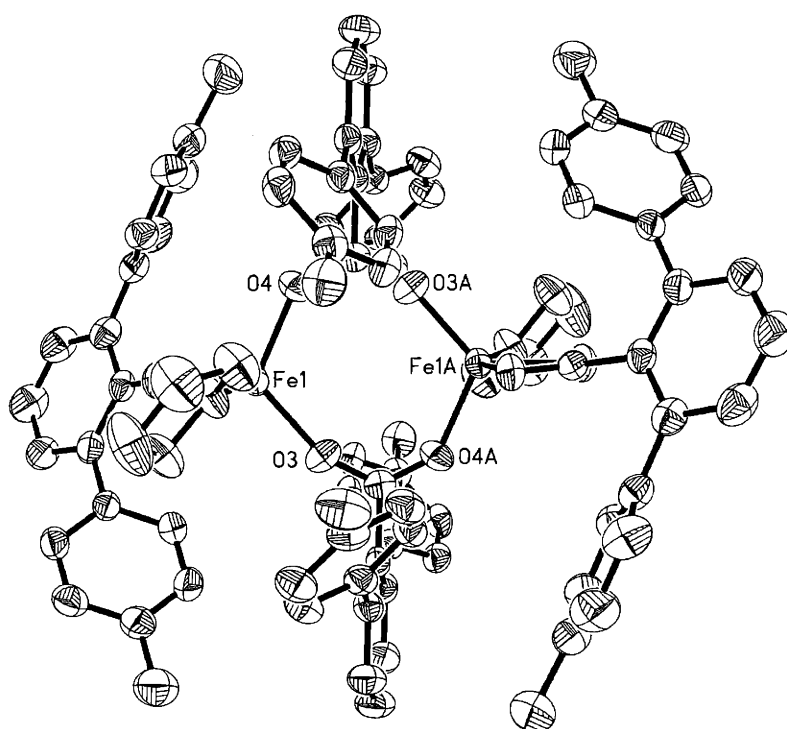


Figure 1.3. ORTEP diagram of $[\text{Fe}_2(\mu\text{-O}_2\text{CAr}^{\text{Tol}})_2(\text{O}_2\text{CAr}^{\text{Tol}})_2(\text{THF})_2]$ (**2**) with thermal ellipsoids at 50% probability.

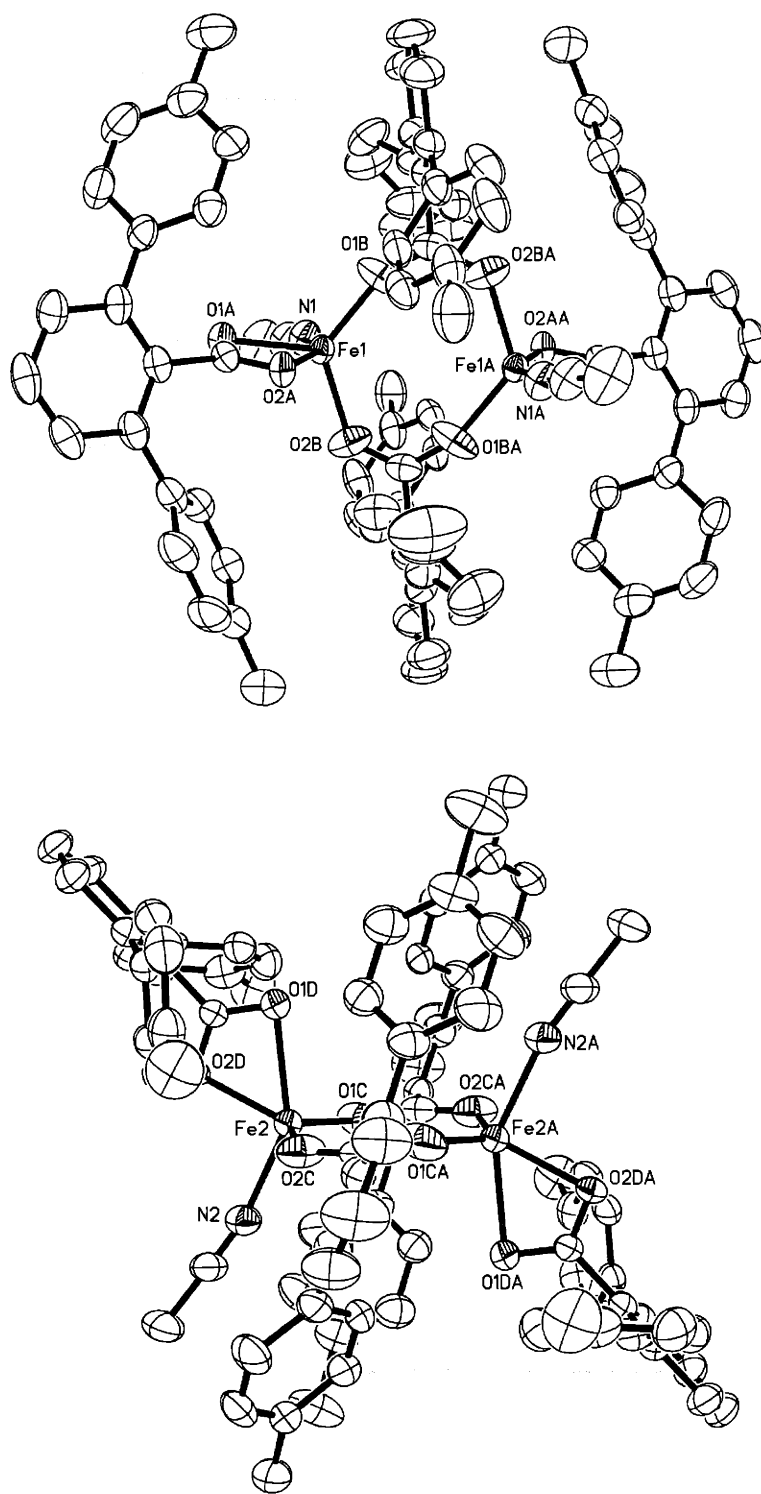


Figure 1.4. ORTEP diagram of $[\text{Fe}_2(\mu\text{-O}_2\text{CAr}^{\text{Tol}})_2(\text{O}_2\text{CAr}^{\text{Tol}})_2(\text{MeCN})_2]$ (3) with thermal ellipsoids at 50% probability: top, molecule 1; bottom, molecule 2.

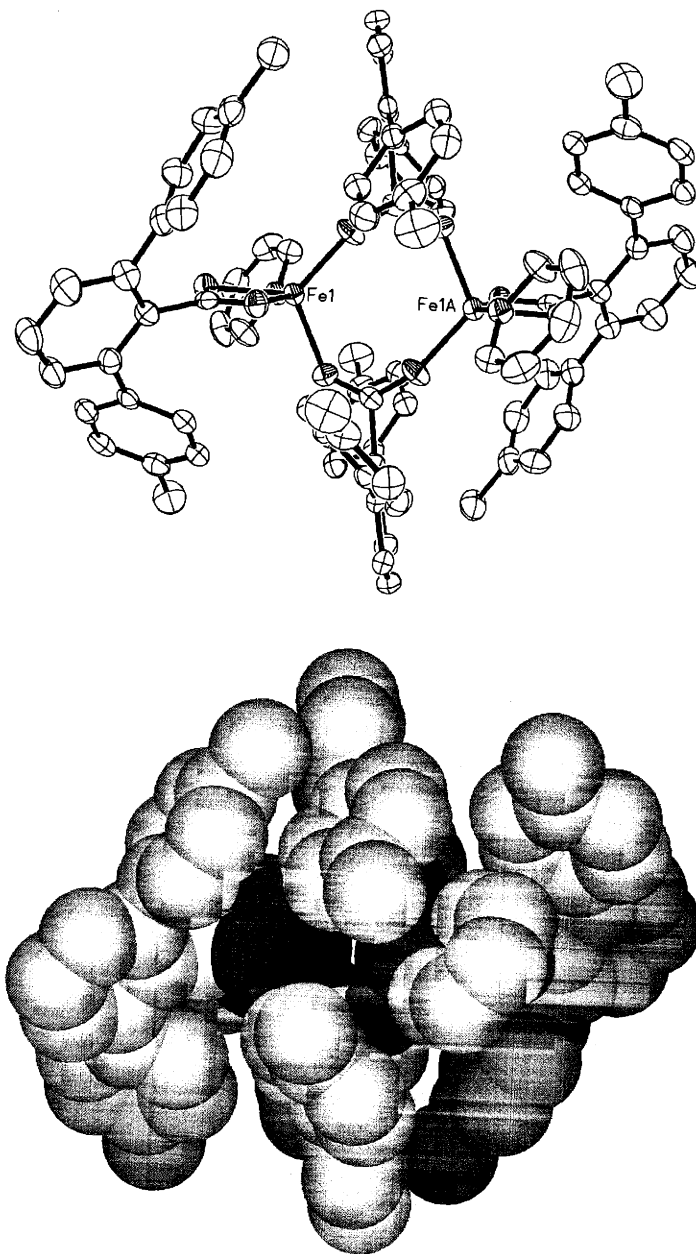


Figure 1.5. Solid-state structure of $[\text{Fe}_2(\mu\text{-O}_2\text{CAr}^{\text{Tol}})_2(\text{O}_2\text{CAr}^{\text{Tol}})_2(\text{C}_5\text{H}_5\text{N})_2]$ (4): top, ORTEP diagram with thermal ellipsoids at 50% probability; bottom, space-filling representation, where N is blue, O is bright red, and Fe is dark red.

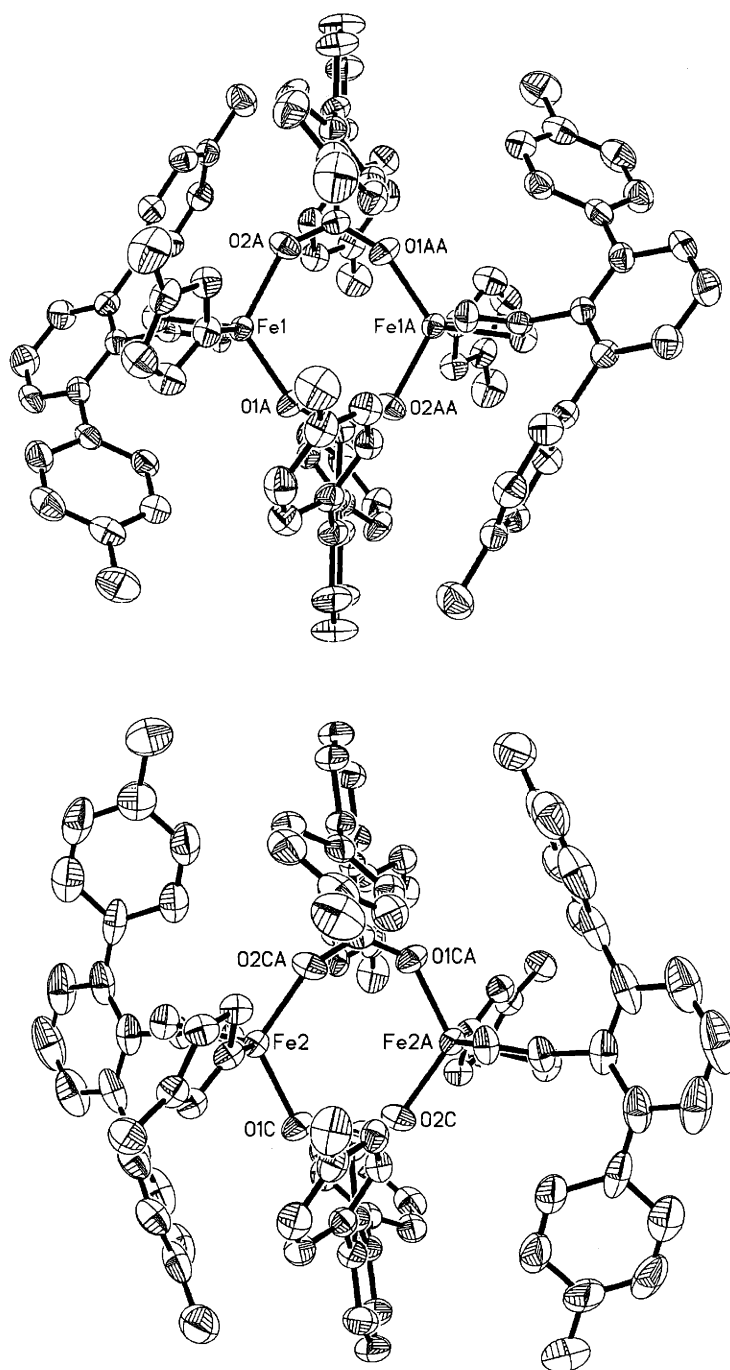


Figure 1.6. ORTEP diagram of $[\text{Fe}_2(\mu\text{-O}_2\text{CAr}^{\text{Tol}})_2(\text{O}_2\text{CAr}^{\text{Tol}})_2(1\text{-MeIm})_2]$ (**5**) with thermal ellipsoids at 50% probability: top, molecule 1; bottom, molecule 2.

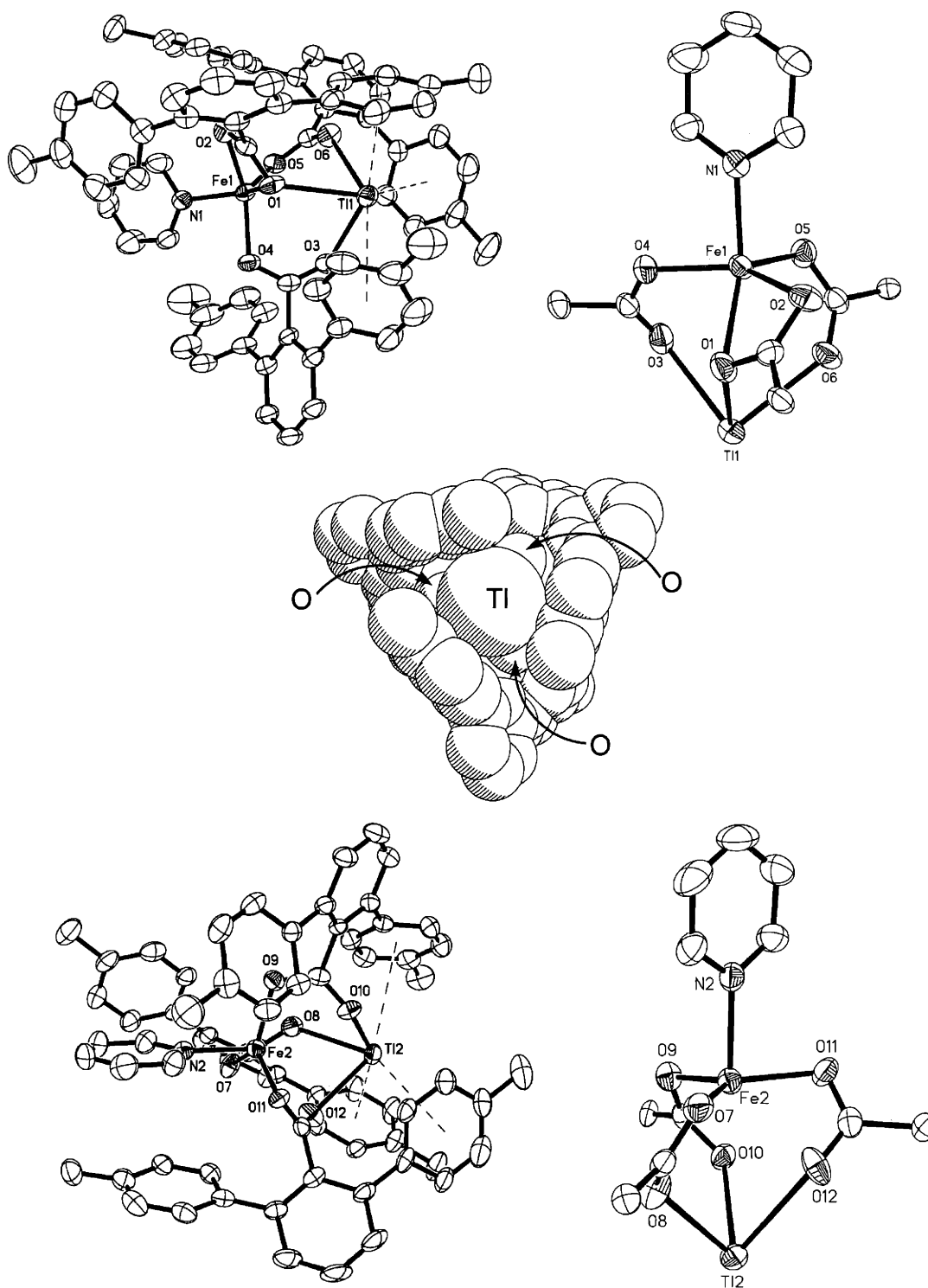


Figure 1.7. ORTEP diagram of [FeTl(μ-O₂CArTol)₃(C₅H₅N)] with thermal ellipsoids at 50% probability (top, molecule 1; bottom, molecule 2) and a space-filling representation of molecule 2 (middle).

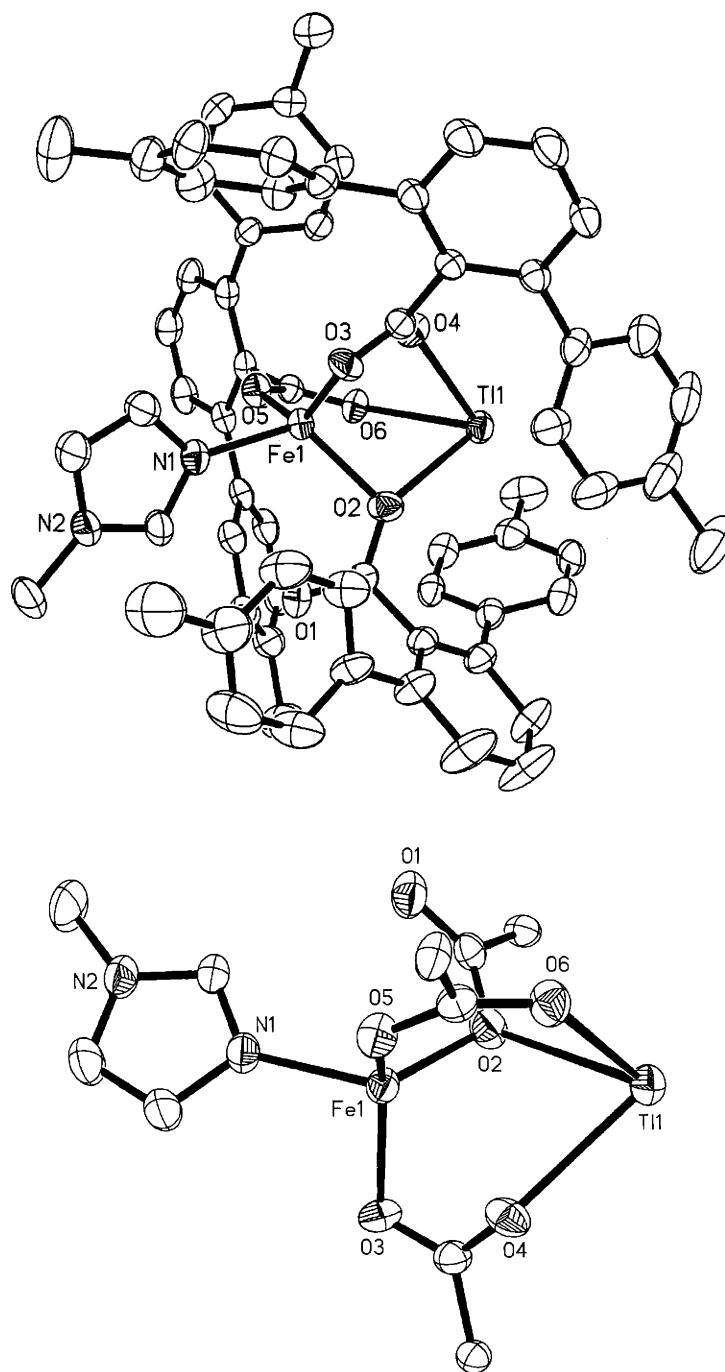


Figure 1.8. ORTEP diagram of $[\text{FeTi}(\mu\text{-O}_2\text{CAr}^{\text{Tol}})_3(1\text{-MeIm})]$ with thermal ellipsoids at 50% probability: top, whole molecule; bottom, core structure.

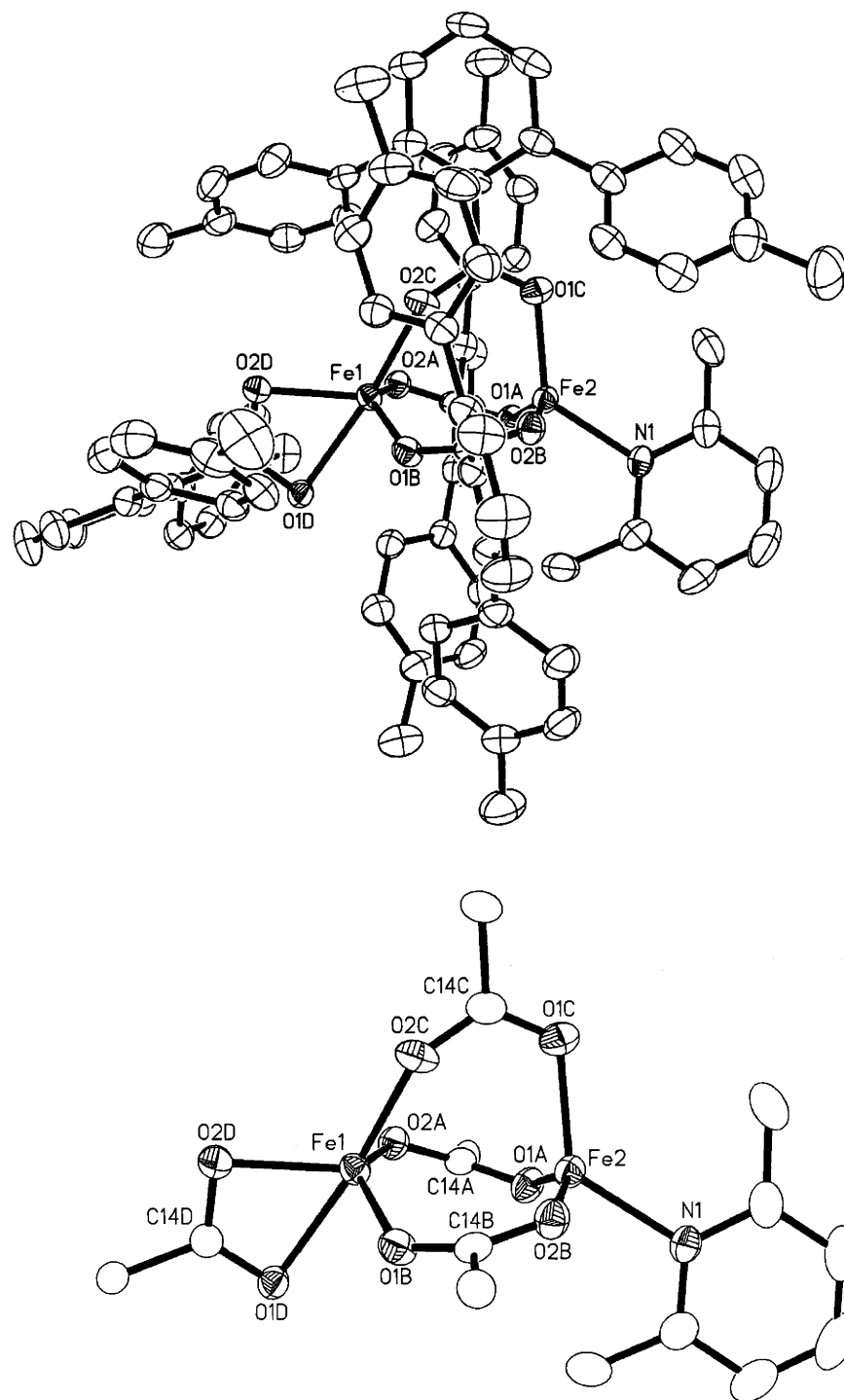


Figure 1.9. ORTEP diagram of [Fe₂(μ-O₂CAr^{Tol})₃(O₂CAr^{Tol})(2,6-lutidine)] (6) with thermal ellipsoids at 50% probability: top, whole molecule; bottom, core structure.

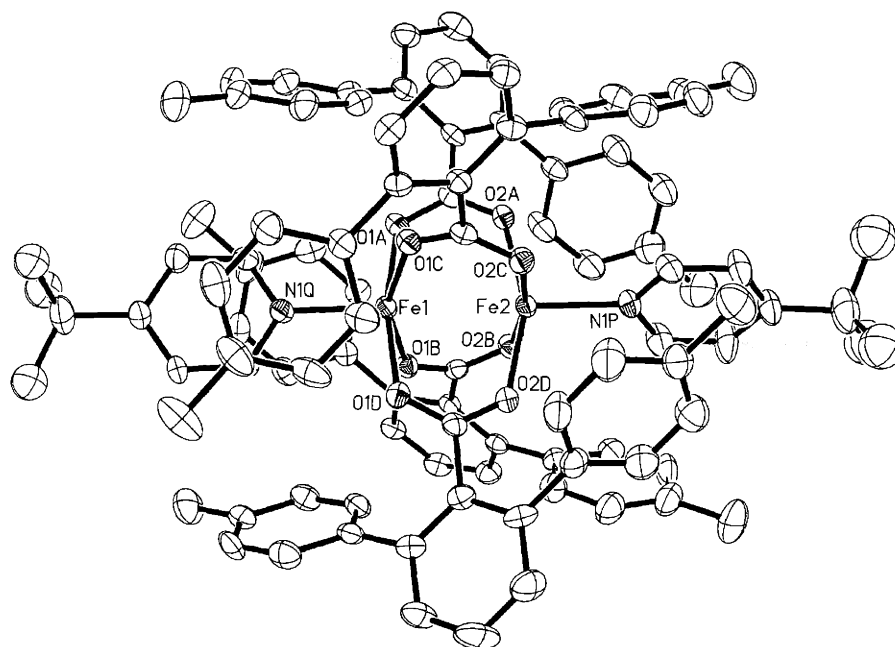


Figure 1.10. ORTEP diagram of $[\text{Fe}_2(\mu\text{-O}_2\text{CAr}^{\text{Tol}})_4(4\text{-}^t\text{BuC}_5\text{H}_4\text{N})_2]$ (7) with thermal ellipsoids at 50% probability.

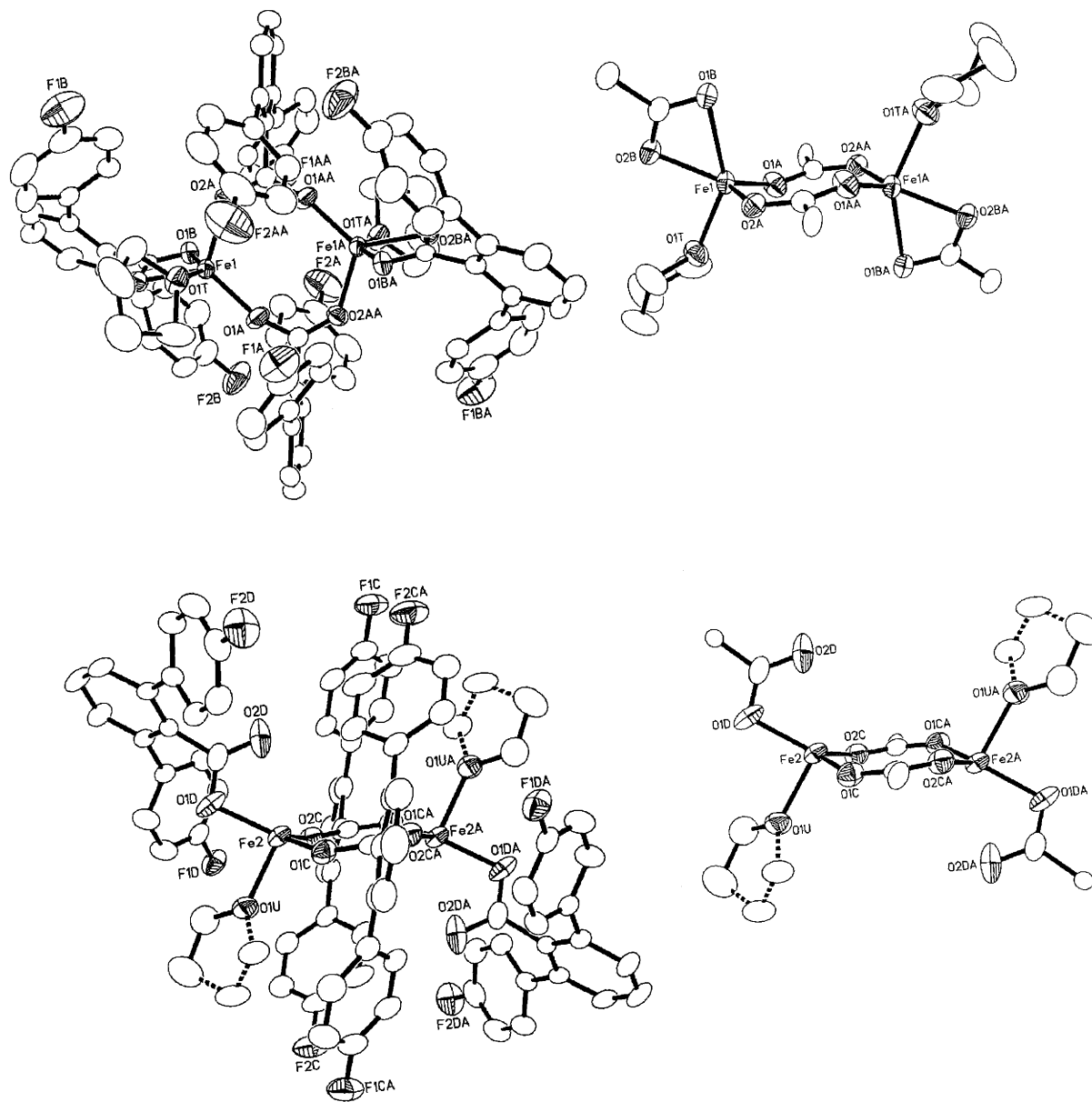


Figure 1.11. ORTEP diagram of $[\text{Fe}_2(\mu\text{-O}_2\text{CAR}^{4\text{-FPh}})_2(\text{O}_2\text{CAR}^{4\text{-FPh}})_2(\text{THF})_2]$ (8) with thermal ellipsoids at 50% probability: top, molecule 1; bottom, molecule 2.

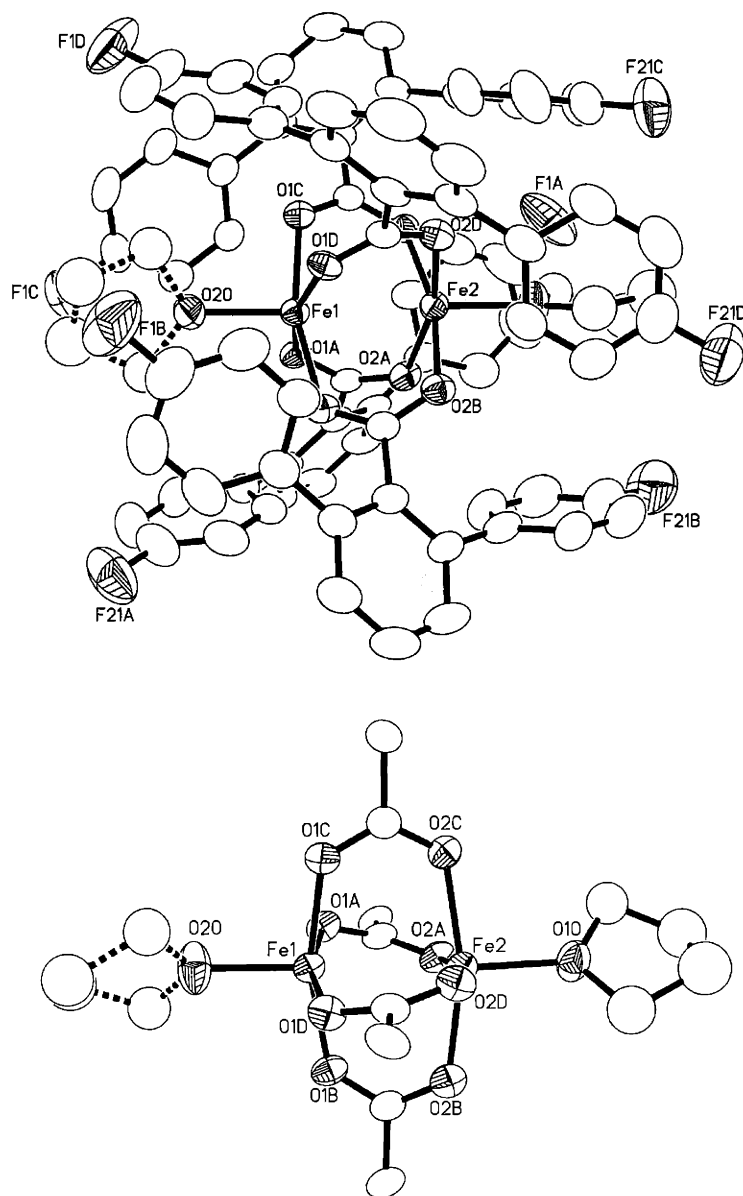


Figure 1.12. ORTEP diagram of [Fe₂(μ-O₂CAr^{4-FPh})₄(THF)₂] (9) with thermal ellipsoids at 50% probability: top, whole molecule; bottom, core structure.

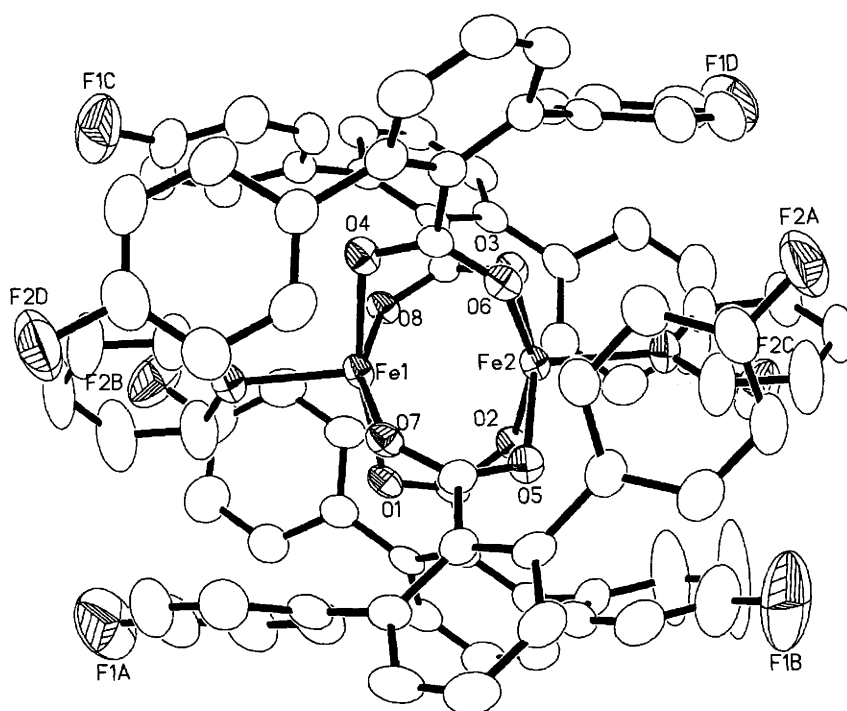


Figure 1.13. ORTEP diagram of $[\text{Fe}_2(\mu\text{-O}_2\text{CAR}^{4\text{-FPh}})_4(\text{C}_5\text{H}_5\text{N})_2]$ (**10**) with thermal ellipsoids at 50% probability.

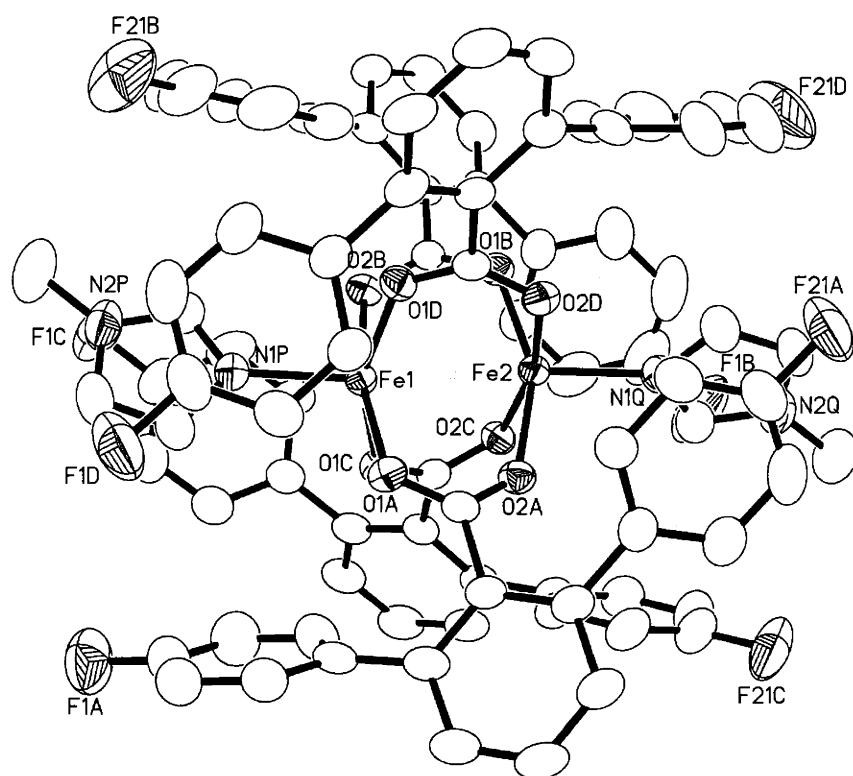


Figure 1.14. ORTEP diagram of $[\text{Fe}_2(\mu\text{-O}_2\text{CAR}^{4\text{-FPh}})_4(1\text{-MeIm})_2]$ (**11**) with thermal ellipsoids at 50% probability.

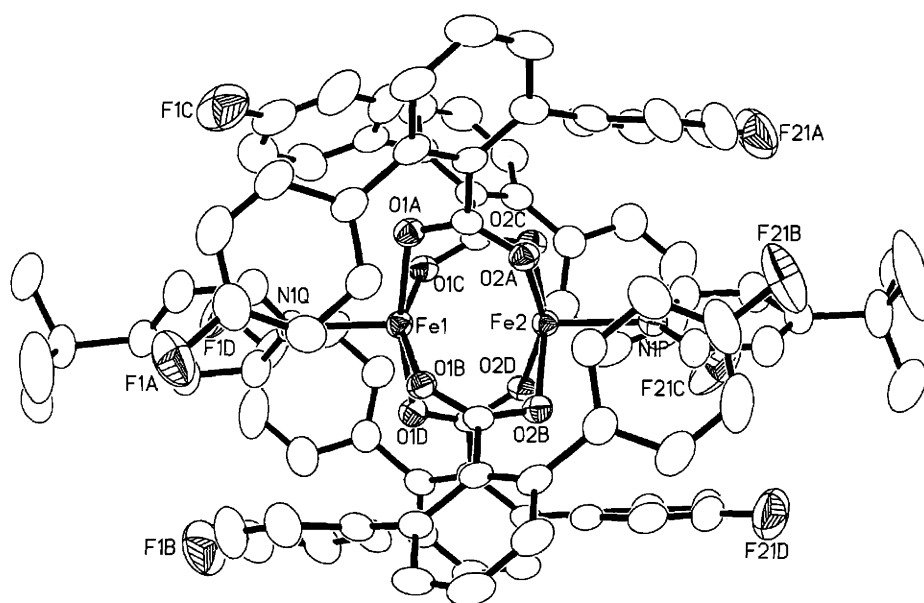


Figure 1.15. ORTEP diagram of [Fe₂(μ-O₂CAr^{4-FPh})₄(4-^tBuC₅H₄N)₂] (12) with thermal ellipsoids at 50% probability.

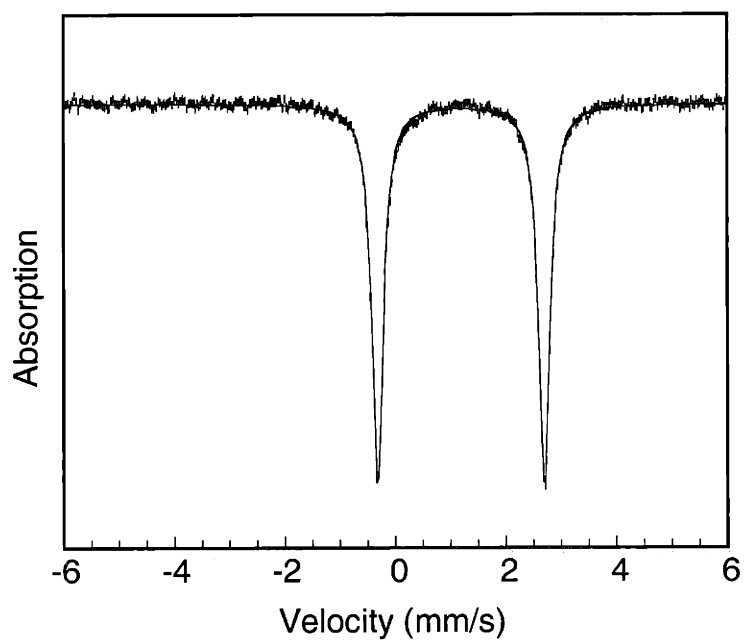


Figure 1.16. Zero-field Mössbauer spectrum (experimental data (|), calculated fit (—)) recorded at 4.2 K for $[\text{Fe}_2(\mu\text{-O}_2\text{CAr}^{\text{Tol}})_2(\text{O}_2\text{CAr}^{\text{Tol}})_2(\text{C}_5\text{H}_5\text{N})_2]$ (**4**) in the solid state. See Table 1.4 for derived Mössbauer parameters.

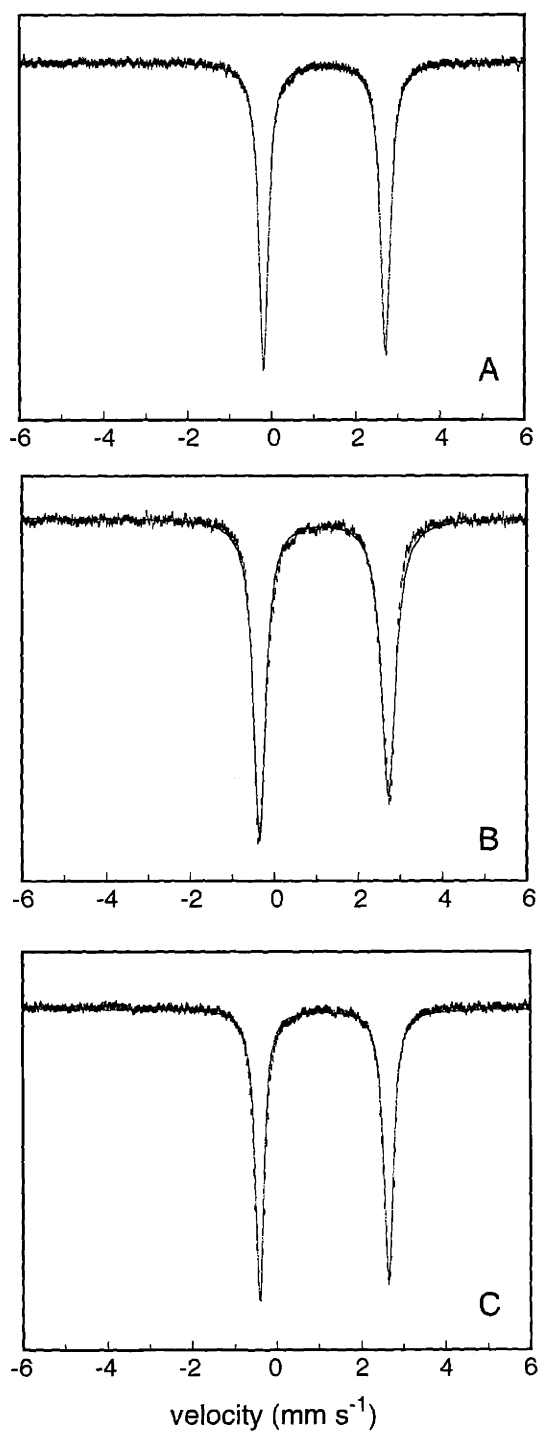


Figure 1.17. Zero-field Mössbauer spectrum (experimental data (|)), calculated fit (—) recorded at 4.2 K for $[\text{Fe}_2(\mu\text{-O}_2\text{CAr}^{\text{Tol}})_2(\text{O}_2\text{CAr}^{\text{Tol}})_2(\text{THF})_2]$ (**2**) (A), $[\text{Fe}_2(\mu\text{-O}_2\text{CAr}^{\text{Tol}})_2(\text{O}_2\text{CAr}^{\text{Tol}})_2(1\text{-MeIm})_2]$ (**5**) (B), and $[\text{Fe}_2(\mu\text{-O}_2\text{CAr}^{\text{Tol}})_4(4\text{-}^t\text{BuC}_5\text{H}_4\text{N})_2]$ (**7**) (C) in the solid state. See Table 1.4 for derived Mössbauer parameters.

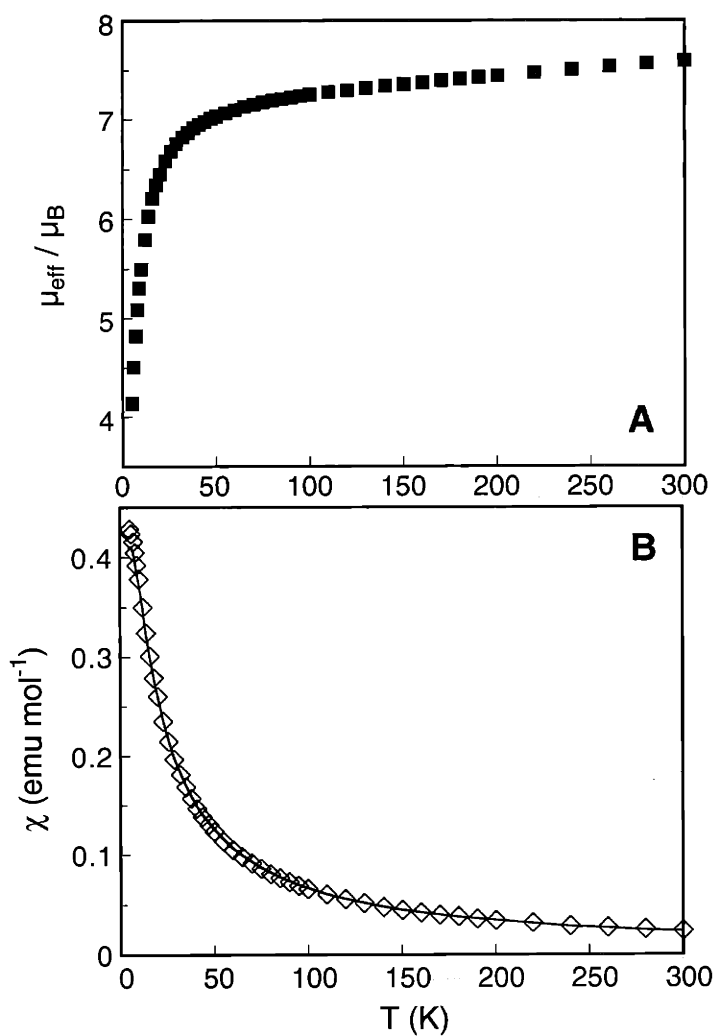


Figure 1.18. Plots of effective moment (μ_{eff}) per molecule versus temperature (A) and molar susceptibility (χ_M) versus temperature (B) for $[\text{Fe}_2(\mu\text{-O}_2\text{CAr}^{\text{Tol}})_2(\text{O}_2\text{CAr}^{\text{Tol}})_2(\text{C}_5\text{H}_5\text{N})_2]$ (**4**). The solid line in B corresponds to the best fit, obtained by using the parameters described in Table 1.4.

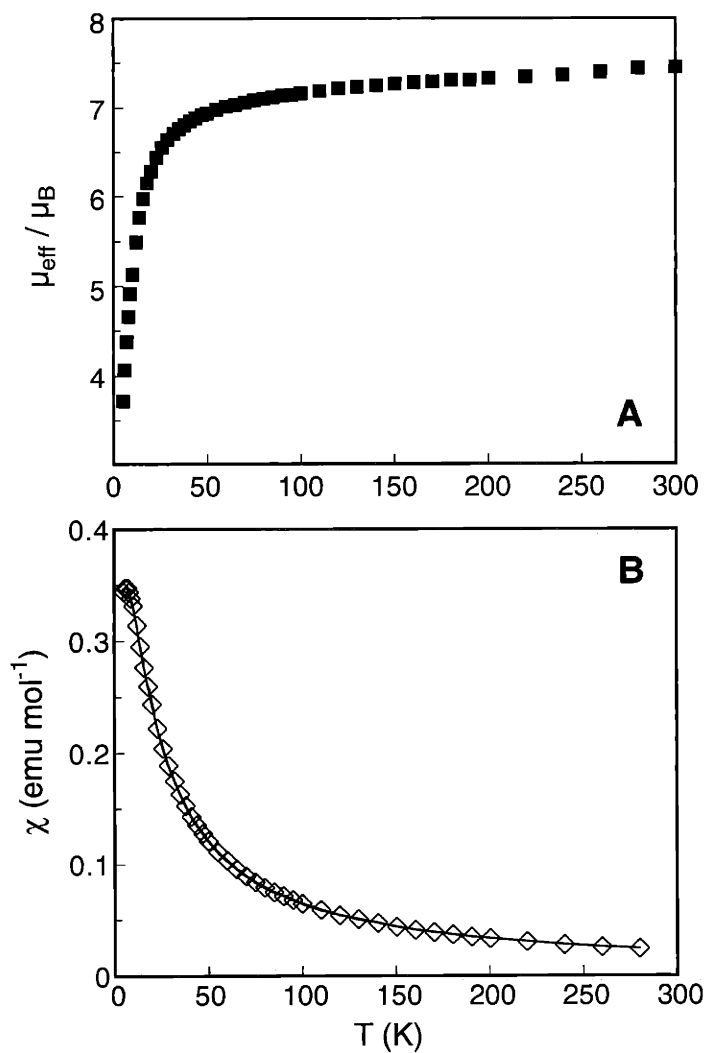


Figure 1.19. Plots of effective moment (μ_{eff}) per molecule versus temperature (A) and molar susceptibility (χ_M) versus temperature (B) for $[\text{Fe}_2(\mu\text{-O}_2\text{CAr}^{\text{Tol}})_2(\text{O}_2\text{CAr}^{\text{Tol}})_2(1\text{-MeIm})_2]$ (5). The solid line corresponds to the best fit, obtained by using the parameters described in Table 1.4.

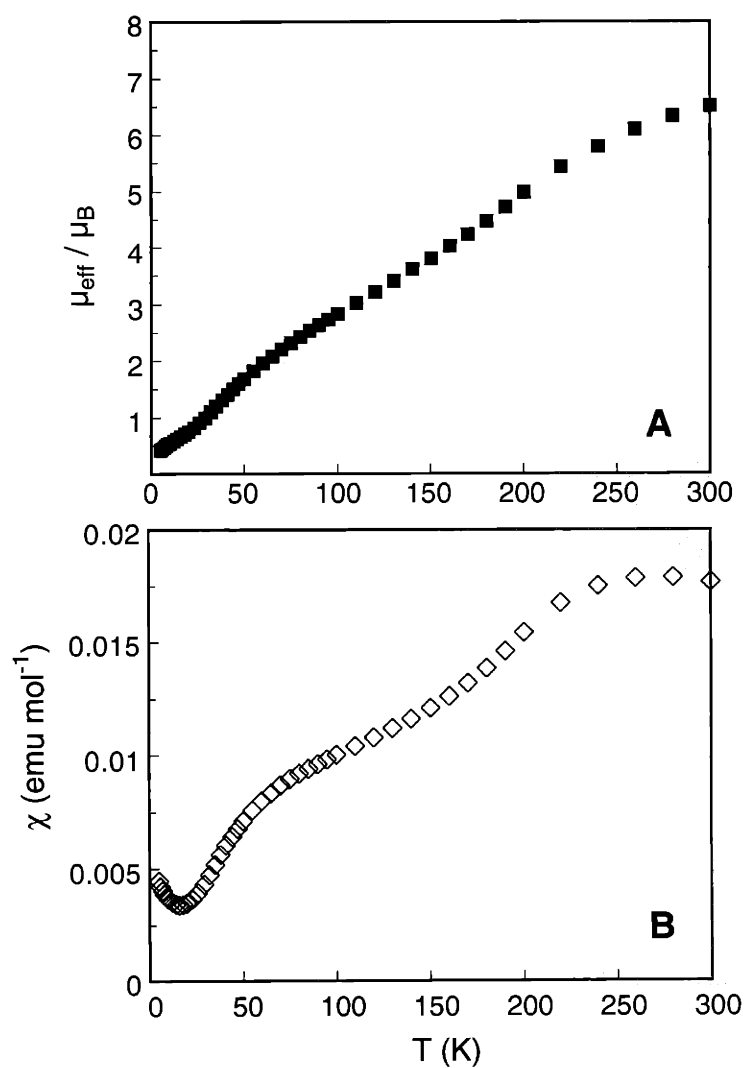


Figure 1.20. Plots of effective moment (μ_{eff}) per molecule versus temperature (A) and molar susceptibility (χ_M) versus temperature (B) for $[\text{Fe}_2(\mu\text{-O}_2\text{CAr}^{\text{Tol}})_4(4\text{-}^t\text{BuC}_5\text{H}_4\text{N})_2]$ (7).

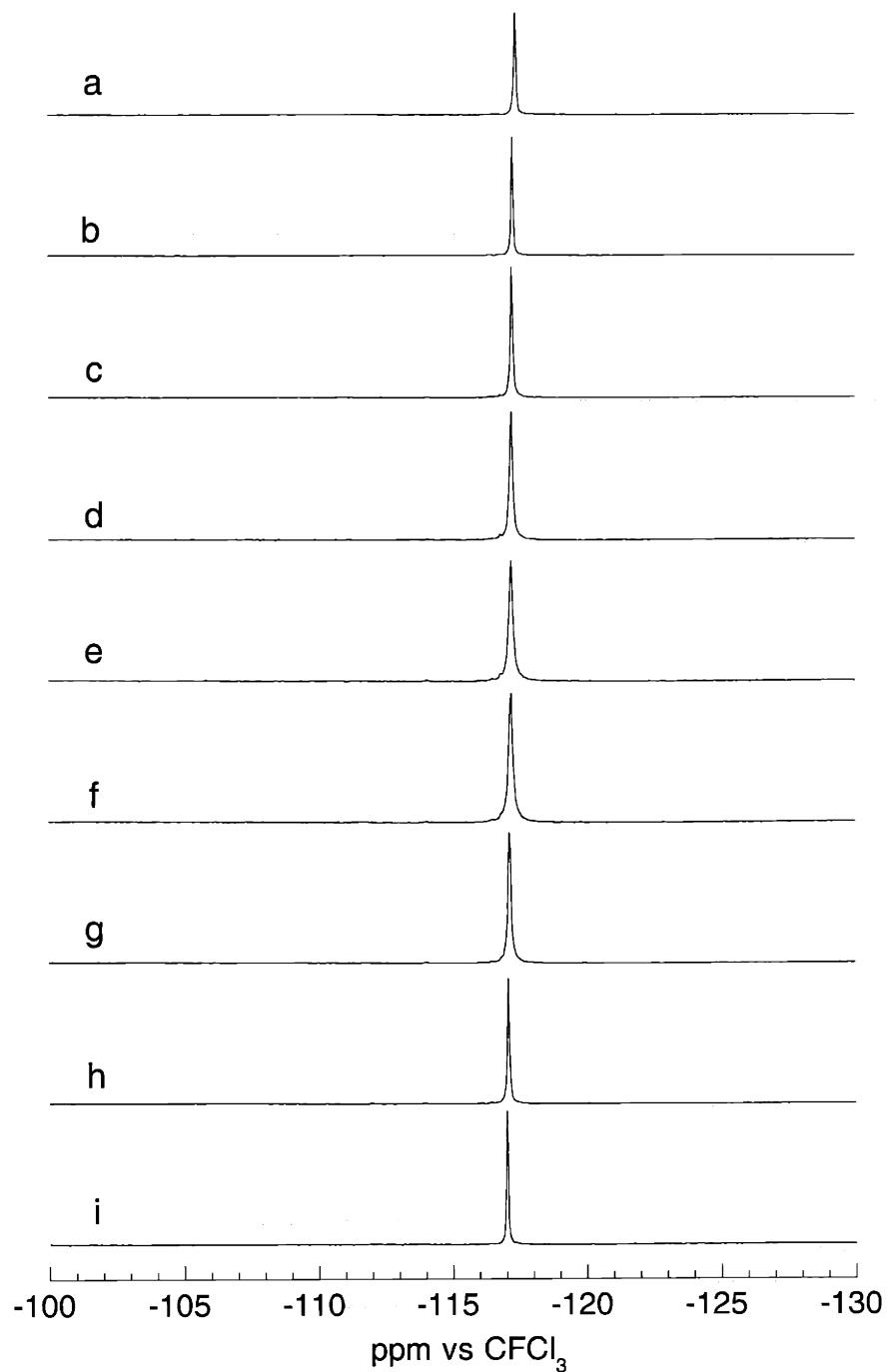


Figure 1.21. Variable temperature ^{19}F -NMR spectra (vs CFCl_3) of $[\text{Fe}_2(\mu\text{-O}_2\text{CAr}^{4\text{-FPh}})_4(4\text{-}^t\text{BuC}_5\text{H}_4\text{N})_2]$ (**12**) in CH_2Cl_2 at 470 MHz. Spectra were acquired at the following temperatures: (a) +20 °C, (b) 0 °C, (c) -10 °C, (d) -20 °C, (e) -30 °C, (f) -40 °C, (g) -50 °C, (h) -60 °C, (i) -70 °C.

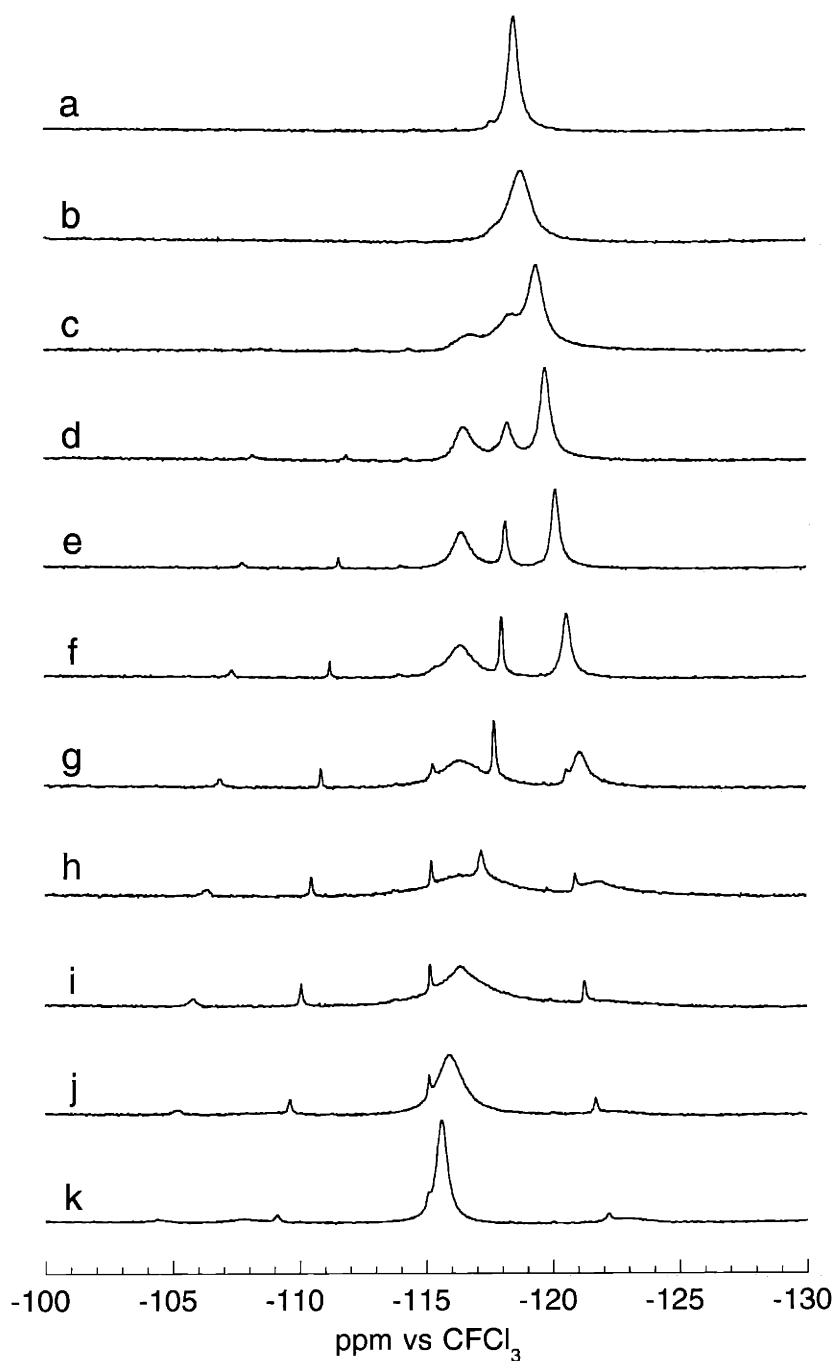


Figure 1.22. Variable temperature ^{19}F -NMR spectra (vs CFCl_3) of $[\text{Fe}_2(\mu\text{-O}_2\text{CAr}^{4\text{-FPh}})_2(\text{O}_2\text{CAr}^{4\text{-FPh}})_2(\text{THF})_2]$ (**8**) in CH_2Cl_2 at 470 MHz. Spectra were acquired at the following temperatures: (a) +20 °C, (b) +10 °C, (c) 0 °C, (d) -10 °C, (e) -20 °C, (f) -30 °C, (g) -40 °C, (h) -50 °C, (i) -60 °C, (j) -70 °C, (k) -80 °C.

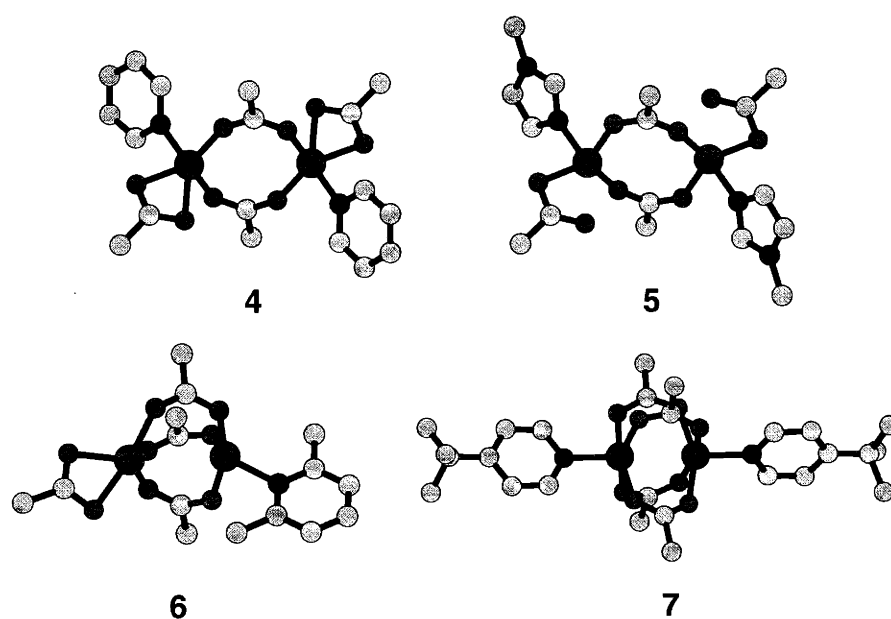


Figure 1.23. Ball and stick representation of the solid-state structures of $[\text{Fe}_2(\mu\text{-O}_2\text{CAr}^{\text{Tol}})_2(\text{O}_2\text{CAr}^{\text{Tol}})_2(\text{C}_5\text{H}_5\text{N})_2]$ (**4**), $[\text{Fe}_2(\mu\text{-O}_2\text{CAr}^{\text{Tol}})_2(\text{O}_2\text{CAr}^{\text{Tol}})_2(1\text{-MeIm})_2]$ (**5**), $[\text{Fe}_2(\mu\text{-O}_2\text{CAr}^{\text{Tol}})_3(\text{O}_2\text{CAr}^{\text{Tol}})(2,6\text{-lutidine})]$ (**6**), and $[\text{Fe}_2(\mu\text{-O}_2\text{CAr}^{\text{Tol}})_4(4\text{-}^t\text{BuC}_5\text{H}_4\text{N})_2]$ (**7**), generated using the crystallographic coordinates. For clarity, all atoms of the $\text{Ar}^{\text{Tol}}\text{CO}_2^-$ ligand, except for the carboxylate groups and the α -carbon atoms, were omitted.

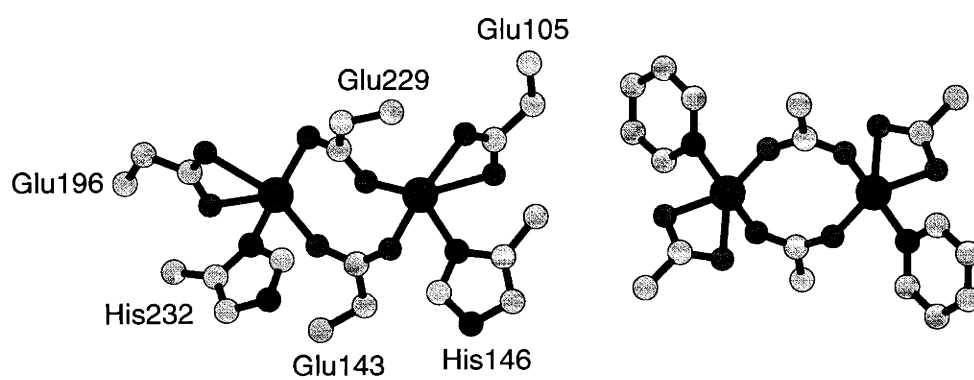


Figure 1.24. Ball and stick representation of the crystallographically determined diiron(II) active site of Δ^9D (left) and 4 (right).

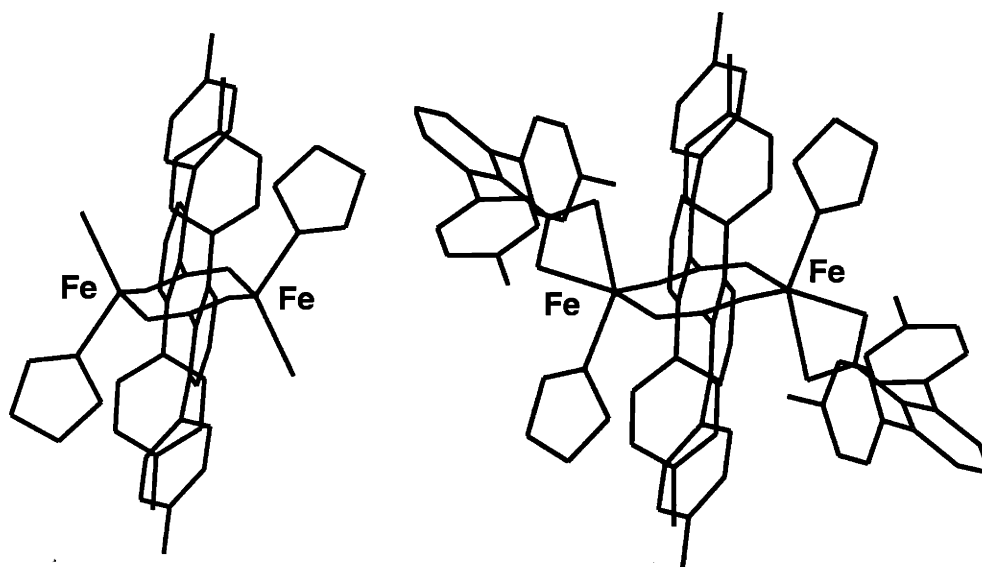


Figure 1.25. Structures of $[\text{Fe}_2(\mu\text{-O}_2\text{CAr}^{\text{Tol}})_2(\text{THF})_2\text{Br}_2]$ (1) (left) and $[\text{Fe}_2(\mu\text{-O}_2\text{CAr}^{\text{Tol}})_2(\text{O}_2\text{CAr}^{\text{Tol}})_2(\text{THF})_2]$ (2) (right), generated using the crystallographic coordinates.

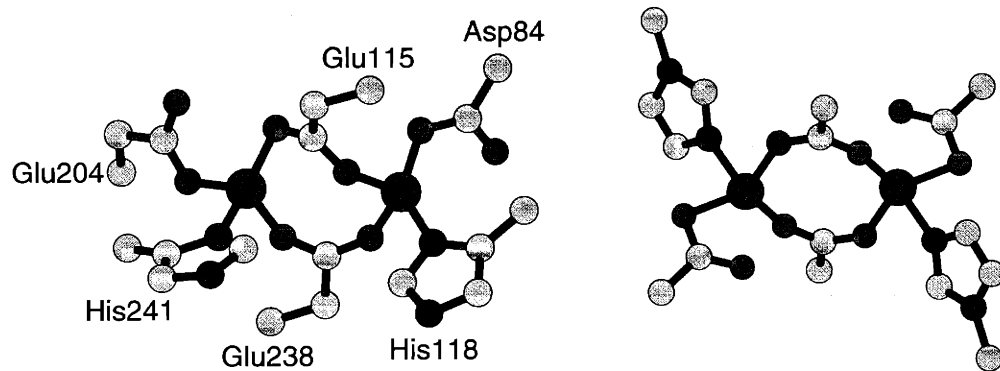


Figure 1.26. Ball and stick representation of the crystallographically determined diiron(II) active site of RNR-R2 (left) and 5 (right).

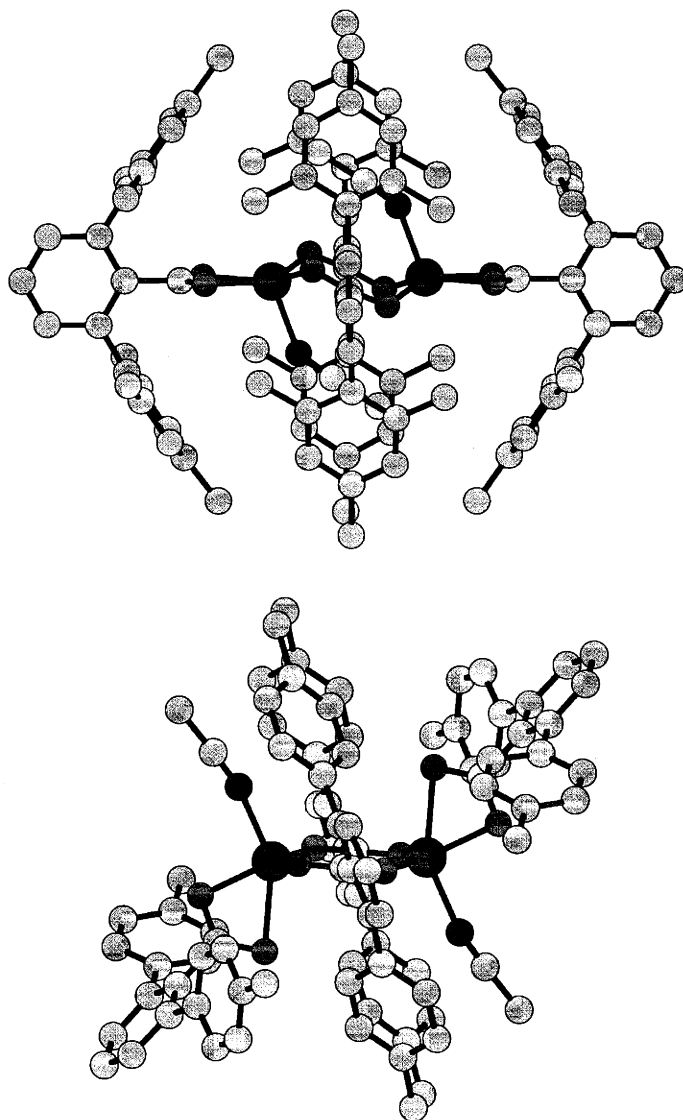


Figure 1.27. Structures of $[\text{Fe}_2(\mu\text{-O}_2\text{CAr}^{\text{Mes}})_2(\text{O}_2\text{CAr}^{\text{Mes}})_2(\text{MeCN})_2]$ (top) and $[\text{Fe}_2(\mu\text{-O}_2\text{CAr}^{\text{Tol}})_2(\text{O}_2\text{CAr}^{\text{Tol}})_2(\text{MeCN})_2]$ (3) (right), generated using the crystallographic coordinates.

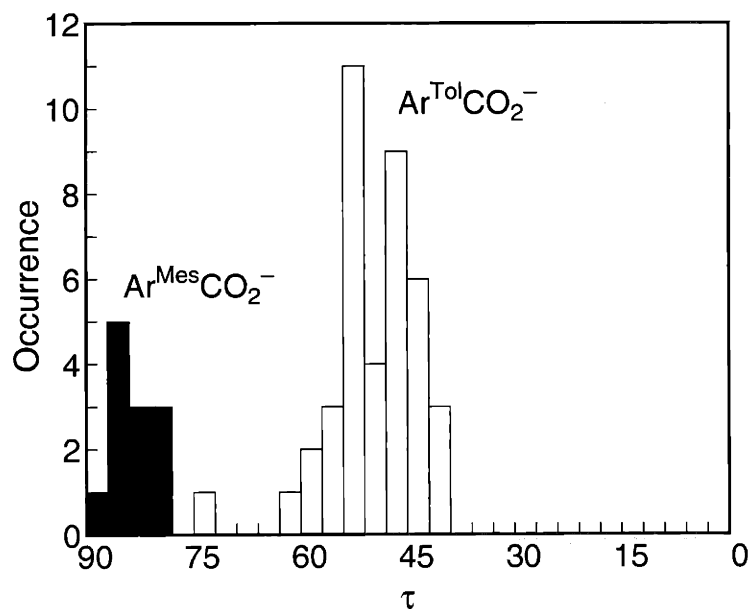
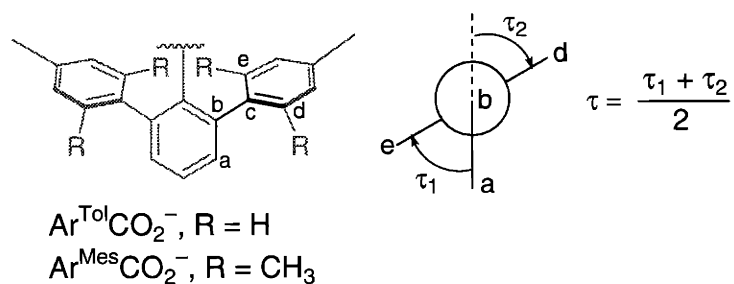


Figure 1.28. Distribution of torsion angles (τ) of $\text{Ar}^{\text{Mes}}\text{CO}_2^-$ (■) and $\text{Ar}^{\text{Tol}}\text{CO}_2^-$ (□) defined as $(\tau_1 + \tau_2)/2$. The values for $\text{Ar}^{\text{Mes}}\text{CO}_2^-$ were obtained from CSD files BAWYUT, BAWZAA, and BAXBIL, corresponding to $[\text{Li}_2(\mu\text{-O}_2\text{CAr}^{\text{Mes}})_2(\text{Et}_2\text{O})_2]$, $[\text{Fe}(\text{O}_2\text{CAr}^{\text{Mes}})_2(1\text{-MeIm})_2]$, and $[\text{Fe}_2(\mu\text{-O}_2\text{CAr}^{\text{Mes}})_2(\text{O}_2\text{CAr}^{\text{Mes}})_2(\text{MeCN})_2]$, respectively. Those of $\text{Ar}^{\text{Tol}}\text{CO}_2^-$ were from 1–8.

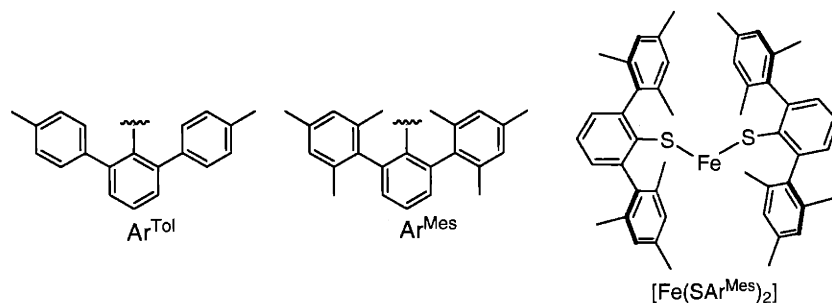
Chapter II

Structural Flexibility within a Sterically Hindered Ligand Platform: Mononuclear Iron(II) Carboxylate Complexes as Subsite Models for Diiron(II) Centers*

Introduction

Coordinationally unsaturated redox-active transition metal ions bind and activate small molecule substrates in living systems.¹ Sulfido-bridged three-coordinate iron centers occur in the nitrogen-fixing FeMo cofactors.² One carboxylate and two histidine ligands bind non-heme iron in selected dioxygen-activating enzymes.³⁻⁵ Efforts to investigate structure-function relationships for such catalytic sites have been greatly assisted by low molecular weight analogs having similar chemical properties.^{6,7}

Sterically hindered ligands are commonly exploited to stabilize low-coordinate metal centers.^{8,9} Among the tactics used to afford steric bulk is the *m*-terphenyl fragment, which can support unusual coordination geometries in mononuclear complexes. The two-coordinate iron(II) thiolate complexes $[\text{Fe}(\text{SAr}^{\text{Mes}})\{\text{N}(\text{SiMe}_3)_2\}]$ and $[\text{Fe}(\text{SAr}^{\text{Mes}})_2]$ illustrate this application.^{10,11} Two mesityl groups flanking the metal binding sites apparently shield them against unwanted oligomerization reactions. Control over coordination number and geometry can thus be achieved by inter-ligand steric interactions in the second coordination sphere.



Recently, we¹²⁻¹⁵ and others^{16,17} have employed the *m*-terphenyl fragment to access coordinationally unsaturated diiron carboxylate complexes. Following a divergent synthetic route, a variety of tetracarboxylate diiron(II) compounds

were prepared from a convenient synthetic precursor, $[\text{Fe}_2(\mu\text{-O}_2\text{CAr}^{\text{Tol}})_2(\text{O}_2\text{CAr}^{\text{Tol}})_2(\text{THF})_2]$ (**1**), where $\text{Ar}^{\text{Tol}}\text{CO}_2^- = 2,6\text{-di}(p\text{-tolyl})\text{benzoate}$.¹² Weakly coordinating THF molecules in **1** are readily displaced by N-donor ligands under mild conditions to afford diiron(II) complexes bearing a close structural resemblance to the active sites of selected non-heme diiron enzymes.^{3,18,19} These ligand substitution reactions, together with the flexible coordination of the terphenyl carboxylates, afforded doubly-, triply-, and quadruply-bridged diiron complexes sharing the common $\{\text{Fe}_2(\text{O}_2\text{CAr}^{\text{Tol}})_4\}$ component.^{12,13,20} In an extension of this approach we explored the chemistry of sterically more demanding monodentate and polydentate N-donor ligands. Our goal was to evaluate how variation in steric bulk and ligand donor strength would affect the nuclearity and coordination geometry of the resulting complexes.

In this chapter are described the synthesis and characterization of neutral mononuclear iron(II) complexes of the carboxylate ligands $\text{Ar}'\text{CO}_2^-$ ($\text{Ar}' = \text{Ar}^{\text{Tol}}$ or $\text{Ar}^{4\text{-tBuPh}}$). Four-, five-, and six-coordinate compounds were readily obtained from a common synthetic precursor with the proper choice of N-donor ligands. Unique structural and physical properties of the compounds $[\text{Fe}(\text{O}_2\text{CAr}')_2\text{L}_n]$ ($\text{L} = 1\text{-BnIm}$ (**3**); 1-MeBzIm (**4**); $2,2'\text{-bipy}$ (**5**); TMEDA (**6**); BPTA (**7**)) are described.¹⁰ The Mössbauer parameters of these compounds were used to facilitate spectral assignment of $[\text{Fe}_2(\mu\text{-O}_2\text{CAr}^{\text{Tol}})_3(\text{O}_2\text{CAr}^{\text{Tol}})(2,6\text{-lutidine})]$ (**2**), which has asymmetric iron centers. Carboxylate shifts upon changes in the N-donor ligands and their structural implications are discussed. A portion of this work has been previously communicated.¹⁵

Experimental Section

General Considerations. All reagents were obtained from commercial suppliers and used as received unless otherwise noted. Dichloromethane was

distilled over CaH₂ under nitrogen. Diethyl ether, pentanes, and THF were saturated with nitrogen and purified by passage through activated Al₂O₃ columns under nitrogen.²¹ The compounds Fe(OTf)₂·2MeCN,²² 2,6-di(*p*-tolyl)benzoic acid (Ar^{Tol}CO₂H),²³⁻²⁵ *N,N'*-bis(2-pyridylmethyl)-*tert*-butylamine (BPTA),²⁶ and [Fe₂(μ-O₂CAr^{Tol})₂(O₂CAr^{Tol})₂(THF)₂] (**1**)¹² were prepared according to literature procedures. The synthesis of 2,6-di(4-*tert*-butylphenyl)benzoic acid (Ar^{*t*BuPh}CO₂H) and [Fe₂(μ-O₂CAr^{Tol})₃(O₂CAr^{Tol})(2,6-lutidine)] (**2**) is reported elsewhere.²⁰ Air-sensitive manipulations were carried out under nitrogen in a Vacuum Atmospheres drybox or by standard Schlenk line techniques.

Physical Measurements. FT-IR spectra were recorded on a Bio Rad FTS-135 instrument with Win-IR software. UV-vis spectra were measured on a Hewlett Packard 8453 diode array spectrophotometer. Mössbauer spectra were obtained on an MS1 spectrometer (WEB Research Co.) with a ⁵⁷Co source in a Rh matrix maintained at room temperature in the MIT Department of Chemistry Instrumentation Facility. Solid samples were prepared by suspending ~0.05 mmol of the powdered material in Apeizon N grease and packing the mixture into a nylon sample holder. All data were collected at 4.2 K and the isomer shift (δ) values are reported with respect to natural iron foil that was used for velocity calibration at room temperature. The spectra were fit to Lorentzian lines by using the WMOSS plot and fit program.²⁷

[Fe(O₂CAr^{Tol})₂(1-BnIm)₂] (**3**). To a rapidly stirred pale yellow CH₂Cl₂ (2 mL) solution of **1** (98 mg, 67 μmol) was added dropwise 1-benzylimidazole (1-BnIm) (43 mg, 0.27 mmol) dissolved in CH₂Cl₂ (1 mL). The resulting colorless solution was stirred for 3 h and filtered. Vapor diffusion of pentanes into the filtrate afforded colorless blocks of **3** (102 mg, 0.105 mmol, 78%), which were suitable for X-ray crystallography. FT-IR (KBr, cm⁻¹) 3141, 3121, 2920, 1608, 1585, 1515, 1497, 1454, 1438, 1400, 1346, 1305, 1283, 1239, 1144, 1106, 1088, 1031, 1020,

946, 940, 838, 820, 800, 783, 765, 752, 736, 725, 708, 693, 655, 544, 458. Anal. Calcd for $C_{62}H_{54}N_4O_4Fe$: C, 76.38; H, 5.58; N, 5.75. Found: C, 75.83; H, 5.92; N, 5.75.

[Fe(O₂CAr^{Tol})₂(1-MeBzIm)₂] (4). To a rapidly stirred pale yellow CH₂Cl₂ (3 mL) solution of **1** (101 mg, 69.1 μmol) was added dropwise 1-methylbenzimidazole (1-MeBzIm) (39 mg, 0.30 mmol) in CH₂Cl₂ (3 mL). The reaction immediately turned into a heterogeneous mixture. Volatile fractions were removed under reduced pressure and the residual off-white solid was extracted into MeOH/MeCN (1:1, 3 mL) and filtered. Vapor diffusion of Et₂O into the filtrate afforded colorless blocks of **4** (103 mg, 0.112 mmol, 81%), which were suitable for X-ray crystallography. FT-IR (KBr, cm⁻¹) 3111, 3056, 2918, 1565, 1513, 1453, 1361, 1297, 1255, 1203, 1186, 1149, 1130, 1111, 1070, 1020, 1006, 916, 882, 855, 835, 821, 802, 784, 763, 586, 541, 524, 454. Anal. Calcd for $C_{58}H_{50}N_4O_4Fe$: C, 75.48; H, 5.46; N, 6.07. Found: C, 75.50; H, 5.42; N, 6.12.

[Fe(O₂CAr^{4-tBuPh})₂(2,2'-bipy)] (5). To a rapidly stirred MeCN (5 mL) solution of Fe(OTf)₂·2MeCN (112 mg, 0.257 mmol) was added NaO₂CAr^{4-tBuPh} (208 mg, 0.509 mmol) to afford a pale yellow solution. A portion of 2,2'-bipyridine (2,2'-bipy) (40 mg, 0.256 mmol) in MeCN (3 mL) was added dropwise. The color of the solution turned dark burgundy red and crystalline material began to deposit within minutes. Dark red blocks of **5** (150 mg, 56%) were isolated and analyzed by X-ray crystallography. FT-IR (KBr, cm⁻¹) 3057, 2962, 2903, 2866, 1598, 1579, 1547, 1513, 1473, 1460, 1442, 1406, 1381, 1363, 1268, 1020, 856, 842, 827, 806, 781, 763, 752, 736, 695, 686, 578; UV-vis (CH₂Cl₂) (λ_{max}, nm (ε, M⁻¹cm⁻¹)) 350 (sh, 290), 537 (200). Anal. Calcd for $C_{64}H_{66}N_2O_4Fe$: C, 78.19; H, 6.77; N, 2.85. Found: C, 78.10; H, 6.83; N, 2.84.

[Fe(O₂CAr^{Tol})₂(TMEDA)] (6). *Method A.* A portion of *N,N,N',N'*-tetramethylethylenediamine (TMEDA) (75 μL, 0.497 mmol) was added dropwise to a rapidly stirred MeCN (10 mL) solution of Fe(OTf)₂·2MeCN (219 mg, 0.502

mmol). The colorless solution was treated with $\text{NaO}_2\text{CAr}^{\text{Tol}}$ (325 mg, 1.00 mmol) and the heterogeneous mixture was stirred overnight. Volatile fractions were removed under reduced pressure and the residual off-white solid was extracted into CH_2Cl_2 (5 mL). Insoluble material was filtered off and pentanes/hexanes (1:1) were allowed to diffuse into the pale yellow filtrate at room temperature. Colorless blocks of **6** (308 mg, 80%) were obtained and analyzed by X-ray crystallography.

Method B. To a rapidly stirred CH_2Cl_2 (3 mL) solution of **1** (153 mg, 0.105 mmol) was added dropwise TMEDA (32 μL , 0.21 mmol). The reaction mixture was stirred for 0.5 h and filtered. Vapor diffusion of pentanes/hexanes (1:1) into the filtrate afforded colorless blocks of **6** (148 mg, 91%). FT-IR (KBr, cm^{-1}) 2916, 2865, 1545, 1514, 1459, 1411, 1382, 1291, 1125, 1111, 1029, 954, 855, 835, 818, 800, 766, 738, 711, 586, 546, 528. Anal. Calcd for $\text{C}_{48}\text{H}_{50}\text{N}_2\text{FeO}_4$: C, 74.41; H, 6.50; N, 3.62. Found: C, 74.56; H, 6.88; N, 3.63.

[Fe(O₂CAr^{Tol})₂(BPTA)] (7). To a rapidly stirred CH_2Cl_2 (2 mL) solution of **1** (102 mg, 69.8 μmol) was added dropwise BPTA (36 mg, 0.14 mmol) dissolved in CH_2Cl_2 (1 mL). The intense yellow solution was stirred for 15 min and volatile fractions were removed under reduced pressure. The residual orange solid was extracted into PhCl (2 mL) and insoluble material was filtered off. Vapor diffusion of pentanes into the yellow filtrate afforded yellow needles of **7** (102 mg, 0.111 mmol, 80%), which were suitable for X-ray crystallography. FT-IR (KBr, cm^{-1}) 3053, 3024, 2974, 2919, 1623, 1606, 1576, 1515, 1477, 1442, 1404, 1372, 1354, 1189, 1149, 1021, 833, 799, 767, 701, 532; UV-vis (CH_2Cl_2) (λ_{max} , nm (ϵ , $\text{M}^{-1}\text{cm}^{-1}$)) 433 (1300). Anal. Calcd for $\text{C}_{58}\text{H}_{55}\text{N}_3\text{O}_4\text{Fe}\cdot\text{C}_6\text{H}_5\text{Cl}$: C, 74.89; H, 5.89; N, 4.09. Found: C, 75.00; H, 6.20; N, 4.14.

X-ray Crystallographic Studies. Intensity data were collected on a Bruker (formerly Siemens) CCD diffractometer with graphite-monochromated Mo $\text{K}\alpha$

radiation ($\lambda = 0.71073 \text{ \AA}$), controlled by a Pentium-based PC running the SMART software package.²⁸ Single crystals were mounted at room temperature on the tips of quartz fibers, coated with Paratone-N oil, and cooled to 188 K under a stream of cold nitrogen maintained by a Bruker LT-2A nitrogen cryostat. Data collection and reduction protocols are described elsewhere.²⁹ The structures were solved by direct methods and refined on F^2 by using the SHELXTL software package.³⁰ Empirical absorption corrections were applied with SADABS,³¹ part of the SHELXTL program package, and the structures were checked for higher symmetry by the program PLATON.³² All non-hydrogen atoms were refined anisotropically unless otherwise noted. Hydrogen atoms were assigned idealized positions and given thermal parameters equivalent to either 1.5 (methyl hydrogen atoms) or 1.2 (all other hydrogen atoms) times the thermal parameter of the carbon atom to which they were attached. The hydrogen atoms associated with the disordered solvent molecules were not included in the refinement. The butyl groups on one of the $\text{Ar}^{4\text{-tBuPh}}\text{CO}_2^-$ ligands in **5** were disordered over two positions. The atoms were equally distributed and refined isotropically. The disordered ethylene carbon atoms of the TMEDA ligand in **6** were equally distributed over two positions and refined isotropically. Each of the chlorine atoms associated with the two PhCl solvent molecules in the structure of **7** were disordered over two positions. One was refined at 0.7 and 0.3 occupancy; the other refined to 0.6 and 0.4. Crystallographic information is provided in Table 2.1.

Results

Synthesis, and structural characterization of $[\text{Fe}(\text{O}_2\text{CAr}^{\text{Tol}})_2(1\text{-BnIm})_2]$ (3**), $[\text{Fe}(\text{O}_2\text{CAr}^{\text{Tol}})_2(1\text{-MeBzIm})_2]$ (**4**), $[\text{Fe}(\text{O}_2\text{CAr}^{4\text{-tBuPh}})_2(2,2'\text{-bipy})]$ (**5**), $[\text{Fe}(\text{O}_2\text{CAr}^{\text{Tol}})_2(\text{TMEDA})]$ (**6**), and $[\text{Fe}(\text{O}_2\text{CAr}^{\text{Tol}})_2(\text{BPTA})]$ (**7**).** Compound **3** was prepared from a reaction between **1** and 1-BnIm in CH_2Cl_2 . Even when a 2:1 ra-

tio of 1-BnIm to **1** was used, only a mononuclear complex was isolated, which incorporated two N-donor ligands per iron(II). The preparation was thus optimized by using > 4 equiv of 1-BnIm per **1**, which afforded colorless blocks of **3** in good yield (78%). The crystal structure of **3** is shown in Figure 2.1; selected bond lengths and angles are listed in Table 2.2. The pseudo-tetrahedral iron center in **3** is coordinated by two monodentate carboxylate and two 1-BnIm ligands. The metrical parameters are normal for high-spin iron(II) centers and comparable to those of related compounds $[\text{Fe}(\text{O}_2\text{CAr}^{\text{Mes}})_2\text{L}_2]$ ($\text{L} = 1\text{-MeIm}$ or pyridine) built on sterically more demanding carboxylate ligands, 2,6-di(mesityl)benzoate ($\text{Ar}^{\text{Mes}}\text{CO}_2^-$).³³

When a similar procedure was used for **1** and 1-MeBzIm, a six-coordinate mononuclear complex **4** was isolated following recrystallization from MeOH/MeCN/Et₂O. The crystal structure of **4** is shown in Figure 2.1; selected bond lengths and angles are listed in Table 2.2. A crystallographic C₂-symmetry bisects the molecule and two symmetry-related bidentate carboxylate and 1-MeBzIm ligands support a highly distorted octahedral iron center. The binding of the carboxylate ligands is asymmetric, as reflected in the two distinct Fe–O distances with $\Delta_{\text{Fe-O}} \sim 0.31 \text{ \AA}$ (Table 2.2). The longer Fe–O bond is positioned trans to the N-donor atoms and the average Fe–O distance of $\sim 2.23 \text{ \AA}$ is significantly longer than that ($\sim 1.99 \text{ \AA}$) in **3**. Despite an increase in coordination number, however, the N–Fe–N angle of 114.99(12)° in **4** is significantly larger than that in **3**, presumably due to the steric interaction between cis-coordinated bulky N-donor ligands. Much smaller N–Fe–N angles of 90.3(1) to 97.6(2)° were obtained for related six-coordinate iron(II) complexes $[\text{Fe}(\text{O}_2\text{CAr}^{\text{Mes}})_2\text{L}_2]$ having sterically less demanding ligands such as 2-picoline or 2,5-lutidine.³³

Ligand substitution reactions of **1** with bidentate imine or amine donors afforded five-coordinate iron(II) complexes **5** and **6** having N₂O₃ donor atom

sets. When a CH_2Cl_2 solution of **1** was treated with 2 equiv of 2,2'-bipy, the color of the solution turned bluish purple and a highly intractable solid material deposited immediately. In order to enhance the solubility of this 2,2'-bipy adduct(s), the less polar $\text{Ar}^{4\text{-tBuPh}}\text{CO}_2^-$ ligand was used to replace $\text{Ar}^{\text{Tol}}\text{CO}_2^-$. Compound **5** was isolated in modest yield (~56%) from a reaction between $\text{Fe}(\text{OTf})_2 \cdot 2\text{MeCN}$, $\text{NaO}_2\text{CAr}^{4\text{-tBuPh}}$, and 2,2'-bipy in a 1:2:1 ratio in MeCN. The use of the polar solvent MeCN apparently facilitates isolation of the neutral product **5**, which precipitates directly from the reaction mixture in analytically pure, crystalline form. The crystal structure of **5** is shown in Figure 2.2; selected bond lengths and angles are available in Table 2.2. Compound **5** has one bidentate and one monodentate carboxylate ligands. The symmetric bonding of the η^2 -carboxylate ($\Delta_{\text{Fe-O}} \cong 0.023 \text{ \AA}$) has Fe–O distances of 2.194(2) and 2.171(2) \AA , which are significantly longer than that of the monodentate carboxylate, 2.015(2) \AA .

Compound **6** can be prepared either by ligand substitution of **1** with 2 equiv of TMEDA or by direct self-assembly from $\text{Fe}(\text{OTf})_2 \cdot 2\text{MeCN}$, $\text{NaO}_2\text{CAr}^{\text{Tol}}$, and TMEDA in a 1:2:1 ratio in THF. Colorless blocks were obtained in excellent yield (80 ~ 91%) following recrystallization from CH_2Cl_2 /pentanes/hexanes. The crystal structure of **6** is shown in Figure 2.2; selected bond lengths and angles are available in Table 2.2. The highly distorted trigonal bipyramidal iron atom ($\text{O}(1\text{A})\text{-Fe}(1)\text{-O}(1\text{B}) = 157.80(6)^\circ$) is coordinated by one bidentate and one monodentate carboxylate, as in **5**. The flexible ethylene linker between the two N donor atoms affords a slightly expanded N–Fe–N angle of $82.66(6)^\circ$ compared with the $75.57(11)^\circ$ value in **5**. Unlike **5**, however, binding of η^2 -carboxylate in **6** is highly asymmetric ($\Delta_{\text{Fe-O}} \cong 0.289 \text{ \AA}$), with a longer Fe(1)–O(2A) bond positioned trans to the amine donors.

Reaction of **1** with 2 equiv of BPTA in CH₂Cl₂ afforded yellow needles of **7** in good yield (80%). The crystal structure of **7** is shown in Figure 2.3; selected bond lengths and angles are available in Table 2.2. X-ray structure analysis revealed two chemically identical but crystallographically inequivalent molecules in the unit cell. The tridentate BPTA ligand binds in a meridional configuration, positioning the two pyridine nitrogen atoms at the pseudoaxial sites of a distorted trigonal bipyramidal. The N(1P)-Fe(1)-N(1Q) angles are 152.28(18) and 153.09(18)°. A pair of monodentate carboxylates and a tertiary amine complete the N₃O₂ donor atom set. The Fe-N_{pyridine} distances of 2.100(4) to 2.137(4) Å in **7** are comparable to the Fe-N_{imidazole/pyridine} distances of 2.074(4) to 2.141(3) Å in **3–5**, but significantly shorter than the Fe-N_{amine} distances of 2.336(4) to 2.353(4) Å. A similar trend was observed for dimanganese(III) and dimanganese(IV) complexes supported by BPTA.²⁶ Compound **7** displays an intense ($\epsilon = 1300 \text{ M}^{-1} \text{ cm}^{-1}$) visible band at $\lambda_{\text{max}} = 433 \text{ nm}$, assigned as a MLCT transition. Similar transitions occur at $\sim 360 \text{ nm}$ in related complexes having comparable ϵ values per iron(II)-pyridine unit ($500\text{--}1000 \text{ M}^{-1} \text{ cm}^{-1}$).³⁴

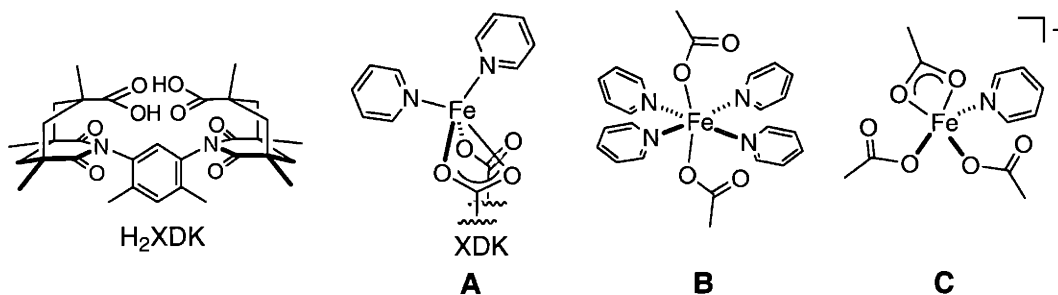
Mössbauer spectroscopy. Zero-field Mössbauer spectra (Figures 2.4 and 2.5) of solid samples of **2–5** and **7** were collected at 4.2 K. The corresponding parameters derived from fits of the spectra are provided in Table 2.3 along with those of related diiron(II) complexes. Consistent with the presence of two distinct iron(II) centers in the dinuclear unit, **2** exhibits two overlapping doublets with equal intensities. Compounds **3–5** and **7** display single sharp ($\Gamma = 0.24 - 0.31 \text{ mm s}^{-1}$) quadrupole doublets. The isomer shifts and quadrupole splittings of these compounds are typical of high-spin iron(II) sites in a N/O coordination environment^{35–37} and comparable to those obtained for related diiron(II) complexes (Table 2.3).²⁰

Discussion

Synthesis of Iron(II) Carboxylate Complexes. Synthetic routes to the Ar^{Tol}CO₂⁻-supported iron(II) complexes developed in this and previous investigations are summarized in Scheme 2.1. The iron(II) centers in these compounds are nestled within the hydrophobic cavity afforded by the *p*-aryl groups flanking the carboxylate group on Ar'CO₂⁻ (Ar' = Ar^{Tol} or Ar^{4-tBuPh}). This steric shield attenuates the propensity of kinetically labile iron-carboxylate units to assemble into higher nuclearity species.³⁸ The nuclearity and coordination geometry of these compounds are apparently dictated by the electronic and steric properties of the N-donor ligands. Structural diversity within the [Fe(O₂CAr^{Tol})₂L₂] modules is further extended by the flexible coordination of the carboxylate ligands, which translate into distinctive Mössbauer parameters obtained for these compounds (*vide infra*).

(a) Core Disassembly upon Ligand Substitution with Monodentate N-Donors. Minimal structural perturbation is introduced into the carboxylate-bridged diiron(II) core of **1** upon displacement of the weakly bound THF ligands by MeCN, pyridine, or 1-methylimidazole.^{12,20} Binding of sterically more demanding monodentate N-donor ligands such as 1-BnIm or 1-MeBzIm, however, dissociates the dinuclear core into mononuclear iron(II) dicarboxylate complexes **3** or **4**. Members of this rare class of iron(II) compounds having two carboxylate and two N-donor ligands were previously prepared by using a dinucleating dicarboxylate XDK¹⁰ or a *m*-terphenyl-derived Ar^{Mes}CO₂⁻ ligand. In [Fe(μ-XDK)(C₅H₅N)₂] (**A**), the iron atom is coordinated by three carboxylate oxygen and two pyridine nitrogen atoms.³⁴ Four- or six-coordinate iron(II) centers can be stabilized within the [Fe(O₂CAr^{Mes})₂L₂] platform.³³ Related mononuclear iron(II) complexes [Fe(OAc)₂(C₅H₅N)₄] (**B**) and [Fe(OAc)₃(C₅H₅N)]⁻ (**C**) can be prepared by chemical reduction of a basic iron acetate cluster

$[\text{Fe}_3\text{O}(\text{OAc})_6(\text{C}_5\text{H}_5\text{N})_3]$ in a mixture of pyridine and AcOH.^{39,40} Without an effective steric shield or conformational rigidity, however, these compounds exist in equilibrium with higher nuclearity species in solution.



The shift in the coordination number from four-coordinate in **3** to six-coordinate in **4** results from a change in the carboxylate denticity and correlates with the electron density at the metal center. Coordination of the less electron-donating ligand 1-MeBzIm ($\text{pK}_a = 5.7$) compared to 1-BnIm ($\text{pK}_a = 6.7$)^{41,42} enhances the Lewis acidity at the metal center, inducing a carboxylate shift from monodentate to bidentate chelating. NMR studies of low-spin cobalt(III) complexes⁴³ as well as a structural analysis of iron(II) complexes $[\text{Fe}(\text{O}_2\text{CAr}^{\text{Mes}})_2\text{L}_2]$ ($\text{L} = \text{N}$ donor ligands)³³ support this notion.

(b) Effects of Conformationally Restricted Bidentate N-Donors. The five-coordinate complexes **5** and **6** are favored when 2,2'-bipy and TMEDA, respectively, are employed. Although an identical N_2O_3 donor atom set occurs in **5** and **6**, the bidentate ligands in these complexes have significantly different donor abilities, as indicated by the pK_a values of 4.3 for 2,2'-bipy⁴⁴ and 9.0 for TMEDA⁴⁵. Both the electronic and steric properties of the ligands in **6** suggest that it, like **3**, might adopt a four-coordinate geometry due to the enhanced donor ability of the amine groups as well as the steric crowding induced by four methyl groups on TMEDA. Compound **5**, on the other hand, might favor six-

coordination, since 2,2'-bipy has a pK_a value even lower than that (5.7) of 1-MeBzIm. The solid state structures of **5** and **6**, however, indicate the failure of these simple arguments to predict the correct geometry, since both are five-coordinate. The ligands 2,2'-bipy and TMEDA afford smaller N-Fe-N bite angles ($75.6 - 82.7^\circ$) than that (98.9°) in **3**, promoting coordination numbers higher than four. These bidentate ligands, however, are conformationally restrictive and may not allow the structural rearrangement required to alleviate steric crowding in six-coordinate complexes.

Recent DFT calculations of $[\text{Zn}(\text{OAc})_x(\text{Im})_y\text{L}_z]^{n+}$ models revealed an energetically very flat potential surface of carboxylate coordination, which allows barrierless interconversion between different carboxylate binding modes.⁴⁶ If similar isoenergetic processes are operative for the $[\text{Fe}(\text{O}_2\text{CAr}^{\text{Tol}})_2\text{L}_n]$ module, the correlation between electronic and stereochemical properties becomes less than straightforward.

(c) Flexible Tridentate N-Donor Ligand. Binding of the three nitrogen atoms of BPTA afforded the five-coordinate iron(II) complex **7**, which has two monodentate carboxylate ligands. Amine/imine mixed-donor ligands derived from the *N,N*-bis(2-pyridylmethyl)amine (BPA) module have been extensively employed to stabilize biomimetic polymanganese clusters.^{26,47-49} Unlike TACN⁻¹⁰ or HBpz₃⁻¹⁰ derived tridentate ligands, conformationally flexible BPA analogs allow both facial and meridional coordination.^{48,50} This feature prompted us to investigate the structural properties of its iron(II) complexes. In order to prevent the formation of unwanted bis(chelate) compounds $[\text{Fe}(\text{BPA})_2]\text{X}_2$,⁵¹ a *tert*-butyl group was installed on the amine nitrogen atom. As shown in Figure 2.3, meridional coordination of BPTA provides a pair of *cis* oriented coordination sites for carboxylate binding. Monodentate coordination of the carboxylate ligands alleviates steric crowding between the $\text{Ar}^{\text{Tol}}\text{CO}_2^-$ ligands

and *tert*-butyl group on BPTA. Carboxylate shifts⁵² thus allow both N₂O₃ and N₃O₂ donor combinations without a change in overall coordination number for 5–7.

Mössbauer spectroscopy. Mössbauer spectroscopy is an excellent method for establishing the oxidation and spin states of iron atoms.³⁵ Among biologically relevant oxidation and spin states, only high-spin ($S = 2$) iron(II) has a unique range of isomer shift (δ) values.^{36,37} The coordination environment and degree of metal-ligand covalency can be deduced from the quadrupole splitting parameter, ΔE_Q , which reflects the electric field gradient (EFG) generated by the charges surrounding the iron site. Mössbauer parameters obtained for well-defined iron carboxylate complexes thus can be used to aid the assignment of spectra for structurally related biological iron clusters. Even for structurally characterized iron model compounds, however, an assignment of quadrupole doublets to individual subsites can be ambiguous when multiple asymmetric iron(II) centers occur within a given molecule.^{34,53,54} We therefore investigated the Mössbauer parameters of the mononuclear iron(II) complexes prepared here as subsite models that can be used to deconvolute more complicated spectra obtained for structurally related polyiron clusters.

Compound **2** is one such species, in which there are two distinct iron sites, Fe(1) (four-coordinate) and Fe(2) (five-coordinate), within the dinuclear unit. The asymmetric coordination environment of the two iron atoms in **2** results in two overlapping quadrupole doublets displayed in the 4.2 K zero-field Mössbauer spectra (Figure 2.4). Valence bond theory dictates that the lower-coordinate Fe(1) site should have greater s-character relative to Fe(2) and a negatively shifted δ value. The quadrupole doublet having the small isomer shift of 1.05 mm s⁻¹ is therefore assigned to Fe(1) and the one with the larger isomer shift of 1.23 mm s⁻¹ to Fe(2). This assignment requires that the smaller ΔE_Q value (2.18

mm s⁻¹) belongs to Fe(1), which indeed displays a more symmetric tetrahedral coordination sphere. Consistent with this analysis is the observation that, in the four-coordinate complex **3**, the δ and ΔE_Q values lie at the low end of the range ($\delta = 1.08 - 1.16$ mm s⁻¹; $\Delta E_Q = 2.46 - 3.52$ mm s⁻¹) of parameters for [Fe(O₂CAr')₂L_n] compounds (Table 2.3). The subspectrum of **2** displaying the larger ΔE_Q value (2.80 mm s⁻¹) is assigned to the more asymmetric, highly distorted five-coordinate atom Fe(2). Comparable quadrupole splittings (2.90 – 3.02 mm s⁻¹) were obtained for **1** and [Fe₂(μ -O₂CAr^{Tol})₂(O₂CAr^{Tol})₂(C₅H₅N)₂],¹² in which analogous five-coordinate iron(II) centers are coordinated by O₅ and NO₄ donor sets, respectively. Deviations from a perfectly symmetric distribution of donor atoms are reflected in similarly large ΔE_Q values of 2.82 – 3.52 mm s⁻¹ exhibited by **4**, **5**, and **7**.

As summarized in Table 2.3, a distribution of ΔE_Q values occurs for the [Fe(O₂CAr')₂L₂] series of compounds. Asymmetry in coordination geometry as well as the positioning of different donor atoms apparently reinforce the intrinsic EFG of high-spin iron(II). A rigorous correlation between the Mössbauer parameters and overall stereochemistry of the iron(II) complexes cannot be made, however, in part owing to the limited number of well-defined basis sets available. Analysis of the Mössbauer data of **2** as described above, however, clearly demonstrates that mononuclear complexes can serve as effective subsite models for higher nuclearity species. It remains to be seen whether such an approach is generally applicable to a larger number of examples sharing similar architectural features.

Summary and Conclusions

A series of mononuclear iron(II) complexes were obtained from a common diiron(II) precursor complex. Sterically demanding *m*-terphenyl-derived car-

boxylate ligands stabilize four-, five-, and six-coordinate complexes having rare coordination geometries. Structural variations within the $[\text{Fe}(\text{O}_2\text{CAr}')_2\text{L}_n]$ module are dictated by the steric and electronic properties of the N-donor ligands and accommodated by flexible coordination of the carboxylate ligands. Mössbauer parameters obtained for these compounds were used to assist spectral assignment of a dinuclear complex. Structurally related mononuclear complexes thus may serve as useful subsite models for higher nuclearity species in both synthetic and biological systems.

Acknowledgments. This work was supported by a grant from the National Science Foundation. I thank Ms. J. Kuzelka for help in acquiring the Mössbauer spectra.

References

(*) A slightly modified version of this work has been submitted for publication.

Lee, D.; Lippard, S. J. **2001**

(1) Holm, R. H.; Kennepohl, P.; Solomon, E. I. *Chem. Rev.* **1996**, *96*, 2239-2314.

(2) Stiefel, E. I.; George, G. N. *Bioinorganic Chemistry*; Bertini, I., Gray, H. B., Lippard, S. J. and Valentine, J. S., Ed.; University Science Books: Mill Valley, CA, 1994, pp 365-453.

(3) Feig, A. L.; Lippard, S. J. *Chem. Rev.* **1994**, *94*, 759-805.

(4) Hegg, E. L.; Que, L., Jr. *Eur. J. Biochem.* **1997**, *250*, 625-629.

(5) Solomon, E. I.; Brunold, T. C.; Davis, M. I.; Kemsley, J. N.; Lee, S.-K.; Lehnert, N.; Neese, F.; Skulan, A. J.; Yang, Y.-S.; Zhou, J. *Chem. Rev.* **2000**, *100*, 235-349.

(6) Beinert, H.; Holm, R. H.; Münck, E. *Science* **1997**, *277*, 653-659.

(7) Que, L., Jr.; Ho, R. Y. N. *Chem. Rev.* **1996**, *96*, 2607-2624.

(8) Cummins, C. C. *Prog. Inorg. Chem.* **1998**, *47*, 685-836.

(9) Twamley, B.; Haubrich, S. T.; Power, P. P. *Adv. Organomet. Chem.* **1999**, *44*, 1-65.

(10) Abbreviations used: Ar^{Mes}, 2,6-dimesitylphenyl; XDK, *m*-xylenediamine bis(Kemp's triacid imide); TACN, 1,4,7-triazacyclononane; HBpz₃, hydrotris(1-pyrazolyl)borate; 1-BnIm, 1-benzyl-imidazole; 1-MeBzIm, 1-methylbenzimidazole; 2,2'-bipy, 2,2'-bipyridine; TMEDA, *N,N,N',N'*-tetramethylethylenediamine; BPTA, *N,N'*-bis(2-pyridylmethyl)-*tert*-butylamine.

(11) Ellison, J. J.; Ruhlandt-Senge, K.; Power, P. P. *Angew. Chem., Int. Ed. Engl.* **1994**, *33*, 1178-1180.

(12) Lee, D.; Lippard, S. J. *J. Am. Chem. Soc.* **1998**, *120*, 12153-12154.

(13) Lee, D.; Du Bois, J.; Petasis, D.; Hendrich, M. P.; Krebs, C.; Huynh, B. H.; Lippard, S. J. *J. Am. Chem. Soc.* **1999**, *121*, 9893-9894.

- (14) Lee, D.; Krebs, C.; Huynh, B. H.; Hendrich, M. P.; Lippard, S. J. *J. Am. Chem. Soc.* **2000**, *122*, 5000–5001.
- (15) Lee, D.; Lippard, S. J. *J. Am. Chem. Soc.* **2001**, *123*, 4611–4612.
- (16) Hagadorn, J. R.; Que, L., Jr.; Tolman, W. B. *J. Am. Chem. Soc.* **1998**, *120*, 13531–13532.
- (17) Hagadorn, J. R.; Que, L., Jr.; Tolman, W. B.; Prisecaru, I.; Münck, E. *J. Am. Chem. Soc.* **1999**, *121*, 9760–9761.
- (18) Wallar, B. J.; Lipscomb, J. D. *Chem. Rev.* **1996**, *96*, 2625–2657.
- (19) Du Bois, J.; Mizoguchi, T. J.; Lippard, S. J. *Coord. Chem. Rev.* **2000**, *200–202*, 443–485.
- (20) D. Lee, S. J. Lippard, submitted for publication.
- (21) Pangborn, A. B.; Giardello, M. A.; Grubbs, R. H.; Rosen, R. K.; Timmers, F. J. *Organometallics* **1996**, *15*, 1518–1520.
- (22) Hagen, K. S. *Inorg. Chem.* **2000**, *39*, 5867–5869.
- (23) Du, C.-J. F.; Hart, H.; Ng, K. -K. D. *J. Org. Chem.* **1986**, *51*, 3162–3165.
- (24) Saednya, A.; Hart, H. *Synthesis* **1996**, 1455–1458.
- (25) Chen, C.-T.; Siegel, J. S. *J. Am. Chem. Soc.* **1994**, *116*, 5959–5960.
- (26) Mok, H. J.; Davis, J. A.; Pal, S.; Mandal, S. K.; Armstrong, W. H. *Inorg. Chim. Acta* **1997**, *263*, 385–394.
- (27) Kent, T. A. *WMOSS v2.5: Mössbauer Spectral Analysis Software*; WEB Research Co.: Minneapolis, MN, 1998.
- (28) *SMART v5.05: Software for the CCD Detector System*; Bruker AXS: Madison, WI, 1998.
- (29) Feig, A. L.; Bautista, M. T.; Lippard, S. J. *Inorg. Chem.* **1996**, *35*, 6892–6898.
- (30) Sheldrick, G. M. *SHELXTL97-2: Program for the Refinement of Crystal Structures*; University of Göttingen, Germany, 1997.

- (31) Sheldrick, G. M. *SADABS: Area-Detector Absorption Correction*; University of Göttingen, Germany, 1996.
- (32) Spek, A. L. *PLATON, A Multipurpose Crystallographic Tool*; Utrecht University: Utrecht, The Netherlands, 1998.
- (33) Hagadorn, J. R.; Que, L., Jr.; Tolman, W. B. *Inorg. Chem.* **2000**, *39*, 6086-6090.
- (34) LeCloux, D. D.; Barrios, A. M.; Mizoguchi, T. J.; Lippard, S. J. *J. Am. Chem. Soc.* **1998**, *120*, 9001-9014.
- (35) Kurtz, D. M., Jr. *Chem. Rev.* **1990**, *90*, 585-606.
- (36) Gütlich, P.; Ensling, J. *Inorganic Electronic Structure and Spectroscopy*; Solomon, E. I. and Lever, A. B. P., Ed.; John Wiley & Sons: New York, 1999; Vol. I, pp 161-211.
- (37) Münck, E. *Physical Methods in Bioinorganic Chemistry: Spectroscopy and Magnetism*; Que, L., Jr., Ed.; University Science Books: Sausalito, CA, 2000, pp 287-319.
- (38) Lippard, S. J. *Angew. Chem., Int. Ed. Engl.* **1988**, *27*, 344-361.
- (39) Singh, B.; Long, J. R.; Papaefthymiou, G. C.; Stavropoulos, P. *J. Am. Chem. Soc.* **1996**, *118*, 5824-5825.
- (40) Singh, B.; Long, J. R.; de Biani, F. F.; Gatteschi, D.; Stavropoulos, P. *J. Am. Chem. Soc.* **1997**, *119*, 7030-7047.
- (41) Avdeef, A.; Comer, J. E. A.; Thomson, S. J. *Anal. Chem.* **1993**, *65*, 42-29.
- (42) Catalán, J.; Claramunt, R. M.; Elguero, J.; Laynez, J.; Menéndez, M.; Anvia, F.; Quian, J. H.; Taagepera, M.; Taft, R. W. *J. Am. Chem. Soc.* **1988**, *110*, 4105-4111.
- (43) Connolly, J. A.; Kim, J. H.; Banaszczyk, M.; Drouin, M.; Chin, J. *Inorg. Chem.* **1995**, *34*, 1094-1099.
- (44) Tijou, E. M.; Fruchier, A.; Pellegrin, V.; Tarrago, G. *J. Heterocyclic Chem.* **1989**, *26*, 893-898.

- (45) Reddy, P. R.; Reddy, M. H. *J. Chem. Soc., Dalton Trans.* **1985**, 239-242.
- (46) Ryde, U. *Biophys. J.* **1999**, 77, 2777-2787.
- (47) Pal, S.; Chan, M. K.; Armstrong, W. H. *J. Am. Chem. Soc.* **1992**, 114, 6398-6406.
- (48) Pal, S.; Olmstead, M. M.; Armstrong, W. H. *Inorg. Chem.* **1995**, 34, 4708-4715.
- (49) Mandal, S. K.; Armstrong, W. H. *Inorg. Chim. Acta* **1995**, 229, 261-270.
- (50) Ito, M.; Takita, Y.-S.; Sakai, K.; Tubomura, T. *Chem. Lett.* **1998**, 1185-1186.
- (51) Butcher, R. J.; Addison, A. W. *Inorg. Chim. Acta* **1989**, 158, 211-215.
- (52) Rardin, R. L.; Tolman, W. B.; Lippard, S. J. *New J. Chem.* **1991**, 15, 417-430.
- (53) Tolman, W. B.; Liu, S.; Bentsen, J. G.; Lippard, S. J. *J. Am. Chem. Soc.* **1991**, 113, 152-164.
- (54) Herold, S.; Lippard, S. J. *J. Am. Chem. Soc.* **1997**, 119, 145-156.

Table 2.1. Summary of X-ray Crystallographic Data

	3	4	5·2MeCN	6	7·PhCl
formula	FeC ₆₂ H ₅₄ N ₄ O ₄	FeC ₅₈ H ₅₀ N ₄ O ₄	FeC ₆₈ H ₇₂ N ₄ O ₄	FeC ₄₈ H ₅₀ N ₂ O ₄	FeC ₆₄ H ₅₉ N ₃ O ₄ Cl
fw	974.9	922.87	1065.15	774.75	1025.44
space group	$P\bar{1}$	C2/c	$P\bar{1}$	P2 ₁ /n	$P\bar{1}$
a, Å	12.7648(4)	14.453(17)	14.1779(12)	12.4478(4)	13.3303(4)
b, Å	14.5563(5)	23.21(2)	14.4349(13)	19.9561(6)	16.6989(4)
c, Å	15.4066(6)	15.667(10)	14.7856(13)	17.2865(5)	26.8209(6)
α, deg	73.8100(10)		78.700(3)		99.7700(10)
β, deg	67.795(2)	114.03(5)	84.547(2)	110.7520(10)	102.9470(10)
γ, deg	84.0580(10)		83.7120(10)		104.31
V, Å ³	2545.26(15)	4800(8)	2941.0(4)	4015.5(2)	5475.4(2)
Z	2	4	2	4	4
ρ _{calc} , g/cm ³	1.272	1.277	1.203	1.282	1.244
T, °C	-85	-85	-85	-85	-85
μ(Mo Kα), mm ⁻¹	0.349	0.366	0.308	0.423	0.375
θ limits, deg	1.81–28.30	1.75–28.29	1.94–28.34	1.62–28.31	1.61–28.30
total no. of data	16198	4892	18565	24856	34765
no. of unique data	11287	3479	12990	9231	24237
no. of params	640	310	690	522	1333
R (%) ^a	6.80	3.80	6.21	4.06	7.03
wR ² (%) ^b	11.10	9.40	14.23	9.27	12.10
max, min peaks, e/Å ³	0.310, -0.341	0.197, -0.225	0.445, -0.339	0.355, -0.413	0.291, -0.328
$a R = \Sigma F_o - F_c / \Sigma F_o \cdot b wR^2 = \{\Sigma [w(F_o^2 - F_c^2)^2] / \Sigma [w(F_o^2)^2]\}^{1/2}$.					

Table 2.2. Selected Bond Lengths (Å) and Angles (deg) for **3**, **4**, **5·2MeCN**, **6**, and **7·PhCl**^a

	bond length		bond angle	
3	Fe(1)–O(1)	1.989(3)	O(1)–Fe(1)–O(3)	147.58(13)
	Fe(1)–O(3)	1.996(3)	O(1)–Fe(1)–N(1)	107.68(14)
	Fe(1)–N(1)	2.074(4)	O(3)–Fe(1)–N(1)	95.25(14)
	Fe(1)–N(3)	2.121(4)	O(1)–Fe(1)–N(3)	90.13(14)
			O(3)–Fe(1)–N(3)	109.02(14)
			N(1)–Fe(1)–N(3)	98.89(15)
4	Fe(1)–O(1)	2.076(3)	O(1)–Fe(1)–O(1A)	156.77(1)
	Fe(1)–O(2)	2.384(2)	O(1)–Fe(1)–N(1)	107.93(8)
	Fe(1)–N(1)	2.128(2)	O(1)–Fe(1)–N(1A)	84.75(8)
			O(1)–Fe(1)–O(2)	58.58(7)
			O(1)–Fe(1)–O(2A)	102.22(8)
			N(1)–Fe(1)–O(2)	93.72(9)
			N(1)–Fe(1)–O(2A)	139.58(7)
			O(2)–Fe(1)–O(2A)	79.51(11)
			N(1)–Fe(1)–N(1A)	114.99(12)
5·2MeCN	Fe(1)–O(1A)	2.194(2)	O(1A)–Fe(1)–O(2A)	60.08(9)
	Fe(1)–O(2A)	2.171(2)	O(1A)–Fe(1)–O(1B)	100.92(9)
	Fe(1)–O(1B)	2.015(2)	O(1B)–Fe(1)–N(1)	141.94(11)
	Fe(1)–N(1)	2.131(3)	O(1B)–Fe(1)–N(2)	112.81(10)
	Fe(1)–N(2)	2.141(3)	O(1B)–Fe(1)–O(2A)	101.80(10)
			N(1)–Fe(1)–O(2A)	112.95(10)
			N(2)–Fe(1)–O(2A)	101.85(10)
			N(1)–Fe(1)–O(1A)	84.19(10)
			N(2)–Fe(1)–O(1A)	144.82(10)
			N(1)–Fe(1)–N(2)	75.57(11)
6	Fe(1)–O(1A)	2.0641(14)	O(1A)–Fe(1)–O(1B)	157.80(6)
	Fe(1)–O(2A)	2.3527(14)	O(1A)–Fe(1)–O(2A)	59.07(5)
	Fe(1)–O(1B)	1.9590(13)	O(1B)–Fe(1)–O(2A)	104.11(5)
	Fe(1)–N(1)	2.1868(16)	O(1A)–Fe(1)–N(1)	103.28(6)
	Fe(1)–N(2)	2.2119(16)	O(1A)–Fe(1)–N(2)	91.06(6)
			O(1B)–Fe(1)–N(1)	96.89(6)
			O(1B)–Fe(1)–N(2)	100.73(6)
			N(1)–Fe(1)–O(2A)	114.16(6)
			N(2)–Fe(1)–O(2A)	147.65(6)
			N(1)–Fe(1)–N(2)	82.66(6)

^a Number in parentheses are estimated standard deviations of the last significant figures. Atoms are labeled as indicated in Figures 2.1 – 2.3.

Table 2.2, continued. Selected bond lengths (Å) and angles (deg) for **3**, **4**, **5**·2MeCN, **6**, and **7**·PhCl ^a

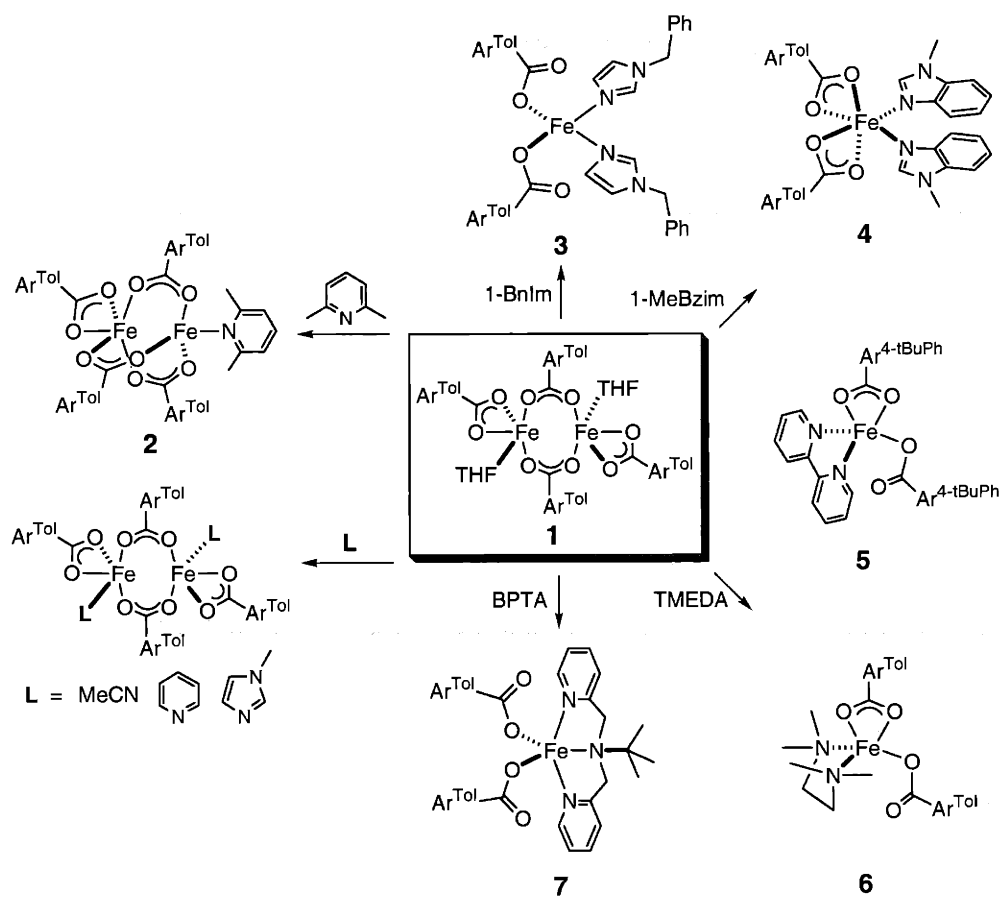
bond length		bond angle			
7·PhCl	Fe(1)–O(1A)	2.116(3) ^b	O1A-Fe1-O1B	87.80(14) ^b	
		2.150(3) ^c		91.68(13) ^c	
	Fe(1)–O(1B)	2.007(3) ^b	O1A-Fe1-N1P	101.40(14) ^b	
		1.995(3) ^c		98.98(15) ^c	
	Fe(1)–N(1Q)	2.121(4) ^b	O1A-Fe1-N1Q	96.72(14) ^b	
		2.100(4) ^c		96.74(15) ^c	
	Fe(1)–N(1P)	2.137(4) ^b	O1A-Fe1-N01	142.17(14) ^b	
		2.122(4) ^c		142.12(13) ^c	
	Fe(1)–N(01)	2.353(4) ^b	O1B-Fe1-N1P	91.92(15) ^b	
				93.50(14) ^c	
		2.336(4) ^c	O1B-Fe1-N1Q	109.69(14) ^b	
				107.76(15) ^c	
			O1B-Fe1-N01	129.76(13) ^b	
				125.96(13) ^c	
	N1P-Fe1-N1Q		N1P-Fe1-N1Q	152.28(18) ^b	
				153.09(18) ^c	
		N1P-Fe1-N01			76.28(15) ^b
					77.25(17) ^c
N1Q-Fe1-N01			76.53(15) ^b		
			77.25(17) ^c		

^a Number in parentheses are estimated standard deviations of the last significant figures. Atoms are labeled as indicated in Figures 2.1 – 2.3. ^b Molecule 1. ^c Molecule 2.

Table 2.3. 4.2 K Zero-Field Mössbauer Parameters for $[\text{Fe}_2(\mu\text{-O}_2\text{CAr}^{\text{Toh}})_3(\text{O}_2\text{CAr}^{\text{Toh}})(2,6\text{-lutidine})]$ (2), $[\text{Fe}(\mu\text{-O}_2\text{CAr}^{\text{Toh}})_2(1\text{-BnIm})_2]$ (3), $[\text{Fe}(\text{O}_2\text{CAr}^{\text{Toh}})_2(1\text{-MeBzIm})_2]$ (4), $[\text{Fe}(\text{O}_2\text{CAr}^{4\text{-tBuPh}})_2(2,2'\text{-bipy})]$ (5), $[\text{Fe}(\text{O}_2\text{CAr}^{\text{Toh}})_2(\text{BPTA})]$ (7), and Related Diiron(II) Complexes.

compound	δ (mm s ⁻¹)	ΔE_{Q} (mm s ⁻¹)	Γ_{L} (mm s ⁻¹)	Γ_{R} (mm s ⁻¹)	coord. number	ref
2	1.05(2)	2.18(2)	0.31	0.31	site 1 4	this work
	1.23(2)	2.80(2)	0.28	0.28	site 2 5	
3	1.08(2)	2.46(2)	0.26	0.31	4	this work
4	1.16(2)	2.82(2)	0.24	0.26	6	this work
5	1.13(2)	2.91(2)	0.29	0.28	5	this work
7	1.10(2)	3.52(2)	0.26	0.26	5	this work
$[\text{Fe}_2(\mu\text{-O}_2\text{CAr}^{\text{Toh}})_2(\text{O}_2\text{CAr}^{\text{Toh}})_2(\text{THF})_2]$	1.26(2)	2.90(2)	0.27	0.28	5 ^a	20
$[\text{Fe}_2(\mu\text{-O}_2\text{CAr}^{\text{Toh}})_2(\text{O}_2\text{CAr}^{\text{Toh}})_2(\text{C}_5\text{H}_5\text{N})_2]$	1.19(2)	3.02(2)	0.25	0.25	5 ^a	20

^a Two iron atoms are symmetry-related



Scheme 2.1.

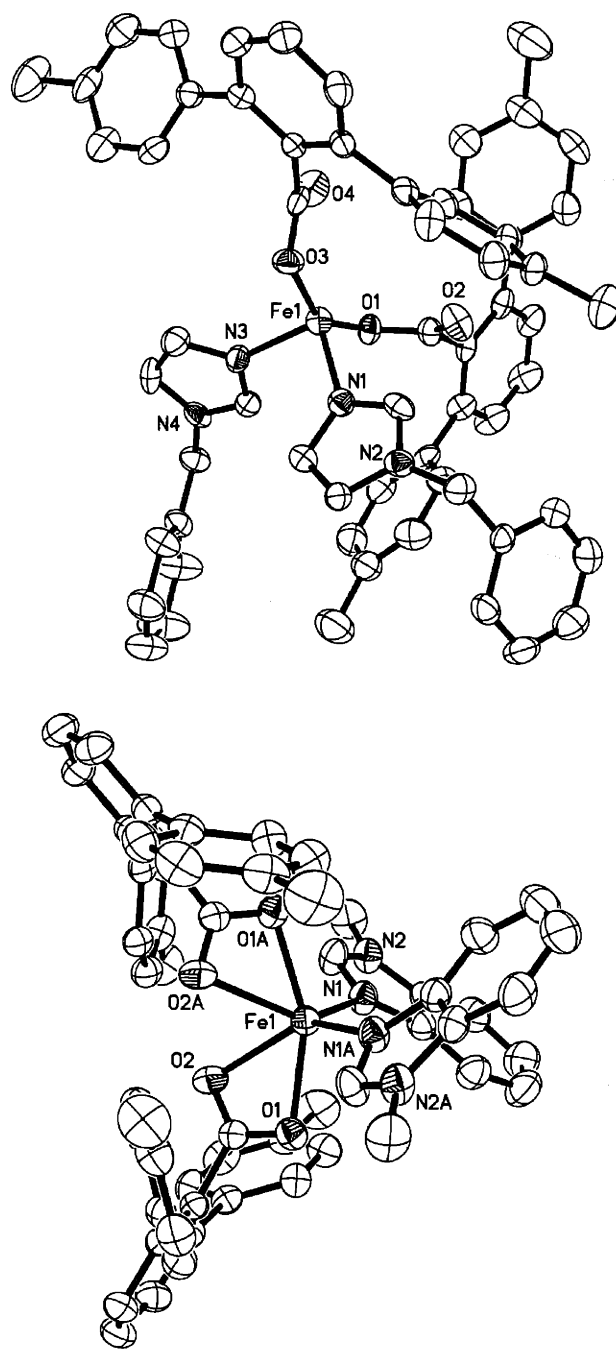


Figure 2.1. ORTEP diagrams of $[\text{Fe}(\text{O}_2\text{CAr}^{\text{Tol}})_2(1\text{-BnIm})_2]$ (3) (top) and $[\text{Fe}(\text{O}_2\text{CAr}^{\text{Tol}})_2(1\text{-MeBzIm})_2]$ (4) (bottom) with thermal ellipsoids at 50% probability.

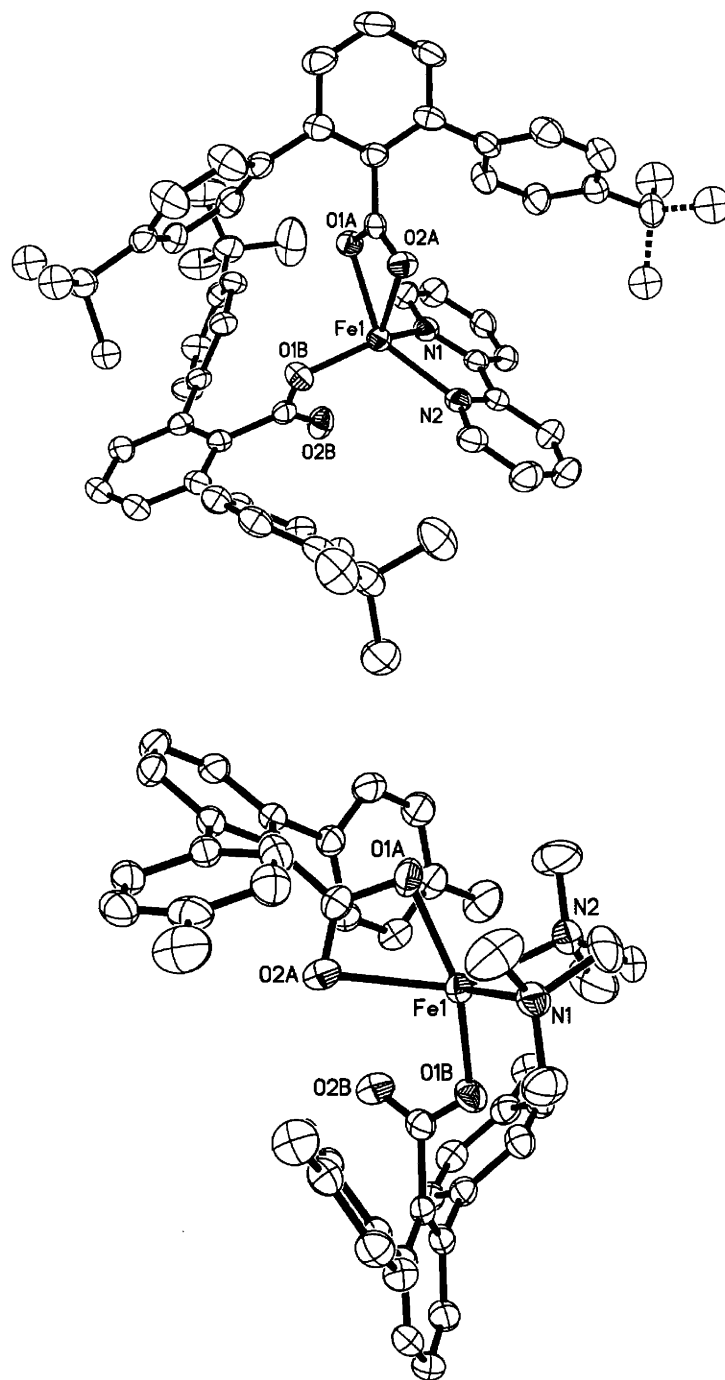


Figure 2.2. ORTEP diagrams of $[\text{Fe}(\text{O}_2\text{CAr}^{4\text{-tBuPh}})_2(2,2'\text{-bipy})]$ (5) (top) and $[\text{Fe}(\text{O}_2\text{CAr}^{\text{Tol}})_2(\text{TMEDA})]$ (6) (bottom) with thermal ellipsoids at 50% probability.

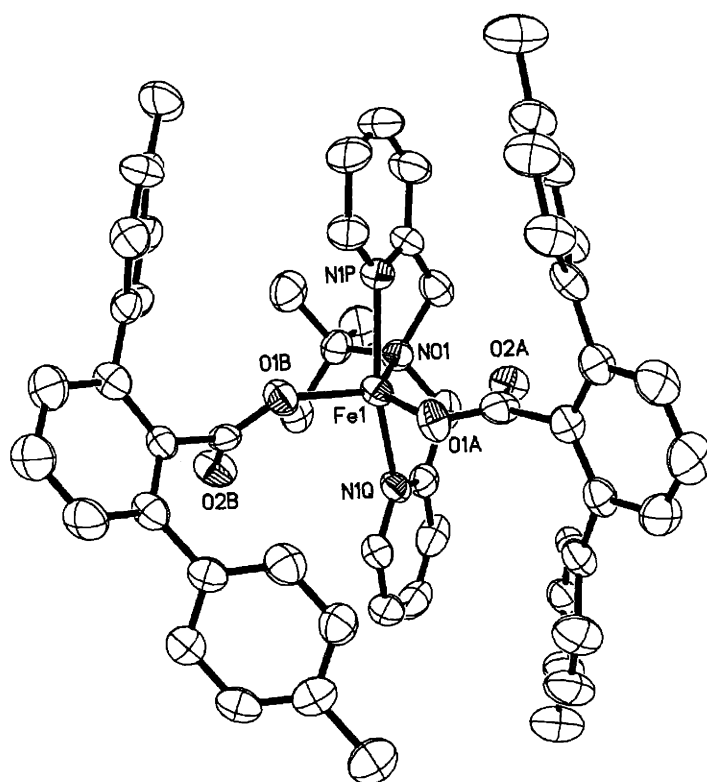


Figure 2.3. ORTEP diagram of [Fe(O₂CAr^{Tol})₂(BPTA)] (7) with thermal ellipsoids at 50% probability.

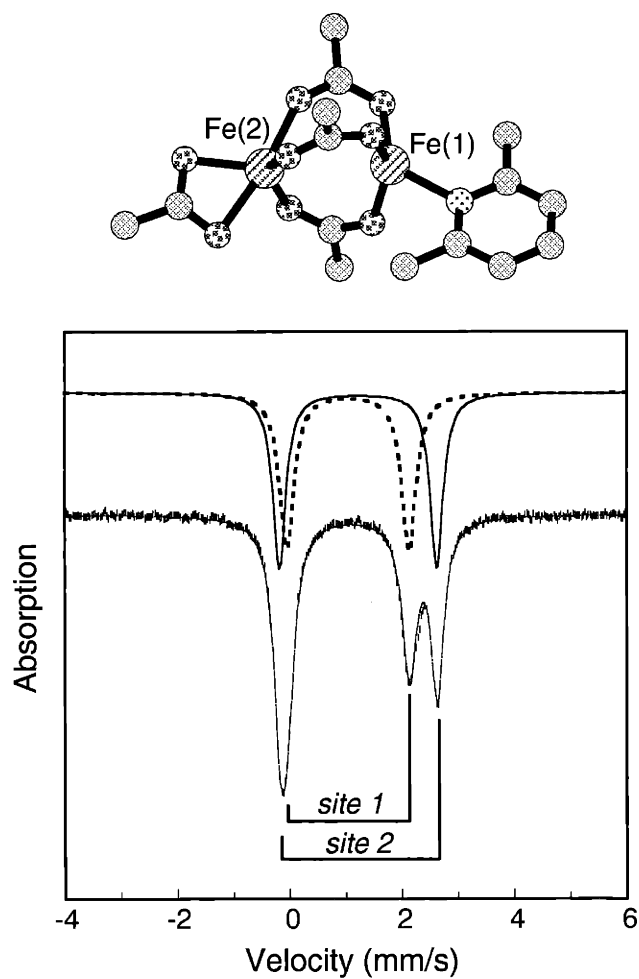


Figure 2.4. Zero-field Mössbauer spectra (experimental data (|), calculated fit (—)) recorded at 4.2 K for a solid sample of [Fe₂(μ-O₂CAr^{Tol})₃(O₂CAr^{Tol})(2,6-lutidine)] (2). The upper curves show two subsets for the calculated spectra. See Table 2.3 for derived Mössbauer parameters.

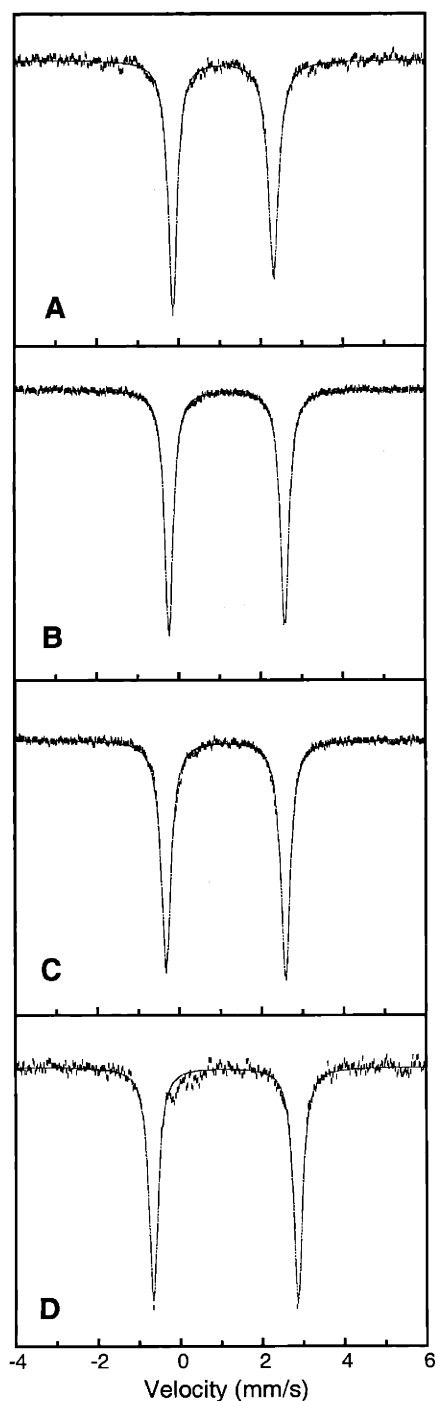


Figure 2.5. Zero-field Mössbauer spectra (experimental data (|), calculated fit(–)) recorded at 4.2 K for solid samples of $[\text{Fe}(\text{O}_2\text{CAr}^{\text{Tol}})_2(1\text{-BnIm})_2]$ (**3**) (A); $[\text{Fe}(\text{O}_2\text{CAr}^{\text{Tol}})_2(1\text{-MeBzIm})_2]$ (**4**) (B); $[\text{Fe}(\text{O}_2\text{CAr}^{4\text{-tBuPh}})_2(2,2'\text{-bipy})]$ (**5**) (C); $[\text{Fe}(\text{O}_2\text{CAr}^{\text{Tol}})_2(\text{BPTA})]$ (**7**) (D). See Table 2.3 for derived Mössbauer parameters.

Chapter III

Functional Mimic of Dioxygen-Activating Centers in Non-Heme Diiron Enzymes: Mechanistic Implications of Paramagnetic Intermediates in the Reactions between Diiron(II) Complexes and Dioxygen*

Introduction

Structural modules comprising two iron atoms ligated by four carboxylate and two imidazole residues occur in selected non-heme diiron enzymes that activate dioxygen.¹ The hydroxylase component of methane monooxygenase (MMOH),^{2,3} the R2 component of ribonucleotide reductase (RNR-R2),^{4,5} and stearyl-acyl carrier protein (ACP) Δ^9 -desaturase (Δ^9D)^{6,7} are representative of such metalloenzymes, in which coordinatively unsaturated dimetallic centers are used to harness the oxidizing power of dioxygen. In the enzyme reaction cycle, highly reactive intermediates are accessed through controlled delivery of reducing equivalents to the metal-bound O₂-derived ligands. Notable functional features of this enzyme family include the evolution of distinctive higher oxidation state intermediates from essentially identical initial dioxygen-adducts (Scheme 3.1). Current information points toward the involvement of high-valent iron(IV) species in C–H activation by MMOH and tyrosine oxidation by RNR-R2. The mechanism(s) by which reductive activation of an O–O bond affords reactive iron-oxo units, however, is not fully understood. Specifically, two-electron reduction of the peroxide ligand by iron in (peroxo)diiron(III) species affords a Fe(IV)Fe(IV) center in MMOH_Q,⁸⁻¹⁰ whereas delivery of one external electron is required for a conversion to the Fe(III)Fe(IV) core in RNR-R2 X.¹¹ The fate of these O₂-derived intermediates might be affected by carboxylate shifts,¹² the functional relevance of which needs to be elucidated in conjunction with the dynamic core conversions implicated in the catalytic cycle.²

Well-defined synthetic analogs having chemical properties comparable to those of non-heme diiron enzymes have complemented our understanding of biological dioxygen activation.^{1c,1f,13-15} Several examples are now available in which reactions between diiron(II) complexes and O₂ afford (peroxo)diiron(III) species,¹⁶⁻²² the mechanisms of formation and decay of which have been investi-

gated by kinetic techniques.^{20,22-26} A few (peroxo)diiron(III) complexes have been isolated at low temperatures and structurally characterized,^{16b,17c,18} providing insights into the geometric and electronic structures of the transient enzyme intermediates.^{1g,27-31} High-valent di(μ -oxo)iron(III)iron(IV) complexes were prepared by reactions between diiron(III) complexes and H_2O_2 , and studied as spectroscopic and structural models for RNR-R2 X.³² Related Fe(III)Fe(IV) species were accessed by one-electron chemical oxidation of a di(μ -oxo)diiron(III) precursor³³ or by reactions between a diiron(II) precursor and O_2 at low temperatures.²² Most of the model compounds investigated so far, however, are built on polyamine/imine donor ligands, a coordination environment significantly different from those of the carboxylate-rich active sites in MMOH and RNR-R2. Integrating a parallel functional chemistry into a well-defined structural replica of the non-heme diiron enzymes is a long-standing problem in bioinorganic chemistry, the solution to which would provide significant insights into the underlying chemical principles of enzyme action.

Recently, we reported that tetracarboxylate diiron(II) complexes $[\text{Fe}_2(\mu\text{-O}_2\text{CAr}^{\text{Tot}})_2(\text{O}_2\text{CAr}^{\text{Tot}})_2(\text{C}_5\text{H}_5\text{N})_2]$ (**1a**) or $[\text{Fe}_2(\mu\text{-O}_2\text{CAr}^{\text{Tot}})_4(4\text{-}^t\text{BuC}_5\text{H}_4\text{N})_2]$ (**2a**), where $\text{Ar}^{\text{Tot}}\text{CO}_2^- = 2,6\text{-di}(p\text{-tolyl})\text{benzoate}$, react with dioxygen in CH_2Cl_2 at -78°C to afford thermally-sensitive intermediates having broad intense visible absorptions at $660 - 670\text{ nm}$.^{34,35} EPR and Mössbauer data were consistent with the existence of an equimolar amount of Fe(II)Fe(III) and Fe(III)Fe(IV) species as major components of these intermediates.³⁵ A mechanism for this unprecedented process was proposed (eq 1), based solely on the observed reaction stoichiometry.



In this chapter, we present a full description of the reactions of **1a** and **2a** with dioxygen. Spectroscopic and reactivity properties of the metastable reaction intermediates are described and compared with those of independently synthesized mixed-valence compounds. Kinetic studies revealed simultaneous development of both Fe(III)Fe(IV) and Fe(II)Fe(III) species from the reactions between diiron(II) precursor molecules and dioxygen at low temperatures. Mechanistic implications of this novel transformation are discussed and compared with other synthetic and biological systems, highlighting the importance of regulated electron trafficking in reductive activation of dioxygen.

Experimental Section

General Considerations. All reagents were obtained from commercial suppliers and used as received unless otherwise noted. Dichloromethane was distilled over CaH₂ under nitrogen. Diethyl ether, pentanes, and THF were saturated with nitrogen and purified by passage through activated Al₂O₃ columns under nitrogen.³⁶ The compounds [H(OEt₂)₂](BAR'₄)^{37,38} and 3,3',5,5'-tetra-*tert*-butyl-1,1'-bi-2,2'-phenol³⁹ were synthesized according to literature procedures. Syntheses of the compounds [Fe₂(μ-O₂CAr^{Tol})₂(O₂CAr^{Tol})₂(C₅H₅N)₂] (**1a**),³⁴ [Fe₂(μ-O₂CAr^{Tol})₄(4-*t*-BuC₅H₄N)₂] (**2a**),³⁵ [Fe₂(μ-O₂CAr^{Tol})₄(C₅H₅N)₂](OTf) (**1mv**), and [Fe₂(μ-O₂CAr^{Tol})₄(4-*t*-BuC₅H₄N)₂](PF₆) (**2mv**)⁴⁰ were reported previously. Dioxygen (99.994%, BOC Gases) was dried by passing the gas stream through a column of Drierite. ¹⁸O-Enriched dioxygen (99%) was supplied by ICON, NY. All air-sensitive manipulations were carried out under nitrogen in a Vacuum Atmospheres drybox or by standard Schlenk line techniques. Manometric experiments were performed according to a literature procedure,^{41a} with [IrCl(CO)(PPh₃)₂] as a standard.

$[\text{Fe}_2(\mu\text{-OH})_2(\mu\text{-O}_2\text{CAr}^{\text{Tol}})_2(\text{O}_2\text{CAr}^{\text{Tol}})_2(\text{C}_5\text{H}_5\text{N})_2]$ (**1c**). Compound **1a** (55 mg, 37 μmol) was suspended in 20 mL of CH_2Cl_2 and cooled to $-78\text{ }^\circ\text{C}$ in a dry ice/acetone bath. Dry dioxygen was bubbled directly into the reaction mixture for 10 min and the resulting dark emerald green solution was stirred under dioxygen for 0.5 h. The reaction was purged with Ar for 0.5 h to remove unreacted O_2 and the solution was gradually warmed to room temperature. The reaction mixture was concentrated to a dark greenish-yellow residue, which was extracted into CH_2Cl_2 and filtered. Greenish-yellow blocks of **1c** $\cdot 1.5\text{CH}_2\text{Cl}_2$ (54 mg, 33 μmol , 90%), which were suitable for X-ray crystallography, were obtained by recrystallization from CH_2Cl_2 /pentanes ($-30\text{ }^\circ\text{C}$ to room temperature). FT-IR(KBr, cm^{-1}) 3547, 3052, 3023, 2920, 2864, 1728, 1608, 1586, 1515, 1488, 1450, 1408, 1377, 1328, 1306, 1218, 1187, 1144, 1110, 1070, 1043, 1019, 820, 802, 786, 767, 736, 717, 695, 642, 584, 545, 530, 522. Anal. Calcd for $\text{C}_{94}\text{H}_{80}\text{O}_{10}\text{N}_2\text{Fe}_2$: C, 74.80; H, 5.34; N 1.86. Found: C, 74.54; H, 5.37; N 1.85.

$[\text{Fe}_2(\mu\text{-OH})_2(\mu\text{-O}_2\text{CAr}^{\text{Tol}})_2(\text{O}_2\text{CAr}^{\text{Tol}})_2(4\text{-}^t\text{BuC}_5\text{H}_4\text{N})_2]$ (**2c**). This compound was prepared from **2a** (260mg, 0.164 mmol) by a procedure analogous to that used to obtain **1c** from **1a**. Greenish yellow blocks of **2c** (200mg, 0.123 mmol, 75%), which were suitable for X-ray crystallography, deposited upon vapor diffusion of hexanes/pentanes (1:1) into a concentrated (5 mL) oxygenation reaction mixture. FT-IR (KBr, cm^{-1}) 3054, 3022, 2965, 2920, 2868, 1618, 1587, 1561, 1527, 1515, 1501, 1454, 1422, 1406, 1377, 1329, 1305, 1272, 1143, 1111, 1070, 1031, 1020, 831, 819, 802, 785, 766, 736, 694, 584, 568, 545, 523. Anal. Calcd for $\text{C}_{102}\text{H}_{96}\text{O}_{10}\text{N}_2\text{Fe}_2$: C, 75.55; H, 5.97; N, 1.73. Found: C, 75.85; H, 6.26; N, 1.73.

Oxygenation of 1a and 2a. In a typical reaction, compound **1a** or **2a** was dissolved in freshly distilled CH_2Cl_2 and loaded into a vessel fitted with a rubber septum. The solution was cooled to $-78\text{ }^\circ\text{C}$ in a dry ice/acetone bath. Dioxygen

was bubbled directly into the solution, resulting in a color change from yellow to dark emerald green, indicating the formation of **1b** or **2b**.

X-ray Crystallographic Studies. Intensity data were collected on a Bruker (formerly Siemens) CCD diffractometer with graphite-monochromated Mo K α radiation ($\lambda = 0.71073 \text{ \AA}$), controlled by a Pentium-based PC running the SMART software package.⁴² Single crystals were mounted at room temperature on the tips of quartz fibers, coated with Paratone-N oil, and cooled to 188 K under a stream of cold nitrogen maintained by a Bruker LT-2A nitrogen cryostat. Data collection and reduction protocols are described elsewhere.⁴³ The structures were solved by direct methods and refined on F^2 by using the SHELXTL software package.⁴⁴ Empirical absorption corrections were applied with SADABS,⁴⁵ part of the SHELXTL program package, and the structures were checked for higher symmetry by the program PLATON.⁴⁶ All non-hydrogen atoms were refined anisotropically unless otherwise noted. Hydrogen atoms were assigned idealized positions and given thermal parameters equivalent to either 1.5 (methyl hydrogen atoms) or 1.2 (all other hydrogen atoms) times the thermal parameter of the carbon atom to which they were attached. The hydrogen atoms associated with the bridging hydroxides in **1c** and **2c** were located in the difference Fourier map and refined isotropically; those associated with disordered solvent molecules were not included in the refinement. Each of the three CH₂Cl₂ molecules identified in the structure of **1c** was disordered over three positions. The *tert*-butyl group of one of the molecules in the asymmetric unit of **2c** is distributed over two positions and refined isotropically. The lattice solvent molecules found in the structure of **2c** were modeled as disordered CH₂Cl₂ and hexane. Crystallographic information is provided in Table 3.1.

Physical Measurements. ¹H-NMR spectra were recorded on a Varian Mercury 300 spectrometer; chemical shifts are reported versus tetramethylsilane

and were referenced to the residual solvent peaks. FT-IR spectra were recorded on a Bio Rad FTS-135 instrument with Win-IR software. UV-vis spectra were recorded on a Hewlett-Packard 8452A diode array spectrophotometer. The low-temperature UV-vis experiments were executed by using a custom-made quartz cuvette with a 1-cm path length fused into a vacuum-jacketed dewar. Low-temperature titration was monitored by using a Spectral Instruments Model 440 CCD Array UV-vis spectrophotometer in conjunction with a remote fiber-optic dip probe with a 1-cm path length.

Resonance Raman Spectroscopy. A Coherent Innova 90 Kr⁺ laser with an excitation wavelength of 647.1 nm and 50 mW of power was used to acquire Raman data. A 0.6 m single monochromator (1200 grooves/nm grating), with an entrance slit of 100 μm , and a TE-CCD-1100-PB-VISAR detector (Princeton Instruments, Inc.) cooled to $-40\text{ }^{\circ}\text{C}$ were used in a standard backscattering configuration. A holographic notch filter (Kaiser Optical Systems) was used to attenuate Rayleigh scattering. Spectra were collected in CH_2Cl_2 solution at $-78\text{ }^{\circ}\text{C}$ with the same low-temperature dewar used in UV-vis studies. Solutions were made as concentrated as possible, $\sim 10\text{ mM}$ in the best cases, to ensure an optimal signal-to-noise ratio. A total of 400 scans, each with a 1-s exposure time, were typically collected for each sample. Raman shifts were calibrated with DMF as an external standard. The data were processed on a Gateway 2000 computer using WIN-SPEC 3.2.1 software (Princeton Instruments, Inc.).

Mössbauer Spectroscopy. Field-dependent Mössbauer spectra were acquired on a spectrometer equipped with a Janis 12 CNDT/SC SuperVaritemp cryostat and an 8 T superconducting magnet. Zero-field Mössbauer spectra were obtained at 4.2 K on an MS1 spectrometer (WEB Research Co.). The spectrometer was operated in constant acceleration mode in transmission geometry. Zero velocity of the Mössbauer spectra refers to the centroid of the room temperature

spectrum of metallic Fe-foil. Solid samples of **2b** were prepared by concentrating the oxygenation product of **2a** (100 mg) in CH₂Cl₂ (3 mL) at -78 °C by using a diffusion pump operating at < 10⁻⁵ mm Hg. A dark green solid material thus isolated was suspended in BN and stored at 77 K. A solid sample of **2c** was prepared by suspending ~0.02 mmol of the powdered material in Apeizon N grease and packing the mixture into a nylon sample holder. A frozen solution sample of **2c** was prepared in THF by loading 1 mL of a ~20 mM solution into a nylon sample holder and freezing it at 77 K.

The Mössbauer spectra of **2b** were analyzed by using the spin Hamiltonian (eq 2), in which H_e represents the electronic properties of the diiron clusters

$$H_S = H_e + H_{hf} \quad (2)$$

and H_{hf} describes the hyperfine interactions of the iron nuclei with their surrounding electrons. The electronic part, H_e , contains the zero-field and Zeeman interactions (eq 3) and H_{hf} contains the quadrupolar (the first summation)

$$H_e = D \left[\mathbf{S}_z^2 - \frac{S(S+1)}{3} + \frac{E}{D} (\mathbf{S}_x^2 - \mathbf{S}_y^2) \right] + \beta \mathbf{S} \cdot \mathbf{g} \cdot \mathbf{H} \quad (3)$$

and magnetic (the second summation) hyperfine interactions (eq 4). All symbols

$$H_{hf} = \sum_{i=1}^2 \frac{eQ(V_{zz})_i}{4} \left[\mathbf{I}_{zi}^2 - \frac{I_i(I_i+1)}{3} + \frac{\eta}{3} (\mathbf{I}_{xi}^2 - \mathbf{I}_{yi}^2) \right] + \sum_{i=1}^2 (\mathbf{S} \cdot \mathbf{A}_i \cdot \mathbf{I}_i - g_n \beta_n \mathbf{H} \cdot \mathbf{I}_i) \quad (4)$$

have their usual meaning. The symbol \mathbf{S} represents the total electronic spin of the ground state of the diiron clusters, and \mathbf{A} is the magnetic hyperfine tensor

describing the interaction between the total spin \mathbf{S} and the individual iron nuclear spins, \mathbf{I}_i . The Mössbauer spectra of **2c** were fit to Lorentzian lines by using the WMOSS plot and fit program.⁴⁷

EPR Spectroscopy. X-band (9 GHz) EPR spectra were recorded on a Bruker 300 spectrometer equipped with an Oxford ESR 910 cryostat for low temperature measurements and a Bruker bimodal cavity for generation of the microwave fields parallel and transverse to the static field. Q-band (35 GHz) EPR spectra were recorded on a Bruker 200 spectrometer equipped with a low temperature microwave probe and a locally constructed cryogenic system. For both instruments, the microwave frequency was calibrated by a frequency counter and the magnetic field was calibrated with an NMR gauss meter. The Oxford thermocouple temperature was calibrated using a carbon glass resistor temperature probe (CGR-1-1000 Lake Shore Cryotronics). For X and Q-band EPR, the magnetic field modulation was 100 kHz unless noted otherwise. All experimental data were collected under non-saturation conditions.

EPR Simulations. Interpretation of the EPR spectra utilizes the spin Hamiltonian given in eq 3. Simulations of the EPR spectra are calculated from diagonalization of eq 3 with a locally written program. The powder pattern is generated for a uniform spherical distribution of the magnetic field vector \mathbf{B} . The transition intensities are calculated from the square of the transition moment. The spectral line width is dominated by D-strain and simulations use distributions of the D and E/D to give the correct line width. The distributions are specified as σ_D and $\sigma_{E/D}$.

The simulations are generated with careful consideration of all intensity factors, both theoretical and instrumental. This approach allows direct comparison of simulated spectra to the absolute intensity scale of the experimental spectrum having a known sample concentration. The only unknown factor relating

the spin concentration to signal intensity is an instrumental one that depends on the microwave detection system. This factor, however, is determined by the spin standard, CuEDTA, for which the copper concentration was accurately determined from plasma emission spectroscopy.

Magnetic Susceptibility Measurements. Magnetic susceptibility data for solid samples of **1c** and **2c** were measured between 5 K and 300 K with applied magnetic fields of 0.1 T using a Quantum Design MPMS SQUID susceptometer. Samples were loaded in gel capsules and suspended in plastic straws. The susceptibilities of the straw and gel capsule were independently determined at the same temperature range and field for correction of their contribution to the total measured susceptibility. Underlying diamagnetism of the sample was calculated from Pascal's constants.⁴⁸ The molar magnetic susceptibility data were fit to the expression derived from the spin-only isotropic HDvV exchange Hamiltonian $\mathcal{H} = -2J\mathbf{S}_1 \cdot \mathbf{S}_2$, where $\mathbf{S}_1 = \mathbf{S}_2 = 5/2$. This expression is given in eq 5, where $x = J/kT$. No corrections were made for TIP or paramagnetic impurities.

$$\chi_M = \frac{N g^2 \mu_B^2}{kT} \frac{2e^{2x} + 10e^{6x} + 28e^{12x} + 60e^{20x} + 110e^{30x}}{1 + 3e^{2x} + 5e^{6x} + 7e^{12x} + 9e^{20x} + 11e^{30x}} \quad (5)$$

Titration of 2b with Cp₂Fe or Cp*₂Fe. A CH₂Cl₂ solution of **2a**, typically 4.5 mM, was cooled to -78 °C and subjected to an O₂ purge for 5 min. The development of **2b** was followed by UV-vis spectroscopy for 1 h, during which time the 670 nm absorption reached a maximum. Excess O₂ was removed by bubbling argon through the solution for > 20 min. Aliquots of either Cp₂Fe or Cp*₂Fe in CH₂Cl₂ were delivered to the solution under argon by using a gas-tight microsyringe. Spectral measurements were made after each addition and corrected for dilution.

EPR Kinetics. Kinetic experiments were performed in calibrated EPR tubes. A CH_2Cl_2 solution sample of **2a** (1.12 mM) was prepared in a drybox and each 300 μL aliquot was loaded into an EPR tube fitted with a rubber septum. The samples were brought out, placed under a positive Ar pressure, and held at $-78\text{ }^\circ\text{C}$. Dioxygen (2.5 mL) was bubbled through the solution over a period of 30 sec by injection from a gas-tight syringe. The reactions were kept at $-78\text{ }^\circ\text{C}$ for varying periods of time (1 – 45 min) and quenched by flash-freezing the EPR tubes at 77 K. The amount of $S = 9/2$ species was determined relative to a quantitative simulation by using the spectral parameters given in Figure 3.7. This value was later confirmed, to within 10 % of the concentration, by a pure sample of **2mv** of known concentration. The $S = 1/2$ component was quantitated by double integration of the EPR signal.

Generation of 2b in the Presence of H^+ . Solution samples of **2a** (1.21 mM) mixed with $[\text{H}(\text{OEt}_2)_2](\text{BAR}'_4)$ (0.63 mM) were prepared in CH_2Cl_2 and loaded into calibrated EPR tubes. Oxygenation was carried out in a manner similar to that described for EPR kinetics (see above) and the reaction was quenched after incubation for 5 min. The amounts of $S = 9/2$ and $S = 1/2$ components were quantitated and compared with those of a kinetics sample quenched after an identical period of time.

Ligand Recovery. A CH_2Cl_2 (30 mL) suspension of **1a** (102 mg, 69.4 μmol) was cooled to $-78\text{ }^\circ\text{C}$. Dioxygen was bubbled through the solution for 5 min and the resulting dark emerald green solution was stirred for 0.5 h. Unreacted dioxygen was removed by bubbling Ar through the solution for 0.5 h. The solution was warmed to room temperature and quenched by adding an aq HCl solution (10%, 20 mL). The organic layer was separated and the aqueous layer was extracted with 3 x 20 mL portions of CH_2Cl_2 . The combined extracts were dried over MgSO_4 , filtered, and concentrated under reduced pressure to afford

Ar^{Tol}CO₂H as an off-white solid (79 mg, 0.261 mmol, 94% recovery yield). ¹H NMR (300 MHz, CD₂Cl₂) 7.52 (t, 1H), 7.35 (d, 2H), 7.31 (d, 4H), 7.22 (d, 4H), 2.41 (s, 6H); FT-IR (thin film deposited from CD₂Cl₂ solution on NaCl, cm⁻¹) 3027, 2925, 1699, 1516, 1455, 1294, 816, 803, 781. LRMS (EI): *m/z* 302 (M⁺).

Reactions of 1b with 2,4,6-Tri-*tert*-butylphenol. A CH₂Cl₂ solution (10 mL) of 1a (0.37 mM) was purged with dioxygen at -78 °C to afford 1b. Excess O₂ was removed by bubbling Ar through the solution. A portion of 2,4,6-tri-*tert*-butylphenol (8.1 μmol, 2.2 equiv) in CH₂Cl₂ (30 μL) was added and the spectral change was monitored by UV-vis spectroscopy. A similarly prepared sample of 1b was transferred to a pre-cooled EPR tube containing an equal volume of Ar-purged toluene. The mixture was rapidly frozen at 77 K and analyzed by X-band EPR spectroscopy. The spectra were compared with those of 2,4,6-tri-*tert*-butylphenoxy radical generated independently by a chemical method.⁴⁹

Reaction of 2b with 2,4-Di-*tert*-butylphenol. A CH₂Cl₂ solution (10 mL) of 2a (204 mg, 0.129 mmol) was purged with O₂ at -78 °C to afford 2b. The dark green solution was stirred for 2 h at -78 °C and excess oxygen was removed by Ar bubbling. A portion of 2,4-di-*tert*-butylphenol (55 mg, 0.27 mmol) was added as a solid. The mixture was warmed to room temperature to afford an intense blue solution. Volatile fractions were removed and the remaining solid material was extracted into CH₂Cl₂ (25 mL). A portion of aq HCl (10%, 15 mL) was added and the organic layer was separated. The aqueous layer was extracted with 4 x 25 mL portions of CH₂Cl₂. The combined extracts were dried over MgSO₄, filtered, and concentrated under reduced pressure to provide a pale yellow residue. The mixture (203 mg, 98% overall recovery yield) comprised Ar^{Tol}CO₂H, 2,4-di-*tert*-butylphenol, and 3,3',5,5'-tetra-*tert*-butyl-1,1'-bi-2,2'-phenol, as judged by comparison with the ¹H-NMR spectra of authentic samples. The amount of the 2,2'-biphenol product (26 μmol, 40% based on 2a) was determined by comparison of

the integration of the methyl group peaks (1.45 ppm and 1.33 ppm) against the methyl proton signals from the unreacted 2,4-di-*tert*-butylphenol (1.41 ppm and 1.30 ppm).

Reaction of 2mv with 2,4-Di-*tert*-butyl-phenol. To a dark green CH₂Cl₂ (10 mL) solution of 2mv (114 mg, 65.8 μmol) was added 2,4-di-*tert*-butylphenol (58 mg, 0.28 mmol) under nitrogen. The reaction mixture was stirred for 2 h at room temperature and quenched by adding aq HCl (10%, 15 mL). The components in the CH₂Cl₂ layer were isolated and analyzed as described above. The mixture (124 mg, 91% overall recovery yield) was composed of Ar^{Tol}CO₂H and unreacted 2,4-di-*tert*-butylphenol, as judged by comparison with the ¹H-NMR spectra of authentic samples. No coupling product, 3,3',5,5'-tetra-*tert*-butyl-1,1'-bi-2,2'-phenol, was detected.

Results

Reactions of Diiron(II) Complexes [Fe₂(μ-O₂CAr^{Tol})₂(O₂CAr^{Tol})₂-(C₅H₅N)₂] (1a) and [Fe₂(μ-O₂CAr^{Tol})₄(4-^tBuC₅H₄N)₂] (2a) with O₂. (a) **UV-vis Spectroscopy.** Oxygenation of a CH₂Cl₂ solution of 1a at -78 °C resulted in the formation of a deep green species 1b with a broad (ν_{1/2} ≅ 3700 cm⁻¹) visible absorption centered at ~660 nm (ν ≅ 15200 cm⁻¹; ε = 1600 M⁻¹cm⁻¹) (Figure 3.1A). Since 1a cannot be regenerated from 1b by evacuation or Ar-purging, this process is effectively irreversible. Addition of 2 equiv of [H(OEt₂)₂](BAR'₄) did not alter the intensity of the absorption. Although stable for > 6 h at -78 °C, 1b rapidly decays to a pale yellow solution upon warming to room temperature (Figure 3.1A).

Exposure of 2a to O₂ under similar conditions resulted in analogous irreversible color change from bright yellow to deep green (Figure 3.1B). The buildup of a broad (ν_{1/2} ≅ 3400 cm⁻¹) visible absorption of 2b centered at ~670

nm ($\nu \cong 14900 \text{ cm}^{-1}$; $\epsilon = 1700 \text{ M}^{-1}\text{cm}^{-1}$) was monitored by UV-vis spectroscopy at $-78 \text{ }^\circ\text{C}$, affording $t_{1/2} \cong 7.7 \text{ min}$ under the conditions employed (gentle purging with O_2 for 1 min) (Figure 3.2). The thermal stability of **2b** is comparable to that of **1b**; no diminution in the intensity of the absorption band occurs up to 12 h at $-78 \text{ }^\circ\text{C}$. Upon warming to room temperature, however, **2b** decays to a bright yellow material (Figure 3.1B).

(b) Resonance Raman Spectroscopy. Raman spectra were obtained for **1b** and **2b** in CH_2Cl_2 at $-78 \text{ }^\circ\text{C}$. As shown in Figure 3.3, upon excitation at 647.1 nm, a strong resonance enhanced peak appeared at 851 cm^{-1} for **1b**. This feature is absent both in the precursor compound **1a** and in the decomposition product of **1b**. Although this frequency falls into the right range for the O–O stretching mode of a (μ -peroxo)diiron(III) species (Table 3.2), no shift in the peak position was observed for samples prepared by reacting **1a** with either ^{18}O -labeled dioxygen (**1b***) (Figure 3.3) or a 50:50 mixture of ^{16}O : ^{18}O -labeled material under identical conditions (data not shown). A similar result was obtained for **2b**, which also exhibits a resonance enhanced vibration at 851 cm^{-1} (Figure 3.4). Raman spectra were obtained for mixed-valence Fe(II)Fe(III) compounds **1mv** and **2mv** in CH_2Cl_2 . Under conditions similar to those used for **1b** and **2b**, resonance enhanced peaks appear at 851 cm^{-1} for both **1mv** and **2mv** (Figure 3.5).

(c) EPR Spectroscopy. Figure 3.6 displays the EPR spectra obtained for frozen CH_2Cl_2 samples of **2b**.³⁵ A strong isotropic $g = 2$ signal and a less intense absorption at $g = 10$ were observed. Quantitation of these two species accounted for 70% of the total iron, the former signal contributing 40% and the latter 30%. The broad X-band signal at $g = 2$, with a width of ca 28 G, originates from an $S = 1/2$ species which shows resolved g -anisotropy at Q-band (see inset). The two simulations overlaid on the data use the same parameter set of $g = 1.986, 1.997,$ and 2.011 . This g -anisotropy is similar to that of the RNR-R2 X ($g = 1.994, 1.999,$

and 2.007) signal,^{11c,d} which arises from the antiferromagnetically (AF) coupled Fe(III)Fe(IV) core in this enzyme intermediate. The signals at $g = 10$ (X- and Q-band) and $g = 4.3$ and 2.8 (Q-band) originate from an $S = 9/2$ species and the simulations overlaid on the data were obtained with $D = 1.2 \text{ cm}^{-1}$, $E/D = 0.013$, and $g = 2.00$. The resonances near $g = 4$ in Q-band for both parallel and perpendicular modes are from an intradoublet transition and are not included in the simulation. The $g = 19$ (X-band) and possibly the $g = 29$ (Q-band) signals are from the diiron(III) species, whereas the $g = 16$ signal (Q-band) and its simulation are from unreacted **2a**, which account for 20% and 10% of the total iron, respectively. There was no evidence for population of an excited state up to 150 K both for $S = 1/2$ and $S = 9/2$ signals, indicating exchange interactions of $|2J| > 200 \text{ cm}^{-1}$ for the former and $> 50 \text{ cm}^{-1}$ for the latter ($\mathcal{H} = -2J\mathbf{S}_1 \cdot \mathbf{S}_2$).

Figure 3.7 displays X-band (A) and Q-band (B) EPR spectra obtained for a frozen CH_2Cl_2 sample of **2mv**. The signal observed at $g = 9.5$ and 2.0 in X-band perpendicular mode ($B_1 \perp B$) originates from a transition between the ground doublet within the $S = 9/2$ manifold. In the strong field limit, the transition occurs between $m_s = \pm 1/2$ states. The signal at $g = 4.3$ originates from trace contamination ($\sim 2\%$) of rhombic Fe(III) ($S = 5/2$). In Q-band perpendicular mode ($h\nu = 1.2 \text{ cm}^{-1}$), three distinct transitions were observed. For $S = 9/2$ complexes with $E/D \sim 0$, we expect resonances to occur at $g = 10, 10, \text{ and } 2$ ($m_s = \pm 1/2$), and $g = 0, 0, \text{ and } 6$ ($m_s = \pm 3/2$), based on the standard diagrams of g_{obs} vs E/D .⁵⁰ For $D \leq h\nu$, as is the case here, however, significant mixing of the doublets occurs, thus invalidating such diagrams. The signals at $g = 8.9$ and 2.9 originate from the ground ($m_s = \pm 1/2$) and first excited state doublets ($m_s = \pm 3/2$) of the $S = 9/2$ manifold, respectively. The signal at $g = 4.2$ is novel and originates from an interdoublet transition between the $m_s = +1/2$ and $-3/2$ levels. From the simulation overlaid on the data of Figure 3.7 were obtained $D = 1.13 \text{ cm}^{-1}$ and $E/D =$

0.007. The lineshapes are determined by D -strain, which is modeled with distributions in the parameters D and E/D of Gaussian width σ_D and $\sigma_{E/D}$, respectively. The spectral fit determines both parameters independently, with values of $\sigma_D = 0.03$ and $\sigma_{E/D} = 0.004$. The EPR spectra of **2mv** and the $S = 9/2$ component in **2b** are essentially identical, indicating that a valence-delocalized Fe(II)Fe(III) species is generated by the reaction between **2b** and dioxygen at -78 °C.

Anaerobic thawing at -60 °C of the frozen CH_2Cl_2 solution sample of **2b** resulted in the total loss of the signals arising from $S = 1/2$ and $S = 9/2$ species and buildup of two new signals in the X-band EPR spectra (Figure 3.8). The signal at $g = 4.3$ (Figure 3.8A), constituting ca 20% of the diiron starting material, originates from a rhombic Fe(III) system ($S = 5/2$). Figure 3.8B displays the parallel mode EPR spectra indicating the appearance of a new signal at $g = 10.2$, which was tentatively assigned to an AF coupled diiron(III) species. An identical $g = 10.2$ signal was observed, when the reaction between **2a** and dioxygen was conducted at room temperature. This signal, however, is different from the $g = 19.8$ signal of **2c**, which arises from a transition within the $S = 5$ manifold of ferromagnetically coupled diiron(III) centers (vide infra). This result clearly indicates that **2c** is not an immediate oxygenation product of **2a**.

(d) Mössbauer Spectroscopy. Field Orientation Dependence. Figure 3.9 displays the Mössbauer spectra of a solid powder sample of **2b** recorded at 4.2 K with a 50-mT magnetic field applied parallel (A) and perpendicular (B) to the γ rays.³⁵ The spectra may be deconvoluted into three major components. A central quadrupole doublet (marked by brackets) with apparent Mössbauer parameters of $\Delta E_Q = 1.13$ mm/s and $\delta = 0.54$ mm/s is assigned to an AF coupled diiron(III) species (30% of total iron). A magnetically split spectrum with well-resolved peaks at -3.8 , -1.7 , $+2.0$ and $+4.9$ mm/s can be assigned to the $S = 1/2$

species (36% of total iron). The remaining component (34% of total iron) is a broad and featureless spectrum with absorption extending from -7 mm/s to $+7$ mm/s. Of the three diiron species mentioned above, only the spectrum of the $S = 1/2$ species is expected to have a strong dependence on the orientation of the applied field with respect to the direction of the γ rays. Consequently, a difference spectrum (Figure 3.9C) of the spectra shown in Figure 3.9A and 3.9B will cancel most of the contributions from the other species and reveal the field orientation dependence of the $S = 1/2$ species. Analysis of the data yields parameters that compare very well with Fe(III)Fe(IV) centers in previously reported RNR-R2 X ,^{11c} MMOH-Q X ,⁵¹ and a related model compound.^{32b} In particular, the observed isomer shifts, 0.55 and 0.12 mm/s, for the two iron sites indicate unambiguously that the $S = 1/2$ component is a Fe(III)Fe(IV) species.

Spectral Deconvolution. In a complementary approach, the Mössbauer spectra were recorded in higher magnetic fields (4T – 8T) and deconvoluted into the foregoing three spectral components through an iterative process. Shown in Figure 3.10A is the Mössbauer spectrum of a solid sample of **2b** (hashed lines) recorded at 4.2 K in a magnetic field of 8 T applied parallel to the γ -ray beam. The two well-resolved outermost lines at -6.2 mm/s and 7.7 mm/s are closely matched, in both positions and shapes, by those of the spectrum of a solid sample of **2mv** (solid line) recorded under identical experimental conditions,⁴⁰ indicating that they arise from the valence-delocalized $S = 9/2$ Fe(II)Fe(III) species. Due to the fact that these outer lines do not overlap with spectral features arising from the other components, which show absorptions in the central region of the spectrum, they can be used to estimate the relative concentration of the $S = 9/2$ component in **2b**. By matching the intensities of these outer lines to that of spectrum of solid **2b**, it is estimated that 45% of the total iron in the green mixture is in the form of $[\text{Fe}_2(\mu\text{-O}_2\text{CAr}^{\text{Tol}})_4(4\text{-}^t\text{BuC}_5\text{H}_4\text{N})_2]^+$ (see the caption of Figure

3.10A), an amount slightly higher than that estimated from the 50-mT spectral analysis (vide supra).

Removal of the contribution of $[\text{Fe}_2(\mu\text{-O}_2\text{CAr}^{\text{Tol}})_4(4\text{-}^t\text{BuC}_5\text{H}_4\text{N})_2]^+$ from the raw data of **2b** yields the spectrum shown in Figure 3.10B. The lines at -2.7 mm/s and $+3.4$ mm/s are well resolved and can be assigned to the valence-trapped Fe(III)Fe(IV) species. The solid line shown in Figure 3.10B is a theoretical simulation of this species using the parameters presented in Table 3.3 and accounts for 36% of the total iron absorption. Removal of this component from the spectrum shown in Figure 3.10B yields the spectrum (Figure 3.10C) arising from a diiron(III) species, which shows features at -1 mm/s, 0.5 mm/s, and 2.1 mm/s. In contrast to the two components described above, for which the major absorption lines are well separated from the spectral features of the other species, the signals for the diiron(III) species overlap with other absorptions. Consequently, the exact shape and absorption peaks of this component are less well defined. Nonetheless, the major features of this component can readily be seen in the raw experimental spectrum shown in Figure 3.10A. The central peak at 0.5 mm/s is clearly apparent and the peaks at -1 mm/s and 2.1 mm/s appear as shoulders. The theoretical simulation of this component, which is plotted as a solid line in Figure 3.10C, was calculated by using the parameters given in the caption of Figure 3.10 and assuming diamagnetism ($S = 0$). The Mössbauer parameters, which are typical of N/O-coordinate high-spin Fe(III) ions,⁵²⁻⁵⁴ and the diamagnetism are consistent with the assignment that this component represents an AF coupled diiron(III) species. This component accounts for approximately 19% of the total intensity, and the large line width indicates the presence of some microheterogeneity.

Valence-Delocalized Fe(II)Fe(III) Species. As mentioned above, a major spectral component observed in the spectrum of **2b** recorded at 4.2 K and 8 T is

accurately represented by the spectrum of a solid sample of **2mv** recorded under the same conditions. This result indicates that **2b** includes the valence-delocalized Fe(II)Fe(III) cation $[\text{Fe}_2(\mu\text{-O}_2\text{CAr}^{\text{Tol}})_4(4\text{-}^t\text{BuC}_5\text{H}_4\text{N})_2]^+$. To illustrate this point, a spectrum of solid **2mv** (Figure 3.11A) is compared to the Fe(II)Fe(III) component in **2b** (Figure 3.11B). The similarities between these two spectra are obvious. The latter spectrum was obtained from the raw experimental data by removing the contributions of the other two components, which were simulated by using the parameters listed in Table 3.3 and the caption of Figure 3.10. In Figure 3.11C is shown the Fe(II)Fe(III) component in **2b** recorded at 4.2 K in an applied field of 4 T. This spectrum consists of a single six-line pattern, indicating that both iron sites contribute identical Mössbauer spectra. This observation demonstrates unequivocally that the Fe(II)Fe(III) component in **2b** is a valence-delocalized cluster, $[\text{Fe}_2(\mu\text{-O}_2\text{CAr}^{\text{Tol}})_4(4\text{-}^t\text{BuC}_5\text{H}_4\text{N})_2]^+$. EPR and SQUID measurements demonstrate that $[\text{Fe}_2(\mu\text{-O}_2\text{CAr}^{\text{Tol}})_4(4\text{-}^t\text{BuC}_5\text{H}_4\text{N})_2]^+$ has a $S = 9/2$ ground state.⁴⁰ Furthermore, the zero-field parameters have been determined by EPR spectroscopy and are $D = 1.2 \text{ cm}^{-1}$ and $E/D = 0.013$.³⁵ For the analysis of the Mössbauer spectrum of the $[\text{Fe}_2(\mu\text{-O}_2\text{CAr}^{\text{Tol}})_4(4\text{-}^t\text{BuC}_5\text{H}_4\text{N})_2]^+$ component in **2b**, we use eqs 3 and 4, and assume that the electronic relaxation is slow compared to the ^{57}Fe nuclear Larmor precession and that $E/D = 0.013$. With these assumptions, the parameter D can be determined from the field-dependent Mössbauer data for the following reasons. The size of the magnetic splitting of a Mössbauer spectrum depends on the magnitude of the internal field, $\langle \mathbf{S} \rangle \cdot \mathbf{A}$, where $\langle \mathbf{S} \rangle$ represents the spin expectation value at the Fe-sites. For the case of $D \approx g\beta H$, which describes the current situation, the expectation values for the three components, $\langle S_x \rangle$, $\langle S_y \rangle$ and $\langle S_z \rangle$, of $\langle \mathbf{S} \rangle$ depend sensitively on the ratio of $D/g\beta H$. Consequently, it is possible to determine the value of D from the field-dependence of the spectra. Such an analysis gives $D = 1.2 \pm 0.2 \text{ cm}^{-1}$, which is in excellent agreement with the value determined by EPR spectroscopy.³⁵

From the analysis of the Mössbauer spectra, other characteristic parameters can also be determined (Table 3.4). Theoretical simulations using these parameters are plotted in Figure 3.11 as solid lines overlaid with the corresponding experimental spectra. The agreement between theory and experiment is excellent. In Table 3.4, the parameters determined for $[\text{Fe}_2(\mu\text{-O}_2\text{CAr}^{\text{Tol}})_4(4\text{-}^t\text{BuC}_5\text{H}_4\text{N})_2]^+$ are compared with those of related valence-delocalized Fe(II)Fe(III) compounds. The Mössbauer parameters of a valence-delocalized compound are the arithmetic means of those of the corresponding pure Fe(II) and Fe(III) sites in the same ligand environment.⁵⁵ Accordingly, the ranges of isomer shifts (0.74 – 0.84 mm/s) and magnitudes of quadrupole splittings (1.86 – 2.14 mm/s) observed for valence-delocalized $S = 9/2$ Fe(II)Fe(III) compounds are between the typical values for N/O coordinated high-spin Fe(III) and N/O coordinated high-spin Fe(II) sites.⁵⁶⁻⁵⁹ In comparison with these values, the isomer shift, $\delta = 0.65$ mm/s, and quadrupole splitting, $|\Delta E_Q| = 0.63$ mm/s, determined for **2mv**, are significantly smaller. The smaller isomer shift observed for **2mv** can in part be explained by the fact that the iron centers are five coordinate. The origin of the smaller quadrupole splitting, however, is unclear. For the compound $[\text{Fe}_2(\mu\text{-OH})_3(\text{Me}_3\text{TACN})_2]^{2+}$ the value of the quadrupole splitting, $\Delta E_Q = -2.14$ mm/s, was attributed to the delocalized electron being in a d_{z^2} orbital.⁵⁶ More recently, the interaction between the two Fe-centered d_{z^2} orbitals (with the Fe–Fe vector defining the z-axis) was identified as a mechanism for promoting the electron delocalization between the two Fe sites.⁶⁰ The reduced magnitude of the quadrupole splitting in **2mv**, $\Delta E_Q = -0.63$ mm/s, however, indicates that the orbital ground state of **2mv** is not a pure d_{z^2} orbital, but rather a quantum admixture, possibly of d_{z^2} and d_{xy} orbitals. Since d_{z^2} and d_{xy} orbitals generate opposite electric field gradients,⁶¹ a quantum admixture of these two orbitals would reduce the magnitude of the quadrupole splitting. DFT calculations are currently in progress to gain further insights into the electronic structure of **2mv** and to understand these unusual Mössbauer parameters.⁶²

Valence-Trapped Fe(III)Fe(IV) Species. The contributions of the Fe(II)Fe(III) and diiron(III) components can be removed from the experimental spectra of **2b** by using theoretical spectra simulated with the parameters listed in Table 3.4 and the caption of Figure 3.10. This treatment generates a spectrum corresponding to the Fe(III)Fe(IV) component in **2b**. Figure 3.12 displays the Mössbauer spectra (hash marks) of the Fe(III)Fe(IV) species in **2b** recorded at 4.2 K in a parallel applied field of 4 T (A) or 8 T (B). These spectra can be deconvoluted into two equal intensity spectral components corresponding to two valence-localized Fe sites. Each site contributes approximately 18% of the total iron absorption. Characteristic parameters obtained for the two Fe sites are listed in Table 3.3, and theoretical simulations of each individual component are displayed in Figure 3.12 above the experimental spectra. The solid lines overlaid with the experimental spectra are the superpositions of the two individual spectral components. The observation that the magnetic splitting of one of the components (depicted as dashed lines above the data) *increases* whereas that of the other component (shown as solid lines above the data) *decreases* with increasing applied field demonstrates the antiparallel orientation of the individual spins of the Fe sites in the ground state and establishes unambiguously the AF coupling nature of Fe(III)Fe(IV). The different field dependence is reflected in different signs of the **A**-tensors. The Fe-site with a negative **A**-tensor has an isomer shift, $\delta = 0.56$ mm/s, typical of a high-spin Fe(III) ion with N/O coordination. In accord with this assignment, the **A**-tensor of this site is rather isotropic, as expected for high-spin Fe(III) compounds. The second Fe-site has a positive **A**-tensor with significant anisotropy (about 30%). The isomer shift of this site, $\delta = 0.19$ mm/s, is below the typical range for high-spin Fe(III) ions, and is assigned to a high-spin Fe(IV) site. The anisotropy of the **A**-tensor is consistent with this assignment. Similar valence-trapped Fe(III)Fe(IV) clusters have been observed for the RNR-

R2 reaction intermediate X,^{11a,c} the state MMOH-Q_x, which is a cryoreductively generated one-electron-reduced intermediate Q from the MMOH reaction cycle,⁵¹ and the model compound [Fe₂(μ-O)₂(6-Me-TPA)₂]³⁺.^{32b} As presented in Table 3.3, the Mössbauer parameters of the Fe(III)Fe(IV) component in **2b** compare very well with those of RNR-R2 X and MMOH-Q_x. This result indicates that, compared with the nitrogen-rich donor atom sets in [Fe₂(μ-O)₂(6-Me-TPA)₂]³⁺,^{32b,37} the coordination environment of the enzyme intermediate is better reproduced by the tetracarboxylate ligand system employed in this investigation.

(e) Manometric Studies. Dioxygen uptake was monitored by manometric measurements (3 replicate runs) for the reaction between O₂ and **2a** in CH₂Cl₂ at -78 °C. Compound **2a** consumed 0.75 ± 0.1 equivalents of O₂ to provide **2b**. This substoichiometric consumption of dioxygen contrasts with the 1:1 stoichiometry observed for the formation of discrete (peroxo)diiron(III) species in other studies.^{17b,20}

(f) EPR Kinetic Studies. The relatively slow formation rate of paramagnetic intermediates at -78 °C allowed us to monitor the buildup of *S* = 1/2 and *S* = 9/2 components in **2b** by X-band EPR spectroscopy as a function of time. Identical solution samples of **2a** were prepared in CH₂Cl₂ and reactions were initiated by injecting known amounts of dioxygen at -78 °C. Following different incubation times at -78 °C, each sample was frozen at 77 K and analyzed by X-band EPR spectroscopy. Shown in Figure 3.13 is a plot of the concentration of *S* = 1/2 and *S* = 9/2 components as a function of time. The concentrations were determined from quantitation of the EPR signals at *g* = 2 and 9.5, respectively. Both components build up at the same rate and exist in the same relative amounts throughout the reaction. A pseudo-first order fit to the data is shown in Figure 3.13, which gave *k*_{obs} = 0.18 ± 0.02 min⁻¹ at -78 °C. This result is a strong

evidence that the processes leading to the formation of $S = 1/2$ and $S = 9/2$ components in **2b** are coupled to one another. The reaction approaches completion at > 45 min, affording ca 38% of the $S = 1/2$ and 36% of $S = 9/2$ components (based on **2a**).

The presence of a proton source significantly affects the development of the $S = 1/2$ and $S = 9/2$ species. Figure 3.14 shows the EPR spectra of **2b** quenched 5 min after oxygenation at -78 °C. When 0.5 equiv of $[\text{H}(\text{OEt}_2)_2](\text{BAr}'_4)$ was added to **2a** prior to reaction with O_2 , the amount of the $S = 9/2$ component formed is negligibly affected, whereas the amount of $S = 1/2$ component is significantly reduced from 19% (without H^+) to 2% (with H^+) of the diiron(II) starting material **2a**. This result indicates that the Fe(III)Fe(IV) species has ligand fragments that are susceptible to protonation. Changes in the metal oxidation states may be triggered by ligand protonation, resulting in the loss of the AF coupled Fe(III)Fe(IV) component in **2b**.

Reactions of the Oxygenation Intermediates with External Reagents. (a) Cp_2Fe and Cp^*_2Fe . Addition of Cp_2Fe to a CH_2Cl_2 solution of **2b** at -78 °C did not perturb the electronic absorption at 670 nm, whereas Cp^*_2Fe completely abolished this transition. This finding requires that the reduction potential of **2b** lie between -130 mV and $+460$ mV vs SCE.⁶³ A redox titration of **2b** was therefore carried out by monitoring the decay of the 670 nm absorption band as a function of Cp^*_2Fe added under Ar at -78 °C. Typical UV-vis traces are displayed in Figure 3.15. An average oxidizing equivalent of 0.45 ± 0.04 (3 replicate runs) was determined for the $\lambda_{\text{max}} = 670$ nm chromophore in **2b**.

(b) Oxidation of Phenol Substrates. Both **1b** and **2b** act as one-electron oxidants and proton acceptors. Addition of 2.2 equiv of 2,4,6-tri-*tert*-butylphenol to a CH_2Cl_2 solution of **1b** at -78 °C did not result in any change in the UV-vis spectra. Upon warming to room temperature, however, absorption peaks de-

velop at 383 and 401 nm, which are characteristic of the 2,4,6-tri-*tert*-butylphenoxy radical (Figure 3.16A).⁶⁴ Formation of the phenoxy radical was further confirmed by an EPR signal at $g = 2.0045$ in a sample prepared under similar conditions (Figure 3.16B). At room temperature, the reaction mixture remains blue. When 2,4-di-*tert*-butylphenol was allowed to react with **2b**, the 3,3',5,5'-tetra-*tert*-butyl-1,1'-bi-2,2'-phenol coupling product was obtained in ~40% yield based on **2a**. Upon warming from -78 °C to room temperature, the color of the solution turned blue, as for **1b**. A mononuclear iron(III) complex $[\text{Fe}(\text{O}_2\text{CAr}^{\text{Tol}})_2(2,4\text{-}^t\text{Bu}_2\text{C}_6\text{H}_3\text{O})(4\text{-}^t\text{BuC}_5\text{H}_4\text{N})]$ (Figure 3.17)⁶⁵ was isolated by vapor diffusion of pentanes into the reaction mixture, indicating that the blue color arises from a phenoxide-to-Fe(III) LMCT band.⁶⁶ No 2,4-di-*tert*-butylphenol coupling product was detected when a similar reaction was carried out with the Fe(II)Fe(III) compound **2mv**.

Di(μ -hydroxo)di(μ -carboxylato)diiron(III) Complexes $[\text{Fe}_2(\mu\text{-OH})_2(\mu\text{-O}_2\text{CAr}^{\text{Tol}})_2(\text{O}_2\text{CAr}^{\text{Tol}})_2\text{L}_2]$, L = $\text{C}_5\text{H}_5\text{N}$ (1c**) and $4\text{-}^t\text{BuC}_5\text{H}_4\text{N}$ (**2c**). (a) **Synthesis and Structural Characterization.** Quadruply-bridged diiron(III) complexes **1c** and **2c** were isolated as thermal decomposition products of **1b** and **2b**, respectively. The crystal structures are shown in Figures 3.18 and 3.19; selected bond lengths and angles are listed in Table 3.5. In both cases, two chemically identical but crystallographically inequivalent molecules were identified in the unit cell, each sitting on an inversion center. The structures of **1c** and **2c** are essentially the same, having two iron atoms bridged by two hydroxide and two μ -1,3 carboxylate ligands. Assignment of the single atom bridging ligands as hydroxide is supported by the Fe–O distances of 1.949(3) – 2.012(2) Å, as well as by the location and refinement of the associated hydrogen atoms in the X-ray structure determination. The Fe···Fe distances of 2.8322(8) – 2.8843(9) Å in **1c** and **2c** are significantly below the range (3.089(2) – 3.155(3) Å) obtained for doubly-bridged**

$\{\text{Fe}_2(\mu\text{-OH})_2\}^{4+}$ cores,^{67,68} and lie between 2.95(1) Å and 2.714(2) Å observed for $\{\text{Fe}_2(\mu\text{-O})(\mu\text{-OH})\}^{3+}$ ⁶⁹ and $\{\text{Fe}_2(\mu\text{-O})_2\}^{2+}$ ⁷⁰ core fragments, respectively. This trend nicely demonstrates the systematic shortening of the metal...metal distances in the $\{\text{M}_2\text{L}_2\}^{n+}$ rhombic cores by decreasing the M-L distances, as well as by increasing the number of bridging units. For comparison, a Fe...Fe distance of 2.9788(6) Å was obtained for the triply-bridged $\{\text{Fe}_2(\mu\text{-OH})_2(\mu\text{-O}_2\text{CR})\}^{3+}$ unit in $[\text{Fe}_2(\mu\text{-OH})_2(\mu\text{-O}_2\text{CAr}^{\text{Tol}})(\text{O}_2\text{CAr}^{\text{Tol}})_3(\text{N-Bnen})(\text{N,N-Bn}_2\text{en})]$,⁷¹ the first structural model compound of the diiron(III) core in MMOH. The Fe-O_{hydroxide}-Fe angles in **1c** and **3c** range from 92.34(10) to 93.42(12)°. The two terminal η^1 -carboxylate ligands are hydrogen bonded to the bridging hydroxide groups (O_{hydroxide}...O_{carboxylate} = 2.725(4) – 2.888(3) Å). Binding of the two pyridine ligands, disposed anti across the Fe-Fe vector, completes the pseudo-octahedral coordination spheres of the two iron(III) centers.

For edge-shared octahedral metal centers, quadruply-bridged units consisting of two hydroxide and two Ar^{Tol}CO₂⁻ ligands can only be accommodated by a trans-disposition of the μ -1,3 carboxylates across the $\{\text{M}_2(\mu\text{-OH})_2\}^{n+}$ plane, a configuration that alleviates steric interactions between the *p*-tolyl groups. An analogous dicobalt(III) complex was recently synthesized and structurally characterized,⁷² suggesting that the $\{\text{M}_2(\mu\text{-OH})_2(\mu\text{-O}_2\text{CR})_2\}^{2+}$ core fragment may be a general structural motif for quadruply-bridged trivalent dimetallics supported by Ar^{Tol}CO₂⁻ and related ligands.

(b) Mössbauer and Magnetic Properties. Zero-field Mössbauer spectra of both solid and solution samples of **2c** were collected at 4.2 K. The spectrum of powdered **2c** displays a relatively sharp ($\Gamma = 0.36 - 0.39 \text{ mm s}^{-1}$) quadrupole doublet (Figure 3.20A) with $\delta = 0.49(2) \text{ mm s}^{-1}$ and $\Delta E_{\text{Q}} = 1.01(2) \text{ mm s}^{-1}$, values typical for high spin Fe(III) ions.⁵²⁻⁵⁴ Identical Mössbauer parameters were obtained for the frozen THF solution states (Figure 3.20B). Although the peaks are

significantly broadened ($\Gamma = 0.52 - 0.53 \text{ mm s}^{-1}$) in the latter case, this result indicates that the integrity of the diiron(III) core is maintained in solution.

Compounds **1c** and **2c** display weak ferromagnetic coupling, affording $S = 5$ ground spin states. Plots of the effective magnetic moment (μ_{eff}) and molar susceptibility (χ_M) versus temperature for **1c** and **2c** are presented in Figures 3.21 and 3.22, respectively. At temperatures above $\sim 150 \text{ K}$, the effective magnetic moment is essentially constant at $8.4 \mu_B$ (for **1c**) and $8.5 \mu_B$ (for **2c**), values consistent with the presence of two uncoupled $S = 5/2$ centers with $g = 2.00$ (calculated spin-only value of $\mu_{\text{eff}} = 8.37 \mu_B$). Upon lowering the temperature, μ_{eff} gradually increases to $10.23 \mu_B$ and $10.37 \mu_B$ at 5 K for **1c** and **2c**, respectively. These values are close to the theoretical moment of $10.95 \mu_B$ calculated for an $S_{\text{tot}} = 5$ spin state arising from two ferromagnetically coupled $S = 5/2$ centers with $g = 2.00$. The magnetic susceptibility data were fit by using an expression derived from the spin-only isotropic HDvV exchange Hamiltonian $\mathcal{H} = -2J\mathbf{S}_1 \cdot \mathbf{S}_2$, where $\mathbf{S}_1 = \mathbf{S}_2 = 5/2$. The best fit was obtained for $J = +0.69(4) \text{ cm}^{-1}$ for **1c** (Figure 3.21) and $J = +0.70(4) \text{ cm}^{-1}$ for **2c** (Figure 3.22) by fixing $g = 2.00$.

Compounds **1c** and **2c** belong to a rare class of diiron(III) clusters displaying ferromagnetic interactions. Other examples include $[\text{Fe}_2(\text{salmp})_2]$,³⁷ in which two phenoxide bridging ligands mediate weak ferromagnetic coupling ($J = +1.21 \text{ cm}^{-1}$) between two high-spin Fe(III) centers separated by $3.063(1) \text{ \AA}$ ($\text{Fe}-\text{O}_{\text{phenoxide}}-\text{Fe} = 97.06(9)^\circ$).⁷³ Structurally related di(μ -hydroxo)diiron(III) compounds, $[\text{L}^2_2\text{Fe}_2(\mu\text{-OH})_2]$ ³⁷ ($\text{Fe}\cdots\text{Fe} = 3.155(3) \text{ \AA}$; $\text{Fe}-\text{O}_{\text{hydroxide}}-\text{Fe} = 102.8(3)^\circ$) and $[(\text{dipic})\text{Fe}(\mu\text{-OH})_2(\text{H}_2\text{O})_2]$ ³⁷ ($\text{Fe}\cdots\text{Fe} = 3.089(2) \text{ \AA}$; $\text{Fe}-\text{O}_{\text{hydroxide}}-\text{Fe} = 103.6(2)^\circ$), however, display weak AF interactions with $J = -10.4 \text{ cm}^{-1}$ and -11.4 cm^{-1} , respectively.^{67,68} The smaller $\text{Fe}-\text{O}_{\text{hydroxide}}-\text{Fe}$ angles in **1c** and **2c**, owing to the presence of two μ -1,3 carboxylate ligands, may lead to a crossover from antiferromagnetism to ferromagnetism. The large number of possible exchange path-

ways between two high-spin Fe(III) centers, however, precludes a straightforward magnetostructural correlation.

Discussion

Spectroscopic Identification of Intermediates in the Reaction of [Fe₂(O₂CAr^{Tol})₄L₂] Complexes with Dioxygen. Oxygenation of **1a** and **2a** in CH₂Cl₂ at -78 °C generates thermally sensitive intermediates **1b** and **2b**, which decay to afford **1c** and **2c**, respectively, as the isolated products (Scheme 3.2). The electronic structures of **1b** and **2b** were probed by various spectroscopic techniques. EPR and Mössbauer studies provide compelling evidence that **2b** comprises equimolar amounts of Fe(III)Fe(IV) and Fe(II)Fe(III) as major components. Independent chemical synthesis and spectroscopic characterization of the Fe(II)Fe(III) complexes, **1mv** and **2mv**,⁴⁰ enabled us to understand fully the contribution of each paramagnetic component to the overall spectroscopic properties of **1b** and **2b**.

The intense ($\epsilon = 1600 \sim 1700 \text{ M}^{-1}\text{cm}^{-1}$, based on [Fe₂]) visible transitions at 660 ~ 670 nm as well as the thermal instability of **1b** and **2b** are reminiscent of the properties of (peroxo)diiron(III) clusters. Peroxide-to-iron(III) LMCT transitions in these units usually occur at 500 – 800 nm with extinction coefficients exceeding ~1000 M⁻¹cm⁻¹ (Table 3.2), values significantly above those (390 – 520 M⁻¹cm⁻¹) of the 674 – 688 nm absorption maxima displayed by valence-trapped Fe(II)Fe(III) complexes [Fe₂(μ -O)(μ -O₂CR)₂(Me₃TACN)₂]⁺ (R = CH₃ or C₆H₅).^{37,74} No isotope-sensitive O–O vibrations, however, were detected in the resonance Raman spectra of **1b**. UV-vis data of **1mv** and **2mv**⁴⁰ now unambiguously establish that the optical transitions of **1b** and **2b** actually arise from the mixed-valence Fe(II)Fe(III) components, [Fe₂(μ -O₂CAr^{Tol})₄(C₅H₅N)₂]⁺ ($\lambda_{\text{max}} = 660 \text{ nm}$; $\epsilon = 2900 \text{ M}^{-1}\text{cm}^{-1}$) and [Fe₂(μ -O₂CAr^{Tol})₄(4-^tBuC₅H₄N)₂]⁺ ($\lambda_{\text{max}} = 670 \text{ nm}$; $\epsilon = 3200 \text{ M}^{-1}$

cm⁻¹), respectively. In Figure 3.23 are displayed the UV-vis spectra of **2b** and **2mv** scaled such that the absorption maxima match one another. The $\lambda_{\text{max}} = 670$ nm chromophore of **2b** is perfectly accounted for by the inter-valence charge transfer (IVCT) band of the Fe(II)Fe(III) cation that constitutes ~54% of the total diiron concentration. This result is consistent with the ~0.45 oxidizing equivalent of **2b** determined by redox titration with Cp₂*Fe. The mixed-valence species **2mv** (Fe^{II}Fe^{III}/Fe^{II}Fe^{II} = +244 mV vs SCE)⁷⁵ acts as one-electron oxidant toward Cp₂*Fe (Fe^{II}/Fe^{III} = -130 mV vs SCE)⁶³ to afford **2a** and Cp₂*Fe⁺. A similar analysis can be made with **1b**, for which the corresponding **1mv** component has $\lambda_{\text{max}} \cong 665$ nm. Comparison of the extinction coefficients indicates that **1b** comprises ~55% of **1mv**. Taken together, these results indicate that the dark green color of **1b** and **2b** arises predominantly from the Fe(II)Fe(III), not the Fe(III)Fe(IV), component in the oxygenation reaction mixture. For comparison, the Fe(III)Fe(IV) chromophore in RNR-R2 X has an absorption band at ~360 nm and none at higher wavelengths.^{11b}

The resonance enhanced peak at 851 cm⁻¹ in the Raman spectra of **1b** and **2b** originates from the Fe(II)Fe(III) components **1mv** and **2mv**, respectively, and is thus not affected by ¹⁸O labeling. At present, we do not have an assignment for this vibration, which is observed upon excitation of the IVCT band of the valence-delocalized Fe(II)Fe(III) cores.

Mechanistic Considerations. Formation of Fe(III)Fe(IV) and Fe(II)Fe(III) species from a reaction between an Fe(II)Fe(II) precursor and dioxygen is an unprecedented process among non-heme diiron systems. Based on the spectroscopic and kinetic data obtained here and in other investigations,^{35,40} we propose the working mechanism depicted in Scheme 3.3 to account for this novel chemical transformation.

(a) Carboxylate Shifts. In the solution state, we presume an equilibrium between doubly-bridged (**A**, Scheme 3.3) and quadruply-bridged (**B**, Scheme 3.3) isomers of the $[\text{Fe}_2(\text{O}_2\text{CAr}^{\text{Tol}})_4\text{L}_2]$ module. This postulate reflects the fact that both **1a** and **2b** display essentially identical reactivity patterns toward dioxygen, affording reaction intermediates **1b** and **2b** having comparable spectral properties (*vide supra*). Given the distinctively different solid state structures of **1a** (isomer **A**) and **2b** (isomer **B**), this result is quite unexpected. The steric environments of the coordinatively unsaturated metal centers in **A** and **B** are significantly different, as indicated by space-filling representations (Figure 3.24). Open coordination sites on the five-coordinate iron atoms in **A** are readily accessible to exogenous ligands, whereas the coordination sites available for the sixth ligand in **B** lies along the Fe–Fe vector buried inside the hydrophobic cavity. Core rearrangement is thus required for **B** before dioxygen binding.

Variable temperature ^{19}F -NMR studies indicated that a related compound $[\text{Fe}_2(\text{O}_2\text{CAr}^{4\text{-FPh}})_4(\text{THF})_2]$ can exist in both isomeric forms **A** and **B**, the relative populations of which strongly depends on the temperature.⁷⁶ In CH_2Cl_2 at -80°C , **A** is a dominant isomer for $[\text{Fe}_2(\text{O}_2\text{CAr}^{4\text{-FPh}})_4(\text{THF})_2]$, although both **A** and **B** are present at room temperature. Such flexibility is illustrated by structural characterization of the mixed-valence Fe(II)Fe(III) compounds $[\text{Fe}_2(\mu\text{-O}_2\text{CAr}^{\text{Tol}})_4\text{L}_2]\text{X}$ ($\text{L} = \text{THF}, \text{C}_5\text{H}_5\text{N}$; $\text{X}^- = \text{PF}_6^-, \text{OTf}^-$).⁴⁰ Here, a **B**-type core forms following one-electron oxidation of an **A**-type core without any apparent steric penalty. These findings corroborate speculation that both isomeric forms, **A** and **B**, can be accessed by **1a** and **2a** under certain conditions. Formal double carboxylate shifts between μ -1,3 bridging and η^2 -terminal positions would allow core interconversion between **A** and **B** to occur by a triply-bridged intermediate **C**. We propose that the quadruply-bridged isomer **B** dominates the solution population of both **1a** and **2a** at low temperatures.

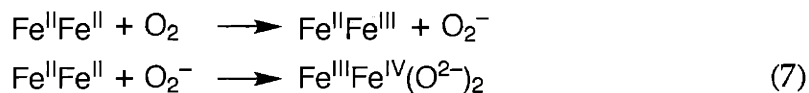
(b) Nature of the Initial O₂-Adduct(s). As mentioned above, core re-arrangement in **B** is required to provide a dioxygen binding site. Shifts of one or two bridging carboxylate ligands in **B** would afford **C** or **A** as functionally competent isomers. Reaction of the diiron(II) species with dioxygen leads to an initial adduct **D**, which, by analogy to the RNR-R2 and MMOH intermediates,¹ is most likely either a peroxo-type Fe^{III}₂(O₂²⁻) or a Q-type Fe^{IV}₂(O²⁻)₂ unit. Although rapid reaction with **B** (vide infra) precluded detailed investigation of **D** under the conditions employed, the sterically more hindered analog of **1a**, [Fe₂(μ-O₂CAr^{Mes})₂(O₂CAr^{Mes})₂(MeCN)₂],³⁷ reacts with dioxygen to afford a (peroxo)diiron(III) intermediate.²¹ A (peroxo)diiron(III) intermediate precedes the assembly of a {Fe^{III}Fe^{IV}(O²⁻)₂}³⁺ core in reactions between [Fe₂(μ-OH)₂(6-Me₃-TPA)₂]²⁺ and dioxygen.^{22,37}

(c) Paramagnetic Intermediates. The first spectroscopically observable intermediates **1b** and **2b** contain equimolar amounts of Fe(II)Fe(III) (**E**) and Fe(III)Fe(IV) (**F**) species as major constituents. The spectroscopic properties of **E** match perfectly those of **1mv** and **2mv**, indicating that **E** indeed is a one-electron oxidized form of **B**, [Fe₂(μ-O₂CAr^{Tol})₂L₂]⁺ (L = C₅H₅N or 4-^tBuC₅H₄N). Formation of a 1:1 mixture of **E** and **F** requires formal four-electron oxidation of two molecules of diiron(II) precursors. This metal oxidation is coupled to four-electron reduction of dioxygen, formally affording two oxo groups. Accordingly, **F** is formulated as Fe^{III}Fe^{IV}(O²⁻)₂ (eq 6).

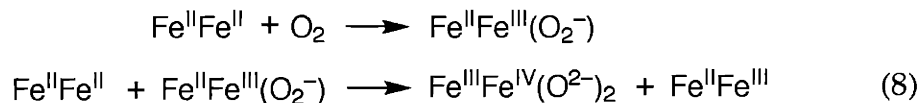


The nature of the oxidant effecting one-electron oxidation of **B** to **E** has significant implications about the chemistry we observe. Both dioxygen and a metal-based oxidant might promote outer-sphere electron transfer (ET), a process

that would preserve the structural integrity of the diiron(II) precursor. Outer sphere ET from **B** to O₂ would generate **E** and a superoxide anion. Formal three-electron reduction of the latter by **B** would afford **F** (eq 7). The first step in this



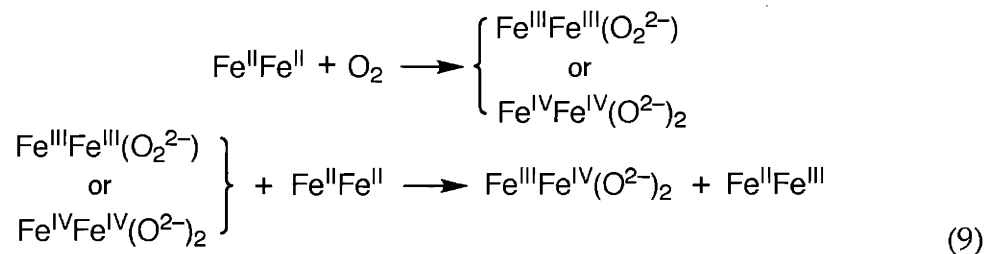
conversion has been previously implicated in the formation of mixed-valence Fe(II)Fe(III) compounds having at least one single atom bridging ligand. Controlled oxygenation of coordinatively saturated diiron(II) precursors having {Fe₂(μ-OH)(μ-O₂CR)₂}⁺ cores afforded the corresponding valence-trapped Fe(II)Fe(III) compounds.^{74,77,78} A similar observation was made for [Fe₂(μ-OⁱPr)₂(μ-O₂CAr^{Mes})(O₂CAr^{Mes})₂], prepared by outer-sphere electron transfer from [Fe₂(μ-O₂CAr^{Mes})₂(O₂CAr^{Mes})₂(MeCN)₂] in CH₂Cl₂/ⁱPrOH.⁵⁸ Considering the high oxidation potential (Fe^{II}Fe^{II}/Fe^{II}Fe^{III} = +284 mV vs NHE)^{40,75} of **2a** in CH₂Cl₂, however, we can rule out the outer-sphere one-electron reduction of dioxygen (O₂/O₂⁻ = -330 mV vs NHE)⁷⁹ as a coupled process for the formation of **E**. Alternatively, inner-sphere ET from metal-bound O₂ might be invoked (eq 8). In order to account for the simultaneous formation of an equimolar quantity of **F**, however, the superoxide complex would have to be selectively and completely



trapped by another equivalent of **B**, which seems unlikely. Moreover, there is no precedent for the three-electron reduction of superoxide by iron(II) compounds.

Instead, we propose that **D** acts as a one-electron oxidant toward **B**, affording the observed 1:1 mixture of **E** and **F** (eq 9). The coupled formation of **E**

and **F** is fully consistent with the EPR kinetic data. Although rapid ET from **B** to **D** presumably prevents accumulation of a detectable amount of **D** under the conditions employed, the kinetic data provide compelling evidence for the presence of an intermediate preceding **E** and **F**, the most reasonable candidates being either a peroxo- or a Q-type dioxygen adduct.



(d) Oxidation of Phenol Substrates: Functional Mimic of RNR-R2 X.

The high-valent Fe(III)Fe(IV) species **F** effects oxidation of phenol substrates. The ~40% yield of the coupled biphenol product from 2,4-di-*tert*-butylphenol is close to the upper limit (50% based on diiron(II) precursor) of **F** in the proposed mechanism (Scheme 3.3; eq 6), and consistent with the quantitation afforded by EPR and Mössbauer spectroscopy. Control experiments with the Fe(II)Fe(III) compound **2mv**, which cannot oxidize the phenols, confirmed that the oxidizing power of **2b** originates from **F**, which acts both as a one-electron oxidant and a proton acceptor. This process closely parallels the mechanism of RNR-R2, in which a high-valent Fe(III)Fe(IV) intermediate **X** oxidizes an adjacent tyrosine residue. Related $\{\text{Fe}^{\text{III}}\text{Fe}^{\text{IV}}(\mu\text{-O})_2\}^{3+}$ core fragments supported on polypyridyl ligands effect similar transformations.^{22,80}

(e) Reactivity and Magnetic Properties: Structural Implications for Fe(III)Fe(IV). Different reactivity patterns of **E** and **F** toward H^+ indicate that **F** has ligand unit(s), the protonation of which alters magnetic coupling between the metal centers. Addition of 0.5 equiv of H^+ prior to oxygenation only slightly af-

affected the amount of **E** generated, whereas a 10-fold decrease was observed for **F** as determined by EPR spectroscopy. Consistent with this finding, the contribution of **E** to the visible absorption of **1b** was not affected by addition of 2 equiv H^+ at $-78\text{ }^\circ\text{C}$. This result indicates that the structural integrity of the $[\text{Fe}_2(\text{O}_2\text{CAr}^{\text{Tol}})_4\text{L}_2]^+$ cation (**E**) is maintained in the presence of H^+ , whereas protonation of the putative O_2 -derived ligand(s) significantly decreases the stability of **F** as well as increasing its rate of reduction. The formulation of the **F** core as $\{\text{Fe}^{\text{III}}\text{Fe}^{\text{IV}}(\text{O}^{2-})_2\}^{3+}$ is compatible with such an observation. Protonation of the oxo groups in $\{\text{Fe}^{\text{III}}\text{Fe}^{\text{IV}}(\text{O}^{2-})_2\}^{3+}$ may trigger reduction of the Fe(IV) center to Fe(III), affording an Fe(III)Fe(III) species. At this point, we cannot conclusively determine which species serves as an electron donor for **F**. Since the amount of **E** produced upon oxygenation is only slightly affected in the presence of H^+ , we believe that both **B** and **E** could act as reductants for **F**.

The large exchange coupling constant of $|2J| > 200\text{ cm}^{-1}$ ($\mathcal{H} = -2J\mathbf{S}_1 \cdot \mathbf{S}_2$), estimated for **F** by EPR spectroscopy, implies the presence of an efficient superexchange pathway.^{1g} We propose that at least one of the oxo groups within the $\{\text{Fe}^{\text{III}}\text{Fe}^{\text{IV}}(\text{O}^{2-})_2\}^{3+}$ core in **F** acts as a bridging ligand, mediating the strong net AF interaction between the Fe(III) and Fe(IV) sites. A valence-localized Fe(III)Fe(IV) complex having a $\{\text{Fe}_2(\mu\text{-O})_2\}^{3+}$ core exhibits a large coupling, $|2J| > 80\text{ cm}^{-1}$ ($\mathcal{H} = -2J\mathbf{S}_1 \cdot \mathbf{S}_2$).^{32b} Although the correlation between J and the shortest Fe–O–Fe pathway has been well-established for (μ -oxo)diiron(III) complexes,⁸¹ an analogous magnetostructural correlation is not available for the Fe(III)Fe(IV) units, largely owing to the limited number of well-defined basis sets available.

(d) Decay of the Intermediates and Isolation of a Diiron(III) Complex.

Mechanistic information about the decomposition of **E** and **F** is currently unavailable. Studies of **1mv** and **2mv** reveal that **E** is thermally stable but rapidly decomposes in the presence of dioxygen at room temperature.⁴⁰ Decomposition

of **E** upon warming thus can be partially ascribed to reactions with residual dioxygen. Alternatively, reactions between **E** and **F** may occur at elevated temperatures, although preliminary EPR data suggest that their decay processes are not coupled.

The EPR spectra obtained for a thermal decay product of **2b** display spectral patterns distinctively different from that of **2c**. This result clearly indicates that **2c** is not an immediate reaction product of **2b**. Although the $\{\text{Fe}_2(\mu\text{-OH})_2\}^{4+}$ core in **1c** or **2c** are reminiscent of analogous $\{\text{Cu}_2(\mu\text{-OH})_2\}^{2+}$ cores obtained following C-H activation by high-valent $\{\text{Cu}_2(\mu\text{-O})_2\}^{2+}$ intermediates,⁴¹ no ligand oxidation was observed in the present investigation. The good to excellent isolated yields (75 – 90%) of **1c** and **2c** also strongly suggest that not all of the oxygen atoms in the OH^- bridging ligands originate from O_2 . Incorporation of adventitious H_2O in the crystallization media most likely contribute to the assembly of the $\{\text{Fe}_2(\mu\text{-OH})_2\}^{4+}$ core from the initial thermal decay product(s), the details of which were not further investigated.

(e) Branching Pathways. In addition to the major intermediates **E** and **F** described above, a diiron(III) component was detected in EPR and Mössbauer samples of **2b**. Although the mechanism depicted in Scheme 3.3 does not account for the formation of this diiron(III) product, it must arise either through a reaction between **E** and **F** or via a branching pathway involving the diiron(II) precursor and dioxygen. Such processes could be operative in the concentrated (> 10 mM) diiron solutions used for the manometry, EPR, and Mössbauer studies. The stoichiometry of O_2 consumption (0.75 ± 0.1 equiv per diiron(II)) exceeds that (0.50) expected solely from the chemistry of eq 6, implying the involvement of additional, unidentified oxygenation processes. Thermal decay or reactions with **E** may be responsible for the detection of less than a quantitative amount of

F in the Mössbauer sample, which required solvent removal at $-78\text{ }^{\circ}\text{C}$ over a period of $> 18\text{ h}$ to prepare.

Biomimetic Formation of Fe(III)Fe(IV) Species: Relevance to RNR-R2.

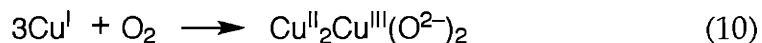
A high-valent Fe(III)Fe(IV) species has now been prepared by reaction of dioxygen with $[\text{Fe}_2(\text{O}_2\text{CR})_4\text{L}_2]$ diiron(II) complexes, a process that closely mimics the formation of the enzyme intermediate RNR-R2 X (Scheme 3.1). Prior to our previous communication of this chemistry,³⁵ no synthetic system existed that utilized dioxygen as a terminal oxidant to access the Fe(IV) state from Fe(II) precursors. Analogous high-valent non-heme Fe(III)Fe(IV) compounds had previously been obtained only by oxidation of di(μ -oxo)diiron(III) precursors with H_2O_2 ,³² and in these cases polypyridyl ligands unlike those in the proteins were employed.

One external electron is required to balance the equation for the formation of a tyrosyl radical and the (μ -oxo)diiron(III) core describing the reaction between reduced RNR-R2 and O_2 (Scheme 3.1). The source of this extra electron and its injection point along the reaction coordinate are currently unclear. Subsequent to our communication of this RNR-R2 model chemistry,³⁵ another synthetic system was reported, in which a polypyridine-supported diiron(II) center reacts with dioxygen to afford a (peroxo)diiron(III) species.^{22,26} In the presence of one equiv of H^+ , this intermediate transformed into a Fe(III)Fe(IV) complex, and again the source of the extra electron needed for the conversion of the former to the latter was not established. A recent mechanistic proposal suggests that, in RNR-R2, the diiron clusters are functionally distinctive, one reacting with dioxygen and the other supplying reducing equivalents.⁸² Although the requisite Fe(II)Fe(III) intermediate has yet to be identified in the biological system, the mechanism depicted in Scheme 3.3 suggests that carboxylate-bridged diiron(II) centers can indeed function to supply the required electron by ET. It still re-

mains to be determined, however, whether the ET occurs directly to a (per-oxo)diiron(III) unit or whether conversion to a Q-type transient intermediate is involved that accepts the electron to afford the Fe(III)Fe(IV) intermediate X.

Self-hydroxylating monooxygenase reactivities occur in certain mutants of RNR-R2,⁸³ which strongly support a unifying theory connecting the chemistry of non-heme dioxygen-activating centers. A similar one-electron reduction of the high-valent diiron(IV) species in MMOH_Q could be effectively blocked either by the lack of an efficient ET pathway or by the binding of other MMO component proteins. Conformational changes in the primary metal coordination sphere might be induced by such binding events, which could shift the redox window to avoid deleterious quenching of the oxidizing equivalents.

Comparison with Copper(I) Dioxygen Activation. Advances in copper dioxygen chemistry have complemented our understanding of the parallel processes in diiron systems.⁸⁴ Reactions between a mononuclear copper(I) complex and O₂ afforded a trinuclear intermediate [L₃Cu^{II}₂Cu^{III}(μ-O)₂]³⁺, as indicated by eq 10.⁸⁵ Despite apparent differences in the reaction stoichiometry and structural outcome, the chemical principles underlying eqs 6 and 10 are strikingly similar.



In the reductive activation of dioxygen by iron, four electrons are supplied by three iron(II) centers within two dimeric units (eq 6), whereas for copper three individual copper(I) ions contribute four reducing equivalents (eq 10) to cleave the O–O bond. The results are two distinguishable mixed-valence dinuclear clusters for the former and one trinuclear mixed-valence cluster for the latter. Steric shielding provided by the bulky *m*-terphenyl units apparently helps to sustain the dinuclear cores of **1a** and **2a** during their reactions with dioxygen.

Summary and Perspective

Tetracarboxylate diiron(II) complexes react with dioxygen to access the Fe(IV) oxidation state, a process that parallels the chemistry of several non-heme diiron enzymes. The spectroscopic and functional properties of the Fe(III)Fe(IV) species faithfully reproduce features of the enzyme intermediate RNR-R2 X. Spectroscopic and kinetic studies revealed the simultaneous formation of both Fe(II)Fe(III) and Fe(III)Fe(IV) species in this transformation, the mechanistic implications of which relate well to a recent proposal for the enzyme. The untimely ET from the low-valent starting material to putative high-valent dioxygen-adduct(s), as proposed in this investigation, poses a significant challenge for future work to access dioxygen-activating model compounds that functionalize hydrocarbons. Bulky ligand fragments have been frequently exploited to shield highly reactive species against unwanted side reactions. Although the steric hindrance provided by such constructs may suppress reactions involving bond-forming processes, deleterious ET reactions may still occur even between well-shielded small molecules. Uncontrolled electron trafficking may quench a reactive intermediate before it accumulates in amounts sufficient to effect the chemical transformations of interest. A detailed understanding of this process would undoubtedly facilitate efforts to gain better control over the oxidizing power of dioxygen in synthetic constructs.

Acknowledgment. This work was supported by grants from the National Science Foundation and National Institute of General Medical Sciences. The EPR studies discussed here were carried out in collaboration with Prof. Michael P. Hendrich and Mr. Brad Pierce (Carnegie Mellon University). The Mössbauer studies were done in collaboration with Prof. Boi Hanh Huynh and Dr. Carsten

Krebs (Emory University). I thank Dr. Justin Du Bois for many helpful discussions, Dr. Amy M. Barrios and Ms. Joey Bautista for performing the resonance Raman experiment, and Ms. Jane Kuzelka for assistance in acquiring the Mössbauer spectra.

References

- (*) Part of this work has appeared previously in references 34 and 35, © 1998, 1999 American Chemical Society. A slightly modified version of this work has been submitted for publication. Lee, D.; Pierce, B.; Krebs, C.; Hendrich, M. P.; Huynh, B. H.; Lippard, S. J. **2001**
- (1) (a) Feig, A. L.; Lippard, S. J. *Chem. Rev.* **1994**, *94*, 759-805. (b) Wallar, B. J.; Lipscomb, J. D. *Chem. Rev.* **1996**, *96*, 2625-2657. (c) Que, L., Jr.; Dong, Y. *Acc. Chem. Res.* **1996**, *29*, 190-196. (d) Lange, S. J.; Que, L., Jr. *Curr. Opin. Chem. Biol.* **1998**, *2*, 159-172. (e) Stahl, S. S.; Lippard, S. J. *Iron Metabolism: Inorganic Biochemistry and Regulatory Mechanisms*; Ferreira, G. C., Moura, J. J. G. and Franco, R., Ed.; Wiley-VCH: Weinheim, 1999, pp 303-321. (f) Du Bois, J.; Mizoguchi, T. J.; Lippard, S. J. *Coord. Chem. Rev.* **2000**, *200-202*, 443-485. (g) Solomon, E. I.; Brunold, T. C.; Davis, M. I.; Kemsley, J. N.; Lee, S.-K.; Lehnert, N.; Neese, F.; Skulan, A. J.; Yang, Y.-S.; Zhou, J. *Chem. Rev.* **2000**, *100*, 235-349.
- (2) Merckx, M.; Kopp, D. A.; Sazinsky, M. H.; Blazyk, J. L.; Müller, J.; Lippard, S. *J. Angew. Chem., Int. Ed. Engl.* **2001**, *40*, 2782-2807.
- (3) Whittington, D. A.; Lippard, S. J. *Handbook of Metalloproteins*; Messerschmidt, A., Huber, R., Poulos, T. and Wieghardt, K., Ed.; John Wiley & Sons: Chichester, 2001, pp 712-724.
- (4) Logan, D. T.; Su, X.-D.; Åberg, A.; Regnström, K.; Hajdu, J.; Eklund, H.; Nordlund, P. *Structure* **1996**, *4*, 1053-1064.
- (5) Stubbe, J.; van der Donk, W. A. *Chem. Rev.* **1998**, *98*, 705-762.
- (6) Lindqvist, Y.; Huang, W.; Schneider, G.; Shanklin, J. *EMBO J.* **1996**, *15*, 4081-4092.
- (7) Yang, Y.-S.; Broadwater, J. A.; Pulver, S. C.; Fox, B. G.; Solomon, E. I. *J. Am. Chem. Soc.* **1999**, *121*, 2770-2783.

- (8) Lee, S.-K.; Fox, B. G.; Froland, W. A.; Lipscomb, J. D.; Münck, E. *J. Am. Chem. Soc.* **1993**, *115*, 6450-6451.
- (9) Liu, K. E.; Valentine, A. M.; Wang, D.; Huynh, B. H.; Edmondson, D. E.; Salifoglou, A.; Lippard, S. J. *J. Am. Chem. Soc.* **1995**, *117*, 10174-10185.
- (10) Shu, L.; Nesheim, J. C.; Kauffmann, K.; Münck, E.; Lipscomb, J. D.; Que, L., Jr. *Science* **1997**, *275*, 515-518.
- (11) (a) Ravi, N.; Bollinger, J. M., Jr.; Huynh, B. H.; Edmondson, D. E.; Stubbe, J. *J. Am. Chem. Soc.* **1994**, *116*, 8007-8014. (b) Bollinger, J. M., Jr.; Tong, W. H.; Ravi, N.; Huynh, B. H.; Edmondson, D. E.; Stubbe, J. *J. Am. Chem. Soc.* **1994**, *116*, 8015-8023. (c) Sturgeon, B. E.; Burdi, D.; Chen, S.; Huynh, B. H.; Edmondson, D. E.; Stubbe, J.; Hoffman, B. M. *J. Am. Chem. Soc.* **1996**, *118*, 7551-7557. (d) Burdi, D.; Sturgeon, B. E.; Tong, W. H.; Stubbe, J.; Hoffman, B. M. *J. Am. Chem. Soc.* **1996**, *118*, 281-282. (e) Willems, J.-P.; Lee, H.-I.; Burdi, D.; Doan, P. E.; Stubbe, J.; Hoffman, B. M. *J. Am. Chem. Soc.* **1997**, *119*, 9816. (f) Burdi, D.; Willems, J.-P.; Riggs-Gelasco, P.; Antholine, W. E.; Stubbe, J.; Hoffman, B. M. *J. Am. Chem. Soc.* **1998**, *120*, 12910-12919.
- (12) Rardin, R. L.; Tolman, W. B.; Lippard, S. J. *New J. Chem.* **1991**, *15*, 417-430.
- (13) Que, L., Jr. *J. Chem. Soc., Dalton Trans.* **1997**, 3933-3940.
- (14) Westerheide, L.; Pascaly, M.; Krebs, B. *Curr. Opin. Chem. Biol.* **2000**, *4*, 235-241.
- (15) Tolman, W. B.; Spencer, D. J. E. *Curr. Opin. Chem. Biol.* **2001**, *5*, 188-195.
- (16) (a) Kitajima, N.; Tamura, N.; Amagai, H.; Fukui, H.; Moro-oka, Y.; Mizutani, Y.; Kitagawa, T.; Mathur, R.; Heerwegh, K.; Reed, C. A.; Randall, C. R.; Que, L., Jr.; Tatsumi, K. *J. Am. Chem. Soc.* **1994**, *116*, 9071-9085. (b) Kim, K.; Lippard, S. J. *J. Am. Chem. Soc.* **1996**, *118*, 4914-4915.
- (17) (a) Ménage, S.; Brennan, B. A.; Juarez-Garcia, C.; Münck, E.; Que, L., Jr. *J. Am. Chem. Soc.* **1990**, *112*, 6423-6425. (b) Dong, Y.; Ménage, S.; Brennan, B.

- A.; Elgren, T. E.; Jang, H. G.; Pearce, L. L.; Que, L., Jr. *J. Am. Chem. Soc.* **1993**, *115*, 1851-1859. (c) Dong, Y.; Yan, S.; Young, V. G., Jr.; Que, L., Jr. *Angew. Chem., Int. Ed. Engl.* **1996**, *35*, 618-620.
- (18) Ookubo, T.; Sugimoto, H.; Nagayama, T.; Masuda, H.; Sato, T.; Tanaka, K.; Maeda, Y.; Okawa, H.; Hayashi, Y.; Uehara, A.; Suzuki, M. *J. Am. Chem. Soc.* **1996**, *118*, 701-702.
- (19) Dong, Y.; Zang, Y.; Shu, L.; Wilkinson, E. C.; Que, L., Jr. *J. Am. Chem. Soc.* **1997**, *119*, 12683-12684.
- (20) LeCloux, D. D.; Barrios, A. M.; Mizoguchi, T. J.; Lippard, S. J. *J. Am. Chem. Soc.* **1998**, *120*, 9001-9014.
- (21) Hagadorn, J. R.; Que, L., Jr.; Tolman, W. B. *J. Am. Chem. Soc.* **1998**, *120*, 13531-13532.
- (22) MacMurdo, V. L.; Zheng, H.; Que, L., Jr. *Inorg. Chem.* **2000**, *39*, 2254-2255.
- (23) Feig, A. L.; Lippard, S. J. *J. Am. Chem. Soc.* **1994**, *116*, 8410-8411.
- (24) Feig, A. L.; Becker, M.; Schindler, S.; van Eldik, R.; Lippard, S. J. *Inorg. Chem.* **1996**, *35*, 2590-2601.
- (25) Feig, A. L.; Masschelein, A.; Bakac, A.; Lippard, S. J. *J. Am. Chem. Soc.* **1997**, *119*, 334-342.
- (26) Kryatov, S. V.; Rybak-Akimova, E. V.; MacMurdo, V. L.; Que, L., Jr. *Inorg. Chem.* **2001**, *40*, 2220-2228.
- (27) Valentine, A. M.; Stahl, S. S.; Lippard, S. J. *J. Am. Chem. Soc.* **1999**, *121*, 3876-3887.
- (28) Lee, S.-K.; Lipscomb, J. D. *Biochemistry* **1999**, *38*, 4423-4432.
- (29) Bollinger, J. M., Jr.; Krebs, C.; Vicol, A.; Chen, S.; Ley, B. A.; Edmondson, D. E.; Huynh, B. H. *J. Am. Chem. Soc.* **1998**, *120*, 1094-1095.
- (30) Broadwater, J. A.; Ai, J.; Loehr, T. M.; Sanders-Loehr, J.; Fox, B. G. *Biochemistry* **1998**, *37*, 14664-14671.

- (31) Brunold, T. C.; Tamura, N.; Kitajima, N.; Moro-oka, Y.; Solomon, E. I. *J. Am. Chem. Soc.* **1998**, *120*, 5674-5690.
- (32) (a) Dong, Y.; Fujii, H.; Hendrich, M. P.; Leising, R. A.; Pan, G.; Randall, C. R.; Wilkinson, E. C.; Zang, Y.; Que, L., Jr.; Fox, B. G.; Kauffmann, K.; Münck, E. *J. Am. Chem. Soc.* **1995**, *117*, 2778-2792. (b) Dong, Y.; Que, L., Jr.; Kauffmann, K.; Münck, E. *J. Am. Chem. Soc.* **1995**, *117*, 11377-11378. (c) Hsu, H.-F.; Dong, Y.; Shu, L.; Young, V. G., Jr.; Que, L., Jr. *J. Am. Chem. Soc.* **1999**, *121*, 5230-5237.
- (33) Zheng, H.; Yoo, S. J.; Münck, E.; Que, L., Jr. *J. Am. Chem. Soc.* **2000**, *122*, 3789-3790.
- (34) Lee, D.; Lippard, S. J. *J. Am. Chem. Soc.* **1998**, *120*, 12153-12154.
- (35) Lee, D.; Du Bois, J.; Petasis, D.; Hendrich, M. P.; Krebs, C.; Huynh, B. H.; Lippard, S. J. *J. Am. Chem. Soc.* **1999**, *121*, 9893-9894.
- (36) Pangborn, A. B.; Giardello, M. A.; Grubbs, R. H.; Rosen, R. K.; Timmers, F. J. *Organometallics* **1996**, *15*, 1518-1520.
- (37) Abbreviations used: $[\text{BAr}'_4]^-$, $[(3,5-(\text{CF}_3)_2\text{C}_6\text{H}_3)_4\text{B}]^-$; H_2XDK = *m*-xylylenediamine bis(Kemp's triacid imide); BXDK = the benzyl derivative of XDK; dipic, 2,6-pyridinedicarboxylate; H_3dfmp , 2,6-diformyl-4-methylphenoldioxime; HPTB = anion of *N,N,N',N'*-tetrakis(2-benzimidazolylmethyl)-2-hydroxyl-1,3-diaminopropane; L^1 , [2+2] condensation product of propylenediamine and 2,6-diformyl-4-methylphenol; L^2 , *N,N'*-ethylenebis(salicylamine); L^3 , *N,N,N',N'*-tetramethyl-(1*R*,2*R*)-cyclohexanediamine; Me_3TACN , 1,4,7-trimethyl-1,4,7-triazacyclononane; 6- Me_3 -TPA = tris(6-methyl-2-pyridylmethyl)amine; OAc^- , acetate; Ph-bimp = 2,6-bis[bis(2-(1-methyl-4,5-diphenylimidazolyl)methyl)aminomethyl]-4-methylphenolate; PhCyCO_2H = 1-phenylcyclohexanecarboxylic acid; pz' = 3,5-bis-(isopropyl)pyrazolyl; H_3salmp , 2-bis(salicylideneamino)methylphenol.

- (38) Brookhart, M.; Grant, B.; Volpe, A. F., Jr. *Organometallics* **1992**, *11*, 3920-3922.
- (39) van der Linden, A.; Schaverien, C. J.; Meijboom, N.; Ganter, C.; Orpen, A. G. *J. Am. Chem. Soc.* **1995**, *117*, 3008-3021.
- (40) Lee, D.; Krebs, C.; Huynh, B. H.; Hendrich, M. P.; Lippard, S. J. *J. Am. Chem. Soc.* **2000**, *122*, 5000-5001.
- (41) (a) Mahapatra, S.; Halfen, J. A.; Wilkinson, E. C.; Pan, G.; Wang, X.; Young, V. G., Jr.; Cramer, C. J.; Que, L., Jr.; Tolman, W. B. *J. Am. Chem. Soc.* **1996**, *118*, 11555-11574. (b) Mahapatra, S.; Halfen, J. A.; Tolman, W. B. *J. Am. Chem. Soc.* **1996**, *118*, 11575-11586.
- (42) *SMART v5.05: Software for the CCD Detector System*; Bruker AXS: Madison, WI, 1998.
- (43) Feig, A. L.; Bautista, M. T.; Lippard, S. J. *Inorg. Chem.* **1996**, *35*, 6892-6898.
- (44) Sheldrick, G. M. *SHELXTL97-2: Program for the Refinement of Crystal Structures*; University of Göttingen, Germany, 1997.
- (45) Sheldrick, G. M. *SADABS: Area-Detector Absorption Correction*; University of Göttingen, Germany, 1996.
- (46) Spek, A. L. *PLATON, A Multipurpose Crystallographic Tool*; Utrecht University: Utrecht, The Netherlands, 1998.
- (47) Kent, T. A. *WMOSS v2.5: Mössbauer Spectral Analysis Software*; WEB Research Co.: Minneapolis, MN, 1998.
- (48) Carlin, R. L. *Magnetochemistry*; Springer-Verlag: New York, 1986.
- (49) Goldberg, D. P.; Koulougliotis, D.; Brudvig, G. W.; Lippard, S. J. *J. Am. Chem. Soc.* **1995**, *117*, 3134-3144.
- (50) Krebs, C.; Davydov, R.; Baldwin, J.; Hoffman, B. M.; Bollinger, J. M., Jr.; Huynh, B. H. *J. Am. Chem. Soc.* **2000**, *122*, 5327-5336.

- (51) Valentine, A. M.; Tavares, P.; Pereira, A. S.; Davydov, R.; Krebs, C.; Hoffman, B. M.; Edmondson, D. E.; Huynh, B. H.; Lippard, S. J. *J. Am. Chem. Soc.* **1998**, *120*, 2190-2191.
- (52) Kurtz, D. M., Jr. *Chem. Rev.* **1990**, *90*, 585-606.
- (53) Gütlich, P.; Ensling, J. *Inorganic Electronic Structure and Spectroscopy*; Solomon, E. I. and Lever, A. B. P., Ed.; John Wiley & Sons: New York, 1999; Vol. I, pp 161-211.
- (54) Münck, E. *Physical Methods in Bioinorganic Chemistry: Spectroscopy and Magnetism*; Que, L., Jr., Ed.; University Science Books: Sausalito, CA, 2000, pp 287-319.
- (55) Blondin, B.; Girerd, J.-J. *Chem. Rev.* **1990**, *98*, 1359-1376.
- (56) Ding, X.-Q.; Bominaar, E. L.; Bill, E.; Winkler, H.; Trautwein, A. X.; Drüeke, S.; Chaudhuri, P.; Wieghardt, K. *J. Chem. Phys.* **1990**, *92*, 178-186.
- (57) Dutta, S. K.; Ensling, J.; Werner, R.; Flörke, U.; Haase, W.; Gütlich, P.; Nag, K. *Angew. Chem., Int. Ed. Engl.* **1997**, *36*, 152-155.
- (58) Hagadorn, J. R.; Que, L., Jr.; Tolman, W. B.; Prisecaru, I.; Münck, E. *J. Am. Chem. Soc.* **1999**, *121*, 9760-9761.
- (59) Krebs, C. Ph.D. Thesis; Ruhr-Universität Bochum: Germany, 1997.
- (60) Gamelin, D. R.; Bominaar, E. L.; Kirk, M. L.; Wieghardt, K.; Solomon, E. I. *J. Am. Chem. Soc.* **1996**, *118*, 8085-8097.
- (61) Rodriguez, J. H.; Ok, H. N.; Xia, Y.-M.; Debrunner, P. G.; Hinrichs, B. E.; Meyer, T.; Packard, N. H. *J. Phys. Chem.* **1996**, *100*, 6849-6862.
- (62) Rodriguez, J. H.; Lee, D.; Lippard, S. J., unpublished results.
- (63) Connelly, N. G.; Geiger, W. E. *Chem. Rev.* **1996**, *96*, 877-910.
- (64) Altwicker, E. R. *Chem. Rev.* **1967**, *67*, 475-531.

- (65) Crystal data for $[\text{Fe}(\text{O}_2\text{CAr}^{\text{Tot}})_2(2,4\text{-}^t\text{Bu}_2\text{C}_6\text{H}_3\text{O})(4\text{-}^t\text{BuC}_5\text{H}_4\text{N})]$: space group $P2_1/n$ with $a = 17.9762(6) \text{ \AA}$, $b = 14.4378(5) \text{ \AA}$, $c = 23.7130(7) \text{ \AA}$, $\beta = 104.1780(10)^\circ$, $V = 5966.9(3) \text{ \AA}^3$, $Z = 4$, $R = 7.76\%$, $wR^2 = 17.28\%$.
- (66) Lever, A. B. P. *Inorganic Electronic Spectroscopy*; 2nd ed.; Elsevier Science Publishers B. V.: Amsterdam, The Netherlands, 1984.
- (67) Borer, L.; Thalken, L.; Ceccarelli, C.; Glick, M.; Zhang, J. H.; Reiff, W. M. *Inorg. Chem.* **1983**, *22*, 1719-1724.
- (68) Thich, J. A.; Ou, C. C.; Powers, D.; Vasiliou, B.; Mastropaolo, D.; Potenza, J. A.; Schugar, H. J. *J. Am. Chem. Soc.* **1976**, *98*, 1425-1433.
- (69) Zang, Y.; Pan, G.; Que, L., Jr.; Fox, B. G.; Münck, E. *J. Am. Chem. Soc.* **1994**, *116*, 3653-3654.
- (70) Zang, Y.; Dong, Y.; Que, L., Jr.; Kauffmann, K.; Münck, E. *J. Am. Chem. Soc.* **1995**, *117*, 1169-1170.
- (71) Lee, D.; Lippard, S. J. *J. Am. Chem. Soc.* **2001**, *123*, 4611-4612.
- (72) Lee, D.; Hung, P.-L.; Spingler, B.; Lippard, S. J., submitted for publication.
- (73) Snyder, B. S.; Patterson, G. S.; Abrahamson, A. J.; Holm, R. H. *J. Am. Chem. Soc.* **1989**, *111*, 5214-5223.
- (74) Payne, S. C.; Hagen, K. S. *J. Am. Chem. Soc.* **2000**, *122*, 6399-6410.
- (75) $\text{Fc}/\text{Fc}^+ = 0.46 \text{ V vs SCE}$; $\text{Fc}/\text{Fc}^+ = 0.40 \text{ V vs NHE}$.⁶³
- (76) Lee, D.; Lippard, S. J., submitted for publication.
- (77) Bossek, U.; Hummel, H.; Weyhermüller, T.; Bill, E.; Wieghardt, K. *Angew. Chem., Int. Ed. Engl.* **1995**, *34*, 2642-2645.
- (78) Cohen, J. D.; Payne, S.; Hagen, K. S.; Sanders-Loehr, J. *J. Am. Chem. Soc.* **1997**, *119*, 2960-2961.
- (79) Bertini, I.; Gray, H. B.; Lippard, S. J.; Valentine, J. S. *Bioinorganic Chemistry*; University Science Books: Mill Valley, CA, 1994.
- (80) Kim, C.; Dong, Y.; Que, L., Jr. *J. Am. Chem. Soc.* **1997**, *119*, 3635-3636.

- (81) Gorun, S. M.; Lippard, S. J. *Inorg. Chem.* **1991**, *30*, 1625-1630.
- (82) Miller, M. A.; Gobena, F. T.; Kauffmann, K.; Münck, E.; Que, L., Jr.; Stankovich, M. T. *J. Am. Chem. Soc.* **1999**, *121*, 1096-1097.
- (83) (a) Ormö, M.; deMaré, F.; Regnström, K.; Åberg, A.; Sahlin, M.; Ling, J.; Loehr, T. M.; Sanders-Loehr, J.; Sjöberg, B.-M. *J. Biol. Chem.* **1992**, *267*, 8711-8714. (b) Åberg, A.; Ormö, M.; Nordlund, P.; Sjöberg, B.-M. *Biochemistry* **1993**, *32*, 9845-9850. (c) Ormö, M.; Regnström, K.; Wang, Z.; Que, L., Jr.; Sahlin, M.; Sjöberg, B.-M. *J. Biol. Chem.* **1995**, *270*, 6570-6576. (d) Baldwin, J.; Voegtli, W. C.; Khidekel, N.; Moënné-Loccoz, P.; Krebs, C.; Pereira, A. S.; Ley, B. A.; Huynh, B. H.; Loehr, T. M.; Riggs-Gelasco, P. J.; Rosenzweig, A. C.; Bollinger, J. M., Jr. *J. Am. Chem. Soc.* **2001**, *ASAP*.
- (84) (a) Tolman, W. B. *Acc. Chem. Res.* **1997**, *30*, 227-237. (b) Liang, H.-C.; Dahan, M.; Karlin, K. D. *Curr. Opin. Chem. Biol.* **1999**, *3*, 168-175. (c) Mahadevan, V.; Klein Gebbink, R. J. M.; Stack, T. D. P. *Curr. Opin. Chem. Biol.* **2000**, *4*, 228-234.
- (85) Cole, A. P.; Root, D. E.; Mukherjee, P.; Solomon, E. I.; Stack, T. D. P. *Science* **1996**, *273*, 1848-1850.

Table 3.1. Summary of X-ray Crystallographic Data

	1c·3CH₂Cl₂	2c·3.5CH₂Cl₂·0.5C₆H₁₂
formula	Fe ₂ C ₉₇ H ₈₀ N ₂ O ₁₀ Cl ₆	Fe ₂ C _{109.5} H ₉₆ N ₂ O ₁₀ Cl ₇
fw	1758.03	1945.55
space group	<i>P</i> $\bar{1}$	<i>P</i> $\bar{1}$
<i>a</i> , Å	13.7957(2)	14.7583(8)
<i>b</i> , Å	15.4489(2)	14.9097(8)
<i>c</i> , Å	22.27310(10)	24.8019(14)
α , deg	91.8950(10)	91.9500(10)
β , deg	102.2890(10)	93.9610(10)
γ , deg	103.7510(10)	110.9620(10)
<i>V</i> , Å ³	4487.78(9)	5074.0(5)
<i>Z</i>	2	2
ρ_{calc} , g/cm ³	1.301	1.273
<i>T</i> , °C	-85	-85
μ (Mo K α), mm ⁻¹	0.561	0.518
θ limits, deg	1.36 – 28.20	1.47 – 28.29
total no. of data	26809	32216
no. of unique data	18901	22510
no. of params	1102	1203
<i>R</i> (%) ^{<i>a</i>}	6.32	6.64
<i>wR</i> ² (%) ^{<i>b</i>}	17.05	17.55
max, min peaks, e/Å ³	0.915, -1.050	0.926, -0.914

^{*a*} $R = \Sigma ||F_o| - |F_c|| / \Sigma |F_o|$. ^{*b*} $wR^2 = \{\Sigma[w(F_o^2 - F_c^2)^2] / \Sigma[w(F_o^2)^2]\}^{1/2}$.

Table 3.2. Spectroscopic Properties of Peroxo Diiron(III) Enzyme Intermediates and Their Synthetic Analogs

	λ_{\max} (nm)	ϵ ($M^{-1}cm^{-1}$)	ν_{O-O} (cm^{-1})	ref
MMOH (<i>M. capsulatus</i>) ^a	725	1800		27
	420	4000		
MMOH (<i>M. trichosporium</i> OB3b) ^b	700	2500		28
RNR-R2 D84E mutant	700	1500	890	29
$\Delta 9D$	700	1100–1200	898	30
	350	1100		
$[Fe_2(\mu-O_2)(\mu-O_2CCH_2Ph)_2(HB(pz')_3)_2]^{37}$	694	2650	888	16b
$[Fe_2(\mu-O_2)(\mu-O_2CPh)(N-Et-HPTB)]^{2+ 37}$	588	1500	900	17
$[Fe_2(\mu-O_2)(\mu-O_2CPh)(Ph-bimp)]^{2+ 37}$	500–800	1700		18
$[Fe_2(\mu-O_2)(\mu-O)(6-Me_3-TPA)_2]^{2+ 37}$	494	1100	848	19
	648	1200		
	846	230		
$[Fe_2(\mu-O_2)(\mu-BXDK)(O_2CPhCy)_2(py)_2]^{37}$	580	1500	864	20
$[Fe_2(\mu-O_2CAR^{Mes})_2(O_2CAR^{Mes})_2(MeCN)_2]^{37} + O_2$	540	2300	885	21

^a *Methylococcus capsulatus* (Bath). ^b *Methylosinus trichosporium* OB3b.

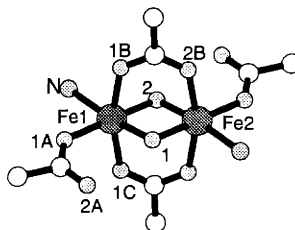
Table 3.3. Mössbauer Parameters of the Fe(III)Fe(IV) Component in **2b** and Related Valence-Trapped Fe(III)Fe(IV) Centers Having $S = 1/2$ Ground State.

		δ (mm/s)	ΔE_Q (mm/s)	η	A_{xx} (MHz)	A_{yy} (MHz)	A_{zz} (MHz)	ref
2b	Fe(III)	0.56	0.9	-0.3	-75	-70.5	-75	this work
	Fe(IV)	0.19	0.8	-1	26	37.5	23.8	
RNR-R2 X	Fe(III)	0.56	-0.9	0.5	-74.2	-72.2	-73.2	11a,c
	Fe(IV)	0.26	-0.6	2.7	27.5	36.8	36.8	
MMOH-Q _x	Fe(III)	0.48	-0.9	0.2	-70	-75	-75	51
	Fe(IV)	0.14	-0.6	0.9	26	30	32	
[Fe ₂ (μ -O) ₂ (6-Me-TPA) ₂] ³⁺ ³⁷	Fe(III)	0.48	1.6	1.0	-64.5	-64.5	-64.5	32b
	Fe(IV)	0.08	0.5	1.0	20	36.5	36.5	

Table 3.4. Mössbauer Parameters of the Fe(II)Fe(III) Component in **2b**, $[\text{Fe}_2(\mu\text{-O}_2\text{CAr}^{\text{Tot}})_4(4\text{-}^t\text{BuC}_5\text{H}_4\text{N})_2]^+$, and Related Valence-Delocalized Fe(II)Fe(III) Centers Having $S = 9/2$ Ground State.

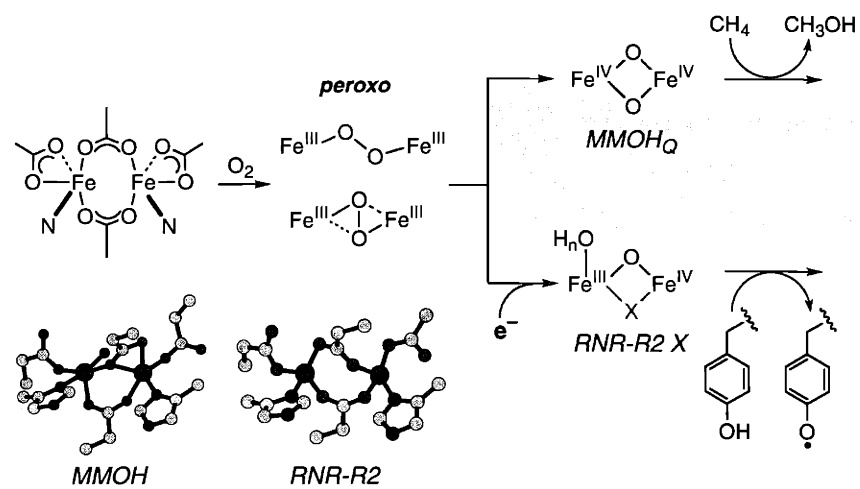
	δ (mm/s)	ΔE_Q (mm/s)	η	A_{xx} (MHz)	A_{yy} (MHz)	A_{zz} (MHz)	ref
$[\text{Fe}_2(\mu\text{-O}_2\text{CAr}^{\text{Tot}})_4(4\text{-}^t\text{BuC}_5\text{H}_4\text{N})_2]^+$	0.65	-0.63	0	-15.2	-15.8	-20.7	this work
$[\text{Fe}_2(\mu\text{-OH})_3(\text{Me}_3\text{TACN})_2]^{2+}$ ³⁷	0.74	-2.14	0	-14.5	-14.5	-18.5	56
$[\text{PhB}\{\text{Fe}_2(\mu\text{-dfmp})_3\}\text{BPh}]$ ³⁷	0.82	-1.86	0	-14.8	-14.8	-17.0	59
$[\text{L}^1\text{Fe}_2(\mu\text{-OAc})_2]^+$ ³⁷	0.84	2.09	0.1	a	a	a	57
$[\text{Fe}_2(\mu\text{-O}^i\text{Pr})_2(\mu\text{-O}_2\text{CAr}^{\text{Mes}})(\text{O}_2\text{CAr}^{\text{Mes}})_2]$ ³⁷	0.76	2.0	0.7	a	a	a	58

^a Only the internal fields, 43.5 T for ref 57 and 41.0 T for ref 58, along the magnetic uniaxis have been reported.

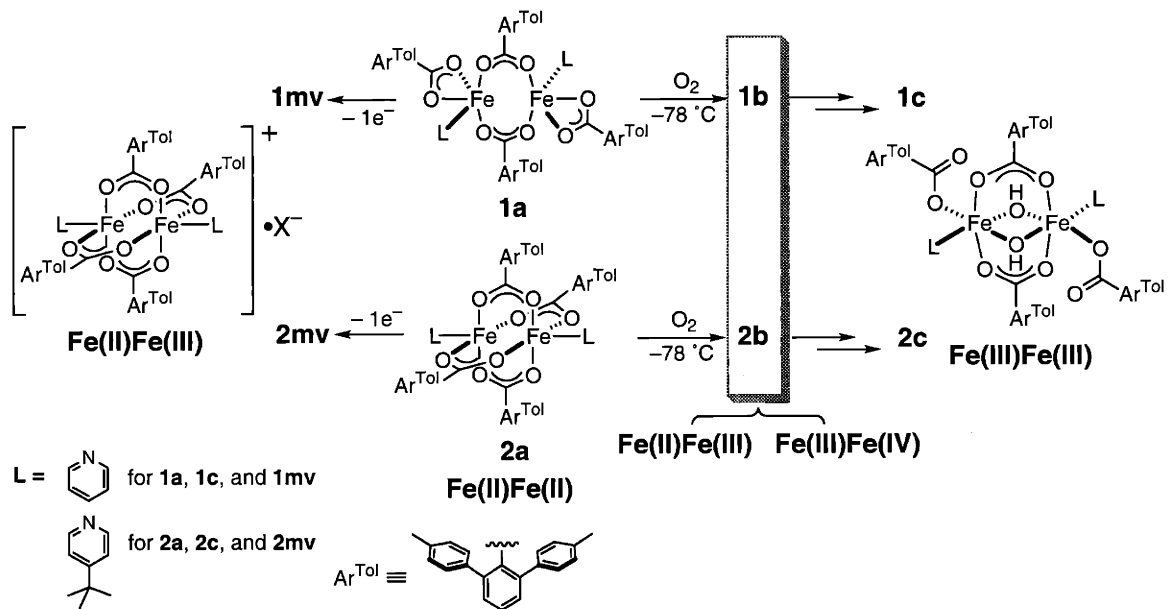
Table 3.5. Selected Bond Lengths (Å) and Angles (deg) for **1c** and **2c**.^a

	1c		2c	
	molecule 1	molecule 2	molecule 1	molecule 2
Fe1...Fe2	2.8843(9)	2.8473(8)	2.8432(8)	2.8322(8)
Fe1–O1	1.986(2)	1.976(2)	1.949(3)	1.955(2)
Fe1–O2	2.012(2)	1.969(3)	1.957(3)	1.955(2)
Fe1–O1A	1.970(2)	1.964(2)	1.966(2)	1.965(2)
Fe1–O1B	2.076(2)	2.096(2)	2.082(2)	2.081(2)
Fe1–O1C	2.040(2)	2.060(2)	2.055(2)	2.048(2)
Fe1–N	2.148(3)	2.144(3)	2.136(3)	2.127(3)
O1...O2A	2.888(3)	2.773(4)	2.725(4)	2.736(4)
Fe1–O1–Fe2	92.34(10)	92.38(11)	93.42(12)	92.82(11)
O1–Fe1–O2	87.66(10)	87.62(11)	86.58(12)	87.18(11)

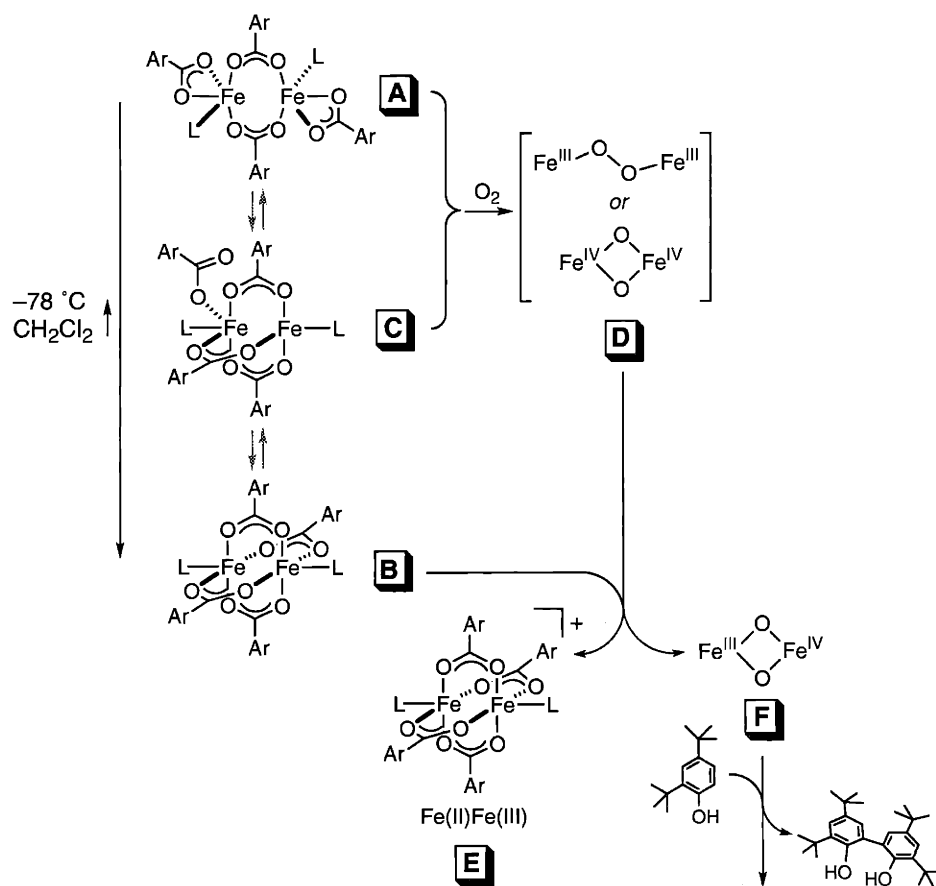
^a Numbers in parentheses are estimated standard deviations of the last significant figures.



Scheme 3.1



Scheme 3.2.



Scheme 3.3.

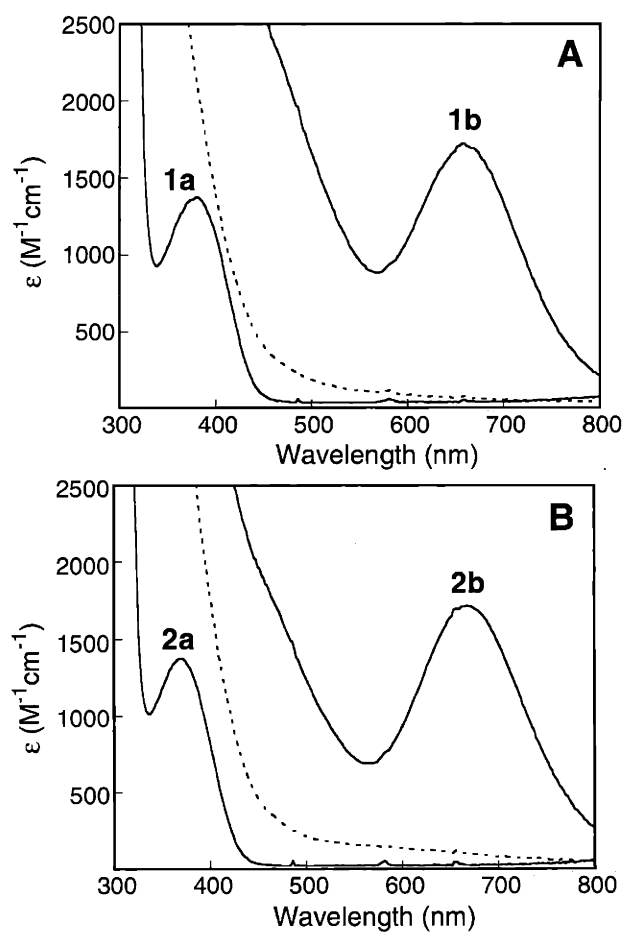


Figure 3.1. Electronic absorption spectra for the formation of dioxygen adducts of diiron(II) complexes in CH_2Cl_2 at -78°C and their thermal decay products (.....): (A) $[\text{Fe}_2(\mu\text{-O}_2\text{CAr}^{\text{Tol}})_2(\text{O}_2\text{CAr}^{\text{Tol}})_2(\text{C}_5\text{H}_5\text{N})_2]$ (**1a**); (B) $[\text{Fe}_2(\mu\text{-O}_2\text{CAr}^{\text{Tol}})_4(4\text{-}^t\text{BuC}_5\text{H}_4\text{N})_2]$ (**2a**).

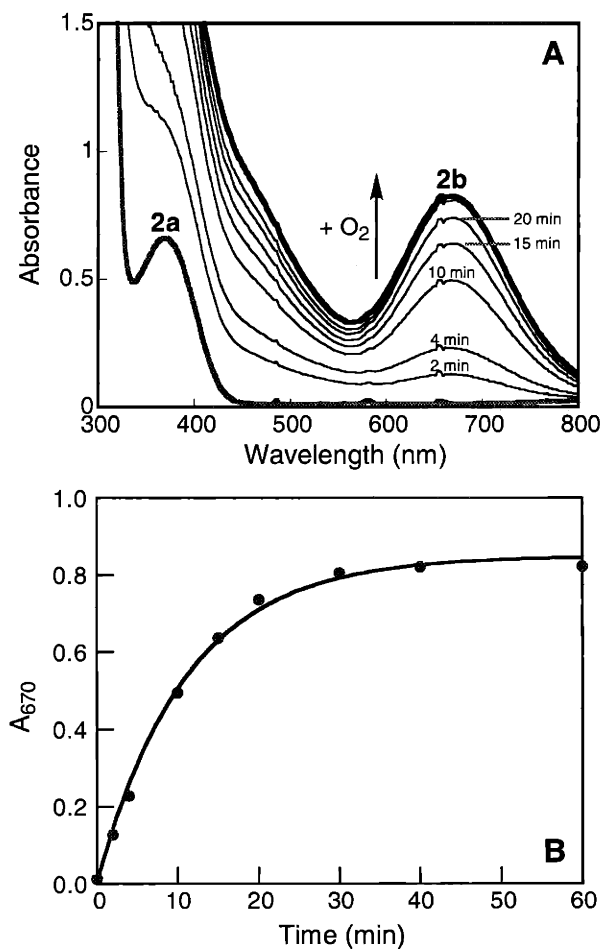


Figure 3.2. Kinetic data for the reaction of $[\text{Fe}_2(\mu\text{-O}_2\text{CAr}^{\text{Tol}})_4(4\text{-}^t\text{BuC}_5\text{H}_4\text{N})_2]$ (**2a**) with O_2 in CH_2Cl_2 at $-78\text{ }^\circ\text{C}$: (A) UV-vis traces for the development of **2b**; (B) plot of A_{670} versus time and a fit to a first-order exponential buildup ($t_{1/2} = 7.7\text{ min}$).

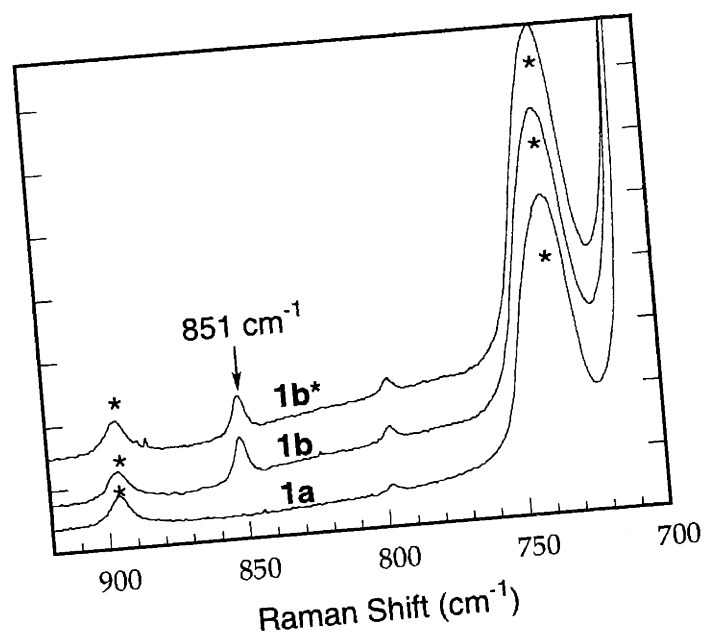


Figure 3.3. Resonance Raman spectra of fluid solutions of $[\text{Fe}_2(\mu\text{-O}_2\text{CAr}^{\text{Tol}})_2(\text{O}_2\text{CAr}^{\text{Tol}})_2(\text{C}_5\text{H}_5\text{N})_2]$ (**1a**), $[\text{Fe}_2(\mu\text{-O}_2\text{CAr}^{\text{Tol}})_2(\text{O}_2\text{CAr}^{\text{Tol}})_2(\text{C}_5\text{H}_5\text{N})_2] + {}^{16}\text{O}_2$ (**1b**), and $[\text{Fe}_2(\mu\text{-O}_2\text{CAr}^{\text{Tol}})_2(\text{O}_2\text{CAr}^{\text{Tol}})_2(\text{C}_5\text{H}_5\text{N})_2] + {}^{18}\text{O}_2$ (**1b***) in CH_2Cl_2 at -78°C ; excitation wavelength = 647.1 nm. Solvent features are labeled with asterisk.

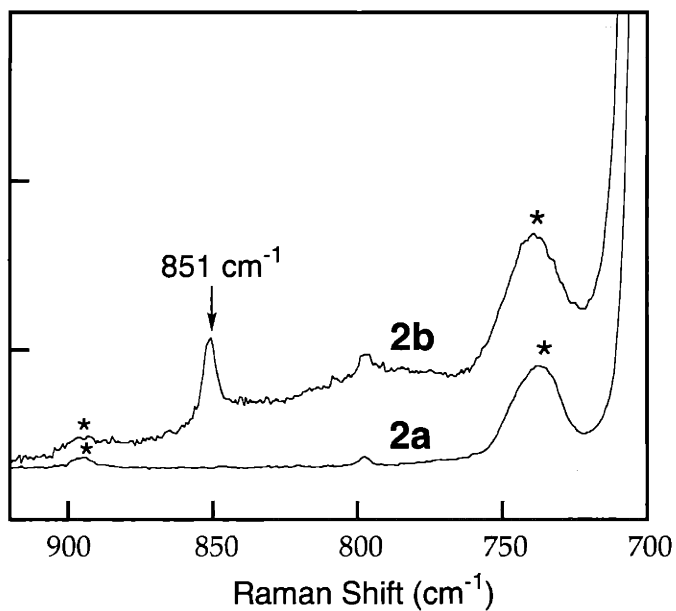


Figure 3.4. Resonance Raman spectra of fluid solutions of $[\text{Fe}_2(\mu\text{-O}_2\text{CAr}^{\text{Tol}})_4(4\text{-}^t\text{BuC}_5\text{H}_4\text{N})_2]$ (**2a**) and $[\text{Fe}_2(\mu\text{-O}_2\text{CAr}^{\text{Tol}})_4(4\text{-}^t\text{BuC}_5\text{H}_4\text{N})_2] + {}^{16}\text{O}_2$ (**2b**) in CH_2Cl_2 at $-78\text{ }^\circ\text{C}$; excitation wavelength = 647.1 nm. Solvent features are labeled with asterisk.

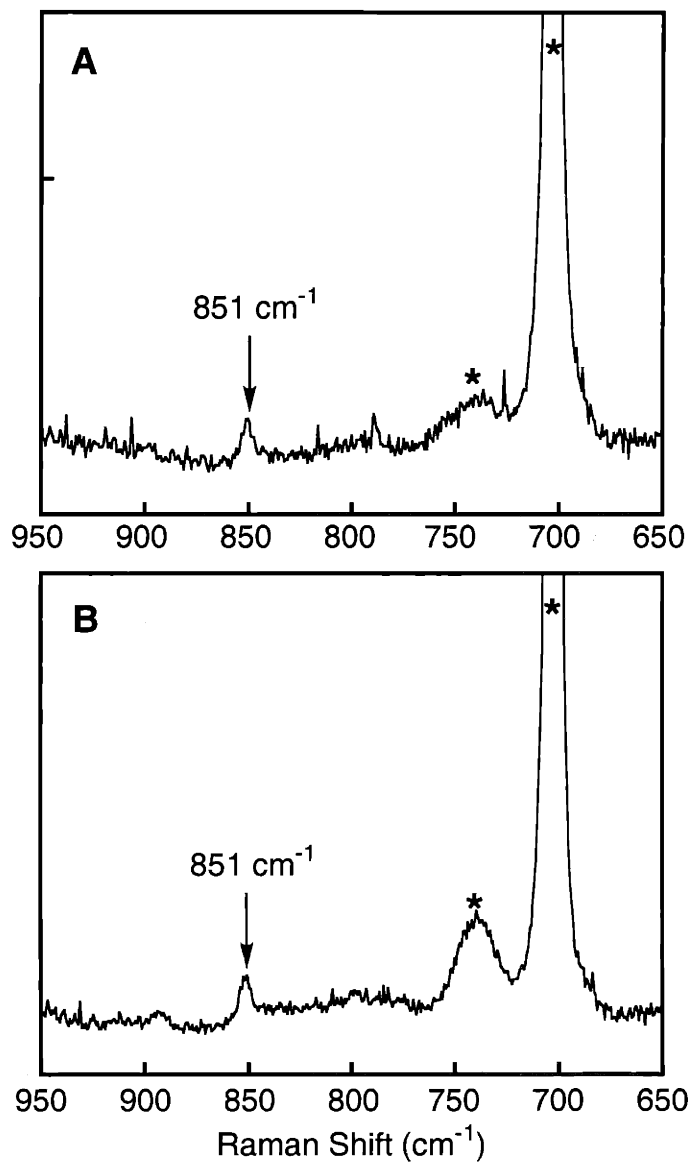


Figure 3.5. Resonance Raman spectra of fluid solutions of $[\text{Fe}_2(\mu\text{-O}_2\text{CAr}^{\text{Tol}})_4\text{-(C}_5\text{H}_5\text{N)}_2](\text{OTf})$ (**1mv**) (A) and $[\text{Fe}_2(\mu\text{-O}_2\text{CAr}^{\text{Tol}})_4(4\text{-}^t\text{BuC}_5\text{H}_4\text{N)}_2](\text{PF}_6)$ (**2mv**) (B) in CH_2Cl_2 at $-78\text{ }^\circ\text{C}$; excitation wavelength = 647.1 nm. Solvent features are labeled with asterisk.

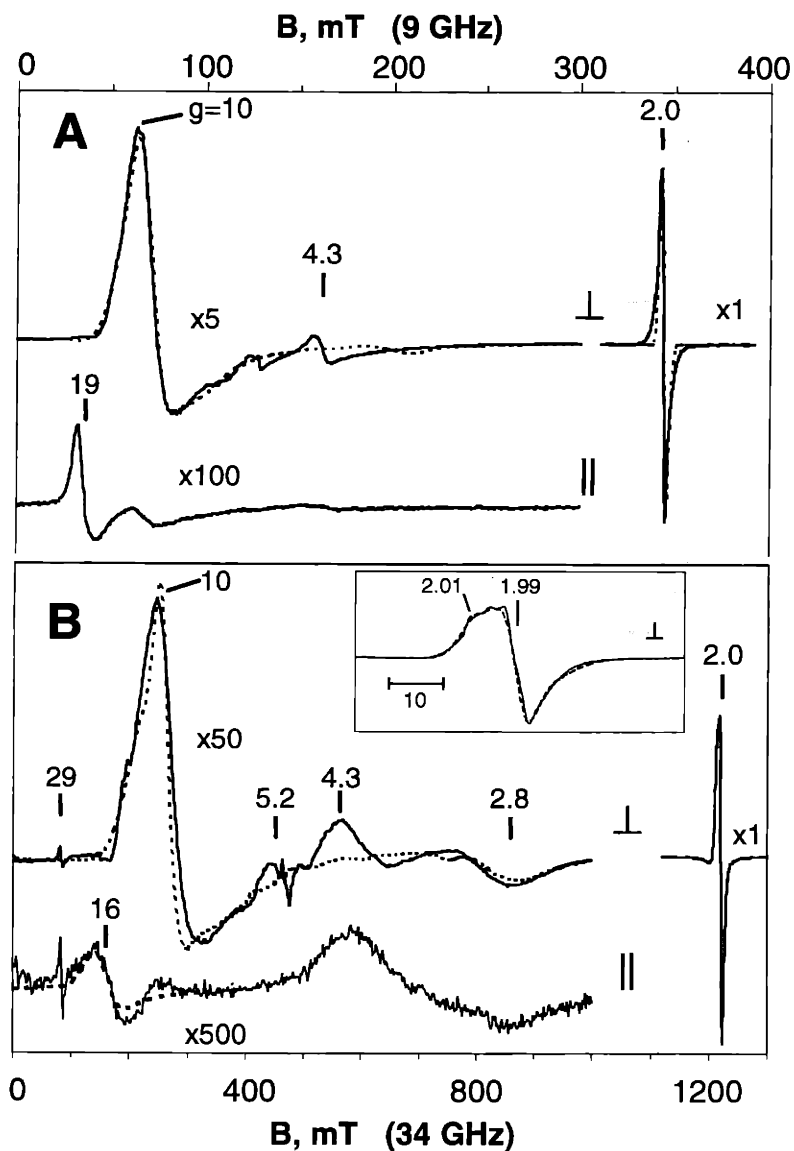


Figure 3.6. X-band (A, 9.4 GHz) and Q-band (B, 34.1 GHz) EPR spectra of a frozen CH_2Cl_2 solution of **2b** for microwave fields parallel and perpendicular to the static field. Dashed lines are quantitative simulations for the $S=1/2$ and $S=9/2$ species discussed in the text. The inset is a magnified view of the Q-band $g=2$ signal. Sample temperatures are <12 K and relative signal gains are shown on the figure.

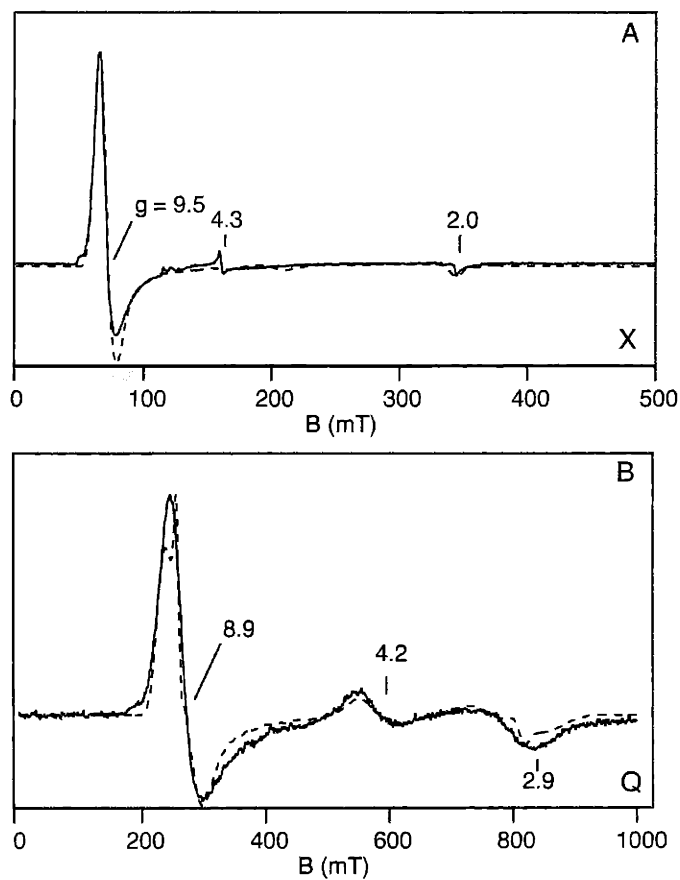


Figure 3.7. X-band (A) and Q-band (B) EPR spectra (solid lines) of a frozen CH_2Cl_2 solution sample of 2mv measured at 11 K and 6 K, respectively. Simulations (dashed lines) are calculated for $g = 2.0261$; $D = 1.13 \text{ cm}^{-1}$; $\sigma_D = 0.03 \text{ cm}^{-1}$; $E/D = 0.007$; $\sigma_{E/D} = 0.004$. EPR conditions: frequency, 9.62 GHz (X-band) and 34.2 GHz (Q-band); microwave power, 0.2 mW (X-band) and 0.02 mW (Q-band).

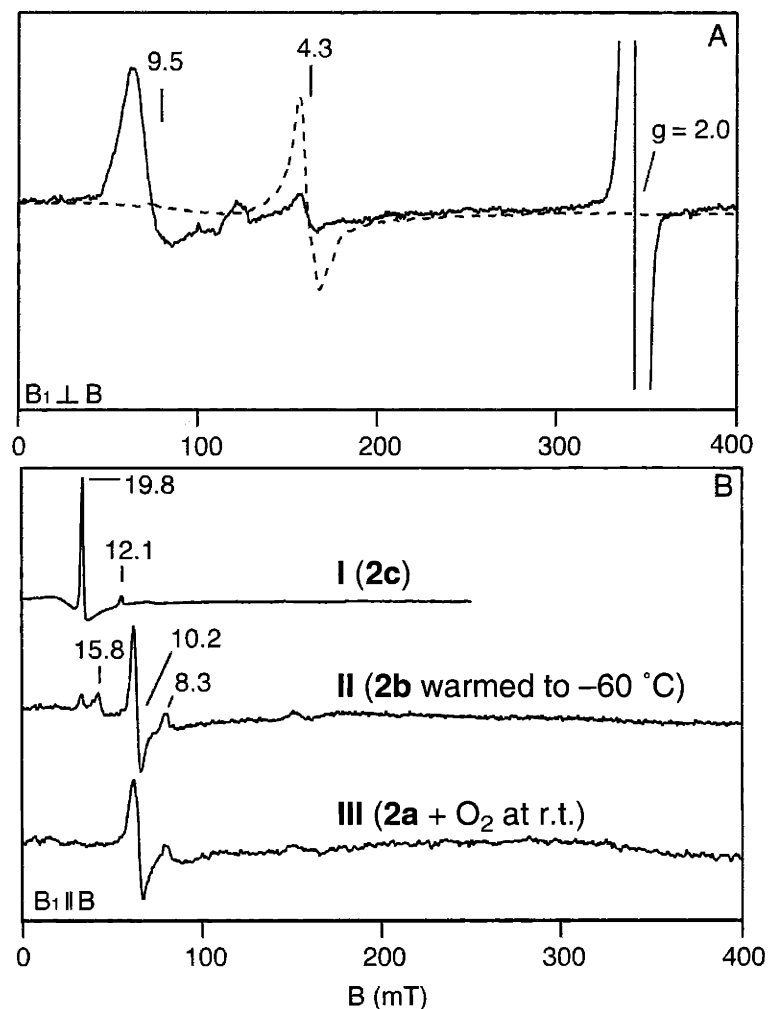


Figure 3.8. (A) Perpendicular mode ($B_1 \perp B$) X-band (9.62 GHz, 10 K) EPR spectra of a frozen CH_2Cl_2 solution sample of **2b** (solid line) and its thermolysis product (dashed line) prepared by thawing **2b** for 1 hour under a He atmosphere at -60°C and re-freezing. (B) Parallel mode ($B_1 \parallel B$) X-band (9.26 GHz) EPR spectra of **2c** (I), thermolysis product of **2b** (II), and a sample prepared by exposing a CH_2Cl_2 solution of **2a** to dioxygen at room temperature and freezing (III). Spectra I and III were measured at 10 K, II at 18 K.

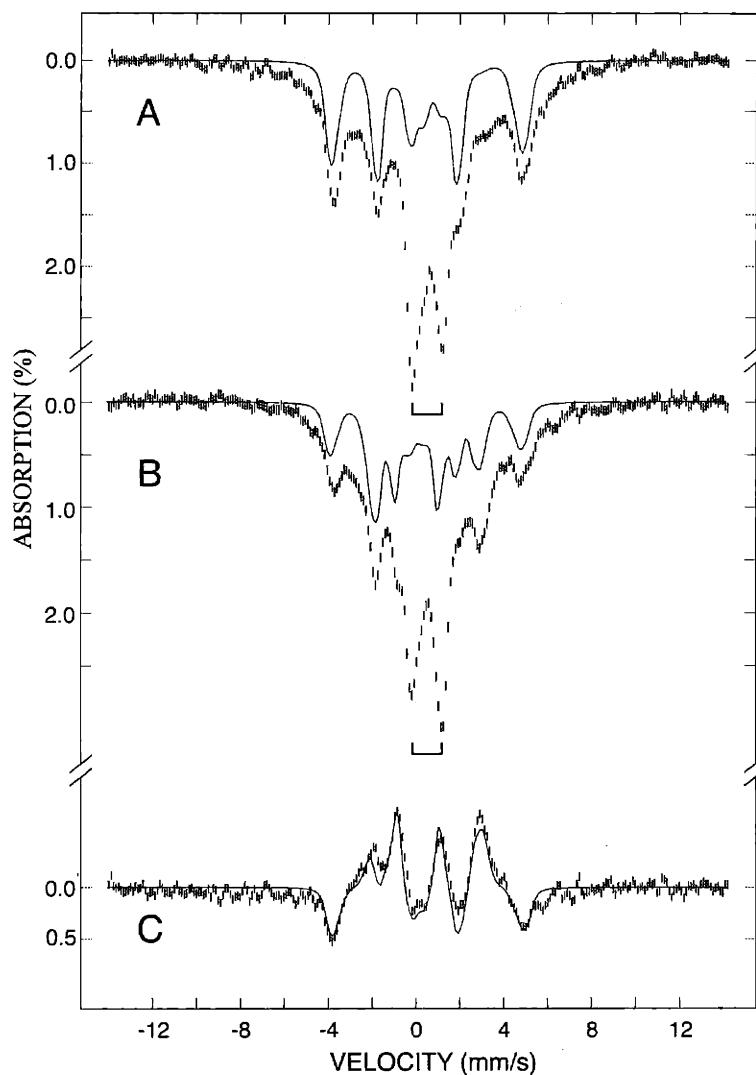


Figure 3.9. Mössbauer spectra of the solid powder sample of **2b** recorded at 4.2 K with a 50-mT magnetic field applied parallel (A) and perpendicular (B) to the γ -rays. Spectrum C is a difference spectrum of the spectra shown in A and B. The solid lines are theoretical simulations of the $S = 1/2$ species using the parameters: $\delta = 0.55$ mm/s, $\Delta E_Q = 1.1$ mm/s, $\eta = 1.0$, $A_{xx} = -71.9$ MHz, $A_{yy} = -71.1$ MHz, and $A_{zz} = -72.7$ MHz for site 1; $\delta = 0.12$ mm/s, $\Delta E_Q = 0.6$ mm/s, $\eta = -1.0$, $A_{xx} = 31.5$ MHz, $A_{yy} = 27.4$ MHz, and $A_{zz} = 31.5$ MHz for site 2. The theoretical spectra are normalized to 36% of the total iron absorption.

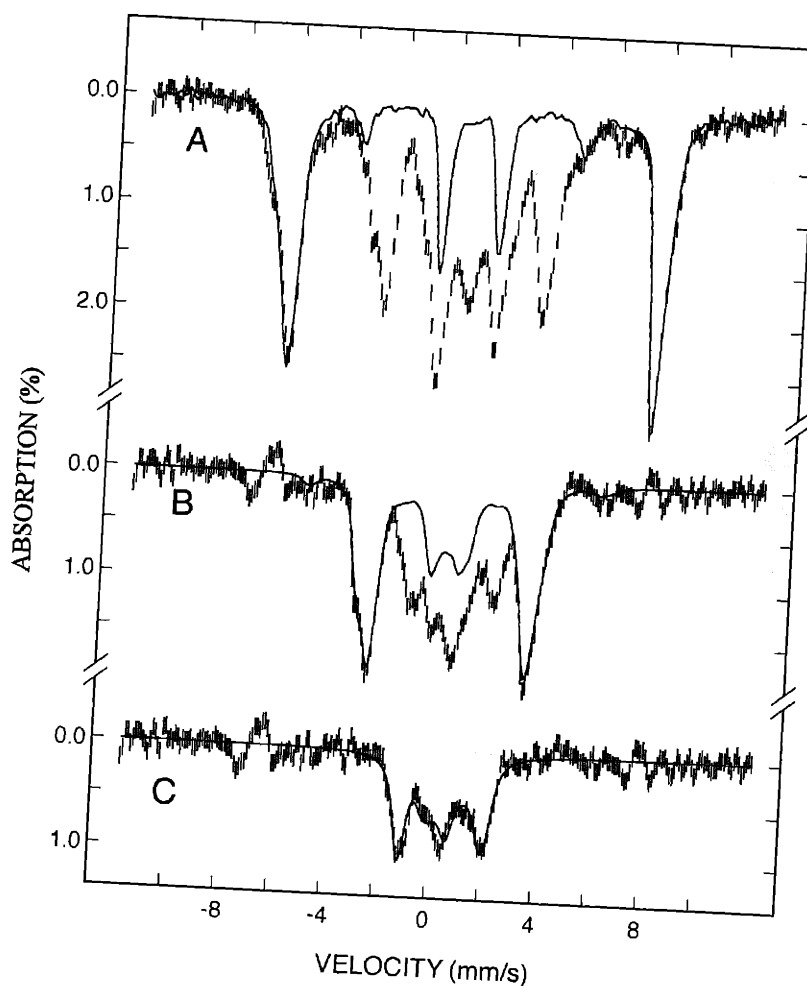


Figure 3.10. Deconvolution of the Mössbauer spectrum of the solid powder sample of **2b** recorded at 4.2 K in an applied field of 8 T. (A) Raw data of **2b** (hash marks) and the spectrum of a solid sample of $[\text{Fe}_2(\mu\text{-O}_2\text{CAr}^{\text{Tol}})_4(4\text{-}^t\text{BuC}_5\text{H}_4\text{N})_2](\text{PF}_6)$ (**2mv**) (solid line) scaled to 45% of the absorption intensity of the hash-marked spectrum. (B) The hash-marked spectrum is generated by subtracting the solid-line spectrum of A from the hash-marked spectrum of A. The solid line is a theoretical simulation of the Fe(III)Fe(IV) species using parameters from Table 3.3 and corresponds to 36% of the total iron absorption. (C) The hash-marked spectrum is generated by subtracting the solid-line spectrum of B from the hash-marked spectrum of B. The solid line is a theoretical simulation using $\delta = 0.54$ mm/s, $\Delta E_Q = 1.05$ mm/s, $\eta = 0.4$, and line-width = 0.55 mm/s, and assuming diamagnetism.

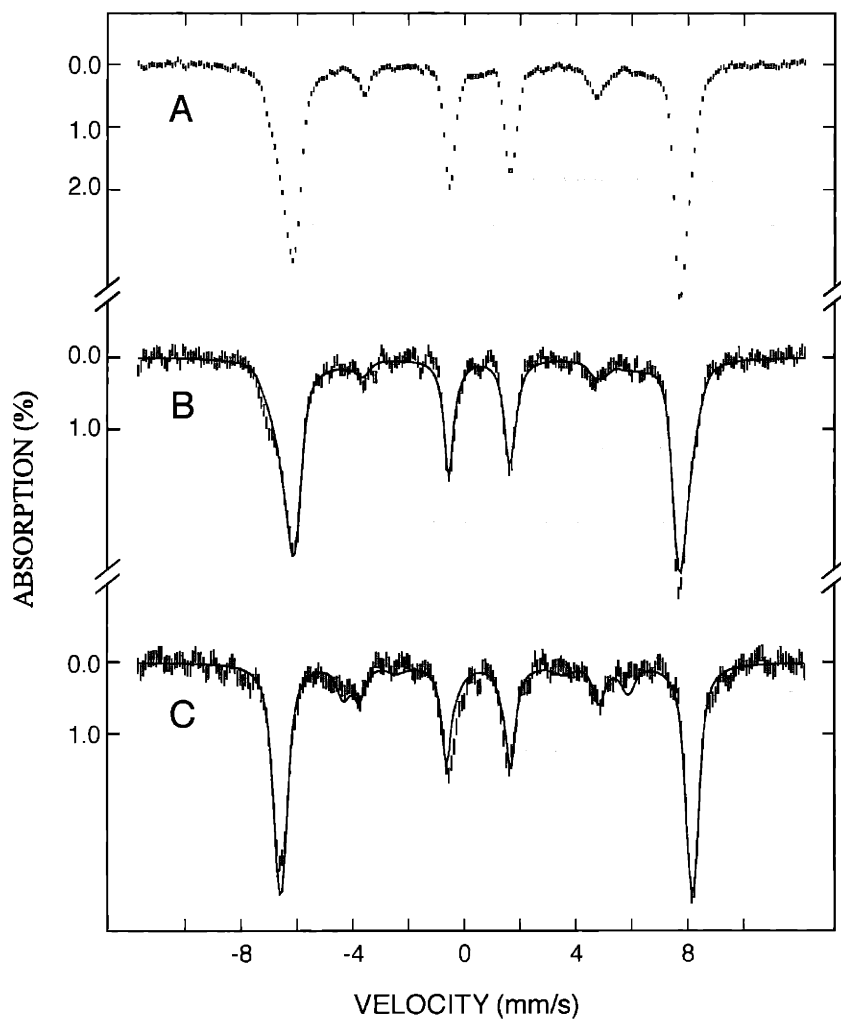


Figure 3.11. 4.2-K Mössbauer spectra of $[\text{Fe}_2(\mu\text{-O}_2\text{CAr}^{\text{Tol}})_4(4\text{-}^t\text{BuC}_5\text{H}_4\text{N})_2](\text{PF}_6)$ (**2mv**) in the form of solid (A) and the Fe(II)Fe(III) component in **2b** (B, C). The spectra in A and B are recorded in a parallel applied field of 8 T, and the spectrum in C is recorded in 4 T. The spectra in (B) and (C) were prepared by removing the contributions of the Fe(III)Fe(IV) (36%) and the diferric species (19%) from the raw data using theoretical spectra of Fe(III)Fe(IV) and the diiron(III) species simulated with parameters listed in Table 3.3 and quoted in the caption of Figure 3.10.

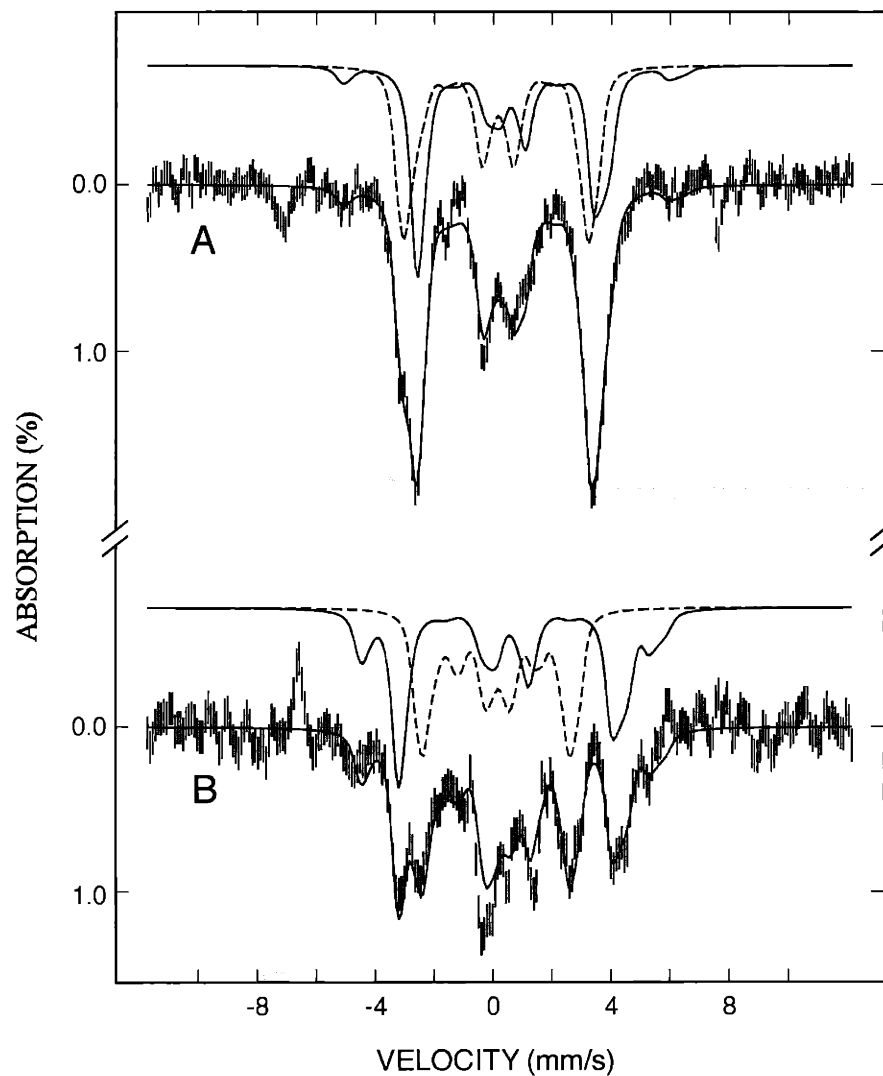


Figure 3.12. 4.2 K Mössbauer spectra of the Fe(III)Fe(IV) component in the solid powder sample of **2b** in applied fields of 4 T (A) and 8 T (B). The hash-marked spectra were prepared by removing the contributions of Fe(II)Fe(III) (45%) and the diiron(III) cluster (19%) from the raw data using theoretical spectra simulated with parameters listed in Table 3.4 and quoted in the caption of Figure 3.10. The solid lines overlaid with the experimental data are theoretical simulations of Fe(III)Fe(IV) using parameters listed in Table 3.3. The spectra of the Fe(III) and Fe(IV) sites are plotted above the experimental data as solid and dashed lines, respectively.

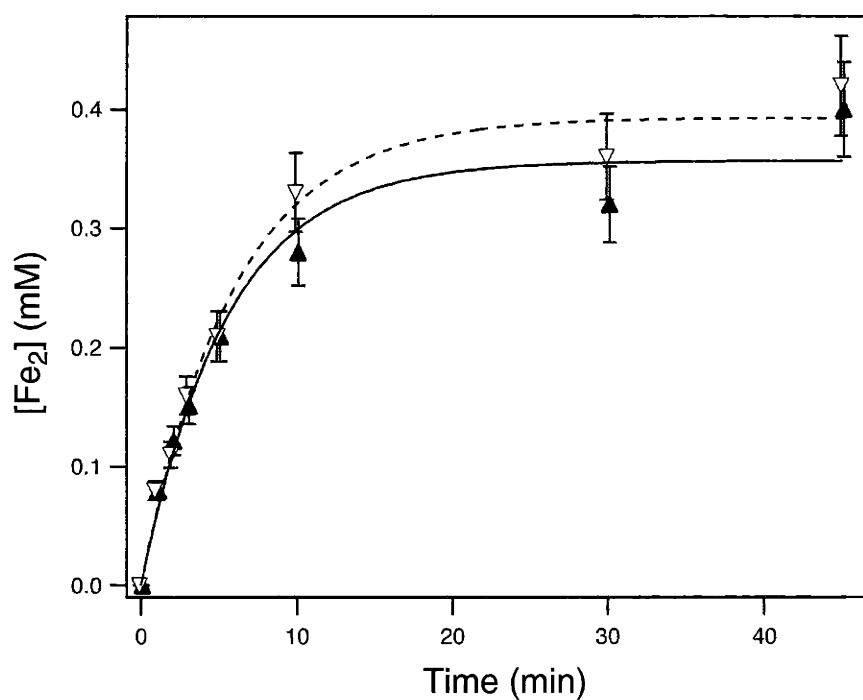


Figure 3.13. Time-dependent development of the $S = 1/2$ (∇) and $S = 9/2$ (\blacktriangle) components in **2b** as determined by X-band EPR spectra of freeze-quenched samples prepared by oxygenating **2a** (1.12 mM) in CH_2Cl_2 at -78°C . Fits to experimental data for the $S = 1/2$ (dashed line) and $S = 9/2$ (solid line) species indicate $k_{\text{obs}} = 0.18 \pm 0.02 \text{ min}^{-1}$. Spin quantitation was carried out as described in the experimental section.

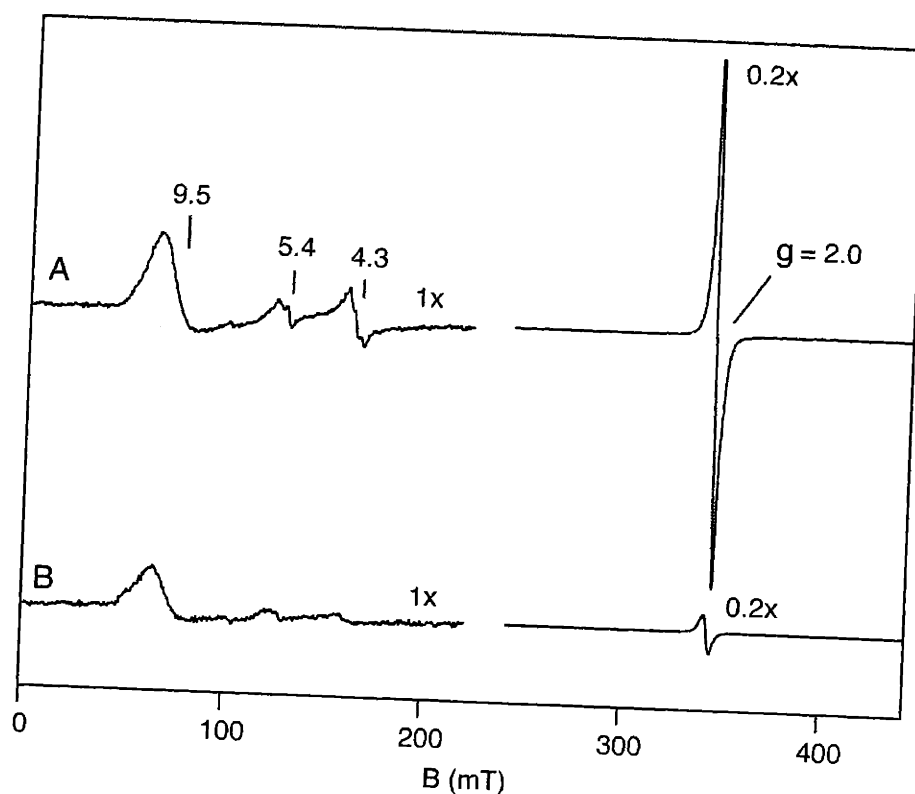


Figure 3.14. X-band EPR spectra of a frozen CH_2Cl_2 solution of **2b** obtained by quenching the reaction 5 min after exposing **2a** to dioxygen at -78°C , in the absence (A) and presence (B) of $[\text{H}(\text{OEt}_2)_2](\text{BAr}'_4)$ (0.5 equiv per Fe_2). The $S = 1/2$ and $S = 9/2$ species are observed at $g = 2.0$ and 9.5 , respectively. The signals at $g = 5.4$ and 4.3 are from contaminating species. EPR conditions: frequency, 9.62 GHz ; T , 12 K ; microwave power, 0.02 mW ; modulation amplitude, 1.0 mT .

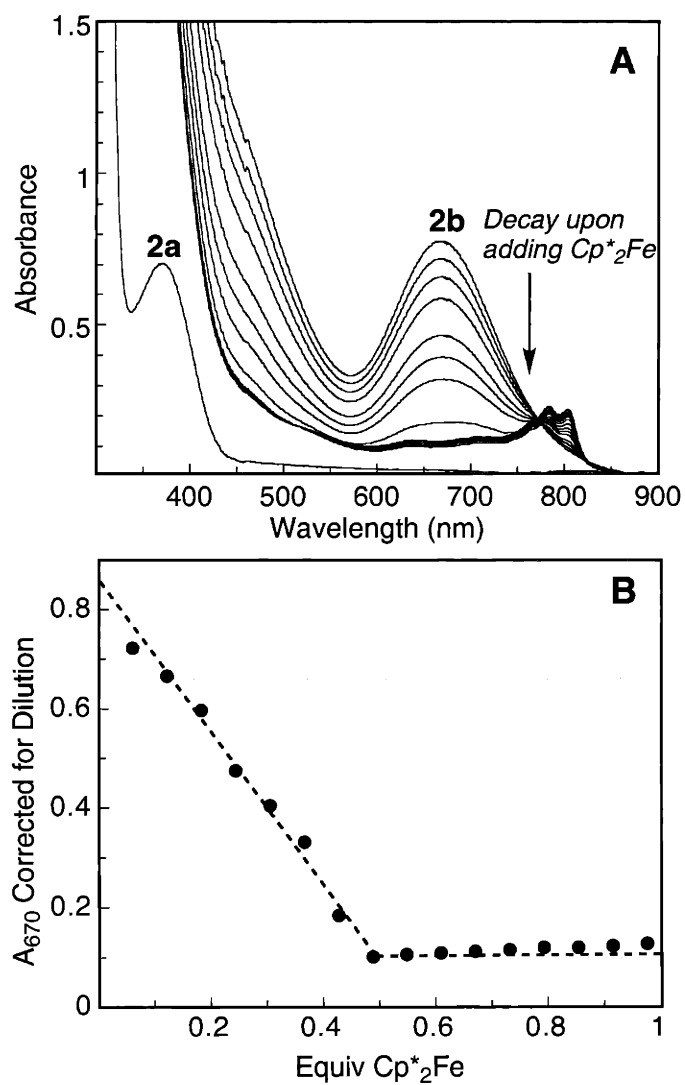


Figure 3.15. (A) Representative UV-vis spectra for the reaction of **2b** with Cp*₂Fe in CH₂Cl₂ at -78 °C. The spectral traces track the decay of the $\lambda_{\text{max}} = 670$ chromophore upon addition of Cp*₂Fe. (B) A plot of A₆₇₀ versus equiv (per **2a**) of Cp*₂Fe added. The values are corrected for dilution.

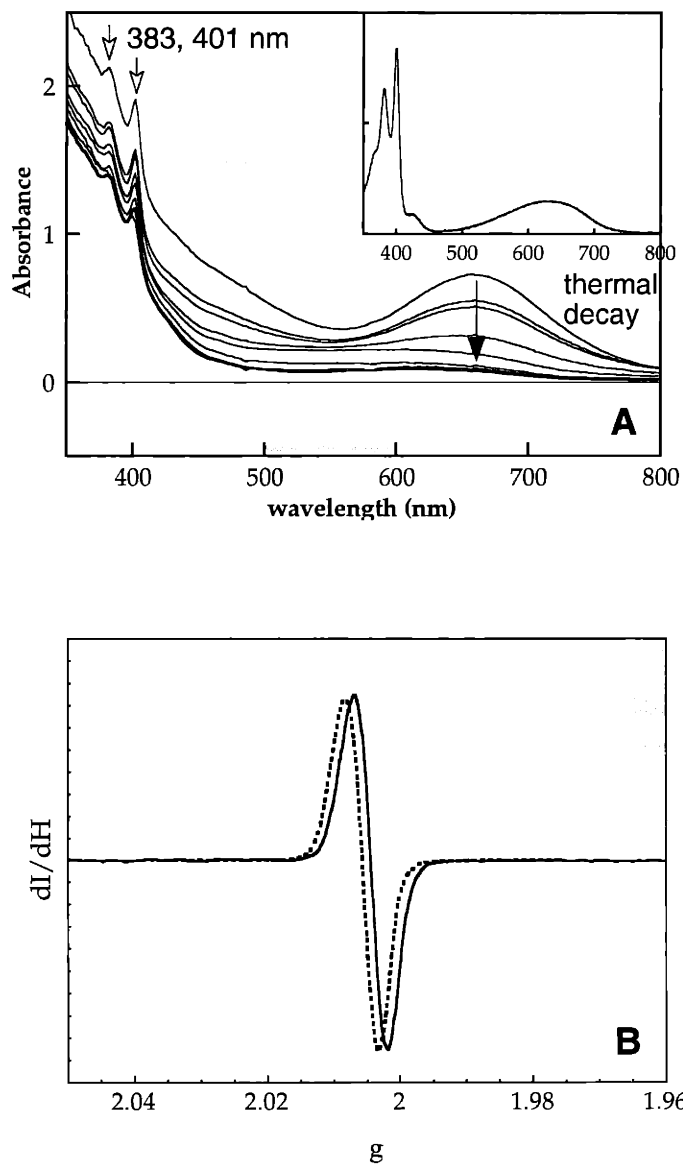


Figure 3.16. (A) Reaction of 2,4,6-tri-*tert*-butylphenol with **1b** in CH_2Cl_2 followed by UV/vis spectra from -78°C to room temperature (Inset : electronic absorption spectrum of 2,4,6-tri-*tert*-butylphenoxy radical in CH_2Cl_2 at room temperature). (B) EPR spectrum (—) of the reaction mixture of 2,4,6-tri-*tert*-butylphenol and **1b** at 77K in toluene/ CH_2Cl_2 ($g = 2.0045$), compared with that (.....) of 2,4,6-tri-*tert*-butylphenoxy radical under identical conditions ($g = 2.0057$).

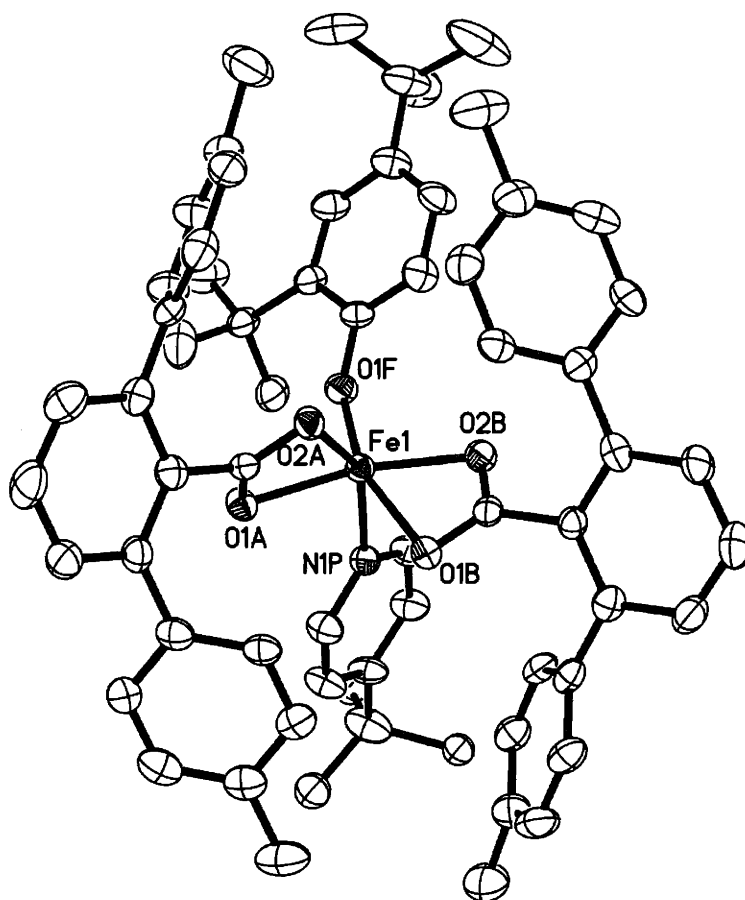


Figure 3.17. ORTEP diagram of $[\text{Fe}(\text{O}_2\text{CAr}^{\text{Tol}})_2(2,4\text{-}^t\text{Bu}_2\text{C}_6\text{H}_3\text{O})(4\text{-}^t\text{BuC}_5\text{H}_4\text{N})]$ with thermal ellipsoids at 50% probability.

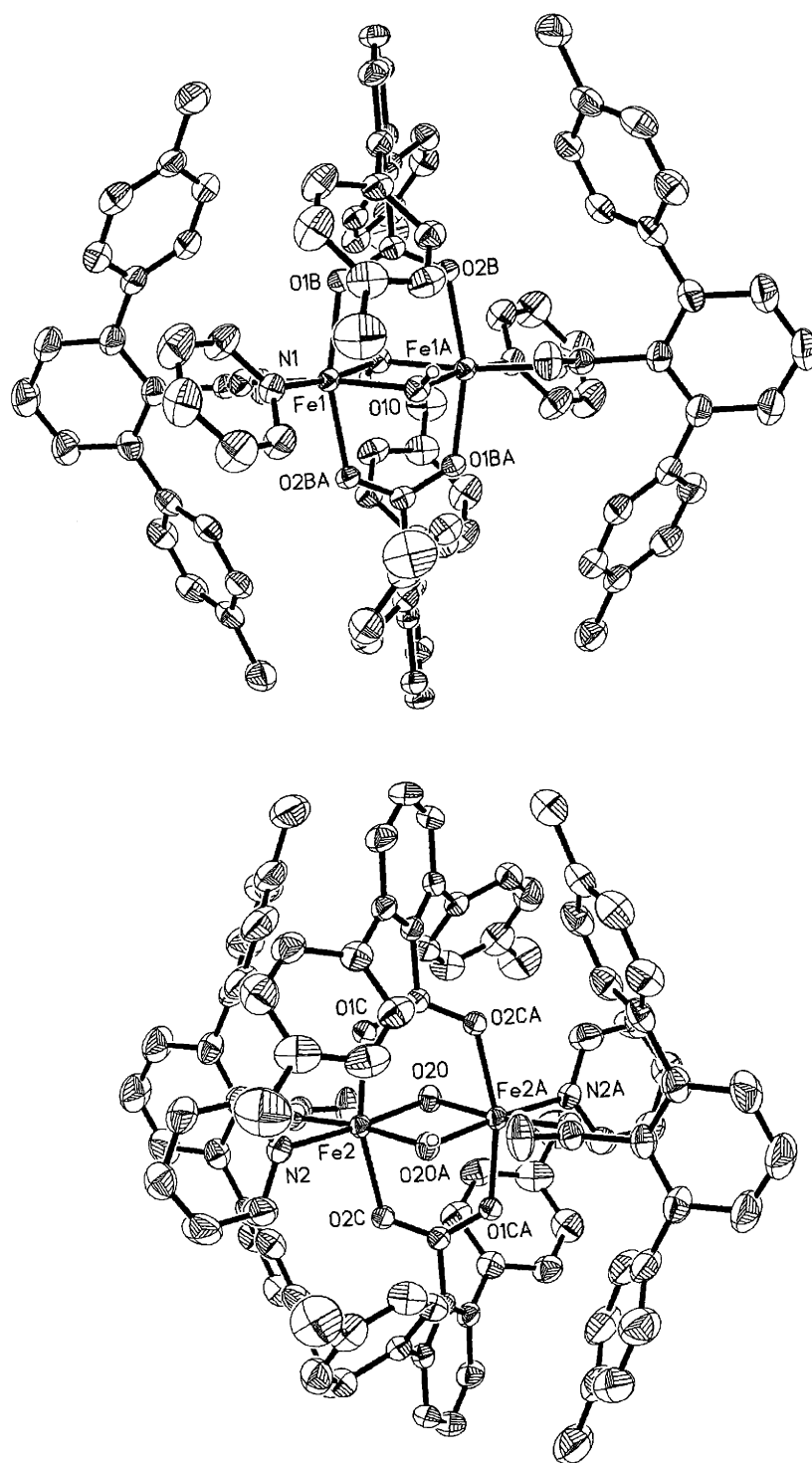


Figure 3.18. ORTEP diagram of $[\text{Fe}_2(\mu\text{-OH})_2(\mu\text{-O}_2\text{CAr}^{\text{Tol}})_2(\text{O}_2\text{CAr}^{\text{Tol}})_2(\text{C}_5\text{H}_5\text{N})_2]$ (**1c**) with thermal ellipsoids at 50% probability. Top, molecule 1; bottom, molecule 2.

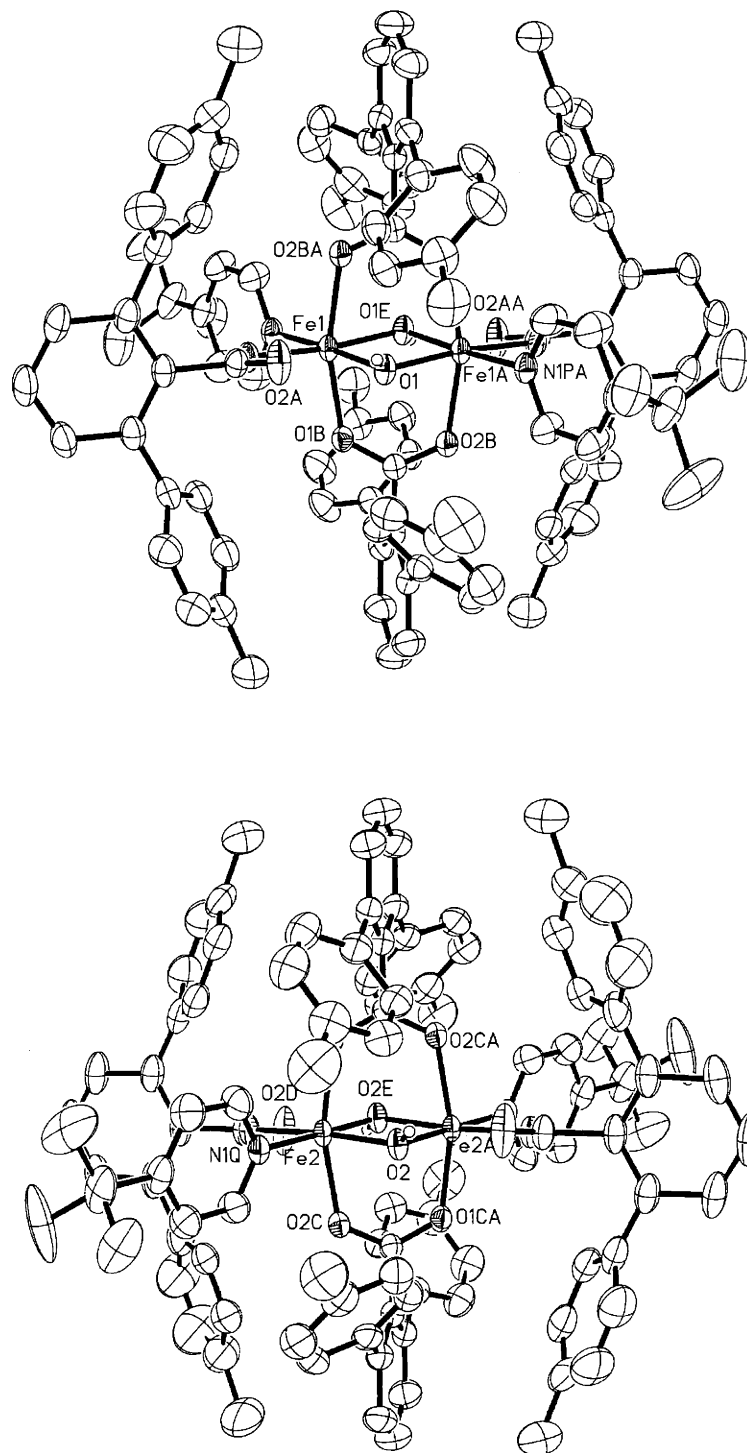


Figure 3.19. ORTEP diagram of $[\text{Fe}_2(\mu\text{-OH})_2(\mu\text{-O}_2\text{CAr}^{\text{Tol}})_2(\text{O}_2\text{CAr}^{\text{Tol}})_2\text{-}(4\text{-}^t\text{BuC}_5\text{H}_4\text{N})_2]$ (**2c**) with thermal ellipsoids at 50% probability. Top, molecule 1; bottom, molecule 2.

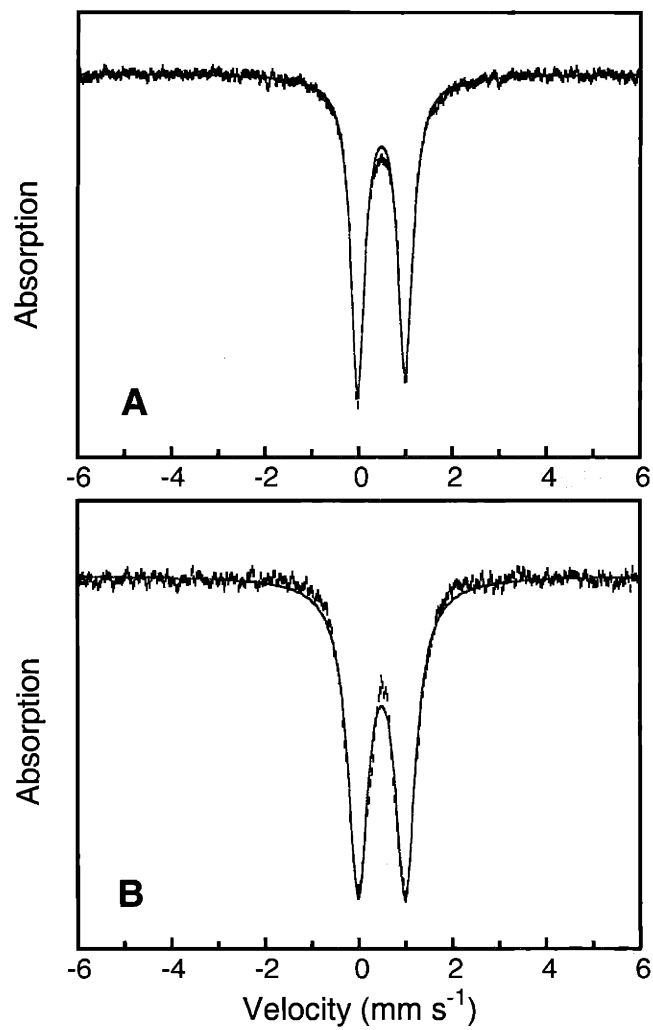


Figure 3.20. Zero-field Mössbauer spectra (experimental data (|), calculated fit (-)) recorded at 4.2 K for $[\text{Fe}_2(\mu\text{-OH})_2(\mu\text{-O}_2\text{CAr}^{\text{Tol}})_2(\text{O}_2\text{CAr}^{\text{Tol}})_2]^{2-}$ ($4\text{-}^t\text{BuC}_5\text{H}_4\text{N}_2$) (**2c**) (A) as a solid state sample, (B) as a THF frozen solution sample.

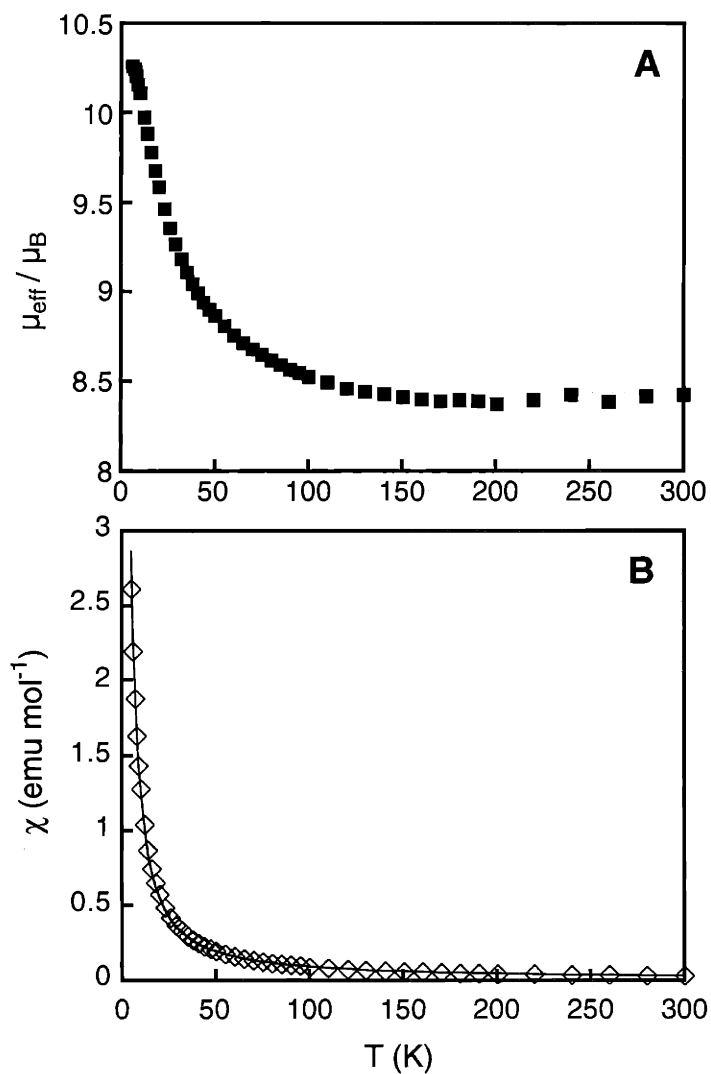


Figure 3.21. Plots of effective moment (μ_{eff}) per molecule versus temperature (A) and molar susceptibility (χ_M) versus temperature (B) for $[\text{Fe}_2(\mu\text{-OH})_2(\mu\text{-O}_2\text{CAr}^{\text{Tol}})_2(\text{O}_2\text{CAr}^{\text{Tol}})_2(\text{C}_5\text{H}_5\text{N})_2]$ (**1c**). The solid line in B corresponds to the best fit, obtained by parameters described in the text.

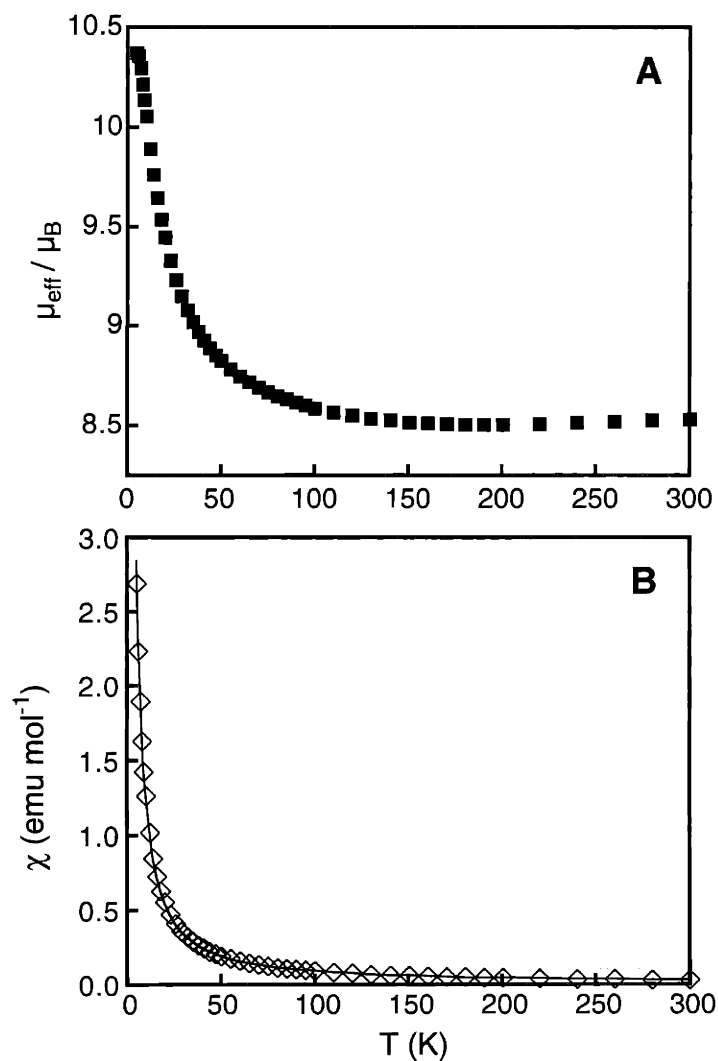


Figure 3.22. Plots of effective moment (μ_{eff}) per molecule versus temperature (A) and molar susceptibility (χ_M) versus temperature (B) for $[\text{Fe}_2(\mu\text{-OH})_2(\mu\text{-O}_2\text{CAr}^{\text{Tol}})_2(\text{O}_2\text{CAr}^{\text{Tol}})_2(4\text{-}^t\text{BuC}_5\text{H}_4\text{N})_2]$ (**2c**). The solid line in B corresponds to the best fit, obtained by parameters described in the text.

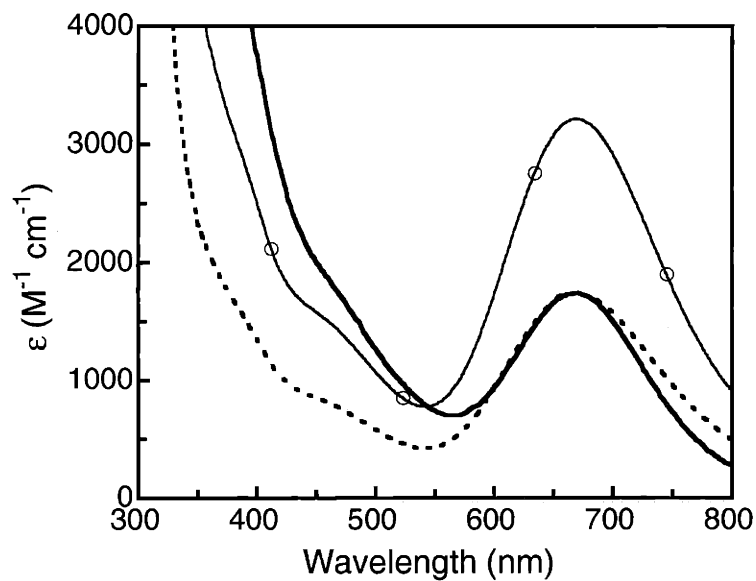


Figure 3.23. Comparison of the electronic absorption spectra of $[\text{Fe}_2(\mu\text{-O}_2\text{CAr}^{\text{Tol}})_4(4\text{-}^t\text{BuC}_5\text{H}_4\text{N})_2](\text{PF}_6)$ (**2mv**) (solid line with O) and **2b** (solid line) in CH_2Cl_2 . The dotted line represents the spectrum of **2mv** scaled to 54% to match the absorption maximum of **2b** at 670 nm.

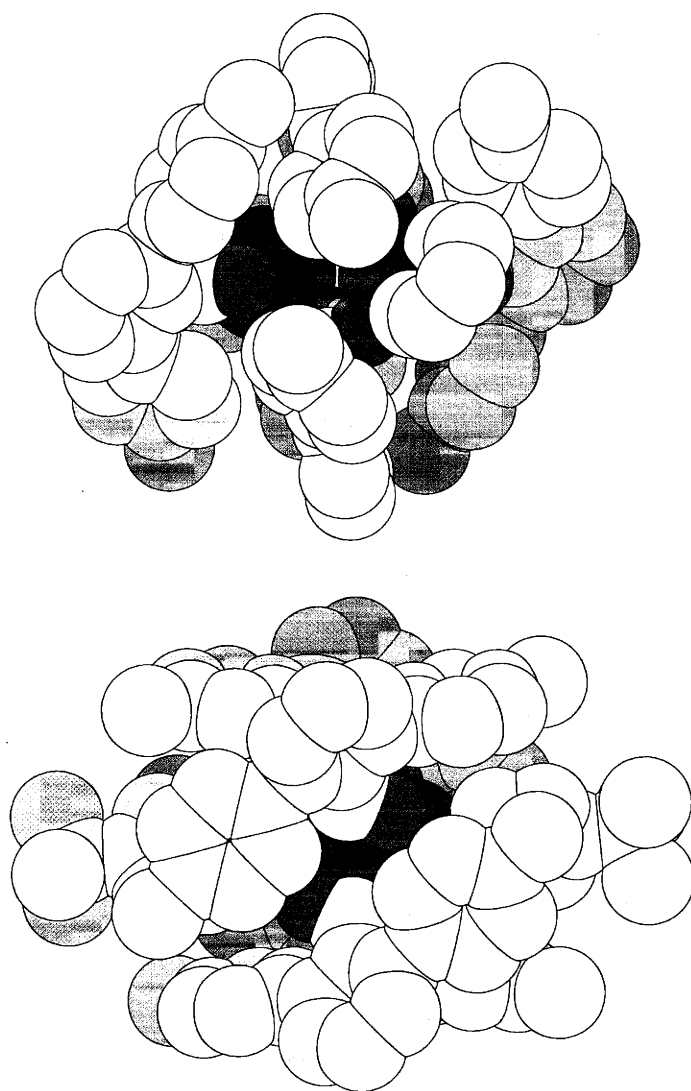


Figure 3.24. Space-filling representations of $[\text{Fe}_2(\mu\text{-O}_2\text{CAr}^{\text{Tol}})_2(\text{O}_2\text{CAr}^{\text{Tol}})_2\text{-}(\text{C}_5\text{H}_5\text{N})_2]$ (**1a**) (top) and $[\text{Fe}_2(\mu\text{-O}_2\text{CAr}^{\text{Tol}})_4(4\text{-}^t\text{BuC}_5\text{H}_4\text{N})_2]$ (**2a**) (bottom) generated using the crystallographic coordinates, where N is blue, O is bright red, and Fe is dark red.

Use of Sterically Hindered Carboxylate Ligands to Model
Structural and Functional Features of
Dioxygen-Activating Centers in Non-Heme Diiron Enzymes

by

Dongwhan Lee

B.S., Chemistry, Seoul National University, Seoul, Korea (1993)

M.S., Chemistry, Seoul National University, Seoul, Korea (1996)

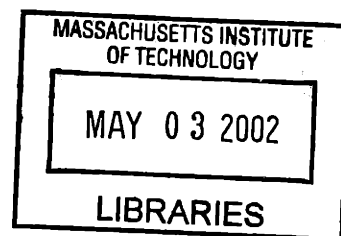
SUBMITTED TO THE DEPARTMENT OF CHEMISTRY IN PARTIAL
FULFILLMENT OF THE REQUIREMENT FOR THE DEGREE OF

DOCTOR OF PHILOSOPHY IN CHEMISTRY
AT THE
MASSCHUSETTS INSTITUTE OF TECHNOLOGY

February 2002

© 2002 Massachusetts Institute of Technology
All rights reserved

ARCHIVES



Signature of Author: _____

Lee Dongwhan

Department of Chemistry
September 17, 2001

Certified by: _____

Stephen J. Lippard

Stephen J. Lippard
Thesis Supervisor

Accepted by: _____

Rt 25

Robert W. Field
Chairman, Departmental Committee on Graduate Studies

V.2

Chapter IV

Structural and Spectroscopic Studies of Valence-Delocalized Diiron(II,III) Complexes Supported by Carboxylate-Only Bridging Ligands*

Introduction

Metalloproteins having valence-delocalized $\text{Cu}_2(\text{I,II})$ or $\text{Fe}_2(\text{II,III})$ sites are important participants in biological electron transfer (ET) reactions.¹⁻³ By delocalizing the charge over multiple nuclei, distortions associated with redox processes are significantly reduced, thus lowering Frank-Condon barriers for ET.⁴ Electron trafficking through such clusters is tightly regulated by a delicate interplay between geometric and electronic factors, the understanding of which has been greatly assisted by bioinorganic modeling studies.^{2,3,5,6}

The Cu_A centers in cytochrome c oxidase and nitrous oxide reductase use $\text{Cu(I)Cu(I)}/\text{Cu}_2(\text{I,II})$ redox couple for inter- and intraprotein ET.⁷⁻⁹ The short $\text{Cu}\cdots\text{Cu}$ distances (~ 2.44 Å) revealed by X-ray crystallography¹⁰⁻¹³ indicate direct $\text{Cu}-\text{Cu}$ bonding, which is crucial for valence delocalization at low-symmetry protein sites.¹⁴ Comparison with a model complex¹⁵ suggests that overlap between $3d_{x^2-y^2}$ orbitals is responsible for strong electronic coupling in Cu_A , although indirect superexchange via bridging cysteine thiolate ligands also occurs.¹⁴

Iron-sulfur clusters in electron transferases participate in many biological ET processes.^{5,9} The sulfido bridging ligands in $[\text{2Fe}-\text{2S}]$ clusters mediate strong antiferromagnetic coupling and afford valence-trapped Fe(II)Fe(III) units upon reduction of the metal center.^{16,17} Similar vibronic trapping affords the $S = 1/2$ ground spin state for oxo- or hydroxo-bridged Fe(II)Fe(III) centers.¹⁸⁻²² Valence delocalized $\text{Fe}_2(\text{II,III})$ units with a ground spin state of $S = 9/2$, however, occur in two mutant forms of a $[\text{2Fe}-\text{2S}]$ ferredoxin,^{23,24} and at $[\text{2Fe}-\text{2S}]$ subsites within mixed-valence $[\text{4Fe}-\text{4S}]$ or $[\text{3Fe}-\text{4S}]$ clusters.¹⁶ This interesting phenomenon, whereby valence localization shifts to delocalization upon formal dimerization of the $\{\text{Fe}_2\text{S}_2\}^+$ units has yet to be understood.²⁵ The resonance energy associated

with valence-delocalization affects the cluster redox potential^{26,27} as well as the rate of ET.²⁸

Studies of discrete valence delocalized Fe₂(II,III) complexes can provide insights into the physical origin of parallel spin alignment observed in biological systems. Prior to this work, few synthetic diiron complexes, [Fe₂(μ-OH)₃(Me₃TACN)₂]²⁺ ²⁹ (**A**),³⁰ [L¹Fe₂(μ-OAc)₂]⁺ ²⁹ (**B**),³¹ and [Fe₂(μ-OⁱPr)₂(μ-O₂CAr^{Mes})(O₂CAr^{Mes})₂]²⁹ (**C**)³² were structurally characterized, having S = 9/2 ground spin states that arise from valence-delocalized Fe₂(II,III) cores (Figure 4.1). Various spectroscopic techniques were applied to understand the magnetic and electronic interactions between the metal centers in these compounds. Mössbauer spectroscopy provided the most compelling evidence for equivalent iron sites within the valence-delocalized diiron(II,III) cores.^{30b,31a,32} In addition, Fe L-edge X-ray absorption spectroscopy (XAS) was employed to probe the electronic structure of valence-trapped and -delocalized diiron(II,III) complexes.^{30c} Although Fe K-edge and pre-edge (1s → 3d region) XAS both can provide geometric and electronic structural information,^{2,33} this technique has not been used to address issues concerning electron delocalization in iron dimers.

Previously, we communicated the first example of valence-delocalized Fe₂(II,III) complexes having no single-atom bridging ligand(s).³⁴ One-electron oxidation of tetracarboxylate diiron(II) precursor compounds afforded a series of (μ-1,3-carboxylato)diiron(II,III) complexes having class III mixed-valence behavior. Characteristic six-line patterns were observed in magnetic Mössbauer spectra recorded at 4.2 K, revealing that the extra electron in the S = 9/2 spin system is delocalized over two metal centers. The iron atoms are thus rendered equivalent on the Mössbauer time scale (~10⁻⁷ s). In this chapter, we present a full description of the synthesis and spectroscopic properties of the compounds [Fe₂(μ-O₂CAr^{Tol})₄L₂]^X, where Ar^{Tol}CO₂⁻ = 2,6-di(*p*-tolyl)benzoate; L = 4-^tBuC₅H₄N (**1b**),

C₅H₅N (**2b**), and THF (**3b**); X = PF₆⁻ (**1b** and **3b**) and OTf⁻ (**2b**). Electrochemical studies revealed significantly different redox behavior for tetracarboxylate diiron(II) complexes having doubly- versus quadruply-bridged cores. Analytically pure Fe(II)Fe(III) complexes **1b–3b** were obtained by chemical oxidation of the diiron(II) precursor compounds and structurally characterized. The *S* = 9/2 ground spin state of these compounds was confirmed by magnetic susceptibility measurements. X-ray absorption spectroscopic (XAS) experiments disclosed the valence-delocalized nature of **1b–3b**, further substantiating the previous assignment made by Mössbauer spectroscopy. Notably, the “extra” electron in the Fe₂(II,III) clusters remain delocalized even in the X-ray photoexcited states, demonstrating that XAS can be a useful probe for investigating this class of compounds.

Experimental Section

General Considerations. All reagents were obtained from commercial suppliers and used as received unless otherwise noted. Dichloromethane was distilled over CaH₂ under nitrogen. Diethyl ether, pentanes, and THF were saturated with nitrogen and purified by passage through activated Al₂O₃ columns under nitrogen.³⁵ The compounds [Fe₂(μ-O₂CAr^{Tol})₄(4-^tBuC₅H₄N)₂] (**1a**), [Fe₂(μ-O₂CAr^{Tol})₂(O₂CAr^{Tol})₂(C₅H₅N)₂] (**2a**), [Fe₂(μ-O₂CAr^{Tol})₂(O₂CAr^{Tol})₂(THF)₂] (**3a**), and [Fe₂(μ-OH)₂(μ-O₂CAr^{Tol})₄(4-^tBuC₅H₄N)₂] (**1c**) were prepared as described previously.^{36,37} All synthetic procedures and air-sensitive manipulations were carried out under nitrogen in a Vacuum Atmospheres drybox or by standard Schlenk line techniques.

[Fe₂(μ-O₂CAr^{Tol})₄(4-^tBuC₅H₄N)₂](PF₆) (**1b**). To a rapidly stirred deep yellow CH₂Cl₂ solution (5 mL) of **1a** (128 mg, 81 μmol) was added dropwise a CH₂Cl₂ (3 mL) suspension of [Cp₂Fe](PF₆) (30 mg, 91 μmol). The reaction mix-

ture was dark emerald green following the addition. The solution was stirred for 1 h and volatile fractions were removed under reduced pressure. The solid residue was washed with pentanes (10 mL) and filtered. Recrystallization from CH₂Cl₂/pentanes afforded **1b** (86 mg, 50 μmol, 62%) as dark green microcrystalline material, which was analyzed by X-ray crystallography. FT-IR (KBr, cm⁻¹) 3024, 2962, 2923, 2870, 1618, 1583, 1514, 1497, 1440, 1405, 1386, 1306, 1272, 1232, 1211, 1187, 1153, 1110, 1069, 1030, 844, 810, 792, 762, 728, 704, 586, 557, 530, 488; UV-vis (CH₂Cl₂, λ_{max}, nm (ε, M⁻¹cm⁻¹)) 670 (3200), 450 (sh, 1600), 380 (sh, 3100). Anal. Calcd for C₁₀₂H₉₄N₂O₈F₆Fe₂P: C, 70.71; H, 5.47; N, 1.62. Found: C, 71.16; H, 5.85; N, 1.62.

[Fe₂(μ-O₂CAr^{Tol})₄(C₅H₅N)₂](OTf) (**2b**). To a rapidly stirred CH₂Cl₂ (5 mL) suspension of **2a** (113 mg, 77 μmol) was added dropwise AgOTf (22 mg, 88 μmol) suspended in CH₂Cl₂ (5 mL). The heterogeneous mixture was stirred for 1 h and filtered through Celite. The dark green filtrate was concentrated to ca 5 mL. Vapor diffusion of pentanes into the resulting solution afforded dark brown crystals of **2b** (90 mg, 55 μmol, 71%), which were suitable for X-ray crystallography. FT-IR (KBr, cm⁻¹) 3025, 2919, 1610, 1583, 1513, 1485, 1437, 1406, 1384, 1304, 1265, 1222, 1184, 1265, 1222, 1184, 1148, 1110, 1067, 1044, 1031, 1016, 845, 814, 790, 761, 727, 712, 704, 692, 636, 584, 528, 487, 416; UV-vis (CH₂Cl₂, λ_{max}, nm (ε, M⁻¹cm⁻¹)) 665 (2900), 455 (sh, 1800), 385 (sh, 3400). Anal. Calcd for C₉₅H₇₈N₂O₁₁F₃Fe₂S: C, 70.24; H, 4.84; N, 1.72. Found: C, 70.62; H, 4.98; N, 1.64.

[Fe₂(μ-O₂CAr^{Tol})₄(THF)₂](PF₆) (**3b**). This compound was prepared from **3a** (154 mg, 105 μmol) and [Cp₂Fe](PF₆) (40 mg, 121 μmol) by a procedure analogous to that used to obtain **1b**. Blue-purple blocks (117 mg, 73 μmol, 60%) were afforded following vapor diffusion of pentanes into the CH₂Cl₂ solution of this material. Single crystals suitable for X-ray crystallography were obtained similarly from pentanes and a chlorobenzene solution of this material. FT-IR (KBr,

cm⁻¹) 3025, 2919, 1583, 1566, 1521, 1436, 1382, 1305, 1270, 1236, 1210, 1190, 1154, 1110, 1076, 1019, 957, 917, 860, 761, 727, 705, 585, 556, 528, 492; UV-vis (CH₂Cl₂, λ_{max}, nm (ε, M⁻¹cm⁻¹)) 620 (2700), 450 (sh, 1600), 385 (sh, 3200). Anal. Calcd for C₉₂H₈₄O₁₀F₆Fe₂P: C, 68.79; H, 5.27. Found: C, 68.23; H, 5.39.

X-ray Crystallographic Studies. Intensity data were collected on a Bruker (formerly Siemens) CCD diffractometer with graphite-monochromated Mo Kα radiation (λ = 0.71073 Å), controlled by a Pentium-based PC running the SMART software package.³⁸ Single crystals were mounted at room temperature on the tips of quartz fibers, coated with Paratone-N oil, and cooled to 188 K under a cold stream of nitrogen maintained by a Bruker LT-2A nitrogen cryostat. Data collection and reduction protocols are described elsewhere.³⁹ Empirical absorption corrections were applied with SADABS,⁴⁰ part of the SHELXTL program package. The possibility of higher symmetry was checked by the program PLATON.⁴¹ All non-hydrogen atoms were refined anisotropically unless otherwise noted. Hydrogen atoms were assigned idealized positions and given thermal parameters equivalent to either 1.5 (methyl hydrogen atoms) or 1.2 (all other hydrogen atoms) times the thermal parameter of the carbon atom to which they are attached. The hydrogen atoms associated with the disordered solvent molecules were not included in the refinement. The structure of **2b** contains a lattice CH₂Cl₂ molecule, disordered over three positions, which was refined isotropically. In the structure of **3b**, each coordinated THF molecule contains two carbon atoms disordered over two positions. In each case the atoms were distributed over two positions and refined isotropically. The PF₆⁻ anion in the structure of **3b** is disordered over two positions and was refined isotropically. Crystallographic information is provided in Table 4.1. The structure of **1b** was not fully refined owing to severe disorder in the PF₆⁻ counterion and the solvent molecules. This compound crystallizes in triclinic space group $P\bar{1}$ with $a = 16.472(5)$

\AA , $b = 16.706(5) \text{ \AA}$, $c = 17.888(5) \text{ \AA}$, $\alpha = 108.243(5)^\circ$, $\beta = 90.614(5)^\circ$, $\gamma = 90.587(5)^\circ$, and $Z = 2$.

Physical Measurements. FT-IR spectra were recorded on a Bio Rad FTS-135 instrument with Win-IR software. UV-vis spectra were recorded on a Hewlett Packard 8453 diode array spectrophotometer. UV-vis-NIR spectra were obtained using a Cary 17 spectrophotometer modified by On-Line Instrument Systems (OLIS) to introduce computer control. 4.2 K Mössbauer spectra were measured and analyzed as described previously.⁴² Samples were prepared by suspending a finely ground solid material of **1b** (50 mg) in BN (30 mg).

Electrochemistry. Cyclic voltammetric measurements were carried out in a Vacuum Atmospheres drybox under nitrogen with an EG&G model 263 potentiostat. A three-electrode configuration consisting of a 1.75-mm² platinum working electrode, a Ag/AgNO₃ (0.1 M in MeCN with 0.5 M (Bu₄N)PF₆ reference electrode, and a platinum mesh auxiliary electrode was used. The supporting electrolyte was 0.5 M (Bu₄N)PF₆ in CH₂Cl₂. All cyclic voltammograms were externally referenced to the Cp₂Fe/Cp₂Fe⁺ couple.

Magnetic Susceptibility Measurements. The magnetic susceptibility of polycrystalline powders of **1b–3b** was measured between 5 K and 300 K with applied magnetic fields of 0.1 T using a Quantum Design MPMS SQUID susceptometer. Samples were loaded in gel capsules under nitrogen and suspended in plastic straws. Data were corrected for the magnetism of the sample holder, which was independently determined at the same temperature range and field. The underlying diamagnetism of the sample was estimated from Pascal's constants.⁴³

X-ray Absorption Spectroscopy (XAS). X-ray absorption spectra were measured on unfocused wiggler beamline 7-3 at the Stanford Synchrotron Radiation Laboratory (SSRL), with the ring operating at 3 GeV and 50–100 mA.

Solid samples of **1a**, **1c**, and **1b–3b** were prepared by grinding ~30 mg polycrystalline powder with BN and pressing the mixture into a 1 mm thick aluminum sample holder. Samples were maintained at 10 K inside an Oxford Instrument CF-1208 liquid helium continuous flow cryostat. A Si(220) double-crystal monochromator was used, detuned 50% at 7987 eV in order to minimize contamination of the radiation by higher harmonics. Vertical 1-mm pre-monochromator slits were used to define the beam size, minimizing beam divergence and allowing for an energy resolution of $\leq 1 - 1.4$ eV at the Fe K-edge. Spectra were collected in fluorescence mode, using a Lytle detector (an iron chamber equipped with a manganese filter and Soller slits).⁴⁴ The spectrum of Fe foil was collected concomitantly, allowing for internal energy calibration of the data. The first inflection point energy for the Fe foil spectrum was set to 7111.2 eV. The reproducibility in the determination of edge position was < 0.2 eV. K-edge data were measured over the energy range 7105 – 7150 eV. Multiple (4 – 5) scans over the complete energy range were averaged for each sample. For each spectrum, a smooth second-order polynomial was fit to the pre-edge region, then extrapolated across the entire energy range and subtracted from the data.

Results

Electrochemistry of $[\text{Fe}_2(\mu\text{-O}_2\text{CAr}^{\text{Tol}})_4(4\text{-}^t\text{BuC}_5\text{H}_4\text{N})_2]$ (1a**) and $[\text{Fe}_2(\mu\text{-O}_2\text{CAr}^{\text{Tol}})_2(\text{O}_2\text{CAr}^{\text{Tol}})_2(\text{THF})_2]$ (**3a**).** Electrochemical properties of **1a** and **3a** were investigated by cyclic voltammetry, in order to select appropriate 1-electron chemical oxidants to access the Fe(II)Fe(III) oxidation states. Measurement was not made with **2a**, due to its limited solubility in CH_2Cl_2 . Cyclic voltammograms of a CH_2Cl_2 solution of **1a** revealed a reversible oxidation at $E_{1/2} = -216$ mV vs $\text{Cp}_2\text{Fe}^+/\text{Cp}_2\text{Fe}$ ($\Delta E_p = 89$ mV) (Figure 4.2). A broad second oxidation wave occurs at ca +1080 mV, which does not display a corresponding reduction wave in

the return sweep. Under identical conditions, the compound $[\text{Fe}_2(\mu\text{-O}_2\text{C-Ar}^{4\text{-FPPh}})_4(4\text{-}^t\text{BuC}_5\text{H}_4\text{N})_2]$ ^{29,45} exhibited a similarly reversible oxidation step at $E_{1/2} = -16$ mV vs $\text{Cp}_2\text{Fe}^+/\text{Cp}_2\text{Fe}$ ($\Delta E_p = 97$ mV) (Figure 4.3). A positive shift ($\Delta E = +200$ mV) in the oxidation potential is consistent with the coordination of less electron-donating fluoro-substituted ligands $\text{Ar}^{4\text{-FPPh}}\text{CO}_2^-$. A similar shift would place the second oxidation peak of $[\text{Fe}_2(\mu\text{-O}_2\text{C-Ar}^{4\text{-FPPh}})_4(4\text{-}^t\text{BuC}_5\text{H}_4\text{N})_2]$ at +1280 mV, lying at the positive limit of the accessible potential window. No second oxidation step was observed. Compound **3a** displayed a broad oxidation wave, beginning at -150 mV and maximizing at +400 mV. A significantly narrower reduction wave occurred at -195 mV in the return sweep (Figure 4.4A). A similarly irreversible redox behavior was observed even with increased scan rates (50 – 500 mV/s) at a narrower potential sweep range from -720 to +880 mV (Figure 4.4B).

Synthesis and Structural Characterization of $[\text{Fe}_2(\mu\text{-O}_2\text{C-Ar}^{\text{Tol}})_4(4\text{-}^t\text{BuC}_5\text{H}_4\text{N})_2](\text{PF}_6)$ (1b**), $[\text{Fe}_2(\mu\text{-O}_2\text{C-Ar}^{\text{Tol}})_4(\text{C}_5\text{H}_5\text{N})_2](\text{OTf})$ (**2b**), and $[\text{Fe}_2(\mu\text{-O}_2\text{C-Ar}^{\text{Tol}})_4(\text{THF})_2](\text{PF}_6)$ (**3b**).** Reactions of **1a–3a** with 1 equiv of $[\text{Cp}_2\text{Fe}]\text{PF}_6$ or AgOTf in CH_2Cl_2 resulted in an instantaneous color change from yellow to deep forest green. Dark brown-green blocks of **1b–3b** were obtained in good yield (60 ~ 71%), following recrystallization from CH_2Cl_2 /pentanes. These compounds are stable both in the solid state and in solution when protected from exposure to dioxygen or to coordinating solvents such as THF, MeCN, or MeOH. Attempts to access a similar unit by oxidizing $[\text{Fe}_2(\mu\text{-O}_2\text{CCMe}_3)_4(\text{C}_5\text{H}_5\text{N})_2]$ ⁴⁶ with 1 equiv of $[\text{Cp}_2\text{Fe}]\text{PF}_6$ did not lead to any isolable product. The initial dark green reaction mixture gradually decomposed to an orange brown material. Steric shielding provided by the *m*-terphenyl units (Figure 4.5) apparently plays a crucial role in stabilizing the mixed valence diiron(II,III) cores in **1b–3b**.

The solid state structures of **1b–3b** were determined by X-ray crystallography. The molecular structures are shown in Figures 4.5–4.7; selected bond lengths and angles are listed in Table 4.2. Although severe disorder in the PF_6^- counterion and solvent molecules hampered detailed structural refinement of the model for **1b**, its Fe...Fe distance of 2.713(3) Å, as well as the quadruply-bridged core structure, is comparable to the corresponding properties of **2b** and **3b**. In **1b–3b**, the Fe...Fe distances are 2.6633(11) – 2.713(3) Å and four μ -1,3 carboxylate ligands bridge the Fe–Fe vector. This architectural feature is shared by a few structurally characterized paddle-wheel diiron(II) complexes.^{37,45,46} The two iron atoms are crystallographically inequivalent but display similar square-pyramidal coordination comprising four carboxylate oxygen atoms at the base and one N- or O-donor atom at the axial position. In order to minimize inter-ligand steric repulsions, the benzoate rings in the $\text{Ar}^{\text{Tol}}\text{CO}_2^-$ ligands are twisted from the CO_2^- planes by 39.3 – 45.7°. This conformation provides tetragonal pockets on either side of the Fe–Fe vector. The motion of the axial ligand confined within this pocket is significantly restricted. The dihedral angles between the two pyridine planes are 72.3° in **1b** and 62.1° in **2b**. Comparable Fe–O_{carboxylate} distances were observed for each iron within the dimer (Table 4.2).

Physical Properties. Compounds **1b–3b** display intense visible absorption bands at $\lambda_{\text{max}} = 620 - 670 \text{ nm}$ ($\epsilon = 2700 - 3200 \text{ M}^{-1}\text{cm}^{-1}$) and two shoulders at $\sim 380 \text{ nm}$ ($\epsilon = 3100 - 3400 \text{ M}^{-1}\text{cm}^{-1}$) and $\sim 450 \text{ nm}$ ($\epsilon = 1600 - 1800 \text{ M}^{-1}\text{cm}^{-1}$) in CH_2Cl_2 (Figures 4.8 and 4.9; Table 4.3). No other visible-NIR transitions occur up to 1650 nm (Figure 4.10). Since both the pyridine and THF complexes behave similarly, the 620 – 670 nm bands are assigned as intervalence charge transfer (IVCT), rather than LMCT transitions. The experimentally determined width at half-height ($\Delta\nu_{1/2}$) ranges between 3590 and 3970 cm^{-1} for **1b–3b**, values significantly lower than those predicted by Hush's relationship^{47,48} for class II mixed

valence centers ($\Delta v_{1/2} = [2310 v_{\max}]^{1/2} = 5880 - 6120 \text{ cm}^{-1}$). This result strongly indicates that **1b–3b** are valence delocalized diiron(II,III) complexes. Similar IVCT bands are observed at 758 – 1060 nm ($\epsilon = 1250 - 2400 \text{ M}^{-1}\text{cm}^{-1}$) for **A–C** (Figure 4.1; Table 4.3).

The μ_{eff} vs T curves for **1b–3b** are shown in Figure 4.11. The measured values of 10.2 – 11.0 μ_{B} at 300 K are consistent with ground state ferromagnetism. The spin-only moment for an $S = 9/2$ spin state is 9.95 μ_{B} . The effective moment of **1b** decreased slightly, from 11.0 μ_{B} to 10.3 μ_{B} upon cooling from 300 K to 5 K. At temperatures above ~50 K, an essentially constant value of 10.2 and 10.5 μ_{B} was observed for **2b** and **3b**, respectively. Below ~50 K, the moments gradually increased to ~11.0 μ_{B} at 5 K. The observed magnetic behavior was not modeled. Spin-dependent electron delocalization between two paramagnetic centers results in a non-Heisenberg spin ladder with a complicated energy level distribution.^{30d,17}

Mössbauer Spectroscopy. The electronic structure of **1b** was also probed by Mössbauer studies. At 4.2 K and in a weak applied magnetic field (50 mT), the spectrum of a solid powder sample of **1b** is broad and featureless, indicative of intermediate electronic relaxation (data not shown). In a strong applied field (> 3 T), however, the effects of electronic relaxation diminish and well-resolved spectra are obtained. Figure 4.12 shows Mössbauer spectra of **1b** recorded at 4.2 K with a magnetic field of 4 T (spectrum A) and 8 T (spectrum B) applied parallel to the γ -rays. A distinct six-line pattern is observed under these experimental conditions, indicating that the two iron sites contribute identically to the spectra. This observation demonstrates unambiguously that **1b** is valence-delocalized. A detailed analysis of the Mössbauer data is provided in the Chapter III of this thesis. Relevant parameters are summarized in Table 4.2, along with those for **A–C**.

X-ray Absorption Spectroscopy. As shown in Figures 4.13 and 4.14, the Fe K-edge and pre-edge ($1s \rightarrow 3d$ transitions) spectra of **1b–3b** are nearly identical and intermediate in energy between K-edges for structurally related diiron(II) complex **1a** and diiron(III) complex **1c**. Adding K-edge spectra for **1a** and **1c** at a weighted ratio of 50:50 yielded a spectrum comparable in rising edge energy to those of **1b–3b** (Figure 4.14), consistent with the formal description of the oxidation states of the mixed-valence species as Fe(II)Fe(III). K-edges or pre-edges for the mixed-valence complexes, however, are not a simple 50:50 superposition of the Fe(II)Fe(II) and Fe(III)Fe(III) spectra. The difference is clearly manifest by comparing the second-derivatives of the K-edge spectra (Figure 4.15), or more specifically, the second-derivatives of the pre-edge region (Figure 4.16), which highlight individual transitions obscured by the rising edge absorption. Each of the compounds **1b–3b** has a pair of transitions in the pre-edge region, at energies that are almost exactly intermediate between those for **1a** and **1c**. This result suggests that the iron sites in each mixed-valence species are best described as delocalized Fe(2.5)Fe(2.5), rather than localized Fe(II)Fe(III). The spectrum for a localized complex should be the superposition of both Fe(II) and Fe(III) spectra.^{30c}

Discussion

Synthesis, Structures, and Electrochemical Properties of Diiron(II,III) Complexes. Synthetic routes to **1b–3b** are described in Scheme 4.1. Consistent with the oxidation potentials determined for **1a** and **3a**, mixed valence diiron(II,III) complexes **1b–3b** were readily accessed through one electron oxidation by $[\text{Cp}_2\text{Fe}]^+$ ($E'' = +460$ mV vs SCE in CH_2Cl_2) or Ag^+ ($E'' = +1110$ mV vs SCE in CH_2Cl_2). The redox behavior of **1a** and **3a**, as well as the structural outcome of their chemical oxidation, however, differ significantly.

Compound **1a** undergoes minimal structural rearrangement following oxidation to **1b**. Except for a slight but significant shortening of the Fe...Fe distance from 2.8229(9) to 2.713(3) Å, the coordination geometry afforded by the four μ -1,3 bridging carboxylate and two N-donor ligands remains essentially identical. This behavior is consistent with the reversible interconversion between the Fe(II)Fe(II) and Fe(II)Fe(III) species observed by cyclic voltammetry of **1a** in CH₂Cl₂. In contrast, significant core rearrangement accompanies oxidation of the metal centers in **2a** and **3a**. Double carboxylate shifts⁴⁹ from terminal bidentate to μ -1,3 bridging positions (Scheme 4.2) result in the significant shortening ($\Delta_{\text{Fe}\cdots\text{Fe}} = 1.52 \sim 1.62$ Å) of the Fe...Fe distances from 4.2189(13) to 2.6982(13) Å (**2a** \rightarrow **2b**) and 4.2822(7) to 2.6633(11) Å (**3a** \rightarrow **3b**). The irreversible electrochemical behavior of **3a** in CH₂Cl₂ (Figure 4.4) most likely results from such a core rearrangement concomitant with a change in oxidation state.

The broad oxidation wave of **3a** initiates at -150 mV, shifted by +180 mV relative to that of **1a**. This shift is consistent with the coordination of less electron-donating (THF < 4-*tert*-butylpyridine) ligands to the metal. Compared with the broad oxidation wave, however, the corresponding reduction peak of **3a** is significantly narrower (Figure 4.4). This electrochemical behavior is nicely explained by the mechanism postulated in Scheme 4.2. In CH₂Cl₂ at room temperature, **3a** exists as an equilibrium mixture with its quadruply-bridged isomer **3a'**. Such a dynamic core rearrangement was demonstrated by VT ¹⁹F-NMR studies of the related compound [Fe₂(μ -O₂CAr^{4-FPh})₂(O₂CAr^{4-FPh})₂(THF)₂].⁴⁵ Electrochemical oxidation of multiple species at the electrode surface would give account for the broad oxidation peak observed in the cyclic voltammogram. At the return potential, the diffusion layer mainly comprises a single species, **3b**, the one electron reduction of which results in a well-defined and narrow cathodic peak. This behavior can be further evaluated by comparing the energies of the

different structural isomers of $[\text{Fe}_2(\text{O}_2\text{CAr}^{\text{Tot}})_4\text{L}_2]$ in different oxidation states. Such an investigation is in progress.⁵⁰

XAS: Valence-Delocalized Photoexcited States. Central to our analysis of the XAS data in this investigation is the ability to prepare three diiron complexes having different oxidation states but similar N/O ligand combinations and coordination geometry. The effective electron density at the metal can be influenced by changes in the oxidation states or ligand composition, which lead to a shift in the X-ray absorption edge.³³ By minimizing contributions from structural changes, the edge shift can be directly correlated to the redox changes at the metal center.

The XAS results for **1b–3b** have significant implications for the electronic structure of valence-delocalized complexes. The creation of a 1s electron hole via the K-edge absorption is expected to cause excited state relaxation of the Fe electronic configuration. The relaxed configuration might therefore resemble a localized Fe(II)Fe(III) species, even if the complex is delocalized in the ground state. Studies of Ru(II)Ru(III) dimers indicated that X-ray photoemission spectroscopy (XPS) fails to distinguish between a valence-localized and -delocalized ground state.⁵¹ A large decrease in the electron coupling in the photoexcited state may render two metal centers inequivalent, regardless of the situation in the ground state.

The observed pre-edge XAS spectrum of **1b**, however, is fully consistent with a valence-delocalized Fe(2.5)Fe(2.5) description, since the simple linear combination of Fe(II) and Fe(III) sites cannot reproduce the observed spectral pattern. The electronic coupling responsible for the valence delocalization in the ground state may be equally well operative in the X-ray photoexcited state. Previous L-edge XAS studies similarly revealed differences between valence-localized and -delocalized dinuclear Fe(II)Fe(III) complexes.^{30c} The multiplet

structures of spectra for the valence-trapped complexes were well modeled by 50:50 superpositions of L-edge spectra for related Fe(II)Fe(II) and Fe(III)Fe(III) complexes. The spectrum for the valence-delocalized compound **A**, in contrast, displays a broader and less well resolved multiplet structure. The corresponding Fe(II)Fe(II) or Fe(III)Fe(III) complexes, however, are not available for **A** and a direct spectral comparison could not be made. To the best of our knowledge, compounds **1b–3b** represent the first examples of mixed-valence Fe₂(II,III) complexes, where the valence-delocalized nature is retained in excited states produced by X-ray absorption. With such proper calibrations made possible by the existence of structurally related Fe(II)Fe(II) and Fe(III)Fe(III) complexes, XAS should be able to probe the electronic structure of other mixed-valence Fe(II)Fe(III) complexes.

Valence Delocalization. The ground state ferromagnetism of the Fe₂(II,III) compounds **1b–3b** was revealed by magnetic susceptibility studies. Electron delocalization in this $S = 9/2$ spin system was indicated by the essentially identical geometric parameters obtained for the two iron atoms in the dimers in the solid state (Table 4.2). Although static disorder of valence-trapped Fe(II)Fe(III) cations or dynamic disordering due to rapid electron transfer between the metal centers can equally well explain such structural results,⁵² Mössbauer and XAS studies provide a compelling evidence that the diiron(II,III) cores in **1b–1c** remain valence-delocalized on the time scale of $\sim 10^{-16}$ s at < 10 K.

Such valence delocalization between paramagnetic centers is described by double exchange,^{16,17,26,53} a mechanism by which delocalized electrons provide an additional coupling mechanism for the parallel alignment of the spins. Such resonance interaction between metal centers can be mediated either by direct metal–metal orbital overlap or by the bridging ligands. Notable structural features of the previously characterized valence-delocalized diiron(II,III) com-

pounds **A–C** (Figure 4.1) include short metal···metal distances and the presence of single atom bridging ligands. Oxygen atoms supplied by hydroxo, phenoxo, or alkoxo ligands promote short the Fe···Fe distances of 2.509(6) ~ 2.7414(8) Å in **A–C** and can mediate a strong metal–metal resonance interaction. Theoretical studies indicate that a direct σ -type overlap of the two d_{z^2} orbitals are responsible for the valence delocalization in **A**,^{30d} whereas both σ -type interaction between the Fe $d_{x^2-y^2}$ orbitals and Fe–O_{phenoxide} bonding contribute to the similar phenomenon in **B**.^{31b}

Although compounds **1b–3b** feature short Fe···Fe distances comparable to those in **A–C** (Table 4.3), their quadruply-bridged diiron(II,III) cores lack efficient coupling pathways afforded by single atom bridging ligands. Double exchange observed in the $[\text{Fe}_2(\mu\text{-O}_2\text{CAr}^{\text{Tol}})_4\text{L}_2]^+$ module is thus apparently mediated by the direct through-space interaction between the metal centers. Preliminary DFT calculations indicate that π -type overlap between d_{xz} orbitals is responsible for the strong electron delocalization in **1b–3b**, the details of which are currently under investigation.⁵⁴ Collectively, the synthesis and characterization of **1b–3b** significantly expands the class of valence delocalized diiron(II,III) clusters, affording novel basis for correlating the geometric and electronic factors responsible for this novel phenomenon.

Acknowledgment. This work was supported by a grant from the National Science Foundation. The XAS studies discussed here were carried out in collaboration with Prof. Britt Hedman and Keith O. Hodgson and Dr. Jennifer L. DuBois (Stanford University). The Mössbauer studies were done in collaboration with Prof. Boi Hanh Huynh and Dr. Carsten Krebs (Emory University). I thank Mr. Christopher M. Chang of the Nocera group at MIT for assistance in acquiring the UV-vis-NIR spectra.

References

- (*) Part of this work has appeared previously in reference 34, © 2000 American Chemical Society. A slightly modified version of this work has been submitted for publication. Lee, D.; DuBois, J. L.; Hedman, B.; Hodgson, K. O.; Pierce, B.; Hendrich, M. P.; Lippard, S. J. **2001**.
- (1) Holm, R. H.; Kennepohl, P.; Solomon, E. I. *Chem. Rev.* **1996**, *96*, 2239-2314.
- (2) Solomon, E. I.; Hanson, M. A. *Inorganic Electronic Structure and Spectroscopy*; Solomon, E. I. and Lever, A. B. P., Ed.; John Wiley & Sons: New York, 1999; Vol. II, pp 1-129.
- (3) Solomon, E. I.; Randall, D. W.; Glaser, T. *Coord. Chem. Rev.* **2000**, *200-202*, 595-632.
- (4) Marcus, R. A.; Sutin, N. *Biochim. Biophys. Acta* **1985**, *811*, 265-322.
- (5) Beinert, H.; Holm, R. H.; Münck, E. *Science* **1997**, *277*, 653-659.
- (6) Glaser, T.; Hedman, B.; Hodgson, K. O.; Solomon, E. I. *Acc. Chem. Res.* **2000**, *33*, 859-868.
- (7) Ramirez, B. E.; Malmström, B. G.; Winkler, J. R.; Gray, H. B. *Proc. Natl. Acad. Sci.* **1995**, *92*, 11949-11951.
- (8) Ferguson-Miller, S.; Babcock, G. T. *Chem. Rev.* **1996**, *96*, 2889-2907.
- (9) Beinert, H. *Eur. J. Biochem.* **1997**, *245*, 521-532.
- (10) Iwata, S.; Ostermeier, C.; Ludwig, B.; Michel, H. *Nature* **1995**, *376*, 660-669.
- (11) Tsukihara, T.; Aoyama, H.; Yamashita, E.; Tomizaki, T.; Yamaguchi, H.; Shinzawa-Itoh, K.; Nakashima, R.; Yaono, R.; Yoshikawa, S. *Science* **1995**, *269*, 1069-1074.
- (12) Tsukihara, T.; Aoyama, H.; Yamashita, E.; Tomizaki, T.; Yamaguchi, H.; Shinzawa-Itoh, K.; Nakashima, R.; Yaono, R.; Yoshikawa, S. *Science* **1996**, *272*, 1136-1144.

- (13) Brown, K.; Tegoni, M.; Prudêncio, M.; Pereira, A. S.; Besson, S.; Moura, J. J.; Moura, I.; Cambillau, C. *Nature Struct. Biol.* **2000**, *7*, 191-195.
- (14) Gamelin, D. R.; Randall, D. W.; Hay, M. T.; Houser, R. P.; Mulder, T. C.; Canters, G. W.; de Vries, S.; Tolman, W. B.; Lu, Y.; Solomon, E. I. *J. Am. Chem. Soc.* **1998**, *120*, 5246-5263.
- (15) Houser, R. P.; Young, V. G., Jr.; Tolman, W. B. *J. Am. Chem. Soc.* **1996**, *118*, 2101-2102.
- (16) Münck, E.; Papaefthymiou, V.; Surerus, K. K.; Girerd, J.-J. *Metal Clusters in Proteins*; Que, L., Jr., Ed.; American Chemical Society: Washington, D. C., 1988, pp 302-325.
- (17) Blondin, B.; Girerd, J.-J. *Chem. Rev.* **1990**, *98*, 1359-1376.
- (18) Bossek, U.; Hummel, H.; Weyhermuller, T.; Bill, E.; Wieghardt, K. *Angew. Chem., Int. Ed. Engl.* **1995**, *34*, 2642.
- (19) Davydov, R. M.; Ménage, S.; Fontecave, M.; Gräslund, A.; Ehrenberg, A. J. *Biol. Inorg. Chem.* **1997**, *2*, 242-255.
- (20) Cohen, J. D.; Payne, S.; Hagen, K. S.; Sanders-Loehr, J. J. *Am. Chem. Soc.* **1997**, *119*, 2960-2961.
- (21) Payne, S. C.; Hagen, K. S. *J. Am. Chem. Soc.* **2000**, *122*, 6399-6410.
- (22) Mizoguchi, T. J.; Davydov, R. M.; Lippard, S. J. *Inorg. Chem.* **1999**, *38*, 4098-4103.
- (23) Achim, C.; Golinelli, M.-P.; Bominaar, E. L.; Meyer, J.; Münck, E. *J. Am. Chem. Soc.* **1996**, *118*, 8168-8169.
- (24) Achim, C.; Bominaar, E. L.; Meyer, J.; Peterson, J.; Münck, E. *J. Am. Chem. Soc.* **1999**, *121*, 3704-3714.
- (25) Glaser, T.; Rose, K.; Shadle, S. E.; Hedman, B.; Hodgson, K. O.; Solomon, E. I. *J. Am. Chem. Soc.* **2001**, *123*, 442-454.
- (26) Girerd, J.-J. *J. Chem. Phys.* **1983**, *79*, 1766-1775.

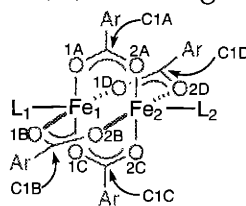
- (27) Mouesca, J. M.; Chen, J. L.; Noodleman, L.; Bashford, D.; Case, D. A. *J. Am. Chem. Soc.* **1994**, *116*, 11898-11914.
- (28) Achim, C.; Bominaar, E. L.; Münck, E. *J. Biol. Inorg. Chem.* **1998**, *3*, 126-134.
- (29) Abbreviations used: Me₃TACN, 1,4,7-trimethyl-1,4,7-triazacyclononane; L¹, [2+2] condensation product of propylenediamine and 2,6-diformyl-4-methylphenoxide; Ar^{Mes}CO₂⁻, 2,6-dimesitylbenzoate; Ar^{4-FPh}CO₂⁻, 2,6-di(4-fluorophenyl)benzoate.
- (30) (a) Drüeke, S.; Chaudhuri, P.; Pohl, K.; Wieghardt, K.; Ding, X.-Q.; Bill, E.; Sawaryn, A.; Trautwein, A. X.; Winkler, H.; Gurman, S. J. *J. Chem. Soc., Chem. Commun.* **1989**, 59-62. (b) Ding, X.-Q.; Bominaar, E. L.; Bill, E.; Winkler, H.; Trautwein, A. X.; Drüeke, S.; Chaudhuri, P.; Wieghardt, K. *J. Chem. Phys.* **1990**, *92*, 178-186. (c) Peng, G.; van Elp, J.; Jang, H.; Que, L., Jr.; Armstrong, W. H.; Cramer, S. P. *J. Am. Chem. Soc.* **1995**, *117*, 2515-2519. (d) Gamelin, D. R.; Bominaar, E. L.; Kirk, M. L.; Wieghardt, K.; Solomon, E. I. *J. Am. Chem. Soc.* **1996**, *118*, 8085-8097. (e) Knapp, M. J.; Krzystek, J.; Brunel, L.-C.; Hendrickson, D. N. *Inorg. Chem.* **1999**, *38*, 3321-3328.
- (31) (a) Dutta, S. K.; Enslin, J.; Werner, R.; Flörke, U.; Haase, W.; Gütlich, P.; Nag, K. *Angew. Chem., Int. Ed. Engl.* **1997**, *36*, 152-155. (b) Saal, C.; Böhm, M. C.; Haase, W. *Inorg. Chim. Acta* **1999**, *291*, 82-90.
- (32) Hagadorn, J. R.; Que, L., Jr.; Tolman, W. B.; Prisecaru, I.; Münck, E. *J. Am. Chem. Soc.* **1999**, *121*, 9760-9761.
- (33) Scott, R. A. *Physical Methods in Bioinorganic Chemistry: Spectroscopy and Magnetism*; Que, L., Jr., Ed.; University Science Books: Sausalito, CA, 2000, pp 465-503.
- (34) Lee, D.; Krebs, C.; Huynh, B. H.; Hendrich, M. P.; Lippard, S. J. *J. Am. Chem. Soc.* **2000**, *122*, 5000-5001.

- (35) Pangborn, A. B.; Giardello, M. A.; Grubbs, R. H.; Rosen, R. K.; Timmers, F. J. *Organometallics* **1996**, *15*, 1518-1520.
- (36) Lee, D.; Lippard, S. J. *J. Am. Chem. Soc.* **1998**, *120*, 12153-12154.
- (37) Lee, D.; Du Bois, J.; Petasis, D.; Hendrich, M. P.; Krebs, C.; Huynh, B. H.; Lippard, S. J. *J. Am. Chem. Soc.* **1999**, *121*, 9893-9894.
- (38) SMART v5.05; Bruker AXS Inc.: Madison, WI, 1998.
- (39) Feig, A. L.; Bautista, M. T.; Lippard, S. J. *Inorg. Chem.* **1996**, *35*, 6892-6898.
- (40) Sheldrick, G. M. *SADABS v2.03: Area-Detector Absorption Correction*; University of Göttingen, Göttingen, Germany, 1999.
- (41) Spek, A. L. *PLATON, A Multipurpose Crystallographic Tool*; Utrecht University: Utrecht, The Netherlands, 1998.
- (42) Liu, K. E.; Valentine, A. M.; Wang, D.; Huynh, B. H.; Edmondson, D. E.; Salifoglou, A.; Lippard, S. J. *J. Am. Chem. Soc.* **1995**, *117*, 10174-10185.
- (43) Carlin, R. L. *Magnetochemistry*; Springer-Verlag: New York, 1986.
- (44) Lytle, F. W.; Sayers, D. E.; Stern, E. A. *Phys. B* **1989**, *158*, 701-722.
- (45) Lee, D.; Lippard, S. J., submitted for publication.
- (46) Randall, C. R.; Shu, L.; Chiou, Y.-M.; Hagen, K. S.; Ito, M.; Kitajima, N.; Lachicotte, R. J.; Zang, Y.; Que, L., Jr. *Inorg. Chem.* **1995**, *34*, 1036-1039.
- (47) Hush, N. S. *Prog. Inorg. Chem.* **1967**, *8*, 391-444.
- (48) Creutz, C. *Prog. Inorg. Chem.* **1983**, *30*, 1-73.
- (49) Rardin, R. L.; Tolman, W. B.; Lippard, S. J. *New J. Chem.* **1991**, *15*, 417.
- (50) Baik, M.-H.; Lee, D.; Lippard, S. J.; Friesner, R., unpublished results.
- (51) Citrin, P. H.; Ginsberg, A. P. *J. Am. Chem. Soc.* **1981**, *103*, 3673-3679.
- (52) Achim, C.; Bominaar, E. L.; Staples, R. J.; Münck, E.; Holm, R. H. *Inorg. Chem.* **2001**, *40*, 4389-4403.
- (53) Noodleman, L.; Baerends, E. J. *J. Am. Chem. Soc.* **1984**, *106*, 2316-2327.
- (54) Rodriguez, J. H.; Lee, D.; Lippard, S. J., unpublished results.

Table 4.1. Summary of X-ray Crystallographic Data

	2b·CH₂Cl₂	3b·3PhCl
formula	C ₉₆ H ₇₈ N ₂ O ₁₁ Cl ₂ F ₃ Fe ₂ S	C ₁₁₀ H ₉₁ O ₁₀ Cl ₃ F ₆ Fe ₂ P
fw	1707.26	1935.85
space group	<i>P</i> $\bar{1}$	<i>P</i> $\bar{1}$
<i>a</i> , Å	14.639(5)	15.454(5)
<i>b</i> , Å	14.886(5)	17.759(5)
<i>c</i> , Å	19.796(5)	19.679(5)
α , deg	87.550(5)	69.225(5)
β , deg	70.660(5)	81.798(5)
γ , deg	89.361(5)	70.115(5)
<i>V</i> , Å ³	4067(2)	4747(2)
<i>Z</i>	2	2
ρ_{calc} , g/cm ³	1.394	1.354
<i>T</i> , °C	-85	-85
$\mu(\text{Mo K}\alpha)$, mm ⁻¹	0.520	0.479
θ limits, deg	2.01 – 22.50	1.76 – 22.50
total no. of data	17280	20062
no. of unique data	10570	12354
no. of params	1058	1179
<i>R</i> (%) ^{<i>a</i>}	5.88	5.72
<i>wR</i> ² (%) ^{<i>b</i>}	12.85	14.47
max, min peaks, e/Å ³	0.760, -0.737	0.691, -1.065

^{*a*} $R = \Sigma ||F_o| - |F_c| | / \Sigma |F_o|$. ^{*b*} $wR^2 = \{\Sigma[w(F_o^2 - F_c^2)^2] / \Sigma[w(F_o^2)^2]\}^{1/2}$.

Table 4.2. Selected Bond Lengths (Å) and Angles (deg) for **2b** and **3b**.^a

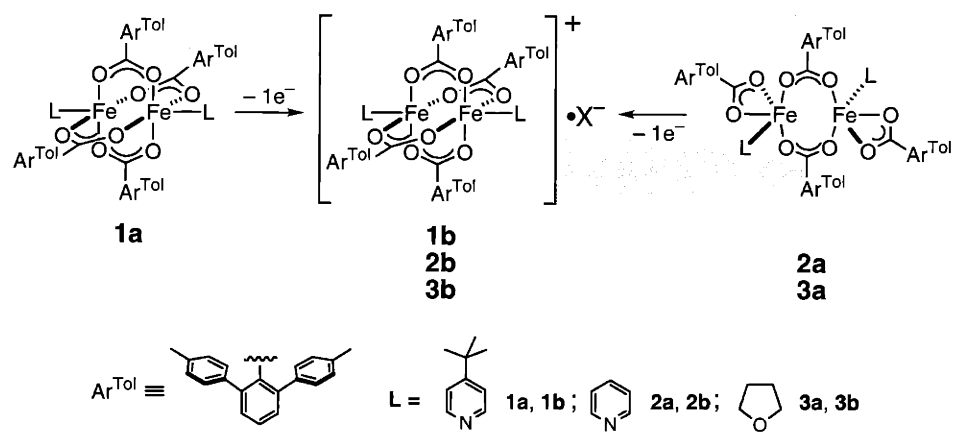
	2b	3b
Fe1...Fe2	2.6982(13)	2.6633(11)
Fe1-O1A	2.011(3)	2.009(3)
Fe1-O1B	2.008(3)	2.016(3)
Fe1-O1C	2.013(4)	2.007(3)
Fe1-O1D	2.012(4)	2.024(3)
Fe1-L1	2.104(4)	2.011(3)
Fe2-O2A	2.015(3)	2.024(3)
Fe2-O2B	1.989(3)	1.994(3)
Fe2-O2C	2.000(3)	2.016(3)
Fe2-O2D	2.005(3)	2.003(3)
Fe2-L2	2.085(4)	2.017(3)
Fe1-O1A-C1A	121.4(3)	122.1(3)
Fe1-O1B-C1B	125.4(3)	120.6(3)
Fe1-O1C-C1C	123.9(3)	126.1(3)
Fe1-O1D-C1D	122.2(3)	123.1(2)
Fe2-O2A-C1A	126.1(3)	125.0(3)
Fe2-O2B-C1B	122.3(3)	124.9(3)
Fe2-O2C-C1C	123.2(3)	120.8(3)
Fe2-O2D-C1D	123.5(3)	122.8(3)

^a Numbers in parentheses are estimated standard deviations of the last significant figures.

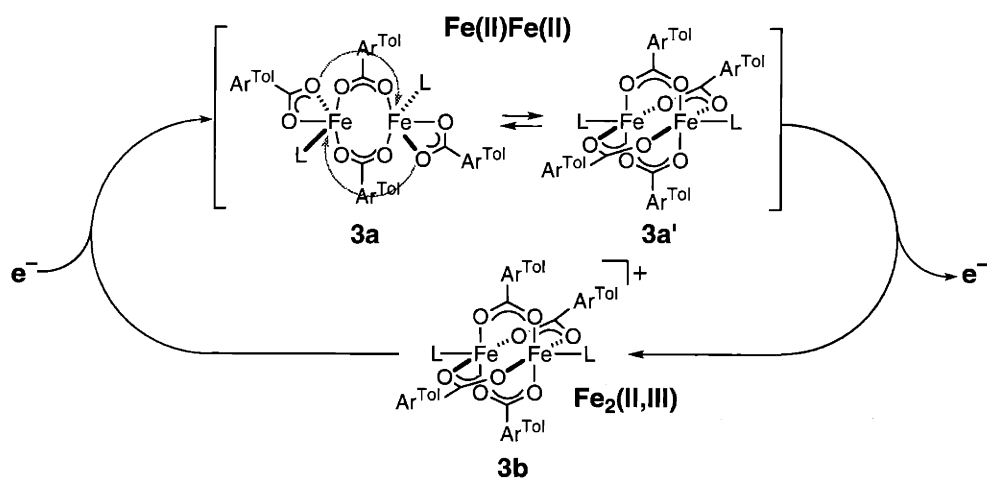
Table 4.3. Summary of Pertinent Structural and Spectroscopic Data for **1b–3b** and Related Mixed-Valence $S = 9/2$ Diiron(II,III) Systems.

	Fe...Fe (Å)	λ_{max} , nm (e, $M^{-1} \text{cm}^{-1}$)	$\Delta V_{1/2}$ calcd ^a (cm^{-1})	$\Delta V_{1/2}$ measured (cm^{-1})	μ_{eff}/μ_B	δ (mm/s)	ΔE_Q (mm/s)	ref
1b	2.713(3)	670 (3200) 450 (1600) ^b 380 (3100) ^b	5880	3590	11.0 ^c	0.65	-0.63	this work
2b	2.6982(13)	665 (2900) 455 (1800) ^b 385 (3400) ^b	5900	3970	10.2 ^c			
3b	2.6633(11)	620 (2700) 450 (1600) ^b 385 (3200) ^b	6120	3670	10.5 ^c			
A	2.509(6)	758 (2400)	5500	3800	10.5 ^d	0.74	-2.14	30a,b,d
B	2.7414(8)	1060 (1250)	4670	3980	10.0 ^e	0.84	2.09	31a
C	2.6241(9)	780 (2000)				0.76	2.0	32

^a $\Delta V_{1/2} = [2310 \nu_{\text{max}}]^{1/2}$ (ref 47, 48). ^b Shoulders determined from derivative spectra. ^c 300 K. ^d 30–300 K. ^e 70–300 K.



Scheme 4.1.



Scheme 4.2.

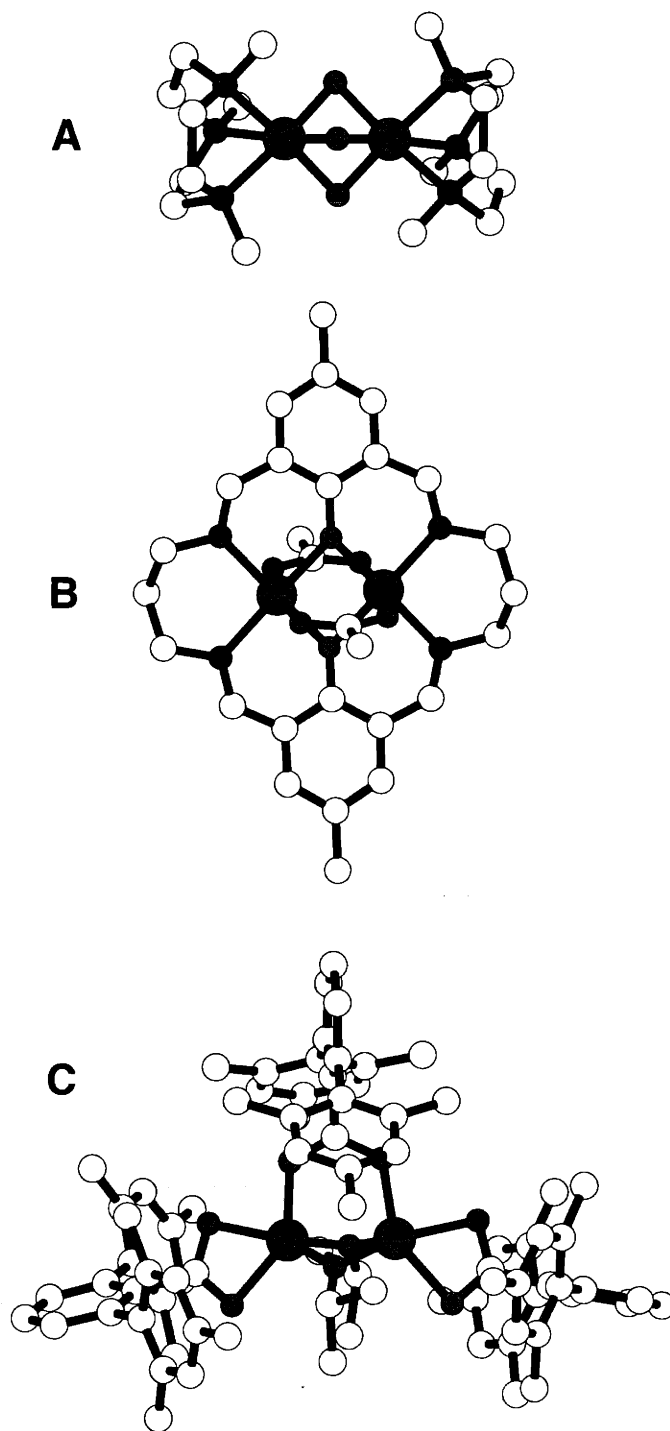


Figure 4.1. Solid-state structures of the cations in $[(\text{Me}_3\text{TACN})_2\text{Fe}(\mu\text{-OH})_3](\text{ClO}_4)_2$ (A), $[\text{L}^1\text{Fe}_2(\mu\text{-OAc})_2](\text{ClO}_4)$ (B), and $[\text{Fe}_2(\mu\text{-O}^i\text{Pr})_2(\mu\text{-O}_2\text{CAr}^{\text{Mes}})(\text{O}_2\text{CAr}^{\text{Mes}})_2]$ (C), generated using the crystallographic coordinates: N is blue, O is bright red, and Fe is dark red.

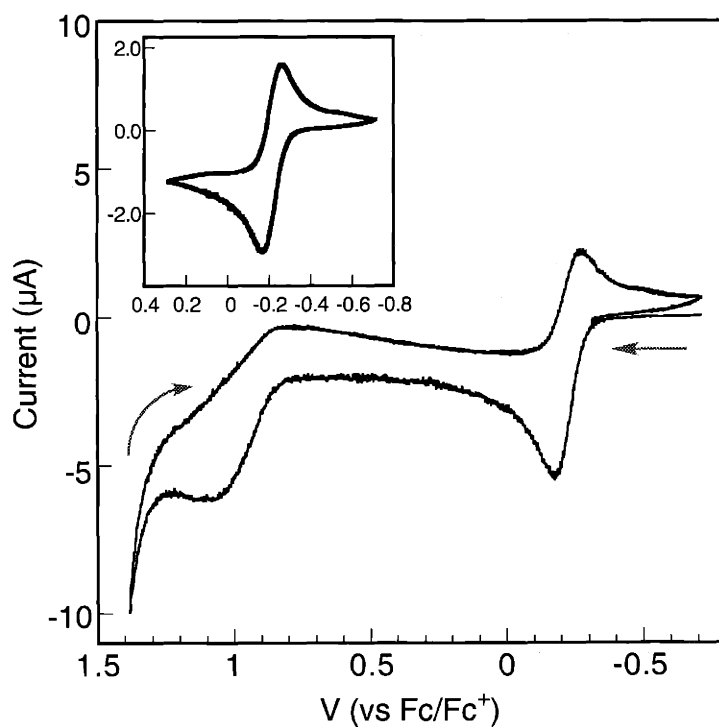


Figure 4.2. Cyclic voltammograms of $[\text{Fe}_2(\mu\text{-O}_2\text{CAr}^{\text{Tol}})_4(4\text{-}^t\text{BuC}_5\text{H}_4\text{N})_2]$ (**1a**) in CH_2Cl_2 with $0.5 \text{ M } (\text{Bu}_4\text{N})(\text{PF}_6)$ as supporting electrolyte and a scan rate of 50 mV/s . The inset shows the reversible wave observed when the experiment was conducted at potentials below $+300 \text{ mV vs Fc/Fc}^+$ (scan rate = 25 mV/s).

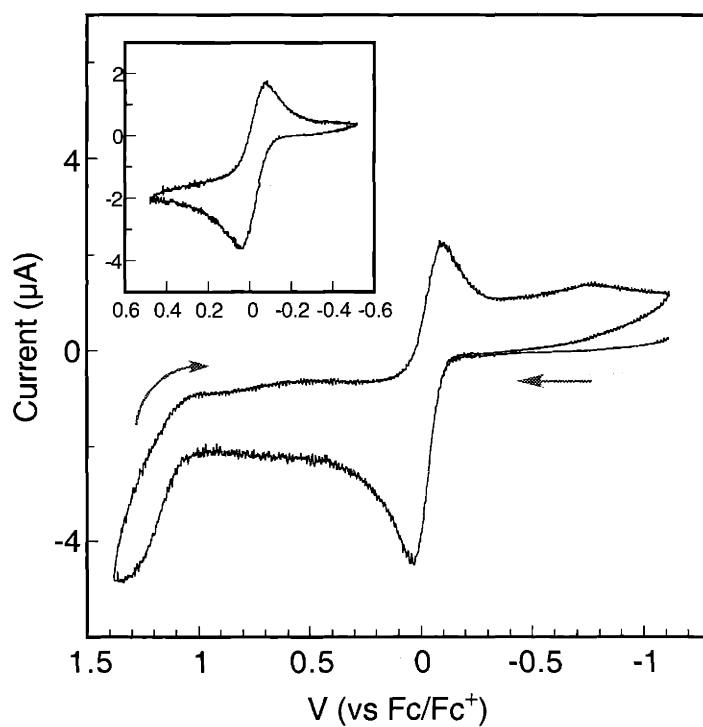


Figure 4.3. Cyclic voltammograms of $[\text{Fe}_2(\mu\text{-O}_2\text{CAr}^{4\text{-FPh}})_4(4\text{-}^t\text{BuC}_5\text{H}_4\text{N})_2]$ in CH_2Cl_2 with 0.5 M $(\text{Bu}_4\text{N})(\text{PF}_6)$ as supporting electrolyte and a scan rate of 50 mV/s. The inset shows the reversible wave observed when the experiment was conducted at potentials below +500 mV vs Fc/Fc^+ (scan rate = 25 mV/s).

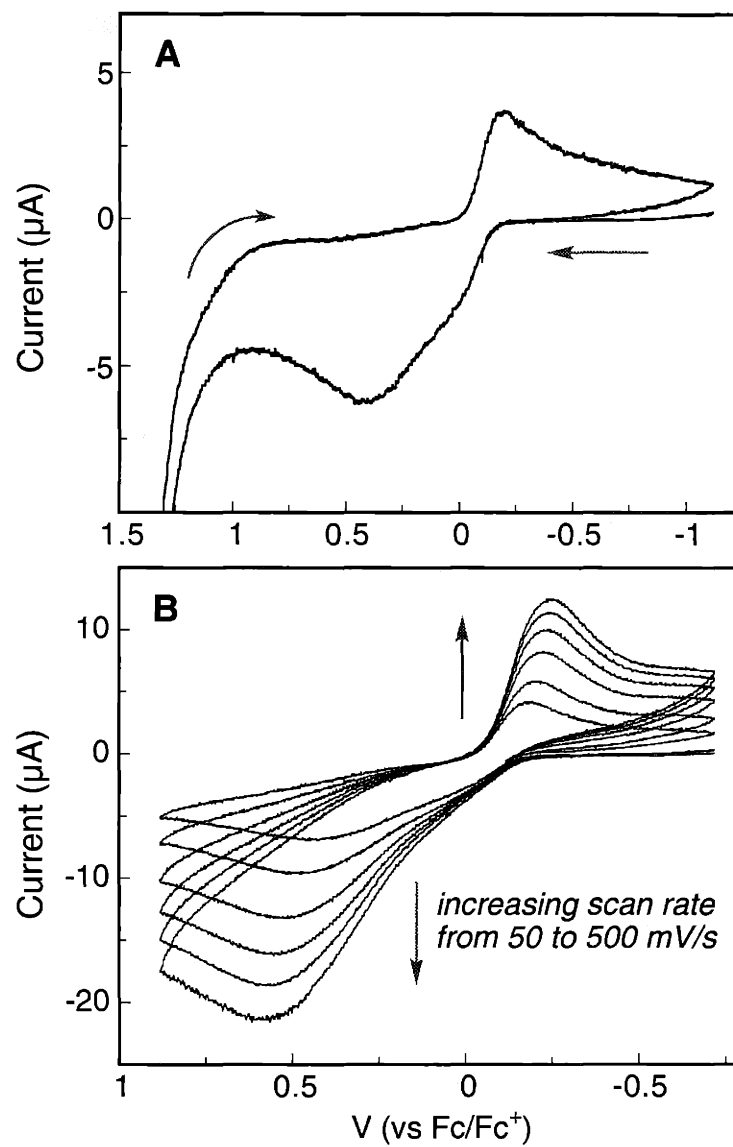


Figure 4.4. Cyclic voltammograms of $[\text{Fe}_2(\mu\text{-O}_2\text{CAr}^{\text{Tol}})_2(\text{O}_2\text{CAr}^{\text{Tol}})_2(\text{THF})_2]$ (**3a**) in CH_2Cl_2 with 0.5 M $(\text{Bu}_4\text{N})(\text{PF}_6)$ as supporting electrolyte and a scan rate of 50 mV/s (A); with increasing scan rates from 50 mV/s to 500 mV/s (B).

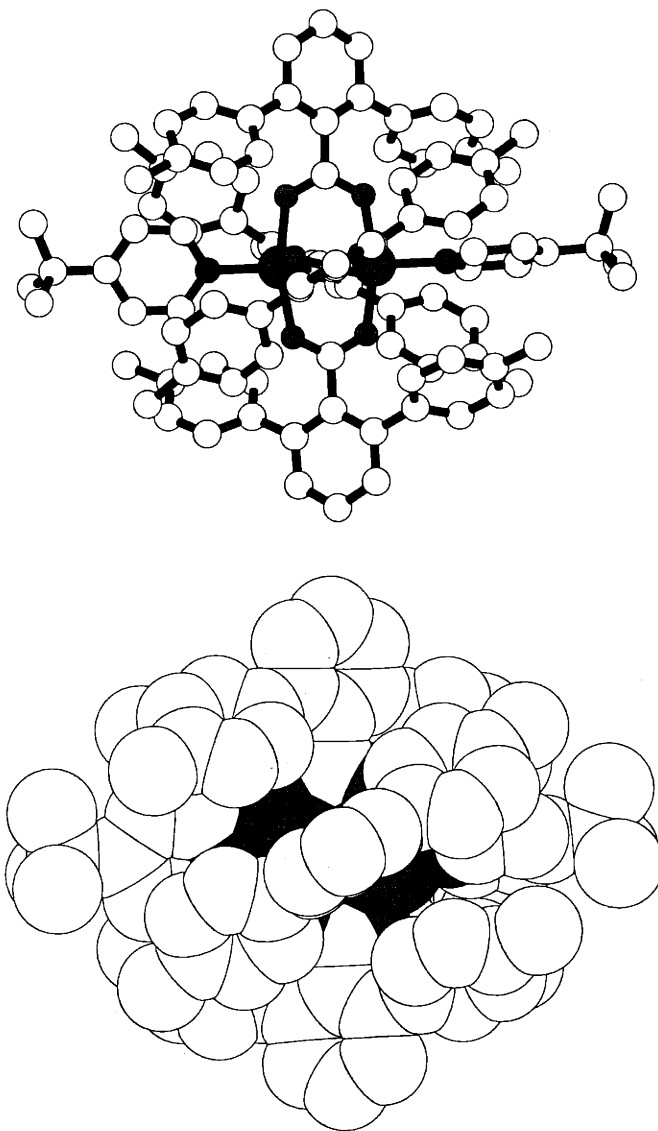


Figure 4.5. Ball and stick (top) and space-filling (bottom) representation of the solid-state structure of $[\text{Fe}_2(\mu\text{-O}_2\text{CAr}^{\text{Tol}})_4(4\text{-}^t\text{BuC}_5\text{H}_4\text{N})_2]^+$ cation generated using the crystallographic coordinates, where N is blue, O is bright red, and Fe is dark red.

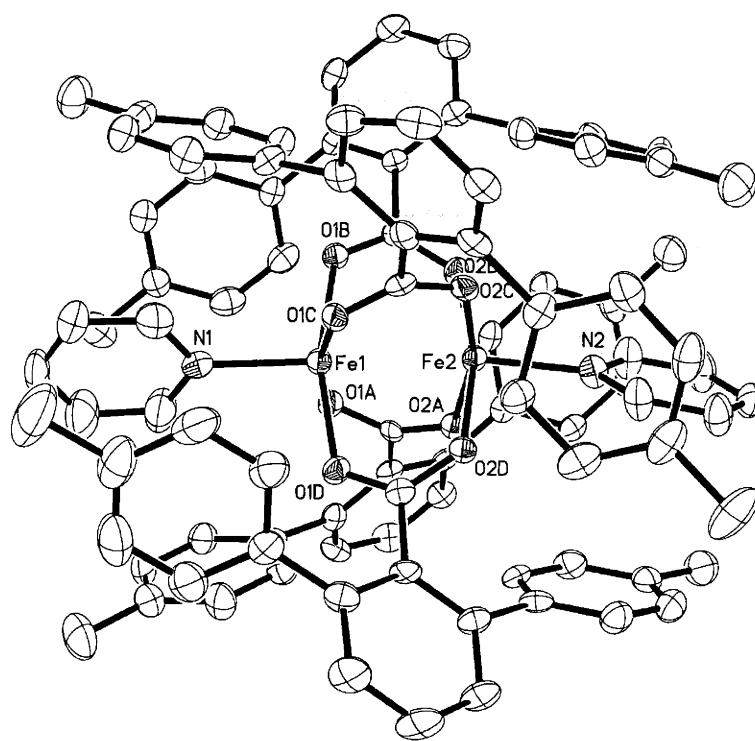


Figure 4.6. ORTEP diagram of the cation in $[\text{Fe}_2(\mu\text{-O}_2\text{CAr}^{\text{Tol}})(\text{C}_5\text{H}_5\text{N})_2](\text{OTf})$ (**2b**) with thermal ellipsoids at 50% probability.

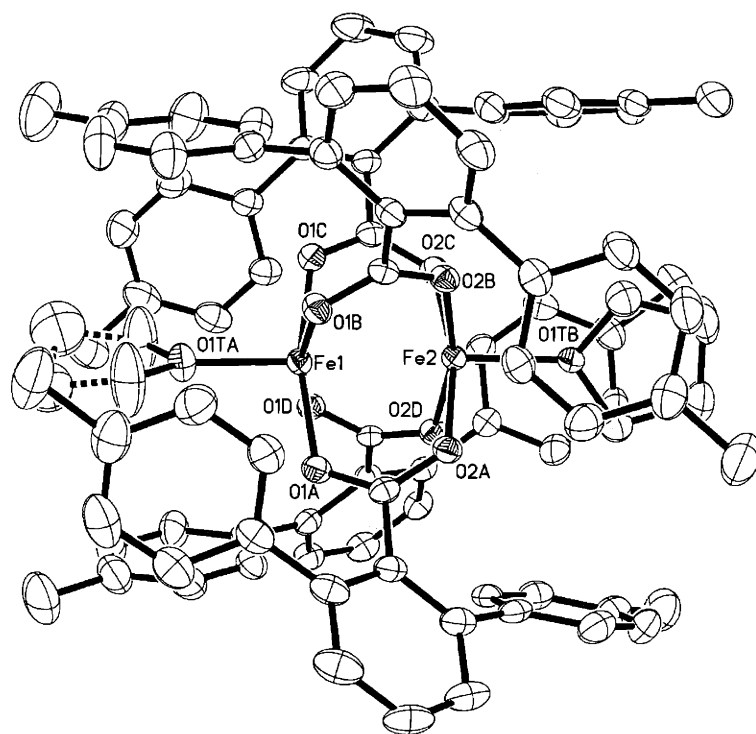


Figure 4.7. ORTEP diagram of the cation in $[\text{Fe}_2(\mu\text{-O}_2\text{CAr}^{\text{Tol}})_4(\text{THF})_2](\text{PF}_6)$ (3b) with thermal ellipsoids at 50% probability.

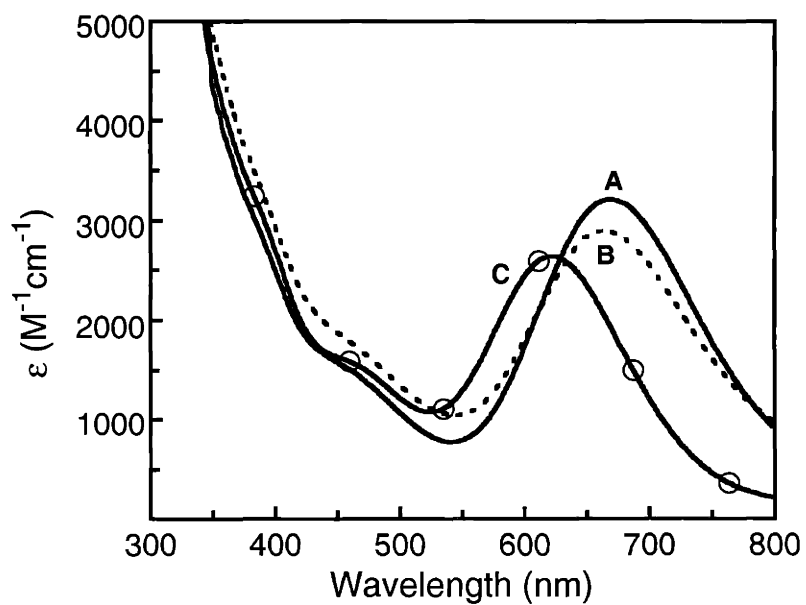


Figure 4.8. Electronic absorption spectra of **1b–3b** in CH_2Cl_2 showing the IVCT transitions. (A) $[\text{Fe}_2(\mu\text{-O}_2\text{CAr}^{\text{Tol}})_4(4\text{-}^t\text{BuC}_5\text{H}_4\text{N})_2](\text{PF}_6)$ (**1b**) (—); (B) $[\text{Fe}_2(\mu\text{-O}_2\text{CAr}^{\text{Tol}})_4(\text{C}_5\text{H}_5\text{N})_2](\text{OTf})$ (**2b**) (.....); (C) $[\text{Fe}_2(\mu\text{-O}_2\text{CAr}^{\text{Tol}})_4(\text{THF})_2](\text{PF}_6)$ (**3b**) (— with circle).

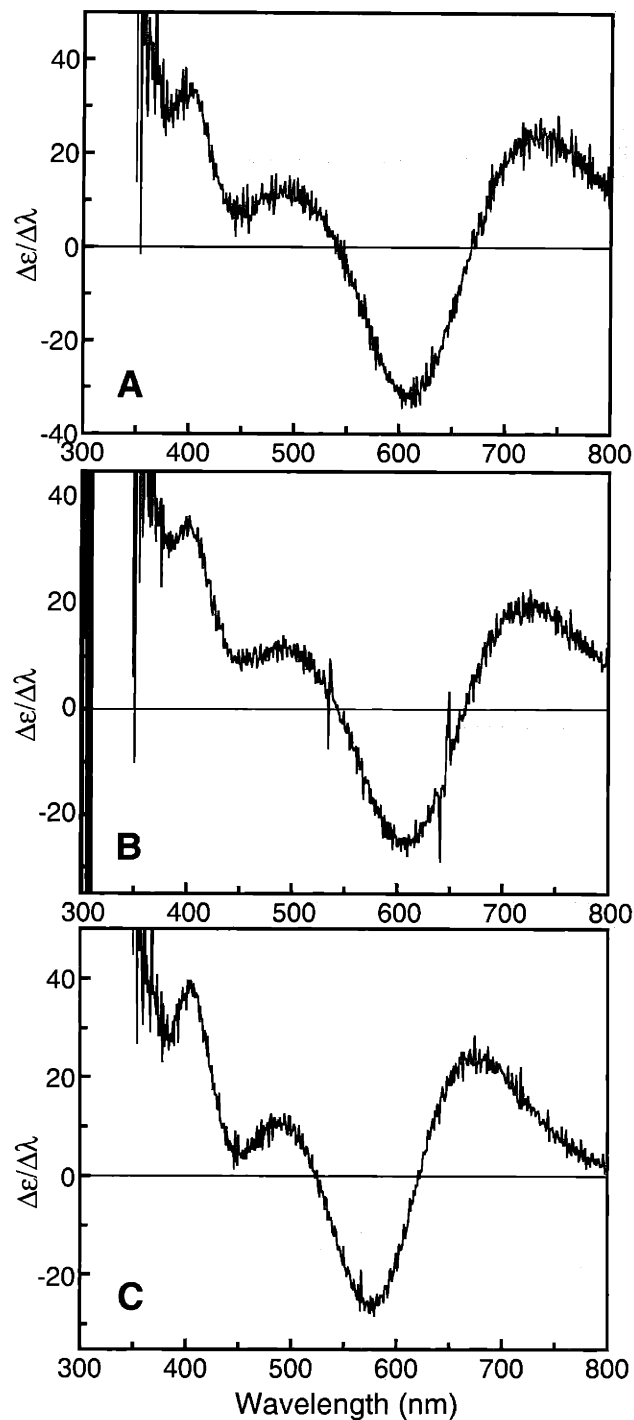


Figure 4.9. First-derivative electronic absorption spectra of **1b–3b** in CH_2Cl_2 . (A) $[\text{Fe}_2(\mu\text{-O}_2\text{CAr}^{\text{Tol}})_4(4\text{-}^t\text{BuC}_5\text{H}_4\text{N})_2](\text{PF}_6)$ (**1b**); (B) $[\text{Fe}_2(\mu\text{-O}_2\text{CAr}^{\text{Tol}})_4(\text{C}_5\text{H}_5\text{N})_2](\text{OTf})$ (**2b**); (C) $[\text{Fe}_2(\mu\text{-O}_2\text{CAr}^{\text{Tol}})_4(\text{THF})_2](\text{PF}_6)$ (**3b**).

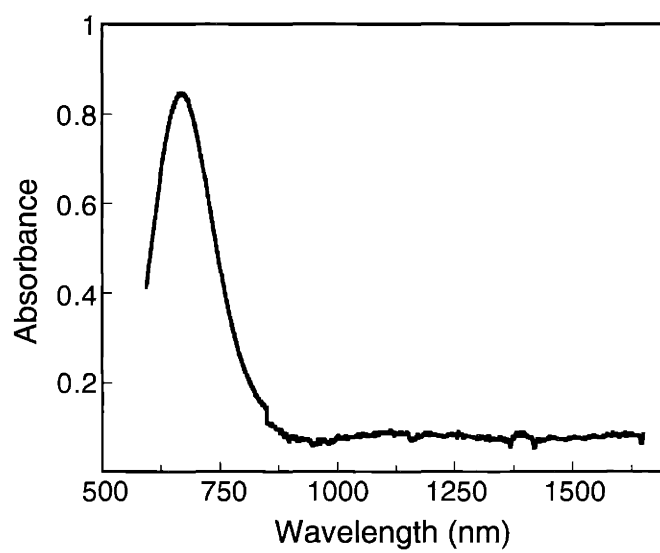


Figure 4.10. Electronic absorption spectra of $[\text{Fe}_2(\mu\text{-O}_2\text{CAr}^{\text{Tol}})_4(4\text{-}^t\text{BuC}_5\text{H}_4\text{N})_2]\text{-}(\text{PF}_6)$ (**1b**) in CH_2Cl_2 .

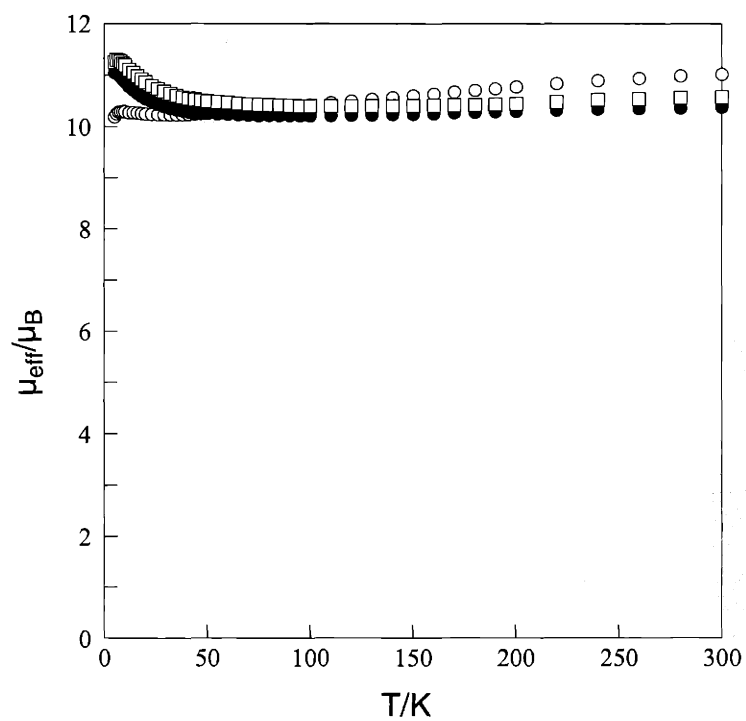


Figure 4.11. Effective magnetic moments, T 5–300 K, for $[\text{Fe}_2(\mu\text{-O}_2\text{CAr}^{\text{Tol}})_4(4\text{-}^t\text{BuC}_5\text{H}_4\text{N})_2](\text{PF}_6)$ (**1b**) (○), $[\text{Fe}_2(\mu\text{-O}_2\text{CAr}^{\text{Tol}})_4(\text{py})_2](\text{OTf})$ (**2b**) (●), and $[\text{Fe}_2(\mu\text{-O}_2\text{CAr}^{\text{Tol}})_4(\text{THF})_2](\text{PF}_6)$ (**3b**) (□).

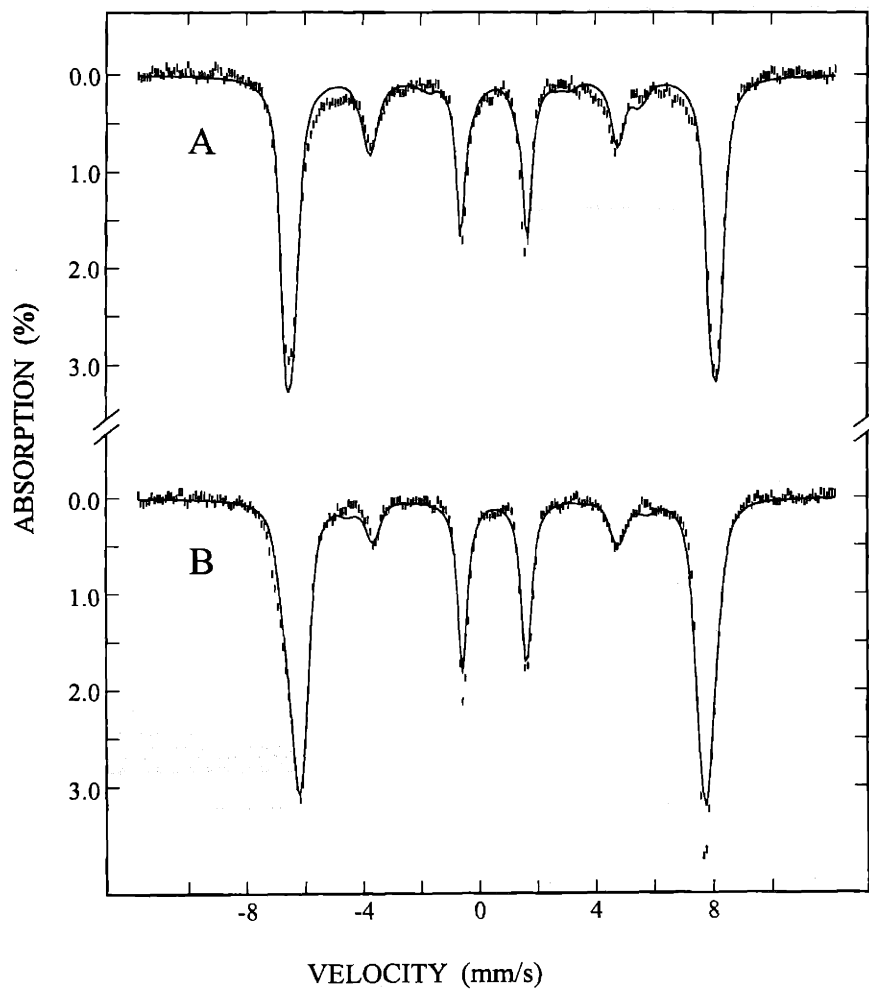


Figure 4.12. Mössbauer spectra of the solid powder sample of $[\text{Fe}_2(\mu\text{-O}_2\text{CAr}^{\text{Tol}})_4(4\text{-}^t\text{BuC}_5\text{H}_4\text{N})_2](\text{PF}_6)$ (**1b**) recorded at 4.2 K with a magnetic field of 4 T (A) and 8 T (B) parallel to the γ -rays. The solid lines are theoretical simulations using the parameters listed in the ref. 34.

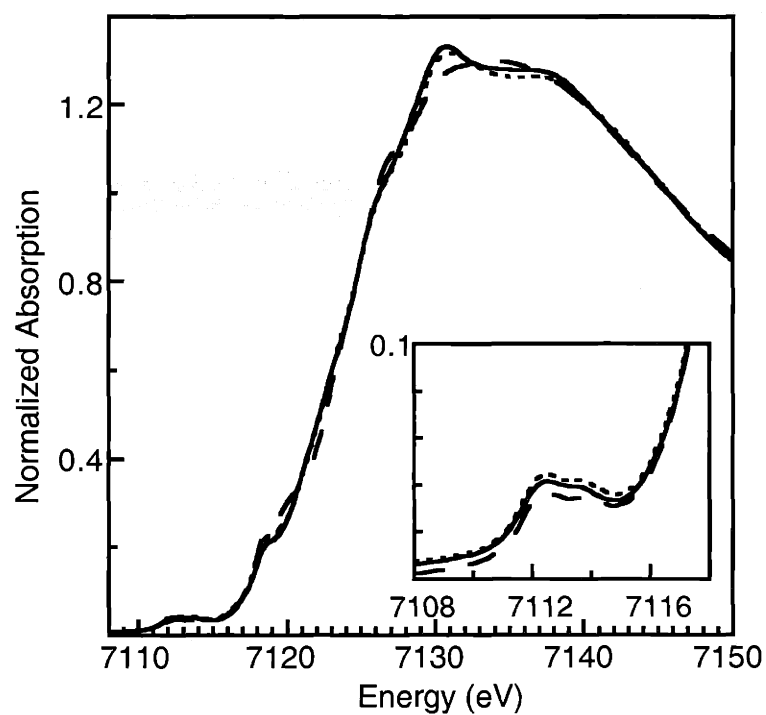


Figure 4.13. Fe K-edge and pre-edge transitions (inset) for $[\text{Fe}_2(\mu\text{-O}_2\text{CAr}^{\text{Tol}})_4(4\text{-}^t\text{BuC}_5\text{H}_4\text{N})_2](\text{PF}_6)$ (**1b**) (—), $[\text{Fe}_2(\mu\text{-O}_2\text{CAr}^{\text{Tol}})_4(\text{C}_5\text{H}_5\text{N})_2](\text{OTf})$ (**2b**) (⋯), and $[\text{Fe}_2(\mu\text{-O}_2\text{CAr}^{\text{Tol}})_4(\text{THF})_2](\text{PF}_6)$ (**3b**) (---). Note the strong similarities in all three edges and pre-edges, suggesting similarities in their geometric and electronic structures, respectively.

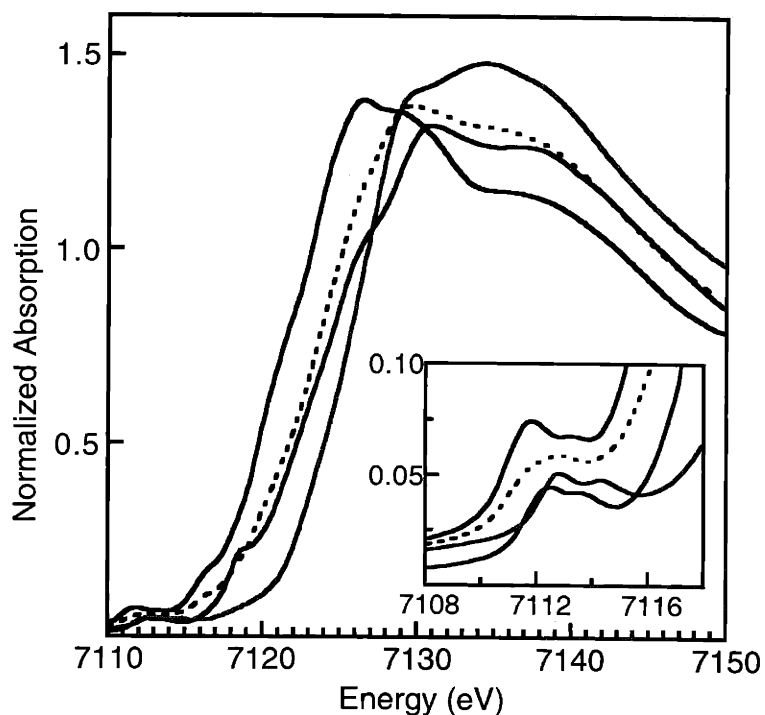


Figure 4.14. Fe K-edge and pre-edge transitions (inset) for $[\text{Fe}_2(\mu\text{-O}_2\text{CAr}^{\text{Tol}})_4(4\text{-}^t\text{BuC}_5\text{H}_4\text{N})_2]$ (**1a**) (blue), $[\text{Fe}_2(\mu\text{-O}_2\text{CAr}^{\text{Tol}})_4(4\text{-}^t\text{BuC}_5\text{H}_4\text{N})_2](\text{PF}_6)$ (**1b**) (green), $[\text{Fe}_2(\mu\text{-OH})_2(\mu\text{-O}_2\text{CAr}^{\text{Tol}})_2(\text{O}_2\text{CAr}^{\text{Tol}})_2(4\text{-}^t\text{BuC}_5\text{H}_4\text{N})_2]$ (**1c**) (red), and a 50:50 weighted addition of the edges for **1a** and **1c** (dashed lines). Note that the edge for the mixed-valence complex **1b** is intermediate in energy between edges for the related diiron(II) complex **1a** and diiron(III) complex **1c**, and comparable to the 50:50 weighted addition of these two edges. Also note that the mixed-valence complex **1b** has only two (rather than four) pre-edge features, which are likewise intermediate in energy between those for diiron(II) and diiron(III) species.

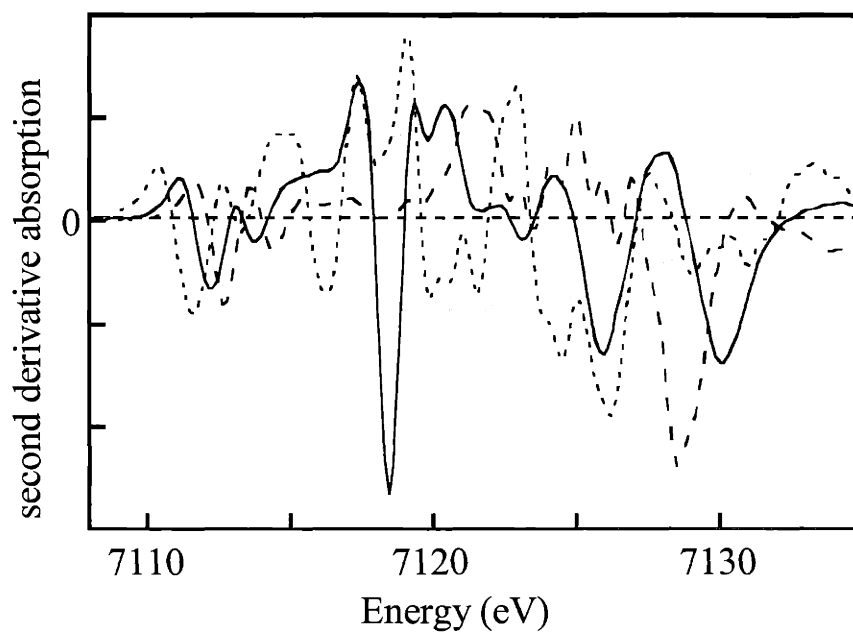


Figure 4.15. Second derivatives of the K-edge spectra for $[\text{Fe}_2(\mu\text{-O}_2\text{CAr}^{\text{Tol}})_4(4\text{-}^t\text{BuC}_5\text{H}_4\text{N})_2]$ (**1a**) (····), $[\text{Fe}_2(\mu\text{-O}_2\text{CAr}^{\text{Tol}})_4(4\text{-}^t\text{BuC}_5\text{H}_4\text{N})_2](\text{PF}_6)$ (**1b**) (—), and $[\text{Fe}_2(\mu\text{-OH})_2(\mu\text{-O}_2\text{CAr}^{\text{Tol}})_2(\text{O}_2\text{CAr}^{\text{Tol}})_2(4\text{-}^t\text{BuC}_5\text{H}_4\text{N})_2]$ (**1c**) (----). Note that the spectrum for the mixed-valence species does not resemble a superposition of the diiron(II) and diiron(III) species, as would be expected for valence-localized complex.

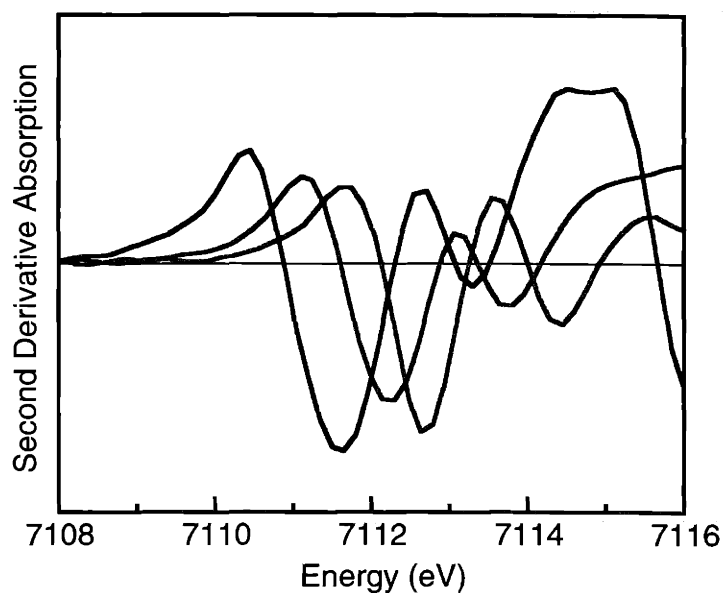


Figure 4.16. Second derivatives of the pre-edge region ($1s \rightarrow 3d$ transition) for $[\text{Fe}_2(\mu\text{-O}_2\text{CAr}^{\text{Tol}})_4(4\text{-}^t\text{BuC}_5\text{H}_4\text{N})_2]$ (**1a**) (blue), $[\text{Fe}_2(\mu\text{-O}_2\text{CAr}^{\text{Tol}})_4(4\text{-}^t\text{BuC}_5\text{H}_4\text{N})_2](\text{PF}_6)$ (**1b**) (green), and $[\text{Fe}_2(\mu\text{-OH})_2(\mu\text{-O}_2\text{CAr}^{\text{Tol}})_2(\text{O}_2\text{CAr}^{\text{Tol}})_2(4\text{-}^t\text{BuC}_5\text{H}_4\text{N})_2]$ (**1c**) (red). Note that the spectrum for the mixed-valence species does not contain individual transitions at the same approximate energies of the related diiron(II) and diiron(III) complexes, as would be expected of a valence-localized complex. Rather, the two transitions for **1b** lie intermediate in energy to those for **1a** and **1c**.

Chapter V

Spectroscopic Studies of a Putative O₂-Adduct of a Carboxylate-Bridged Diiron Complex: Effects of Nitrogen-Rich Coordination in Dioxygen Activation

Introduction

The concept of a *bioinorganic chip* has been suggested to designate architecturally related metal-ligand modules that carry out distinctive functions depending on the nature of the biological circuits in which they are housed.¹ Two different types of iron-containing bioinorganic chips, heme and carboxylate-bridged dinuclear non-heme cofactors, have evolved in nature to harness the oxidizing power of the ubiquitous small molecule substrate, dioxygen.

Heme proteins participate in binding and/or activation of dioxygen. Hemoglobin (Hb) and myoglobin (Mb) are responsible for storage and transport of O₂ in most aerobic organisms,^{2,3} whereas cytochrome P450 (cP450) incorporates one oxygen atom of O₂ into various organic substrates.⁴⁻⁶ Although these proteins are closely related in that five-coordinate heme iron(II) centers bind dioxygen, the chemistry evolving from the initial O₂-adduct is modulated by ligands derived from the protein side chains, as well as by the supply of additional electrons and protons. The imidazole-bound heme sites in Hb and Mb reversibly bind dioxygen as a superoxide ligand, which is stabilized by hydrogen-bonding interaction with a distal histidine residue.⁷ Enzymes belonging to the cP450 family utilize heme-thiolate modules to activate dioxygen to access oxo iron(IV)-porphyrin radical cations that effect a wide range of organic transformations. Formal four-electron reduction of dioxygen is assisted by the controlled delivery of electrons and protons, as well as by the ligation of the strongly electron donating cysteine thiolate.

Analogous strategies are adopted in carboxylate-bridged non-heme diiron proteins that process dioxygen in an analogous fashion. Hemerythrin (Hr), a protein that reversibly binds dioxygen, utilizes a (μ -hydroxo)di(μ -carboxylato)diiron(II) unit supported by five histidine imidazole groups.⁸ The open coordination site on one iron atom is used to bind and release dioxygen, a

process that induces minimal structural reorganization in the first coordination sphere. Structurally related di(μ -carboxylato)-diiron(II) centers occur in the hydroxylase component of soluble methane monooxygenase (MMOH), the R2 subunit of ribonucleotide reductase (RNR-R2), and stearyl-acyl carrier protein (ACP) Δ^9 desaturase ($\Delta 9D$).⁹ In these enzymes, four carboxylate and two histidine ligands support coordinatively unsaturated diiron(II) units that bind and activate dioxygen. Their anion-rich environment is significantly different from the neutral, nitrogen-rich coordination in Hr. In dioxygen-activating enzymes, structurally flexible and more electron-donating carboxylate ligands enable access to a high-valent diiron(IV) species following O–O bond cleavage of the (peroxo)diiron(III) precursor.

The shift in function from dioxygen-binding to dioxygen-activation is apparently dictated by the ancillary ligands that support *bioinorganic chips* comprising two iron atoms bridged by two carboxylate residues. In this chapter, we demonstrate this principle by using small synthetic surrogates. Previously, we¹⁰⁻¹³ and others^{14,15} assembled biomimetic tetracarboxylate diiron(II) complexes by using *m*-terphenyl-derived carboxylate ligands, $\text{Ar}^{\text{Tol}}\text{CO}_2^-$ or $\text{Ar}^{\text{Mes}}\text{CO}_2^-$.¹⁶ Two such compounds, $[\text{Fe}_2(\mu\text{-O}_2\text{CAr}^{\text{Tol}})_2(\text{O}_2\text{CAr}^{\text{Tol}})_2(\text{C}_5\text{H}_5\text{N})_2]$ and $[\text{Fe}_2(\mu\text{-O}_2\text{CAr}^{\text{Tol}})_4-(4\text{-}^t\text{BuC}_5\text{H}_4\text{N})_2]$, react with dioxygen at low temperature to afford a mixed-valent iron(III)iron(IV) species,^{11,17} a process that closely mimics the chemistry of RNR-R2.^{9,18} We reasoned that formal replacement of the two terminal bidentate carboxylate ligands by neutral amine ligands would significantly alter electron donation to the metal centers. Such an electronic modification could destabilize the transition state leading to the iron(IV)-containing species and allow us to trap the preceding intermediate, a putative (peroxo)diiron(III) complex. Accordingly, we prepared and structurally characterized two carboxylate-bridged diiron(II) complexes $[(\text{Me}_3\text{TACN})_2\text{Fe}_2(\mu\text{-}$

$\text{O}_2\text{CAr}^{\text{Tol}})_2\text{L}_2](\text{OTf})_2$ (L = MeCN (**1a**); H₂O (**2a**)).¹⁶ Upon reaction with dioxygen at low temperature, **1a** affords the intensely colored diamagnetic intermediate **1b**, which decays into (μ -oxo)diiron(III) product(s) **1c**. The spectroscopic properties of this metastable dioxygen adduct are described herein and compared with those of related systems. The biological implications of such structure–function relationships are also discussed.

Experimental Section

General Considerations. All reagents were obtained from commercial suppliers and used as received unless otherwise noted. Dichloromethane and acetonitrile were distilled over CaH₂ under nitrogen. Diethyl ether, THF, and pentanes were saturated with nitrogen and purified by passage through activated Al₂O₃ columns under nitrogen.¹⁹ Dioxygen (99.994%, BOC Gases) was dried by passing the gas stream through a column of Drierite. ¹⁸O-Enriched dioxygen (99%) was supplied by ICON, N.Y. The compounds Fe(OTf)₂·2MeCN²⁰ and Ar^{Tol}CO₂H²¹ were prepared according to literature procedures. Air-sensitive manipulations were carried out under nitrogen in a Vacuum Atmospheres drybox or by standard Schlenk line techniques.

$[(\text{Me}_3\text{TACN})_2\text{Fe}(\mu\text{-O}_2\text{CAr}^{\text{Tol}})_2(\text{MeCN})_2](\text{OTf})_2$ (**1a**). To a rapidly stirred MeCN solution (10 mL) of Fe(OTf)₂·2MeCN (229 mg, 0.52 mmol) was added dropwise neat Me₃TACN¹⁶ (100 μ L, 0.52 mmol). The color of the solution turned dark violet. The reaction mixture was stirred for 2 h and treated with NaO₂CAr^{Tol} (177 mg, 0.55 mmol) and MeCN (10 mL). The heterogeneous mixture was stirred for 4 h to afford a pale yellow solution. Volatile fractions were removed under reduced pressure and the residual beige solid was extracted into CH₂Cl₂ (5 mL). Insoluble material was filtered off and MeCN (0.5 mL) was added to the filtrate. Vapor diffusion of Et₂O afforded X-ray quality colorless

blocks of **1a** (234 mg, 0.16 mmol, 63%). FT-IR (KBr, cm^{-1}) 2862, 2838, 2820, 2293, 2264, 1599, 1517, 1494, 1461, 1448, 1384, 1367, 1263, 1224, 1151, 1063, 1031, 1013, 993, 893, 836, 821, 804, 783, 769, 747, 719, 698, 635, 580, 550, 527, 518. Anal. Calcd for $\text{C}_{66}\text{H}_{82}\text{N}_8\text{O}_{10}\text{F}_6\text{Fe}_2\text{S}_2 \cdot 0.75\text{CH}_2\text{Cl}_2$: C, 53.42; H, 5.61; N, 7.47. Found: C, 53.27; H, 5.85; N, 7.74.

$[(\text{Me}_3\text{TACN})_2\text{Fe}_2(\mu\text{-O}_2\text{CAr}^{\text{Tol}})_2(\text{H}_2\text{O})_2](\text{OTf})_2$ (**2a**). This compound was prepared in a similar manner to **1a**. Following extraction of the beige solid into CH_2Cl_2 , the filtrate was treated with Ar-saturated H_2O (2 equiv) and evaporated to dryness. Recrystallization of the residual solid material from $\text{CH}_2\text{Cl}_2/\text{Et}_2\text{O}$ afforded pale yellow blocks of **2a** (260 mg, 0.187 mmol, 36%), suitable for X-ray crystallography. This crystalline material readily loses solvent to afford an ivory powder. FT-IR (KBr, cm^{-1}) 3623, 3276, 3170, 2920, 2866, 2823, 1591, 1571, 1516, 1466, 1450, 1382, 1302, 1285, 1243, 1224, 1181, 1158, 1083, 1066, 1029, 1014, 991, 894, 835, 822, 808, 796, 770, 747, 731, 718, 699, 637, 580. Anal. Calcd for $\text{C}_{62}\text{H}_{80}\text{N}_6\text{O}_{12}\text{F}_6\text{Fe}_2\text{S}_2$: C, 53.53; H, 5.80; N, 6.04. Found C, 53.37; H, 5.99; N, 6.13.

X-ray Crystallographic Studies. Intensity data were collected on a Bruker (formerly Siemens) CCD diffractometer with graphite-monochromated Mo $\text{K}\alpha$ radiation ($\lambda = 0.71073 \text{ \AA}$), controlled by a Pentium-based PC running the SMART software package.²² Single crystals were mounted at room temperature on the tips of quartz fibers, coated with Paratone-N oil, and cooled to 188 K under a stream of cold nitrogen maintained by a Bruker LT-2A nitrogen cryostat. Data collection and reduction protocols are described elsewhere.²³ The structures were solved by direct methods and refined on F^2 by using the SHELXTL software package.²⁴ Empirical absorption corrections were applied with SADABS,²⁵ part of the SHELXTL program package, and the structures were checked for higher symmetry by the program PLATON.²⁶ All non-hydrogen atoms were refined anisotropically unless otherwise noted. Hydrogen atoms were assigned

idealized positions and given thermal parameters equivalent to either 1.5 (methyl hydrogen atoms) or 1.2 (all other hydrogen atoms) times the thermal parameter of the carbon atom to which they were attached. The hydrogen atoms associated with the coordinated water molecules in **2a** were located in the difference Fourier map and refined isotropically; those of the disordered solvent molecules were not included in the refinement. One of the two triflate counterions in **1a** was disordered over two positions. The atoms were distributed at 0.55 and 0.45 occupancies and refined isotropically. The CH₂Cl₂ solvent molecule in the structure of **2a** was distributed over two positions (0.6 and 0.4 occupancies). The triflate anion was disordered over two positions and refined to 0.75 and 0.25 occupancies. Pertinent crystallographic information is provided in Table 5.1.

Generation of a Dioxygen Adduct. In a typical reaction, a THF solution of **1a** was placed in a vessel that was subsequently sealed with a rubber septum and cooled to -78 °C in a dry ice/acetone bath. Dry dioxygen was bubbled directly into the cold solution via a stainless steel needle. The solution immediately turned dark blue-green, indicating the formation of **1b**.

Physical Measurements. FT-IR spectra were recorded on a Bio Rad FTS-135 instrument with Win-IR software. UV-vis spectra were recorded on a Hewlett Packard 8453 diode array spectrophotometer. Low-temperature UV-vis experiments were executed by using a custom-made quartz cuvette with a 1-cm path length fused into a vacuum-jacketed dewar. EPR spectra were recorded on a Bruker Model 300 ESP X-band spectrometer operating at 9.42 GHz. Liquid helium temperatures were maintained with an Oxford Instruments EPR 900 cryostat, and liquid nitrogen temperatures were obtained with an EPR finger dewar. For all measurements ~5 mM frozen solutions were prepared in THF.

Resonance Raman Spectroscopy. A Coherent Innova 90 Kr⁺ laser with an excitation wavelength of 647.1 nm and 50 mW of power was used to acquire Ra-

man data. A 0.6 m single monochromator (1200 grooves/nm grating), with an entrance slit of 100 μm , and a TE-CCD-1100-PB-VISAR detector (Princeton Instruments, Inc.) cooled to $-40\text{ }^{\circ}\text{C}$ were used in a standard backscattering configuration. A holographic notch filter (Kaiser Optical Systems) was used to attenuate Rayleigh scattering. Spectra were collected in THF solution at $-78\text{ }^{\circ}\text{C}$ with the same low-temperature dewar used in UV-vis studies. Solutions were made as concentrated as possible, $\sim 10\text{ mM}$, to ensure an optimal signal-to-noise ratio. A total of 200 scans, each with a 1 s exposure time, were typically collected for each sample. Raman shifts were calibrated with DMF as an external standard. The data were processed on a Gateway 2000 computer using WINSPEC 3.2.1 software (Princeton Instruments, Inc.).

^{57}Fe Mössbauer Spectroscopy. Mössbauer spectra were obtained on an MS1 spectrometer (WEB Research Co.) with a ^{57}Co source in a Rh matrix maintained at room temperature in the MIT Department of Chemistry Instrumentation Facility. Solid samples were prepared by suspending $\sim 0.04\text{ mmol}$ of the powdered material in Apeizon N grease and packing the mixture into a nylon sample holder. A frozen THF solution sample ($\sim 15\text{ mM}$) of **1a** was made by freezing at 77 K. Oxygenation of **1a** in THF was conducted at $-78\text{ }^{\circ}\text{C}$. Dry dioxygen (60 mL) was carefully delivered through a saturated THF solution of **1a** ($\sim 15\text{ mM}$, 1 mL) and the resulting dark blue-green solution of **1b** was kept at $-78\text{ }^{\circ}\text{C}$ for 10 min. The nylon sample holder was held in thermal contact with an acetone/dry ice bath throughout the reaction. The reaction was quenched by freezing the mixture at 77 K. After the measurement was complete, the frozen solution sample was slowly warmed to room temperature. The resulting red-orange thermolysis product **1c** was subsequently frozen at 77 K and re-measured. All data were collected at 4.2 K and the isomer shift (δ) values are reported with respect to natural iron foil that was used for velocity calibration at

room temperature. The spectra were fit to Lorentzian lines by using the WMOSS plot and fit program.²⁷

X-ray Absorption Spectroscopy. Samples of **1a**, its dioxygen-adduct (**1b**), and the thermolysis product (**1c**) were prepared as 8 mM solutions in THF. Pre-cooled Delrin XAS sample cells with Mylar windows were filled by submersion in the respective solutions. Samples were kept frozen in liquid N₂ until used. A sample of ~30 mg solid **1a** was ground with BN and pressed into a 1-mm thick aluminum sample holder for XAS measurements.

X-ray absorption spectra (XAS) were measured on unfocused wiggler beamline 7-3 at the Stanford Synchrotron Radiation Laboratory (SSRL), with the ring operating at 3 GeV and 50–100 mA. Samples were maintained at 10 K inside an Oxford Instruments CF-1208 liquid helium continuous flow cryostat. A Si(220) double-crystal monochromator was used, detuned 50% at 7987 eV in order to minimize contamination of the radiation by higher harmonics. Vertical 1-mm pre-monochromator slits were used to define the beam size, minimizing beam divergence and allowing for an energy resolution of ≤ 1 –1.4 eV at the Fe K-edge. Spectra for the frozen solution samples were measured in fluorescence mode, using a Lytle detector (an ion chamber with manganese filter and soller slits).²⁸ The spectrum for the solid sample of **1a** was measured via transmission, using ion chambers as detectors. For all experimental spectra, the spectrum of Fe foil was collected concomitantly, allowing for internal energy calibration of the data. The first inflection point energy for the Fe foil spectrum was set to 7111.2 eV. Reproducibility in the determination of the edge position was < 0.2 eV. K-edge and EXAFS data were measured over the energy range 6786–7987 eV. Multiple scans over the complete energy range were averaged for each sample (12 scans for the frozen solution; 5 scans for the solid). Although EXAFS data

were collected to $k = 17 \text{ \AA}^{-1}$, spectra were truncated at 13 \AA^{-1} due to noise in the data at higher values of k .

For each spectrum, a smooth second-order polynomial was fit to the pre-edge region, then extrapolated across the entire energy range and subtracted from the data. A three-segment spline (polynomial curves of orders 2, 3, and 3) was fit to and subtracted from the EXAFS region, and the data normalized at 7130 eV, using the SPLINE program (written by Dr. Paul Ellis). EXAFS data were then k^3 -weighted, where the photoelectron wave vector $k = [2m_e/(E - E_0)/(h/2\pi)^2]^{1/2}$, E is energy, E_0 is the energy of onset of the EXAFS, and m_e is the mass of an electron.²⁹ Phase and amplitude functions ($\phi_{as}(k)$ and $A_s(k)$) calculated by FEFF 6.0³⁰ were used in creating a simulated EXAFS spectrum, which was adjusted by a least-squares fitting process to match the data (using the EXAFSPAK programs by Dr. G. N. George, SSRL, which utilize the public domain MINPAK fitting library).³¹ Absorber-scatterer distances (R_{as}) and Debye-Waller factors (σ_{as}^2) were varied for each equivalent set of backscattering atoms. Coordination numbers (N_s) were generally kept constant, according to the known crystal structure of **1a**. Alternatively, coordination numbers were fixed in accordance with the known ratio of the component species in the sample (for **1b**). Other parameters included in the fits were E_0 and S_0^2 , where S_0^2 is the many-body amplitude reduction factor accounting for spectral dampening due to shake-up or shake-off processes.²⁹ E_0 was allowed to vary within ranges defined by fits to similar, crystallographically characterized diiron(II) and diiron(III) complexes. S_0^2 was fixed at 0.9. Fits were constructed in a building-up process, where components to the fit were included on the basis of visual improvement to the EXAFS fit and reduction in a goodness-of-fit parameter R , where $R = R^2/[(2\Delta k\Delta R'/\pi) - \text{no. variables in fit}]$, $R = [\sum k^6(\chi_{\text{obs}} - \chi_{\text{calc}})^2/N]^{1/2}$, N = the num-

ber of points in the EXAFS spectrum, Δk = range over which EXAFS was fit (here, 3 – 13 \AA^{-1}), and $\Delta R'$ = range of FT over which the fit was made (here, $R' = 0 - 5 \text{\AA}$).

Results

Synthesis and Structural Characterization of $[(\text{Me}_3\text{TACN})_2\text{Fe}_2(\mu\text{-O}_2\text{CAr}^{\text{Tol}})_2\text{L}_2](\text{OTf})_2$, L = MeCN (1a**) and H₂O (**2a**).** Reaction of equimolar amounts of $\text{Fe}(\text{OTf})_2 \cdot 2\text{MeCN}$, Me_3TACN , and $\text{NaO}_2\text{CAr}^{\text{Tol}}$ in anhydrous MeCN afforded colorless blocks of **1a** in good yield (63%) following recrystallization from $\text{CH}_2\text{Cl}_2/\text{MeCN}/\text{Et}_2\text{O}$. A related compound **1b** can be conveniently prepared by doping a CH_2Cl_2 solution of crude **1a** with > 2 equiv of H₂O (Scheme 5.1) and isolating the product by recrystallization from $\text{CH}_2\text{Cl}_2/\text{Et}_2\text{O}$. The solid state structures of **1a** and **2a** are displayed in Figures 5.1 and 5.2; selected bond lengths and angles are listed in Table 5.2.

X-ray crystallography revealed two chemically identical but crystallographically inequivalent molecules of **1a** in the unit cell. As shown in Figure 5.1, the two iron atoms in **1a** are related by a crystallographic inversion symmetry and linked by two μ -1,3 bridging carboxylate ligands. Relatively long Fe...Fe distances of 4.6787(15) – 4.7127(13) \AA are accommodated by opening the $\text{C}_{\text{carboxylate}}\text{-O-Fe}$ angles, which range from 145.0(3) to 158.0(3) $^\circ$. Such a structural motif is shared by the diiron(II) complexes $[\text{Fe}_2(\mu\text{-O}_2\text{CAr}^{\text{Tol}})_2(\text{O}_2\text{CAr}^{\text{Tol}})_2\text{L}_2]$ (L = THF, MeCN, $\text{C}_5\text{H}_5\text{N}$, or 1-MeIm), in which the steric interaction between the *p*-tolyl groups is minimized by the trans disposition of the $\text{Ar}^{\text{Tol}}\text{CO}_2^-$ ligands.^{10,17} Four nitrogen atoms from the Me_3TACN and MeCN ligands complete the coordination spheres of the pseudo-octahedral iron atoms in **1a**.

Formal displacement of the MeCN ligands in **1a** by H₂O molecules affords **2a**, in which minimal perturbation is introduced to the overall coordination geometry. The metal centers remain pseudo-octahedral with metrical parameters

normal for high-spin iron(II) (Table 5.2). The Fe...Fe distance of 4.5852(9) Å in **2a**, however, is significantly shortened relative to that of **1a**. This core contraction is reflected in the decreased C_{carboxylate}-O-Fe angles of 140.6(2) – 141.3(2)°. An attenuated steric crowding between the {(Me₃TACN)Fe(H₂O)}²⁺ units and the bridging Ar^{Tol}CO₂⁻ ligands in **2a**, compared with that between {(Me₃TACN)Fe(MeCN)}²⁺ and Ar^{Tol}CO₂⁻ in **1a**, may be responsible for such a structural variation, as highlighted in Figure 5.3.

UV-vis Studies of the Reactions between [(Me₃TACN)₂Fe₂(μ-O₂CAr^{Tol})₂(MeCN)₂](OTf)₂ (1a**) and O₂.** Exposure of a colorless THF solution of **1a** to dioxygen at -78 °C induced an instantaneous color change to dark blue-green. As shown in Figure 5.4, the dioxygen-adduct **1b** exhibits a broad visible absorption band centered at ~640 nm (ε ≈ 2000 M⁻¹cm⁻¹). The energy and intensity of this transition is comparable to those of well-characterized (peroxo)diiron(III) species exhibiting peroxide-to-iron(III) LMCT transitions (Table 5.3).³²⁻⁴⁷ In strongly coordinating solvents such as EtCN, no reaction occurs between **1a** and O₂ at -78 °C, as judged by UV-vis spectroscopy. At -78 °C, **1b** decays to a yellow species (Figure 5.4B) with an estimated half-life of ~20 min. Upon warming to room temperature, the yellow solution turns orange red, as monitored by the buildup of a pair of visible peaks at 485 and 525 nm as well as weaker bands centered at ~750 nm of **1c** (Figure 5.4C). The positions and intensities of the lower energy bands fall in the range observed in other (μ-oxo)di(μ-carboxylato)diiron(III) complexes.^{48,49} This set of absorption bands arises from the ⁶A₁ → ⁴T₂ LF transition of high-spin iron(III) in an octahedral coordination environment.⁵⁰ The sharp 525 nm transition is assigned as components of the LF-independent ⁶A₁ → ⁴A₁ spin flip transition, and the broad absorption at 485 nm as the singlet in-plane π oxo-to-Fe(III) CT transition, in analogy to the properties of [(Me₃TACN)₂Fe(μ-O)(μ-OAc)₂]²⁺.^{16,51,52}

Mössbauer Spectroscopy. Figures 5.5A and 5.5B display the 4.2 K zero-field Mössbauer spectra of **1a** and **2a** in the solid state; the corresponding parameters derived from fits of the spectra are provided in Table 5.4, along with those of related diiron(II) complexes.^{10,17,53-55} As expected for two iron centers related by crystallographic inversion symmetry, single sharp ($\Gamma = 0.27 - 0.32 \text{ mm s}^{-1}$) quadrupole doublets were obtained for **1a** and **2a**. In THF, however, significant broadening of the peaks ($\Gamma = 0.38 - 0.39 \text{ mm s}^{-1}$) occurs for **1a** (Figure 5.6A). The spectrum was deconvoluted into two subspectra having similar isomer shift (δ) but different quadrupole splitting (ΔE_Q) parameters. These values are comparable to those of **1a** in the solid state, indicating that the dimetallic core structure is retained in THF. The inequivalent iron sites of **1a** in solution may result from partial dissociation of the MeCN ligands or ligand substitution by the THF solvent molecule, as suggested by EXAFS studies (vide infra). The δ and ΔE_Q parameters of **1a** and **2a** are typical of high-spin iron(II) sites in a N/O coordination environment.^{48,56,57}

Mössbauer samples of **1b** were prepared by oxygenating a THF solution of **1a** at -78°C . Given the thermal instability of **1b**, the reaction was quenched by freezing the solution before a substantial decay of the dioxygen adduct occurs. Under the conditions employed, the freeze-quenched sample contains $\sim 40\%$ of **1a** (Figure 5.6B), the contribution of which was subtracted by its independently obtained parameters. This treatment greatly simplified the spectral analysis. The Mössbauer spectrum of **1b** reveals a slightly asymmetric quadrupole doublet, which was fit to two subspectra of equal intensities (Figure 5.7; Table 5.4). The isomer shift (0.52 and 0.66 mm s^{-1}) and quadrupole splitting (1.17 and 1.36 mm s^{-1}) parameters are within the range for high-spin iron(III) sites and comparable to those determined for (peroxo)diiron(III) clusters (Table 5.3). The two quadrupole doublets of **1b** may reflect inequivalent iron coordination environ-

ments in the dinuclear unit. Alternatively, they may result from two distinct diiron species existing in a 1:1 ratio. Although the former explanation is favored, we do not have any evidence to rule out the latter interpretation.

A single sharp quadrupole doublet was obtained for the thermal decay product **1c** (Figure 5.8), which was obtained by warming **1b** to room temperature. The corresponding Mössbauer parameters of $\delta = 0.50(2) \text{ mm s}^{-1}$ and $\Delta E_Q = 1.84(2) \text{ mm s}^{-1}$ are typical for high-spin (μ -oxo)diiron(III) species, which have characteristically large ΔE_Q values.⁴⁸

EPR Spectroscopy. The dioxygen adduct **1b** is EPR silent at 4 K and 77 K, implying a $S = 0$ ground spin state arising from antiferromagnetically (AF) coupled diiron(III) centers. In other (peroxo)diiron(III) complexes, similar AF coupling is mediated by μ -1,2 bridging peroxide ligands.^{42,58} The reaction pathway leading to the formation of a diamagnetic intermediate from **1a** is significantly different from that traversed by $[\text{Fe}_2(\mu\text{-O}_2\text{CAr}^{\text{Tol}})_2(\text{O}_2\text{CAr}^{\text{Tol}})_2(\text{C}_5\text{H}_5\text{N})_2]$ or $[\text{Fe}_2(\mu\text{-O}_2\text{CAr}^{\text{Tol}})_4(4\text{-}^t\text{BuC}_5\text{H}_4\text{N})_2]$, which afford equimolar amounts of paramagnetic intermediates upon reaction with dioxygen.^{11,17}

Resonance Raman Spectroscopy. In order to obtain evidence for the metal-bound peroxo unit, resonance Raman spectra were acquired for **1b** in THF at $-78 \text{ }^\circ\text{C}$. As displayed in Figure 5.9, **1b** prepared with $^{16}\text{O}_2$ exhibits broad, weakly resonance enhanced peaks at 837 and 858 cm^{-1} . Although these vibrations fall within the range expected for (μ -1,2-peroxo)diiron(III) clusters (Table 5.3), repeated attempts to locate isotope sensitive O–O vibrations were not successful with fluid samples labeled with ^{18}O (Figure 5.9). This failure can be ascribed to photolysis of the intermediates, spectral overlap with solvent peaks, or the possibility that **1b** does not have a metal-bound peroxide ligand. No attempts were made to prepare frozen solution samples of **1b** to enhance its stability during the measurement.

X-ray Absorption Spectroscopy. Fe K-edges for **1a** in the solid state and in the frozen THF solution are very similar in shape and nearly overlap in energy (Figure 5.10). This result suggests substantial structural agreement between the complex in the solid and solution states. Discrepancies between the two edge spectra may be due to the increased vibrational disorder in solutions relative to solids, effecting broadening of individual edge features, or could be due to structural differences.

The Fe K-edges for THF solutions of **1a**, the oxygenation product **1a** + O₂, and the thermolysis product **1c**, are compared in Figure 5.11. The K-edge for **1a** + O₂ is intermediate in energy between edges for **1a** and **1c**, reflecting the expected mixed Fe(II)/Fe(III) composition of the sample estimated from Mössbauer spectra to consist of 40% unreacted **1a** and 60% peroxide-level intermediate **1b**. To obtain an approximate edge for the putative peroxide species in **1a** + O₂, a weighted edge spectrum for **1a** was subtracted from the spectrum for **1a** + O₂ and the resulting spectrum renormalized (at 7150 eV). The weighting reflected the expected ~40% unreacted **1a** in the sample. This subtracted spectrum resembles the spectrum for **1c**, both in energy and shape, suggesting that the iron atoms in the putative peroxide species **1b** are in the +3 oxidation states. It also suggests that the putative peroxide **1b** is structurally similar to **1c**, because the edge spectrum serves as a sensitive structural "fingerprint".

The pre-edge for **1c** (inset, Figure 5.11) has a two-peaked structure with a weak transition at ~7113 eV and a more intense one at ~7114.5 eV. This pattern is highly characteristic of a (μ-oxo)diiron(III) unit.⁵⁹ The pre-edge for **1a** + O₂, or for the subtracted spectrum (**1b** = [**1a** + O₂] - 40%), appears to have two transitions of more comparable intensities. This behavior is characteristic of a more octahedral (centrosymmetric) iron(III) environment.⁵⁹

EXAFS data measured for **1a** in the solid state and in a frozen THF solution are similar but not identical (Figure 5.12). Differences in the spectra are also evident in the Fourier transforms (FT) of their EXAFS. Because the Fe...Fe distance is exceptionally long in the reduced complex (4.6787(15) – 4.7127(13) Å), it is not possible directly to assess whether the dinuclear complex is intact in solution, although the measured distances to the coordinated ligands in the solid/solution are mostly in agreement. Fits to the data reveal at least one structural difference. The coordination sphere for **1a** in the solid state is well-modeled by two O/N ligands at 2.06 Å with four additional O/N ligands at 2.21 Å, consistent with crystallographic distances to the two carboxylate oxygen and four Me₃TACN/CH₃CN-derived nitrogen donor atoms, respectively. However, data for **1a** in THF are best modeled by two O/N ligands at 2.06 Å, three O/N ligands at 2.22 Å, and a longer O/N ligand 2.58 Å (Figures 5.13 and 5.14). This suggests that a labile CH₃CN molecule is potentially substituted by triflate or a molecule of solvent in solution, at a longer bonding distance.

The EXAFS for **1b** similarly has a long Fe–O/N distance (1 O/N at 2.55 Å) as part of the best fit (Table 5.5 and Figure 5.15). Other coordinated ligands include 0.6 O/N at 1.94 Å, 1.4 O/N at 2.09 Å, and 3 O/N at 2.22 Å. The latter two distances are roughly consistent with the Fe–O_{carboxylate} and Fe–N_{amine} distances observed in the crystal structure of the diiron(II) precursor **1a**. The short Fe–O/N interaction (1.94 Å) is present with a stoichiometry of one O/N per iron, accounting for 60% of total iron species. This interaction is therefore potentially due to the Fe–O_{peroxide} bonding. The EXAFS derived model containing one short bond per iron in this putative peroxo species further suggests a μ -1,2 peroxide, rather than a symmetrically bridging side-on peroxide, which would have two equivalent Fe–O_{peroxide} bonds per iron. Finally, an Fe...Fe scattering interaction at 3.09 Å (one Fe per peroxo-iron) was included as part of the best fit. This dis-

tance is more consistent with known cis μ -1,2-peroxo complexes ($\text{Fe}\cdots\text{Fe} = 3.14 - 3.33 \text{ \AA}$)^{41,46} rather than with the μ -1,2 peroxo diiron(III) complex having a gauche Fe–O–O–Fe conformation ($\text{Fe}\cdots\text{Fe} = 4.01 \text{ \AA}$).⁴⁰ It is also possible that this Fe \cdots Fe vector is actually due to some contamination of the sample by the thermolysis product. An identical Fe \cdots Fe distance was also found for **1c**, although with a considerably smaller Debye-Waller factor (Table 5.5). Mössbauer spectra of **1b** (Figure 5.7), however, revealed no contamination with **1c** (Figure 5.8). This result suggests that the similarities in the XAS for **1b** and **1c** are due to real structural congruences between the putative peroxo diiron(III) and its thermolysis product.

Consistent with the observed pre-edge feature, EXAFS data for **1c** are best modeled by the inclusion of a short, presumably Fe–O_{oxo} interaction at 1.78 Å, with a stoichiometry of one per iron. Two additional O/N ligands at 2.04 Å and three at 2.20 Å, consistent with Fe–O_{carboxylate} and Fe–N_{amine} distances, respectively, were also measured. Finally, an Fe \cdots Fe vector of 3.10 Å was determined, with a stoichiometry of 1 per iron (Figure 5.16). Hence structural features determined for **1c** are consistent with an oxo-bridged diiron(III) complex, with one or both carboxylates potentially retained as bridging ligands to help enforce the short Fe \cdots Fe distance.

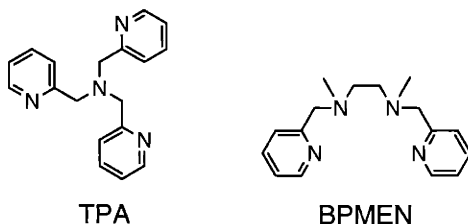
Discussion

Doubly-bridged Diiron(II) Cores Capped by Neutral N-donor Ligands.

Dicationic $\{\text{Fe}_2(\mu\text{-O}_2\text{CAr}^{\text{Tol}})_2(\text{Me}_3\text{TACN})_2\}^{2+}$ modules were assembled, in which a doubly-bridged diiron(II) center is supported by neutral tridentate ancillary ligands. Previous attempts to access similar units through self-assembly from simple iron(II) salts, $\text{MO}_2\text{CAr}^{\text{Tol}}$ (M = Na or Tl), and other polydentate N-donor ligands afforded neutral mono- or dinuclear complexes having two carboxylate ligands per iron.^{13,17} The doubly-bridged diiron(II) core motif in **1a** and **2a** is

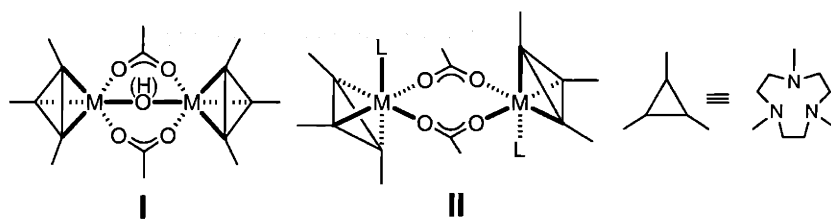
shared by $[\text{Fe}_2(\mu\text{-OAc})_2(\text{TPA})_2](\text{BPh}_4)_2$ ¹⁶ and $[\text{Fe}_2(\mu\text{-OAc})_2(\text{BPMEN})_2](\text{ClO}_4)_2$ ¹⁶ having octahedral coordination at each iron atom and an N_4O_2 donor atom set.^{60,61} In these compounds, significantly shorter Fe...Fe distances of 4.288(2) – 4.382(2) Å result from the presence of less sterically demanding acetate bridging ligands (see Table 5.2).

Unlike the tetradentate ligands TPA or BPMEN, the N_4 donor atom sets for each iron center in **1a** are derived from a tridentate ligand Me_3TACN and a MeCN molecule. In solution, the terminally bound MeCN ligands can be readily replaced, as exemplified by the isolation of **2a** from a reaction between **1a** and H_2O (Scheme 5.1). Mössbauer and EXAFS studies of **1a** in THF also indicate partial loss of terminal ligand(s). Dissociation of the MeCN ligand from the formal six-coordinate iron atoms in **1a** provides open coordination sites for exogenous ligand binding. Reactions between **1a** and dioxygen thus can proceed on the dimetallic platform, whereas $[\text{Fe}_2(\mu\text{-OAc})_2(\text{TPA})_2]^{2+}$ dissociates into two monomeric units to provide binding sites for O_2 .⁶⁰ No intermediate was observed in the autoxidation of this compound with 0.5 equiv of O_2 , which afforded (μ -oxo)diiron(III) products.⁶⁰



The positioning of the two μ -1,3 bridging ligands across the Fe–Fe vector in **1a** and **2b** is a consequence of the steric repulsion between the *p*-tolyl groups on $\text{Ar}^{\text{Tol}}\text{CO}_2^-$. TACN¹⁶-derived tridentate ligands usually promote face-shared octahedral geometry (**I**) for triply-bridged dimetallic centers such as $\{\text{Fe}_2(\mu\text{-X})(\mu\text{-$

$\text{O}_2\text{CR})_2\}^{\text{n}+}$, where $\text{X} = \text{O}^{2-}$ or OH^- .⁶²⁻⁶⁸ The V-shaped $\text{Ar}^{\text{Tot}}\text{CO}_2^-$, however, cannot accommodate **I** but affords a doubly-bridged core **II**. This spatial arrangement apparently minimizes inter-ligand steric crowding. As a consequence, the sixth coordination sites of each metal center in **II** are available for a monodentate ligand L, the dissociation of which allows binding of dioxygen. Open coordination sites in **I** can only be accessed by the shifting of the μ -1,3 bridging carboxylates,⁶⁹ an energetically less favorable process for sterically demanding ligands.⁶⁶⁻⁶⁸



Proposed O_2 -Activation Mechanism. From the structural and spectroscopic studies of **1a**, **1b**, and **1c** emerges a working mechanism, depicted in Scheme 5.2. Dissociation of the MeCN ligand from **1a** provides an open coordination site. Binding of O_2 affords intermediate **1b** featuring two inequivalent iron(III) centers with a short metal...metal separation (3.09 Å). Structures **A** or **B** can accommodate these structural requirements. In **A**, the iron atoms are rendered inequivalent owing to the different coordination mode of the bridging peroxide ligand, whereas the configuration of the ancillary ligands supporting the cis μ -1,2-peroxo diiron(III) unit in **B** can eliminate any local symmetry. Steric crowding in the dimetallic cores of **A** or **B** may require shifts of the carboxylate ligands from the μ -1,3 bridging positions. Structure **A** resembles that of the H_{peroxo} intermediate as computed by density functional theory.^{70,71} Intermediate **1b** decays at -78°C and eventually converts to **1c**, a species containing a (μ -

oxo)diiron(III) core. The short Fe...Fe distance (3.10 Å) and the characteristic UV-vis features of **1c** are consistent with a bent Fe–O–Fe unit supported by additional bridging unit(s). Although mechanistic information detailing the conversion of **1b** to **1c** conversion is currently unavailable, decay of (peroxo)diiron(III) intermediates to (μ-oxo)diiron(III) products is a well-documented phenomenon.^{69,72,73} A more definitive proof of the foregoing postulated mechanism will require vibrational spectroscopic evidence for the metal-bound O–O unit, as well as a detailed kinetic analysis of the development and decay of **1b**.

Effects of Nitrogen-Rich Coordination on Dioxygen Activation. Ancillary ligands modulate the structural and reactivity properties of the {Fe₂(μ-O₂CAr^{Tol})₂}²⁺ core. Relative to the diiron(II) compounds [Fe₂(μ-O₂CAr^{Tol})₂(O₂CAr^{Tol})₂L₂] (L = THF, MeCN, C₅H₅N, or 1-MeIm),^{10,17} the overall charge of the dinuclear units in **1a** and **2a** is increased by 2. A less electron-donating primary coordination sphere apparently affects the oxygenation reaction pathway of **1a**, which is significantly different from that traversed by the neutral diiron(II) compounds [Fe₂(μ-O₂CAr^{Tol})₂(O₂CAr^{Tol})(C₅H₅N)₂] and [Fe₂(μ-O₂CAr^{Tol})₄(4-^tBuC₅H₄N)₂].^{10,11} Whereas mixed-valent iron(III)iron(IV) species are afforded following reaction of these neutral diiron(II) compounds with O₂ at –78 °C, a diamagnetic peroxo-type intermediate evolves from **1a** under similar conditions. These processes closely mimic the chemistry of non-heme diiron *bioinorganic chips* involved in dioxygen-binding versus dioxygen-activation. In the Ar^{Tol}CO₂[–]-supported diiron(II) systems, access to high-valent iron(IV) species is apparently facilitated by an anion-rich coordination environment, whereas neutral donor groups stabilize the preceding O₂-adduct. Generalizations about structure–function relationships in non-heme diiron proteins, however, must be viewed with caution, especially given the nitrogen-rich ligand environment adopted by the dioxygen-activating enzyme alkane ω-hydroxylase (AlkB).^{74,75}

Polypyridyl-derived tetradentate ligands also can support mono-⁷⁶⁻⁷⁸ and dinuclear⁷⁹⁻⁸³ complexes that stabilize iron(IV) or iron(V) oxidation states. It remains to be seen how these phenomena can be rationalized in terms of the stereoelectronic factors of the ligand environment in biological or synthetic systems.

Acknowledgments. This work was supported by grants from the National Science Foundation and National Institute of General Medical Sciences. The XAS studies discussed here were carried out in collaboration with Profs. Britt Hedman and Keith O. Hodgson, and Dr. Jennifer L. DuBois (Stanford University). I thank Dr. Amy M. Barrios and Ms. Joey Bautista for performing the resonance Raman experiment, and Ms. Jane Kuzelka for assistance in acquiring the Mössbauer spectra.

References

- (1) Lippard, S. J.; Berg, J. M. *Principles of Bioinorganic Chemistry*; University Science Books: Mill Valley, CA, 1994.
- (2) Niederhoffer, E. C.; Timmons, J. H.; Martell, A. E. *Chem. Rev.* **1984**, *84*, 137-203.
- (3) Collman, J. P.; Fu, L. *Acc. Chem. Res.* **1999**, *32*, 455-463.
- (4) Sono, M.; Roach, M. P.; Coulter, E. D.; Dawson, J. H. *Chem. Rev.* **1996**, *96*, 2841-2887.
- (5) Newcomb, M.; Toy, P. H. *Acc. Chem. Res.* **2000**, *33*, 449-455.
- (6) Silverman, R. B. *The Organic Chemistry of Enzyme-Catalyzed Reactions*; Academic Press: San Diego, CA, 2000.
- (7) Pauling, L. *Nature* **1964**, *203*, 182-183.
- (8) Stenkamp, R. E. *Chem. Rev.* **1994**, *94*, 715-726.
- (9) (a) Feig, A. L.; Lippard, S. J. *Chem. Rev.* **1994**, *94*, 759-805. (b) Wallar, B. J.; Lipscomb, J. D. *Chem. Rev.* **1996**, *96*, 2625-2657. (c) Que, L., Jr.; Dong, Y. *Acc. Chem. Res.* **1996**, *29*, 190-196. (d) Lange, S. J.; Que, L., Jr. *Curr. Opin. Chem. Biol.* **1998**, *2*, 159-172. (e) Stahl, S. S.; Lippard, S. J. *Iron Metabolism*; Ferreira, G. C., Moura, J. J. G. and Franco, R., Ed.; Wiley-VCH: Weinheim, 1999, pp 303-321. (f) Du Bois, J.; Mizoguchi, T. J.; Lippard, S. J. *Coord. Chem. Rev.* **2000**, *200*-202, 443-485. (g) Merckx, M. K., D. A.; Sazinsky, M. H.; Blazyk, J. L.; Müller, J.; Lippard, S. J. *Angew. Chem., Int. Ed. Engl.* **2001**, *40*, 2782-2807.
- (10) Lee, D.; Lippard, S. J. *J. Am. Chem. Soc.* **1998**, *120*, 12153-12154.
- (11) Lee, D.; Du Bois, J.; Petasis, D.; Hendrich, M. P.; Krebs, C.; Huynh, B. H.; Lippard, S. J. *J. Am. Chem. Soc.* **1999**, *121*, 9893-9894.
- (12) Lee, D.; Krebs, C.; Huynh, B. H.; Hendrich, M. P.; Lippard, S. J. *J. Am. Chem. Soc.* **2000**, *122*, 5000-5001.
- (13) Lee, D.; Lippard, S. J. *J. Am. Chem. Soc.* **2001**, *123*, 4611-4612.

- (14) Hagadorn, J. R.; Que, L., Jr.; Tolman, W. B. *J. Am. Chem. Soc.* **1998**, *120*, 13531-13532.
- (15) Hagadorn, J. R.; Que, L., Jr.; Tolman, W. B.; Prisecaru, I.; Münck, E. *J. Am. Chem. Soc.* **1999**, *121*, 9760-9761.
- (16) Abbreviations used: Ar^{Tol}CO₂⁻, 2,6-di(p-tolyl)benzoate; Ar^{Mes}CO₂⁻, 2,6-dimesitylbenzoate; TPA, tris(2-pyridylmethyl)amine; BPMEN, *N,N'*-dimethyl-*N,N'*-bis(2-pyridylmethyl)ethylene-1,2-diamine; pz', 3,5-bis(isopropyl)pyrazolyl; Ph-bimp, 2,6-bis[bis{2-(1-methyl-4,5-diphenylimidazolyl)methyl}aminomethyl]-4-methylphenolate; HPTB, anion of *N,N,N',N'*-tetrakis(2-benzimidazolylmethyl)-2-hydroxyl-1,3-diaminopropane; HO₂CPhCy, 1-phenylcyclohexanecarboxylic acid; BXDK, the benzyl derivative of XDK; H₂XDK, *m*-xylylenediamine bis(Kemp's triacid imide); 6-Me₃-TPA, tris(6-methyl-2-pyridylmethyl)amine; L¹, 1,2-bis[2-(bis(2-pyridyl)methyl)-6-pyridyl]ethane; TMEDA, *N,N,N',N'*-tetramethylethylenediamine; Ph₄DBA²⁻, dibenzofuran-4,6-bis(diphenylacetate); TACN, 1,4,7-triazacyclononane; Me₃TACN, 1,4,7-trimethyl-1,4,7-triazacyclononane
- (17) Lee, D.; Lippard, S. J., submitted for publication.
- (18) Stubbe, J.; van der Donk, W. A. *Chem. Rev.* **1998**, *98*, 705-762.
- (19) Pangborn, A. B.; Giardello, M. A.; Grubbs, R. H.; Rosen, R. K.; Timmers, F. J. *Organometallics* **1996**, *15*, 1518-1520.
- (20) Hagen, K. S. *Inorg. Chem.* **2000**, *39*, 5867-5869.
- (21) (a) Du, C.-J. F.; Hart, H.; Ng, K.-K. D. *J. Org. Chem.* **1986**, *51*, 3162-3165. (b) Saednya, A.; Hart, H. *Synthesis* **1996**, 1455-1458. (c) Chen, C.-T.; Siegel, J. S. *J. Am. Chem. Soc.* **1994**, *116*, 5959-5960.
- (22) SMART v5.05; Bruker AXS Inc.: Madison, WI, 1998.
- (23) Feig, A. L.; Bautista, M. T.; Lippard, S. J. *Inorg. Chem.* **1996**, *35*, 6892-6898.

- (24) Sheldrick, G. M. *SHELXTL v5.1: Program for the Refinement of Crystal Structures 97-2*; University of Göttingen, Göttingen, Germany, 1998.
- (25) Sheldrick, G. M. *SADABS v2.03: Area-Detector Absorption Correction*; University of Göttingen, Göttingen, Germany, 1999.
- (26) Spek, A. L. *PLATON, A Multipurpose Crystallographic Tool*; Utrecht University: Utrecht, The Netherlands, 1998.
- (27) Kent, T. A. *WMOSS v2.5: Mössbauer Spectral Analysis Software*; Minneapolis, 1998.
- (28) Lytle, F. W.; Sayers, D. E.; Stern, E. A. *Phys. B* **1989**, *158*, 701-722.
- (29) Riggs-Gelasco, P. J.; Stemmler, T. L.; Penner-Hahn, J. E. *Coord. Chem. Rev.* **1995**, *144*, 245-286.
- (30) Mustre de Leon, J.; Rehr, J. J.; Zabinsky, S. I.; Albers, R. C. *Phys. Rev. B* **1991**, *44*, 4146-4156.
- (31) This software is available free and can be downloaded from the world wide web. See <http://www-ssrl.slac.stanford.edu/exafspak.html>.
- (32) Valentine, A. M.; Stahl, S. S.; Lippard, S. J. *J. Am. Chem. Soc.* **1999**, *121*, 3876-3887.
- (33) Liu, K. E.; Valentine, A. M.; Wang, D.; Huynh, B. H.; Edmondson, D. E.; Salifoglou, A.; Lippard, S. J. *J. Am. Chem. Soc.* **1995**, *117*, 10174-10185.
- (34) Lee, S.-K.; Lipscomb, J. D. *Biochemistry* **1999**, *38*, 4423-4432.
- (35) Shu, L.; Nesheim, J. C.; Kauffmann, K.; Münck, E.; Lipscomb, J. D.; Que, L., Jr. *Science* **1997**, *275*, 515-518.
- (36) Bollinger, J. M., Jr.; Krebs, C.; Vicol, A.; Chen, S.; Ley, B. A.; Edmondson, D. E.; Huynh, B. H. *J. Am. Chem. Soc.* **1998**, *120*, 1094-1095.
- (37) Moëne-Loccoz, P.; Baldwin, J.; Ley, B. A.; Loehr, T. M.; Bollinger, J. M., Jr. *Biochemistry* **1998**, *37*, 14659-14663.

- (38) Broadwater, J. A.; Ai, J.; Loehr, T. M.; Sanders-Loehr, J.; Fox, B. G. *Biochemistry* **1998**, *37*, 14664-14671.
- (39) Broadwater, J. A.; Achim, C.; Münck, E.; Fox, B. G. *Biochemistry* **1999**, *38*, 12197-12204.
- (40) Kim, K.; Lippard, S. J. *J. Am. Chem. Soc.* **1996**, *118*, 4914-4915.
- (41) Ookubo, T.; Sugimoto, H.; Nagayama, T.; Masuda, H.; Sato, T.; Tanaka, K.; Maeda, Y.; Okawa, H.; Hayashi, Y.; Uehara, A.; Suzuki, M. *J. Am. Chem. Soc.* **1996**, *118*, 701-702.
- (42) Dong, Y.; Ménage, S.; Brennan, B. A.; Elgren, T. E.; Jang, H. G.; Pearce, L. L.; Que, L., Jr. *J. Am. Chem. Soc.* **1993**, *115*, 1851-1859.
- (43) Ménage, S.; Brennan, B. A.; Juarez-Garcia, C.; Münck, E.; Que, L., Jr. *J. Am. Chem. Soc.* **1990**, *112*, 6423-6425.
- (44) Dong, Y.; Yan, S.; Young, V. G., Jr.; Que, L., Jr. *Angew. Chem., Int. Ed. Engl.* **1996**, *35*, 618-620.
- (45) LeCloux, D. D.; Barrios, A. M.; Mizoguchi, T. J.; Lippard, S. J. *J. Am. Chem. Soc.* **1998**, *120*, 9001-9014.
- (46) Dong, Y.; Zang, Y.; Shu, L.; Wilkinson, E. C.; Que, L., Jr. *J. Am. Chem. Soc.* **1997**, *119*, 12683-12684.
- (47) Kodera, M.; Taniike, Y.; Itoh, M.; Tanahashi, Y.; Shimakoshi, H.; Kano, K.; Hirota, S.; Iijima, S.; Ohba, M.; Okawa, H. *Inorg. Chem.* **2001**, ASAP.
- (48) Kurtz, D. M., Jr. *Chem. Rev.* **1990**, *90*, 585-606.
- (49) Mizoguchi, T. J.; Lippard, S. J. *Inorg. Chem.* **1997**, *36*, 4526-4533.
- (50) Reem, R. C.; McCormick, J. M.; Richardson, D. E.; Devlin, F. J.; Stephens, P. J.; Musselman, R. L.; Solomon, E. I. *J. Am. Chem. Soc.* **1989**, *111*, 4688-4704.
- (51) Brown, C. A.; Remar, G. J.; Musselman, R. L.; Solomon, E. I. *Inorg. Chem.* **1995**, *34*, 688-717.

- (52) Solomon, E. I.; Brunold, T. C.; Davis, M. I.; Kemsley, J. N.; Lee, S.-K.; Lehnert, N.; Neese, F.; Skulan, A. J.; Yang, Y.-S.; Zhou, J. *Chem. Rev.* **2000**, *100*, 235-349.
- (53) Okamura, M. Y.; Kolotz, I. M.; Johnson, C. E.; Winter, M. R. C.; Williams, R. J. P. *Biochemistry* **1969**, *8*, 1951-1958.
- (54) Mizoguchi, T. J.; Lippard, S. J. *J. Am. Chem. Soc.* **1998**, *120*, 11022-11023.
- (55) Mizoguchi, T. J.; Kuzelka, J.; Spingler, B.; DuBois, J. L.; Davydov, R. M.; Hedman, B.; Hodgson, K. O.; Lippard, S. J. *Inorg. Chem.* **2001**, *in press*.
- (56) Gütlich, P.; Ensling, J. *Inorganic Electronic Structure and Spectroscopy*; Solomon, E. I. and Lever, A. B. P., Ed.; John Wiley & Sons: New York, 1999; Vol. I, pp 161-211.
- (57) Münck, E. *Physical Methods in Bioinorganic Chemistry: Spectroscopy and Magnetism*; Que, L., Jr., Ed.; University Science Books: Sausalito, CA, 2000, pp 287-319.
- (58) Kitajima, N.; Tamura, N.; Amagai, H.; Fukui, H.; Moro-oka, Y.; Mizutani, Y.; Kitagawa, T.; Mathur, R.; Heerwegh, K.; Reed, C. A.; Randall, C. R.; Que, L., Jr.; Tatsumi, K. *J. Am. Chem. Soc.* **1994**, *116*, 9071-9085.
- (59) Westre, T. E.; Kennepohl, P.; DeWitt, J. G.; Hedman, B.; Hodgson, K. O.; Solomon, E. I. *J. Am. Chem. Soc.* **1997**, *119*, 6297-6314.
- (60) Ménage, S.; Zang, Y.; Hendrich, M. P.; Que, L., Jr. *J. Am. Chem. Soc.* **1992**, *114*, 7786-7792.
- (61) Hazell, R.; Jensen, K. B.; McKenzie, C. J.; Toftlund, H. *J. Chem. Soc., Dalton Trans.* **1995**, 707-717.
- (62) Wieghardt, K.; Pohl, K.; Gebert, W. *Angew. Chem. Int. Ed. Engl.* **1983**, *22*, 727.
- (63) Spool, A.; Williams, I. D.; J., L. S. *Inorg. Chem.* **1985**, *24*, 2156-2162.
- (64) Chaudhuri, P.; Wieghardt, K.; Nuber, B.; Weiss, J. *Angew. Chem., Int. Ed. Engl.* **1985**, *24*, 778-779.

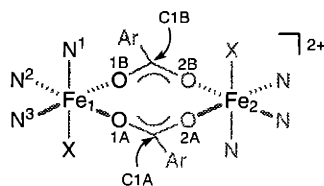
- (65) Hartman, J. R.; Rardin, R. L.; Chaudhuri, P.; Pohl, K.; Wieghardt, K.; Nuber, B.; Weiss, J.; Papaefthymiou, G. C.; Frankel, R. B.; Lippard, S. J. *J. Am. Chem. Soc.* **1987**, *109*, 7387–7396.
- (66) Bossek, U.; Hummel, H.; Weyhermüller, T.; Bill, E.; Wieghardt, K. *Angew. Chem., Int. Ed. Engl.* **1995**, *34*, 2642–2645.
- (67) Cohen, J. D.; Payne, S.; Hagen, K. S.; Sanders-Loehr, J. J. *Am. Chem. Soc.* **1997**, *119*, 2960–2961.
- (68) Payne, S. C.; Hagen, K. S. *J. Am. Chem. Soc.* **2000**, *122*, 6399–6410.
- (69) Feig, A. L.; Masschelein, A.; Bakac, A.; Lippard, S. J. *J. Am. Chem. Soc.* **1997**, *119*, 334–342.
- (70) Siegbahn, P. E. M. *Inorg. Chem.* **1999**, *38*, 2880–2889.
- (71) Dunietz, B. D.; Beachy, M. D.; Cao, Y.; Whittington, D. A.; Lippard, S. J.; Friesner, R. A. *J. Am. Chem. Soc.* **2000**, *122*, 2828–2839.
- (72) Feig, A. L.; Lippard, S. J. *J. Am. Chem. Soc.* **1994**, *116*, 8410–8411.
- (73) Feig, A. L.; Becker, M.; Schindler, S.; van Eldik, R.; Lippard, S. J. *Inorg. Chem.* **1996**, *35*, 2590–2601.
- (74) Shanklin, J.; Achim, C.; Schmidt, H.; Fox, B. G.; Münck, E. *Proc. Natl. Acad. Sci. USA* **1997**, *94*, 2981–2986.
- (75) Austin, R. N.; Chang, H.-K.; Zylstra, G. J.; Groves, J. T. *J. Am. Chem. Soc.* **2000**, *122*, 11747–11748.
- (76) Lange, S. J.; Miyake, H.; Que, L., Jr. *J. Am. Chem. Soc.* **1999**, *121*, 6330–6331.
- (77) Miyake, H.; Chen, K.; Lange, S. J.; Que, L., Jr. *Inorg. Chem.* **2001**, *40*, 3534–3538.
- (78) Chen, K.; Que, L., Jr. *J. Am. Chem. Soc.* **2001**, *123*, 6327–6337.
- (79) Dong, Y.; Fujii, H.; Hendrich, M. P.; Leising, R. A.; Pan, G.; Randall, C. R.; Wilkinson, E. C.; Zang, Y.; Que, L., Jr.; Fox, B. G.; Kauffmann, K.; Münck, E. *J. Am. Chem. Soc.* **1995**, *117*, 2778–2792.

- (80) Dong, Y.; Que, L., Jr.; Kauffmann, K.; Münck, E. *J. Am. Chem. Soc.* **1995**, *117*, 11377-11378.
- (81) Hsu, H.-F.; Dong, Y.; Shu, L.; Young, V. G., Jr.; Que, L., Jr. *J. Am. Chem. Soc.* **1999**, *121*, 5230-5237.
- (82) Zheng, H.; Yoo, S. J.; Münck, E.; Que, L., Jr. *J. Am. Chem. Soc.* **2000**, *122*, 3789-3790.
- (83) MacMurdo, V. L.; Zheng, H.; Que, L., Jr. *Inorg. Chem.* **2000**, *39*, 2254-2255.

Table 5.1. Summary of X-ray Crystallographic Data

	1a ·CH ₂ Cl ₂	2a ·2CH ₂ Cl ₂
formula	C ₆₇ H ₈₄ N ₈ O ₁₀ Cl ₂ F ₆ Fe ₂ S ₂	C ₆₄ H ₈₀ N ₆ O ₁₂ Cl ₄ F ₆ Fe ₂ S ₂
fw	1522.14	1556.96
space group	<i>P</i> $\bar{1}$	<i>P</i> 2 ₁ / <i>c</i>
<i>a</i> , Å	13.7111(5)	12.1014(2)
<i>b</i> , Å	16.1389(5)	19.3605(4)
<i>c</i> , Å	18.5093(4)	16.2147(3)
α , deg	85.3430(10)	
β , deg	82.5590(10)	104.2940(10)
γ , deg	65.5390(10)	
<i>V</i> , Å ³	3695.03(19)	3681.32(12)
<i>Z</i>	2	2
ρ_{calc} , g/cm ³	1.368	1.405
<i>T</i> , °C	-85	-85
μ (Mo K α), mm ⁻¹	0.596	0.671
θ limits, deg	1.64 – 28.27	1.74 – 28.28
total no. of data	23337	22815
no. of unique data	16303	8490
no. of params	868	451
<i>R</i> (%) ^{<i>a</i>}	7.75	6.63
<i>wR</i> ² (%) ^{<i>b</i>}	18.82	16.71
max, min peaks, e/Å ³	1.096, -0.827	1.079, -1.146

$$^a R = \sum | |F_o| - |F_c| | / \sum |F_o|. \quad ^b wR^2 = \{ \sum [w(F_o^2 - F_c^2)^2] / \sum [w(F_o^2)^2] \}^{1/2}.$$

Table 5.2. Selected Bond Lengths (Å) and Angles (deg) for **1a** and **2a**.^a

	1a		2a
	molecule 1	molecule 2	
Fe1...Fe2	4.7127(13)	4.6787(15)	4.5852(9)
Fe1-N1	2.210(4)	2.209(4)	2.216(3)
Fe1-N2	2.260(4)	2.269(4)	2.258(3)
Fe1-N3	2.271(4)	2.287(5)	2.250(3)
Fe1-O1A	2.073(3)	2.072(3)	2.089(2)
Fe1-O1B	2.056(3)	2.097(3)	2.085(2)
Fe1-X ^b	2.194(5)	2.191(6)	2.139(3)
N1-Fe1-N2	79.10(15)	79.22(16)	79.05(12)
N1-Fe1-N3	78.80(16)	78.83(17)	80.00(12)
N1-Fe1-O1A	93.42(15)	96.70(15)	96.41(11)
N1-Fe1-O1B	94.51(16)	92.63(15)	93.20(11)
N2-Fe1-N3	78.55(16)	78.40(16)	79.49(12)
N3-Fe1-O1A	87.38(15)	87.88(15)	88.71(11)
O1A-Fe1-O1B	105.51(14)	105.33(14)	100.41(10)
O1B-Fe1-N2	88.07(15)	88.12(15)	91.07(11)
X-Fe1-N2	91.28(16)	90.61(19)	95.46(12)
X-Fe1-N3	90.36(17)	91.5(2)	99.70(12)
X-Fe1-O1A	93.77(15)	91.36(17)	89.08(11)
X-Fe1-O1B	94.34(16)	94.87(17)	86.26(11)
N1-Fe1-X	166.69(16)	167.16(19)	174.48(12)
N2-Fe1-O1A	165.08(15)	166.18(15)	167.91(11)
N3-Fe1-O1B	165.92(15)	165.13(15)	169.23(11)
C1B-O1B-Fe1 ^c	158.0(3)	145.0(3)	140.6(2)
C1A-O1A-Fe1 ^d	150.3(3)	155.6(3)	141.3(2)

^a Numbers in parentheses are estimated standard deviations of the last significant figures. ^b X = N_{MeCN} for **1a** and O_{water} for **2a**. ^c C1B-O1B-Fe1 and C1A-O2A-Fe2 are identical. ^d C1A-O1A-Fe1 and C1B-O2B-Fe2 are identical.

Table 5.3. Spectroscopic Properties of Peroxo Diiron(III) Enzyme Intermediates and Their Synthetic Analogs.

	λ_{max} (nm)	ϵ ($\text{M}^{-1} \text{cm}^{-1}$)	δ (mm s^{-1})	ΔE_{O} (mm s^{-1})	$\nu_{\text{O-O}}$ (cm^{-1})	Fe...Fe (\AA)	ref
MMOH (<i>M. capsulatus</i>) ^a	725	1800	0.66	1.51			32,33
	420	4000					
MMOH (<i>M. trichosporium</i> OB3b) ^b	700	2500	0.67	1.51			9b,34,35
RNR-R2 D84E mutant	700	1500	0.63	1.58	890		36,37
$\Delta 9\text{D}$	700	1100-1200	0.68	1.90	898		38,39
	350	1100	0.64	1.06			
$[\text{Fe}_2(\mu\text{-O}_2)(\mu\text{-O}_2\text{CCH}_2\text{Ph})_2\{\text{HB}(\text{pz}')_3\}_2]^{16}$	694	2650	0.66	1.40	888	4.007(4)	40
$[\text{Fe}_2(\mu\text{-O}_2)(\mu\text{-O}_2\text{CPh})(\text{Ph-bimp})]^{2+,16}$	500-800	1700	0.58	0.74		3.327(2)	41
			0.65	1.70			
$[\text{Fe}_2(\mu\text{-O}_2)(\mu\text{-O}_2\text{CPh})(\text{N-Et-HPTB})]^{2+,16}$	588	1500	0.52(2)	0.72(2)	900	3.462(3) ^c	42-44
$[\text{Fe}_2(\mu\text{-O}_2)(\mu\text{-BXDK})(\text{O}_2\text{CPhCy})_2(\text{py})_2]^{16}$	580	1500	0.47	0.88	864		45
			0.63	1.20			
$[\text{Fe}_2(\mu\text{-O}_2)(\mu\text{-O})(6\text{-Me}_3\text{-TPA})_2]^{2+,16}$	494	1100	0.54(2)	1.68(4)	848	3.14 ^d	46
	648	1200					
	846	230					
$[\text{Fe}_2(\mu\text{-O}_2\text{CAr}^{\text{Mes}})_2(\text{O}_2\text{CAr}^{\text{Mes}})_2(\text{MeCN})_2]^{16} + \text{O}_2$	540	2300			885 ^e		14
$[\text{Fe}_2(\mu\text{-O}_2)(\mu\text{-O})(\text{L}^1)]^{2+,16}$	510	1300	0.53(8)	1.67(8)	816		47
	605	1310					
$[(\text{Me}_3\text{TACN})_2\text{Fe}_2(\mu\text{-O}_2\text{CAr}^{\text{Tot}})_2(\text{MeCN})_2]^{2+} + \text{O}_2$	640	2000	0.52(4)	1.17(4)			this work
			0.66(4)	1.36(4)			

^a *Methylococcus capsulatus* (Bath). ^b *Methylosinus trichosporium* OB3b. ^c Determined for $[\text{Fe}_2(\mu\text{-O}_2)(\text{N-Et-HPTB})(\text{Ph}_3\text{PO})_2]^{3+}$.^d Determined by EXAFS. ^e Shifted by 14 cm^{-1} with $^{18}\text{O}_2$.

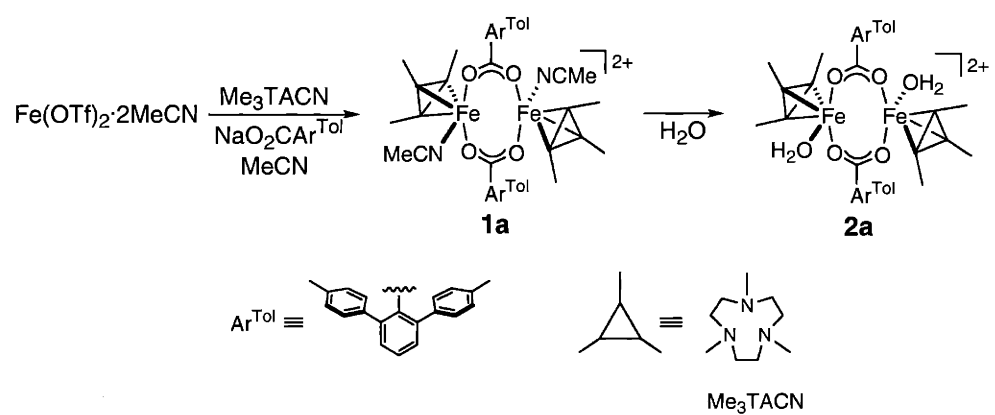
Table 5.4. 4.2 K Zero-field Mössbauer Parameters for $[(\text{Me}_3\text{TACN})_2\text{Fe}_2(\mu\text{-O}_2\text{CAR}^{\text{Toh}})_2(\text{MeCN})_2](\text{OTf})_2$ (**1a**), $[(\text{Me}_3\text{TACN})_2\text{Fe}_2(\mu\text{-O}_2\text{CAR}^{\text{Toh}})_2(\text{H}_2\text{O})_2](\text{OTf})_2$ (**2a**), **1b**, **1c**, and Related Diron Clusters.

	δ (mm s ⁻¹)	ΔE_Q (mm s ⁻¹)	Γ_L (mm s ⁻¹)	Γ_R (mm s ⁻¹)	ref
1a (solid)	1.23(2)	2.48(2)	0.29	0.27	this work
2a (solid)	1.23(2)	3.06(2)	0.29	0.32	this work
Hr	1.20	2.89			50
$[\text{Fe}(\mu\text{-OH})(\mu\text{-Ph}_4\text{DBA})(\text{TMEDA})_2(\text{OTf})]$	1.21(2)	2.87(2)			52
$[\text{Fe}_2(\mu\text{-O}_2\text{CAR}^{\text{Toh}})_2(\text{O}_2\text{CAR}^{\text{Toh}})_2(\text{C}_5\text{H}_5\text{N})_2]$	1.19(2)	3.02(2)			10, 17
1a (in THF)	1.17(2)	2.93(2)	0.38	0.38	site 1 this work
	1.23(2)	2.41(2)	0.39	0.39	site 2
1b (in THF)	0.52(4)	1.17(4)	0.49	0.49	site 1 this work
	0.66(4)	1.36(4)	0.44	0.44	site 2
1c (in THF)	0.50(2)	1.84(2)	0.40	0.37	this work

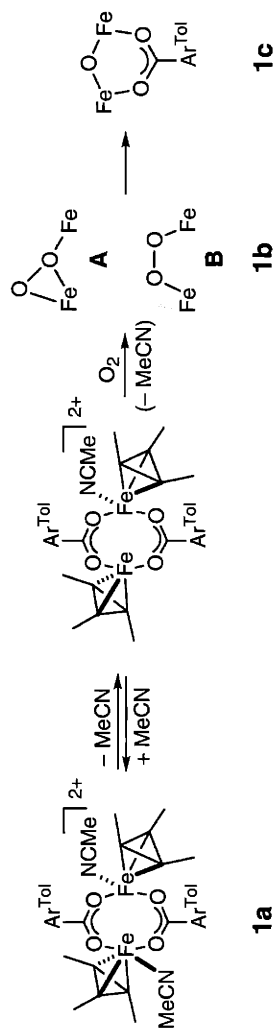
Table 5.5. EXAFS Fit Results for **1a**, **1b**, and **1c**.

sample	fit ^a	Fe...O/N ^b			Fe...Fe			Fe...C			E ₀ (eV)	R (%)
		N _s	R(Å)	σ ²	N _s	R(Å)	σ ²	N _s	R(Å)	σ ²		
1a ^c	1	2	2.06	0.003				8	3.05	0.009	7121.2	30.2
		4	2.21	0.006				3	3.48	0.005		
	2	2	2.08	0.003				8	3.05	0.009	7121.8	28.3
		3	2.21	0.006				3	3.48	0.005		
		1	2.58	0.002								
	1a ^d	1	2	2.04	0.004				8	3.08	0.008	7122.0
4			2.22	0.004				3	3.60	0.004		
2		2	2.06	0.004				8	3.07	0.008	7121.8	23.3
		3	2.22	0.003				3	3.59	0.006		
		1	2.58	0.001								
1b ^d		1	0.6	1.89	0.005	0.6	3.09	0.005	3	3.54	0.005	7122.2
	1.4		2.03	0.007				6	3.01	0.005		
	4		2.20	0.006								
	2	0.6	1.94	0.004	0.6	3.09	0.005	2	3.54	0.005	7122.8	22.1
		1.4	2.09	0.007				6	3.01	0.008		
		3	2.22	0.006								
1		2.55	0.002									
1c ^d	1	1	1.79	0.004	0.6	3.10	0.001	6	2.97	0.003	7121.1	29.2
		2	2.04	0.005				3	3.53	0.004		
		3	2.20	0.005								

^a Where present, the paired fits 1 and 2 illustrate the effect of including a long (~2.6 Å) Fe-O/N scattering interaction on the goodness-of-fit parameter, R. ^b Here, N_s = number of equivalent backscatterers, R = absorber-scatterer distance, and σ² is the Debye-Waller factor (in Å²). ^c Solid suspended in BN. ^d Frozen solution in THF.



Scheme 5.1.



Scheme 5.2.

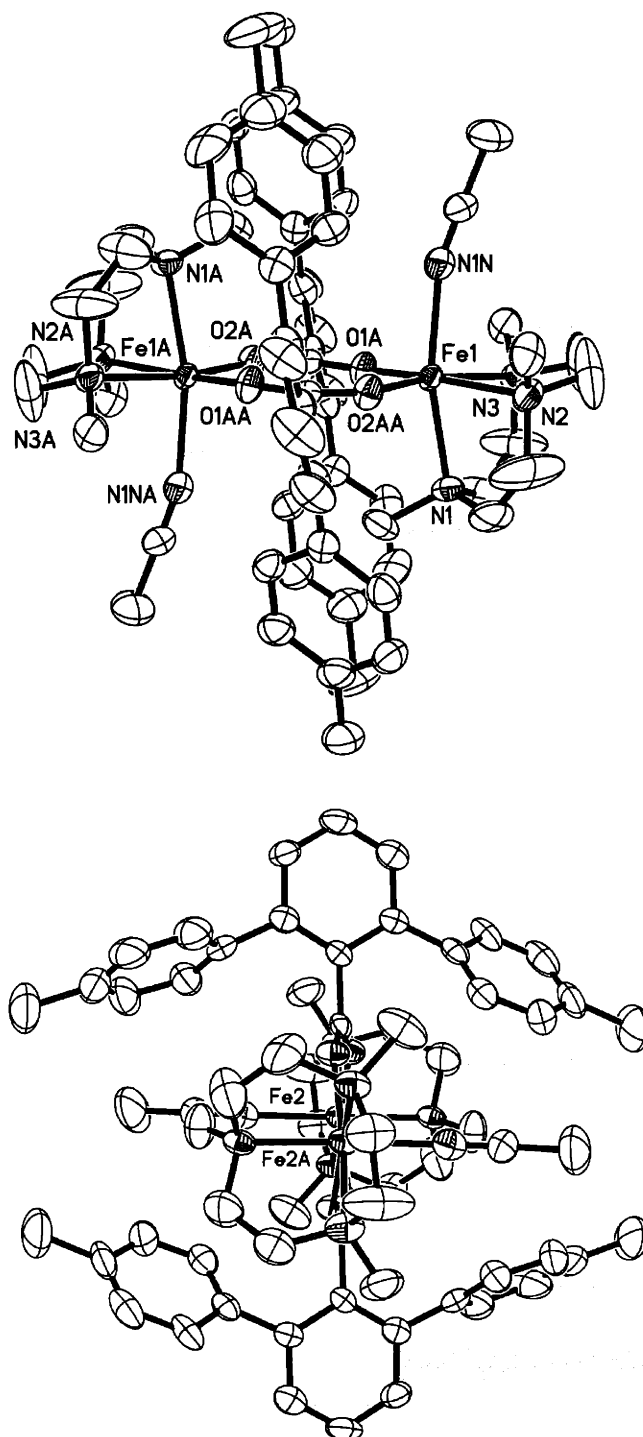


Figure 5.1. ORTEP diagram of $[\text{Fe}_2(\mu\text{-O}_2\text{CAr}^{\text{Tol}})_2(\text{Me}_3\text{TACN})_2(\text{MeCN})_2]^{2+}$ (**1a**) with thermal ellipsoids at 50% probability; top, molecule 1; bottom, molecule 2.

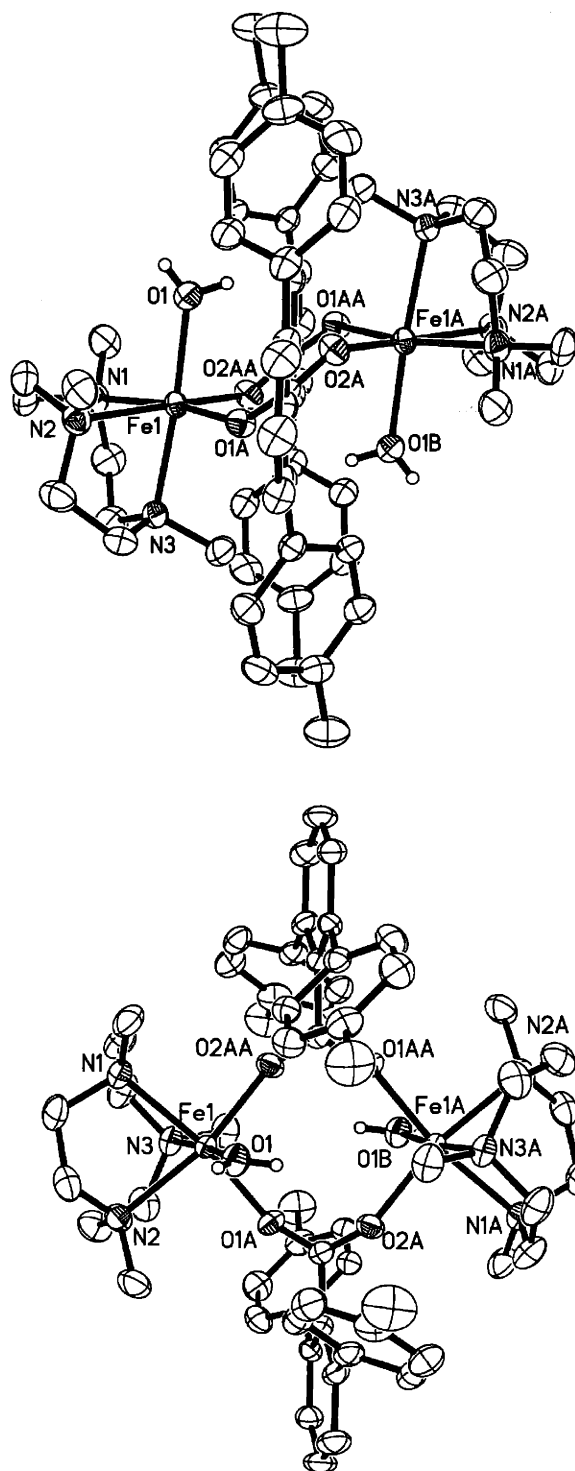


Figure 5.2. ORTEP diagram of $[\text{Fe}_2(\mu\text{-O}_2\text{CAr}^{\text{Tol}})_2(\text{Me}_3\text{TACN})_2(\text{H}_2\text{O})_2]^{2+}$ (**2a**) with thermal ellipsoids at 50% probability.

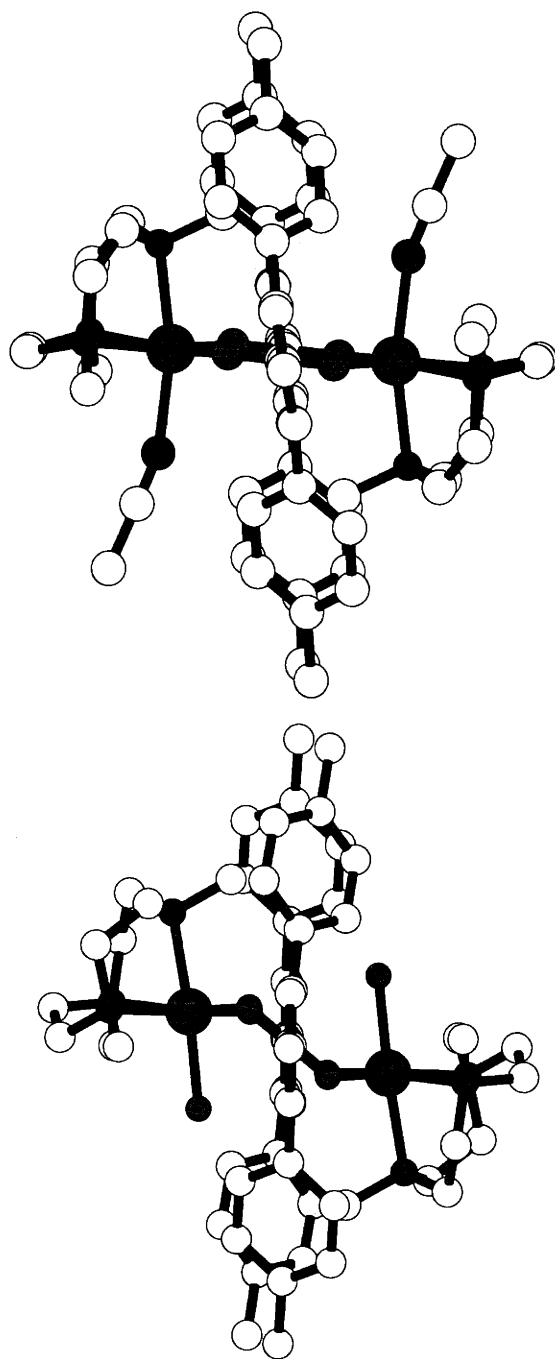


Figure 5.3. Comparison of the solid state structures of $[(\text{Me}_3\text{TACN})_2\text{Fe}_2(\mu\text{-O}_2\text{CAr}^{\text{Tol}})_2(\text{MeCN})_2]^{2+}$ (**1a**) (top) and $[(\text{Me}_3\text{TACN})_2\text{Fe}_2(\mu\text{-O}_2\text{CAr}^{\text{Tol}})_2(\text{H}_2\text{O})_2]^{2+}$ (**1b**) (bottom).

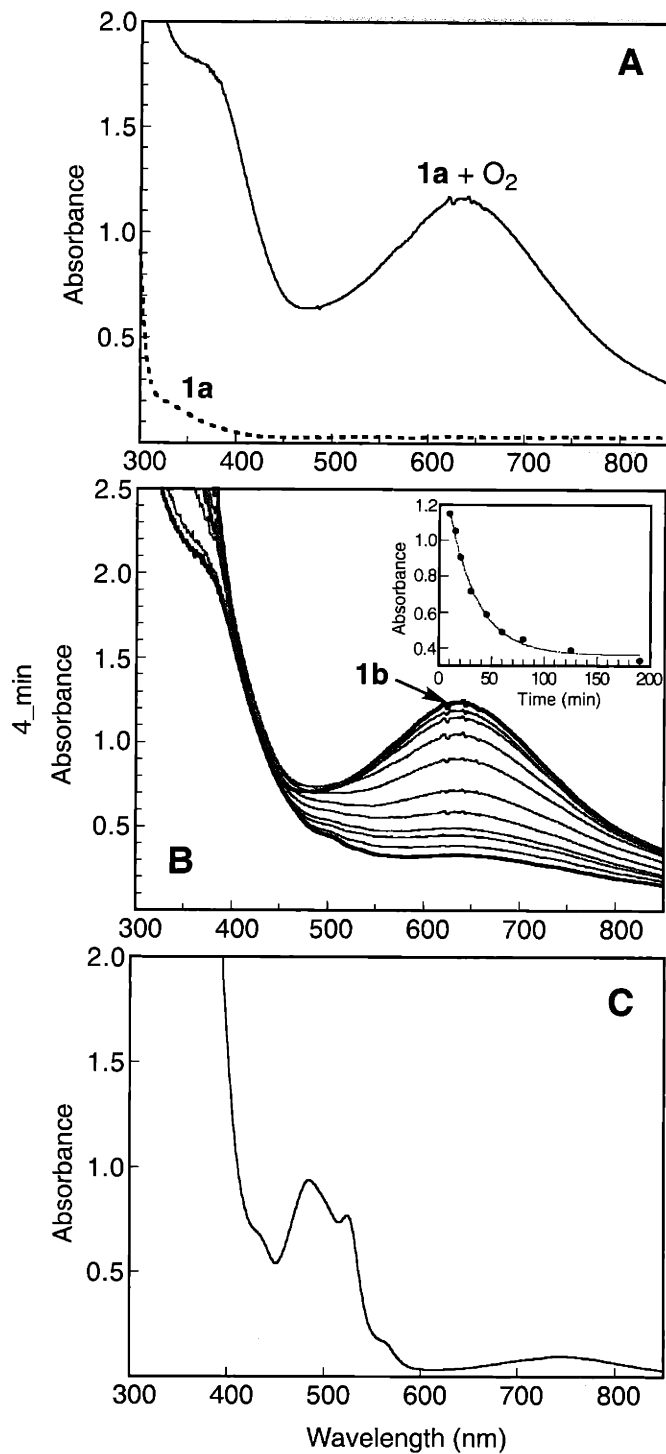


Figure 5.4. Electronic absorption spectra of (A) $[(\text{Me}_3\text{TACN})_2\text{Fe}_2(\mu\text{-O}_2\text{CAr}^{\text{Tot}})_2(\text{MeCN})_2](\text{OTf})_2$ (**1a**) (0.63 mM) in THF at -78°C before (.....) and after (—) addition of dioxygen, (B) the decay of **1b** from 4 min to 190 min in THF at -78°C (inset: a plot of A_{640} versus time and a fit to a first-order exponential decay), and (C) **1c** formed by warming **1b** to 25°C in air.

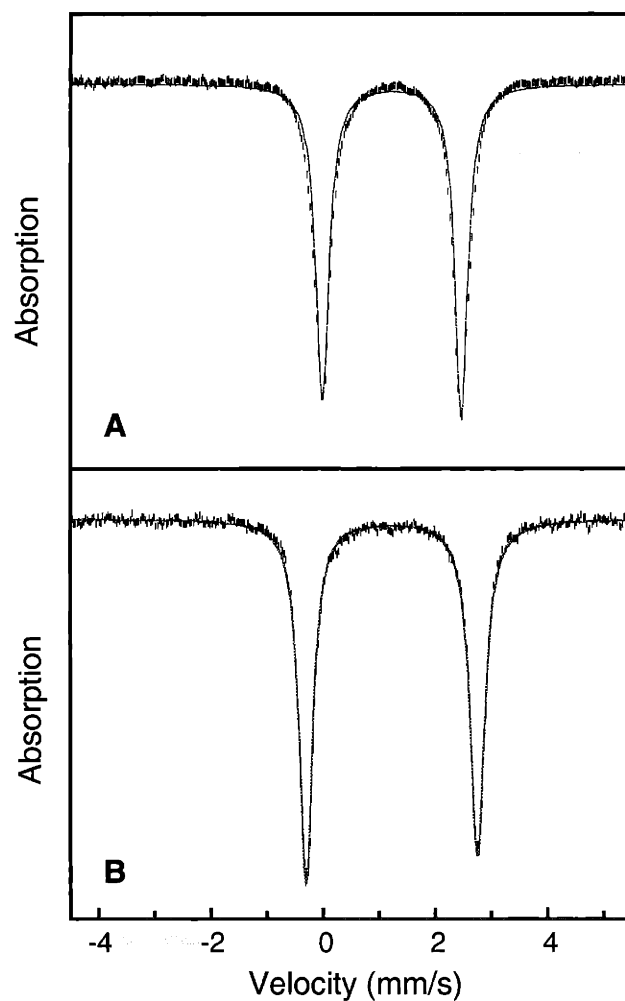


Figure 5.5. Zero-field Mössbauer spectra (experimental data (|), calculated fit (–)) recorded at 4.2 K for (A) $[(\text{Me}_3\text{TACN})_2\text{Fe}_2(\mu\text{-O}_2\text{CAr}^{\text{Tol}})_2(\text{MeCN})_2](\text{OTf})_2$ (**1a**) and (B) $[(\text{Me}_3\text{TACN})_2\text{Fe}_2(\mu\text{-O}_2\text{CAr}^{\text{Tol}})_2(\text{H}_2\text{O})_2](\text{OTf})_2$ (**1b**) in the solid state. See Table 5.4 for derived Mössbauer parameters.

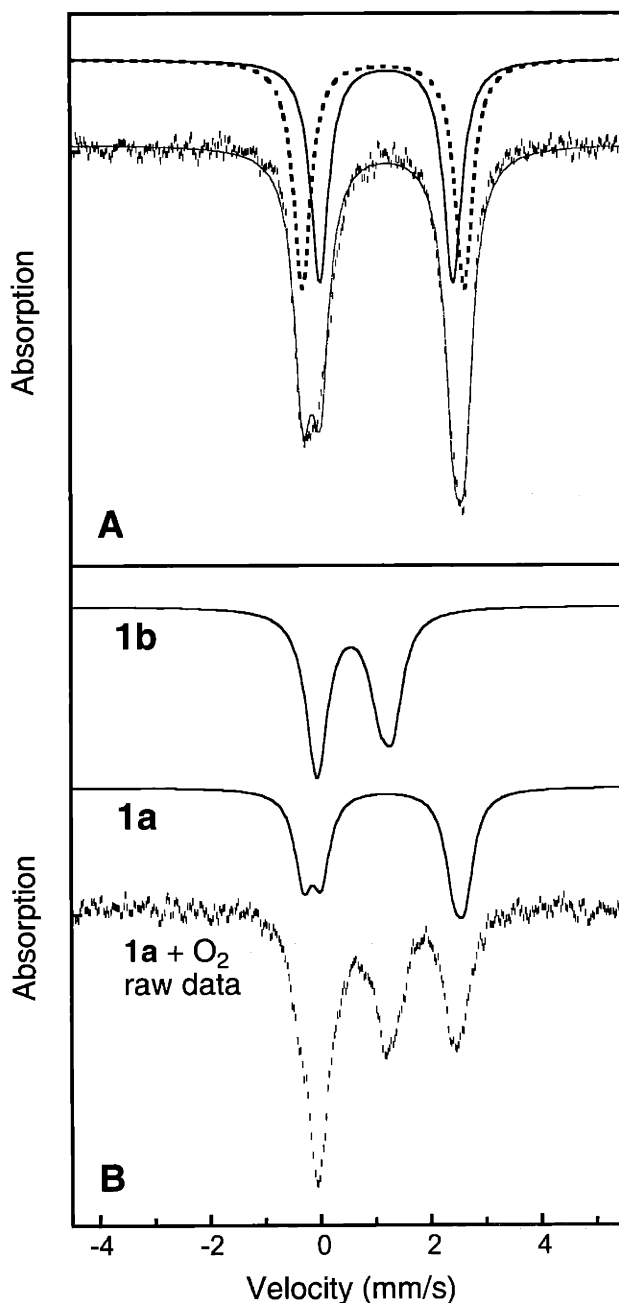


Figure 5.6. Zero-field Mössbauer spectra (experimental data (|), calculated fit (–)) recorded at 4.2 K of (A) $[(\text{Me}_3\text{TACN})_2\text{Fe}_2(\mu\text{-O}_2\text{CAr}^{\text{Tot}})_2(\text{MeCN})_2](\text{OTf})_2$ (**1a**) as a THF frozen solution, and (B) **1a** + O_2 as a THF solution. The upper curves of A show two subspectra for the calculated spectra (see Table 5.4 for derived Mössbauer parameters). The upper curves of B show contributions of **1b** and **1a** (~40% of total iron; approximated as two quadrupole doublets simulated using the parameters in Table 5.4) to the experimental data.

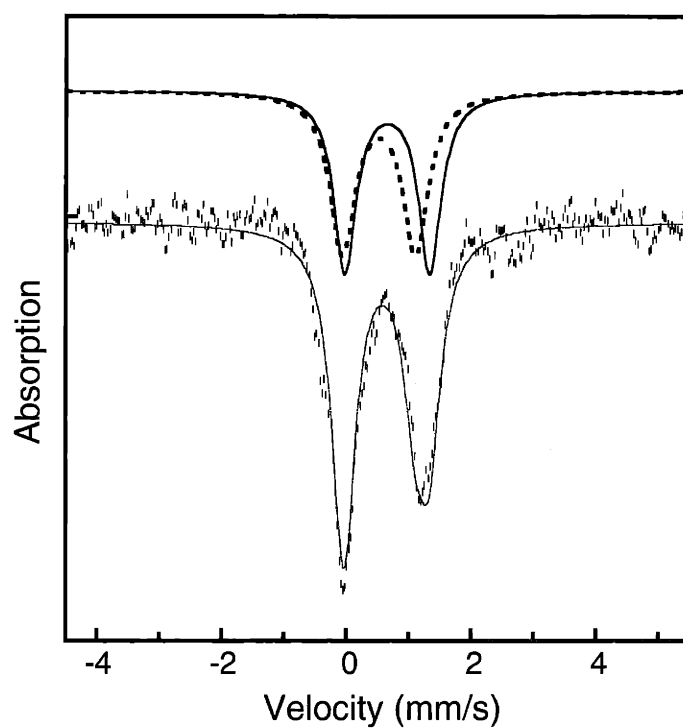


Figure 5.7. Zero-field Mössbauer spectra (experimental data (|), calculated fit (—)) recorded at 4.2 K of **1b** as a THF solution. Contribution of unreacted **1a** was removed from the experimental data (see the text). The upper curves show two subspectra for the calculated spectrum (see Table 5.4 for derived Mössbauer parameters).

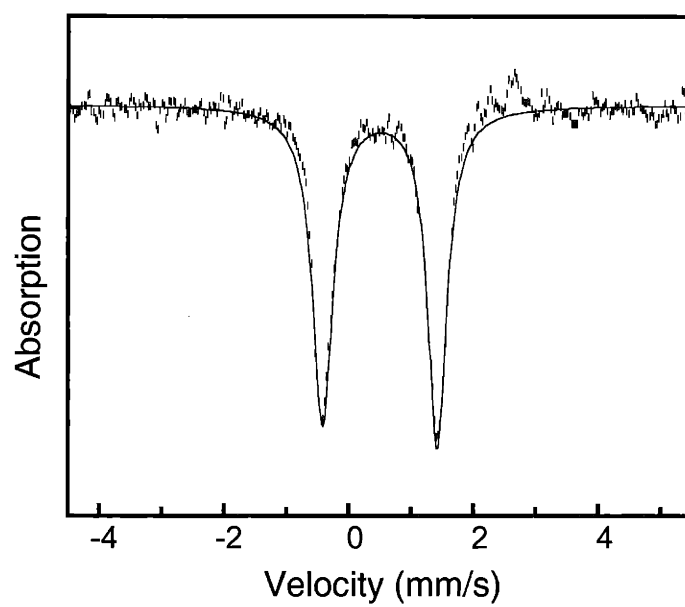


Figure 5.8. Zero-field Mössbauer spectra (experimental data (|), calculated fit (–)) recorded at 4.2 K of **1c** as a THF solution. See Table 5.4 for derived Mössbauer parameters.

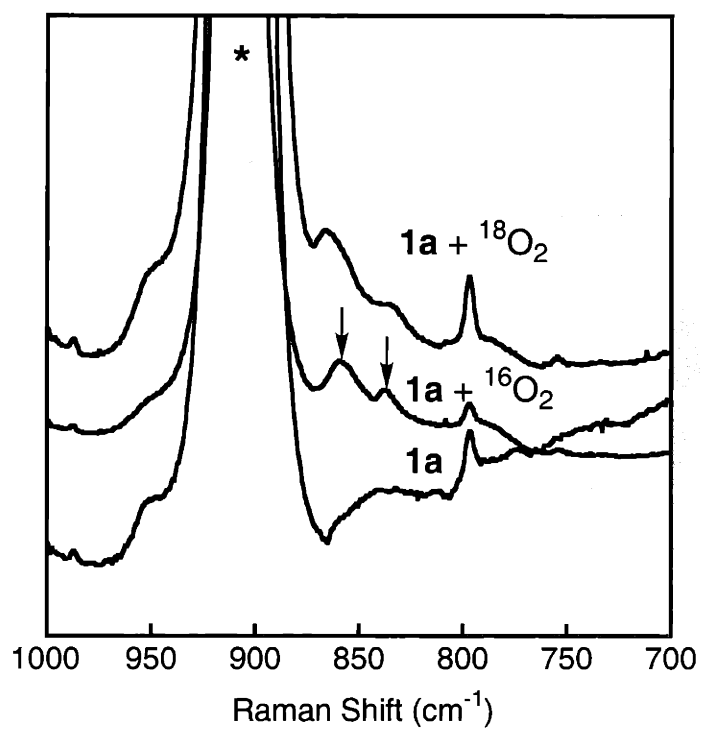


Figure 5.9. Resonance Raman spectra of fluid solutions of [(Me₃TACN)₂Fe₂-(μ-O₂CAr^{Tol})₂(MeCN)₂](OTf)₂ (**1a**), **1a** + ¹⁶O₂ (**1b**), and **1a** + ¹⁸O₂ in THF at -78 °C; excitation wavelength = 647.1 nm. Solvent features are labeled with asterisk.

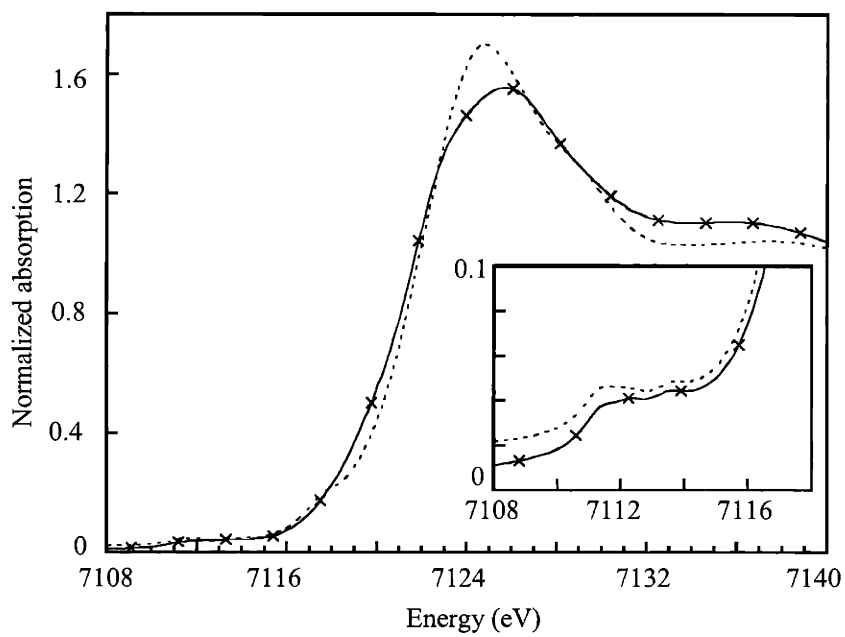


Figure 5.10. Fe K-edge and pre-edge transitions (inset) for **1a** in THF (solid line with x) and in the solid state (dotted line).

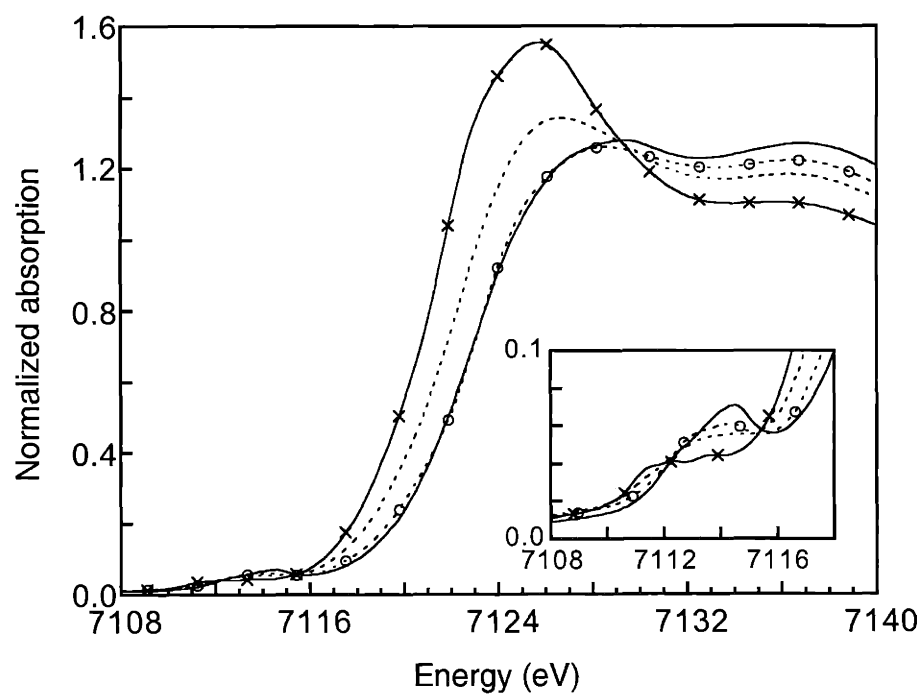


Figure 5.11. Fe K-edge and pre-edge transitions (inset) for **1a** (solid lines with x), **1a** + O₂ (dotted lines), and the putative peroxo diiron(III) species **1b** ([**1a** + O₂] - 40%[**1a**]) (dotted lines with circles), and **1c** (solid line).

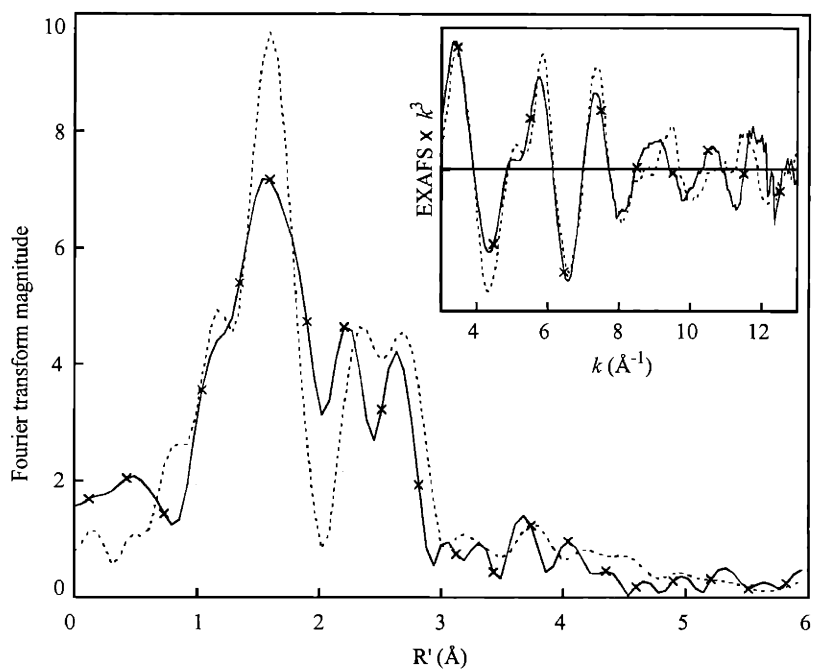


Figure 5.12. EXAFS (inset) and Fourier transformed EXAFS for **1a** in THF (solid lines with x) and in the solid state (dotted lines).

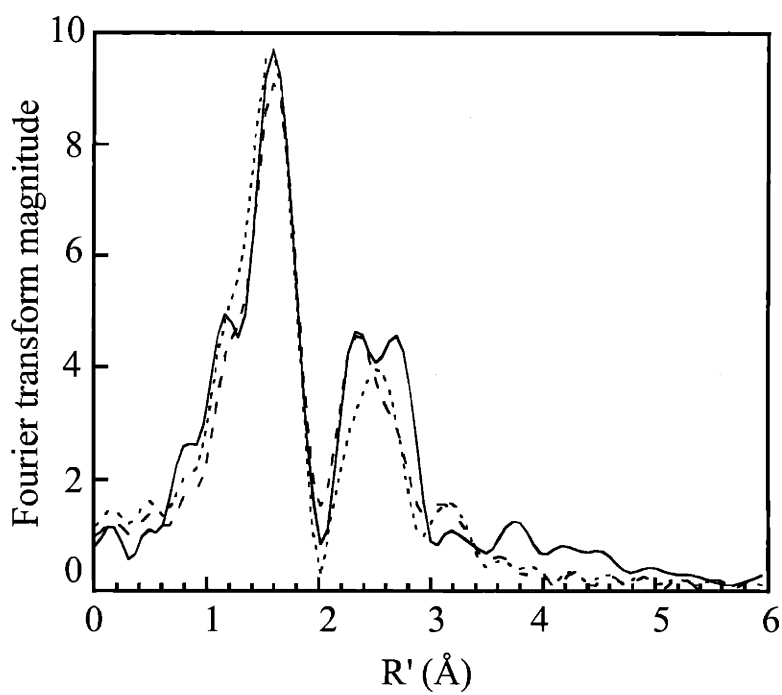


Figure 5.13. Fourier transform data (solid line) and fits for **1a**. The dotted line shows fit 1 (see Table 5.5), without the inclusion of a long, ~ 2.6 Å Fe–O/N interaction; the dashed line shows fit 2, which includes this long bond. Both fits are visually and statistically comparable.

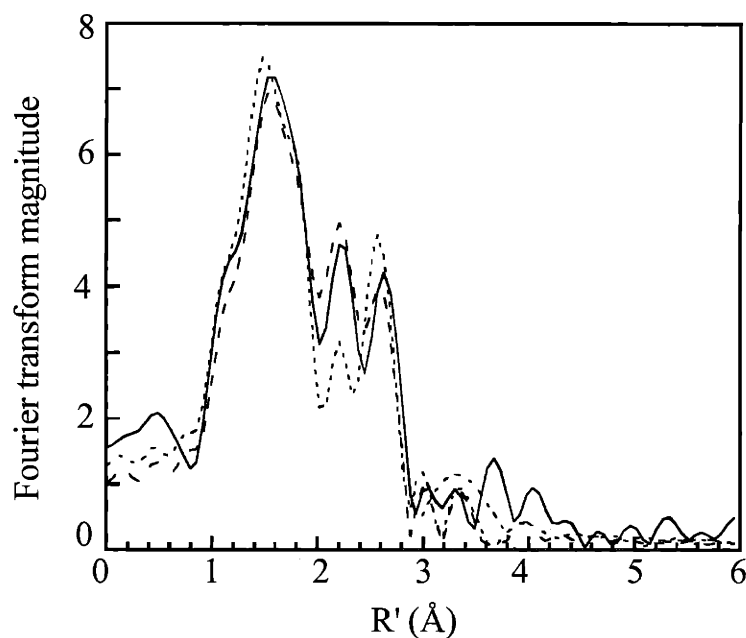


Figure 5.14. Fourier transform data (solid line) and fits for **1a** in the solid state. The dotted line shows fit 1 (see Table 5.5), without the inclusion of a long, ~ 2.6 Å Fe–O/N interaction; the dashed line shows fit 2, which includes this long bond. The fit including the long bond is appreciably better, visually and in terms of R value.

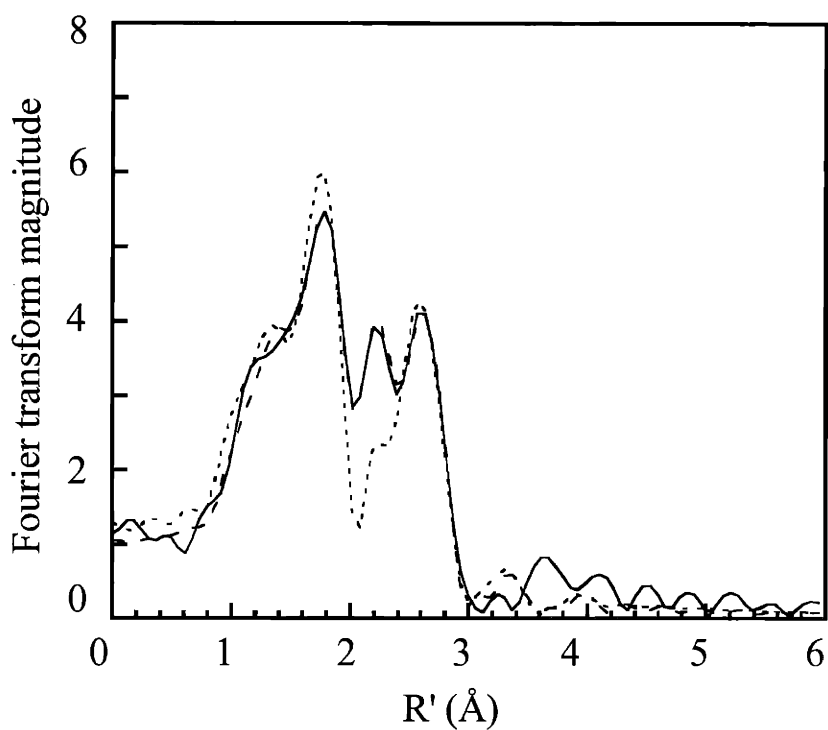


Figure 5.15. Fourier transform data (solid line) and fits for **1b**. The dotted line shows fit 1 (see Table 1), without the inclusion of a long, ~ 2.6 Å Fe–O/N interaction; the dashed line shows fit 2, which includes this long bond. The fit including the long bond is appreciably better, visually and in terms of R value.

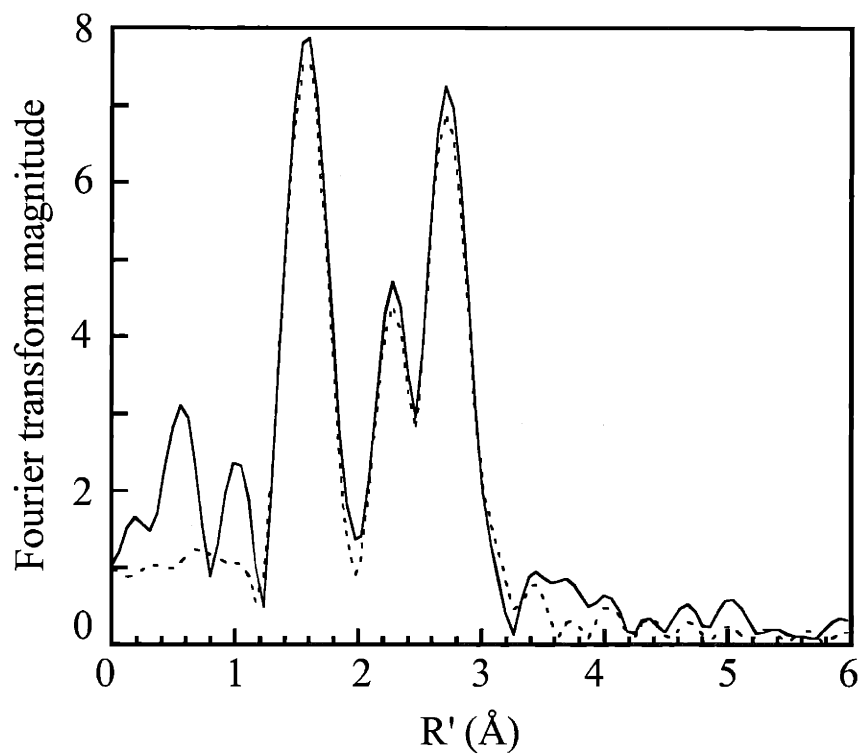


Figure 5.16. Fourier transform data (solid line) and representative best fit (dotted lines) for **1c**.

Chapter VI

**Biomimetic Access to the Elusive $\{\text{Fe}_2(\mu\text{-OH})_2(\mu\text{-O}_2\text{CR})\}^{3+}$
Core of Soluble Methane Monooxygenase Hydroxylase:
Synthesis, Characterization, and Dioxygen Reactivity
Studies of Carboxylate-Bridged Diiron(II) Complexes
Supported by Bidentate Amine Ligands***

Introduction

Selective oxidation of hydrocarbons under ambient conditions is a formidable synthetic task.¹ Certain iron(II)² or copper(I)³ centers in biological systems utilize dioxygen to effect the controlled two-electron oxidation of organic substrates. Chemical strategies adopted by these metalloenzymes for the transfer of metal-bound, dioxygen-derived units to the C–H bonds have attracted considerable scientific interest and engendered an active research area in bioinorganic chemistry.^{4–8} Recent progress in detailing the oxo transfer steps in cytochrome P450 (cP450) enzymes^{2d,9} and their synthetic analogs^{10–13} exemplify how such endeavors can be rewarded by complementary approaches.

The hydroxylase component of methane monooxygenase (MMOH) houses carboxylate-bridged non-heme diiron centers that bind and activate dioxygen.^{2a,2c,2e,14,15} Cleavage of a metal-bound O–O bond affords the highly-reactive di(μ -oxo)diiron(IV) species MMOH_Q ¹⁶ that can insert one oxygen atom into a C–H bond of various substrates including CH_4 . The reaction coordinates traversed by the enzyme intermediates have been predominantly probed by direct biological studies on MMOH itself,¹⁷ and further evaluated by DFT calculations.^{18–22} Parallel progress in non-heme iron modeling chemistry has been hampered, however, by the scarcity of enzyme analogs that integrate biomimetic structural and functional properties into a single system.⁷ Mechanistic information obtained by well-defined low molecular weight analogs can be used to calibrate the geometric and electronic parameters involved in key O–O and C–H bond activation steps of the MMOH reaction cycle.

For some time, we^{23–25} and others^{26,27} have been exploring the chemistry of non-heme diiron complexes supported by *m*-terphenyl-derived carboxylate ligands. Key architectural features of the carboxylate-rich enzyme active sites have been faithfully reproduced in such constructs,^{23,26} some of which display

biomimetic O₂ reactivity properties.^{24,26} Depending on the choice of carboxylate ligands, either (peroxo)diiron(III)²⁶ or high-valent iron(III)iron(IV)²⁴ species were accessed. Effective steric shielding provided by the aryl moieties apparently prevents deleterious bimolecular decompositions of the highly reactive dioxygen-adduct(s) encapsulated therein.

During our investigation of the Ar^{Tol}CO₂⁻-based model system, we realized that some of the oxidizing equivalents of the dioxygen-adduct(s) were being quenched by electron transfer (ET) from the diiron(II) precursor compound (Scheme 6.1).²⁴ According to this mechanistic model, **A** is the major isomer, in equilibrium with **B**, for the [Fe₂(μ-O₂CAr^{Tol})₄L₂] (L = pyridine derivatives) system at low temperatures. The oxygenation reaction is slow since it can only proceed following **A** to **B** conversion via carboxylate shifts.²⁸ Under these conditions, the putative initial O₂-adduct(s) **C** is rapidly reduced by **A**, affording a mixture of Fe(III)Fe(IV) and Fe(II)Fe(III) species as the products. Overlap between the redox windows of **A** and **C** presumably facilitates this unwanted ET process.

In order to generate quantitative amounts of functionally competent high-valent oxo diiron(IV) species, we reasoned it would be advantageous if the **B** were to predominate in solution. Rapid reaction of **B** with dioxygen would prevent the quenching of oxidizing equivalents in **C**. To achieve this goal, we implemented two different synthetic strategies, as depicted in Scheme 6.2. In one, the *m*-terphenyl ligand fragment is laterally expanded (**I**, Scheme 6.2), enhancing inter-ligand steric crowding and thus destabilizing the quadruply-bridged core in **A**. Alternatively, the doubly-bridged isomer (**B'**) is accessed by installing a bidentate ligand at each iron atom (**II**, Scheme 6.3). In the latter case, the six-coordinate isomer **A'** adopts a highly strained coordination geometry that introduces a significant degree of steric crowding at the axial positions. Strategy

I did not lead to the desired results. Instead, reactivity patterns similar to that depicted in Scheme 6.1 were observed,²⁹ or higher nuclearity iron(II) complexes were obtained.³⁰ Strategy II was successfully implemented, however, the details of which are described here.

In this chapter, we present a full description of the synthesis and reactivity studies of carboxylate-bridged diiron(II) complexes supported by sterically hindered carboxylate and diamine ligands. One such compound, $[\text{Fe}_2(\mu\text{-O}_2\text{CAr}^{\text{Tol}})_2(\text{O}_2\text{CAr}^{\text{Tol}})_2(\text{N,N-Bn}_2\text{en})_2]$ (**6**),³¹ reacts with dioxygen to afford the diiron(III) complex $[\text{Fe}_2(\mu\text{-OH})_2(\mu\text{-O}_2\text{CAr}^{\text{Tol}})(\text{O}_2\text{CAr}^{\text{Tol}})_3(\text{N-Bnen})(\text{N,N-Bn}_2\text{en})]$ (**8**).³¹ This chemistry closely parallels the activation of dioxygen by non-heme diiron enzymes and is analogous to the dealkylation of heteroatom-containing substrates effected by cP450. A consequence of this biomimetic oxidative *N*-dealkylation was the synthesis of the long-sought structural model of the diiron core in MMOH_{ox}.³¹ Collectively, these findings represent a significant expansion in scope of structural and reactivity properties of non-heme diiron model compounds. Aspects of this work have been previously communicated.³²

Experimental Section

General Considerations. All reagents were obtained from commercial suppliers and used as received unless otherwise noted. Dichloromethane and acetonitrile were distilled over CaH₂ under nitrogen. Diethyl ether, pentanes, and THF were saturated with nitrogen and purified by passage through activated Al₂O₃ columns under nitrogen.³³ Dioxygen (99.994%, BOC Gases) was dried by passing the gas stream through a column of Drierite. ¹⁸O-enriched dioxygen (99%) was supplied by ICON, NY. The compounds Fe(OTf)₂·MeCN,³⁴ 2,6-di(*p*-tolyl)benzoic acid (Ar^{Tol}CO₂H),³⁵ 2,6-di(4-fluorophenyl)benzoic acid (Ar^{4-FPh}CO₂H),³⁵ 2,6-di(4-*tert*-butylphenyl)benzoic acid (Ar^{4-tBuPh}CO₂H)³⁰ *N,N*-

dibenzylethylenediamine (*N,N*-Bn₂en),^{36,37} and *N,N*-dibenzylpropylamine³⁸ were prepared as described in the literature. The synthesis and characterization of the compounds [Fe₂(μ-O₂CAr^{Tol})₂(O₂CAr^{Tol})₂(THF)₂] (**1**)²³ and [Fe₂(μ-O₂CAr^{Tol})₄(4-^tBuC₅H₄N)₂]²⁴ have been reported. The sodium salts of the carboxylic acids, NaO₂CAr^{Tol}, NaO₂CAr^{4-FPh}, and NaO₂CAr^{4-^tBuPh}, were prepared by treating a MeOH solution of the free acid with 1 equiv of NaOH and removing the volatile fractions under reduced pressure. Air-sensitive manipulations were carried out under nitrogen in a Vacuum Atmospheres drybox or by standard Schlenk line techniques.

Physical Measurements. FT-IR spectra were recorded on a Bio Rad FTS-135 instrument with WIN-IR software. UV-vis spectra were recorded on a Hewlett Packard 8453 diode array spectrophotometer. Mössbauer spectra were obtained on an MS1 spectrometer (WEB Research Co.) with a ⁵⁷Co source in a Rh matrix maintained at room temperature in the MIT Department of Chemistry Instrumentation Facility. Solid samples were prepared by suspending ~0.015 mmol of the powdered material in Apeizon N grease and packing the mixture into a nylon sample holder. All data were collected at 4.2 K and the isomer shift (δ) values are reported with respect to natural iron foil that was used for velocity calibration at room temperature. The spectra were fit to Lorentzian lines by using the WMOSS plot and fit program.³⁹

[Fe₂(μ-O₂CAr^{Tol})₂(O₂CAr^{Tol})₂(*N,N*-Me₂en)₂] (**2**), [Fe₂(μ-O₂CAr^{Tol})₃(O₂CAr^{Tol})(*N,N*-Me₂en)] (**3**) and [Fe(O₂CAr^{Tol})₂(*N,N*-Me₂en)₂] (**4**). To a rapidly stirred CH₂Cl₂ (4 mL) solution of **1** (181 mg, 0.124 mmol) was added dropwise neat *N,N*-Me₂en³¹ (27 μL, 0.25 mmol). The pale yellow reaction mixture was stirred for 0.5 h, mixed with PhCl (1 mL), and layered with pentanes. Pale yellow blocks (87 mg, 47% based on **1**) deposited within a few days and were analyzed by X-ray crystallography. Repeated attempts to isolate analytically

pure **2** were not successful. The major contaminants included **3** and **4** as judged by crystallographic chemical analysis.

$[\text{Fe}_2(\mu\text{-O}_2\text{CAr}^{4\text{-tBuPh}})_2(\text{OTf})_2(\text{N,N-Bn}_2\text{en})_2]$ (**5**). To a rapidly stirred MeCN (10 mL) solution of $\text{Fe}(\text{OTf})_2 \cdot 2\text{MeCN}$ (218 mg, 0.500 mmol) was added a single portion of $\text{NaO}_2\text{CAr}^{4\text{-tBuPh}}$ (210 mg, 0.514 mmol). The reaction mixture clarified within a few minutes. A portion of neat *N,N*-Bn₂en (120 mg, 0.500 mmol) was added dropwise and the resulting pale yellow solution was stirred for 2 h. Volatile fractions were removed and the off-white residual solid material was extracted into CH_2Cl_2 (20 mL). Insoluble material was filtered off and the filtrate was concentrated to ca 10 mL. Vapor diffusion of pentanes into the filtrate afforded colorless blocks of **5** (165 mg, 99.3 μmol , 40%), which were suitable for X-ray crystallography. FT-IR (KBr, cm^{-1}) 3337, 3323, 3276, 2966, 2905, 2870, 1593, 1568, 1456, 1389, 1317, 1240, 1220, 1169, 1032, 849, 752, 703, 635, 578. Anal. Calcd for $\text{C}_{88}\text{H}_{98}\text{N}_4\text{O}_{10}\text{F}_6\text{Fe}_2\text{S}_2$: C, 63.61; H, 5.94; N, 3.37. Found: C, 63.57; H, 5.89; N, 3.37.

$[\text{Fe}_2(\mu\text{-O}_2\text{CAr}^{\text{Tol}})_2(\text{O}_2\text{CAr}^{\text{Tol}})_2(\text{N,N-Bn}_2\text{en})_2]$ (**6**). To a rapidly stirred yellow CH_2Cl_2 solution (10 mL) of **1** (505 mg, 0.346 mmol) was added dropwise neat *N,N*-Bn₂en (166 mg, 0.691 mmol). The resulting pale yellow solution was stirred for 10 min and filtered through Celite. Pale yellow blocks of **6** (608 mg, 98%), suitable for X-ray crystallography, were obtained by vapor diffusion of pentanes/hexanes (1:1) into the filtrate. FT-IR (KBr, cm^{-1}) 3324, 3261, 3052, 3024, 2919, 2794, 1605, 1561, 1515, 1494, 1454, 1410, 1383, 1307, 1268, 1187, 1146, 1110, 1170, 1044, 1020, 977, 855, 820, 801, 784, 765, 748, 736, 701, 584, 544, 521. Anal. Calcd for $\text{C}_{116}\text{H}_{108}\text{N}_4\text{O}_8\text{Fe}_2$: C, 77.50; H, 6.05; N, 3.12. Found: C, 77.22; H, 6.35; N, 3.08.

$[\text{Fe}_2(\mu\text{-O}_2\text{CAr}^{4\text{-FPh}})_2(\text{O}_2\text{CAr}^{4\text{-FPh}})_2(\text{N,N-Bn}_2\text{en})_2]$ (**7**) To a rapidly stirred THF (10 mL) solution of $\text{Fe}(\text{OTf})_2 \cdot 2\text{MeCN}$ (220 mg, 0.504 mmol) was added

dropwise neat *N,N*-Bn₂en (132 μ L, 0.498 mmol). A portion of NaO₂CAr^{4-FPh} (340 mg, 1.02 mmol) was added and the heterogeneous mixture was stirred overnight to afford a pale yellow clear solution. Volatile fractions were removed and the residual pale yellow solid was extracted into CH₂Cl₂ (7 mL). Insoluble material was filtered off. Vapor diffusion of Et₂O into the filtrate afforded pale yellow blocks of **7** (350 mg, 97%), which were suitable for X-ray crystallography. FT-IR (KBr, cm⁻¹) 3324, 3062, 2800, 1606, 1576, 1545, 1512, 1454, 1405, 1382, 1225, 1160, 1117, 1095, 1070, 843, 810, 792, 773, 750, 701, 555, 532. Anal. Calcd for C₁₀₈H₈₄N₄O₈F₈Fe₂: C, 70.90; H, 4.63; N, 3.06. Found: C, 70.52; H, 4.57; N, 3.06.

[Fe₂(μ -OH)₂(μ -O₂CAr^{Tol})(O₂CAr^{Tol})₃(*N*-Bnen)(*N,N*-Bn₂en)] (**8**).³¹ A CH₂Cl₂ solution (10 mL) of **6** (355 mg, 0.195 mmol) was saturated with dry dioxygen at room temperature over a period of 10 min. The dark brown solution was filtered through Celite, concentrated to ca 5 mL, and layered with pentanes at room temperature. Bright yellow blocks of **8** (166 mg, 95.3 μ mol, 49%) were obtained within several days. Yellow blocks of **8**·2PhCl·0.5C₅H₁₂ suitable for X-ray crystallography were obtained by layering pentanes over a saturated PhCl solution of this material at room temperature. FTIR (KBr, cm⁻¹) 3579, 3328, 3275, 3057, 3025, 2920, 1607, 1543, 1515, 1495, 1454, 1407, 1337, 1186, 1144, 1110, 1070, 1021, 1002, 820, 801, 785, 766, 738, 699, 608, 584, 546, 526, 449. Anal. Calcd for C₁₀₉H₁₀₄N₄O₁₀Fe₂: C, 75.17; H, 6.02; N, 3.22. Found: C, 75.30; H, 6.03; N, 3.10.

X-ray Crystallographic Studies. Intensity data were collected on a Bruker (formerly Siemens) CCD diffractometer with graphite-monochromated Mo K α radiation ($\lambda = 0.71073$ Å), controlled by a Pentium-based PC running the SMART software package.⁴⁰ Single crystals were mounted at room temperature on the tips of quartz fibers, coated with Paratone-N oil, and cooled to 188 K under a stream of cold nitrogen maintained by a Bruker LT-2A nitrogen cryostat. Data collection and reduction protocols are described elsewhere.⁴¹ The structures

were solved by direct methods and refined on F^2 by using the SHELXTL software package.⁴² Empirical absorption corrections were applied with SADABS,⁴³ part of the SHELXTL program package, and the structures were checked for higher symmetry by the program PLATON.⁴⁴ All non-hydrogen atoms were refined anisotropically unless otherwise noted. In general, hydrogen atoms were assigned idealized positions and given thermal parameters equivalent to either 1.5 (methyl hydrogen atoms) or 1.2 (all other hydrogen atoms) times the thermal parameter of the carbon atom to which they were attached. The hydrogen atoms associated with the following groups were located in the difference Fourier maps and refined isotropically: NH_2 groups on 2–8; NH group on 8; OH groups on 8. Hydrogen atoms bound to disordered solvent molecules were not included in the refinement. The structure of 2 contains a disordered CH_2Cl_2 molecule. It was distributed over three positions and refined isotropically at occupancies of 0.5, 0.35, and 0.15. The carbon atom α to the primary amine of the N,N - Bn_2en ligand in 6 was distributed over two positions and refined anisotropically at occupancies of 0.75 and 0.25. A disordered CH_2Cl_2 molecule in the structure of 7 was equally distributed over two positions and refined isotropically. The lattice solvent molecules in the structure of 8 were modeled as pentane and chlorobenzene. Crystallographic information is provided in Table 6.1.

General Procedures for Amine N-Dealkylation Studies. Samples (~12 mM $[\text{Fe}_2]$ dissolved in 1.0 mL of CH_2Cl_2) were prepared in the drybox and loaded into a 6 mL glass vial sealed with a rubber septum. For external substrate oxidation studies, N,N -dibenzylpropylamine, 1 equiv with respect to one iron(II) center, was added to the solution. The sample was brought out of the drybox and gently purged with dry O_2 at atmospheric pressure for 5 min with constant stirring. The resulting oxidation mixture was allowed to stir for 0.5 h and a

CH_2Cl_2 solution of 1,2-dichlorobenzene was added as an internal standard. The mixture was filtered through silica gel (0.5 x 1.0 cm) and the filter cake was washed with additional CH_2Cl_2 (2 mL). The combined filtrates were analyzed by GC. No significant changes were observed in the relative amounts of the PhCHO product and internal standard before and after filtration through the silica plug.

GC Analyses. Analyses were carried out on a Hewlett-Packard HP-5970 gas chromatograph connected to a HP-5971 mass analyzer. An Alltech Econo-cap EC-WAX capillary column (30 m x 0.25 mm x 0.25 μm) was used for GC/MS studies. A HP-5 crosslinked 5% PhMe-silicone column (25 m x 0.32 mm x 0.5 μm) was used for GC studies. The following program was used to effect all separations: initial temperature = 50 °C, initial time = 10 min, and a temperature ramp of 50 – 200 °C at 5 °C/min. The product, benzaldehyde, was identified by comparing its retention time and mass spectral pattern to those of an authentic standard. Co-injection with the authentic sample confirmed the assignment. Integrations were acquired by FID detection with a HP-3393 integrator. Quantitations were made by comparison with the 1,2-dichlorobenzene internal standard. Calibration plots for the detector response were prepared for benzaldehyde and 1,2-dichlorobenzene by using stock solutions of known concentrations.

Isotope Labeling Experiments. A colorless CH_2Cl_2 (2.5 mL) solution of **6** (41 mg) was loaded into a Teflon screw-capped Schlenk flask. The sample was degassed by three successive freeze-pump-thaw cycles and placed in a liquid N_2 bath. The headspace was evacuated on a vacuum line and $^{18}\text{O}_2$ was vacuum transferred into the flask. The mixture was allowed to warm to room temperature, resulting in a color change to yellowish green. The reaction

mixture was stirred for 0.5 h and analyzed by GC-MS: $t_R = 9.9$ min, m/z (abundance) = 108.10 (8068, PhCH¹⁸O, M⁺), 106.00 (1048, PhCHO, M⁺)

Results

Synthesis and Structural Characterization of [Fe₂(μ-O₂CAr^{Tol})₂(O₂CAr^{Tol})₂(*N,N*-Me₂en)₂] (2), [Fe₂(μ-O₂CAr^{Tol})₃(O₂CAr^{Tol})(*N,N*-Me₂en)] (3), and [Fe(O₂CAr^{Tol})₂(*N,N*-Me₂en)₂] (4). Compound **2** was prepared from the reaction of **1** with 2 equiv of *N,N*-Me₂en.³¹ Colorless blocks were obtained by recrystallization from CH₂Cl₂/PhCl/pentanes and analyzed by X-ray crystallography. The crystal structure of **2** is shown in Figure 6.1; selected bond lengths and angles are listed in Table 6.2. Displacement of the weakly bound THF molecules in **1** by the bidentate ligand *N,N*-Me₂en induces carboxylate shifts from terminal bidentate to monodentate (Scheme 6.3). The alleviation of steric repulsion between the μ-1,3 bridging and terminal carboxylate ligands in **2** is reflected in the significantly reduced metal...metal distance of 3.4245(5) Å, compared to 4.2822(7) in **1**. Repeated attempts to prepare an analytically pure batch of **2** were unsuccessful, however. Crystallographic chemical analysis of the reaction batch revealed contamination with the triply-bridged dinuclear complex **3**, as well as with the mononuclear compound **4**, obtained as colorless blocks barely distinguishable from **2**. The crystal structures of these compounds are displayed in Figures 6.2 and 6.3. The Fe...Fe distance of 3.1251(8) Å in **3** is considerably shorter than that in the precursor compound **1**, owing to the presence of the three bridging carboxylate ligands. Bidentate terminal coordination by *N,N*-Me₂en and Ar^{Tol}CO₂⁻ ligands complete the highly distorted trigonal bipyramidal coordination of each iron atom. The tertiary amine group on the chelating *N,N*-Me₂en ligand is pointing away from the dimetallic cavity, alleviating inter-ligand steric crowding. The pseudo-octahedral coordination

sphere of **4** comprises N_4O_2 donor atom sets contributed by two bidentate diamine and two monodentate carboxylate ligands. The metrical parameters are normal for a high-spin iron(II) complex.

Synthesis and Characterization of $[Fe_2(\mu-O_2CAR^{4-tBuPh})_2(OTf)_2(N,N-Bn_2en)_2]$ (**5**), $[Fe_2(\mu-O_2CAR^{Tol})_2(O_2CAR^{Tol})_2(N,N-Bn_2en)_2]$ (**6**), and $[Fe_2(\mu-O_2CAR^{4-FPh})_2(O_2CAR^{4-FPh})_2(N,N-Bn_2en)_2]$ (**7**). Compound **5** was prepared from a reaction between equimolar amounts of $Fe(OTf)_2 \cdot 2MeCN$, $NaO_2CAR^{4-tBuPh}$, and $N,N-Bn_2en$ in MeCN. Colorless blocks were obtained in modest yield (~40%) by recrystallization from CH_2Cl_2 /pentanes. When similar attempts were made with NaO_2CAR^{Tol} , a highly intractable solid material was obtained after removal of the solvent (THF or MeCN), precluding any further characterization. The crystal structure of **5** is displayed in Figure 6.4; selected bond lengths and angles are available in Table 6.2. The five-coordinate iron centers in **5** are related by a crystallographic center of inversion and a metal...metal distance of 3.8108(6) Å is spanned by two trans-disposed carboxylate ligands. The diamine ligand $N,N-Bn_2en$ coordinates in bidentate mode, in a manner similar to that of $N,N-Me_2en$ in **2**.

The tetracarboxylate diiron complex **6** was prepared in excellent yield (~98%) via displacement of the THF ligands in **1** by $N,N-Bn_2en$. Analytically pure pale yellow blocks were obtained by recrystallization from CH_2Cl_2 /pentanes/hexanes. A related compound **7** was conveniently accessed through direct self-assembly from $Fe(OTf)_2 \cdot 2MeCN$, NaO_2CAR^{4-FPh} , and $N,N-Bn_2en$ in a 1:2:1 ratio. Pale yellow blocks were obtained in excellent yield (~97%) following recrystallization from CH_2Cl_2 /Et₂O. The crystal structures of **6** and **7** are shown in Figures 6.5 and 6.6; selected bond lengths and angles are listed in Table 6.2. In **6** and **7**, the terminal carboxylates are bidentate and the diamine ligands $N,N-Bn_2en$ are monodentate, the opposite of the situation in **2**. The

significantly lengthened metal...metal distances of 4.3598(8) Å (in **6**) and 3.9854(9) Å (in **7**) compared with that of 3.4245(5) Å in **2** indicates that these structural variations arises from steric crowding within the dimetallic core. The binding of the terminal carboxylate ligands is asymmetric, as reflected in the two distinct Fe–O distances with $\Delta\text{Fe–O} = 0.11 \sim 0.37$ Å (Table 6.2). The longer Fe–O bonds are positioned trans to the N-donor atoms. The ligand compositions of **6** and **7**, with four carboxylate and two N-donor ligands, are similar to those of related compounds $[\text{Fe}_2(\mu\text{-O}_2\text{CAr}^{\text{Tol}})_2(\text{O}_2\text{CAr}^{\text{Tol}})_2\text{L}_2]$, where $\text{L} = \text{C}_5\text{H}_5\text{N}$ or 1-MeIm.²³

Figure 6.7 displays the 4.2 K zero-field Mössbauer spectrum of **6** in the solid state. The Mössbauer parameters, $\delta = 1.19(2)$ mm s⁻¹ and $\Delta E_{\text{Q}} = 2.90(2)$ mm s⁻¹, obtained for a single quadrupole doublet, are typical of high-spin iron(II) centers in a N/O coordination environment⁴⁵⁻⁴⁷ and comparable to those ($\delta = 1.3$ mm s⁻¹; $\Delta E_{\text{Q}} = 2.4 - 3.13$ mm s⁻¹) obtained for MMOH_{red} .^{16b,31,48,49}

Synthesis and Characterization of $[\text{Fe}_2(\mu\text{-OH})_2(\mu\text{-O}_2\text{CAr}^{\text{Tol}})(\text{O}_2\text{CAr}^{\text{Tol}})_3\text{-}(N\text{-Bnen})(N,N\text{-Bn}_2\text{en})]$ (8**).**³¹ Exposure of a colorless CH_2Cl_2 solution of **6** to dioxygen at room temperature resulted in a rapid color change to brownish yellow. Layering of pentanes over the solution afforded bright yellow blocks of **8** in modest yield (~49%). The crystal structure of **8** is shown in Figure 6.8; selected bond lengths and angles are available in Table 6.3. Structural analysis of **8** revealed that one of the $N,N\text{-Bn}_2\text{en}$ ligands in the precursor compound **6** was N -dealkylated to afford a new bidentate ligand $N\text{-Bnen}$ ³¹ bound to Fe(1). The other $N,N\text{-Bn}_2\text{en}$ ligand remains intact and is coordinated to Fe(2) in a monodentate fashion, as in **6**. The two iron atoms have pseudo-octahedral geometry and are linked by one carboxylate and two hydroxide ligands. The assignment of the single atom bridging ligand as hydroxide is supported by the Fe–O distances, which range from 1.9726(17) to 1.9977(17) Å, as well as by the location and refinement of the associated hydrogen atoms in the X-ray structure

determination. Comparable Fe–O_{hydroxo} distances occur in other high-spin iron(III) complexes having the {Fe₂(μ-OH)₂}⁴⁺ core fragments.^{23,24,50,51} The triply-bridged diiron(III) core in **8** is further stabilized by hydrogen-bonding interactions in the second coordination sphere (Figure 6.8). Specifically, the three non-bridging carboxylate ligands are hydrogen bonded to the bridging hydroxides or to the newly derived secondary amine group on the *N*-Bnen ligand, with O_{carboxylate}⋯X (X = O_{hydroxide} or N_{amine}) distances ranging from 2.668(3) to 2.891(3) Å. The Fe⋯Fe distance of 2.9788(6) Å is shorter than the values of 3.089(2) – 3.155(3) Å in the doubly-bridged {Fe₂(μ-OH)₂}⁴⁺ cores,^{50,51} but longer than those (2.8322(8) – 2.8843(9) Å) in the quadruply-bridged {Fe₂(μ-OH)₂(μ-O₂CAr^{Tol})₂}²⁺ cores.^{23,24}

Except for a shoulder at ~330 nm, the UV-vis spectra of **8** (Figure 6.9) are rather featureless and do not display any longer wavelength LMCT transitions, properties consistent with the presence of hydroxo, not oxo, bridging ligands.^{2e,45} The Mössbauer spectrum obtained for a solid sample of **8** at 77 K (Figure 6.10) exhibits a broad ($\Gamma = 0.62 - 0.74 \text{ mm s}^{-1}$) asymmetric quadrupole doublet, indicative of paramagnetic relaxation. At 4.2 K, a narrower ($\Gamma = 0.33 - 0.35 \text{ mm s}^{-1}$) well-resolved single quadrupole doublet was obtained (Figure 6.11), which was fit with $\delta = 0.48(2) \text{ mm s}^{-1}$ and $\Delta E_Q = 0.61(2) \text{ mm s}^{-1}$. These parameters are typical for high-spin iron(III) centers with pseudo-octahedral geometry.⁴⁵⁻⁴⁷ The narrow peak width indicates that the two iron atoms in **8** are indistinguishable under the Mössbauer conditions.

Oxidative N-Dealkylation. Following exposure of CH₂Cl₂ solutions of **6** to dioxygen at room temperature, the reaction mixture was analyzed. Gas chromatographic-mass spectrometric studies revealed the formation of PhCHO in an average yield of 60(5)% based on [Fe₂] (Figure 6.12). The origin of the oxygen atom incorporated into PhCHO was established by use of ¹⁸O₂, which

afforded PhCH¹⁸O as the major isotopomer (90:10 PhCH¹⁸O/PhCH¹⁶O) under similar conditions. This result provides compelling evidence that the *N*-Bnen ligand in **8** is the product of oxidative *N*-dealkylation of **6**. Insertion of an O₂-derived oxygen atom into the benzylic C–H bond affords the α-hydroxylamine, which decomposes to the final products, the dealkylated amine and PhCHO. This process is well-documented for cP450^{2d,52} as well as in copper dioxygen chemistry.^{4,6,53-57} Upon prolonged exposure to air, the labeled oxygen atom of PhCH¹⁸O in the reaction mixture exchanged. We suspect that the small amount of PhCH¹⁶O identified in the reaction mixture may result from reaction of PhCH¹⁸O with trace amounts of H₂O introduced during sample handling.

When a non-coordinating analog of *N,N*-Bn₂en, such as *N,N*-dibenzylpropylamine, was employed as an external substrate in conjunction with either a mononuclear or a dinuclear iron(II) complex, the yield of the *N*-dealkylation product was significantly reduced. Under reaction conditions similar to those used for **6** (2 equiv of amine substrate per Fe^{II}₂), [Fe(O₂CAr^{Tol})₂(TMEDA)]^{31,32} afforded only 1.3(3)%, and [Fe₂(μ-O₂CAr^{Tol})₄(4-^tBuC₅H₄N)₂]^{2,4} 13(1)%, of PhCHO. Even with a 10-fold increase in the substrate loading, the efficiency of the external substrate oxidation is significantly lower than that effected by **6** (Figure 6.13).

Discussion

Synthetic Routes to Diiron(II) Complexes. A range of bidentate *N*-donor ligands was screened to implement strategy II in Scheme 6.2. Initial attempts to install bidentate ligands into the pre-assembled diiron(II) module {Fe₂(μ-O₂CAr^{Tol})₂(O₂CAr^{Tol})₂} resulted in unwanted core disassembly to mononuclear species. For example, sterically demanding diamine ligands, such as TMEDA,³¹ or diamine ligands that afford smaller bite angles, such as 3-dimethyl-

aminopropylamine, afforded five- or six-coordinate monoiron(II) complexes (Scheme 6.3). By proper choice of the diamine ligand, the desired dinuclear complex **2** was obtained but only in a mixture that also contained **3** and **4**, which can be regarded as formal disproportionation products of **2**. A sterically more demanding *N,N*-disubstituted ethylenediamine was thus targeted.

In the design of this new ligand, we intended also to integrate potential substrate fragments as part of the ethylenediamine derivative. By juxtaposing oxidizable C–H bonds to the reactive metal-dioxygen adduct, we planned to achieve the desired functional chemistry in enzyme models that lack substrate binding cavities. A similar strategy has been previously adopted for related copper oxidation chemistry,^{4,6,53-59} as well as metallohydrolase models.^{60,61} We therefore introduced the *N,N*-Bn₂en diamine ligand in the synthesis of the diiron(II) complexes. The sterically more demanding benzyl groups installed on the nitrogen atom effectively blocked the formation of the undesired bis(chelate) complexes, affording analytically pure diiron(II) compounds **5–7**. The primary coordination spheres of **6** and **7** comprise four carboxylate ligands and two N-donor ligands, just like the diiron(II) center in MMOH_{red} and related proteins.^{2a,2c,14,15,62}

Structural Model of MMOH_{ox}. Among several crystal structures of MMOH_{ox}³¹ determined under different conditions,⁶²⁻⁶⁸ two examples feature the {Fe₂(μ-OH)₂(μ-O₂CR)}³⁺ dimetallic core (Figure 6.14),^{62,66} which previously has not been reproduced outside the enzyme environment. Analogous {M₂(μ-OH)₂(μ-O₂CR)}³⁺ units exist in kinetically inert dichromium(III),⁶⁹ dimolybdenum(III),⁷⁰ dicobalt(III),⁷¹ and diruthenium(III)⁷² complexes. A survey of the CSD revealed that triply-bridged {Fe₂(μ-X)(μ-O₂CR)₂}ⁿ⁺ cores comprising a single atom bridge (X = OH[−] or OR[−]) and two μ-1,3 bridging carboxylate ligands are preferred by diiron complexes (C, Scheme 6.4). The steric

hindrance imposed by the *p*-tolyl substituents on the $\text{Ar}^{\text{Tol}}\text{CO}_2^-$ ligand precludes coordination of two bridging carboxylate ligands in the orthogonal positions. As a result, only one carboxylate ligand can be accommodated in the triply-bridged core in **8** (**D**, Scheme 6.4). Alternatively, two bridging $\text{Ar}^{\text{Tol}}\text{CO}_2^-$ ligands can be disposed trans across the $\{\text{Fe}_2(\mu\text{-OH})_2\}^{4+}$ plane, as in $[\text{Fe}_2(\mu\text{-OH})_2(\mu\text{-O}_2\text{CAr}^{\text{Tol}})_2(\text{O}_2\text{CAr}^{\text{Tol}})_2\text{L}_2]$,^{23,24} where $\text{L} = \text{C}_5\text{H}_5\text{N}$ or $4\text{-}^t\text{BuC}_5\text{H}_4\text{N}$ (**E**, Scheme 6.4). This configuration, however, is not allowed for **8**, owing to the bidentate *N*-Bnen ligand that occupies the axial position of Fe(1) (Figure 6.8). Taken together, the unique structural requirements of the bulky $\text{Ar}^{\text{Tol}}\text{CO}_2^-$ and *N*-Bnen ligands play an essential role in assembling the biomimetic $\{\text{Fe}_2(\mu\text{-OH})_2(\mu\text{-O}_2\text{CR})\}^{3+}$ core outside the well-structured four-helix bundle scaffold⁷³ of the enzyme.

Both iron atoms in MMOH_{ox} from *Methylosinus trichosporium* OB3b have distorted octahedral coordination environments.⁶⁶ The metal...metal distance of 2.99 Å is spanned by one carboxylate and two hydroxide bridging ligands, with Fe-O_{hydroxide} distances of 1.71 – 2.17 Å. The Fe...Fe and Fe-O_{hydroxide} distances of 2.9788(6) Å and 1.9726(17) – 1.9977(17) Å, respectively, in **8** support the assignment of the single atom bridging ligands in the enzyme as hydroxide groups. A significantly increased metal...metal distance of 3.2 Å was obtained for MMOH_{ox} isolated from *Methylococcus capsulatus* (Bath), for which one of the single atom bridging ligands was modeled as weakly bound H_3O_2^- ion.⁶² In both structures, two histidine and three carboxylate terminal ligands, along with solvent-derived molecules, complete the NO_5 donor atom sets for each metal. A slightly different ligand combination is adopted by **8**, which has a N_2O_4 set for one iron and a NO_5 set for the other. Hydrogen-bonding interactions in the second coordination sphere apparently strengthen the dimetallic core in **8**. Notably, the hydrogen-bonding interaction between the axial carboxylate ligands

and one of the bridging hydroxide ligands also occurs in the crystal structure of MMOH_{ox} from *M. capsulatus* (Bath).⁶²

Zero-field Mössbauer spectra obtained at 4 K for MMOH_{ox} from *M. capsulatus* (Bath) indicated the presence of two slightly inequivalent high-spin iron(III) sites in a 1:1 ratio.^{16b} Comparable sets of parameters were obtained for the spectra of MMOH_{ox} from *M. trichosporium* OB3b, which were similarly modeled as the sum of two quadrupole doublets.⁴⁸ As summarized in Table 6.4, the isomer shift parameter of **8** is comparable to those of MMOH_{ox} and a structurally related diiron(III) complex $[\text{Fe}_2(\mu\text{-O}_2\text{CAr}^{\text{Tol}})_2(\text{O}_2\text{CAr}^{\text{Tol}})_2(4\text{-}^t\text{BuC}_5\text{H}_4\text{N})_2]$.^{16b,48,74} The significantly different ΔE_{Q} values obtained for **8** and $[\text{Fe}_2(\mu\text{-O}_2\text{CAr}^{\text{Tol}})_2(\text{O}_2\text{CAr}^{\text{Tol}})_2(4\text{-}^t\text{BuC}_5\text{H}_4\text{N})_2]$, both having six-coordinate iron atoms, however, are somewhat unexpected. Deviations from idealized O_h geometry increases the ΔE_{Q} values for a high-spin d^5 system, whereas the δ values are barely influenced by such variations. The two inequivalent iron sites identified for the MMOH_{ox} core (Table 6.4) may reflect such a subtle structural modification in coordination geometry.

Mechanism of Oxidative N-Dealkylation. Although detailed information about the conversion of **6** to **8** is currently unavailable, we postulate the working mechanism depicted in Scheme 6.5. This working hypothesis is based upon mechanistic frameworks previously developed to explain similar chemical transformations effected by cP450^{2d,52} or copper amine complexes,⁵⁴ in which high-valent iron(IV)-oxo porphyrin π -radical or di(μ -oxo)dicopper(III) species were invoked as reactive intermediates that first hydroxylate the C–H bonds α to the nitrogen, affording the corresponding aldehyde or ketone as the final products.

In our chemistry, we postulate the involvement of a reactive dioxygen adduct of **6**, either at the (peroxo)diiron(III) or di(oxo)diiron(IV) oxidation level,

by analogy to the MMOH reaction cycle.^{2a,2c,2e,14} Given the fundamentally nucleophilic nature of well-characterized (peroxo)diiron(III) species supported on tetracarboxylate ligand frameworks,^{75,76} we prefer a di(oxo)diiron(IV) species as the functionally competent unit. A high-valent iron(IV)-oxo species has also been implicated in the catalytic cycle of a mononuclear iron(II) complex $[L^1Fe(MeCN)_2]^{2+}$ ³¹ that, in conjunction with H_2O_2 , catalyzes oxidative N-dealkylation, stereoselective alkane hydroxylation, and olefin epoxidation.⁷⁷ The electrophilic nature of the $\{Cu_2(\mu-O)_2\}^{2+}$ center, which effects α -hydroxylation of the metal-bound alkylamine ligand, is also well-established.⁵⁴

Insertion of the oxygen atom into the benzylic C–H bond of *N,N*-Bn₂en can proceed by at least three distinguishable reaction pathways. Both conventional recoil with hydrogen atom transfer (HAT) (middle, Scheme 6.5) or sequential single electron transfer (SET), deprotonation, and internal electron transfer (bottom, Scheme 6.5) can equally well provide the α -carbon-centered neutral radical. Subsequent oxygen rebound affords the α -hydroxylamine. Alternatively, concerted insertion of the oxygen atom into the C–H bond can be invoked (top, Scheme 6.5). In the key C–H bond activation step, the tertiary amine group of the *N,N*-Bn₂en ligand may remain coordinated to the metal center, as in **5**. In such an event, the coupled Fe(III)-aminium cation radical in the SET pathway can be alternatively formulated as an Fe(IV)-amine. The SET pathway is implicated in cP450-catalyzed oxidative N-dealkylation,^{2d} whereas direct intramolecular attack at the C–H bond is favored for the di(μ -oxo)dicopper(III) system.⁵⁴ Efforts are currently in progress to delineate the mechanism of oxidative *N*-dealkylation effected by the present non-heme diiron model systems.

Summary and Perspective

Synthetic routes were developed to install potential substrates as part of the ligand fragment bound to non-heme diiron(II) model complexes. Reaction of one such compound with O₂ effected the unprecedented oxidative N-dealkylation of a benzylamine fragment. It also afforded the first diiron(III) complex having the $\{\text{Fe}_2(\mu\text{-OH})_2(\mu\text{-O}_2\text{CR})\}^{3+}$ core structure of MMOH_{ox}, which previously has not been replicated outside the enzyme. A well-defined synthetic module is now accessible, the elaboration of which will significantly extend the scope of structural–function studies that can be carried out with dioxygen-activating non-heme diiron(II) model. The reaction coordinates mapped out by such complexes should help to unravel the details of biological C–H activation at the molecular level.

Acknowledgment. This work was supported by a grant from the National Science Foundation. I thank Ms. Jane Kuzelka for help in acquiring the Mössbauer spectra.

References

- (*) Part of this work has appeared previously in reference 32, © 2001 American Chemical Society.
- (1) (a) Shilov, A. E.; Shul'pin, G. B. *Chem. Rev.* **1997**, *97*, 2879-2932. (b) Stahl, S. S.; Labinger, J. A.; Bercaw, J. E. *Angew. Chem., Int. Ed. Engl.* **1998**, *37*, 2180-2192. (c) Shilov, A. E.; Shteinman, A. A. *Acc. Chem. Res.* **1999**, *32*, 763-771.
- (2) (a) Feig, A. L.; Lippard, S. J. *Chem. Rev.* **1994**, *94*, 759-805. (b) Que, L., Jr.; Ho, R. Y. N. *Chem. Rev.* **1996**, *96*, 2607-2624. (c) Wallar, B. J.; Lipscomb, J. D. *Chem. Rev.* **1996**, *96*, 2625-2657. (d) Sono, M.; Roach, M. P.; Coulter, E. D.; Dawson, J. H. *Chem. Rev.* **1996**, *96*, 2841-2887. (e) Solomon, E. I.; Brunold, T. C.; Davis, M. I.; Kemsley, J. N.; Lee, S.-K.; Lehnert, N.; Neese, F.; Skulan, A. J.; Yang, Y.-S.; Zhou, J. *Chem. Rev.* **2000**, *100*, 235-349.
- (3) (a) *Bioinorganic Chemistry of Copper*; Karlin, K. D., Tyeklár, Z., Eds.; Chapman & Hall: New York, 1993. (b) Solomon, E. I.; Sundaram, U. M.; Machonkin, T. E. *Chem. Rev.* **1996**, *96*, 2563-2605.
- (4) Tolman, W. B. *Acc. Chem. Res.* **1997**, *30*, 227-237.
- (5) Liang, H.-C.; Dahan, M.; Karlin, K. D. *Curr. Opin. Chem. Biol.* **1999**, *3*, 168-175.
- (6) Mahadevan, V.; Klein Gebbink, R. J. M.; Stack, T. D. P. *Curr. Opin. Chem. Biol.* **2000**, *4*, 228-234.
- (7) Du Bois, J.; Mizoguchi, T. J.; Lippard, S. J. *Coord. Chem. Rev.* **2000**, *200-202*, 443-485.
- (8) Tolman, W. B.; Spencer, D. J. E. *Curr. Opin. Chem. Biol.* **2001**, *5*, 188-195.
- (9) Newcomb, M.; Toy, P. H. *Acc. Chem. Res.* **2000**, *33*, 449-455.
- (10) (a) Lee, K. A.; Nam, W. J. *Am. Chem. Soc.* **1997**, *119*, 1916-1922. (b) Goh, Y. M.; Nam, W. *Inorg. Chem.* **1999**, *38*, 914-920. (c) Nam, W.; Lim, M. H.; Lee, H. J.; Kim, C. J. *Am. Chem. Soc.* **2000**, *122*, 6641-6647. (d) Nam, W.; Han, H.

- J.; Oh, S.-Y.; Lee, Y. J.; Choi, M.-H.; Han, S.-Y.; Kim, C.; Woo, S. K.; Shin, W. *J. Am. Chem. Soc.* **2000**, *122*, 8677-8684. (e) Nam, W.; Lim, M. H.; Moon, S. K.; Kim, C. *J. Am. Chem. Soc.* **2000**, *122*, 10805-10809.
- (11) Bernadou, J.; Meunier, B. *Chem. Commun.* **1998**, 2167-2173.
- (12) Collman, J. P.; Chien, A. S.; Eberspacher, T. A.; Brauman, J. I. *J. Am. Chem. Soc.* **2000**, *122*, 11098-11100.
- (13) Woggon, W.-D.; Wagenknecht, H.-A.; Claude, C. *J. Inorg. Biochem.* **2001**, *83*, 289-300.
- (14) Merckx, M.; Kopp, D. A.; Sazinsky, M. H.; Blazyk, J. L.; Müller, J.; Lippard, S. *J. Angew. Chem., Int. Ed. Engl.* **2001**, *40*, 2782-2807.
- (15) Whittington, D. A.; Lippard, S. J. *Handbook of Metalloproteins*; Messerschmidt, A., Huber, R., Poulos, T. and Wieghardt, K., Ed.; John Wiley & Sons: Chichester, 2001, pp 712-724.
- (16) (a) Lee, S.-K.; Fox, B. G.; Froland, W. A.; Lipscomb, J. D.; Münck, E. *J. Am. Chem. Soc.* **1993**, *115*, 6450-6451. (b) Liu, K. E.; Valentine, A. M.; Wang, D.; Huynh, B. H.; Edmondson, D. E.; Salifoglou, A.; Lippard, S. J. *J. Am. Chem. Soc.* **1995**, *117*, 10174-10185. (c) Shu, L.; Nesheim, J. C.; Kauffmann, K.; Münck, E.; Lipscomb, J. D.; Que, L., Jr. *Science* **1997**, *275*, 515-518.
- (17) Valentine, A. M.; Stahl, S. S.; Lippard, S. J. *J. Am. Chem. Soc.* **1999**, *121*, 3876-3887.
- (18) Siegbahn, P. E. M.; Crabtree, R. H. *J. Am. Chem. Soc.* **1997**, *119*, 3103-3113.
- (19) Siegbahn, P. E. M. *Inorg. Chem.* **1999**, *38*, 2880-2889.
- (20) Dunietz, B. D.; Beachy, M. D.; Cao, Y.; Whittington, D. A.; Lippard, S. J.; Friesner, R. A. *J. Am. Chem. Soc.* **2000**, *122*, 2828-2839.
- (21) Gherman, B. J.; Dunietz, B. D.; Whittington, D. A.; Lippard, S. J.; Friesner, R. A. *J. Am. Chem. Soc.* **2001**, *123*, 3836-3837.
- (22) Friesner, R. A.; Dunietz, B. D. *Acc. Chem. Res.* **2001**, *34*, 351-358.

- (23) Lee, D.; Lippard, S. J. *J. Am. Chem. Soc.* **1998**, *120*, 12153-12154.
- (24) Lee, D.; Du Bois, J.; Petasis, D.; Hendrich, M. P.; Krebs, C.; Huynh, B. H.; Lippard, S. J. *J. Am. Chem. Soc.* **1999**, *121*, 9893-9894.
- (25) Lee, D.; Krebs, C.; Huynh, B. H.; Hendrich, M. P.; Lippard, S. J. *J. Am. Chem. Soc.* **2000**, *122*, 5000-5001.
- (26) Hagadorn, J. R.; Que, L., Jr.; Tolman, W. B. *J. Am. Chem. Soc.* **1998**, *120*, 13531-13532.
- (27) Hagadorn, J. R.; Que, L., Jr.; Tolman, W. B.; Prisecaru, I.; Münck, E. *J. Am. Chem. Soc.* **1999**, *121*, 9760-9761.
- (28) Rardin, R. L.; Tolman, W. B.; Lippard, S. J. *New J. Chem.* **1991**, *15*, 417-430.
- (29) Lee, D.; Lippard, S. J., unpublished results.
- (30) Lee, D.; Sorace, L.; Caneschi, A.; Lippard, S. J., submitted for publication.
- (31) Abbreviations used: Ar^{Tol}CO₂⁻, 2,6-di(*p*-tolyl)benzoate; Ar^{Mes}CO₂⁻, 2,6-dimesitylbenzoate; MMOH_{ox}, MMOH in the iron(III)iron(III) oxidation state; MMOH_{red}, MMOH in the iron(II)iron(II) oxidation state; *N,N*-Bn₂en, *N,N*-dibenzylethylenediamine; *N,N*-Me₂en, *N,N*-dimethylethylenediamine; *N*-Bnen, *N*-benzylethylenediamine; L¹, *N,N'*-bis(pyridin-2-ylmethyl)-*N,N''*-bis(3,4,5-trimethoxybenzyl)-ethane-1,2-diamine; TMEDA, *N,N,N',N'*-tetramethylethylenediamine
- (32) Lee, D.; Lippard, S. J. *J. Am. Chem. Soc.* **2001**, *123*, 4611-4612.
- (33) Pangborn, A. B.; Giardello, M. A.; Grubbs, R. H.; Rosen, R. K.; Timmers, F. J. *Organometallics* **1996**, *15*, 1518-1520.
- (34) Hagen, K. S. *Inorg. Chem.* **2000**, *39*, 5867-5869.
- (35) (a) Du, C.-J. F.; Hart, H.; Ng, K.-K. D. *J. Org. Chem.* **1986**, *51*, 3162-3165. (b) Saednya, A.; Hart, H. *Synthesis* **1996**, 1455-1458. (c) Chen, C.-T.; Siegel, J. S. *J. Am. Chem. Soc.* **1994**, *116*, 5959-5960.
- (36) Guillaume, D.; Aitken, D. J.; Husson, H.-P. *Synlett* **1991**, 747-749.

- (37) Iwanami, S.; Takashima, M.; Hirata, Y.; Hasegawa, O.; Usuda, S. *J. Med. Chem.* **1981**, *24*, 1224-1230.
- (38) Trapani, G.; Reho, A.; Latrofa, A. *Synthesis* **1983**, 1013-1014.
- (39) Kent, T. A. *WMOSS v2.5: Mössbauer Spectral Analysis Software*; WEB Research Co.: Minneapolis, MN, 1998.
- (40) *SMART v5.05: Software for the CCD Detector System*; Bruker AXS: Madison, WI, 1998.
- (41) Feig, A. L.; Bautista, M. T.; Lippard, S. J. *Inorg. Chem.* **1996**, *35*, 6892-6898.
- (42) Sheldrick, G. M. *SHELXTL97-2: Program for the Refinement of Crystal Structures*; University of Göttingen, Germany, 1997.
- (43) Sheldrick, G. M. *SADABS: Area-Detector Absorption Correction*; University of Göttingen, Germany, 1996.
- (44) Spek, A. L. *PLATON, A Multipurpose Crystallographic Tool*; Utrecht University: Utrecht, The Netherlands, 1998.
- (45) Kurtz, D. M., Jr. *Chem. Rev.* **1990**, *90*, 585-606.
- (46) Gütlich, P.; Ensling, J. *Inorganic Electronic Structure and Spectroscopy*; Solomon, E. I. and Lever, A. B. P., Ed.; John Wiley & Sons: New York, 1999; Vol. I, pp 161-211.
- (47) Münck, E. *Physical Methods in Bioinorganic Chemistry: Spectroscopy and Magnetism*; Que, L., Jr., Ed.; University Science Books: Sausalito, CA, 2000, pp 287-319.
- (48) Fox, B. G.; Hendrich, M. P.; Surerus, K. K.; Andersson, K. K.; Froland, W. A.; Lipscomb, J. D.; Münck, E. *J. Am. Chem. Soc.* **1993**, *115*, 3688-3701.
- (49) Pulver, S.; Froland, W. A.; Fox, B. G.; Lipscomb, J. D.; Solomon, E. I. *J. Am. Chem. Soc.* **1993**, *115*, 12409-12422.
- (50) Thich, J. A.; Ou, C. C.; Powers, D.; Vasiliou, B.; Mastropaolo, D.; Potenza, J. A.; Schugar, H. J. *J. Am. Chem. Soc.* **1976**, *98*, 1425-1433.

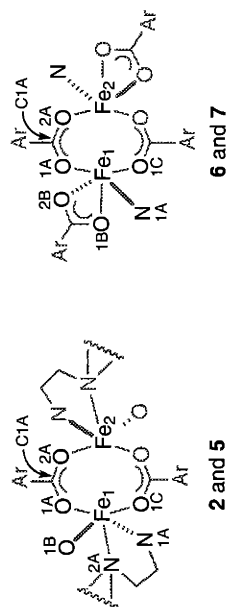
- (51) Borer, L.; Thalken, L.; Ceccarelli, C.; Glick, M.; Zhang, J. H.; Reiff, W. M. *Inorg. Chem.* **1983**, *22*, 1719-1724.
- (52) Silverman, R. B. *The Organic Chemistry of Enzyme-Catalyzed Reactions*; Academic Press: San Diego, CA, 2000.
- (53) Mahapatra, S.; Halfen, J. A.; Wilkinson, E. C.; Pan, G.; Wang, X.; Young, V. G., Jr.; Cramer, C. J.; Que, L., Jr.; Tolman, W. B. *J. Am. Chem. Soc.* **1996**, *118*, 11555-11574.
- (54) Mahapatra, S.; Halfen, J. A.; Tolman, W. B. *J. Am. Chem. Soc.* **1996**, *118*, 11575-11586.
- (55) Mahapatra, S.; Young, V. G., Jr.; Kaderli, S.; Zuberbühler, A. D.; Tolman, W. B. *Angew. Chem., Int. Ed. Engl.* **1997**, *36*, 130-133.
- (56) Mahadevan, V.; Hou, Z.; Cole, A. P.; Root, D. E.; Lal, T. K.; Solomon, E. I.; Stack, T. D. P. *J. Am. Chem. Soc.* **1997**, *119*, 11996-11997.
- (57) Mahadevan, V.; Henson, M. J.; Solomon, E. I.; Stack, T. D. P. *J. Am. Chem. Soc.* **2000**, *122*, 10249-10250.
- (58) Itoh, S.; Taki, M.; Nakao, H.; Holland, P. L.; Tolman, W. B.; Que, L., Jr.; Fukuzumi, S. *Angew. Chem., Int. Ed. Engl.* **2000**, *39*, 398-400.
- (59) Zhang, C. X.; Liang, H.-C.; Kim, E.-I.; Gan, Q.-F.; Tyeklár, Z.; Lam, K.-C.; Rheingold, A. L.; Kaderli, S.; Zuberbühler, A. D.; Karlin, K. D. *Chem. Commun.* **2001**, 631-632.
- (60) He, C.; Lippard, S. J. *J. Am. Chem. Soc.* **1998**, *120*, 105-113.
- (61) Barrios, A. M.; Lippard, S. J. *J. Am. Chem. Soc.* **1999**, *121*, 11751-11757.
- (62) Whittington, D. A.; Lippard, S. J. *J. Am. Chem. Soc.* **2001**, *123*, 827-838.
- (63) Rosenzweig, A. C.; Frederick, C. A.; Lippard, S. J.; Nordlund, P. *Nature* **1993**, *366*, 537-543.
- (64) Rosenzweig, A. C.; Lippard, S. J. *Acc. Chem. Res.* **1994**, *27*, 229-236.

- (65) Rosenzweig, A. C.; Nordlund, P.; Takahara, P. M.; Frederick, C. A.; Lippard, S. J. *Chem. Biol.* **1995**, *2*, 409-418.
- (66) Elango, N.; Radhakrishnan, R.; Froland, W. A.; Wallar, B. J.; Earhart, C. A.; Lipscomb, J. D.; Ohlendorf, D. H. *Protein Sci.* **1997**, *6*, 556-568.
- (67) Whittington, D. A.; Sazinsky, M. H.; Lippard, S. J. *J. Am. Chem. Soc.* **2001**, *123*, 1794-1795.
- (68) Whittington, D. A.; Rosenzweig, A. C.; Frederick, C. A.; Lippard, S. J. *Biochemistry* **2001**, *40*, 3476-3482.
- (69) (a) Fujihara, T.; Fuyuhiko, A.; Kaizaki, S. *Inorg. Chim. Acta* **1998**, *278*, 15-23.
(b) Toftlund, H.; Simonsen, O.; Pedersen, E. *Acta Chem. Scand.* **1990**, *44*, 676-682.
- (70) (a) Wieghardt, K.; Hahn, M.; Swiridoff, W.; Weiss, J. *Inorg. Chem.* **1984**, *23*, 94-99. (b) Kneale, G. G.; Geddes, A. J. *Acta Crystallogr., Sect. B* **1975**, *31*, 1233-1236.
- (71) (a) Dimitrou, K.; Folting, K.; Streib, W. E.; Christou, G. *J. Am. Chem. Soc.* **1993**, *115*, 6432-6433. (b) Sumner, C. E., Jr. *Inorg. Chem.* **1988**, *27*, 1320-1327.
(c) Mandel, G. S.; Marsh, R. E.; Schaefer, W. P.; Mandel, N. S. *Acta Crystallogr., Sect. B* **1977**, *33*, 3185-3188. (d) Maas, G. Z. *Anorg. Allg. Chem.* **1977**, *432*, 203-210.
- (72) Wieghardt, K.; Herrmann, W.; Köppen, M.; Jibril, I.; Huttner, G. Z. *Naturforsch, Teil B* **1984**, *39*, 1335-1343.
- (73) Lombardi, A.; Summa, C. M.; Geremia, S.; Randaccio, L.; Pavone, V.; DeGrado, W. F. *Proc. Natl. Acad. Sci. U.S.A.* **2000**, *97*, 6298-6305.
- (74) Lee, D.; Lippard, S. J., submitted for publication.
- (75) LeCloux, D. D.; Barrios, A. M.; Mizoguchi, T. J.; Lippard, S. J. *J. Am. Chem. Soc.* **1998**, *120*, 9001-9014.

- (76) LeCloux, D. D.; Barrios, A. M.; Lippard, S. J. *Bioorg. Med. Chem.* **1999**, *7*, 763-772.
- (77) Mekmouche, Y.; Ménage, S.; Toia-Duboc, C.; Fontecave, M.; Galey, J.-B.; Lebrun, C.; Pécaut, J. *Angew. Chem., Int. Ed. Engl.* **2001**, *40*, 949-952.

Table 6.1. Summary of X-ray Crystallographic Data

	5	6	7-CH ₂ Cl ₂	8-2PhCl·0.5C ₅ H ₁₂
formula	C ₈₈ H ₉₆ N ₄ O ₁₀ F ₆ Fe ₂ S ₂	Fe ₂ C ₁₁₆ H ₁₀₄ N ₄ O ₈	C ₁₀₉ H ₈₀ N ₄ O ₈ Cl ₂ F ₈ Fe ₂	C _{123.50} H ₁₀₉ N ₄ O ₁₀ Cl ₂ Fe ₂
fw	1659.51	1793.73	1908.37	1991.75
space group	P2 ₁ /c	P $\bar{1}$	P2 ₁ /n	P $\bar{1}$
a, Å	11.7193(3)	11.3953(5)	13.7575(0)	15.0043(18)
b, Å	19.4414(5)	14.7207(7)	21.0669(5)	16.907(2)
c, Å	18.3893(3)	15.2957(7)	17.7305(4)	24.019(3)
α , deg		77.8360(10)		95.570(2)
β , deg	101.6710(10)	72.1730(10)	99.2350(10)	108.017(2)
γ , deg		82.1620(10)		104.939(2)
V, Å ³	4103.19(16)	2380.64(19)	5072.19(17)	5493.8(11)
Z	2	1	2	2
ρ calc, g/cm ³	1.343	1.251	1.250	1.204
T, °C	-85	-85	-85	-85
μ (Mo K α), mm ⁻¹	0.479	0.366	0.410	0.372
θ limits, deg	1.77 - 28.31	1.82 - 28.28	1.51 - 28.27	1.64 - 28.26
total no. of data	30462	15061	31670	48676
no. of unique data	9480	10469	11783	24430
no. of params	513	608	611	1241
R (%) ^a	4.38	5.53	7.23	5.46
wR ² (%) ^b	10.18	11.84	21.16	15.70
max, min peaks, e/Å ³	0.734, -0.580	0.435, -0.397	1.188, -0.698	0.866, -0.905
a R = $\Sigma F_o - F_c / \Sigma F_o $. b wR ² = $\{\Sigma [w(F_o^2 - F_c^2)^2] / \Sigma [w(F_o^2)^2]\}^{1/2}$.				

Table 6.2. Selected Bond Lengths (Å) and Angles (deg) for 2 and 5–7.^a

	2	5	6	7
Fe1...Fe2	3.4245(5)	3.8108(6)	4.3598(8)	3.9854(9)
Fe1-O1A	2.0608(13)	2.0062(15)	1.9608(19)	1.913(3)
Fe1-O1C	2.0437(13)	2.0248(15)	2.007(2)	1.981(3)
Fe1-O1B	2.0557(14)	2.1120(17)	2.1060(19)	2.019(2)
Fe1-O2B			2.2131(19)	2.391(2)
Fe1-N1A	2.2068(17)	2.140(2)	2.127(3)	2.124(3)
Fe1-N2A	2.1838(17)	2.2355(18)		
Fe1-O1A-C1A	129.64(12)	148.53(15)	152.7(2)	155.1(3)
Fe2-O2A-C1A	136.57(12)	127.31(15)	144.8(2)	131.8(3)
N1A-Fe1-N2A	80.36(7)	81.18(7)		

^a Numbers in parentheses are estimated standard deviations of the last significant figures.

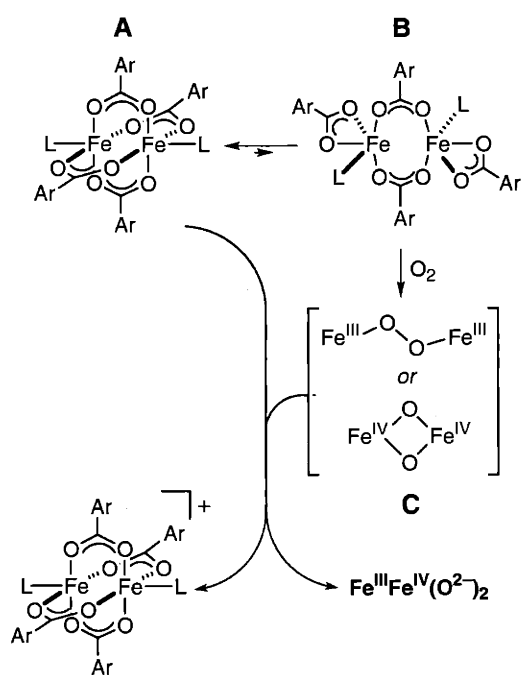
Table 6.3. Selected Bond Lengths (Å) and Angles (deg) for **8**.^a

bond length		bond angle	
Fe(1)···Fe(1A)	2.9788(6)	O(1A)-Fe(1)-O(1)	92.85(7)
		O(1A)-Fe(1)-O(2)	173.12(7)
Fe(1)-O(1)	1.9726(17)	O(1)-Fe(1)-O(2)	80.27(7)
Fe(1)-O(2)	1.9977(17)	O(1A)-Fe(1)-O(1B)	87.61(7)
Fe(1)-O(1A)	1.9664(18)	O(1)-Fe(1)-O(1B)	93.05(7)
Fe(1)-O(1B)	2.0106(17)	O(2)-Fe(1)-O(1B)	92.67(7)
Fe(1)-N(1N)	2.151(2)	O(1A)-Fe(1)-N(1N)	91.20(8)
Fe(1)-N(2N)	2.172(2)	O(1)-Fe(1)-N(1N)	94.12(8)
Fe(2)-O(1)	1.9852(17)	O(2)-Fe(1)-N(1N)	89.36(8)
Fe(2)-O(2)	1.9805(16)	O(1B)-Fe(1)-N(1N)	172.78(8)
Fe(2)-O(2B)	2.1266(16)	O(1A)-Fe(1)-N(2N)	93.54(8)
Fe(2)-O(1C)	2.0045(17)	O(1)-Fe(1)-N(2N)	171.61(8)
Fe(2)-O(1D)	2.0171(17)	O(2)-Fe(1)-N(2N)	93.31(7)
Fe(2)-N(1M)	2.145(2)	O(1B)-Fe(1)-N(2N)	92.64(7)
		N(1N)-Fe(1)-N(2N)	80.32(8)
O(1)···O(2C)	2.681(3)	O(2)-Fe(2)-O(1)	80.39(7)
O(2)···O(2D)	2.668(3)	O(2)-Fe(2)-O(1C)	100.97(7)
N(2N)···O(2A)	2.891(3)	O(1)-Fe(2)-O(1C)	92.40(7)
		O(2)-Fe(2)-O(1D)	93.50(7)
		O(1)-Fe(2)-O(1D)	172.43(7)
		O(1C)-Fe(2)-O(1D)	93.16(7)
		O(2)-Fe(2)-O(2B)	90.35(7)
		O(1)-Fe(2)-O(2B)	85.53(7)
		O(1C)-Fe(2)-O(2B)	168.00(7)
		O(1D)-Fe(2)-O(2B)	90.07(7)
		O(2)-Fe(2)-N(1M)	167.69(8)
		O(1)-Fe(2)-N(1M)	96.70(8)
		O(1C)-Fe(2)-N(1M)	91.06(8)
		O(1D)-Fe(2)-N(1M)	88.34(8)
		O(2B)-Fe(2)-N(1M)	77.48(7)

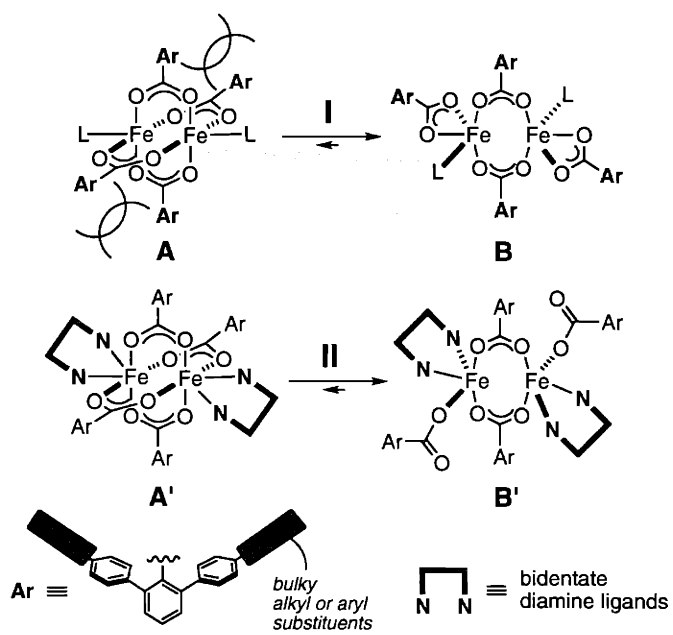
^a Number in parentheses are estimated standard deviations of the last significant figure. Atoms are labeled as indicated in Figure 6.9.

Table 6.4. Mössbauer Parameters of the Diiron(III) Centers in MMOH_{ox} , $[\text{Fe}_2(\mu\text{-OH})_2(\mu\text{-O}_2\text{CAr}^{\text{Tol}})(\text{O}_2\text{CAr}^{\text{Tol}})_3(\text{N-Bnen})(\text{N,N-Bn}_2\text{en})]$ (**8**), and $[\text{Fe}_2(\mu\text{-OH})_2(\mu\text{-O}_2\text{CAr}^{\text{Tol}})_2(\text{O}_2\text{CAr}^{\text{Tol}})_2(4\text{-}^t\text{BuC}_5\text{H}_4\text{N})_2]$ measured at 4 K

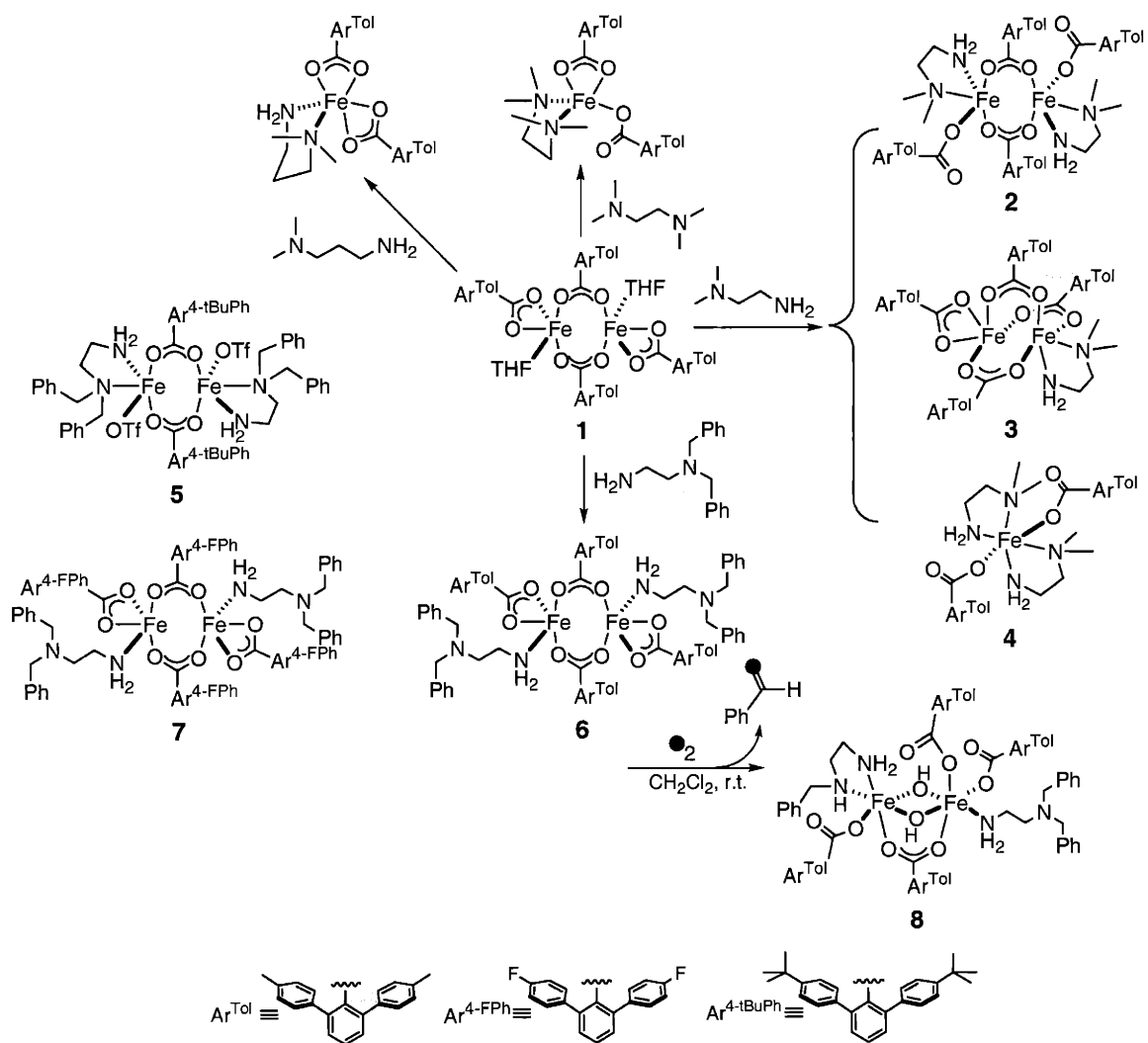
	δ (mm/s)	ΔE_{Q} (mm/s)		ref
MMOH_{ox} (<i>M. capsulatus</i>)	0.51(2)	1.12(3)	site 1	16b
	0.50(2)	0.79(3)	site 2	
MMOH_{ox} (<i>M. trichosporium</i> OB3b)	0.51	1.16	site 1	48
	0.50	0.87	site 2	
8	0.48(2)	0.61(2)		this work
$[\text{Fe}_2(\mu\text{-O}_2\text{CAr}^{\text{Tol}})_2(\text{O}_2\text{CAr}^{\text{Tol}})_2(4\text{-}^t\text{BuC}_5\text{H}_4\text{N})_2]$	0.49(2)	1.01(2)		74



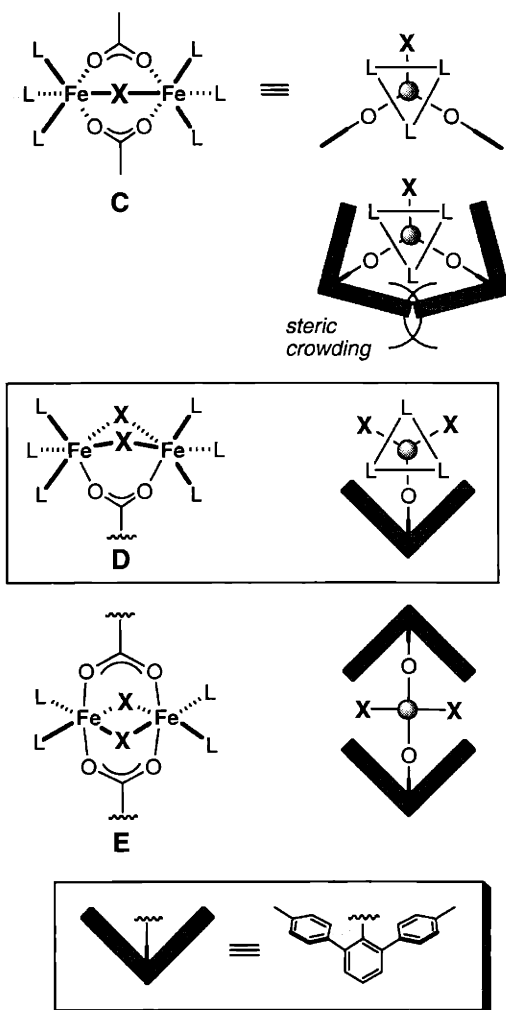
Scheme 6.1.



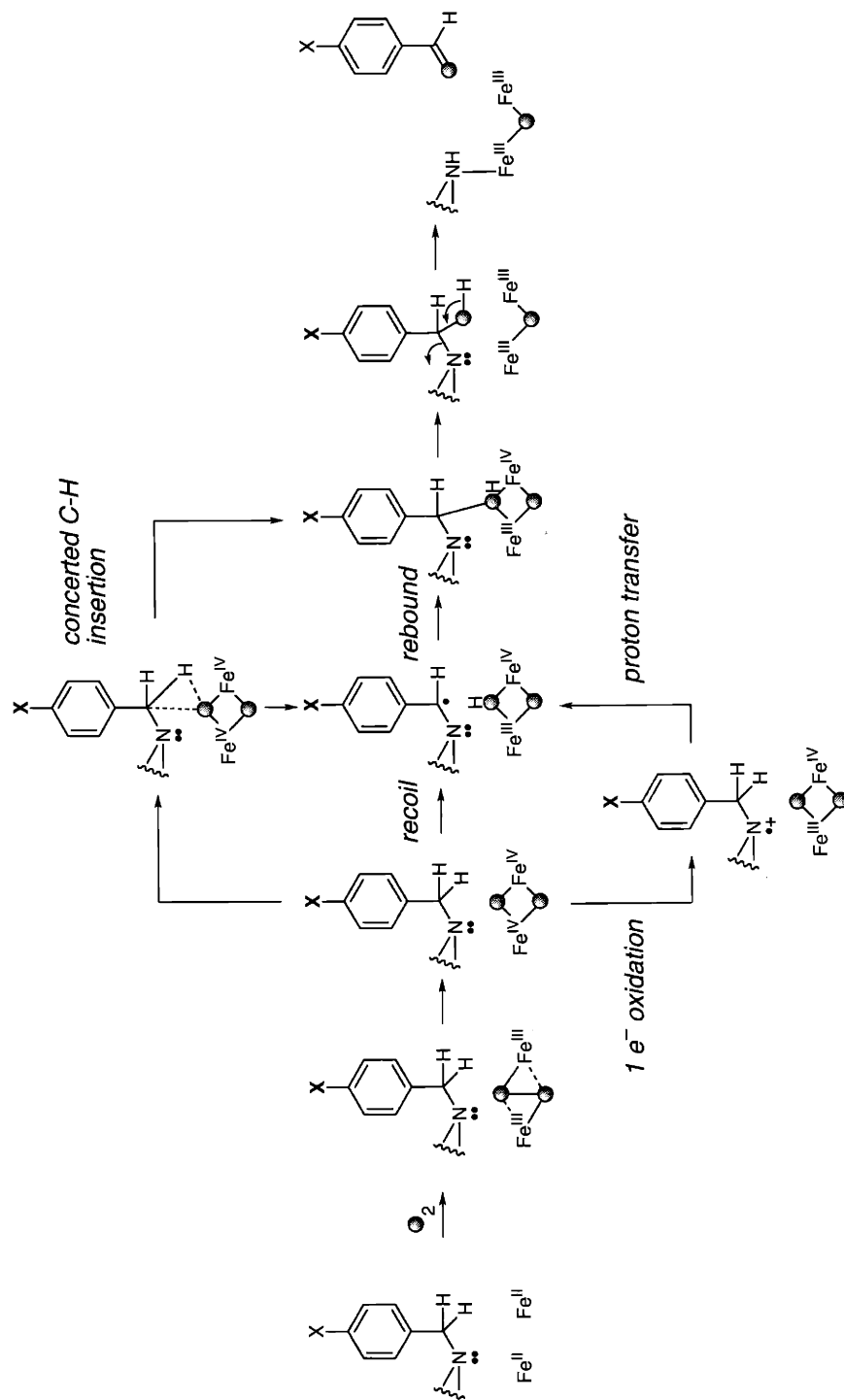
Scheme 6.2.



Scheme 6.3.



Scheme 6.4.



Scheme 6.5.

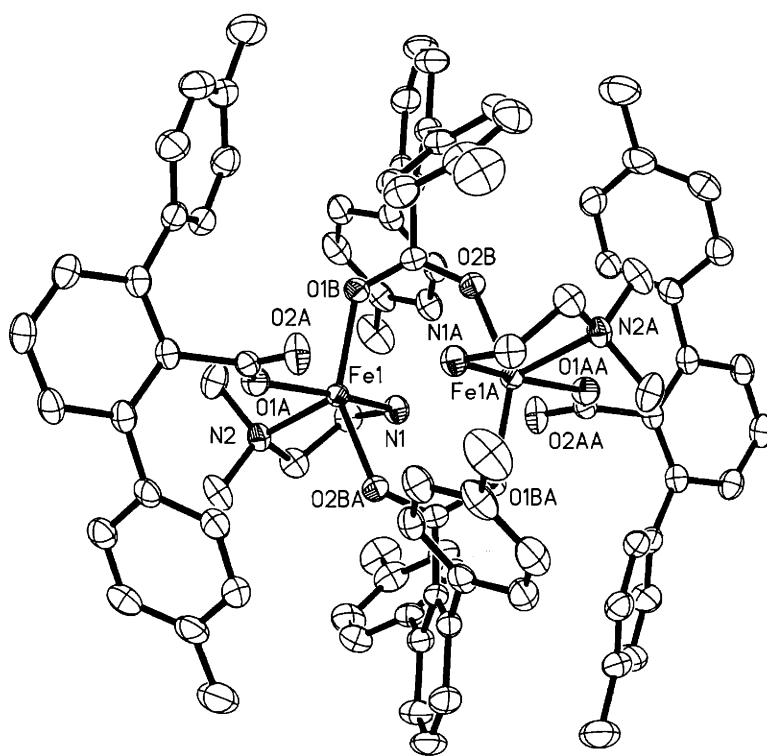


Figure 6.1. ORTEP diagram of $[\text{Fe}_2(\mu\text{-O}_2\text{CAR}^{\text{Tol}})_2(\text{O}_2\text{CAR}^{\text{Tol}})_2(\text{N,N-Me}_2\text{en})_2]$ (2) with thermal ellipsoids at 50% probability.

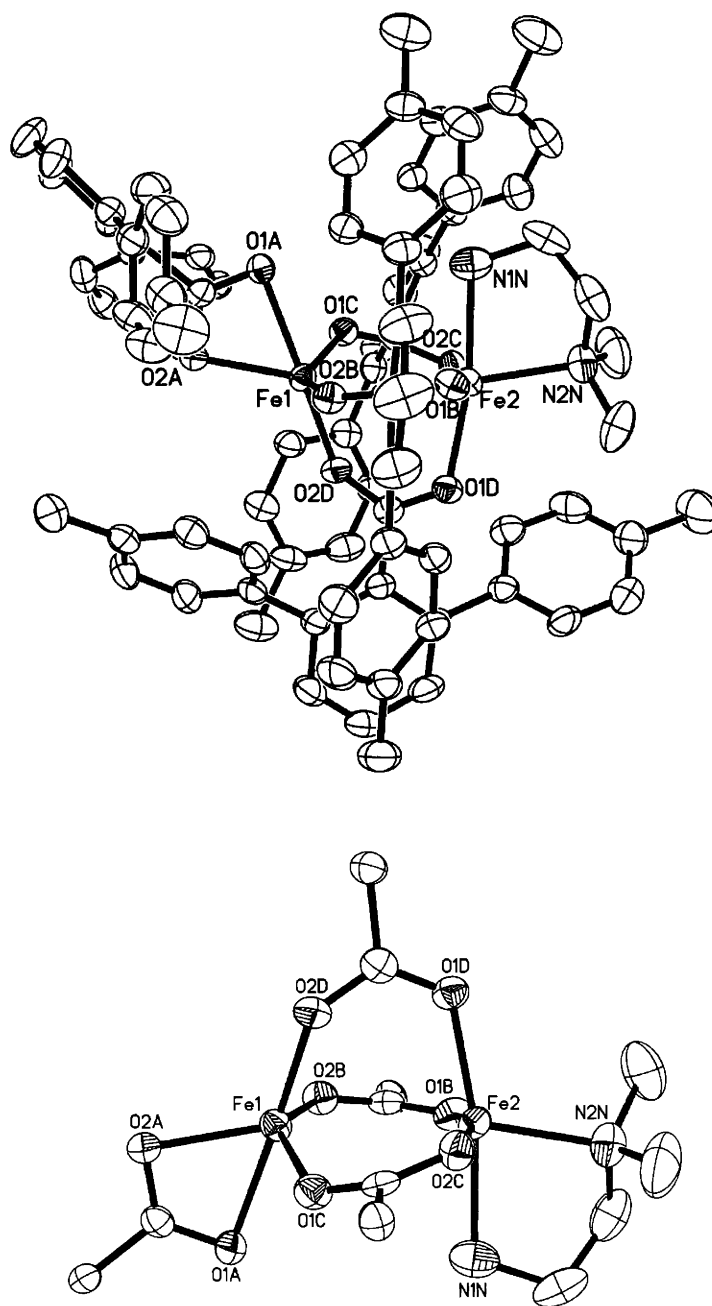


Figure 6.2. ORTEP diagram of $[\text{Fe}_2(\mu\text{-O}_2\text{CAr}^{\text{Tol}})_3(\text{O}_2\text{CAr}^{\text{Tol}})(N,N\text{-Me}_2\text{en})]$ (**3**) with thermal ellipsoids at 50% probability: top, whole molecule; bottom, core structure.

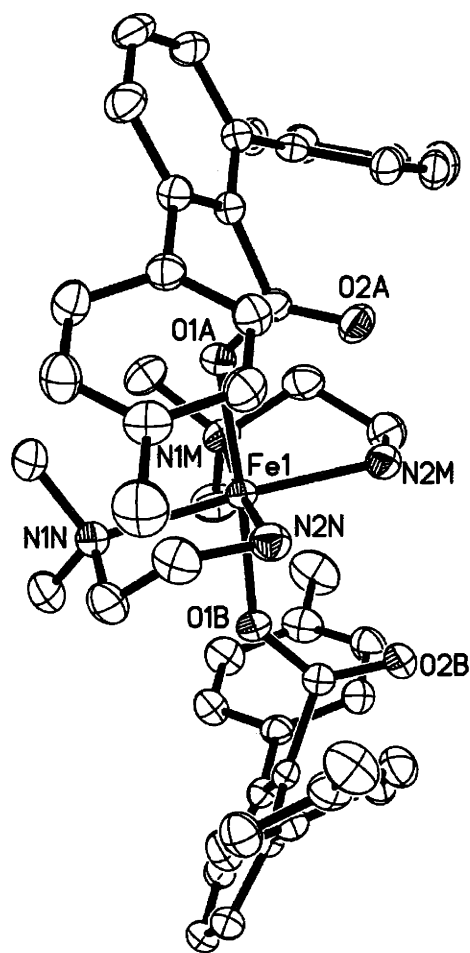


Figure 6.3. ORTEP diagram of $[\text{Fe}(\text{O}_2\text{CAr}^{\text{Tol}})_2(\text{N},\text{N}\text{-Me}_2\text{en})_2]$ (**4**) with thermal ellipsoids at 50% probability.

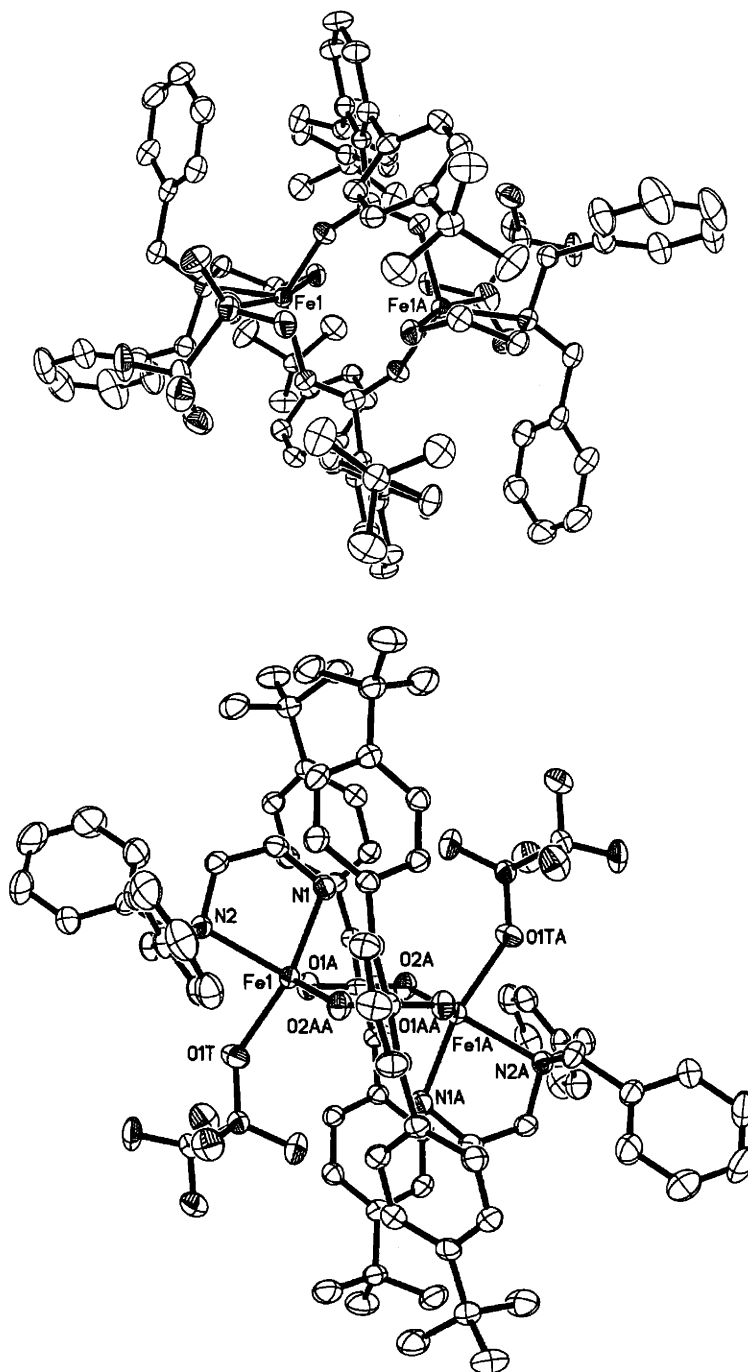


Figure 6.4. ORTEP diagram of $[\text{Fe}_2(\mu\text{-O}_2\text{CAr}^{4\text{-tBuPh}})_2(\text{OTf})_2(\text{N,N-Bn}_2\text{en})_2]$ (5) with thermal ellipsoids at 50% probability.

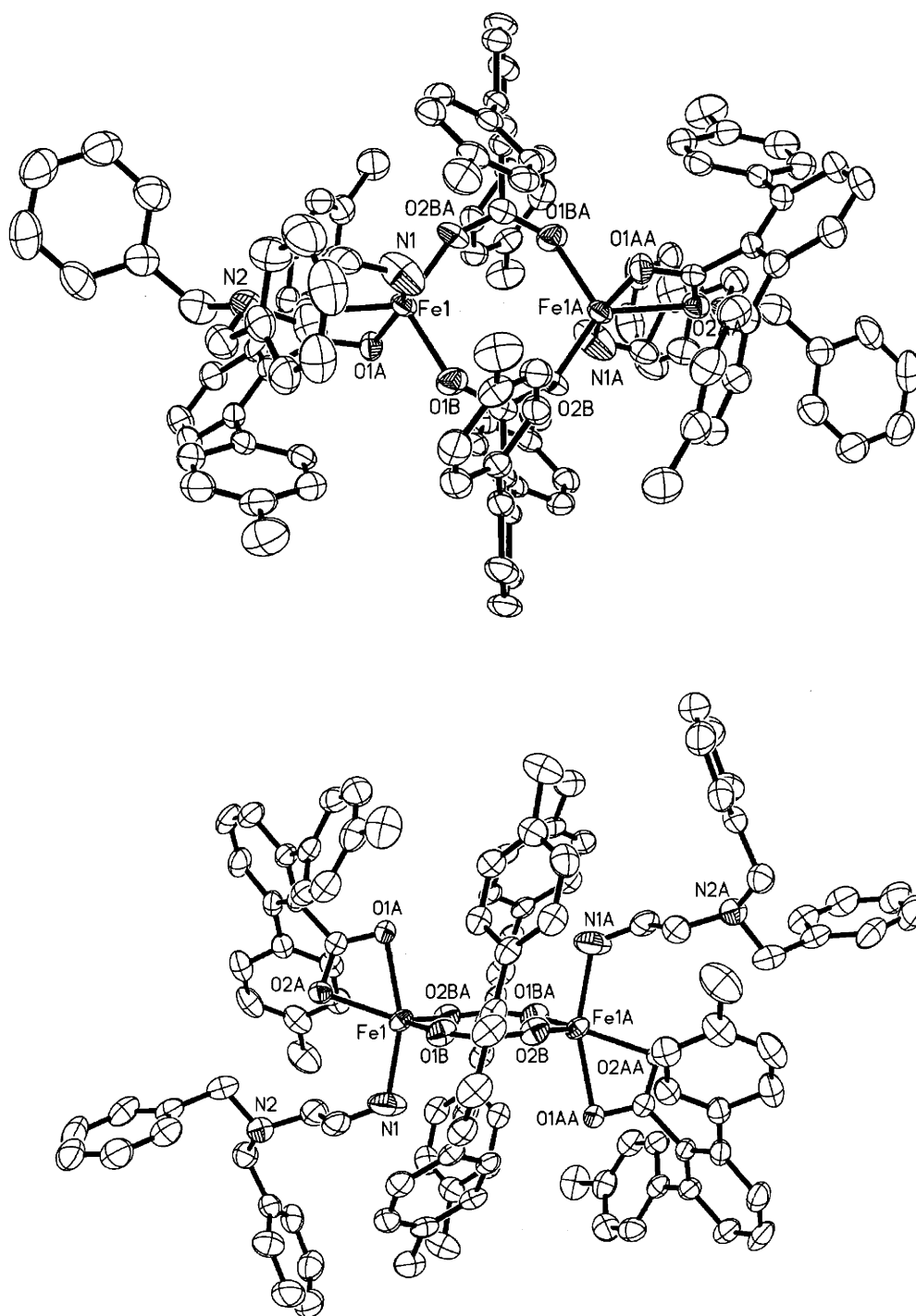


Figure 6.5. ORTEP diagram of $[\text{Fe}_2(\mu\text{-O}_2\text{CAR}^{\text{Tol}})_2(\text{O}_2\text{CAR}^{\text{Tol}})_2(\text{N,N-Bn}_2\text{en})_2]$ (**6**) with thermal ellipsoids at 50% probability.

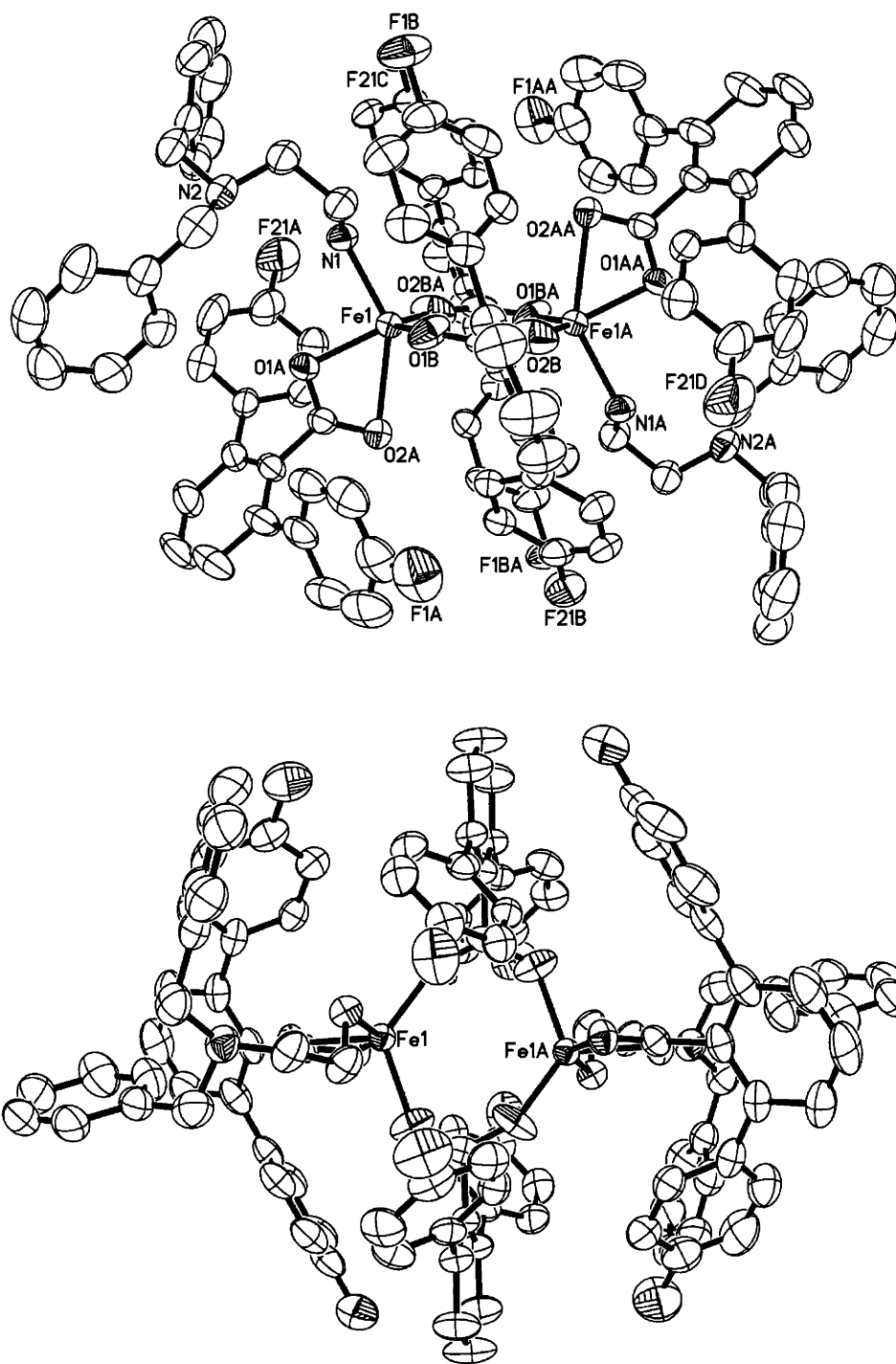


Figure 6.6. ORTEP diagram of $[\text{Fe}_2(\mu\text{-O}_2\text{CAR}^{4\text{-FPh}})_2(\text{O}_2\text{CAR}^{4\text{-FPh}})_2(\text{N,N-Bn}_2\text{en})_2]$ (7) with thermal ellipsoids at 50% probability.

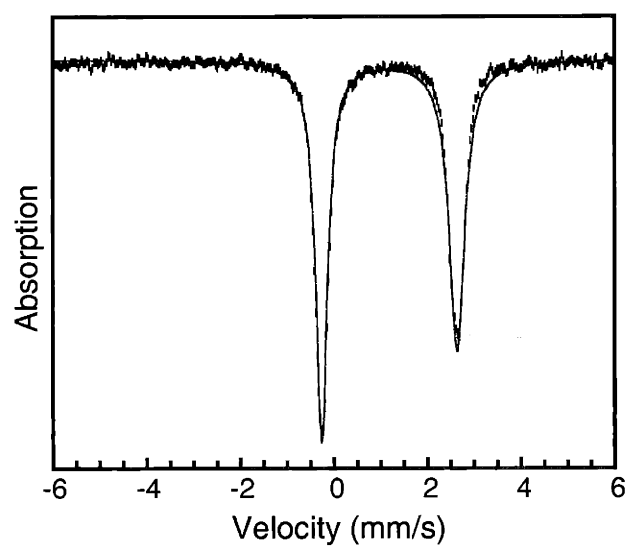


Figure 6.7. Zero-field Mössbauer spectrum (experimental data (|), calculated fit (-)) recorded at 4.2 K for $[\text{Fe}_2(\mu\text{-O}_2\text{CAr}^{\text{Tol}})_2(\text{O}_2\text{CAr}^{\text{Tol}})_2(\text{N,N-Bn}_2\text{en})_2]$ (**6**) in the solid state. See text for derived Mössbauer parameters.

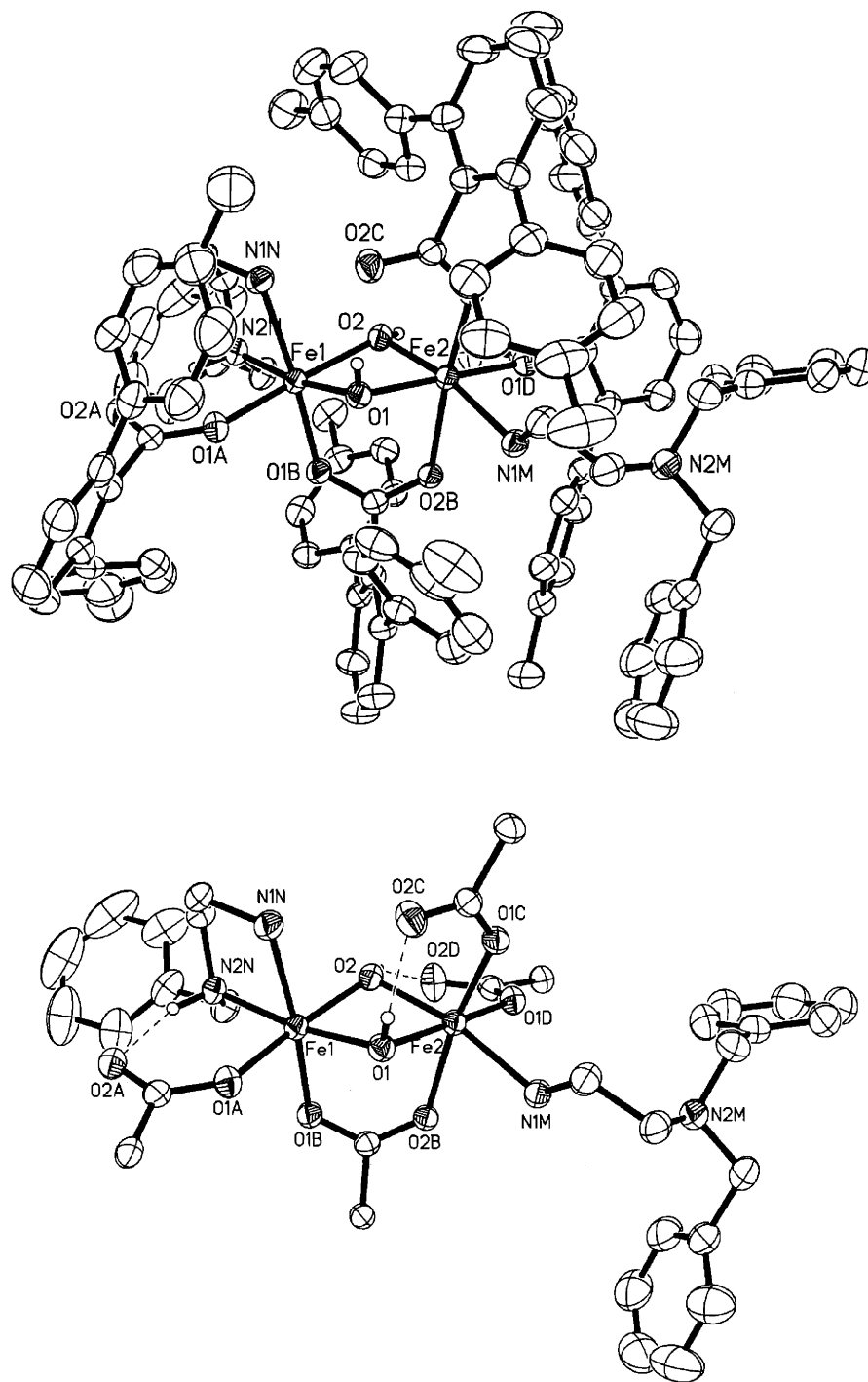


Figure 6.8. ORTEP diagram of $[\text{Fe}_2(\mu\text{-OH})_2(\mu\text{-O}_2\text{CAr}^{\text{Tol}})(\text{O}_2\text{CAr}^{\text{Tol}})_3(\text{N-Bnen})\text{-}(\text{N,N-Bn}_2\text{en})]$ (**8**) with thermal ellipsoids at 50% probability: Top, whole molecule; bottom, core structure.

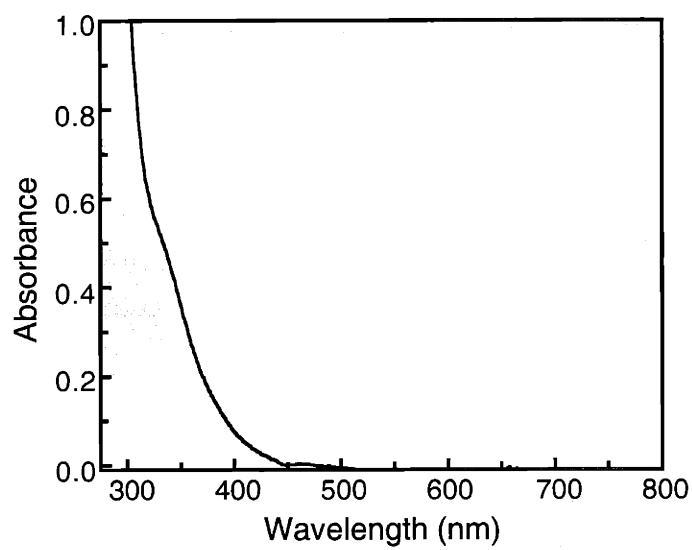


Figure 6.9. Electronic absorption spectrum of $[\text{Fe}_2(\mu\text{-OH})_2(\mu\text{-O}_2\text{CAr}^{\text{Tol}})(\text{O}_2\text{CAr}^{\text{Tol}})_3(\text{N-Bnen})(\text{N,N-Bn}_2\text{en})]$ (**8**) (0.071 mM) in CH_2Cl_2 .

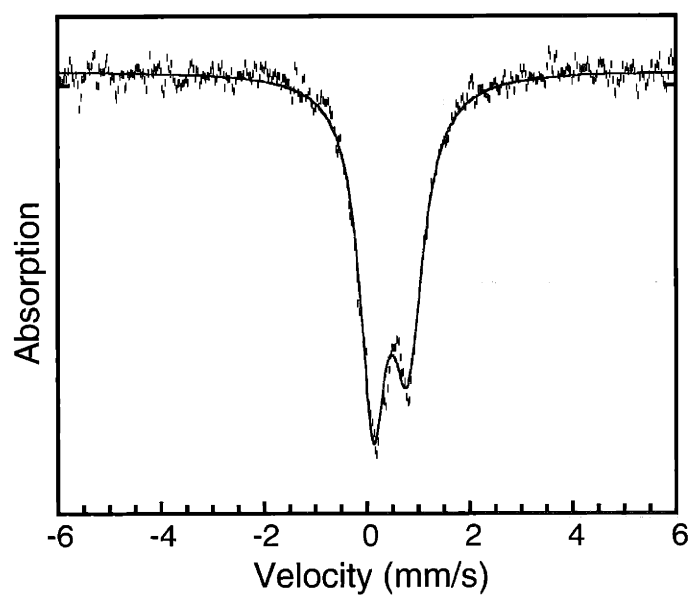


Figure 6.10. Zero-field Mössbauer spectrum (experimental data (|), calculated fit (—)) recorded at 77 K for $[\text{Fe}_2(\mu\text{-OH})_2(\mu\text{-O}_2\text{CAr}^{\text{Tol}})(\text{O}_2\text{CAr}^{\text{Tol}})_3(\text{N-Bnen})\text{-}(\text{N,N-Bn}_2\text{en})]$ (**8**) in the solid state.

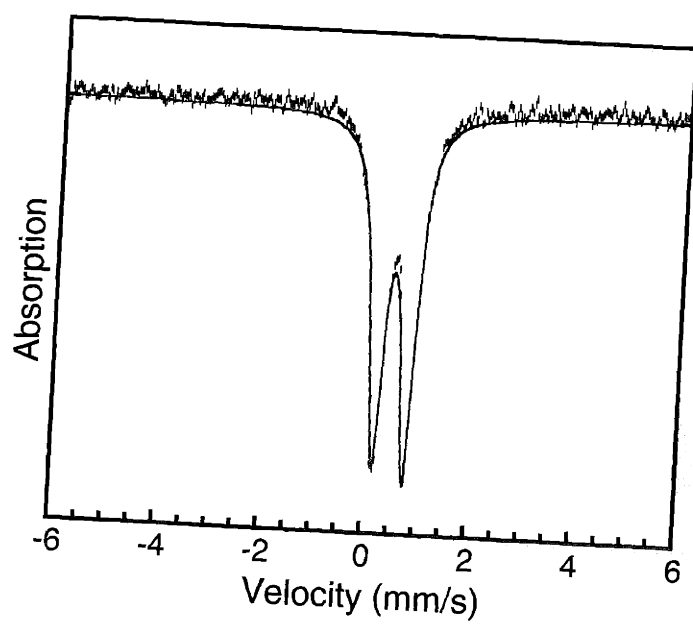


Figure 6.11. Zero-field Mössbauer spectrum (experimental data (|), calculated fit (-)) recorded at 4.2 K for $[\text{Fe}_2(\mu\text{-OH})_2(\mu\text{-O}_2\text{CAr}^{\text{Tol}})(\text{O}_2\text{CAr}^{\text{Tol}})_3(\text{N-Bnen})\text{-}(\text{N,N-Bn}_2\text{en})]$ (**8**) in the solid state. See text for derived Mössbauer parameters.

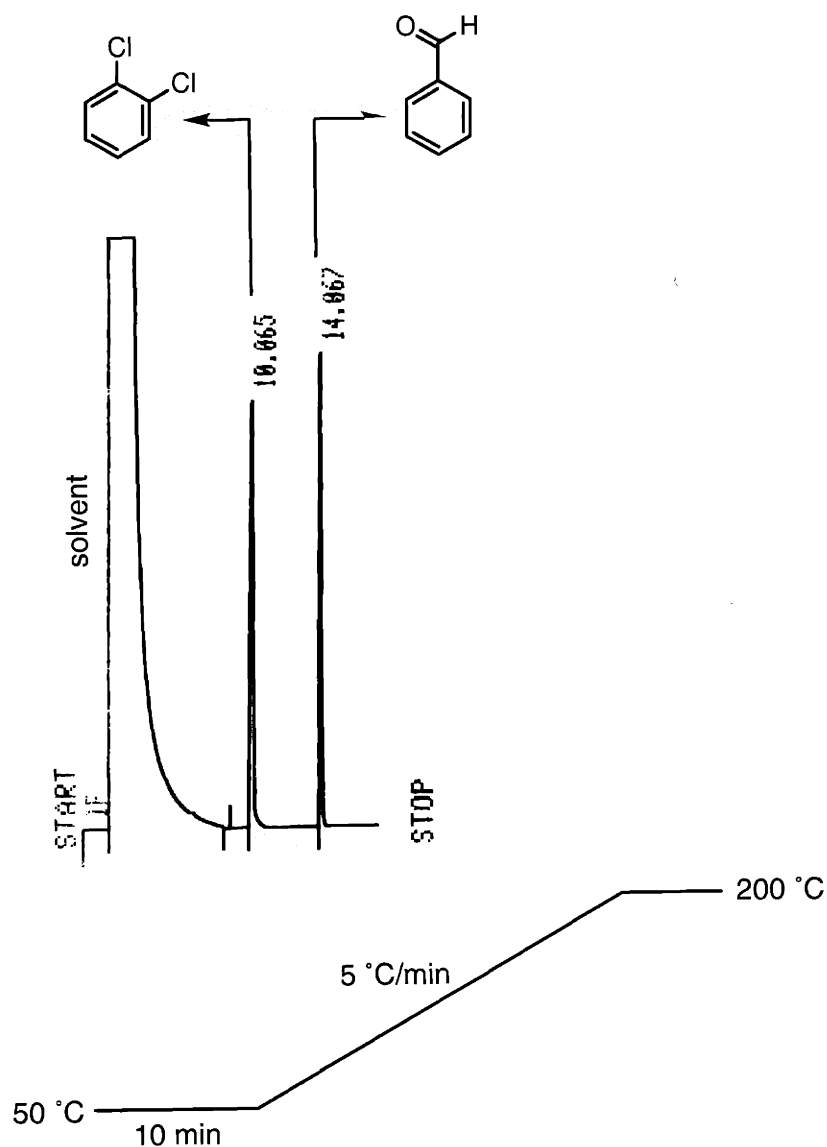


Figure 6.12. A representative GC chromatogram for the oxidative N-dealkylation reactions of **6**. The sample used for this run was derived from a crude reaction mixture filtered through an Al_2O_3 column. The compound 1,2-dichlorobenzene was used as an internal standard. The temperature gradient was programmed as described below the chromatogram.

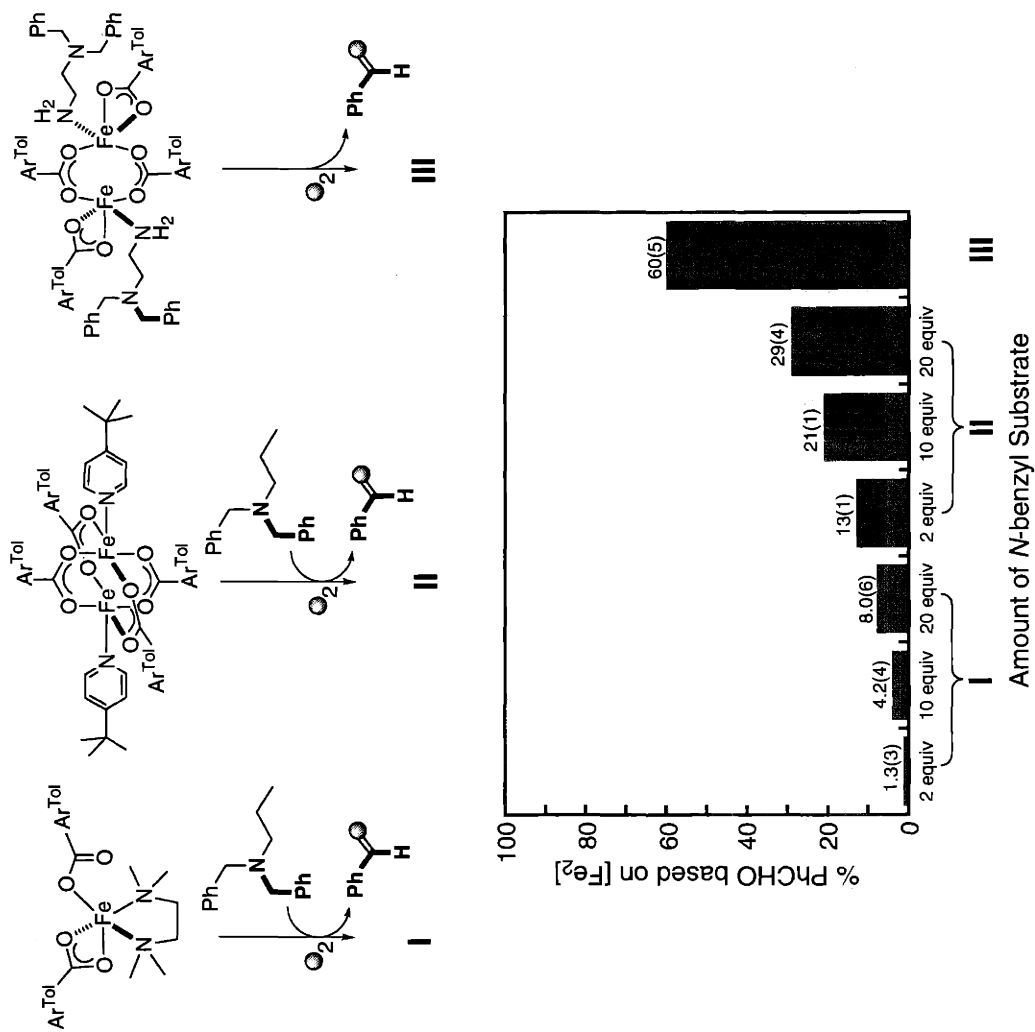


Figure 6.13. Oxidative N-dealkylation of internal versus external substrates by mono- and dinuclear iron(II) complexes.

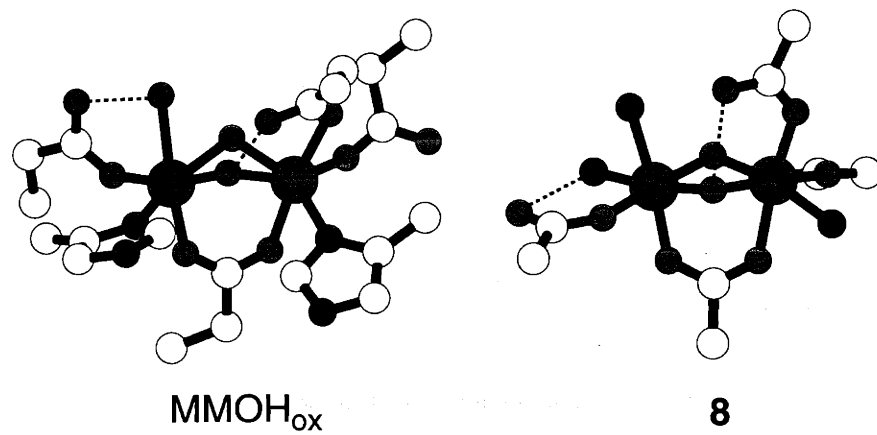


Figure 6.14. Comparison of the diiron(III) core structures of MMOH_{ox} and compound **8**. Hydrogen bonds are represented as broken lines.

Chapter VII

Hydroxo-Bridged Cubane-Type Tetrairon(II) Clusters Supported by Sterically-Hindered Carboxylate Ligands*

Introduction

Multiple metal ions connected by single atom bridging ligands are encountered in proteins participating in electron transfer (ET) reactions.¹⁻³ Maintaining efficient shuttling of electrons while minimizing unwanted redox reactions is a delicate task achieved in living systems, the understanding of which has been a topic of extensive research.^{3,4} For example, cubane-type $\{\text{Fe}_4\text{S}_4\}^{n+}$ clusters occur at the active sites of high-potential iron protein (HiPIP, $n = 2/3$ redox couple) or ferredoxin (Fd, $n = 1/2$ redox couple) electron transferases, and these centers have been the subjects of extensive bioinorganic modeling studies.⁵⁻⁸ Synthetic tetrairon complexes have served as benchmarks for assisting the investigation of their biological counterparts.^{5,8} Insights into the electronic structure of biological clusters at various oxidation states have been gleaned from comparison with their low molecular weight analogs having comparable geometric and spectroscopic properties.²⁻⁴

In contrast to the rich chemistry of $\{\text{Fe}_4\text{S}_4\text{L}_4\}^{n+}$ clusters assembled with a variety of ligand combinations, however, topologically related compounds having oxo- or hydroxo-bridging groups remain unexplored. Considering the ubiquitous nature of oxo- or hydroxo-bridged iron centers in living systems,⁹⁻¹¹ the participation of analogous $\{\text{Fe}_4\text{O}_4\}^{n+}$ or $\{\text{Fe}_4(\text{OH})_4\}^{n+}$ units in biological ET reactions remains an open question.¹² There are only a few iron alkoxide/phenoxide cubes, in which the $\{\text{Fe}_4(\text{OR})_4\}^{n+}$ cores are supported by terminal bidentate ligands or bridging carboxylate groups.¹³⁻¹⁵ A $\{\text{Fe}_4\text{O}_4\}^{4+}$ cuboidal fragment was recently identified within a larger octanuclear cluster.¹² Discrete tetrairon clusters having $\{\text{Fe}_4(\text{OH})_4\}^{n+}$ or $\{\text{Fe}_4\text{O}_4\}^{n+}$ cores, however, are unknown in inorganic chemistry.

Recently, we¹⁶⁻¹⁹ and others^{20,21} have employed *m*-terphenyl-derived carboxylate ligands^{22,23} to model features of non-heme diiron enzyme active

sites.²⁴⁻²⁶ Site isolation of kinetically labile metal centers within a sterically hindered framework allowed access to dinuclear complexes having unprecedented structures and reactivities. The initial success of this approach prompted us to synthesize a bulkier derivative of this versatile ligand and to investigate the effect of the enhanced steric hindrance on the nuclearity and coordination geometry of the resulting complexes. Installing larger alkyl groups on the 4-positions of the flanking aryl substituents on the benzoate moiety should result in a lateral expansion of the *m*-terphenyl unit, which would translate into restricted access to the metal ions buried inside a sterically more encumbered V-shaped cavity.

In this chapter, we describe the synthesis and characterization of a new family of tetrairon(II) clusters. The unprecedented $\{\text{Fe}_4(\mu\text{-OH})_4\}^{4+}$ core is supported by the sterically hindered carboxylate ligand, 2,6-di(4-*tert*-butylphenyl)benzoate ($\text{Ar}^{4\text{-tBuPh}}\text{CO}_2^-$). Unique structural and physical properties of the compounds $[\text{Fe}_4(\mu\text{-OH})_4(\mu\text{-O}_2\text{CAr}^{4\text{-tBuPh}})_2(\mu\text{-OTf})_2\text{L}_4]$ ($\text{L} = \text{C}_5\text{H}_5\text{N}$ (1); 4-*t*-BuC₅H₄N (2); 3-FC₅H₄N (3)) are described. Comparisons are made with compounds having analogous $\{\text{Fe}_4\text{X}_4\}^{n+}$ ($\text{X} = \text{O}, \text{S}$) cores, and the structural integrity of tetrairon fragments upon change in the oxidation state and their biological implications are discussed.

Experimental Section

General Considerations. All reagents were obtained from commercial suppliers and used as received unless otherwise noted. Dichloromethane was distilled over CaH₂ under nitrogen. Diethyl ether, pentanes, and THF were saturated with nitrogen and purified by passage through activated Al₂O₃ columns under nitrogen.²⁷ Fe(OTf)₂·2MeCN was prepared according to literature procedures.²⁸ All synthetic procedures and air-sensitive manipulations were carried

out under nitrogen in a Vacuum Atmospheres drybox or by standard Schlenk line techniques.

Physical Measurements. $^1\text{H-NMR}$ and $^{19}\text{F-NMR}$ spectra were recorded on Varian Mercury 300 MHz and Inova 500 MHz spectrometers, respectively. Chemical shifts of the $^1\text{H-NMR}$ spectra were reported versus tetramethylsilane and referenced to the residual solvent peaks. ^{19}F chemical shifts are reported with reference to external CFCl_3 (0.0 ppm). FT-IR spectra were recorded on a Bio Rad FTS-135 instrument with Win-IR software. Solid samples were pressed into KBr pellets; solution samples were prepared in an airtight Graseby-Specac solution cell with CaF_2 windows. UV-vis spectra were recorded on a Hewlett Packard 8453 diode array spectrophotometer.

2,6-Di(4-*tert*-butylphenyl)benzoic acid ($\text{Ar}^{4\text{-tBuPh}}\text{CO}_2\text{H}$). This compound was prepared by a procedure analogous to that used to synthesize $\text{Ar}^{\text{Tol}}\text{CO}_2\text{H}$,^{29,30} except that 4-*tert*-butylbromobenzene was used instead of 4-methylbromobenzene. Off-white solid material was obtained by recrystallization from hot hexanes/EtOAc (33% purification yield). Mp = 188 °C. $^1\text{H-NMR}$ (300 MHz, CD_2Cl_2 , 20 °C): δ 7.53 (s, 1H), 7.45–7.34 (m, 10H), 1.36 (s, 18H); $^{13}\text{C-NMR}$ (75.47 MHz, CD_2Cl_2 , 20 °C): δ 172.9, 151.3, 140.7, 137.9, 131.8, 130.2, 129.5, 128.6, 125.9, 35.0, 31.6. FT-IR (thin film deposited from CD_2Cl_2 solution on NaCl, cm^{-1}): 3029, 2963, 2904, 2868, 2654, 2553, 1699, 1587, 1513, 1460, 1393, 1363, 1296, 1272, 1136, 1118, 1101, 1018, 954, 838, 807, 780, 750, 712, 679, 593, 575. Anal. Calcd for $\text{C}_{27}\text{H}_{30}\text{O}_2$: C, 83.90; H, 7.82. Found: C, 83.99; H, 7.94. The sodium salt of this compound, $\text{NaO}_2\text{CAr}^{4\text{-tBuPh}}$, was prepared by treating a MeOH solution of the free acid with 1 equiv of NaOH and removing the volatile fractions under reduced pressure.

$[\text{Fe}_4(\mu\text{-OH})_4(\mu\text{-O}_2\text{CAr}^{4\text{-tBuPh}})_2(\mu\text{-OTf})_2(\text{C}_5\text{H}_5\text{N})_4]$ (1). To a rapidly stirred THF (10 mL) solution of $\text{Fe}(\text{OTf})_2 \cdot 2\text{MeCN}$ (435 mg, 0.998 mmol) was added

$\text{NaO}_2\text{CAr}^{4\text{-tBuPh}}$ (209 mg, 0.512 mmol). A portion of pyridine (79 mg, 1.0 mmol) was added and the resulting yellow solution was treated with Et_3N (100 mg, 0.988 mmol). The homogeneous mixture was stirred at room temperature for 0.5 h and treated with Ar-saturated H_2O (25 μL , 1.4 mmol). The color of the solution turned orange yellow. Volatile fractions were removed under reduced pressure and the residual yellow solid was extracted into CH_2Cl_2 (6 mL). Insoluble fractions were filtered off and Et_2O was allowed to diffuse into the filtrate to afford greenish yellow blocks of **1** (320 mg, 48%). FTIR (KBr, cm^{-1}) 3649, 3632, 2966, 2906, 2870, 1602, 1562, 1513, 1487, 1446, 1409, 1385, 1364, 1294, 1215, 1170, 1069, 1041, 1019, 850, 808, 778, 753, 697, 636, 580, 514; UV-vis (CH_2Cl_2) (λ_{max} , nm (ϵ , $\text{M}^{-1}\text{cm}^{-1}$)) 397 (2900). Anal. Calcd for $\text{C}_{76}\text{H}_{82}\text{N}_4\text{O}_{14}\text{F}_6\text{Fe}_4\text{S}_2$: C, 54.43; H, 4.93; N, 3.34; S, 3.82. Found: C, 54.47; H, 5.27; N, 3.17; S, 3.76.

$[\text{Fe}_4(\mu\text{-OH})_4(\mu\text{-O}_2\text{CAr}^{4\text{-tBuPh}})_2(\mu\text{-OTf})_2(4\text{-}^t\text{BuC}_5\text{H}_4\text{N})_4]$ (**2**). This compound was prepared in a manner similar to that described for **1**, except that 4-*tert*-butylpyridine was used instead of pyridine. The reaction mixture was concentrated to an orange-yellow oil, which was extracted into $\text{CH}_2\text{Cl}_2/\text{PhCl}$ (1:2) and filtered. Vapor diffusion of Et_2O into the filtrate afforded yellow crystals of **2** (42%). Yellow blocks suitable for X-ray crystallography were obtained by layering Et_2O over a saturated MeCN solution of this material. FTIR (KBr, cm^{-1}) 3645, 3634, 2966, 2906, 2870, 1615, 1566, 1513, 1502, 1458, 1421, 1384, 1367, 1294, 1273, 1220, 1170, 1071, 1020, 845, 830, 808, 781, 763, 734, 686, 637, 569, 516; UV-vis (CH_2Cl_2) (λ_{max} , nm (ϵ , $\text{M}^{-1}\text{cm}^{-1}$)) 390 (3400). Anal. Calcd for $\text{C}_{76}\text{H}_{82}\text{N}_4\text{O}_{14}\text{F}_6\text{Fe}_4\text{S}_2 \cdot \text{CH}_2\text{Cl}_2$: C, 56.23; H, 5.89; N, 2.82. Found: C, 56.29; H, 6.33; N, 2.83.

$[\text{Fe}_4(\mu\text{-OH})_4(\mu\text{-O}_2\text{CAr}^{4\text{-tBuPh}})_2(\mu\text{-OTf})_2(3\text{-FC}_5\text{H}_4\text{N})_4]$ (**3**). This compound was prepared in a manner similar to that described for **1**, except that 3-fluoropyridine was used instead of pyridine. Yellow blocks of **3** (70%) were obtained by vapor diffusion of pentane into a dichloromethane solution of this

material and analyzed by X-ray crystallography. FTIR (KBr, cm^{-1}) 3644, 3630, 3064, 2966, 2907, 2870, 1608, 1587, 1555, 1514, 1481, 1457, 1435, 1410, 1385, 1365, 1295, 1255, 1236, 1216, 1173, 1120, 1099, 1017, 849, 836, 808, 778, 763, 695, 687, 636, 612, 580, 537, 515; UV-vis (CH_2Cl_2) (λ_{max} , nm (ϵ , $\text{M}^{-1}\text{cm}^{-1}$)) 409 (3500). Anal. Calcd for $\text{C}_{76}\text{H}_{78}\text{N}_4\text{O}_{14}\text{F}_{10}\text{Fe}_4\text{S}_2$: C, 52.19; H, 4.50; N, 3.20. Found: C, 52.14; H, 4.87; N, 2.85.

X-ray Crystallographic Studies. Intensity data were collected on a Bruker (former Siemens) CCD diffractometer with graphite-monochromated Mo $\text{K}\alpha$ radiation ($\lambda = 0.71073 \text{ \AA}$), controlled by a Pentium-based PC running the SMART software package.³¹ Single crystals were mounted at room temperature on the tips of quartz fibers, coated with Paratone-N oil, and cooled to 188 K under a stream of cold nitrogen maintained by a Bruker LT-2A nitrogen cryostat. Data collection and reduction protocols are described elsewhere.³² The structures were solved by direct methods and refined on F^2 by using the SHELXTL software package.³³ Empirical absorption corrections were applied with SADABS,³⁴ part of the SHELXTL program package. All non-hydrogen atoms were refined anisotropically unless otherwise noted. Hydrogen atoms were assigned idealized positions and given thermal parameters equivalent to either 1.5 (methyl hydrogen atoms) or 1.2 (all other hydrogen atoms) times the thermal parameter of the carbon atom to which they were attached. The hydrogen atoms associated with the bridging hydroxide ligands in **2** were located in the difference Fourier map and refined isotropically; those of the disordered solvent molecules were not included in the refinement. One of the butyl groups on the 4-*tert*-butylpyridine ligands in **2** was disordered over two positions. The atoms were equally distributed and refined isotropically. The lattice solvent molecules were modeled as partially occupied CH_2Cl_2 (0.25 occupancy) and Et_2O (0.75 occupancy) and refined isotropically. A half-occupied Et_2O was also found and re-

fined isotropically. Crystallographic information of **2** is provided in Table 7.1. The structures of **1** and **3** were not fully refined due to severe disorder in the bridging triflate anions and solvent molecules. Compound **1** crystallizes in orthorhombic space group $Pna2_1$ with $a = 20.1611(9) \text{ \AA}$, $b = 19.6012(5) \text{ \AA}$, $c = 22.1402(11) \text{ \AA}$, $V = 8749.4(6) \text{ \AA}^3$, and $Z = 4$. Compound **3** crystallizes in the same space group with $a = 20.191(2) \text{ \AA}$, $b = 19.686(2) \text{ \AA}$, $c = 22.071(3) \text{ \AA}$, $V = 8773.0(18) \text{ \AA}^3$, and $Z = 4$. Although detailed structural information is not provided, the core structures of **1** and **3** closely resemble that of **2** (vide infra).

^{57}Fe Mössbauer Spectroscopy. Mössbauer spectra were obtained on an MS1 spectrometer (WEB Research Co.) with a ^{57}Co source in a Rh matrix maintained at room temperature in the MIT Department of Chemistry Instrumentation Facility. Solid samples were prepared by suspending ~ 0.02 mmol of the powdered material in Apeizon N grease and packing the mixture into a nylon sample holder. All data were collected at 4.2 K and the isomer shift (δ) values are reported with respect to natural iron foil that was used for velocity calibration at room temperature. The spectra were fit to Lorentzian lines by using the WMOSS plot and fit program.³⁵

Magnetic Susceptibility. Magnetic susceptibility of a polycrystalline powder of **1** was measured between 2 K and 300 K with applied magnetic fields of 0.1 T and 1 T using a Cryogenic S600 SQUID magnetometer. The sample was prepared under nitrogen, wrapped in Teflon, and quickly transferred to the SQUID vacuum chamber. Each measurement was repeated on two different samples to ensure reproducibility. Data were corrected for the magnetism of the sample holder, which was independently determined at the same temperature range and field. Underlying diamagnetism of the sample was estimated from Pascal's constants.³⁶ Magnetization measurements were performed on the same sample at 2.5 K and 4.5 K with an applied field up to 6 T.

Electrochemistry. Cyclic voltammetric measurements were performed in a Vacuum Atmospheres drybox under nitrogen with an EG&G Model 263 potentiostat. A three-electrode configuration consisting of a 1.75-mm² platinum working electrode, a Ag/AgNO₃ (0.1 M in MeCN with 0.5 M (Bu₄N)(PF₆)) reference electrode, and a platinum mesh auxiliary electrode was used. The supporting electrolyte was 0.5 M (Bu₄N)(PF₆) in CH₂Cl₂. All cyclic voltammograms were externally referenced to the Cp₂Fe/Cp₂Fe⁺ couple.

Results

Synthesis and Structural Characterization of [Fe₄(μ-OH)₄(μ-O₂C-Ar^{4-tBuPh})₂(μ-OTf)₂L₄], L = C₅H₅N (1), 4-^tBuC₅H₄N (2), and 3-FC₅H₄N (3). Reaction of Fe(OTf)₂·2MeCN, NaO₂C-Ar^{4-tBuPh}, OH⁻, and pyridine derivatives in a 2:1:2:2 ratio in THF afforded neutral tetrairon(II) clusters (Scheme 7.1). Extremely air-sensitive yellow blocks of 1–3 were obtained in modest to good yield (42 – 70%) following recrystallization from CH₂Cl₂/Et₂O. Although the solid state structures of 1–3 were unambiguously determined by X-ray crystallography (Figures 7.1 – 7.3), severe disorder in the bridging triflate ligands and solvent molecules hampered detailed structural refinement of the models for 1 and 3.

The crystal structure of 2 is shown in Figure 7.2; selected bond lengths and angles are listed in Table 7.2. Compound 2 has a {Fe₄(μ-OH)₄}⁴⁺ core, which can be best described as interpenetrating Fe₄ and (OH)₄ disphenoids. Each iron atom occupies alternating vertices of the resulting cube and has distorted octahedral geometry with a NO₅ donor atom set (Table 7.2). The assignment of the single atom bridging ligand as hydroxide is supported by the Fe–O distances, which range from 2.081(3) to 2.154(3) Å, as well as by the location and refinement of the associated hydrogen atoms in the X-ray structure determination. Comparable Fe–O_{hydroxo} distances occur in other high-spin iron(II) complexes.³⁷⁻³⁹

The $\{\text{Fe}_4(\mu\text{-OH})_4(\mu\text{-O}_2\text{CAr}^{4\text{-tBuPh}})_2(\mu\text{-OTf})_2\}$ core in **2** can be visualized as arising from the formal dimerization of two orthogonal $\{\text{Fe}_2(\mu\text{-OH})_2(\mu\text{-O}_2\text{CAr}^{4\text{-tBuPh}})\}^+$ units, assisted by two $\mu\text{-1,3}$ triflate ligands. The arrangement of ancillary ligands encapsulating the cubic core is such that the local point group symmetry of **2** is reduced from T_d to D_2 . As a result, **2** can occur in two enantiomeric forms, which crystallize as a racemic mixture. The two $\mu\text{-1,3}$ carboxylate ligands span each diiron(II) unit on parallel faces of a cube, minimizing steric interactions between the bulky 4-*tert*-butylphenyl groups. Such steric interactions apparently play a crucial role in assembling the $\{\text{Fe}_4(\text{OH})_4\}^{4+}$ cores. When attempts were made to access this unit with the sterically less demanding carboxylate ligand 2,6-di(*p*-tolyl)benzoate ($\text{Ar}^{\text{Tol}}\text{CO}_2^-$), only a paddlewheel diiron(II) complex $[\text{Fe}_2(\mu\text{-O}_2\text{CAr}^{\text{Tol}})_4(4\text{-tBuC}_5\text{H}_4\text{N})_2]^{17}$ was isolated under similar reaction conditions.

Depending on the nature of the bridging ligands, systematic variations in the Fe...Fe separations are observed. As shown in Figure 7.2, three different types of diiron(II) subunits are identified in **2**. They are $\{\text{Fe}_2(\mu\text{-OH})_2\}^{2+}$, $\{\text{Fe}_2(\mu\text{-OH})_2(\mu\text{-OTf})\}^+$, and $\{\text{Fe}_2(\mu\text{-OH})_2(\mu\text{-O}_2\text{CAr}^{4\text{-tBuPh}})\}^+$. The Fe...Fe distances decrease with increasing numbers of bridging ligands (Table 7.2). Compared with the intermetallic distances in the $\{\text{Fe}_2(\mu\text{-OH})_2\}^{2+}$ pairs (Fe1...Fe3; Fe2...Fe4), those in the $\{\text{Fe}_2(\mu\text{-OH})_2(\mu\text{-OTf})\}^+$ units (Fe1...Fe4; Fe2...Fe3) are reduced by ca 0.08 Å. These separations are further shortened by ca 0.10 Å when the bridging triflate is replaced by a carboxylate (Fe1...Fe2; Fe3...Fe4). The differences in the O-X (X = C or S) distances, rather than the Fe-O-X (X = C or S) angles, of the bridging ligands are responsible for such a core contraction. The O-C distances (1.255(5) – 1.268(5) Å) are significantly shorter than the O-S distances (1.452(3) – 1.457(3) Å), whereas the Fe-O-C angles (126.3(2) – 129.7(2)°) are comparable to the Fe-O-S angles (122.60(17) – 127.10(17)°). As expected, decrease in the Fe...Fe distances

are accompanied by a diminution in the Fe–O–Fe angles in the $\{\text{Fe}_2(\mu\text{-OH})_2\}^{2+}$ rhombuses (Table 7.2), which may affect the overlap between orbitals participating in magnetic exchange interactions (vide infra).

Electronic Absorption Spectroscopy. Compounds 1–3 exhibit intense visible absorption bands at $\lambda_{\text{max}} = 390 \sim 409$ nm (Figure 7.4), which are assigned as MLCT transitions⁴⁰ by analogy to the similar transitions at ~ 360 nm in related Fe(II)-pyridine units.⁴¹ The observed red shift in the electronic spectra with increasingly more electron-withdrawing pyridine derivatives, 4-*tert*-butylpyridine < pyridine < 3-fluoropyridine, is consistent with such an assignment. The magnitude of ϵ per Fe-pyridine unit ($725 - 875 \text{ M}^{-1}\text{cm}^{-1}$) is comparable to that of other iron(II) complexes having similar ligand combinations.⁴¹

IR Spectroscopy. IR spectra of 1–3 display strong absorptions at $3630 - 3649 \text{ cm}^{-1}$, attributable to the stretching vibrations of the coordinated hydroxide ligands.⁴² As shown in Figure 7.5A, two sharp ν_{OH} bands occur at 3632 and 3649 cm^{-1} for a solid sample of 1. The corresponding ν_{OD} frequencies appear at 2681 and 2691 cm^{-1} for a sample prepared with deuterium-enriched water (Figure 7.5B), which presumably afforded a mixture comprising $[\text{Fe}_4(\mu\text{-OD})_n(\mu\text{-OH})_{4-n}(\mu\text{-O}_2\text{CAr}^{4\text{-tBuPh}})_2(\mu\text{-OTf})_2(\text{C}_5\text{H}_5\text{N})_4]$ ($n = 1-4$). The observed shifts in hydroxide stretching frequencies upon OH to OD substitution ($\Delta\nu_{\text{obsd}} = 951$ and 958 cm^{-1}) are close to those expected from a simple diatomic oscillator model ($\Delta\nu_{\text{calc}} = 989$ and 994 cm^{-1}). Lowering the local symmetry of $\{\text{Fe}_4(\mu\text{-OH})_4\}^{4+}$ from T_d to D_2 would result in the splitting of a single IR-active OH stretching mode (T_2) into three active components (B_1 , B_2 , and B_3), two of which are apparently degenerate. The integrity of the $\{\text{Fe}_4(\mu\text{-OH})_4\}^{4+}$ core in solution was probed by IR spectroscopy in CH_2Cl_2 . As shown in Figure 7.5C, the characteristic OH vibrations of 1 at 3632 and 3649 cm^{-1} are retained with the same relative intensities as those in the solid sample. This result indicates that the cubane structure remains intact in

solution and that the splitting of the OH stretches observed in the solid state does not originate from intermolecular interactions or other solid state effects.

¹⁹F-NMR Spectroscopy. The presence of fluorine nuclei in the bridging triflate and 3-fluoropyridine ligands allowed the use of ¹⁹F-NMR spectroscopy to investigate further the solution structures of **1** and **3**. ¹⁹F-NMR spectroscopy is a good structural probe for paramagnetic iron(II) or cobalt(II) clusters, from which the number and symmetry of the species in solution can often be inferred.⁴³⁻⁴⁶ In CH₂Cl₂ at 20 °C, **1** exhibits a single broad ($\Delta\nu_{1/2} = 393$ Hz) resonance at 55.0 ppm (Figure 7.6A). This signal arises from the μ -1,3 triflate ligands, which are related by pseudo-C₂ symmetry, and is significantly downfield shifted from that (-79.2 ppm) of the free anion, measured independently as a tetrabutylammonium salt. A similar paramagnetic shift to 60.4 ppm was reported for a triflate anion bridging two high-spin iron(II) centers, which is significantly downfield from that of a terminal monodentate triflate (-14.0 ppm).⁴⁶ This behavior appears to reflect the proximity of the fluorine nuclei to two paramagnetic centers.

Under similar conditions, **3** displays two resonances at 52.9 ppm and 61.4 ppm (Figure 7.6B) that arise from the triflate and the 3-fluoropyridine ligands, respectively. Such an assignment is supported by the breadth ($\Delta\nu_{1/2} = 366$ Hz) of the 52.9 ppm resonance, which is comparable to that of the OTf⁻ signal in **1**, as well as by a ~ 3:2 ratio of the integrated intensities. No signal was detected for unbound triflate (-79.2 ppm) or 3-fluoropyridine (-127.6 ppm). The presence of lower or higher-nuclearity species in the solution can be ruled out by the simplicity of the ¹⁹F-NMR pattern, which is consistent with the solid state structure of **3**.

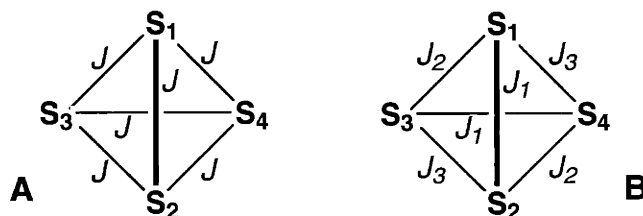
Mössbauer Spectroscopy. Figure 7.7 displays zero-field Mössbauer spectra of the solid samples of **1-3** measured at 4.2 K; the corresponding parameters derived from fits of the spectra are provided in Table 7.3 along with those of

topologically related tetrairon(II) complexes. Although there are four crystallographically unique iron sites in **1–3**, their nearly identical coordination environments produce unresolved Mössbauer spectra. No attempts were made to deconvolute further the single sharp ($\Gamma \sim 0.30 \text{ mm s}^{-1}$) quadrupole doublets. The isomer shifts and quadrupole splittings of **1–3** are typical of high-spin iron(II) sites in a N/O coordination environment^{10,47,48} and comparable to those obtained for related $\{\text{Fe}_4(\text{OR})_4\}^{4+}$ cores (Table 7.3). The similar Mössbauer parameters obtained for **1–3** suggest that the electronic environment around the metal center is not significantly perturbed upon changing the nitrogen donor ligands. This result is also consistent with the minimal structural variations observed in the solid state structures of **1–3**.

Magnetochemistry. The χT vs T curve for **1** is depicted in Figure 7.8; the magnetization curves at 2.5 K and 4.5 K are displayed in Figure 7.9. The measured value of $\chi T = 12.6 \text{ emu K mol}^{-1}$ at 300 K is consistent with the presence of four uncoupled $S = 2$ centers with $g = 2.08$ (expected value of $\chi T = 12.9 \text{ emu K mol}^{-1}$), which is slightly lower than those usually observed for high-spin iron(II) ions.^{36,49,50} Upon lowering the temperature, χT gradually decreases and reaches a plateau of $11.64 \text{ emu K mol}^{-1}$ between 90 K and 35 K. From 35 K to 2 K, however, the value drops from $11.50 \text{ emu K mol}^{-1}$ to $8.3 \text{ emu K mol}^{-1}$. This relatively high χT value indicates that excited magnetic states are still populated at the lowest temperature. This observed magnetic behavior is not easy to rationalize because of the orbitally degenerate ground state (${}^5T_{2g}$) of high-spin octahedral iron(II), which complicates the interpretation of the magnetic data. With a deviation from ideal octahedral geometry, however, the orbital contribution is significantly quenched⁵¹ and its effect on the temperature dependence of the magnetic moment is expected to be very small.^{36,49} Another complicating feature of iron(II) complexes is their large zero-field splitting (ZFS) effects (up to ~ 20

cm^{-1}),⁵² which can affect the χT behavior even at quite high temperatures. In the case of exchange-coupled systems, the ZFS and exchange coupling are often of the same order of magnitude, which makes the interpretation of the magnetic data even less straightforward. Given all these features, only a semi-quantitative explanation for the magnetic behavior of **1** was possible.

In order to minimize the effects from ZFS, only the high temperature region (> 90 K) of the curve was analyzed as a first approximation. A similar approach has been used for a related class of compounds, which exhibit a weak ferromagnetic coupling.¹⁴ In this framework, it is obvious that decrease in χT observed in this region can be attributed to weak antiferromagnetic (AF) coupling between the four magnetic centers. As a first step, we assumed T_d symmetry for the coupling and neglected the differences in the Fe–O–Fe angles and Fe...Fe distances in the cubane structure (Model A). By applying the Hamiltonian in eq



1, the best fit was obtained for $J = 1.2 \text{ cm}^{-1}$ and $g = 2.08$ (Figure 7.8). This treatment affords a $S = 0$ ground state, with the difference in energy between two states being $\Delta E = J S(S+1)/2$.

$$\mathcal{H} = J (\mathbf{S}_1 \cdot \mathbf{S}_2 + \mathbf{S}_1 \cdot \mathbf{S}_3 + \mathbf{S}_1 \cdot \mathbf{S}_4 + \mathbf{S}_2 \cdot \mathbf{S}_3 + \mathbf{S}_2 \cdot \mathbf{S}_4 + \mathbf{S}_3 \cdot \mathbf{S}_4) \quad (1)$$

Alternatively, the six Fe...Fe exchange paths can be grouped into three pairs, each of them experiencing different exchange coupling (Model B). This

subdivision can be made either on the basis of the bridging topology and the corresponding Fe...Fe distances or of the values of Fe-O-Fe angles. For either choice, the Hamiltonian in eq 2 describes the coupling interactions.

$$H = J_1 (\mathbf{S}_1 \cdot \mathbf{S}_2 + \mathbf{S}_3 \cdot \mathbf{S}_4) + J_2 (\mathbf{S}_1 \cdot \mathbf{S}_3 + \mathbf{S}_2 \cdot \mathbf{S}_4) + J_3 (\mathbf{S}_1 \cdot \mathbf{S}_4 + \mathbf{S}_2 \cdot \mathbf{S}_3) \quad (2)$$

This approach yielded for the best fit (Figure 7.8) the following coupling constants: $J_1 = 1.74 \text{ cm}^{-1}$, $J_2 = 1.33 \text{ cm}^{-1}$, and $J_3 = 0.35 \text{ cm}^{-1}$, and with $g = 2.08$. Assuming that the S_1 - S_2 / S_3 - S_4 pairs are the triply-bridged $\{\text{Fe}_2(\mu\text{-OH})_2(\mu\text{-O}_2\text{CAr}^{4\text{-tBuPh}})\}^+$ units, S_1 - S_3 / S_2 - S_4 are the triply-bridged $\{\text{Fe}_2(\mu\text{-OH})_2(\mu\text{-OTf})\}^+$ units, and S_1 - S_4 / S_2 - S_3 are the doubly-bridged $\{\text{Fe}_2(\mu\text{-OH})_2\}^{2+}$ units, the trend is consistent with increasing AF interaction with decreasing Fe...Fe distances (and decreasing Fe-O-Fe angles). As mentioned above, however, the differences in the coupling constants can also originate from the differences in the Fe-O-Fe angles. In particular, the AF interactions should increase with increasing angles, which would strengthen the overlap between the orbitals of the metals involved in metal coupling. The AF interactions decrease with increasing Fe...Fe distance, however. Thus the differences between the coupling constants, $|J_1 - J_2| = 0.41 \text{ cm}^{-1}$ and $|J_2 - J_3| = 0.98 \text{ cm}^{-1}$, favor the former interpretation. The two larger coupling constants (J_1 and J_2) are of similar magnitude and may be affected by coupling pathways mediated by the $\text{Ar}^{4\text{-tBuPh}}\text{CO}_2^-$ and OTf^- bridging ligands. Such pathways are not available for J_3 . As described below, however, care should be exercised not to overinterpret these results for the general purpose of evolving a magnetostructural correlation,¹⁴ given the large number of parameters used to describe the magnetic behavior of this system.

The coupling interactions modeled above are unable to reproduce the experimental data at lower temperatures. The simulated χT curve significantly de-

viates from the experimental data below 90 K. In order to obtain a reasonable simulation for this region, ZFS effects were introduced. For the sake of simplicity, we assumed an energy level pattern based on the one J -model (Model A). Even with this approach the number of parameters is still quite large because there are 8 levels ($S = 1-8$) that are affected by ZFS. Accordingly, only a qualitative analysis of these effects on the calculated curves could be performed. As shown in Figure 7.10, a value of $D = 5 \text{ cm}^{-1}$, chosen arbitrarily because it lies in the expected range for an iron(II) center, for the higher spin states can significantly affect the calculated χT curve, which deviates from the "isotropic" one even at 100 K. Since ZFS apparently increases the magnetic moment at lower temperatures, the experimentally observed behavior may be explained by invoking a subtle balance between exchange coupling and anisotropy, a quantitative determination of which poses a significant challenge. A more detailed analysis should also consider the difference between the three coupling pathways and introduce an anisotropic g tensor,⁵³ which would eventually result in overparameterization of the system and a large correlation between the obtained values, possibly leading to meaningless results.

We therefore conclude that the observed magnetic behavior of **1** results from weak AF coupling between the iron(II) centers, which is accompanied by large ZFS of the excited states. A theoretical curve can be constructed from this model that reproduces the plateau between 90 K and 35 K observed experimentally (Figure 7.8). In support of this model, the magnetization curves (Figure 7.9) clearly indicate that the complex is far from saturation even at 6 T and low temperature (2.5 K). Such behavior further supports the conclusion that weak AF coupling occurs between magnetic centers and that significant ZFS arises from different excited states that are populated at low temperatures.

Electrochemistry. Cyclic voltammograms of a CH_2Cl_2 solution of **1** reveal an oxidation at -10 mV vs $\text{Cp}_2\text{Fe}/\text{Cp}_2\text{Fe}^+$. A broad second oxidation wave occurs at 880 mV, which does not display a corresponding reduction wave in the return sweep (Figure 7.11). The presence of two separate cathodic peaks at -420 mV and -810 mV prompted us to investigate whether these reduction processes may be related to the first oxidation step. With a potential sweep range from -1100 to 700 mV, the first oxidation step approaches quasi-reversible behavior with increased scan rates. At a scan rate of 500 mV/s, the oxidation and reduction peaks maximize at 90 mV and -490 mV, respectively.

Discussion

Three complexes stabilizing the novel $\{\text{Fe}_4(\mu\text{-OH})_4\}^{4+}$ core were readily synthesized with the use of sterically encumbering terphenyl carboxylate ligands. These complexes are stable both in the solid state and in solution when protected from exposure to dioxygen or other oxidizing agents.

Four metal ions and four bridging ligands positioned at alternating corners of a cube describe a well-known unit in inorganic chemistry.¹⁴ Compared with other transition metal ions, however, access to cubic compounds containing oxygen-derived single atom bridging ligands has been quite limited in iron chemistry. There are only four examples of tetrairon(II) clusters having $\{\text{Fe}_4(\mu\text{-OR})_4\}^{n+}$ core fragments. They are $[\text{Fe}_4(\text{DBCat})_4(\text{py})_6]$,¹³ $[\text{Fe}(\text{OMe})(\text{MeOH})(\text{DBM})]_4$,¹⁴ $[\text{Fe}(\text{OMe})(\text{MeOH})(\text{DPM})]_4$,¹⁴ and $[\text{Fe}_4(\text{sae})_4(\text{MeOH})_4]$,¹⁵ where $\text{DBCatH}_2 = 3,5\text{-di-}t\text{-tert-butylcatechol}$, $\text{HDBM} = \text{dibenzoylmethane}$, $\text{HDPM} = \text{dipivaloylmethane}$, and $\text{H}_2\text{sae} = 2\text{-salicylideneamino-1-ethanol}$. The single atom ligands in each of these compounds are derived from either alkoxide or phenoxide ions. Compounds **1–3** represent the first examples of a tetrairon cube having bridging hydroxo ligands, which significantly expands the class of cubic polyiron

clusters. Analogous compounds with $\{M_4(\mu-OH)_4\}^{n+}$ units occur for most first low transition metals including chromium,⁵⁴ manganese,⁵⁵ cobalt,⁵⁶ nickel,⁵⁷ and copper.⁵⁸

Interpretation of the magnetic behavior of compound **1** was complicated by significant anisotropy, ZFS, and orbital contributions related with the $^5T_{2g}$ ground state of iron(II). Although a unique set of magnetic parameters cannot be provided, weak AF coupling and substantial ZFS are evident. Related tetrairon(II) clusters with alkoxide bridging groups, $[Fe(OMe)(MeOH)(DPM)]_4$ ¹⁴ and $[Fe_4(sae)_4(MeOH)_4]$ ¹⁵ display weak ferromagnetic interactions among the iron(II) centers, affording a $S = 8$ spin ground state. The different number of exchange pathways render magnetostructural correlations less than straightforward, but it would appear that triply-bridging methoxide or hydroxide ligands do not provide an efficient exchange coupling pathway between the linked iron(II) centers. Subtle geometrical differences in the M–O–M and O–M–O angles as well as the M···M distances may trigger crossover from ferromagnetic to antiferromagnetic interactions within the $\{Fe_4(OR)_4\}^{4+}$ module.

The quasi-reversible electrochemical behavior of **1** at high scan rates, along with the $\Delta(E_a - E_c)$ dependence on scan rate, indicate that structural rearrangements may accompany oxidation of the tetrairon(II) core. The increased acidity of the oxidized metal centers will favor deprotonation of the bridging hydroxo groups, a phenomenon well documented for (μ -hydroxo)diiron(II) complexes.^{37,59} Structural instability of the $\{Fe_4(\mu-OH)_4\}^{4+}$ core upon a change in oxidation state would be a significant liability if such units were to be used for biological ET reactions. In order to lower the Frank-Condon barrier for ET, minimal inner-sphere reorganization is desirable.⁶⁰ Both synthetic modeling^{1,61,62} and theoretical calculations⁶³ point toward minimal structural changes in $\{Fe_4(\mu-S)_4\}^{n+}$ centers at different physiological oxidation states.

In this context, it is worth noting the electrochemical behavior of a $\{\text{Fe}_4(\mu\text{-O})_4\}^{4+}$ unit embedded in an octairon(III) cluster $[\text{Fe}_8(\mu\text{-O})_4(\mu\text{-pz})_{12}\text{Cl}_4]$; here, an oxo-bridged tetrairon(III) cuboidal fragment is buried inside a “Fe-pyrazolate coat”.¹² In CH_2Cl_2 solution this compound can be sequentially reduced in one-electron steps from tetrairon(III) to tetrairon(II). The first three reduction processes are electrochemically reversible, indicating that no geometric rearrangement accompanies ET. This unusual stability was ascribed to the encapsulation of the $\{\text{Fe}_4(\mu\text{-O})_4\}^{n+}$ core within an inert shell that forces its structural integrity. It should be noted, however, that the bridging oxo groups in this cluster are coordinated to iron(III) sites comprising the “inert shell”, which may help dissipate the developing charge following electrochemical reduction of the core unit. In the absence of such confinement, it is not clear whether the $\{\text{Fe}_4(\mu\text{-O})_4\}^{n+}$ core can undergo similarly reversible redox processes. Discrete tetrairon cubane-type clusters having oxo bridging ligands are yet to be prepared.

With the recent spectroscopic identification⁶⁴ as well as crystallographic characterization⁶⁵ of the all-ferrous iron cube in the Fe protein of the nitrogenase system, the functionally relevant oxidation states of the biological [4Fe-4S] clusters now span from Fe^{II}_4 to $\text{Fe}^{\text{II}}\text{Fe}^{\text{III}}_3$. Although such oxidation states can be accessed chemically or electrochemically by small molecule mimics,^{1,61,62,66} all-ferrous [4Fe-4S] clusters having biologically relevant terminal ligands have not been isolated. Recent XAS studies on Fd, HiPIP, and a [4Fe-4S] model complex revealed that the wide differences in redox windows of seemingly identical tetrairon cores arise from interactions between the first and second coordination spheres.⁶⁷ Specifically, hydrogen-bonding interactions extending to the bridging sulfido groups significantly reduce their covalent interaction with the iron centers, destabilizing higher oxidation states. The $\{\text{Fe}_4(\mu\text{-OH})_4\}$ core in the compounds 1–3 can be formally regarded as a quadruply protonated, hypothetical

{Fe₄(μ-O)₄} unit, an analog of {Fe₄(μ-S)₄} with a lighter chalcogenide. By analogy to the sulfido-bridged core, such protonation of the bridging ligands greatly stabilizes low-valent metal centers, allowing isolation of all-ferrous tetrairon cubes 1–3.

The existence of an oxo-bridged synthetic tetrairon(III) core¹² and the hydroxo-bridged tetrairon(II) complexes 1–3 allows one to envision hypothetical redox processes involving hydroxo-/oxo-bridged cubane clusters. Iron oxyhydroxides and oxides are intermediates in the hydrolytic chemistry involved in the biomineralization of iron.⁶⁸ The nuclearity and coordination geometry of such clusters are controlled by various exogenous ligands including protein side chains that act as templates to direct the structure of the mineral phase.¹¹ With a proper arrangement of the proton donor/acceptor groups in the second coordination sphere, the [4Fe-4O(H)] unit may retain its structural integrity and act as an electron carrier for redox processes. It remains to be seen whether nature has chosen to construct a suitable platform to support such tetranuclear iron clusters for biological ET.

Acknowledgment. This work was supported by a grant from the National Science Foundation. Magnetochemistry part of this chapter was carried out in collaboration with Prof. Andrea Caneschi (University of Florence, Italy) and Mr. Lorenzo Sorace. I thank Ms. Jane Kuzelka for help in acquiring the Mössbauer spectra.

References

- (*) A slightly modified version of this work has been submitted for publication.
Lee, D.; Sorace, L.; Caneschi, A.; Lippard, S. J. **2001**.
- (1) Holm, R. H.; Kennepohl, P.; Solomon, E. I. *Chem. Rev.* **1996**, *96*, 2239-2314.
- (2) Solomon, E. I.; Hanson, M. A. *Inorganic Electronic Structure and Spectroscopy*; Solomon, E. I. and Lever, A. B. P., Ed.; John Wiley & Sons: New York, 1999; Vol. II, pp 1-129.
- (3) Solomon, E. I.; Randall, D. W.; Glaser, T. *Coord. Chem. Rev.* **2000**, *200-202*, 595-632.
- (4) Glaser, T.; Hedman, B.; Hodgson, K. O.; Solomon, E. I. *Acc. Chem. Res.* **2000**, *33*, 859-868.
- (5) Holm, R. H.; Ciurli, S.; Weigel, J. A. *Prog. Inorg. Chem.*; Lippard, S. J., Ed.; John Wiley & Sons, Inc: New York, 1990; Vol. 38, pp 1-74.
- (6) Lippard, S. J.; Berg, J. M. *Principles of Bioinorganic Chemistry*; University Science Books: Mill Valley, CA, 1994.
- (7) Stiefel, E. I.; George, G. N. *Bioinorganic Chemistry*; Bertini, I., Gray, H. B., Lippard, S. J. and Valentine, J. S., Ed.; University Science Books: Mill Valley, CA, 1994.
- (8) Beinert, H.; Holm, R. H.; Münck, E. *Science* **1997**, *277*, 653-659.
- (9) Lippard, S. J. *Angew. Chem., Int. Ed. Engl.* **1988**, *27*, 344-361.
- (10) Kurtz, D. M., Jr. *Chem. Rev.* **1990**, *90*, 585-606.
- (11) Powell, A. K. *Struct. Bonding (Berlin)* **1997**, *88*, 1-38.
- (12) Raptis, R. G.; Georgakaki, I. P.; Hockless, D. C. R. *Angew. Chem., Int. Ed. Engl.* **1999**, *38*, 1632-1634.
- (13) Shoner, S. C.; Power, P. P. *Inorg. Chem.* **1992**, *31*, 1001-1010.
- (14) Taft, K. L.; Caneschi, A.; Pence, L. E.; Delfs, C. D.; Papaefthymiou, G. C.; Lippard, S. J. *J. Am. Chem. Soc.* **1993**, *115*, 11753-11766.

- (15) Oshio, H.; Hoshino, N.; Ito, T. *J. Am. Chem. Soc.* **2000**, *122*, 12602-12603.
- (16) Lee, D.; Lippard, S. J. *J. Am. Chem. Soc.* **1998**, *120*, 12153-12154.
- (17) Lee, D.; Du Bois, J.; Petasis, D.; Hendrich, M. P.; Krebs, C.; Huynh, B. H.; Lippard, S. J. *J. Am. Chem. Soc.* **1999**, *121*, 9893-9894.
- (18) Lee, D.; Krebs, C.; Huynh, B. H.; Hendrich, M. P.; Lippard, S. J. *J. Am. Chem. Soc.* **2000**, *122*, 5000-5001.
- (19) Lee, D.; Lippard, S. J. *J. Am. Chem. Soc.* **2001**, *123*, 4611-4612.
- (20) Hagadorn, J. R.; Que, L., Jr.; Tolman, W. B. *J. Am. Chem. Soc.* **1998**, *120*, 13531-13532.
- (21) Hagadorn, J. R.; Que, L., Jr.; Tolman, W. B.; Prisecaru, I.; Münck, E. *J. Am. Chem. Soc.* **1999**, *121*, 9760-9761.
- (22) Vinod, T. K.; Hart, H. *Topics in Current Chemistry*; Weber, E., Ed.; Springer-Verlag: Berlin, 1994; Vol. 172, pp 119-178.
- (23) Chen, C.-T.; Siegel, J. S. *J. Am. Chem. Soc.* **1994**, *116*, 5959-5960.
- (24) Du Bois, J.; Mizoguchi, T. J.; Lippard, S. J. *Coord. Chem. Rev.* **2000**, *200-202*, 443-485.
- (25) Westerheide, L.; Pascaly, M.; Krebs, B. *Curr. Opin. Chem. Biol.* **2000**, *4*, 235-241.
- (26) Tolman, W. B.; Spencer, D. J. E. *Curr. Opin. Chem. Biol.* **2001**, *5*, 188-195.
- (27) Pangborn, A. B.; Giardello, M. A.; Grubbs, R. H.; Rosen, R. K.; Timmers, F. J. *Organometallics* **1996**, *15*, 1518-1520.
- (28) Hagen, K. S. *Inorg. Chem.* **2000**, *39*, 5867-5869.
- (29) Du, C.-J. F.; Hart, H.; Ng, K.-K. D. *J. Org. Chem.* **1986**, *51*, 3162-3165.
- (30) Saednya, A.; Hart, H. *Synthesis* **1996**, 1455-1458.
- (31) SMART v5.05; Bruker AXS Inc.: Madison, WI, 1998.
- (32) Feig, A. L.; Bautista, M. T.; Lippard, S. J. *Inorg. Chem.* **1996**, *35*, 6892-6898.

- (33) Sheldrick, G. M. *SHELXTL v5.1: Program for the Refinement of Crystal Structures 97-2*; University of Göttingen, Göttingen, Germany, 1998.
- (34) Sheldrick, G. M. *SADABS v2.03: Area-Detector Absorption Correction*; University of Göttingen, Göttingen, Germany, 1999.
- (35) Kent, T. A. *WMOSS: Mössbauer Spectral Analysis Software*; 2.5 ed.; Minneapolis, 1998.
- (36) Carlin, R. L. *Magnetochemistry*; Springer-Verlag: New York, 1986.
- (37) Hartman, J. R.; Rardin, R. L.; Chaudhuri, P.; Pohl, K.; Wieghardt, K.; Nuber, B.; Weiss, J.; Papaefthymiou, G. C.; Frankel, R. B.; Lippard, S. J. *J. Am. Chem. Soc.* **1987**, *109*, 7387–7396.
- (38) Kitajima, N.; Tamura, N.; Tanaka, M.; Moro-oka, Y. *Inorg. Chem.* **1992**, *31*, 3342–3343.
- (39) MacMurdo, V. L.; Zheng, H.; Que, L., Jr. *Inorg. Chem.* **2000**, *39*, 2254–2255.
- (40) Lever, A. B. P. *Inorganic Electronic Spectroscopy*; 2nd ed. ed.; Elsevier Science Publishers B. V.: Amsterdam, The Netherlands, 1984.
- (41) LeCloux, D. D.; Barrios, A. M.; Mizoguchi, T. J.; Lippard, S. J. *J. Am. Chem. Soc.* **1998**, *120*, 9001–9014.
- (42) Nakamoto, K. *Infrared and Raman Spectra of Inorganic and Coordination Compounds*; 5th ed. ed.; Wiley-Interscience: New York, 1997.
- (43) Hagen, K. S.; Lachicotte, R.; Kitaygorodskiy, A.; Elbouadili, A. *Angew. Chem., Int. Ed. Engl.* **1993**, *32*, 1321–1324.
- (44) Lachicotte, R.; Kitaygorodskiy, A.; Hagen, K. S. *J. Am. Chem. Soc.* **1993**, *115*, 8883–8884.
- (45) Hagen, K. S.; Lachicotte, R.; Kitaygorodskiy. *J. Am. Chem. Soc.* **1993**, *115*, 12617–12618.
- (46) Blakesley, D. W.; Payne, S. C.; Hagen, K. S. *Inorg. Chem.* **2000**, *39*, 1979–1989.

- (47) Gütlich, P.; Ensling, J. *Inorganic Electronic Structure and Spectroscopy*; Solomon, E. I. and Lever, A. B. P., Ed.; John Wiley & Sons: New York, 1999; Vol. I, pp 161-211.
- (48) Münck, E. *Physical Methods in Bioinorganic Chemistry: Spectroscopy and Magnetism*; Que, L., Jr., Ed.; University Science Books: Sausalito, CA, 2000, pp 287-319.
- (49) *Theory and Applications of Molecular Paramagnetism*; Boudreaux, E. A. and Mulay, L. N., Ed.; Wiley-Interscience: New York, 1976.
- (50) Girerd, J.-J.; Journaux, Y. *Physical Methods in Bioinorganic Chemistry: Spectroscopy and Magnetism*; Que, L., Jr., Ed.; University Science Books: Sausalito, CA, 2000, pp 321-374.
- (51) Borrás-Almenar, J. J.; Clemente-Juan, J. M.; Coronado, E.; Pali, A. V.; Tsukerblat, B. S. *J. Phys. Chem. A* **1998**, *102*, 200-213.
- (52) Varret, F. *J. Phys. Chem. Solids* **1976**, *37*, 257-263.
- (53) Belanzoni, P.; Re, N.; Rosi, M.; Sgamellotti, A.; Baerends, E. J.; Floriani, C. *Inorg. Chem.* **1996**, *35*, 7776-7785.
- (54) McNeese, T. J.; Mueller, T. E.; Wierda, D. A.; Darensbourg, D. J.; Delord, T. *J. Inorg. Chem.* **1985**, *24*, 3465-3468.
- (55) Copp, S. B.; Holman, K. T.; Sangster, J. O. S.; Subramanian, S.; Zaworotko, M. J. *J. Chem. Soc., Dalton Trans.* **1995**, 2233-2243.
- (56) He, C.; Lippard, S. J. *J. Am. Chem. Soc.* **2000**, *122*, 184-185.
- (57) Aurivillius, B. *Acta Chem. Scand. Ser. A* **1977**, *31*, 501-508.
- (58) Sletten, J.; Sørensen, A.; Julve, M.; Journaux, Y. *Inorg. Chem.* **1990**, *29*, 5054-5058.
- (59) He, C.; Lippard, S. J. *Inorg. Chem.* **2001**, *40*, 1414-1420.
- (60) Marcus, R. A.; Sutin, N. *Biochim. Biophys. Acta* **1985**, *811*, 265-322.
- (61) O'Sullivan, T.; Millar, M. M. *J. Am. Chem. Soc.* **1985**, *107*, 4096-4097.

- (62) Carney, M. J.; Papaefthymiou, G. C.; Frankel, R. B.; Holm, R. H. *Inorg. Chem.* **1989**, *28*, 1497-1503.
- (63) Sigfridsson, E.; Olsson, M. H. M.; Ryde, U. *Inorg. Chem.* **2001**, *40*, 2509-2519.
- (64) Yoo, S. J.; Angove, H. C.; Burgess, B. K.; Hendrich, M. P.; Münck, E. *J. Am. Chem. Soc.* **1999**, *121*, 2534-2545.
- (65) Strop, P.; Takahara, P. M.; Chiu, H.-J.; Angove, H. C.; Burgess, B. K.; Rees, D. C. *Biochemistry* **2001**, *40*, 651-656.
- (66) Goh, C.; Segal, B. M.; Huang, J.; Long, J. R.; Holm, R. H. *J. Am. Chem. Soc.* **1996**, *118*, 11844-11853.
- (67) Glaser, T.; Bertini, I.; Moura, J. J. G.; Hedman, B.; Hodgson, K. O.; Solomon, E. I. *J. Am. Chem. Soc.* **2001**, *123*, 4859-4860.
- (68) Theil, E. C.; Raymond, K. N. *Bioinorganic Chemistry*; Bertini, E., Gray, H. B., Lippard, S. J. and Valentine, J. S., Ed.; University Science Books: Mill Valley, CA, 1994, pp 1-35.

Table 7.1. Summary of X-ray Crystallographic Data

	2.0.25CH ₂ Cl ₂ ·1.25Et ₂ O
formula	Fe ₄ C _{97.25} H ₁₁₄ N ₄ O _{15.25} Cl _{0.5} F ₆ S ₂
fw	2002.17
space group	P2 ₁ /c
<i>a</i> , Å	20.9476(3)
<i>b</i> , Å	23.6601(4)
<i>c</i> , Å	20.9286(3)
α, deg	
β, deg	91.7110(10)
γ, deg	
<i>V</i> , Å ³	10368.1(3)
<i>Z</i>	4
ρ _{calc} , g/cm ³	1.283
<i>T</i> , °C	-85
μ(Mo Kα), mm ⁻¹	0.673
2θ limits, deg	3.9 – 50
total no. of data	76328
no. of unique data	18220
no. of params	1164
<i>R</i> (%) ^{<i>a</i>}	0.0598
<i>wR</i> ² (%) ^{<i>b</i>}	0.1434
max, min peaks, e/Å ³	1.149, ^{<i>c</i>} -0.518

$$^a R = \Sigma ||F_o| - |F_c|| / \Sigma |F_o|. \quad ^b wR^2 = \{\Sigma[w(F_o^2 - F_c^2)^2] / \Sigma[w(F_o^2)^2]\}^{1/2}.$$

^{*c*} This peak occurs in the vicinity of a disordered dichloromethane molecule.

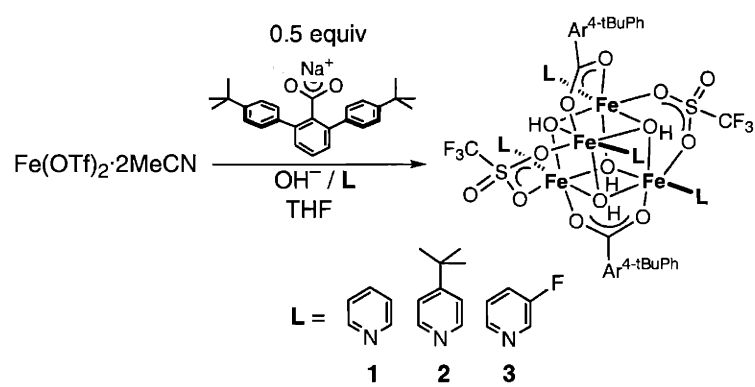
Table 7.2. Selected Bond Lengths (Å) and Angles (deg) for 2.^a

Bond Length		Bond Angle	
Fe(1)···Fe(2)	3.0714(8)	Fe(1)-O(1)-Fe(2)	92.61(12)
Fe(1)···Fe(3)	3.2447(8)	O(1)-Fe(2)-O(2)	85.35(12)
Fe(1)···Fe(4)	3.1700(8)	Fe(1)-O(2)-Fe(2)	92.21(11)
Fe(2)···Fe(3)	3.1647(8)	O(1)-Fe(1)-O(2)	85.66(12)
Fe(2)···Fe(4)	3.2508(8)	Fe(1)-O(1)-Fe(3)	101.53(14)
Fe(3)···Fe(4)	3.0605(8)	O(1)-Fe(3)-O(4)	78.84(12)
Fe(1)-O(1)	2.108(3)	Fe(1)-O(4)-Fe(3)	100.40(13)
Fe(1)-O(2)	2.141(3)	O(1)-Fe(1)-O(4)	79.23(12)
Fe(1)-O(4)	2.090(3)	Fe(1)-O(2)-Fe(4)	97.26(12)
Fe(1)-O(1A)	2.100(3)	O(2)-Fe(4)-O(4)	82.54(11)
Fe(1)-O(1T)	2.231(3)	Fe(1)-O(4)-Fe(4)	97.41(12)
Fe(1)-N(1P)	2.157(3)	O(4)-Fe(1)-O(2)	82.06(11)
Fe(2)-O(1)	2.140(3)	Fe(2)-O(1)-Fe(3)	97.11(13)
Fe(2)-O(2)	2.121(3)	O(1)-Fe(3)-O(3)	82.36(12)
Fe(2)-O(3)	2.076(3)	Fe(2)-O(3)-Fe(3)	97.68(12)
Fe(2)-O(2A)	2.084(3)	O(3)-Fe(2)-O(1)	82.17(12)
Fe(2)-O(1F)	2.263(3)	Fe(4)-O(2)-Fe(2)	101.31(13)
Fe(2)-N(1Q)	2.154(3)	O(2)-Fe(4)-O(3)	78.69(11)
Fe(3)-O(1)	2.081(3)	Fe(2)-O(3)-Fe(4)	100.42(13)
Fe(3)-O(3)	2.127(3)	O(2)-Fe(2)-O(3)	79.59(11)
Fe(3)-O(4)	2.133(3)	Fe(3)-O(3)-Fe(4)	91.26(11)
Fe(3)-O(2B)	2.080(3)	O(4)-Fe(4)-O(3)	86.16(11)
Fe(3)-O(2F)	2.260(3)	Fe(4)-O(4)-Fe(3)	91.80(12)
Fe(3)-N(1R)	2.151(3)	O(3)-Fe(3)-O(4)	86.73(11)
Fe(4)-O(2)	2.082(3)		
Fe(4)-O(3)	2.154(3)		
Fe(4)-O(4)	2.129(3)		
Fe(4)-O(1B)	2.078(3)		
Fe(4)-O(2T)	2.281(3)		
Fe(4)-N(1S)	2.159(3)		

^a Number in parentheses are estimated standard deviations of the last significant figure. Atoms are labeled as indicated in Figure 7.2.

Table 7.3. Zero-Field Mössbauer Parameters for 1–3 and Related Tetrairon(II) Clusters.

compound	T (K)	δ (mm s ⁻¹)	ΔE_Q (mm s ⁻¹)	Γ (mm s ⁻¹)	ref
1	4.2	1.27(2)	2.93(2)	0.30	this work
2	4.2	1.26(2)	3.00(2)	0.30	this work
3	4.2	1.27(2)	2.96(2)	0.31	this work
[Fe(OMe)(MeOH)(DPM)] ₄	4.2	1.25	2.35	0.44	14
[Fe(OMe)(MeOH)(DBM)] ₄	80	1.21	2.52	0.30	14



Scheme 7.1.

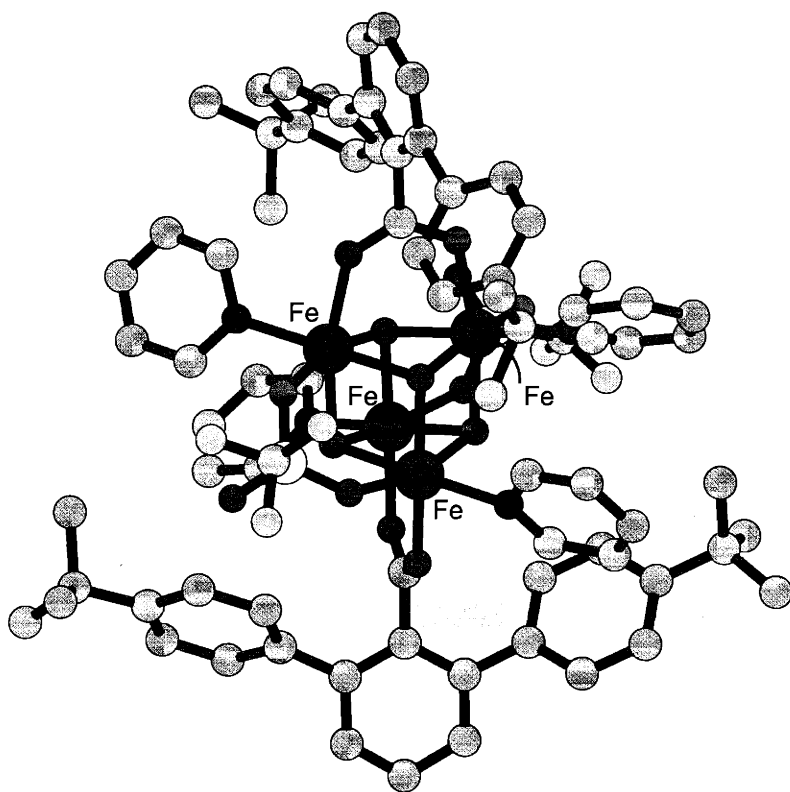


Figure 7.1. Ball and stick representation of the solid-state structure of $[\text{Fe}_4(\mu\text{-OH})_4(\mu\text{-O}_2\text{CAr}^{4\text{-tBuPh}})_2(\mu\text{-OTf})_2(\text{C}_5\text{H}_5\text{N})_4]$ (**1**).

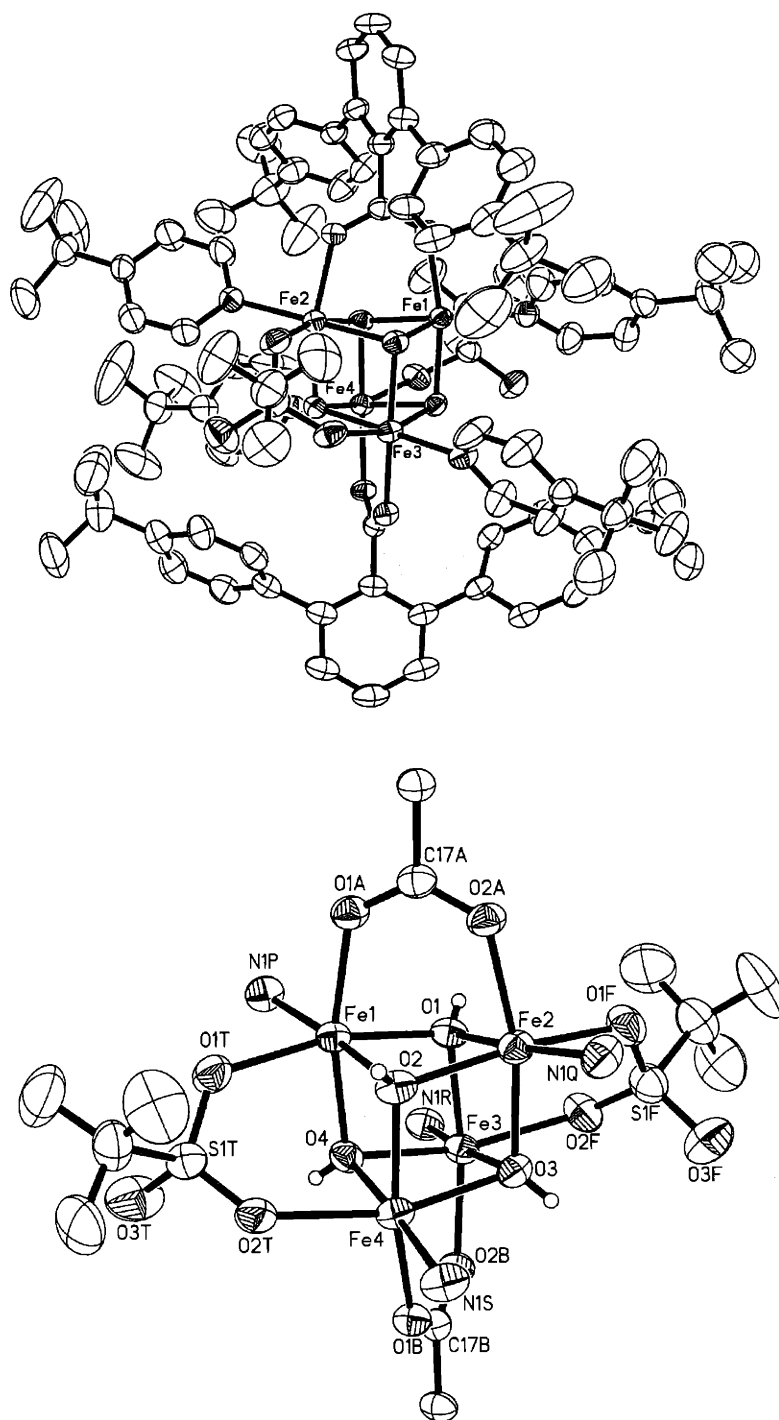


Figure 7.2. ORTEP diagram of $[\text{Fe}_4(\mu\text{-OH})_4(\mu\text{-O}_2\text{CAr}^{4\text{-tBuPh}})_2(\mu\text{-OTf})_2(4\text{-}^t\text{BuC}_5\text{H}_4\text{N})_4]$ (**2**) with thermal ellipsoids at 50% probability: top, whole molecule; bottom, core structure.

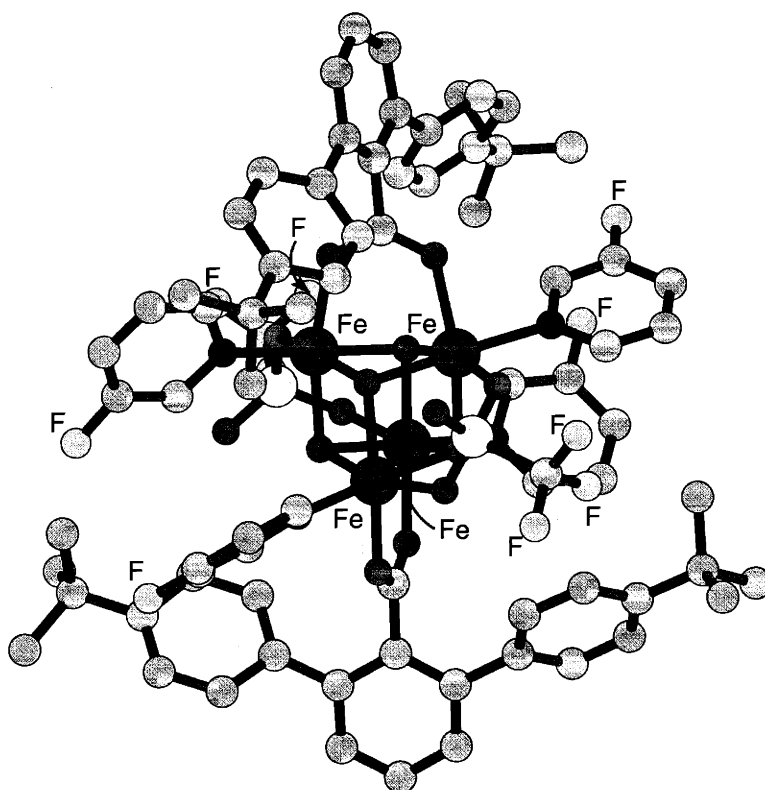


Figure 7.3. Ball and stick representation of the solid-state structure of $[\text{Fe}_4(\mu\text{-OH})_4(\mu\text{-O}_2\text{CAr}^{4\text{-tBuPh}})_2(\mu\text{-OTf})_2(3\text{-FC}_5\text{H}_4\text{N})_4]$ (**3**).

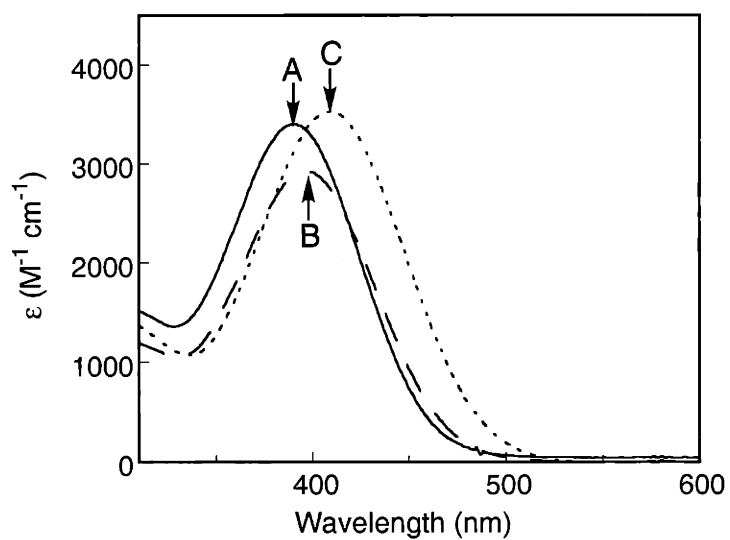


Figure 7.4. Electronic absorption spectra of 1–3 showing the MLCT transitions.

- (A) $[\text{Fe}_4(\mu\text{-OH})_4(\mu\text{-O}_2\text{CAr}^{4\text{-tBuPh}})_2(\mu\text{-OTf})_2(\text{C}_5\text{H}_5\text{N})_4]$ (1) (—);
 (B) $[\text{Fe}_4(\mu\text{-OH})_4(\mu\text{-O}_2\text{CAr}^{4\text{-tBuPh}})_2(\mu\text{-OTf})_2(4\text{-tBuC}_5\text{H}_4\text{N})_4]$ (2) (----);
 (C) $[\text{Fe}_4(\mu\text{-OH})_4(\mu\text{-O}_2\text{CAr}^{4\text{-tBuPh}})_2(\mu\text{-OTf})_2(3\text{-FC}_5\text{H}_4\text{N})_4]$ (3) (.....).

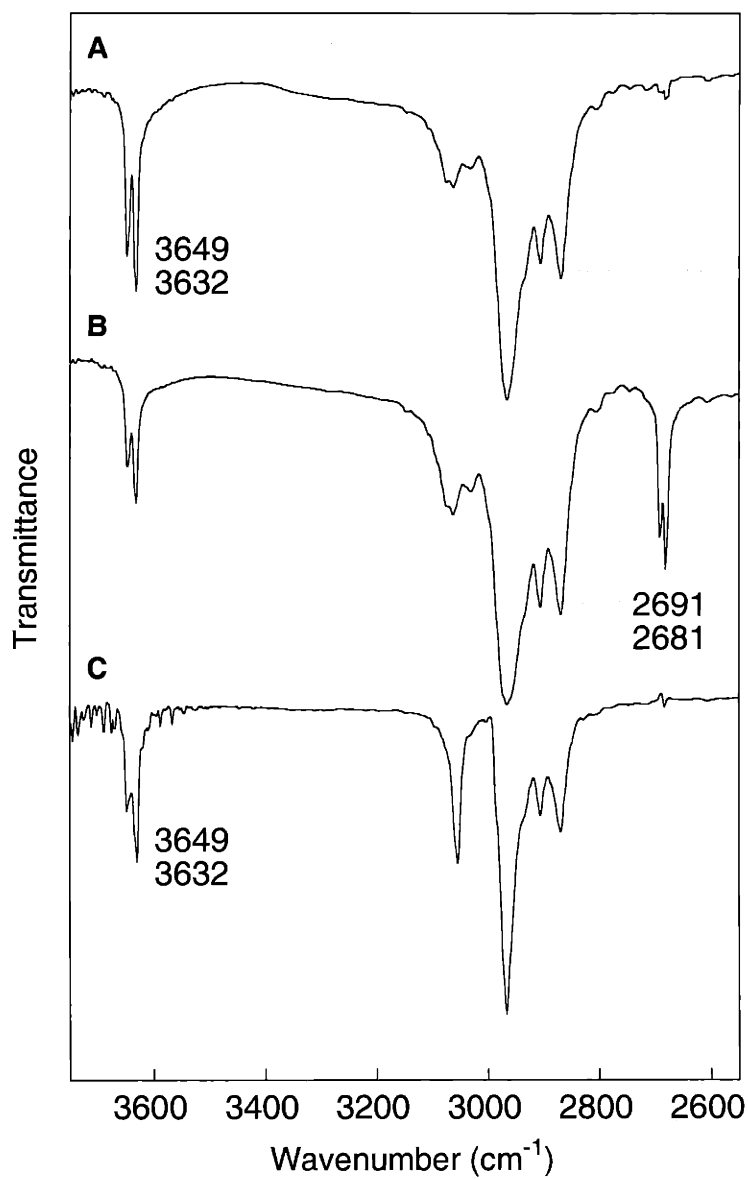


Figure 7.5. IR spectra of $[\text{Fe}_4(\mu\text{-OH})_4(\mu\text{-O}_2\text{CAr}^{4\text{-tBuPh}})_2(\mu\text{-OTf})_2(\text{C}_5\text{H}_5\text{N})_4]$. (A) in KBr; (B) in KBr as a mixture with OD^- substituted cluster $[\text{Fe}_4(\mu\text{-OD})_4(\mu\text{-O}_2\text{CAr}^{4\text{-tBuPh}})_2(\mu\text{-OTf})_2(\text{C}_5\text{H}_5\text{N})_4]$; (C) in CH_2Cl_2 .

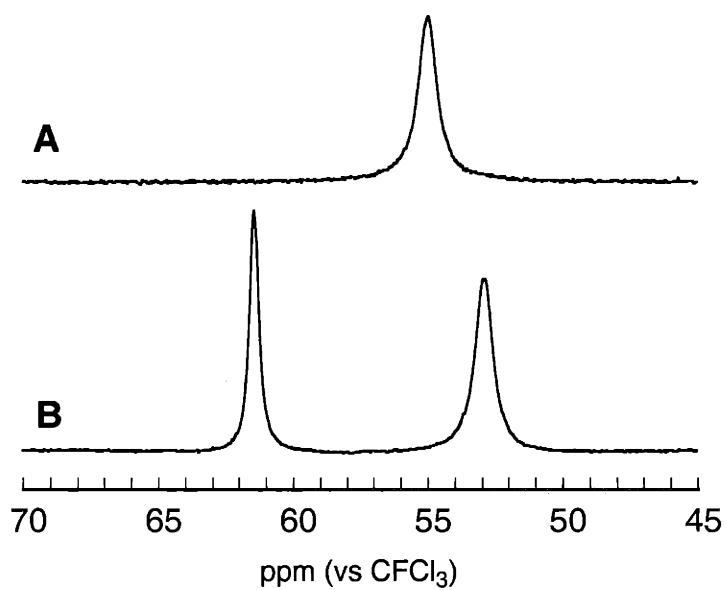


Figure 7.6. 470-MHz ^{19}F -NMR spectra (vs CFCl_3 at 20 °C) of $[\text{Fe}_4(\mu\text{-OH})_4(\mu\text{-O}_2\text{CAr}^{4\text{-tBuPh}})_2(\mu\text{-OTf})_2(\text{C}_5\text{H}_5\text{N})_4]$ (1) (A) and $[\text{Fe}_4(\mu\text{-OH})_4(\mu\text{-O}_2\text{CAr}^{4\text{-tBuPh}})_2(\mu\text{-OTf})_2(3\text{-FC}_5\text{H}_4\text{N})_4]$ (3) (B) in CH_2Cl_2 .

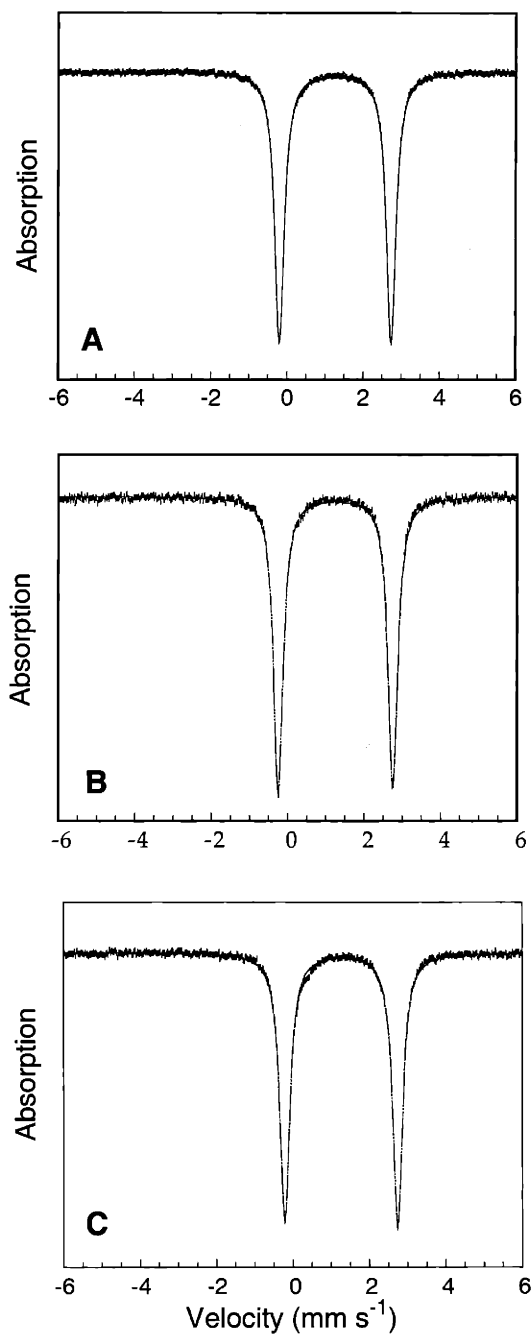


Figure 7.7. Zero-field Mössbauer spectrum (experimental data (|), calculated fit (—)) recorded at 4.2 K for $[\text{Fe}_4(\mu\text{-OH})_4(\mu\text{-O}_2\text{CAR}^{4\text{-tBuPh}})_2(\mu\text{-OTf})_2(\text{C}_5\text{H}_5\text{N})_4]$ (**1**) (A), $[\text{Fe}_4(\mu\text{-OH})_4(\mu\text{-O}_2\text{CAR}^{4\text{-tBuPh}})_2(\mu\text{-OTf})_2(4\text{-tBuC}_5\text{H}_4\text{N})_4]$ (**2**) (B), and $[\text{Fe}_4(\mu\text{-OH})_4(\mu\text{-O}_2\text{CAR}^{4\text{-tBuPh}})_2(\mu\text{-OTf})_2(3\text{-FC}_5\text{H}_4\text{N})_4]$ (**3**) (C) in the solid state. See Table 7.3 for derived Mössbauer parameters.

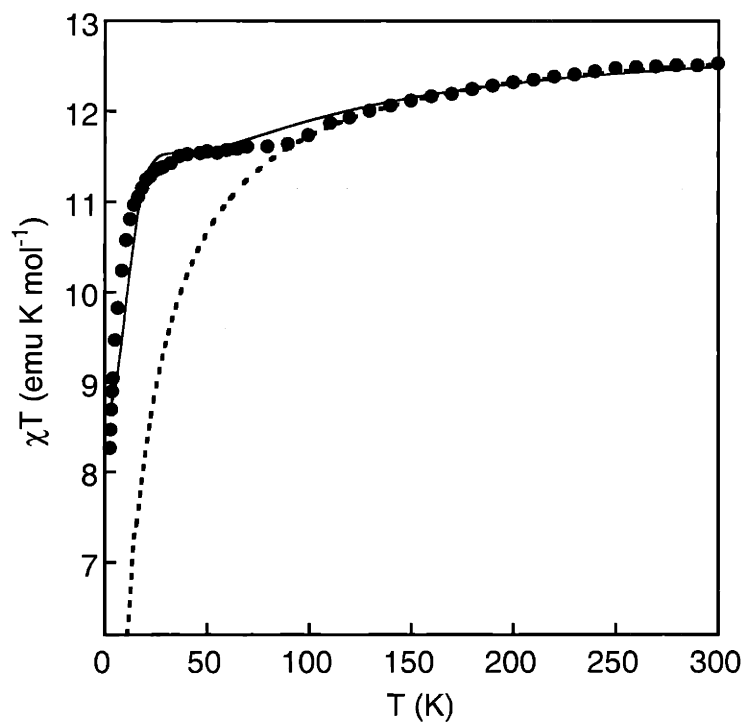


Figure 7.8. Plot of χT versus temperature for $[\text{Fe}_4(\mu\text{-OH})_4(\mu\text{-O}_2\text{CAr}^{4\text{-tBuPh}})_2(\mu\text{-OTf})_2(\text{C}_5\text{H}_5\text{N})_4]$ (**1**) (\bullet). The dashed line is the calculated χT values with the two different isotropic Hamiltonians as described in the text (Models A and B, see text), which afforded two superimposable curves. The solid line was obtained by using the following parameters: $J = 1.2 \text{ cm}^{-1}$; $D = -7.0 \text{ cm}^{-1}$ ($S = 4$); $D = 5.7 \text{ cm}^{-1}$ ($S = 5$); $D = 3.5 \text{ cm}^{-1}$ ($S = 6$); $D = -2.1 \text{ cm}^{-1}$ ($S = 8$). See the text for details of the calculation.

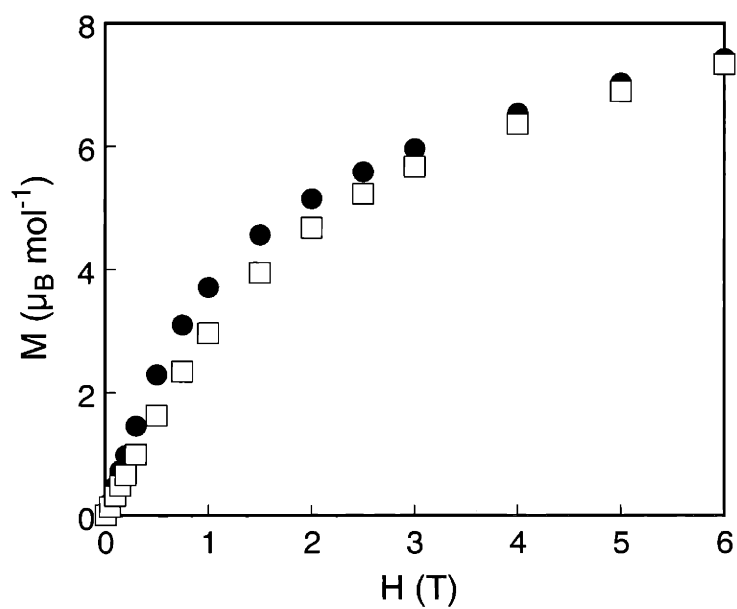


Figure 7.9. Magnetization curves versus field of $[\text{Fe}_4(\mu\text{-OH})_4(\mu\text{-O}_2\text{CAr}^{4\text{-tBuPh}})_2(\mu\text{-OTf})_2(\text{C}_5\text{H}_5\text{N})_4]$ (1) at 2.5 K (●) and 4.5 K (□).

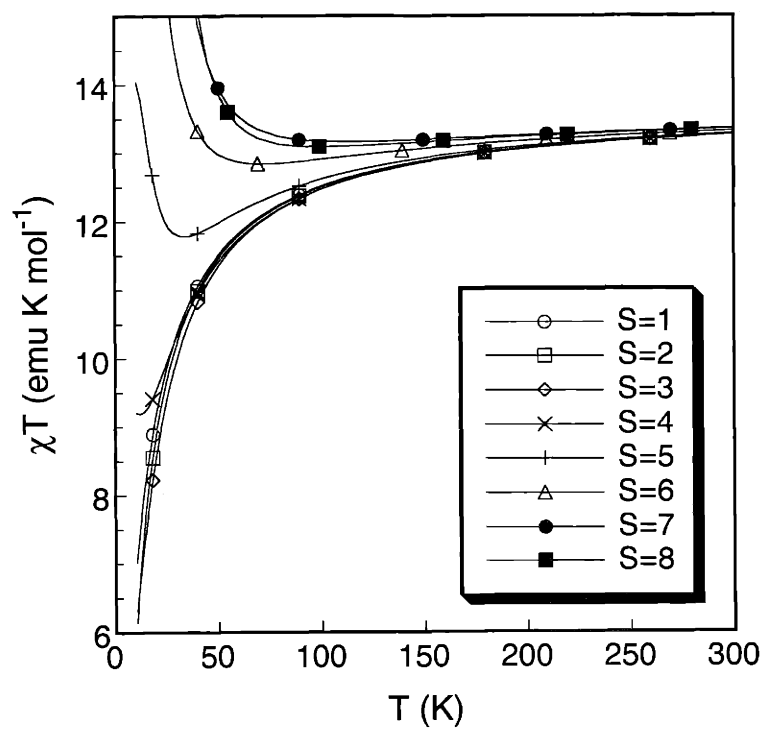


Figure 7.10. Plots of calculated χT versus T for $S = 1-8$ with $D = 5 \text{ cm}^{-1}$. Whereas ZFS has only small effect for lower multiplicity states ($S = 1-3$), its contribution becomes significant for the higher multiplicity states ($S = 4-8$).

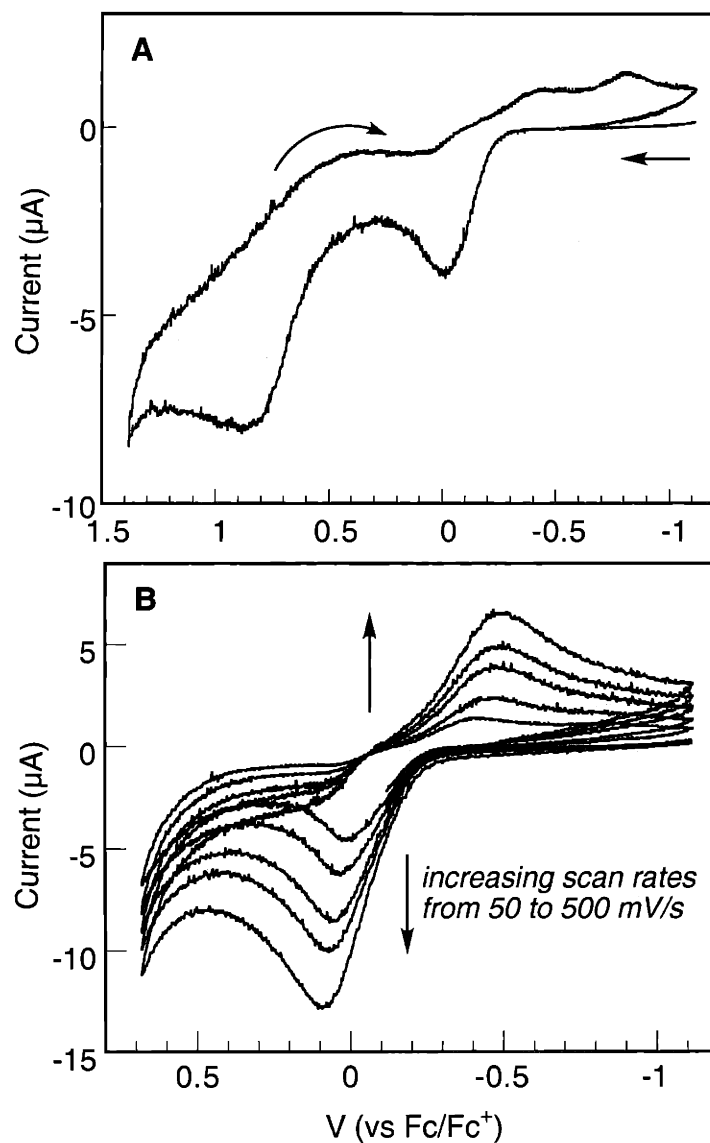


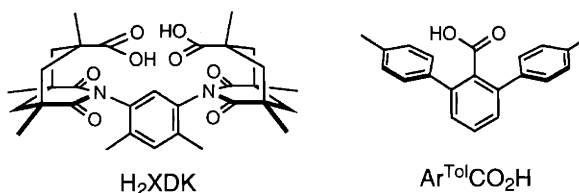
Figure 7.11. Cyclic voltammograms of $[\text{Fe}_4(\mu\text{-OH})_4(\mu\text{-O}_2\text{CAr}^{4\text{-tBuPh}})_2(\mu\text{-OTf})_2(\text{C}_5\text{H}_5\text{N})_4]$ (**1**) in CH_2Cl_2 with 0.5 M $(\text{Bu}_4\text{N})(\text{PF}_6)$ as supporting electrolyte and a scan rate of 50 mV/s (A); with increasing scan rates from 50 mV/s to 500 mV/s (B).

Chapter VIII

Sterically Hindered Carboxylate Ligands Support Water-Bridged Dimetallic Centers That Model Features of Metallohydrolase Active Sites*

Introduction

A structural motif comprising two metal ions supported by four carboxylate and one or two histidine residues is commonly encountered at metalloenzyme active sites.^{1,2} Widely differing organic transformations can be catalyzed at these centers by various metal ions having a seemingly identical chemical architecture. The nature of these transformations has been a topic of great interest. The pre-organized dinucleating carboxylate ligand, XDK,^{3,4} and its derivatives^{5,6} have been extensively used in our laboratory to model features of such enzyme active sites. Discrete dimetallic cores are stabilized by the convergent doubly-bridging carboxylate platform afforded by the XDK ligand family and shielded against unwanted oligomerization reactions. Dimetallic XDK complexes of both redox-active⁵⁻¹¹ and -inactive¹²⁻¹⁶ metal ions have afforded valuable structural and/or functional models for their biological counterparts, providing insights into the underlying chemical principles of metalloenzyme action.



Recently we demonstrated that another conformationally well-defined carboxylate ligand, $\text{Ar}^{\text{Tol}}\text{CO}_2^-$,³ can be used to assemble diiron(II) complexes that bear a close structural and functional resemblance to the active sites of selected non-heme diiron enzymes.¹⁷⁻²⁰ Control over the nuclearity and coordination geometry was achieved by the interlocking nature of the flanking aryl substituents on the benzoate ligands in the complexes. The occurrence of structurally related dimetallic centers in selected metallohydrolases²¹⁻²³ prompted us to

synthesize analogous tetracarboxylate dinuclear complexes of redox inactive metal ions and to compare their structures with those in the biological systems.

In this paper, we describe the synthesis, structural and physical characterization of dicobalt, dinickel, and dizinc complexes coordinated by $\text{Ar}^{\text{Tol}}\text{CO}_2^-$ ligands. Quadruply-bridged dimetallic cores having unprecedented coordination geometries were readily obtained through efficient self-assembly from simple starting materials. From X-ray structural studies of $[\text{Co}_2(\mu\text{-OH}_2)_2(\mu\text{-O}_2\text{CAr}^{\text{Tol}})_2(\text{O}_2\text{CAr}^{\text{Tol}})_2(\text{C}_5\text{H}_5\text{N})_2]$ (**2 a**) and $[\text{Ni}_2(\mu\text{-HO}\cdots\text{H})_2(\mu\text{-O}_2\text{CAr}^{\text{Tol}})_2(\text{O}_2\text{CAr}^{\text{Tol}})_2(\text{C}_5\text{H}_5\text{N})_2]$ (**5**) we could observe a shift of protons on bridging water molecules toward metal-bound carboxylate groups, a process that may be relevant to a key step in the mechanism of metallohydrolases.

Experimental Section

General Procedures and Methods. 2,6-Di(*p*-tolyl)benzoic acid, $\text{Ar}^{\text{Tol}}\text{CO}_2\text{H}$,^{24,25} and *N,N*-dibenzylethylenediamine, *N,N*-Bn₂en,^{26,27} were synthesized according to literature procedures. All other reagents were obtained from commercial suppliers and used as received unless otherwise noted. The reactions of MX_2 ($\text{MX}_2 = \text{CoI}_2$ or NiBr_2), AgOTf, $\text{NaO}_2\text{CAr}^{\text{Tol}}$, and pyridine were carried out under nitrogen in a Vacuum Atmospheres drybox. Solvents used in the drybox were purified by the following methods. Dichloromethane was distilled over CaH_2 under nitrogen and diethyl ether and THF were saturated with nitrogen and purified by passage through activated Al_2O_3 columns under nitrogen.²⁸ FT-IR spectra were recorded on a Bio Rad FTS-135 instrument with Win-IR software. UV-vis spectra were recorded on a Hewlett Packard 8453 diode array spectrophotometer.

$[\text{Co}_2(\mu\text{-O}_2\text{CAr}^{\text{Tol}})_2(\text{O}_2\text{CAr}^{\text{Tol}})_2(\text{C}_5\text{H}_5\text{N})_2]$ (**1**). *Method A.* To a rapidly stirred green THF (10 mL) solution of CoI_2 (79 mg, 0.25 mmol) was added AgOTf

(142 mg, 0.55 mmol) to afford an orange suspension. A portion of $\text{NaO}_2\text{CAr}^{\text{Tol}}$ (165 mg, 0.509 mmol) was added. The heterogeneous mixture was treated with pyridine (21 μL , 0.26 mmol) and allowed to stir overnight. Insoluble fractions were filtered off and the deep blue filtrate was concentrated under reduced pressure. The residual blue solid was extracted into CH_2Cl_2 (5 mL) and insoluble material was filtered off. Vapor diffusion of ether into the filtrate afforded dark blue needles of **1** (102 mg, 68.8 μmol , 55%). Single crystals suitable for X-ray crystallography were obtained by vapor diffusion of pentanes into a concentrated solution of **1** in CH_2Cl_2 /1,2-dichloroethane (4:1).

Method B. To a rapidly stirred pink THF (10 mL) solution of $\text{Co}(\text{NO}_3)_2 \cdot 6\text{H}_2\text{O}$ (148 mg, 0.509 mmol) was added $\text{Ar}^{\text{Tol}}\text{CO}_2\text{H}$ (295 mg, 0.976 mmol). A portion of triethylamine (155 μL , 1.11 mmol) was added and the blue-purple solution was treated with pyridine (41 μL , 0.51 mmol). The deep blue solution was stirred for 2.5 h and concentrated under reduced pressure. The residual dark blue oil was taken into CH_2Cl_2 (4 mL) and filtered. Vapor diffusion of ether into the filtrate afforded blue crystals of **1** (344 mg, 0.232 mmol, 95%) along with colorless needles, which were readily removed by washing with MeCN. FTIR (KBr, cm^{-1}) 3054, 3023, 2917, 2860, 1606, 1515, 1489, 1455, 1448, 1415, 1365, 1305, 1070, 1043, 852, 817, 802, 785, 759, 736, 713, 696, 545, 522; UV-vis (CH_2Cl_2) (λ_{max} , nm (ϵ , $\text{M}^{-1}\text{cm}^{-1}$)) 540 (304), 570 (330), 590 (316), 1100 (40). Anal. Calcd for $\text{C}_{94}\text{H}_{78}\text{N}_2\text{O}_8\text{Co}_2$: C, 76.21; H, 5.31; N, 1.89. Found: C, 75.98; H, 5.53; N, 1.85.

$[\text{Co}_2(\mu\text{-OH}_2)_2(\mu\text{-O}_2\text{CAr}^{\text{Tol}})_2(\text{O}_2\text{CAr}^{\text{Tol}})_2(\text{C}_5\text{H}_5\text{N})_2]$ (**2a**). This compound was obtained by vapor diffusion of pentanes into an aqueous CH_2Cl_2 /acetone solution of **1**. A mixture of acetone/ H_2O (2:1, 3 mL) was added to a CH_2Cl_2 (3 mL) solution of **1** (103 mg, 69.5 μmol), inducing a color change from dark blue to pale pink. The organic layer was separated by filtration through Celite. Red purple blocks of **2** (44 mg, 26 μmol , 37%) suitable for X-ray crystallography were

obtained by vapor diffusion of pentanes into the filtrate at room temperature. Upon heating in vacuo at 60 °C overnight, the crystals readily lose coordinated H₂O and lattice solvent molecules, converting to a dark blue solid of **1** as determined by elemental analysis and FTIR. FTIR (KBr, cm⁻¹) 3549, 3053, 3024, 2919, 2863, 1589, 1515, 1487, 1450, 1407, 1381, 1307, 1265, 1218, 1187, 1150, 1110, 1070, 1042, 1020, 833, 819, 804, 787, 767, 759, 736, 699, 585, 548, 530; UV-vis (CH₂Cl₂) (λ_{max} , nm (ϵ , M⁻¹cm⁻¹)) 520 (60), 550 (69), 588 (64). Anal. Calcd for C₉₄H₈₂N₂O₁₀·Co₂·2CH₂Cl₂: C, 68.33; H, 5.14; N, 1.66. Found: C, 68.39; H, 5.24; N, 1.66.

[Co₂(μ -OH)₂]₂(μ -O₂CAr^{Tol})₂(O₂CAr^{Tol})₂(THF)₂] (**2b**) and [Co₂(μ -OH)₂]₂(μ -O₂CAr^{Tol})₂(O₂CAr^{Tol})₂(*N,N*-Bn₂en)₂] (**2c**). These compounds were obtained in a manner similar to that described for **1** except that THF or *N,N*-dibenzylethylenediamine (*N,N*-Bn₂en) was used instead of pyridine. Violet blocks of **2b** (34%) suitable for X-ray crystallography were obtained by recrystallization from CH₂Cl₂/H₂O/pentanes. Purple blocks of **2c** (64%) were obtained by recrystallization from CH₂Cl₂/H₂O/Et₂O and analyzed by X-ray crystallography.

[Co₂(μ -OH)₂]₂(μ -O₂CAr^{Tol})₂(O₂CAr^{Tol})₂(C₅H₅N)₂] (**3**). A dark blue CH₂Cl₂ (4 mL) solution of **1** (238 mg, 161 μ mol) was treated with H₂O₂ (30% aq, 0.5 mL) to afford a dark brown solution. The organic layer was separated by filtration through Celite. Vapor diffusion of Et₂O into the filtrate afforded dark brown blocks of **3** (64 mg, 42 μ mol, 26%), which were suitable for X-ray crystallography. FTIR (KBr, cm⁻¹) 3354, 3020, 2918, 1604, 1585, 1468, 1516, 1487, 1452, 1399, 1365, 1342, 1305, 1247, 1215, 1185, 1143, 1110, 1035, 1019, 928, 840, 822, 802, 788, 764, 736, 712, 688, 655, 592, 579, 548, 530; UV-vis (CH₂Cl₂) (λ_{max} , nm (ϵ , M⁻¹cm⁻¹)) 610 (310). Anal. Calcd for C₉₄H₈₀N₂O₁₀Co₂: C, 74.50; H, 5.32; N, 1.85. Found: C, 74.39; H, 5.28; N, 1.96.

[Ni₂(μ -O₂CAr^{Tol})₄](C₅H₅N)₂] (**4**). To a rapidly stirred THF (10 mL) suspension of NiBr₂ (60 mg, 0.27 mmol) was added AgOTf (146 mg, 0.568 mmol). A

portion of $\text{NaO}_2\text{CAr}^{\text{Tol}}$ (170 mg, 0.524 mmol) and pyridine (21 μL , 0.26 mmol) was added and the heterogeneous mixture was stirred overnight. Insoluble material was filtered off and the pale green filtrate was concentrated under reduced pressure. The residual green solid was extracted into CH_2Cl_2 (5 mL) and filtered. Vapor diffusion of pentanes into the filtrate afforded green blocks of **4** (135 mg, 91.1 μmol , 70%), which were suitable for X-ray crystallography. FTIR (KBr, cm^{-1}) 3051, 3021, 2918, 2863, 1620, 1584, 1550, 1514, 1487, 1449, 1404, 1385, 1072, 848, 811, 786, 762, 710, 690, 586, 527; UV-vis (CH_2Cl_2) (λ_{max} , nm (ϵ , $\text{M}^{-1}\text{cm}^{-1}$)) 410 (230), 680 (62). Anal. Calcd for $\text{C}_{94}\text{H}_{78}\text{N}_2\text{O}_8\text{Ni}_2$: C, 76.23; H, 5.31; N, 1.89. Found: C, 76.26; H, 5.34; N, 1.83.

$[\text{Ni}_2(\mu\text{-HO}\cdots\text{H})_2(\mu\text{-O}_2\text{CAr}^{\text{Tol}})_2(\text{O}_2\text{CAr}^{\text{Tol}})_2(\text{C}_5\text{H}_5\text{N})_2]$ (**5**). To a rapidly stirred THF (10 mL) suspension of $\text{Ni}(\text{NO}_3)_2\cdot 6\text{H}_2\text{O}$ (77 mg, 0.25 mmol) and $\text{NaO}_2\text{CAr}^{\text{Tol}}$ (166 mg, 0.512 mmol) was added pyridine (20 μL , 0.25 mmol). The heterogeneous mixture was stirred overnight and volatile fractions were removed under reduced pressure. The residual green solid was extracted into CH_2Cl_2 (5 mL) and insoluble material was filtered off. Vapor diffusion of pentanes into the pale green filtrate afforded green blocks of **5** (163 mg, 0.107 mmol, 86%), which were suitable for X-ray crystallography. FTIR (KBr, cm^{-1}) 3527, 3052, 3023, 2918, 2863, 1620, 1608, 1563, 1515, 1487, 1450, 1407, 1382, 1264, 1219, 1187, 1148, 1110, 1071, 1044, 1020, 824, 805, 788, 768, 736, 699, 641, 586, 547, 531; UV-vis (CH_2Cl_2) (λ_{max} , nm (ϵ , $\text{M}^{-1}\text{cm}^{-1}$)) 400 (47), 665 (20), 1100 (10). Anal. Calcd for $\text{C}_{94}\text{H}_{82}\text{N}_2\text{O}_{10}\text{Ni}_2\cdot 2\text{CH}_2\text{Cl}_2$: C, 68.35; H, 5.14; N, 1.66. Found: C, 68.63; H, 5.49; N, 1.63.

$[\text{Zn}_2(\mu\text{-O}_2\text{CAr}^{\text{Tol}})_2(\text{O}_2\text{CAr}^{\text{Tol}})_2(\text{C}_5\text{H}_5\text{N})_2]$ (**6**). To a rapidly stirred THF (15 mL) solution of $\text{Zn}(\text{OTf})_2$ (188 mg, 0.517 mmol) was added $\text{NaO}_2\text{CAr}^{\text{Tol}}$ (336 mg, 1.04 mmol) and pyridine (45 μL , 0.56 mmol). The reaction mixture was stirred for 5 h to afford a clear colorless solution. Volatile fractions were removed under

reduced pressure and the residual white solid was extracted into CH_2Cl_2 (10 mL). Insoluble material was filtered off and vapor diffusion of pentanes into the filtrate afforded **6** (210 mg, 0.141 mmol, 54%) as colorless needles. Colorless blocks suitable for X-ray crystallography were obtained by vapor diffusion of Et_2O into a concentrated CH_2Cl_2 solution of **6** at room temperature. FTIR (KBr, cm^{-1}) 3053, 3025, 2920, 2865, 1605, 1568, 1515, 1489, 1451, 1405, 1372, 1307, 1221, 1187, 1148, 1110, 1070, 1045, 1021, 954, 844, 820, 802, 787, 766, 737, 707, 699, 676, 665. Anal. Calcd for $\text{C}_{94}\text{H}_{78}\text{N}_2\text{O}_8\text{Zn}_2 \cdot 0.25\text{CH}_2\text{Cl}_2$: C, 74.69; H, 5.22; N, 1.85. Found: C, 74.53; H, 5.43; N, 1.78.

X-ray Crystallographic Studies. Intensity data were collected on a Bruker (formerly Siemens) CCD diffractometer with graphite-monochromated Mo $K\alpha$ radiation ($\lambda = 0.71073 \text{ \AA}$), controlled by a Pentium-based PC running the SMART software package.²⁹ Single crystals were mounted at room temperature on the tips of quartz fibers, coated with Paratone-N oil, and cooled to 188 K under a stream of cold nitrogen maintained by a Bruker LT-2A nitrogen cryostat. Data collection and reduction protocols are described elsewhere.³⁰ The structures were solved by direct methods and refined on F^2 by using the SHELXTL software package.³¹ Empirical absorption corrections were applied with SADABS,³² part of the SHELXTL program package, and the structures were checked for higher symmetry by the program PLATON.³³ All non-hydrogen atoms were refined anisotropically unless otherwise noted. Hydrogen atoms were assigned idealized positions and given thermal parameters equivalent to either 1.5 (methyl hydrogen atoms) or 1.2 (all other hydrogen atoms) times the thermal parameter of the carbon atom to which they were attached. The hydrogen atoms associated with the bridging water molecules in **2a–c**, hydroxides in **3**, and water molecules in **5** were located in the difference Fourier map and refined isotropically; those associated with disordered solvent molecules were not included in the refine-

ment. Disordered CH₂Cl₂ solvent molecules in the structures of **1**, **2a**, and **5** were equally distributed over two positions and refined isotropically. In the structure of **2c**, a CH₂Cl₂ solvent molecule was disordered over three positions and refined with 0.5, 0.4, and 0.1 occupancies. The lattice solvent molecules in the structure of **3** were modeled as partially occupied CH₂Cl₂ (0.25 occupancy) and Et₂O (0.75 occupancy) and refined isotropically. Pertinent crystallographic information is provided in Table 8.1.

Results

Preparation and Structural Characterization of Dicobalt(II) Complexes [Co₂(μ-O₂CAr^{Tol})₂(O₂CAr^{Tol})₂(C₅H₅N)₂] (**1**) and [Co₂(μ-OH₂)₂(μ-O₂CAr^{Tol})₂(O₂CAr^{Tol})₂L₂], L = C₅H₅N (**2a**), THF (**2b**), and *N,N*-Bn₂en (**2c**). Reaction of Co(OTf)₂, generated in situ, with 2 equiv of NaO₂CAr^{Tol} and one equiv of pyridine in anhydrous THF, afforded the neutral dicobalt(II) complex **1** in modest yield. The same air-stable compound can be conveniently prepared outside the drybox by reacting Co(NO₃)₂·6H₂O, Ar^{Tol}CO₂H, Et₃N, and pyridine in a 1:2:2:1 ratio in THF (Scheme 8.1). Recrystallization from CH₂Cl₂/Et₂O provided dark blue blocks of **1** in excellent yield (~95%). The crystal structure of **1** is shown in Figures 8.1; selected bond lengths and angles are available in Table 8.2. The geometry of the cobalt(II) centers in **1** is best described as distorted trigonal pyramidal with the pyridine nitrogen atom occupying an axial position. Two cobalt atoms are related by a crystallographic inversion center and their relatively long metal···metal separation of 3.9168(7) Å is spanned by two bridging carboxylates. The remaining coordination sites are occupied by two pyridine and two terminal carboxylates.

When a CH₂Cl₂ solution of **1** was exposed to aqueous organic solvents, the color changed rapidly from dark blue to pale pink. Recrystallization of **1**

from water-saturated CH_2Cl_2 /acetone/pentanes afforded red purple blocks of **2a**. Although this material remains crystalline under ambient conditions, it turns into dark blue powders after heating at 60 °C in vacuo for > 12 h. Loss of lattice solvent as well as bridging water molecules was indicated by FT-IR spectroscopy and elemental analysis, which match the properties of **1**. The crystal structure of **2a** is displayed in Figure 8.2; selected bond lengths and angles are listed in Table 8.2. In the compound **2a**, two octahedral cobalt(II) centers are bridged by two μ -1,3 carboxylate ligands and two water molecules. The Co...Co distance of 3.0562(6) Å is substantially (~0.86 Å) shorter than that in the precursor **1**, owing to the presence of the two bridging water molecules. The assignment of these ligands as water is supported by the Co–O distances, which range from 2.223(2) to 2.304(2) Å, as well as by the location and refinement of the associated hydrogen atoms in the X-ray structure determination (O–H, 0.74(4) and 0.86(4) Å). The two bridging carboxylate groups in **2a** are disposed trans to each other across the $\{\text{Co}_2(\mu\text{-OH}_2)_2\}^{4+}$ plane and the two terminal carboxylates are hydrogen bonded to the bridging water molecules (O...O, 2.559(3) Å). Coordination of two pyridine ligands disposed anti across the Co–Co vector completes the pseudo-octahedral coordination sphere of each cobalt(II) center. Related dicobalt(II) complexes **2b** (Figure 8.3) and **2c** (Figure 8.4) were obtained and structurally characterized. The $\{\text{Co}_2(\mu\text{-OH}_2)_2\}^{4+}$ rhombic core structures and Co...Co distances of 3.0677(6) Å (**2b**) and 3.0521(7) Å (**2c**) are comparable to those of **2a**.

When the optimized synthetic procedure was not strictly followed, co-crystallization of **1** and **2a** occurred. Purple blocks³⁴ obtained from these batches revealed a disordered core structure, which was modeled as a mixture containing 75% of **1** and 25% of **2a**. The structure of **2a** overlaid on **1** (Figure 8.5) clearly indicates that minimal structural reorganization accompanies coordination of additional bridging water ligands. Despite geometrical variations in the

dinuclear cores, the second coordination sphere structures of **1** and **2a** are essentially superimposable, suggesting that interconversion between the two compounds can readily occur by association/dissociation of water molecules.

Preparation and Structural Characterization of $[\text{Co}_2(\mu\text{-OH})_2(\mu\text{-O}_2\text{C-Ar}^{\text{Tol}})_2(\text{O}_2\text{C-Ar}^{\text{Tol}})_2(\text{C}_5\text{H}_5\text{N})_2]$ (3**).** Oxidation of the air-stable complex **1** with H_2O_2 afforded a neutral tetra(carboxylato)dicobalt(III) complex. When a CH_2Cl_2 solution of **1** was treated with excess aq H_2O_2 , the color changed rapidly from blue to dark brown. Dark brownish green blocks of **3** were obtained after recrystallization from $\text{CH}_2\text{Cl}_2/\text{Et}_2\text{O}$ and structurally characterized. The crystal structure is shown in Figure 8.6; selected bond lengths and angles are reported in Table 8.2. The structure of the quadruply bridged dimetallic core unit, as well as the relative orientation of the terminal ligands, in **3** is close to that of the dicobalt(II) complex **2a**, although the corresponding metal-ligand bond lengths are significantly shortened due to the increased oxidation state of the metal center. Compared with the topologically related $\{\text{Co}_2(\mu\text{-OH}_2)_2\}^{4+}$ core in **2a**, the $\{\text{Co}_2(\mu\text{-OH})_2\}^{4+}$ center in **3** has a significantly shortened Co...Co distance of 2.6802(7) Å and shorter $\text{Co}^{\text{III}}\text{-O}_{\text{hydroxo}}$ distances (1.858(2) and 1.865(2) Å). The O–M–O bite angle of the M_2O_2 rhombus slightly diminishes the core contraction in converting **2a** (O–Co–O = 95.10(7)°) to **3** (O–Co–O = 87.92(8)°). The terminal monodentate carboxylate groups are hydrogen bonded to the bridging ligands (O...O, 2.664(3) Å) in a manner similar to that in **2a**.

Preparation and Structural Characterization of Dinickel(II) Complexes $[\text{Ni}_2(\mu\text{-O}_2\text{C-Ar}^{\text{Tol}})_4(\text{C}_5\text{H}_5\text{N})_2]$ (4**) and $[\text{Ni}_2(\mu\text{-HO}\cdots\text{H})_2(\mu\text{-O}_2\text{C-Ar}^{\text{Tol}})_2(\text{O}_2\text{C-Ar}^{\text{Tol}})_2(\text{C}_5\text{H}_5\text{N})_2]$ (**5**).** Compound **4** was synthesized by a route analogous to that used to prepare **1**. Treatment of $\text{Ni}(\text{OTf})_2$ generated in anhydrous THF with 2 equiv of $\text{NaO}_2\text{C-Ar}^{\text{Tol}}$ and 1 equiv of pyridine afforded green blocks of **4** after recrystallization. The crystal structure of **4** is shown in Figure 8.7; selected bond lengths

and angles are listed in Table 8.3. The metal...metal distance is 2.5745(6) Å and there are four bridging carboxylate ligands disposed around a pseudo- C_4 axis along the Ni–Ni vector. The crystallographically inequivalent nickel(II) centers have similar square-pyramidal coordination geometries with average Ni–O distances of 2.019(2) Å for Ni(1) and 2.018(8) Å for Ni(2).

A reaction between $\text{Ni}(\text{NO}_3)_2 \cdot 6\text{H}_2\text{O}$, $\text{NaO}_2\text{CAr}^{\text{Tol}}$, and pyridine in a 1:2:1 ratio in THF afforded green blocks of **5** after recrystallization. The structure is shown in Figure 8.8 and selected bond lengths and angles are reported in Table 8.3. The nickel(II) centers in **5** are spanned by four bridging ligands assigned as a di(μ -aqua)di(μ -carboxylato) unit. The Ni–O distances of 2.137(2) and 2.140(2) Å in the Ni_2O_2 rhombus fall within the range expected for partially deprotonated bridging water molecules. For comparison, the Co– O_{aqua} distances in the $\{\text{Co}_2(\mu\text{-OH}_2)_2\}^{4+}$ core of **2a** are 2.223(2) and 2.304(2) Å, values significantly longer than the Ni– O_{aqua} bond lengths. The metal...metal separation of 2.8923(7) Å is substantially shortened compared with that of **2a**, 3.0562(6) Å. A similar trend was observed between **2a** and **3**, for which core contraction is induced by oxidation of the metal centers as well as by deprotonation of the bridging water ligands. One hydrogen atom associated with the bridging water was located in a difference Fourier map and refined isotropically (O–H, 0.80(4) Å). The other hydrogen atom was located between the two oxygen atoms belonging to the bridging water and terminal monodentate carboxylate ligands, with $\text{O}_{\text{aqua}}\text{-H}$ and $\text{H-O}_{\text{carboxylate}}$ distances of 1.13(5) and 1.37(5) Å, respectively. The short O...O distance of 2.495(3) Å and O–H–O angle of 172(4)° indicate a strong hydrogen bonding interaction that may facilitate formal deprotonation of the bridging water molecules.

The position of the proton between the two oxygen atoms in **5** approaches a symmetric hydrogen bond described by a single-well potential.³⁵ Hydrogen

bonds are usually asymmetric, with the hydrogen atom located closer to the more basic atom.³⁶ In such cases, the hydrogen atom is localized in one well of a double-well potential, a configuration favored even if the two adjacent atoms have the same basicity.^{35,37} As the distance between the donors decreases, however, the barrier height is reduced and eventually disappears. At O...O distances between 2.4 and 2.5 Å, the double-well potential of O...H...O hydrogen bonds becomes a single-well having one centered hydrogen atom.³⁸ Although the different basicity of the two oxygen atoms may not allow an idealized O...H...O single-well potential in the HO...H...O₂CAr^{Tol} unit, the strong hydrogen bonding interaction apparently shifts the position of a proton toward the oxygen atom of a dangling carboxylate. A structural comparison can be made with **2a**, which has very asymmetric O...H distances of 0.74(4) Å and 1.88(4) Å in the HO-H...⁻O₂CAr^{Tol} unit. A longer O...O distance of 2.559(3) Å and a O-H-O angle of 152(4)° substantially deviating from linearity are consistent with weaker hydrogen bonding and a double-well potential in **2a**.

Preparation and Structural Characterization of [Zn₂(μ-O₂CAr^{Tol})₂(O₂CAr^{Tol})₂(C₅H₅N)₂] (6). A tetra(carboxylato)dizinc(II) complex structurally related to **1** was prepared. From a homogeneous THF solution of Zn(OTf)₂, NaO₂CAr^{Tol}, and pyridine in a 1:2:1 ratio, colorless needles of **6** crystallized in modest yield (~54%). The structure of **6** is shown in Figure 8.9; selected bond lengths and angles are listed in Table 8.3. Two zinc(II) centers in **6** are related by a crystallographic center of inversion and bridged by two μ-1,3 carboxylates. Terminal monodentate carboxylate and pyridine ligands complete the coordination spheres of tetrahedral zinc(II) sites, which are separated from each other by 4.0169(9) Å.

Discussion

Structures and Physical Properties. Compounds **1** and **6** belong to a rare class of molecules in which two metal centers are bridged solely by two carboxylate ligands. This structural unit is encountered at diiron(II) centers in the active sites of the R2 subunit of ribonucleotide reductase (RNR-R2)³⁹ and stearyl-ACP Δ^9 desaturase ($\Delta 9D$)⁴⁰ as well as the dicobalt(II) center in the active site of methionine aminopeptidase from *Escherichia coli* (EcMAP).⁴¹ Compound **1** is only the second structurally characterized example of such a bridging unit in synthetic dicobalt(II) chemistry. The other is $[\text{Co}_2(\mu\text{-O}_2\text{CC}_6\text{H}_4\text{CO}_2\text{H})_2(1,10\text{-phen})_4](\text{O}_2\text{CC}_6\text{H}_4\text{CO}_2\text{H})_2$,⁴² in which the two octahedral cobalt(II) centers are separated by 4.765 Å. The *syn,anti*-coordination of μ -1,3-bridging carboxylates expands the Co...Co distance, which is significantly longer than that (3.9168(7) Å) in **1**, which has *syn,syn*-coordination. A diiron(II) analog of **1** and **6** having comparable geometrical parameters was previously reported.¹⁷

Compounds **2a–c** have an unprecedented ligand set connecting the two metal ions. Although triply-bridged (μ -aqua)di(μ -carboxylato)dimetallic cores have been previously observed for diiron(II),^{43–47} dicobalt(II)^{44,45,48,49} or dinickel(II)^{50–52} complexes, a quadruply-bridged di(μ -aqua)di(μ -carboxylato)-dimetallic core is an unknown unit in inorganic chemistry. For edge-shared octahedral metal centers, such a bridging unit can be accommodated only by a trans disposition of the bridging carboxylate ligands across the $\{\text{M}_2(\mu\text{-OH}_2)_2\}^{n+}$ core. This requirement nicely minimizes steric interactions between the *p*-tolyl groups (Figure 8.2). As exemplified by **2a–c**, various neutral donors such as pyridine, THF, or a primary amine can coordinate the $\{\text{Co}_2(\mu\text{-OH}_2)_2(\mu\text{-O}_2\text{CAr}^{\text{Tol}})_2(\text{O}_2\text{CAr}^{\text{Tol}})_2\}$ fragment. The fact that the structure can be accommodated in a co-crystal of **1** and **2a** (Figure 8.3) allows us to assess the minimal degree by which uptake and loss of additional ligands requires rearrangement be-

tween the precursor and adduct. Such a structural change upon ligand association/dissociation may be relevant to the reaction cycle of metallohydrolases, for which a similarly minimal movement of protein side chains would facilitate rapid turnover. Even in the solid state, **2a** readily loses its bridging water molecules to afford the anhydrous complex **1**.

An increase in the oxidation state of a Lewis acidic metal center decreases the pK_a value of coordinated water, as exemplified by the formation of the di(μ -hydroxo)dicobalt core upon oxidation of **2a** to **3**. Although detailed mechanistic information is not available, either outer sphere electron transfer from **2a** followed by deprotonation of bridging water molecules or O–O homolysis of a (μ -1,2-hydroperoxo)dicobalt(II) intermediate can equally well explain the formation of the di(μ -hydroxo)di(μ -carboxylato)dicobalt(III) complex **3** (Scheme 8.2) from **1** and aq H_2O_2 . Structurally related di(μ -hydroxo)di(μ -carboxylato)diiron(III) complexes were previously obtained by reactions of $[Fe_2(\mu-O_2CAR^{Tol})_2(O_2CAR^{Tol})_2(C_5H_5N)_2]$ or $[Fe_2(\mu-O_2CAR^{Tol})_4(4-tBuC_5H_4N)_2]$ with dioxygen, which afforded $[Fe_2(\mu-OH)_2(\mu-O_2CAR^{Tol})_2(O_2CAR^{Tol})_2L_2]$ ($L = C_5H_5N$ or $4-tBuC_5H_4N$) as isolated products.^{17,18} The $Co^{III}-O_{hydroxo}$ distances in **3** are substantially shorter than those in the $Fe^{III}-O_{hydroxo}$ core (1.949(3) – 2.012(2) Å)^{17,18} but are comparable to $Co^{III}-O_{hydroxo}$ distances of ~ 1.90 Å for a low-spin cobalt(III) site in mixed-valence complex $[Co_2(\mu-OH)(\mu-OAc)_2(Me_3TACN)_2](ClO_4)_2$.^{3,53} A $d-d$ band at 610 nm ($\epsilon = 310 M^{-1}cm^{-1}$) is assigned to the ${}^1A_{1g} \rightarrow {}^1T_{1g}$ transition, by analogy to the similar 559 nm transition observed for low-spin dicobalt(III) $[Co_2(\mu-OH)(\mu-OAc)_2(Me_3TACN)_2](ClO_4)_3$.⁵³ Non-corrin mononuclear low-spin cobalt(III) centers occur in cobalt-containing nitrile hydratases that hydrolyze nitrile functional groups to afford amide products.⁵⁴ A cobalt-bound hydroxide group has been proposed as a direct nucleophile or a general base to deprotonate a water molecule that attacks the $C\equiv N$ triple bonds. Metal-bound

phosphodiester substrates can be attacked by a bridging oxide in dicobalt(III) complexes.^{55,56} The guanidium moiety anchored on a (μ -hydroxo)dicobalt(II) core is hydrolyzed by intramolecular attack of the bridging hydroxide ion.¹⁶

Compound **4**, assembled under strictly anhydrous conditions, features a quadruply-bridged dinickel(II) core with a short Ni...Ni distance (2.5745(6) Å). This value lies at the low end of the range (2.603(2)–2.754(3) Å) obtained for related paddle-wheel dinickel(II) complexes.^{52,57,58} For comparison, a substantially longer M...M distance of 2.8229(9) Å occurs in a diiron(II) analog of **4**, [Fe₂(μ -O₂CAr^{Tol})₄(4-^tBuC₅H₄N)₂].¹⁸

Unlike the dicobalt(II) complexes **1** and **2a**, however, a dramatic structural rearrangement occurs upon incorporation of two bridging water molecules into the dimetallic core of **4**. Formal carboxylate shifts⁵⁹ of two Ar^{Tol}CO₂⁻ ligands from μ -1,3-bridging to terminal monodentate open up binding sites for additional bridging water ligands, the coordination of which is stabilized by hydrogen bonding interaction with the terminal ligands. Structurally related dinickel(II) complexes with triply-bridged {Ni₂(μ -OH)(μ -O₂CR)₂}⁺ or {Ni₂(μ -OH₂)(μ -O₂CR)₂}²⁺ cores have Ni...Ni distances of 3.400(3) to 3.676(3) Å, values significantly longer than the 2.8923(7) Å value in quadruply-bridged **5**. The unprecedented {M₂(μ -HO...H)₂(μ -O₂CR)₂} bridging motif in **5** reveals “proton shifts” that can be regarded as a snapshot of an intermediate in the proton transfer step from Lewis acid-bound water to a nearby general base. This partial deprotonation of the bridging water molecules shortens the metal-oxygen bond lengths. For comparison, the Ni–O distances of 2.156(8) and 2.153(9) Å in [Ni₂(μ -OH₂)(μ -O₂CCF₃)₂(O₂CCF₃)₂(tmeda)₂]⁵⁰ are significantly longer than the 2.014(7) Å distance in [Ni₂(μ -OH)(μ -OAc)₂(Me₃TACN)₂](ClO₄).⁶⁰ A similar comparison can be made between the M–O distances in the M₂O₂ cores of **2a** and **5**, which have H₂O and HO...H bridging ligands, respectively (Tables 8.2 and 8.3). A dif-

ference in Lewis acidity at the metal center may translate into such a structural variation under identical ligand environments, although the pK_a values of coordinated water in $[M(H_2O)_6]^{2+}$ are comparable for Co^{2+} (9.85) and Ni^{2+} (9.86) at 25 °C.⁶¹ The pK_a value of metal-bound water molecules is affected by the metal ion and its oxidation states as well as by the ancillary ligands and local dielectric.²¹

Proton Shifts in Carboxylate-Bridged Dimetallic Centers. A survey of structurally characterized carboxylate-bridged dicobalt(II) or dinickel(II) complexes reveals an intriguing trend between the protonation state of the bridging H_2O/OH^- ligands and the composition of the ancillary ligands supporting the dimetallic core. Nitrogen-rich coordination with neutral amine/imine donors promotes the formation of (μ -hydroxo)di(μ -carboxylato) cores (**A**, Figure 8.10) for cobalt(II)^{53,62} or nickel(II),⁶⁰ whereas anion-rich coordination favors (μ -aqua)di(μ -carboxylato) centers (**B** and **C**, Figure 8.10). Dinickel(II) compounds exclusively afford **B**.⁵⁰⁻⁵² Depending on the choice of ligands, both **B**^{44,45,48,49} and **C**^{46,47} are accessible for cobalt(II). In both cases, the stability of the triply-bridged dimetallic centers is enhanced by the hydrogen bonding interaction between bridging water and terminal carboxylate ligands. Even when the water molecule is bound to two metal ions, however, an anion-rich coordination environment apparently suppresses deprotonation.

Extensive studies of many enzymes have revealed carboxylate-bridged dimetallic centers at their active sites. The underlying structural and functional role of carboxylate-rich donor sets supporting such units is not fully elucidated. For example, in addition to providing structural flexibility to the dimetallic unit in the catalytic cycle, the carboxylate ligands coordinating iron centers in non-heme diiron enzymes donate electrons to help cleave the O–O bond of the initial dioxygen-adduct(s), enabling access to high-valent diiron(IV) species.⁶³⁻⁶⁵ A similar carboxylate-rich ligand environment, however, may be a liability for met-

allohydrolases such as aminopeptidases or phosphohydrolases, in which the oxidation states of the low-valent metal ions do not change during catalysis. The Lewis acidity of the protein-bound metal centers would be significantly attenuated by an anion-rich first coordination sphere, rendering metal-bound nucleophiles less reactive. This situation is quite different from the histidine-rich active sites in both mononuclear and dinuclear metallohydrolases, including carboxypeptidase A, thermolysin, carbonic anhydrase, or urease.^{1,21,22,66} Understanding the role of carboxylate-rich centers under this seemingly unfavorable situation can provide mechanistic insight into hydrolytic chemistry catalyzed by Lewis-acidic metal centers.

The dimetallic core structures of **1**, **2a**, **3**, and **5** provide, within an identical ancillary ligand architecture, sequential snapshots of the biomimetic activation of bridging water molecules (Figure 8.11). A detailed structural description is now available for the protonation states of the metal-bound water molecules and shuttling of protons between adjacent oxygen atoms. The results presented here prompt us to propose that metal-bound carboxylate residues in enzyme active sites may act similarly as a general base to assist activation of bridging water molecules, a process facilitated by the thermodynamically favored five-membered chelate ring shown in Scheme 8.3. Strong hydrogen bonding with the dangling carboxylate oxygen atom helps to polarize the HO...H bonds, priming them for heterolytic cleavage to form OH⁻ and H⁺. The leaving proton is shuttled to the non-coordinating oxygen atom of the terminal carboxylate, thus attenuating the donor ability of this anionic ligand. Such decreased electron donation from the terminal ligand can translate into an increased Lewis acidity of the metal ion, which may be beneficial for activation of incoming electrophilic substrates. The minimal nuclear motion accompanying this process can significantly lower the kinetic barrier for fast enzymatic turnover.

Biological Relevance: Dicobalt(II) Centers in Methionine Aminopeptidases. Mechanistic insights gleaned from the structural analyses of small molecules described above can be used to help understand related systems in biology. Methionine aminopeptidase (MAP) is a cobalt-dependent enzyme that removes the N-terminal methionine of nascent polypeptide chains.⁵⁴ Such modification is crucial for functional regulation, intracellular targeting, and degradation of proteins. Previous structural characterization of methionine aminopeptidase from *E. coli* (EcMAP) identified four carboxylate (two Asp and two Glu) and one histidine residues surrounding the catalytic dicobalt(II) core (Figure 8.12).⁴¹ A recent structural determination of a MAP from *Pyrococcus furiosus* (PfMAP) revealed structurally analogous dicobalt(II) centers in the active sites.⁶⁷ In PfMAP, two cobalt(II) ions are bridged by two carboxylate groups and one water molecule, rendering each cobalt(II) site distorted trigonal bipyramidal (Figure 8.12).

Comparison of the core structures of EcMAP and PfMAP indicates that a minimal structural change occurs upon incorporation of water molecules into the first coordination sphere of the dicobalt(II) core, similarly to the interconversion between **1** and **2a**. Across a second water molecule there extends a hydrogen bonding network from the bridging water molecule to the terminally bound carboxylate group (E187) of PfMAP. Such a secondary interaction may assist deprotonation of the bridging water molecule, a process modeled by compounds **2a** and **5**. A recent structural analysis of the EcMAP protein-inhibitor complex also points toward a mechanism in which the terminal carboxylate (E204) facilitates proton transfer from the metal-bound nucleophile.⁶⁸

Summary and Conclusions

Discrete dicobalt(II), dicobalt(III), dinickel(II), and dizinc(II) complexes **1–6** have been efficiently assembled with the use of sterically hindered *m*-

terphenyl-derived carboxylate ligands. Structural analyses of these complexes indicate that additional bridging ligands can be readily accommodated within the tetra(carboxylato)dimetallic unit. Unprecedented structural cores, $\{M_2(\mu-OH_2)_2(\mu-O_2CR)_2\}^{n+}$ and $\{M_2(\mu-HO\cdots H)_2(\mu-O_2CR)_2\}^{n+}$, were identified. Strong-hydrogen bonding interactions with the terminal carboxylate groups should assist deprotonation of bridging water molecules. These groups thus could be activated by the dual action of Lewis acidic metal center and metal-bound general base, a process that may be relevant to the action of selected metallohydrolases having carboxylate-bridged dinuclear centers.

Acknowledgment. This work was supported by a grant from the National Science Foundation. Part of the synthesis described here was carried out by Ms. Pei-Lin Hung (UROP participant). I thank Dr. Bernhard Spingler for assistance in X-ray crystallography.

References

- (*) A slightly modified version of this work has been submitted for publication.
Lee, D.; Hung, P.-L.; Spingler, B.; Lippard, S. J. **2001**.
- (1) Lippard, S. J.; Berg, J. M. *Principles of Bioinorganic Chemistry*; University Science Books: Mill Valley, CA, 1994.
- (2) Holm, R. H.; Kennepohl, P.; Solomon, E. I. *Chem. Rev.* **1996**, *96*, 2239-2314.
- (3) Abbreviations: H₂XDK, m-xylenediamine bis(Kemp's triacid imide); Ar^{Tol}CO₂H, 2,6-di(*p*-tolyl)benzoic acid; Me₃TACN, 1,4,7-trimethyl-1,4,7-triazacyclononane
- (4) Rebek, J., Jr.; Marshall, L.; Wolak, R.; Parris, K.; Killoran, M.; Askew, B.; Nemeth, D.; Islam, N. *J. Am. Chem. Soc.* **1985**, *107*, 7476-7481.
- (5) Herold, S.; Lippard, S. J. *J. Am. Chem. Soc.* **1997**, *119*, 145-156.
- (6) LeCloux, D. D.; Lippard, S. J. *Inorg. Chem.* **1997**, *36*, 4035-4046.
- (7) Watton, S. P.; Masschelein, A.; Rebek, J., Jr.; Lippard, S. J. *J. Am. Chem. Soc.* **1994**, *116*, 5196-5205.
- (8) Herold, S.; Pence, L. E.; Lippard, S. J. *J. Am. Chem. Soc.* **1995**, *117*, 6134-6135.
- (9) LeCloux, D. D.; Barrios, A. M.; Mizoguchi, T. J.; Lippard, S. J. *J. Am. Chem. Soc.* **1998**, *120*, 9001-9014.
- (10) LeCloux, D. D.; Davydov, R.; Lippard, S. J. *J. Am. Chem. Soc.* **1998**, *120*, 6810-6811.
- (11) LeCloux, D. D.; Davydov, R.; Lippard, S. J. *Inorg. Chem.* **1998**, *37*, 6814-6826.
- (12) Yun, J. W.; Tanase, T.; Pence, L. E.; Lippard, S. J. *J. Am. Chem. Soc.* **1995**, *117*, 4407-4408.
- (13) Yun, J. W.; Tanase, T.; Lippard, S. J. *Inorg. Chem.* **1996**, *35*, 7590-7600.
- (14) Tanase, T.; Watton, S. P.; Lippard, S. J. *J. Am. Chem. Soc.* **1994**, *116*, 9401-9402.
- (15) Tanase, T.; Yun, J. W.; Lippard, S. J. *Inorg. Chem.* **1996**, *35*, 3585-3594.
- (16) He, C.; Lippard, S. J. *J. Am. Chem. Soc.* **1998**, *120*, 105-113.

- (17) Lee, D.; Lippard, S. J. *J. Am. Chem. Soc.* **1998**, *120*, 12153-12154.
- (18) Lee, D.; Du Bois, J.; Petasis, D.; Hendrich, M. P.; Krebs, C.; Huynh, B. H.; Lippard, S. J. *J. Am. Chem. Soc.* **1999**, *121*, 9893-9894.
- (19) Lee, D.; Krebs, C.; Huynh, B. H.; Hendrich, M. P.; Lippard, S. J. *J. Am. Chem. Soc.* **2000**, *122*, 5000-5001.
- (20) Lee, D.; Lippard, S. J. *J. Am. Chem. Soc.* **2001**, *123*, 4611-4612.
- (21) Wilcox, D. E. *Chem. Rev.* **1996**, *96*, 2435-2458.
- (22) Lipscomb, W. N.; Sträter, N. *Chem. Rev.* **1996**, *96*, 2375-2433.
- (23) Sträter, N.; Lipscomb, W. N.; Klabunde, T.; Krebs, B. *Angew. Chem. Int. Ed. Engl.* **1996**, *35*, 2024-2055.
- (24) Du, C.-J. F.; Hart, H.; Ng, K.-K. *D. J. Org. Chem.* **1986**, *51*, 3162-3165.
- (25) Saednya, A.; Hart, H. *Synthesis* **1996**, 1455-1458.
- (26) Guillaume, D.; Aitken, D. J.; Husson, H.-P. *Synlett* **1991**, 747-749.
- (27) Iwanami, S.; Takashima, M.; Hirata, Y.; Hasegawa, O.; Usuda, S. *J. Med. Chem.* **1981**, *24*, 1224-1230.
- (28) Pangborn, A. B.; Giardello, M. A.; Grubbs, R. H.; Rosen, R. K.; Timmers, F. J. *Organometallics* **1996**, *15*, 1518-1520.
- (29) SMART v5.05; Bruker AXS Inc.: Madison, WI, 1998.
- (30) Feig, A. L.; Bautista, M. T.; Lippard, S. J. *Inorg. Chem.* **1996**, *35*, 6892-6898.
- (31) Sheldrick, G. M. *SHELXTL v5.1: Program for the Refinement of Crystal Structures 97-2*; University of Göttingen, Göttingen, Germany, 1998.
- (32) Sheldrick, G. M. *SADABS v2.03: Area-Detector Absorption Correction*; University of Göttingen, Göttingen, Germany, 1999.
- (33) Spek, A. L. *PLATON, A Multipurpose Crystallographic Tool*; Utrecht University: Utrecht, The Netherlands, 1998.

- (34) Crystal data for **1+2a** (0.75:0.25): space group $P\bar{1}$ with $a = 10.7046(2)$ Å, $b = 14.5339(2)$ Å, $c = 14.8319(1)$ Å, $\alpha = 109.834(1)^\circ$, $\beta = 102.072(1)^\circ$, $\gamma = 95.894(1)^\circ$, $V = 2084.49(5)$ Å³, $Z = 1$, $R = 6.15\%$, $wR^2 = 15.5\%$.
- (35) (a) Hamilton, W. C.; Ibers, J. A. *Hydrogen Bonding in Solids*; Benjamin: New York, 1968. (b) Vinogradov, S. N.; Linnell, R. H. *Hydrogen Bonding*; Van Nostrand Reinhold: New York, 1971.
- (36) Emsley, J. *Chem. Soc. Rev.* **1980**, *9*, 91-124.
- (37) Perrin, C. L.; Kim, Y.-J. *J. Am. Chem. Soc.* **1998**, *120*, 12641-12645.
- (38) Peinel, G. *Chem. Phys. Lett.* **1979**, *65*, 324-326.
- (39) Logan, D. T.; Su, X.-D.; Åberg, A.; Regnström, K.; Hajdu, J.; Eklund, H.; Nordlund, P. *Structure* **1996**, *4*, 1053-1064.
- (40) Lindqvist, Y.; Huang, W.; Schneider, G.; Shanklin, J. *EMBO J.* **1996**, *15*, 4081-4092.
- (41) Roderick, S. L.; Matthews, B. W. *Biochemistry* **1993**, *32*, 3907-3912.
- (42) Poleti, D.; Karanovic, L.; Bogdanovic, G. A.; Biré, A. S.-D. *Acta Crystallogr., Sect. C* **1999**, *55*, 2061-2063.
- (43) Hagen, K. S.; Lachicotte, R. *J. Am. Chem. Soc.* **1992**, *114*, 8741-8742.
- (44) Hagen, K. S.; Lachicotte, R.; Kitaygorodskiy, A.; Elbouadili, A. *Angew. Chem., Int. Ed. Engl.* **1993**, *32*, 1321-1324.
- (45) Hagen, K. S.; Lachicotte, R.; Kitaygorodskiy *J. Am. Chem. Soc.* **1993**, *115*, 12617-12618.
- (46) Coucouvanis, D.; Reynolds, R. A., III; Dunham, W. R. *J. Am. Chem. Soc.* **1995**, *117*, 7570-7571.
- (47) Reynolds, R. A., III; Dunham, W. R.; Coucouvanis, D. *Inorg. Chem.* **1998**, *37*, 1232-1241.
- (48) Turpeinen, U.; Ahlgrén, M.; Hämäläinen, R. *Acta Crystallogr., Sect. B* **1982**, *38*, 1580-1583.

- (49) Turpeinen, U.; Hämäläinen, R.; Reedijk, J. *Polyhedron* **1987**, *6*, 1603-1610.
- (50) Ahlgrén, M.; Turpeinen, U. *Acta Crystallogr., Sect. B* **1982**, *38*, 276-279.
- (51) Kennard, C. H. L.; O'reilly, E. J.; Smith, G. *Polyhedron* **1984**, *3*, 689-693.
- (52) Eremenko, I. L.; Nefedov, S. E.; Sidorov, A. A.; Golubnichaya, M. A.; Danilov, P. V.; Ikorskii, V. N.; Shvedenkov, Y. G.; Novotortsev, V. M.; Moiseev, I. I. *Inorg. Chem.* **1999**, *38*, 3764-3773.
- (53) Chaudhuri, P.; Querbach, J.; Wieghardt, K.; Nuber, B.; Weiss, J. J. *Chem. Soc., Dalton Trans.* **1990**, 271-278.
- (54) Kobayashi, M.; Shimizu, S. *Eur. J. Biochem.* **1999**, *261*, 1-9.
- (55) Wahnou, D.; Lebuis, A.-M.; Chin, J. *Angew. Chem., Int. Ed. Engl.* **1995**, *34*, 2412-2414.
- (56) Williams, N. H.; Cheung, W.; Chin, J. J. *Am. Chem. Soc.* **1998**, *120*, 8079-8087.
- (57) Hirashima, N.; Husebye, S.; Kato, M.; Maartmann-Moe, K.; Muto, Y.; Nakashima, M.; Tokii, T. *Acta Chem. Scand.* **1990**, *44*, 984-989.
- (58) Morooka, M.; Ohba, S.; Nakashima, M.; Tokii, T.; Muto, Y.; Kato, M.; Steward, O. W. *Acta Crystallogr., Sect. C* **1992**, *48*, 1888-1894.
- (59) Rardin, R. L.; Tolman, W. B.; Lippard, S. J. *New J. Chem.* **1991**, *15*, 417-430.
- (60) Chaudhuri, P.; Küppers, H.-J.; Wieghardt, K.; Gehring, S.; Haase, W.; Nuber, B.; Weiss, J. J. *Chem. Soc., Dalton Trans.* **1988**, 1367-1370.
- (61) Sillén, L. G.; Martell, A. E. *Stability Constants of Metal-Ion Complexes*; The Chemical Society: London, 1971.
- (62) Lachicotte, R.; Kitaygorodskiy, A.; Hagen, K. S. *J. Am. Chem. Soc.* **1993**, *115*, 8883-8884.
- (63) Solomon, E. I.; Brunold, T. C.; Davis, M. I.; Kemsley, J. N.; Lee, S.-K.; Lehnert, N.; Neese, F.; Skulan, A. J.; Yang, Y.-S.; Zhou, J. *Chem. Rev.* **2000**, *100*, 235-349.

- (64) Du Bois, J.; Mizoguchi, T. J.; Lippard, S. J. *Coord. Chem. Rev.* **2000**, *200–202*, 443–485.
- (65) Merckx, M.; Kopp, D. A.; Sazinsky, M. H.; Blazyk, J. L.; Müller, J.; Lippard, S. *J. Angew. Chem., Int. Ed. Engl.* **2001**, *in press*.
- (66) Bertini, I.; Gray, H. B.; Lippard, S. J.; Valentine, J. S. *Bioinorganic Chemistry*; University Science Books: Mill Valley, CA, 1994.
- (67) Tahirov, T. H.; Oki, H.; Tsukihara, T.; Ogasahara, K.; Yutani, K.; Ogata, K.; Izu, Y.; Tsunasawa, S.; Kato, I. *J. Mol. Biol.* **1998**, *284*, 101-124.
- (68) Lowther, W. T.; Zhang, Y.; Sampson, P. B.; Honek, J. F.; Matthews, B. W. *Biochemistry* **1999**, *38*, 14810-14819.

Table 8.1. Summary of X-ray Crystallographic Data

	1·2CH ₂ Cl ₂	2a·2CH ₂ Cl ₂	3·0.5CH ₂ Cl ₂ ·1.5Et ₂ O	4·1.5CH ₂ Cl ₂
formula	C ₂ O ₂ C ₉₆ H ₇₈ N ₂ O ₈ Cl ₄	C ₂ O ₂ C ₉₆ H ₈₂ N ₂ O ₁₀ Cl ₄	C ₂ O ₂ C _{100.5} H ₈₂ N ₂ O _{11.5} Cl	Ni ₂ C _{95.50} H ₈₁ N ₂ O ₈ Cl ₃
fw	1647.26	1683.30	1654.99	1608.39
space group	P $\bar{1}$	P2 ₁ /n	P2 ₁ /n	P $\bar{1}$
a, Å	10.6629(14)	16.3156(5)	17.6721(17)	14.5501(17)
b, Å	14.5496(19)	14.6729(5)	13.8244(13)	15.2644(18)
c, Å	14.7554(19)	18.0830(6)	18.1499(17)	19.321(2)
α , deg	109.868(2)			88.881(2)
β , deg	103.561(2)	102.725(1)	106.268(1)	81.516(2)
γ , deg	95.425(2)			75.843(2)
V, Å ³	2054.5(5)	4222.7(2)	4256.6(7)	4114.8(8)
Z	1	2	2	2
ρ calc, g/cm ³	1.331	1.324	1.291	1.298
T, °C	-85	-85	-85	-85
μ (Mo K α), mm ⁻¹	0.593	0.580	0.485	0.613
θ limits, deg	1.70 – 28.28	1.52 – 28.26	1.88 – 28.31	1.94 – 28.30
total no. of data	18501	26036	37897	25919
no. of unique data	9276	9650	10081	18017
no. of params	527	523	523	1017
R (%) ^a	4.77	4.88	5.48	4.95
wR ² (%) ^b	12.50	12.53	12.12	13.19
Max, min peaks, e/Å ³	0.834, -0.366	0.771, -1.043	0.551, -0.439	0.940, -0.878

$${}^a R = \Sigma ||F_o| - |F_c|| / \Sigma |F_o|, \quad {}^b wR^2 = \{ \Sigma [w(F_o^2 - F_c^2)^2] / \Sigma [w(F_o^2)^2] \}^{1/2}.$$

Table 8.1, continued. Summary of X-ray Crystallographic Data

	5-2CH ₂ Cl ₂	6-2Et ₂ O
Formula	Ni ₂ C ₉ H ₈₂ N ₂ O ₁₀ Cl ₄	Zn ₂ C ₁₀₂ H ₉₈ N ₂ O ₁₀
fw	1682.86	1642.56
space group	<i>P</i> 2 ₁ / <i>c</i>	<i>P</i> $\bar{1}$
<i>a</i> , Å	11.5584(2)	10.556(2)
<i>b</i> , Å	16.0409(2)	14.765(3)
<i>c</i> , Å	23.4924(3)	15.480(3)
α , deg		108.470(4)
β , deg	100.213(1)	94.371(4)
γ , deg		108.870(4)
<i>V</i> , Å ³	4286.65(11)	2122.1(7)
<i>Z</i>	2	1
ρ calc, g/cm ³	1.304	1.285
<i>T</i> , °C	-85	-85
μ (Mo K α), mm ⁻¹	0.624	0.628
θ limits, deg	1.76 – 28.30	1.69 – 28.26
total no. of data	37509	13402
no. of unique data	10072	9346
no. of params	544	523
<i>R</i> (%) ^a	6.06	5.08
<i>wR</i> ² (%) ^b	13.75	10.30
Max, min peaks, e/Å ³	0.593, -0.615	0.499, -0.522

^a $R = \Sigma ||F_o| - |F_c|| / \Sigma |F_o|$. ^b $wR^2 = \{\Sigma [w(F_o^2 - F_c^2)^2] / \Sigma [w(F_o^2)^2]\}^{1/2}$.

Table 8.2. Selected Bond Lengths (Å) and Angles (deg) for 1·2CH₂Cl₂, 2a·2CH₂Cl₂, and 3·0.5CH₂Cl₂·1.5Et₂O^a

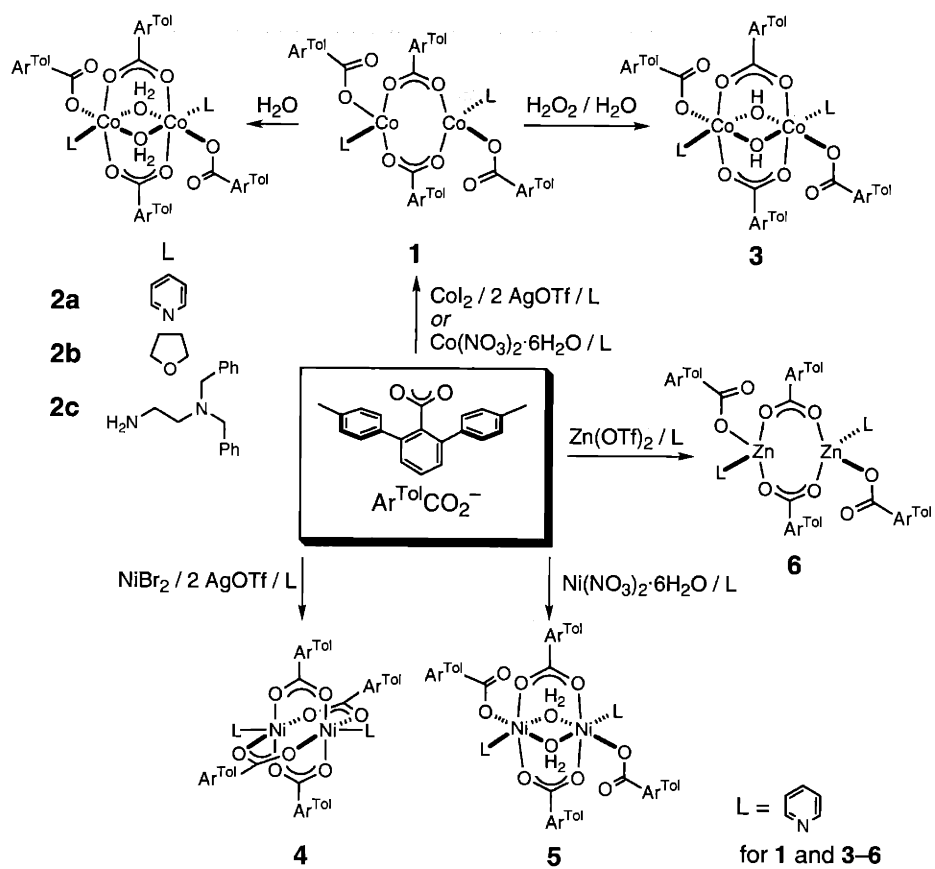
	bond length		bond angle	
1·2CH ₂ Cl ₂	Co(1)···Co(1A)	3.9168(7)	O(1A)-Co(1)-N(1)	94.86(8)
	Co(1)-O(1A)	1.9466(16)	O(1B)-Co(1)-O(1A)	111.47(7)
	Co(1)-O(1B)	1.9292(16)	O(1B)-Co(1)-O(2BA)	127.65(7)
	Co(1)-O(2BA)	1.9353(16)	O(1B)-Co(1)-N(1)	101.42(8)
	Co(1)-N(1)	2.049(2)	O(2BA)-Co(1)-O(1A)	113.86(7)
			O(2BA)-Co(1)-N(1)	99.49(8)
2a·2CH ₂ Cl ₂	Co(1)···Co(1A)	3.0562(6)	O(1A)-Co(1)-O(1)	83.10(7)
	Co(1)-O(1)	2.3043(19)	O(1A)-Co(1)-O(1C)	84.91(7)
	Co(1)-O(1C)	2.2230(18)	O(1A)-Co(1)-N(1)	97.16(7)
	Co(1)-O(1A)	2.0220(16)	O(1B)-Co(1)-O(1A)	102.67(7)
	Co(1)-O(1B)	2.0147(16)	O(1B)-Co(1)-O(1C)	90.24(7)
	Co(1)-O(2AA)	2.0592(16)	O(1B)-Co(1)-O(2AA)	97.31(7)
	O(1C)···O(2B)	2.559(3)	O(1B)-Co(1)-N(1)	89.63(7)
	O(1C)-H(1)	0.74(4)	O(2AA)-Co(1)-N(1)	94.91(7)
	O(1C)-H(2)	0.86(4)	O(2AA)-Co(1)-O(1C)	83.03(7)
	O(2B)···H(1)	1.88(4)	O(2AA)-Co(1)-O(1)	78.17(7)
			N(1)-Co(1)-O(1)	84.83(7)
			O(1)-Co(1)-O(1C)	95.10(7)
			Co(1)-O(1)-Co(1A)	84.90(7)
		O(1C)-H(1)-O(2B)	152(4)	
3·0.5CH ₂ Cl ₂ · 1.5Et ₂ O	Co(1)···Co(1A)	2.6802(7)	O(1)-Co(1)-O(1A)	88.04(8)
	Co(1)-O(1)	1.8653(17)	O(1)-Co(1)-O(1B)	95.38(7)
	Co(1)-O(1C)	1.8582(18)	O(1)-Co(1)-O(2AA)	83.50(8)
	Co(1)-O(1A)	1.9477(18)	O(1B)-Co(1)-N(1)	85.54(8)
	Co(1)-O(1B)	1.9085(17)	O(1B)-Co(1)-O(1A)	94.09(8)
	Co(1)-O(2AA)	1.9064(18)	O(1C)-Co(1)-O(2AA)	89.58(8)
	Co(1)-N(1)	1.935(2)	O(1C)-Co(1)-N(1)	91.42(8)
	O(1)···O(2B)	2.664(3)	O(1C)-Co(1)-O(1A)	82.32(8)
	O(1)-H(1)	0.89(4)	O(2AA)-Co(1)-O(1B)	94.45(8)
	O(2B)···H(1)	2.25(4)	O(2AA)-Co(1)-N(1)	92.40(9)
			N(1)-Co(1)-O(1A)	95.94(9)
			O(1)-Co(1)-O(1C)	87.92(8)
			Co(1)-O(1)-Co(1A)	92.08(7)
		O(1)-H(1)-O(2B)	108(3)	

^a Number in parentheses are estimated standard deviations of the last significant figure. Atoms are labeled as indicated in Figures 8.1, 8.2, 8.6, and 8.11.

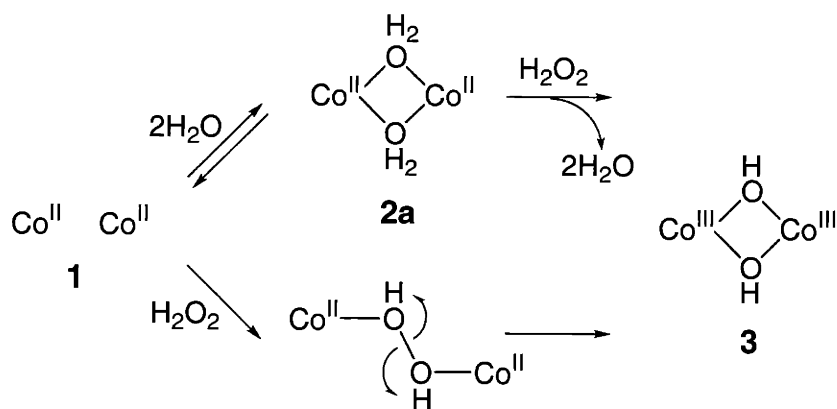
Table 8.3. Selected Bond Lengths (Å) and Angles (deg) for 4·1.5CH₂Cl₂, 5·2CH₂Cl₂, and 6·2Et₂O^a

	bond length		bond angle	
4·1.5CH ₂ Cl ₂	Ni(1)···Ni(2)	2.5745(6)	N(1N)-Ni(1)-O(1A)	96.90(8)
	Ni(1)-O(1A)	2.0208(18)	N(1N)-Ni(1)-O(1B)	95.89(8)
	Ni(1)-O(1B)	2.0172(18)	N(1N)-Ni(1)-O(1C)	95.10(8)
	Ni(1)-O(1C)	2.0197(18)	N(1N)-Ni(1)-O(1D)	95.79(8)
	Ni(1)-O(1D)	2.0165(19)	O(1B)-Ni(1)-O(1A)	88.20(7)
	Ni(1)-N(1N)	1.994(2)	O(1B)-Ni(1)-O(1C)	90.55(7)
	Ni(2)-O(2A)	2.0090(18)	O(1D)-Ni(1)-O(1A)	91.53(7)
	Ni(2)-O(2B)	2.0250(18)	O(1D)-Ni(1)-O(1C)	87.27(7)
	Ni(2)-O(2C)	2.0144(18)	N(11N)-Ni(2)-O(2A)	97.61(8)
	Ni(2)-O(2D)	2.0237(18)	N(11N)-Ni(2)-O(2B)	97.12(8)
	Ni(2)-N(11N)	1.995(2)	N(11N)-Ni(2)-O(2C)	95.16(8)
			N(11N)-Ni(2)-O(2D)	93.55(8)
			O(2A)-Ni(2)-O(2B)	92.19(7)
			O(2A)-Ni(2)-O(2D)	88.07(8)
		O(2C)-Ni(2)-O(2B)	86.47(7)	
		O(2C)-Ni(2)-O(2D)	90.89(7)	
5·2CH ₂ Cl ₂	Ni(1)···Ni(1A)	2.8923(7)	O(2A)-Ni(1)-O(1)	88.46(8)
	Ni(1)-O(1)	2.137(2)	O(2A)-Ni(1)-O(1B)	97.89(8)
	Ni(1)-O(1C)	2.140(2)	O(2A)-Ni(1)-N(1P)	88.57(9)
	Ni(1)-O(2A)	2.018(2)	O(2A)-Ni(1)-O(2BA)	95.44(8)
	Ni(1)-O(1B)	2.024(2)	O(1B)-Ni(1)-O(1)	86.19(8)
	Ni(1)-O(2BA)	2.078(2)	O(1B)-Ni(1)-O(1C)	86.45(8)
	Ni(1)-N(1P)	2.042(2)	O(1B)-Ni(1)-N(1P)	96.97(9)
	O(1)···O(1A)	2.495(3)	O(2BA)-Ni(1)-O(1)	82.67(8)
	O(1)-H(1)	1.13(5)	O(2BA)-Ni(1)-O(1C)	80.95(8)
	O(1)-H(2)	0.80(4)	N(1P)-Ni(1)-O(1C)	87.87(9)
	O(1A)-H(1)	1.37(5)	N(1P)-Ni(1)-O(2BA)	94.85(9)
			O(1)-Ni(1)-O(1C)	94.90(7)
			Ni(1)-O(1)-Ni(1A)	85.10(7)
		O(1)-H(1)-O(1A)	172(4)	
6·2Et ₂ O	Zn(1)···Zn(1A)	4.0169(9)	O(1A)-Zn(1)-N(1N)	94.74(9)
	Zn(1)-O(1A)	1.973(2)	O(1B)-Zn(1)-O(1A)	115.22(9)
	Zn(1)-O(1B)	1.928(2)	O(1B)-Zn(1)-O(2BA)	124.61(9)
	Zn(1)-O(2BA)	1.9374(19)	O(1B)-Zn(1)-N(1N)	100.28(9)
	Zn(1)-N(1N)	2.061(2)	O(2BA)-Zn(1)-O(1A)	112.50(9)
			O(2BA)-Zn(1)-N(1N)	102.19(9)

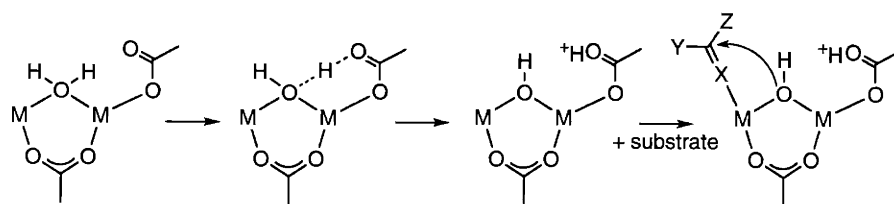
^a Number in parentheses are estimated standard deviations of the last significant figure. Atoms are labeled as indicated in Figures 8.7, 8.8, 8.9, and 8.11.



Scheme 8.1.



Scheme 8.2.



Scheme 8.3.

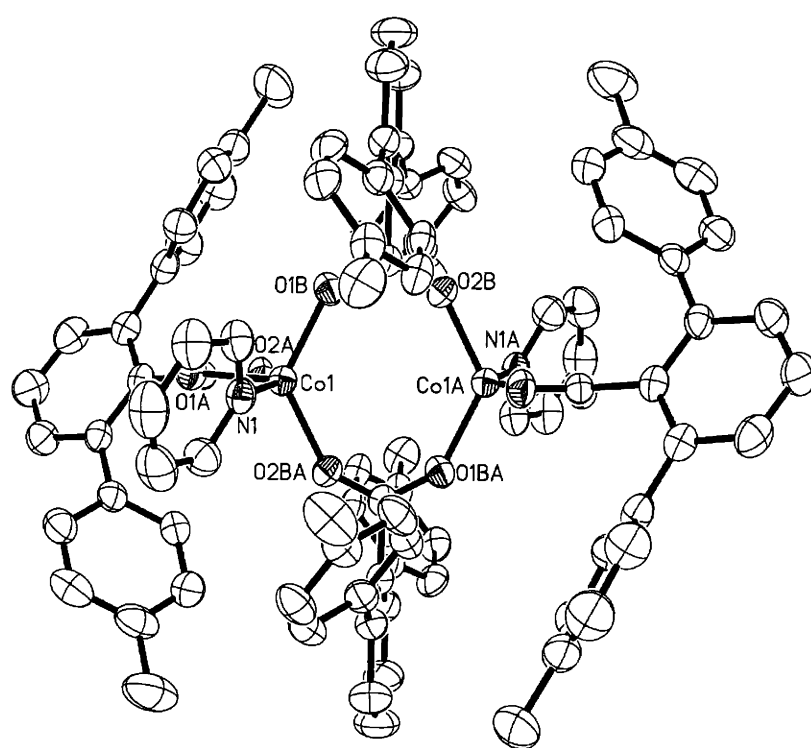


Figure 8.1. ORTEP drawing of $[\text{Co}_2(\mu\text{-O}_2\text{CAr}^{\text{Tol}})_2(\text{O}_2\text{CAr}^{\text{Tol}})_2(\text{C}_5\text{H}_5\text{N})_2]$ (1) showing 50% probability thermal ellipsoids for all non-hydrogen atoms.

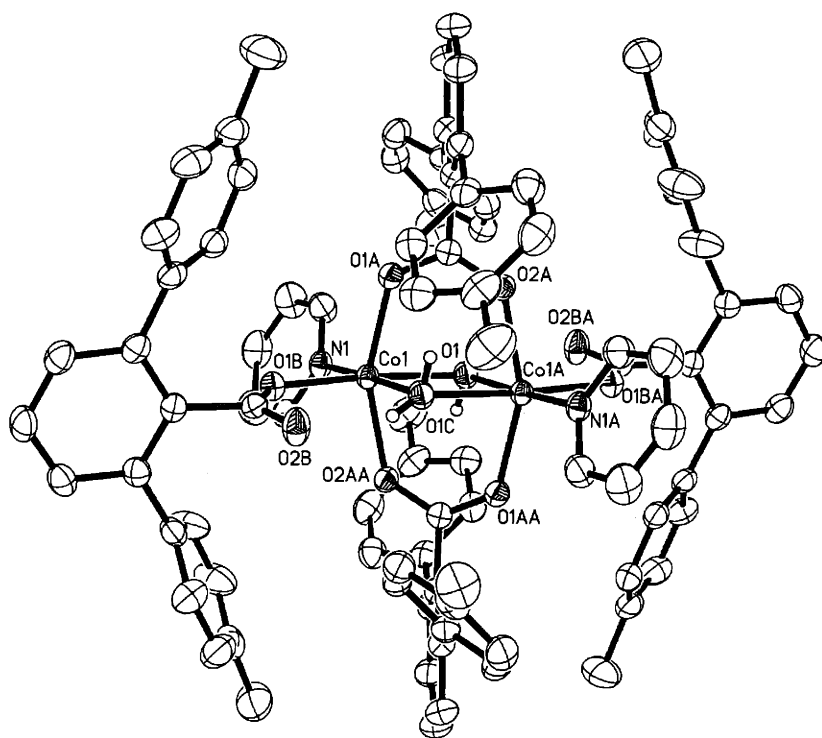


Figure 8.2. ORTEP drawing of $[\text{Co}_2(\mu\text{-OH})_2(\mu\text{-O}_2\text{CAr}^{\text{Tol}})_2(\text{O}_2\text{CAr}^{\text{Tol}})_2\text{-}(\text{C}_5\text{H}_5\text{N})_2]$ (**2a**) showing 50% probability thermal ellipsoids for all non-hydrogen atoms.

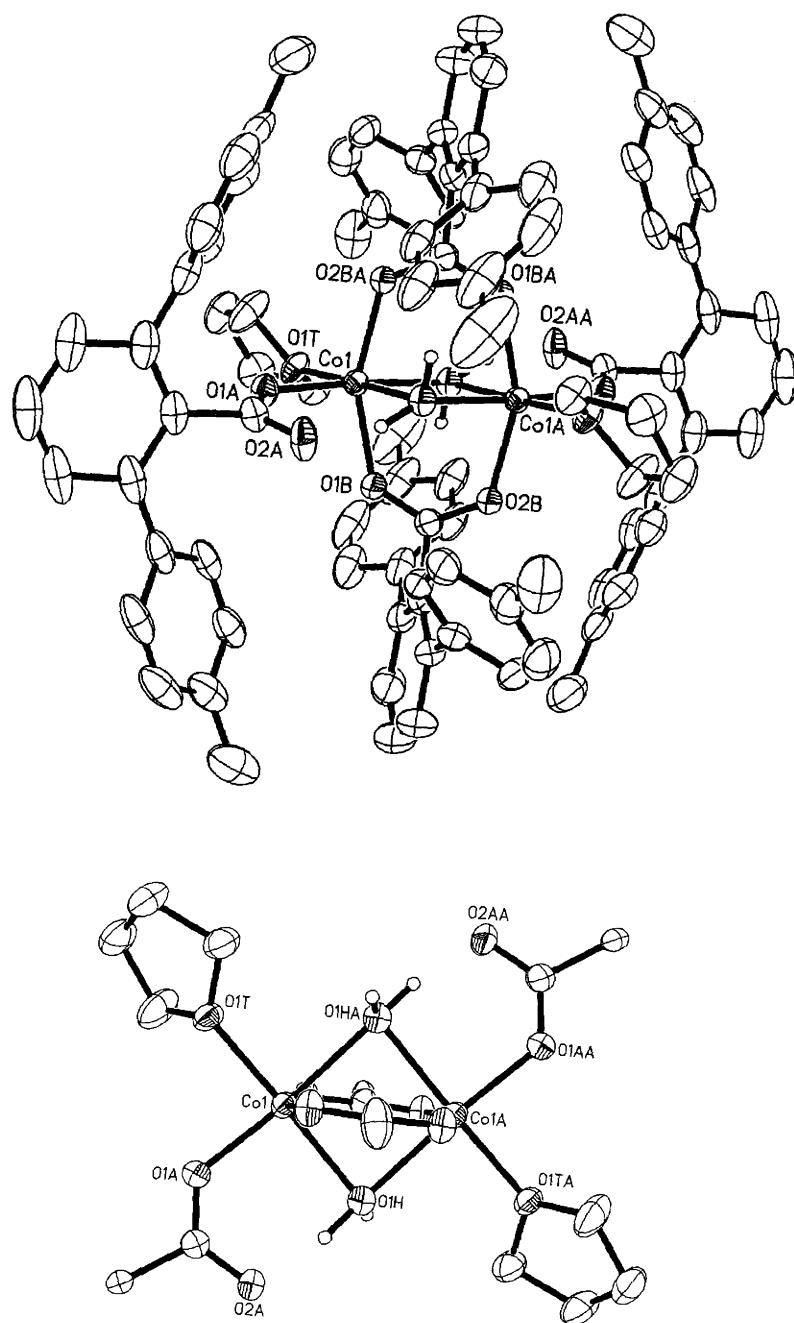


Figure 8.3. ORTEP diagram of $[\text{Co}_2(\mu\text{-OH})_2(\mu\text{-O}_2\text{CAr}^{\text{Tol}})_2(\text{O}_2\text{CAr}^{\text{Tol}})_2(\text{THF})_2]$ (2b) with thermal ellipsoids at 50% probability. Top, whole molecule; bottom, core structure

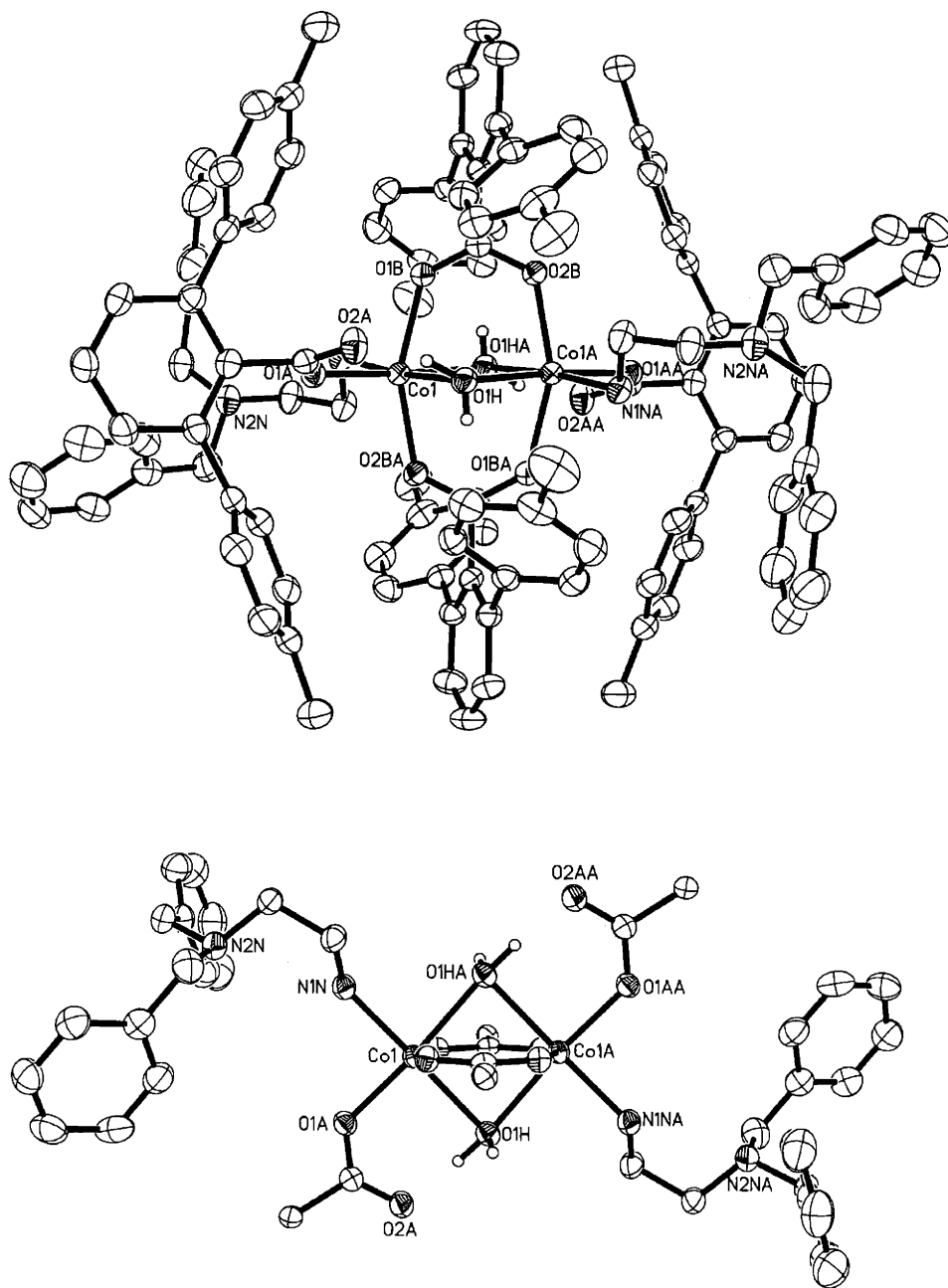


Figure 8.4. ORTEP diagram of $[\text{Co}_2(\mu\text{-OH}_2)_2(\mu\text{-O}_2\text{CAr}^{\text{Tol}})_2(\text{O}_2\text{CAr}^{\text{Tol}})_2\text{-}(N,N\text{-Bn}_2\text{en})_2]$ (**2c**) with thermal ellipsoids at 50% probability.

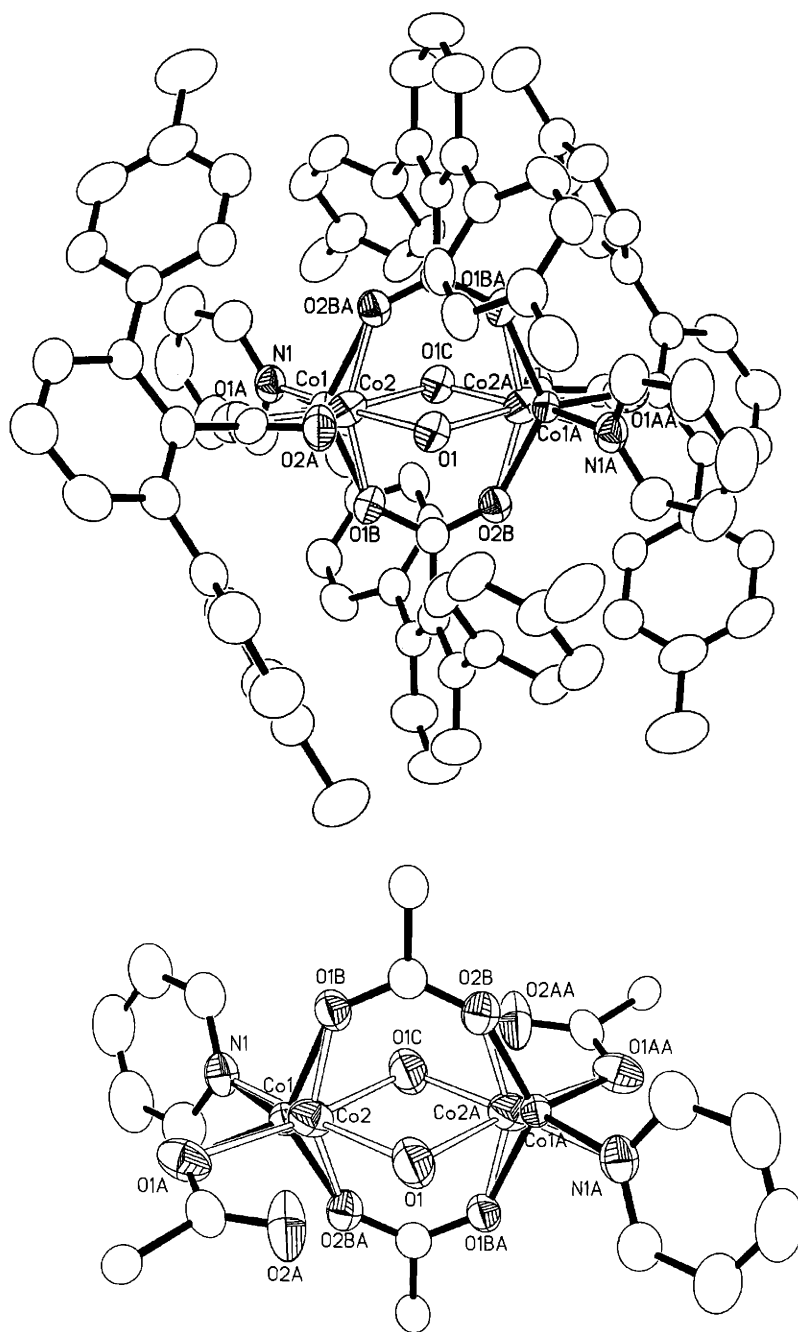


Figure 8.5. ORTEP diagram of a mixture of $[\text{Co}_2(\mu\text{-O}_2\text{CAr}^{\text{Tol}})_2(\text{O}_2\text{CAr}^{\text{Tol}})_2(\text{C}_5\text{H}_5\text{N})_2]$ (**1**) and $[\text{Co}_2(\mu\text{-OH}_2)_2(\mu\text{-O}_2\text{CAr}^{\text{Tol}})_2(\text{O}_2\text{CAr}^{\text{Tol}})_2(\text{C}_5\text{H}_5\text{N})_2]$ (**2a**) with thermal ellipsoids at 50% probability. The disordered core structure was modeled as 75% **1** and 25% **2a**. Top, whole molecule; bottom, core structure.

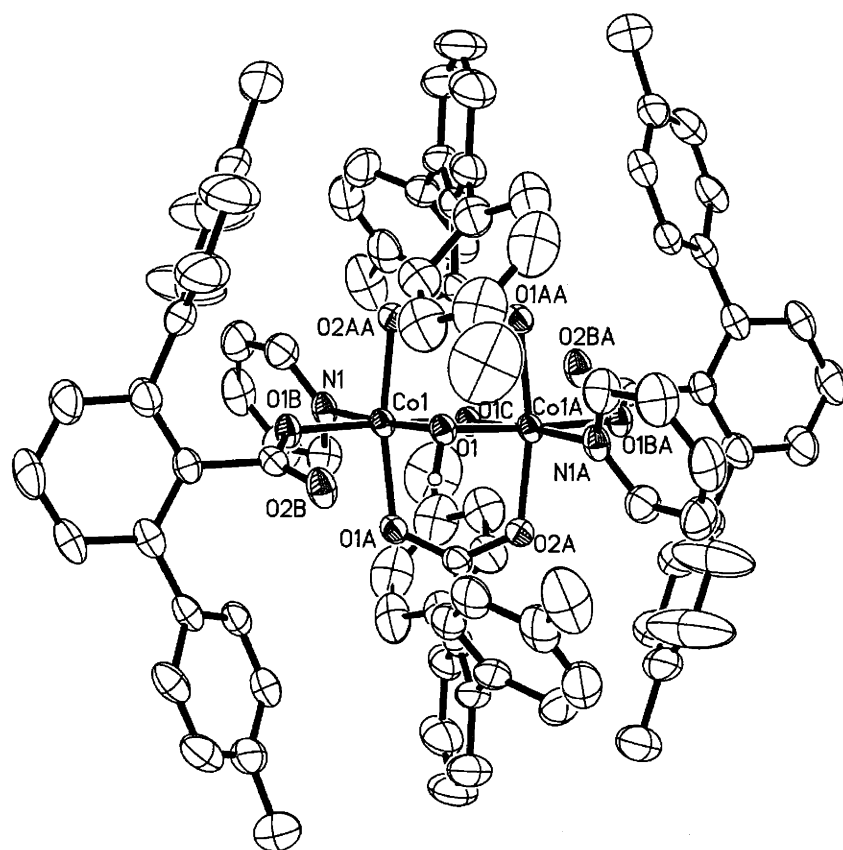


Figure 8.6. ORTEP drawing of $[\text{Co}_2(\mu\text{-OH})_2(\mu\text{-O}_2\text{CAr}^{\text{Tol}})_2(\text{O}_2\text{CAr}^{\text{Tol}})_2(\text{C}_5\text{H}_5\text{N})_2]$ (3) showing 50% probability thermal ellipsoids for all non-hydrogen atoms.

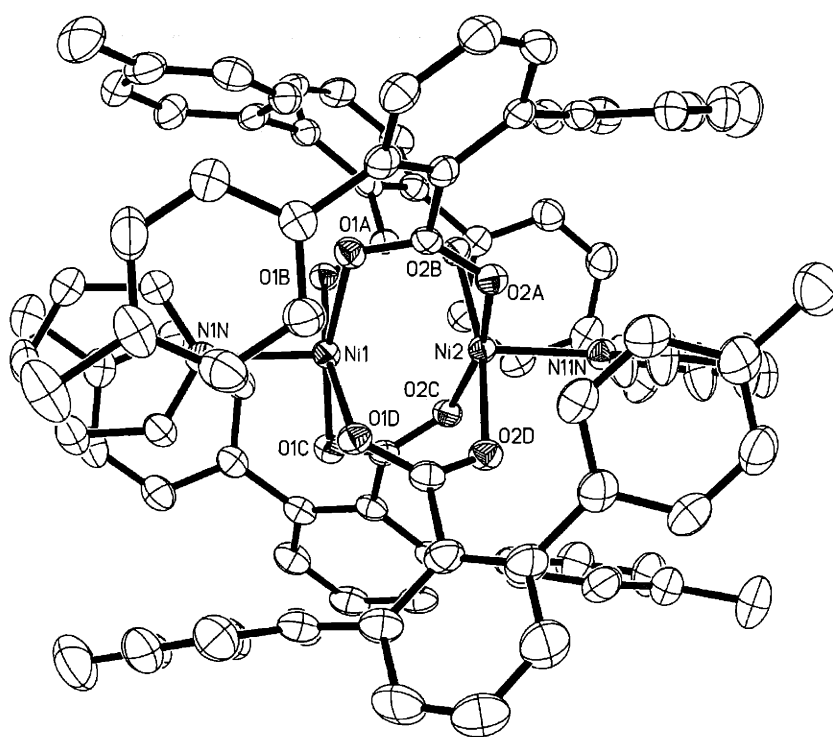


Figure 8.7. ORTEP drawing of [Ni₂(μ-O₂CAr^{Tol})₄(C₅H₅N)₂] (**4**) showing 50% probability thermal ellipsoids for all non-hydrogen atoms.

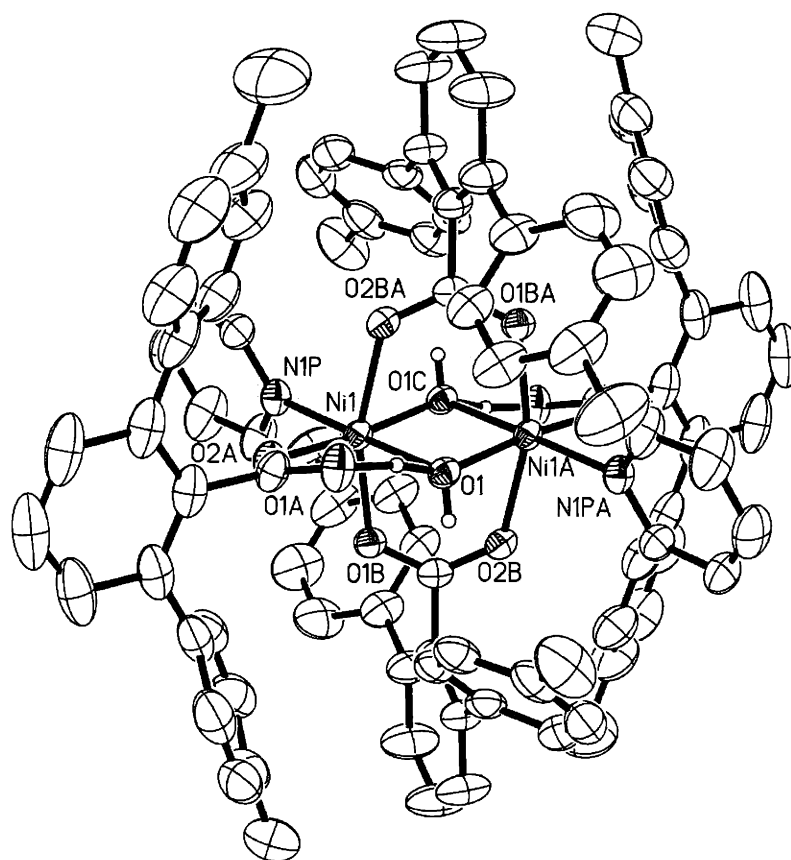


Figure 8.8. ORTEP drawing of $[\text{Ni}_2(\mu\text{-HO}\cdots\text{H})_2(\mu\text{-O}_2\text{CAr}^{\text{Tol}})_2(\text{O}_2\text{CAr}^{\text{Tol}})_2\text{-}(\text{C}_5\text{H}_5\text{N})_2]$ (**5**) showing 50% probability thermal ellipsoids for all non-hydrogen atoms.

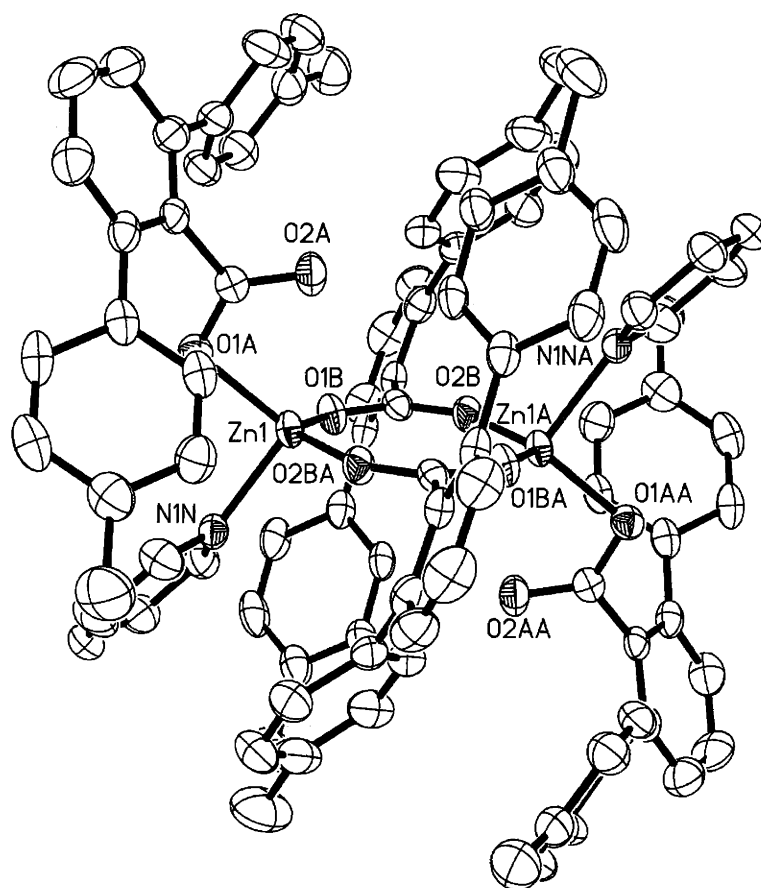


Figure 8.9. ORTEP drawing of $[\text{Zn}_2(\mu\text{-O}_2\text{CAr}^{\text{Tol}})_2(\text{O}_2\text{CAr}^{\text{Tol}})_2(\text{C}_5\text{H}_5\text{N})_2]$ (**6**) showing 50% probability thermal ellipsoids for all non-hydrogen atoms.

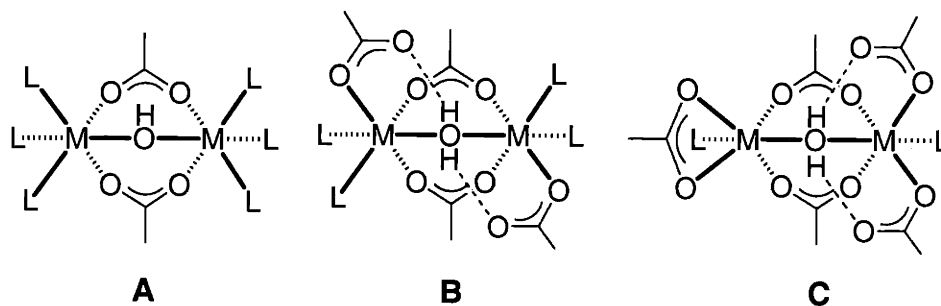


Figure 8.10. Schematic representation of carboxylate-bridged dimetallic centers having hydroxo (**A**) or aqua (**B** and **C**) bridging ligands.

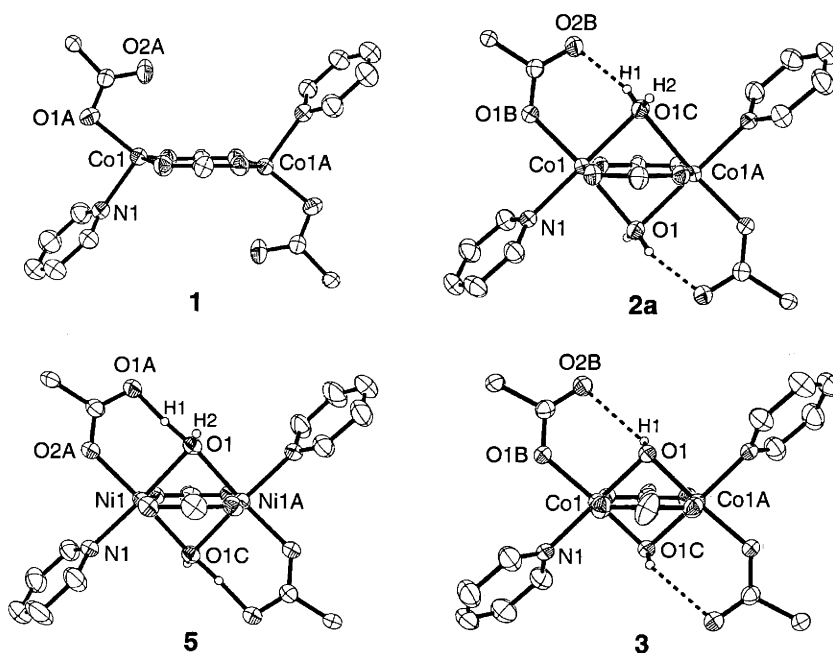


Figure 8.11. Core structures of $[\text{Co}_2(\mu\text{-O}_2\text{CAr}^{\text{Tol}})_2(\text{O}_2\text{CAr}^{\text{Tol}})_2(\text{C}_5\text{H}_5\text{N})_2]$ (**1**), $[\text{Co}_2(\mu\text{-OH})_2(\mu\text{-O}_2\text{CAr}^{\text{Tol}})_2(\text{O}_2\text{CAr}^{\text{Tol}})_2(\text{C}_5\text{H}_5\text{N})_2]$ (**2a**), $[\text{Ni}_2(\mu\text{-HO}\cdots\text{H})_2(\mu\text{-O}_2\text{CAr}^{\text{Tol}})_2(\text{O}_2\text{CAr}^{\text{Tol}})_2(\text{C}_5\text{H}_5\text{N})_2]$ (**5**), and $[\text{Co}_2(\mu\text{-OH})_2(\mu\text{-O}_2\text{CAr}^{\text{Tol}})_2(\text{O}_2\text{CAr}^{\text{Tol}})_2(\text{C}_5\text{H}_5\text{N})_2]$ (**3**). For clarity, all atoms of the 2,6-di(*p*-tolyl)-benzoates, except for the carboxylate groups and α -carbon atoms, were omitted.

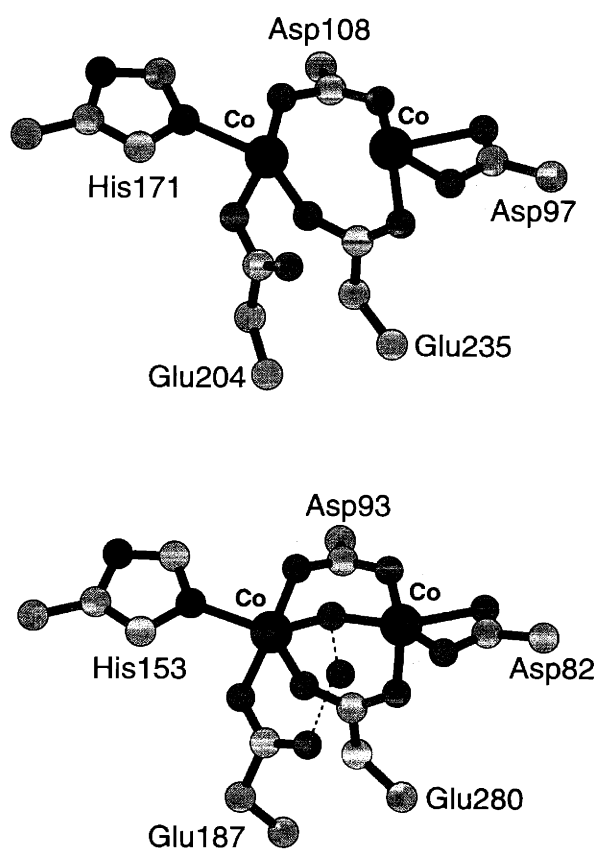


Figure 8.12. Structures of the dicobalt centers in methionine aminopeptidases from *E. coli* (EcMAP, top) and *P. furiosus* (PfMAP, bottom). Hydrogen bonds between water molecules and carboxylate residue in PfMAP are presented as broken lines. Generated from PDB files 1MAT and 1XGS, respectively.

Biographical Note

The author was born in Kyungju, Korea on November 22, 1970 and grown up in Taegu, before he undertook a major in chemistry at Seoul National University (SNU). From 1991 to 1993, he conducted undergraduate research in the laboratory of Professor Junghun Suh. From there he was introduced to the fascinating world of biomimetic chemistry. After completing military service, he continued his study at SNU under the supervision of Professors Junghun Suh and Myunghyun Paik Suh, and received a MS degree in organic chemistry in 1996. Following completion of his graduate studies, he will pursue postdoctoral research in the laboratory of Professor Timothy M. Swager at MIT.

Dongwhan Lee

Education	Massachusetts Institute of Technology	Cambridge, MA
Fall 1996–Fall 2001	Ph.D. in Chemistry, February 2002 Thesis in Inorganic Chemistry under Professor Stephen J. Lippard Title: "Use of Sterically Hindered Carboxylate Ligands to Model Structural and Functional Features of Dioxygen-Activating Centers in Non-Heme Diiron Enzymes"	
Fall 1994–Spring 1996	Seoul National University M.S. in Chemistry, August 1996 Thesis in Organic Chemistry under Professors Junghun Suh and Myunghyun Paik Suh Title: "Reactions of Nickel(II) and Nickel(I) Complexes of Multiaza Macrocyclic Ligands" Honors/Awards: Outstanding Thesis Award	Seoul, Korea
Spring 1989–Fall 1992	Seoul National University B.S. in Chemistry, February 1993 Honors/Awards: Summa cum Laude.	Seoul, Korea

Publications

- [1] "Properties and crystal structure of square-planar *R,S,R,S*-(1,3,6,8,12,15-hexaazatricyclo-[13.3.1^{8,12}])icosane)nickel(II) perchlorate and kinetics of its isomerization to the *R,R,S,S*-configuration", Lee, D.; Suh, M. P.; Lee, J. W. *J. Chem. Soc., Dalton Trans.* **1997**, 577–584.
- [2] "Structural and Functional Models of the Dioxygen-Activating Centers of Non-Heme Diiron Enzymes Ribonucleotide Reductase and Soluble Methane Monooxygenase", Lee, D.; Lippard, S. J. *J. Am. Chem. Soc.* **1998**, *120*, 12153–12154.
- [3] "Formation of Fe(III)Fe(IV) Species from the Reaction between a Diiron(II) Complex and Dioxygen: Relevance to Ribonucleotide Reductase Intermediate X", Lee, D.; Du Bois, J.; Petasis, D.; Hendrich, M. P.; Krebs, C.; Huynh, B. H.; Lippard, S. J. *J. Am. Chem. Soc.* **1999**, *121*, 9893–9894.
- [4] "Epoxidation of an alkene promoted by various nickel(II) multiaza macrocyclic complexes", Lee, D.; Bang, H.; Suh, M. P. *J. Mol. Cat. A* **2000**, *151*, 71–78.
- [5] "Valence-Delocalized Diiron(II,III) Cores Supported by Carboxylate-Only Bridging Ligands", Lee, D.; Krebs, C.; Huynh, B. H.; Hendrich, M. P.; Lippard, S. J. *J. Am. Chem. Soc.* **2000**, *122*, 5000–5001.
- [6] "Diiron Complexes of 1,8-Naphthyridine-Based Dinucleating Ligands as Models for Hemerythrin" He, C.; Barrios, A. M.; Lee, D.; Kuzelka, J.; Davydov, R. M.; Lippard, S. J. *J. Am. Chem. Soc.* **2000**, *122*, 12683–12690.
- [7] "Oxidative N-Dealkylation of a Carboxylate-Bridged Diiron(II) Precursor Complex by Reaction with O₂ Affords the Elusive {Fe₂(μ-OH)₂(μ-O₂CR)}³⁺ Core of Soluble Methane Monooxygenase Hydroxylase", Lee, D.; Lippard, S. J. *J. Am. Chem. Soc.* **2001**, *123*, 4611–4612.

Presentations

- [1] "Modeling the Diiron Active Site of Methane Monooxygenase: The Chemistry of Mono(μ-carboxylato)diiron Complexes" Lee, D.; Lippard, S. J. 216th National ACS Meeting, Boston, MA, August 23–27, 1998.
- [2] "Modeling the Dioxygen-Activating Centers in Non-Heme Diiron Enzymes", Department of Chemistry Spring Seminar Series, Boston College, March 19, 2001.
- [3] "Cubane-Type Tetrairon(II) Clusters Supported by Sterically Hindered Carboxylate Ligands" Lee, D.; Lippard, S. J. 221st National ACS Meeting, San Diego, CA, April 1–5, 2001.